

Direct Detection of Light Dark Matter with Electrons, Phonons, and Magnons

Thesis by
Tanner Trickle

In Partial Fulfillment of the Requirements for the
Degree of
Doctor of Philosophy

The logo for the California Institute of Technology (Caltech), featuring the word "Caltech" in a bold, orange, sans-serif font.

CALIFORNIA INSTITUTE OF TECHNOLOGY
Pasadena, California

2022
Defended May 19, 2022

© 2022

Tanner Trickle
ORCID: 0000-0003-1371-4988

All rights reserved

ACKNOWLEDGEMENTS

While it is certainly not possible to acknowledge everyone that has helped me create this thesis, I will do my best to credit some of the most important people. I will begin by thanking my parents, Kathy and Carl Trickle, and brother, Tyler Trickle, for their everlasting encouragement. I want to thank my fiancé Moriah Morgan, who has been with me since I started studying physics; her continual support, and infectious ambition motivate me on a daily basis. I would not be the physicist, or person, I am today without them, and I am eternally grateful they are a part of my life.

Professionally, no one has helped me more than my advisor Kathryn M. Zurek. Her creativity and passion for physics is contagious, and her patience and guidance has steered me in the right direction throughout graduate school. I would like to thank the other professors I have had the pleasure of working with: Marco Bernardi, Sinéad M. Griffin, Michele Papucci, Stephen Taylor, and Mark B. Wise. I have learned a tremendous amount from each of them, and consider myself lucky to have worked on projects with them. I have also had the opportunity to work with many outstanding postdocs between Berkeley and Caltech: Jeff A. Dror, Andrea Mitridate, Harikrishnan Ramani, and Zhengkang Zhang. Each of them has been an excellent example of what a postdoctoral researcher should be.

I want to thank my high school physics teacher Jim Reichling, from whom I first learned physics and who sparked the fascination I have today. I also want to thank my all of the friends I made throughout graduate school, especially Zachary Pagel, whose many conversations about physics, and not about physics, I especially appreciated. Lastly, I want to thank Moriah's and my dog, Turbo, who has been an endless source of happiness.

This material is based upon work supported by the U.S. Department of Energy, Office of Science, Office of High Energy Physics, under Award Number DE-SC0011632.

ABSTRACT

Discovering the nature of dark matter (DM) remains one of the most important outstanding questions in particle physics. While the astrophysical evidence for its existence continues to accumulate, we know very little about its fundamental constituents, and how it connects to the Standard Model. Terrestrial direct detection experiments offer a unique experimental perspective. Detection of a signal would be the first evidence for non-gravitational interactions between DM and ordinary matter, a crucial clue in understanding the particle nature of DM. Moreover detection in a laboratory is less susceptible to astrophysical uncertainties which accompany indirect detection strategies, and offer a wider vantage than colliders with the ability to swap target materials and search for modulation effects. In this dissertation I will discuss searching for DM with the current state-of-the-art direct detection experiments based on electronic excitations, as well as a potential direction for future experiments based on phonon and magnon excitations.

Previous generations of direct detection experiments utilized nuclear recoil to search for DM particles. While this process is well suited for DM candidates with masses above typical nuclear masses, $\mathcal{O}(\text{GeV})$, sensitivity drops precipitously for lighter DM. New physical processes must be utilized to facilitate the search for well-motivated light, sub-GeV, DM candidates. Electronic excitations are one such process which can probe DM candidates which have enough energy to excite electrons across the band gap. I will discuss many aspects of this DM-induced excitation rate which were developed in this work: the most advanced first-principles calculations of DM scattering and absorption signals using density functional theory (DFT) input, daily modulation effects in anisotropic crystal targets, comparisons of a wide variety of potential detector targets, theoretical development of a non-relativistic effective field theory (NR EFT) to aid in the calculation of DM absorption rates, as well as a study of interactions in cutting edge small gap, spin-orbit coupled targets.

While direct detection experiments using electronic excitations are currently underway, to reach even lower DM masses, which do not carry enough energy to excite states across the band gap, new ideas must be explored. Collective excitations, such as phonons and magnons, exist below the electronic band gap and offer an exciting future for direct detection experiments. Detectors searching for single phonon excitations are currently in development, whereas those based on magnons are in their infancy. Similar to the electronic excitations we will discuss a myriad of topics involving single phonon and magnon excitations: an EFT of DM-collective excitation scattering for general UV theories, potential uses for detection of axion DM, as well as advanced first-principles calculations, detailed study of the directional

detectability in anisotropic crystal targets, and comparisons across a variety of candidate target materials.

PUBLISHED CONTENT AND CONTRIBUTIONS

- H.-Y. Chen, A. Mitridate, T. Trickle, Z. Zhang, M. Bernardi, and K. M. Zurek, “Dark Matter Direct Detection in Materials with Spin-Orbit Coupling,” *arXiv:2202.11716 [cond-mat, physics:hep-ph]* (Feb., 2022) . <http://arxiv.org/abs/2202.11716>. TT participated in the conception of this project, aided in the derivation of the new dark matter-electron interaction rates, implemented and computed all dark matter-electron interaction rates with EXCEED-DM, created Figures 2-6, and participated in the writing of the manuscript
- A. Mitridate, T. Trickle, Z. Zhang, and K. M. Zurek, “Dark matter absorption via electronic excitations,” *JHEP* **09** (September, 2021) 123, [arXiv:2106.12586 \[hep-ph\]](https://arxiv.org/abs/2106.12586). <http://arxiv.org/abs/2106.12586>. TT participated in the conception of this project, aided in the derivation of the novel dark matter induced electronic absorption rate formulas, created the Fortran package EXCEED-DM to compute the dark matter - electron absorption rates, created all the Figures, and participated in the writing of the manuscript
- A. Coskuner, T. Trickle, Z. Zhang, and K. M. Zurek, “Directional detectability of dark matter with single phonon excitations: Target comparison,” *Physical Review D* **105** (Jan., 2022) 015010. <https://link.aps.org/doi/10.1103/PhysRevD.105.015010>. TT participated in the conception of this project, helped develop the Python package, PhonoDark, to compute the dark matter single-phonon scattering rate, and participated in the writing of the manuscript
- T. Trickle, Z. Zhang, and K. M. Zurek, “Effective Field Theory of Dark Matter Direct Detection With Collective Excitations,” *Phys. Rev. D* **105** (9, 2020) 015001, [arXiv:2009.13534 \[hep-ph\]](https://arxiv.org/abs/2009.13534). TT participated in the conception of this project, aided in the derivation of the effective field theory for phonon and magnon excitations, developed and utilized the program PhonoDark to compute the dark matter single-phonon excitation rates, helped in the numeric calculation of dark matter single-magnon scattering, created all the Figures, and participated in the writing of the manuscript
- A. Mitridate, T. Trickle, Z. Zhang, and K. M. Zurek, “Detectability of Axion Dark Matter with Phonon Polaritons and Magnons,” *Phys. Rev. D* **102** (5, 2020) 095005, [arXiv:2005.10256 \[hep-ph\]](https://arxiv.org/abs/2005.10256). TT participated in the conception of this project, aided in the derivation of the axion absorption rate formulas, numerically computed all of the absorption rates, created Figures 2-5, and participated in the writing of the manuscript

- S. M. Griffin, K. Inzani, T. Trickle, Z. Zhang, and K. M. Zurek, “Multichannel direct detection of light dark matter: Target comparison,” *Phys. Rev. D* **101** (2020) no. 5, 055004, [arXiv:1910.10716 \[hep-ph\]](#). TT aided in the derivation of the dark matter induced scattering rates, created the preliminary versions of PhonoDark and EXCEED-DM tools which compute dark matter single-phonon, electron excitation rates, respectively, created all Figures with the exception of the crystal structures and electronic band structures, and participated in the writing of the manuscript
- T. Trickle, Z. Zhang, K. M. Zurek, K. Inzani, and S. Griffin, “Multi-Channel Direct Detection of Light Dark Matter: Theoretical Framework,” *JHEP* **03** (2020) 036, [arXiv:1910.08092 \[hep-ph\]](#). TT aided in the derivation of the dark matter induced scattering rates, created the preliminary versions of PhonoDark and EXCEED-DM tools which compute dark matter single-phonon, electron excitation rates, respectively, created Figures 3-6, and participated in the writing of the manuscript
- T. Trickle, Z. Zhang, and K. M. Zurek, “Detecting Light Dark Matter with Magnons,” *Phys. Rev. Lett.* **124** (2020) no. 20, 201801, [arXiv:1905.13744 \[hep-ph\]](#). TT participated in the conception of this project, aided in the derivation of the novel dark matter-magnon scattering rate calculation, helped perform the numeric calculation of the scattering rates, created Figure 2, and participated in the writing of the manuscript
- S. M. Griffin, K. Inzani, T. Trickle, Z. Zhang, and K. M. Zurek, “Extended calculation of dark matter-electron scattering in crystal targets,” *Phys. Rev. D* **104** (5, 2021) 095015, [arXiv:2105.05253 \[hep-ph\]](#). TT participated in the conception of this project, aided in the derivation of the novel dark matter induced electronic scattering rate formulas, created the Fortran package EXCEED-DM to compute the dark matter - electron scattering rates, created all of the Figures, and participated in the writing of the manuscript

TABLE OF CONTENTS

Acknowledgements	iii
Abstract	iv
Published Content and Contributions	vi
Table of Contents	vii
List of Illustrations	xi
List of Tables	xxv
Chapter I: Introduction	1
1.1 The Evidence for Dark Matter	2
1.2 Theoretical Motivation for Light Dark Matter Models	7
1.3 Direct Detection Preliminaries	12
1.4 Summary	18
Chapter II: Multi-Channel Direct Detection of Light Dark Matter: Theoretical Framework	23
2.1 Introduction	23
2.2 General Framework for Spin-Independent Dark Matter Scattering	27
2.3 Nuclear Recoils	37
2.4 Electron Transitions	40
2.5 Single Phonon Excitations	44
2.6 Conclusions	54
Chapter III: Multi-Channel Direct Detection of Light Dark Matter: Target Comparison	57
3.1 Introduction	57
3.2 Detection Channels	59
3.3 Target Comparison: Kinetically Mixed Light Dark Photon Mediator	63
3.4 Target Comparison: Hadrophilic Scalar Mediator	69
3.5 Conclusions	77
I Collective Excitations	78
Chapter IV: Directional Detectability of Dark Matter With Single Phonon Excitations: Target Comparison	79
4.1 Introduction	79
4.2 Directional Detection With Single Phonon Excitations	81
4.3 Target Comparison	90
4.4 Conclusions	94
Chapter V: Detecting Light Dark Matter With Magnons	96
5.1 Introduction	96
5.2 Magnons In Magnetically Ordered Materials	99
5.3 Magnon Excitation From Dark Matter Scattering	100
5.4 Projected Reach	101

5.5 Discussion	104
5.6 Conclusions	105
Chapter VI: Detectability of Axion Dark Matter With Phonon Polaritons and Magnons	107
6.1 Introduction	107
6.2 General Formalism For Absorption Rate Calculations	112
6.3 Selection Rules And Ways Around Them	118
6.4 Axion Couplings And Detection Channels	121
6.5 Projected Sensitivity	124
6.6 Conclusions	129
Chapter VII: Effective Field Theory of Dark Matter Direct Detection With Collective Excitations	131
7.1 Introduction	131
7.2 Effective Field Theory Calculation of Dark Matter Induced Collective Excitations	133
7.3 Application to Benchmark Models	153
7.4 Conclusions	166
II Electronic Excitations	168
Chapter VIII: Extended Calculation of Dark Matter Electron Scattering In Crystal Targets	169
8.1 Introduction	169
8.2 Electronic States	173
8.3 Electronic Transition Rates	179
8.4 Projected Sensitivity	187
8.5 Conclusions	190
Chapter IX: Dark Matter Absorption via Electronic Excitations	205
9.1 Introduction	205
9.2 Dark Matter Couplings to Non-relativistic Electrons	208
9.3 In-medium Self-energies and Absorption Rates	212
9.4 Dark Matter Absorption in Crystals	220
9.5 Dark Matter Absorption in Superconductors	225
9.6 Conclusions	229
Chapter X: Dark Matter Direct Detection In Materials With Spin-Orbit Coupling . .	231
10.1 Introduction	231
10.2 DM Interaction Rate Formalism	232
10.3 Detection Rates in ZrTe_5	238
10.4 Conclusions	242
Chapter XI: Conclusions	244
Appendix A: DFT Calculation Details for BN	246
Appendix B: Calculations of Target Properties	247
B.1 Calculation Details for Electronic Band Structures and Wavefunctions	249
B.2 Calculation Details for Phonon Spectra	250
B.3 Parameters in Table 3.1	250
Appendix C: Additional Target Comparison Plots	251
Appendix D: Daily Modulation Amplitudes for Additional Materials	263

Appendix E: Calculation of the Modulation Reach	265
Appendix F: Supplemental Material: Additional Details of the Magnon Rate Calculation	266
Appendix G: Photon-Phonon Mixing	270
Appendix H: General form of the magnon Hamiltonian	274
Appendix I: Diagonalization of Quadratic Hamiltonians	276
Appendix J: Nonrelativistic Matching for a Fermion Field	278
Appendix K: Projection of Angular Momentum Operators	280
Appendix L: Velocity Integrals	282
Appendix M: Estimation of Single Phonon Excitation Rate in YIG	285
Appendix N: Self-Energy Calculations	287
N.1 General Result for the One-Loop Self-Energy	287
N.2 Real Part of the One-Loop Self-Energy in a Metal	288
N.3 Imaginary Part of the Two-Loop Self-Energy in a Metal	290
Appendix O: Absorption in Anisotropic Targets	298
Appendix P: Numerical Details	300
P.1 Density Functional Theory (DFT)	300
P.2 DM Interaction Constraint Convergence and Dielectric Function	300
Appendix Q: Generalized Self-Energies	304
Appendix R: Analytic Approximations in Dirac Materials	309
Bibliography	312

LIST OF ILLUSTRATIONS

<i>Number</i>	<i>Page</i>
2.1	25
<p>Illustration of kinematic regimes probed via the three detection channels considered in this paper. For an incoming DM particle with velocity $v = 10^{-3}$, the momentum transfer q and energy deposition ω are bounded by $\omega \leq qv - q^2/2m_\chi$, shown by the shaded regions for three DM masses. Nuclear recoils require $\omega = q^2/2m_N$ for a given type of nucleus, shown by the solid lines for helium and several elements in existing or proposed crystal targets. Standard calculations assuming scattering off individual nuclei break down below a few meV (a few hundred meV) for superfluid He (crystal targets), where we truncate the lines. Electron transitions can be triggered for ω above the band gap, which is $\mathcal{O}(\text{eV})$ for typical semiconductors, as shown by the dashed line. The end point at $q \sim 10 \text{ keV}$ corresponds to a few times αm_e, above which valence electron wavefunctions are suppressed, and only (semi-)core electrons can contribute (which requires ω to be much higher than the band gap). Single phonon excitations are relevant for $\omega \lesssim \mathcal{O}(100 \text{ meV})$ in typical crystals, as shown by the dotted line. The momentum transfer can be up to $q \sim \sqrt{m_N \omega_{\text{ph}}} \sim \mathcal{O}(100 \text{ keV})$ with ω_{ph} the phonon energies, above which the rate is suppressed by the Debye-Waller factor. We see that a GeV-mass DM can be probed by all three channels; a 10 MeV DM is out of reach in conventional nuclear recoil searches, but can be searched for via electron transitions in semiconductors and single phonon excitations in crystals; a sub-MeV DM cannot even trigger electron transitions in eV-gap materials, but can still be detected via single phonon excitations.</p>	
2.2	43
<p>Crystal structure of hexagonal boron nitride (left), its corresponding first Brillouin zone (middle) and DFT-calculated electronic band structure (right) with the Fermi level set to zero. The letters shown in the Brillouin zone plot mark several of the high-symmetry points, and the orange lines mark Brillouin zone paths along which electronic band structure is plotted. The discontinuities in the band structure occur from taking a discontinuous path through the Brillouin zone, indicated by “ ” on the horizontal axis.</p>	

2.3 Total rate of electron transitions R in hexagonal BN, normalized to its daily average $\langle R \rangle$ as a function of time (left), and differential rates at several times of the day assuming $\bar{\sigma}_e = 10^{-37} \text{ cm}^2$ (right), for a 5, 10, 100 MeV DM scattering via a light mediator. 44

2.4 Projected reach for DM scattering via a heavy (left, $m_\phi \gtrsim 400 \text{ MeV}$) or light (right, $m_\phi = 1 \text{ eV}$) scalar mediator coupling to nucleons ($f_p = f_n, f_e = 0$), assuming 1 kg-yr exposure with a GaAs target, 3 signal events and no background. Both single phonon production (purple, assuming energy thresholds $\omega_{\text{min}} = 1, 10, 30 \text{ meV}$) and nuclear recoils (red, assuming $\omega_{\text{min}} = 0.5, 1 \text{ eV}$) are complementary in probing currently unconstrained parameter space. The heavy mediator case is free from stellar constraints for $m_\phi \gtrsim 400 \text{ MeV}$ [10], and the neutrino floor is taken from Ref. [11]. Currently, the best experimental nuclear recoil constraints in this region of parameter space are from DarkSide-50 [12] (assuming binomial fluctuations), and XENON1T (combined limits from [13, 14]). We also show the constraint from CRESST-II [15], which is stronger than the DarkSide-50 constraint at low masses assuming no fluctuation in energy quenching. A more complete collection of nuclear recoil constraints can be found in Refs. [12, 14, 16]. For a light mediator with $m_\phi = 1 \text{ eV}$, fifth force experiments provide the dominant constraint on mediator-nucleon couplings [10]. Meanwhile, the mediator- χ coupling is constrained by DM self interactions (SIDM) if χ makes up all the DM [10], or just by perturbativity (Pert.) if χ is a DM subcomponent (in which case the projected reach can be easily rescaled). 51

2.5 Differential rate of single phonon excitations in a GaAs target for $m_\chi = 0.1, 1, 10 \text{ MeV}$, assuming a heavy (left) or light (right) scalar mediator coupling to nucleons ($f_p = f_n, f_e = 0$), with $\bar{\sigma}_n = 10^{-43} \text{ cm}^2$ and $\omega_{\text{min}} = 1 \text{ meV}$. Contributions from momentum transfer within the first Brillouin zone are shown in dash. Umklapp processes account for the differences between solid and dashed histograms. 52

2.6 Projected reach for a 5% subcomponent of DM scattering via a light (1 eV) hadrophobic scalar (left) or $U(1)_{B-L}$ vector (right) mediator, assuming 1 kg-yr exposure with a GaAs target, 3 signal events and no background. Single phonon excitation reach is shown in purple, assuming energy thresholds $\omega_{\min} = 1, 10, 30$ meV. Pink regions are excluded when taking into account the strongest constraint on the mediator-SM coupling – red giant (RG) stars and fifth force experiments for the two models respectively [10] – together with perturbativity (Pert.) of the mediator- χ coupling. In the $U(1)_{B-L}$ case, the gray region is excluded by stellar production of χ [17]. 54

3.1 Projected reach from single phonon excitations (dashed) and electron transitions (solid) for DM scattering mediated by a kinetically mixed light dark photon (the smallest-gap target InSb suffers from slow convergence in the electronic transition calculation at $m_\chi < 1$ MeV, for which we show results of the two most accurate runs with solid and dotted curves, see Appendix B.1 for details). Nuclear recoils (not shown) can also probe this model, but the conclusion on which targets are superior is the same as for the light hadrophilic mediator model. A detector threshold of 1 meV is used for the phonon calculations, and all transitions with energy deposition greater than the band gaps are included in electron excitations. The freeze-in benchmark is taken from Refs. [18, 19], corrected by including plasmon decay for sub-MeV DM [20]. Stellar constraints are from Ref. [17] and direct detection constraints are from DAMIC [21], DarkSide-50 [12], SENSEI [22], SuperCDMS [23], XENON10 [24, 25], and XENON100 [12, 26].²² 65

3.2 Single phonon and nuclear recoil reach for a light ($m_\phi = 1$ eV) hadrophilic scalar mediator. 1, 20, and 100 meV thresholds are shown for the single phonon reach (solid, dashed, and dotted respectively), and 500 meV threshold is assumed for the nuclear recoil reach (dot-dashed). For $m_\phi = 1$ eV the dominant constraint on f_n is from fifth force experiments [10]. If m_χ makes up all the DM then the dominant constraint on y_χ is from DM self-interactions (SIDM) [10]. If m_χ is only a subcomponent, we only require perturbativity $y_\chi < 1$ (Pert.); in this case the reach curves can be easily rescaled.⁶⁶ 70

3.3 Single phonon and nuclear recoil reach for a massive ($m_\phi \gtrsim 400$ MeV) hadrophilic scalar mediator. 1, 20, and 100 meV thresholds are shown for the single phonon reach (solid, dashed, and dotted respectively), and 500 meV threshold is assumed for the nuclear recoil reach (dot-dashed). There are no stellar constraints for $m_\phi \gtrsim 400$ MeV [10]. Currently, the best experimental nuclear recoil constraints in this region of parameter space are from DarkSide-50 [12] (assuming binomial fluctuations), and XENON1T (combined limits from [13, 14]). We also show the constraint from CRESST-II [15], which is stronger than the DarkSide-50 constraint at low masses assuming no fluctuation in energy quenching. A more complete collection of nuclear recoil constraints can be found in Refs. [12, 16, 27]. The neutrino floor is taken from Ref. [11].66⁶ 71

4.1 **Top:** To understand the kinematic function, $g(\mathbf{q}, \omega)$, defined in Eq. (4.11), we plot $v_* \equiv \frac{q}{2m_\chi} + \frac{\omega}{q}$ as a function of q (blue) for various m_χ and ω values. Comparing v_* to v_e and $v_e + v_{\text{esc}}$ we can qualitatively reconstruct the shape of $g(\mathbf{q}, \omega)$, as discussed in the text. **Bottom:** $g(\mathbf{q}, \omega)$ vs. q for several fixed m_χ, ω values, with varying $\hat{\mathbf{q}} \cdot \hat{\mathbf{v}}_e$. The kinematic function weights different $\hat{\mathbf{q}}$ directions according to their angle with respect to $\mathbf{v}_e(t)$, which ultimately leads to a daily modulating rate. 84

4.2 Comparison between the various sources of anisotropy a in SiO₂ target, for an example DM mass for each benchmark model. A 1 meV energy threshold is assumed in all cases. As discussed in the text, anisotropy in the $\mathbf{Y}_j \cdot \boldsymbol{\epsilon}_{\nu, \mathbf{k}, j}$ factor in Eq. (4.7) is the dominant factor in determining the daily modulation pattern. 86

4.3 **Left:** Daily modulation for a h-BN target with various experimental thresholds, ω_{min} , assuming dark photon mediated scattering and $m_\chi = 100$ keV. **Right:** Differential rate at $t = 0$ for the same process assuming $\bar{\sigma}_e = 10^{-43}$ cm². The daily modulation pattern is drastically different depending on whether the optical phonon modes just below 100 meV are included or excluded. 88

4.4 Effect of the crystal target orientation on the daily modulation pattern, for a sapphire target and the light dark photon mediator model as an example. The default orientation is the one adopted in Refs. [7, 28, 29] for which $\mathbf{v}_e(t)$ is given by Eq. (4.10), and the alternative orientation is achieved by rotating the crystal z axis by 60° clockwise around $\hat{\mathbf{n}} = (\hat{\mathbf{x}} + \hat{\mathbf{y}} + \hat{\mathbf{z}})/\sqrt{3}$ (or equivalently, a -60° right-handed rotation around $\hat{\mathbf{n}}$.) 88

4.5 **Top:** Projected reach for the dark photon mediator model assuming 1 meV and 20 meV detector energy thresholds and one kg-year exposure. Solid curves show the 95% confidence level (CL) exclusion limits in the case of zero observed events, assuming no background. Dashed curves and the associated $\pm 1\sigma$ bands show the modulation reach for DM masses with more than 1% daily modulation, i.e., cross sections for which we can reject the non-modulating hypothesis and establish the statistical significance of a modulating signal, as explained in App. E. **Bottom:** Daily modulation amplitudes f_{mod} , defined in Eq. (4.15), for the same energy thresholds. Results are shown only for m_χ values where a material has substantial reach and $f_{\text{mod}} > 10^{-2}$. The exact DM mass corresponding to a specific bar can be read off from the left edge of that bar. 89

4.6 Same as Fig. 4.5, for the light hadrophilic scalar mediator model. 91

4.7 Same as Fig. 4.5, for the heavy hadrophilic scalar mediator model. 92

4.8 **Left:** Daily modulation for an h-BN target with various DM masses, assuming dark photon mediated scattering and $\omega_{\text{min}} = 1$ meV. The change in modulation pattern is a result of the kinematically favored $\hat{\mathbf{q}} \cdot \hat{\mathbf{v}}_e$ increasing from -1 toward 0 as m_χ increases. During the transition between different modulation patterns, an intermediate mass value around 20 keV features a reduced modulation amplitude, which explains the peak in the modulation reach curve in the top-left panel of Fig. 4.5. A similar effect is also observed for the hadrophilic scalar mediator models in Figs. 4.6 and 4.7. **Right:** Differential rates at $t = 0$ for several higher m_χ assuming $\bar{\sigma}_e = 10^{-43}$ cm². Another transition between modulation patterns occurs when new phonon modes become dominant as m_χ increases, resulting in a second reduced modulation mass point, around 200 keV, in Fig. 4.5. 93

5.1 Projected reach for the DM models in Table 5.1 for a YIG target, assuming three events with kilogram-year exposure, for several magnon detection thresholds ω_{min} (solid). Also shown are the results of a Heisenberg ferromagnet with the same mass and spin densities as YIG, and the same magnon dispersion as the low-energy gapless modes of YIG, for $\omega_{\text{min}} = 1$ meV (dashed); they coincide with the YIG curves for 0.02 MeV $\lesssim m_\chi \lesssim 0.1$ MeV, which can be understood from the effective theory argument in the text. The gray contours show the model parameters in the magnon sensitivity regions, which astrophysical and cosmological constraints on specified UV completions can be mapped onto (see text). For the pseudo-mediated model, we consider a DM subcomponent to evade SIDM constraints, and let g_e saturate the white dwarf cooling bound. 103

6.1	Spectra of gapped phonon polaritons and magnons at zero momentum for several representative targets considered in this work. These collective excitations have typical energies of $\mathcal{O}(1-100)$ meV, and can be utilized to search for axion DM in the mass window $m_a \sim \mathcal{O}(1-100)$ meV. Longer lines with darker colors correspond to the resonances in Figs. 6.3, 6.4 and 6.5, while the shorter ones with lighter colors represent modes with suppressed couplings to axion DM due to selection rules.	108
6.2	Dispersion of phonon polaritons in GaAs near the center of the 1BZ, $k \sim \omega$. The mixing between the photon and TO phonons is maximal at $\omega \sim k$. At $k \ll \omega$, the TO phonon-like modes are degenerate with the LO phonon mode (blue line), while at $\omega \gg k$ they approach their unperturbed value (dotted blue line), and an LO-TO splitting is present.	114
6.3	Projected reach on $g_{a\gamma\gamma}$ from axion absorption onto phonon polaritons in Al_2O_3 , CaWO_4 , GaAs and SiO_2 , in an external 10 T magnetic field, averaged over the magnetic field directions, assuming 3 events per kilogram-year. Also shown are predictions of the KSVZ and DFSZ QCD axion models, and horizontal branch (HB) star cooling constraints [30].	126
6.4	Similar to Fig. 6.3, but with the external magnetic field oriented in the \hat{x} (\hat{z}) direction in the left (right) panel. The strength of axion-phonon couplings depends on the orientation of the magnetic field, and different resonances can be selected by changing the magnetic field direction.	127
6.5	Projected reach on g_{aee} from axion-to-magnon conversion, compared with DFSZ (assuming $0.28 \leq \tan \beta \leq 140$) and KSVZ model predictions, as well as white dwarf (WD) constraints from Ref. [31]. The suppression of axion-magnon couplings is alleviated by using the three strategies discussed in the main text: lifting gapless magnon modes by an external magnetic field (YIG target in a 1 T magnetic field, compared to the scanning scheme of Ref. [32]), anisotropic interactions (NiPS_3 target), and using targets with nondegenerate g -factors (hypothetical toy models based on YIG, referred to as YIG_o and YIG_t). For all the cases considered we assume 3 events per kilogram-year exposure, and take the magnon width to frequency ratio γ/ω to be 10^{-2} (solid) or 10^{-5} (dashed).	128

7.1 Projected reach on the standard SD model listed in Table 7.2 from single magnon (red) and phonon (blue) excitations in YIG. The phonon rate is estimated in two ways, as discussed in the text, which lead to the solid and dashed curves, respectively. Since this model generates only the S response, magnons are seen to have better sensitivity than phonons. 157

7.2 Comparison of the total detection rate in models with a light (left panel) or heavy (right panel) scalar mediator. The couplings to SM fermions are taken proportional to their masses, $g_p = g_n = \frac{m_p}{m_e} g_e$, and we fix $g_\chi g_e = 10^{-13}$. Each curve is labeled with the model type as in Table 7.2 and the excitation type (phonon or magnon) that can probe each model. The phonon curves assume SiO₂ (solid) and GaAs (dashed) targets, and the magnon curves assume YIG (solid) and α -RuCl₃ (dashed) targets. 159

7.3 Projected reach on the multipole DM models listed in Table 7.2, assuming dark photon-like couplings to SM particles: $g_p = -g_e, g_n = 0$. The left panel shows the hierarchy of sensitivities of single phonon excitations, in GaAs and in SiO₂, to the three multipole DM models, together with the SI interaction model for comparison. The center and right panels focus on the magnetic dipole and anapole DM models, respectively, and compare the phonon reach of GaAs and SiO₂ (via the N response), and the magnon reach of YIG (via the S response) and α -RuCl₃ (via both S and L responses); these models are best probed by magnons, though the phonon sensitivity with an optimal target like SiO₂ may be competitive. 161

7.4 Projected reach on the ($\mathbf{L} \cdot \mathbf{S}$)-interacting DM model in Table 7.2, assuming coupling only to electrons, and $\kappa = 0$. Single phonon excitations in GaAs and SiO₂ targets (via the N response) and single magnon excitations in YIG and α -RuCl₃ targets (via the S response) are seen to cover complementary regions of parameter space. 164

8.1 Schematic representation of electronic states in Si (left) and Ge (right), divided into core, valence (“val”), conduction (“cond”) and free. Shaded regions indicate the range of energies for each type of electronic states. In a scattering process, electrons transition from either core or valence states, below the Fermi surface at $E = 0$, to conduction or free states above the band gap E_g . As outlined in Sec. 8.1 and explained in detail in Sec. 8.2, we compute the valence and conduction states numerically using DFT (including all-electron reconstruction), model the core states semi-analytically with RHF wave functions, and treat the free states as plane waves. 171

- 8.2 Selection of results from Sec. 8.4, for DM-electron scattering via a heavy mediator in a Ge target. **Left:** Contribution from each of the four transition types, valence to conduction ($v \rightarrow c$), valence to free ($v \rightarrow f$), core to conduction ($c \rightarrow c$), and core to free ($c \rightarrow f$) to the scattering rate binned in energy deposition (with $\Delta\omega = 1$ eV) for a 1 GeV DM at a given reference cross section $\bar{\sigma}_e = 10^{-40}$ cm². **Right:** 95% C.L. projected limit (3 events) on $\bar{\sigma}_e$ assuming 1 kg-year exposure, for energy thresholds corresponding to 1 and 5 electron-hole pairs. We compare our results with **QEdark** calculations in Refs. [33, 34] and the semi-analytic model of Lee et al [35]; see text for details. 172
- 8.3 Comparison of the Bloch wave function magnitudes, defined in Eq. (8.7), computed with DFT with (red, “AE”) and without (blue, “no AE”) AE reconstruction, and the semi-analytic core approximation of Eq. (8.9) (green, “core”). Shaded bands indicate the maximum and minimum values across all the bands belonging to the state type indicated in the upper right corner of each panel. AE reconstruction, discussed in Sec. 8.2, recovers the large momentum behavior of the electronic wave functions. Core electronic states, such as those shown in the right panels and discussed in Sec. 8.2, can be well modeled semi-analytically with atomic wave functions, as seen by the good agreement between the “core” and “AE” curves. When applicable, the semi-analytic parameterization is advantageous since the electronic wave functions are then known to arbitrarily large momentum. 192
- 8.4 Calculated band structures of Si (left) using a PBE xc-functional within DFT and Ge (right) using a hybrid functional HSE06. The band gaps have been scissor corrected to their measured values near zero temperature, 1.11 eV and 0.67 eV for Si and Ge, respectively. The Fermi level is set to 0 eV in both panels. 193
- 8.5 DM-electron scattering rate from valence to conduction bands binned in energy deposition (with $\Delta\omega = 1$ eV) for 1 GeV DM, light (top row) and heavy (bottom row) mediators, assuming $\bar{\sigma}_e = 10^{-40}$ cm², computed with vs. without AE reconstruction. Valence states included are the first four bands below the band gap, and conduction states included are all bands up to $E_{\text{dft}} = 60$ eV. . . 194
- 8.6 DM-electron scattering rate from valence to conduction ($v \rightarrow c$) bands and from valence bands to free states ($v \rightarrow f$) binned in energy deposition (with $\Delta\omega = 1$ eV) for 1 GeV DM, light (top row) and heavy (bottom row) mediators, assuming $\bar{\sigma}_e = 10^{-40}$ cm². The upper edge of the shaded region corresponds to using Z_{eff} from Eq. (8.15), while the bottom edge corresponds to $Z_{\text{eff}} = 1$. . 195

- 8.7 DM-electron scattering rate from core states to conduction bands binned in energy deposition (with $\Delta\omega = 5$ eV) for 1 GeV DM, light (top row) and heavy (bottom row) mediators, assuming $\bar{\sigma}_e = 10^{-40}$ cm². The core states are labelled by the corresponding atomic orbitals, and the conduction states up to $E_{\text{dft}} = 60$ eV are included. For comparison we also show the $v \rightarrow c$ contribution (after AE reconstruction) from Fig. 8.5 in gray. 196
- 8.8 Contribution to the DM-electron scattering rate binned in energy deposition (with $\Delta\omega = 1$ eV) from 3d electrons to conduction bands in Ge, for 1 GeV DM, light (left) and heavy (right) mediators, assuming $\bar{\sigma}_e = 10^{-40}$ cm². The three curves in each panel are computed using DFT with and without AE reconstruction, and using the semi-analytic core wave functions. 197
- 8.9 DM-electron scattering rate from core states to conduction bands ($c \rightarrow c$) and to free states ($c \rightarrow f$) binned in energy deposition (with $\Delta\omega = 10$ eV) for 1 GeV DM, light (top row) and heavy (bottom row) mediators, assuming $\bar{\sigma}_e = 10^{-40}$ cm². As in the $v \rightarrow f$ calculation in Fig. 8.6, the upper edge of the shaded bands corresponds to Z_{eff} from Eq. (8.15), and the lower edge corresponds to $Z_{\text{eff}} = 1$. 198
- 8.10 Dielectric function $\epsilon(q, \omega)$, given by Eq. (8.46) with the parameters in Table 8.1, of Si (left) and Ge (right) used to incorporate screening effects. The solid line indicates the edge of the kinematically accessible region $\omega \lesssim qv$. The dashed line is the band gap of the target. While the static dielectric can be $\mathcal{O}(10)$, in the kinematically allowed region $\epsilon(q, \omega)$ is an $\mathcal{O}(1)$ number, leading to an $\mathcal{O}(1)$ effect on the scattering rates when the latter are dominated by small q, ω transitions. 199
- 8.11 Effect of screening on the binned rate (top row, for 1 GeV DM) and total rate (bottom row, as a function of m_χ) from $v \rightarrow c$ transitions for DM models with a light (red) and heavy (blue) mediator. The unscreened rate $R^{\text{no scr}}$ is obtained with $\epsilon = 1$, and the screened rate R^{scr} is obtained with the model of the dielectric function given in Eq. (8.46). 200

8.12	DM-electron scattering rate binned in energy deposition (with $\Delta\omega = 1$ eV for 1 GeV DM, light (top row) and heavy (bottom row) mediators, from all four transition types: valence to conduction ($v\rightarrow c$), valence to free ($v\rightarrow f$), core to conduction ($c\rightarrow c$), and core to free ($c\rightarrow f$). We assume $\bar{\sigma}_e = 10^{-40}$ cm ² , and take $Z_{\text{eff}} = 1$ for all effective charges in the Fermi factor. Note that the $c\rightarrow c$ and $c\rightarrow f$ transitions involve semi-analytic treatment of 2p (3d) states and below in Si (Ge), which has been validated with DFT calculations including AE reconstruction; see Fig. 8.3. We also overlay the binned rate from Ref. [34] which computed the $v\rightarrow c$ contribution using QEdark (treating 3d states in Ge as valence, without including AE reconstruction effects).	201
8.13	DM-electron scattering rate as a function of the DM mass, for light (top row) and heavy (bottom row) mediators, from all four transition types: valence to conduction ($v\rightarrow c$), valence to free ($v\rightarrow f$), core to conduction ($c\rightarrow c$), and core to free ($c\rightarrow f$). We assume $\bar{\sigma}_e = 10^{-40}$ cm ² , take $Z_{\text{eff}} = 1$ for all effective charges in the Fermi factor, and show results for several threshold Q values which significantly impact the $v\rightarrow c$ contribution.	202
8.14	95% C.L. exclusion reach (3 events) assuming 1 kg-year exposure, $Q \geq 1$, for light (top row) and heavy (bottom row) mediators. The results shown are from this work, Griffin et al. [6], Essig et al. [33], Lee et al. [35], and Knapen et al. [36] (with and without screening). See Sec. 8.4 for detailed comparison.	203
8.15	95% C.L. exclusion reach (3 events) assuming 1 kg-year exposure, $Q \geq 10$, for light (top row) and heavy (bottom row) mediators. The results shown are from this work and Essig et al. [33]. See Sec. 8.4 for detailed comparison.	204
9.1	Comparison between different terms contributing to the scalar DM absorption rate, defined in Eq. (9.57), for Si, Ge and Al-SC targets assuming $q = 10^{-3}m_\phi$. Dashed curves indicate negative values. In all three targets we see that $\mathcal{R}_{\bar{v}^2, \bar{v}^2}$ dominates over the entire DM mass range considered. This term comes from an NLO operator in the NR EFT (underlined in Table 9.1) and cannot be directly related to the target's optical properties (i.e. the complex conductivity/dielectric function). For Si and Ge, the calculation of $\mathcal{R}_{\bar{v}^2, \mathbf{1}}$ is technically challenging as explained in Sec. 9.4; however, it is parameterically the same order in q as $\mathcal{R}_{\mathbf{1}, \mathbf{1}}$ and therefore expected to be also subdominant compared to $\mathcal{R}_{\bar{v}^2, \bar{v}^2}$	221

- 9.2 Projected 95% C.L. reach (3 events with no background) with semiconductor crystal (Si, Ge) and superconductor (Al-SC) targets for the vector and pseudoscalar DM models defined in Eq. (9.3), assuming 1 kg-yr exposure. We compare our theoretically calculated reach (solid) against the data-driven approach utilizing the target material’s measured conductivity/dielectric [37, 38] (dashed). For Si and Ge, the data-driven approach was taken in previous works [39, 40], with which we find good agreement. For Al-SC, our theoretical calculation reproduces the results in Ref. [41] (dotted) up to the choice of overall normalization factor. Also shown are existing direct detection limits from XENON10/100 [40], stellar cooling constraints from the Sun (assuming Stückelberg mass for vector DM) [42] and white dwarfs (WD) [31], and pseudoscalar couplings corresponding to the QCD axion in KSVZ and DFSZ (for $0.28 \leq \tan \beta \leq 140$) models [43]. 222
- 9.3 Projected 95% C.L. reach (3 events with no background) with semiconductor crystal (Si, Ge) and superconductor (Al-SC) targets, for the scalar DM model defined in Eq. (9.3), assuming 1 kg-yr exposure. In contrast to the vector and pseudoscalar cases shown in Fig. 9.2, the projections here cannot be derived from the target’s optical properties. Differences compared to Hochberg et al. [41] and Gelmini et al. [44] in the Al-SC case are discussed in detail in Sec. 9.5. Also shown are existing constraints from fifth force [45] and red giant (RG) cooling [46]. 223
- 10.1 ZrTe₅ band structure computed using DFT with SOC (solid lines) and without SOC (dashed lines). The inset highlights the low energy (low E) band dispersion, whose details are sampled using a denser \mathbf{k} -point grid. The band gap for the SOC band structure is set to the experimental value of 23.5 meV [47], and the No SOC band structure is shifted accordingly, which gives a larger band gap of 81.6 meV. 236

10.2	Comparison of projected 95% C.L. reach (3 events, no background) assuming one kg-year exposure for scalar (left), pseudoscalar (center) and vector (right) DM. We compare our results with (solid) and without (dotted) SOC for electronic absorption in a ZrTe_5 target (red), with the ones for semiconductor silicon (Si, blue) and germanium (Ge, green) targets [2], superconducting aluminum (Al-SC, brown) [2]), phononic absorption in polar materials [28, 48] (GaAs in orange and SiO_2 in purple), and previous estimates for ZrTe_5 (teal) [29]. We also show the projected constraints combining the SOC energy levels with the No SOC wave functions, (“Partial SOC”, red, dashed) to explicitly show the effect of the spin dependent wave functions. Constraints are expressed in terms of the commonly adopted parameters shown in Eq. (10.29). Shaded red bands correspond to different parameterizations of the electron width $\delta \in [10^{-1.5}, 10^{-0.5}]\omega$ used in calculating the self-energies (see e.g., Eq. (Q.17)), with the solid line corresponding to $\delta = 10^{-1}\omega$. Thin lines indicate results obtained by rescaling the optical data. Also shown are the direct detection limits from XENON10/100 [40], fifth force constraints [45], and stellar cooling constraints from red giants (RG) [46], and white dwarfs (WD) [31]. For the pseudoscalar scenario we also report the couplings corresponding to the QCD axion in KSVZ and DFSZ models, for $0.28 \leq \tan \beta \leq 140$ [43].	239
10.3	Projected constraints on DM-electron scattering cross sections at the 95% C.L. (three events, no background) assuming one kg-year exposure for two benchmark models shown in Eq. (10.1). Left: SI model with a light mediator ($\mathcal{F}_{\text{med}} = (q_0/q)^2$), screened with the static dielectric shown in Fig P.3. The red solid (dashed) curve shows the constraints with (without) the inclusion of SOC effects. For comparison we also show projected constraints from single phonon excitations in GaAs (orange) and SiO_2 (purple) computed with PhonoDark [4] (assuming an energy threshold of $\omega_{\text{min}} = 20 \text{ meV}$), electronic excitations in an aluminum superconductor [49] (brown), and previous estimates for ZrTe_5 (teal) [29]. We also show the projected constraints combining the SOC energy levels with the No SOC wave functions, (“Partial SOC”, red, dashed) to explicitly show the effect of the spin dependent wave functions. Stellar constraints (gray) are taken from Ref. [17] and the freeze-in benchmark (orange) is taken from Ref. [20]. Right: SD model with a heavy mediator ($\mathcal{F}_{\text{med}} = 1$). Curves labelled “low/high E ” include transitions restricted to the low/high E regions discussed in Sec. 10.3.	241
C.1	Crystal structures of targets in Table 3.1.	252

C.2	First Brillouin zones of targets in Table 3.1, with high symmetry points labeled.	253
C.3	Calculated electronic band structures of targets in Table 3.1.	254
C.4	Calculated electronic band structures of targets in Table 3.1.	255
C.5	Phonon dispersions calculated with VASP and phonopy [50] including non-analytic corrections. The path through the high symmetry points is found using SeeK-path [51].	256
C.6	Phonon dispersions calculated with VASP and phonopy [50] including non-analytic corrections. The path through the high symmetry points is found using SeeK-path [51].	257
C.7	Same as Fig. 3.1, but with different materials. For reference, gray lines are CsI, Si, and Al ₂ O ₃ taken from Fig. 3.1.	258
C.8	Same as Fig. 3.1, but with different materials. For reference, gray lines are CsI, Si, and Al ₂ O ₃ taken from Fig. 3.1.	258
C.9	Same as Fig. 3.1, but with different materials. For reference, gray lines are CsI, Si, and Al ₂ O ₃ taken from Fig. 3.1.	259
C.10	Same as Fig. 3.2, but with different materials. For reference, gray lines are CsI, Si, and Al ₂ O ₃ taken from Fig. 3.2.	259
C.11	Same as Fig. 3.2, but with different materials. For reference, gray lines are CsI, Si, and Al ₂ O ₃ taken from Fig. 3.2.	260
C.12	Same as Fig. 3.2, but with different materials. For reference, gray lines are CsI, Si, and Al ₂ O ₃ taken from Fig. 3.2.	260
C.13	Same as Fig. 3.3, but with different materials. For reference, gray lines are CsI, Si, and Al ₂ O ₃ taken from Fig. 3.3.	261
C.14	Same as Fig. 3.3, but with different materials. For reference, gray lines are CsI, Si, and Al ₂ O ₃ taken from Fig. 3.3.	261
C.15	Fig. 3.3 with different materials. Gray lines are CsI, Si, and Al ₂ O ₃ taken from Fig. 3.3.	262
D.1	Daily modulation amplitudes for the dark photon mediator model. Solid and dashed curves assume energy thresholds of 1 meV and 20 meV, respectively. Among the materials studied, only those that have a modulation amplitude greater than 1% for at least one m_χ value (at which the material has substantial reach) are shown. As in the lower panels of Figs. 4.5, 4.6 and 4.7 in the main text, the low mass values where the rate diminishes are excluded for each material. Therefore the shown modulation amplitudes correspond to the mass values where the materials have reach.	263
D.2	Same as Fig. D.1, for the light hadrophilic scalar mediator model.	264

D.3	Same as Fig. D.1, for the heavy hadrophilic scalar mediator model.	264
F.1	Calculated magnon dispersion of YIG along the high symmetry lines in the first Brillouin zone.	267
P.1	Convergence of the constraints on DM absorption, for the models discussed in Sec. 10.3, with respect to the \mathbf{k} point sampling (\mathbf{k} -grid) and plane wave energy cutoff, E_{cut} . The first row includes SOC effects while the second row does not. Absorption rates were computed by adding the contributions from the low E and high E regions, and the first (second) value in the legends corresponds to the parameter used in the low (high) E calculation. For example, the red dotted line corresponds to a calculation in which the low (high) E region was sampled on an $8 \times 8 \times 8$ ($10 \times 10 \times 10$) Monkhorst-Pack grid in the 1BZ, with $E_{\text{cut}} = 650$ (200) eV. All curves assume a width parameter of $\delta = 10^{-1}\omega$	301
P.2	Convergence of the constraints on DM scattering, for the models discussed in Sec. 10.3, with respect to the \mathbf{k} point sampling (\mathbf{k} -grid) and plane wave energy cutoff, E_{cut} . The first row includes SOC effects while the second row does not. The collection of constraints dominant at the lowest masses corresponds to the low E transitions, and the other set corresponds to the high E transitions. Similar to Fig. P.1, the E_{cut} parameters in the legend correspond to the values used for the low/high E regions.	302
P.3	Magnitude of the dielectric function of ZrTe_5 computed with SOC (solid), without SOC (dotted), and a combination of the calculations with and without SOC (dashed), as described in Sec. 10.3. The directional dependence of the dielectric function is due to the anisotropic nature of ZrTe_5 . Note that while non-local corrections are not included in this figure we found they have a small $\mathcal{O}(10\%)$ effect. These results are obtained with an electronic broadening of $\delta = 10^{-1}\omega$	303

LIST OF TABLES

<i>Number</i>	<i>Page</i>
<p>3.1 Target materials studied in this work and their key parameters. The four blocks contain materials currently in use in nuclear recoil experiments, those considered for proposed near-future experiments, those with superior properties for some specific DM models discussed in this paper, and the remaining ones in alphabetical order, respectively. Sensitivity of electron transitions relies heavily on the band gap E_g, for which experimental values are shown (those with asterisks are measured at low temperature). Nuclear recoils and acoustic phonon excitations in the nucleon-coupling benchmark model are largely determined by the speed of sound of longitudinal acoustic phonons \bar{c}_s^{LA} and atomic mass numbers A_j. For optical phonon excitations in the light dark photon mediated model, relevant parameters are the Born effective charges \bar{Z}^*, high-frequency dielectric constant $\bar{\epsilon}_\infty$, optical phonon energies $\bar{\omega}_O$ as well as A_j, all of which combine into a quality factor Q, defined in Eq. (3.27), which determines the reach at high mass. Barred quantities are properly averaged values; see Appendix B.3 for details.</p>	75
<p>3.2 Summary of our results. The material properties relevant for the optimization of target are: atomic mass number A, proton number Z, electronic band gap E_g, speed of sound c_s, optical phonon energy ω_O, average phonon energy ω_{ph}, as well as Born effective charges and the high-frequency dielectric constant that enter the quality factor Q. Achieving lower detector energy thresholds ω_{min} is also crucial in several cases.</p>	76
<p>5.1 Dark matter models, having Lagrangian \mathcal{L}, with SD interactions considered in this work; these models are particularly well-motivated when DM does not carry a charge of any type, see e.g., Refs. [52–63]. χ is a spin-1/2 DM particle, and V, ϕ are ultralight (typically \ll eV) spin-1, spin-0 mediators, respectively. g_χ, g_e are dimensionless couplings, and Λ_χ is the effective theory cutoff. In the non-relativistic limit, these Lagrangians reduce to the operators \hat{O}_χ^α (with Cartesian coordinates $\alpha = 1, 2, 3$), as in Eq. (5.4). $q \equiv \mathbf{q}$ is the momentum transfer, and $\hat{S}_\chi^\alpha = \sigma^\alpha/2$ is the DM spin operator. $\bar{\sigma}_e$ is the reference cross section defined in Eq. (5.11) that we will use to present the reach.</p>	98

- 6.1 Summary of the potentially detectable channels identified in Sec. 6.4. The axion field a is given by Eq. (6.3), ρ_a is its energy density, and \mathbf{v}_a is its velocity. The axion couplings $g_{a\gamma\gamma}$ and $g_{ae\bar{e}}$ are defined in Eqs. (6.1) and (6.2), and given by Eqs. (6.31) and (6.32) for the QCD axion. ε_∞ is the high-frequency dielectric constant due to electronic screening, \mathbf{Z}_j^* is the Born effective charge tensor of the ion, g_j is the Landé g -factor, ρ_T is the target’s mass density, and γ is the resonance width. 111
- 7.1 Types of couplings between a spin- $\frac{1}{2}$ fermion ψ and a scalar (vector) mediator ϕ (V_μ). The (effective) currents are defined by $\mathcal{L} \supset g_X \phi J_X$ ($X = S, P$) or $g_X V_\mu J_X^\mu$ ($X = V, A, \text{edm}, \text{mdm}, \text{ana}, V2$), upon integration by parts in the last four cases. The expressions following the arrows are the leading operators in the NR reduction of the currents (assuming scattering kinematics), which appear between the nonrelativistic fields ψ^- and ψ^+ — see e.g., Eq. (7.9). These will be used to derive the NR operators generated by specific DM models involving tree-level exchange of a scalar or vector mediator in Table 7.2. 137
- 7.2 Benchmark models of spin- $\frac{1}{2}$ DM χ coupling to SM fermions $\psi = p, n, e$. Each model is matched onto the NR EFT by multiplying the currents $J_\chi J_\psi$ (defined in Table 7.1) and the mediator propagator, and accounting for in-medium effects (if present) according to Eq. (7.14). The leading order nonvanishing coefficients $c_i^{(\psi)}$ for the operators $\mathcal{O}_i^{(\psi)}$ (defined in Table 7.3) are listed in the second to last column. For the multipole DM models, $\delta\tilde{\mu}_\psi \equiv \tilde{\mu}_\psi - 1$ where $\tilde{\mu}_\psi$ is half the Landé g -factor of ψ ($\tilde{\mu}_p \simeq 2.8$, $\tilde{\mu}_n \simeq -1.9$, $\tilde{\mu}_e \simeq 1$). The last column lists the lattice degrees of freedom which enter the scattering potential, Eq. (7.30). All models can excite phonons, and models with S or L response generated by DM-electron coupling can also excite magnons. 140
- 7.3 NR effective operators relevant for DM scattering defined in Eq. (7.11), organized into four categories, and the (point-like and composite) crystal responses generated. Here χ is the DM and ψ is a SM particle that can be the proton, neutron or electron. \mathbf{q} is the momentum transfer from the DM to the SM target. $\mathbf{v}^\perp \equiv \frac{\mathbf{P}}{2m_\chi} - \frac{\mathbf{K}}{2m_\psi}$, defined in Eq. (7.13), is the component of the relative velocity perpendicular to \mathbf{q} . Previous calculations [6–8, 28, 64] focused on phonon and magnon excitations via \mathbf{v}^\perp -independent couplings to charge and spin, corresponding to the first and third categories listed here. In this work we extend the calculations to all operators. 142

8.1	Parameters used in the model of dielectric function, Eq. (8.46), of Si and Ge from Ref. [65], which accounts for in-medium screening effects on the transition rate.	187
9.1	Summary of results for scalar and pseudoscalar DM ϕ coupling to electron ψ . The effective operators at LO and NLO in the NR ($1/m_e$) expansion are shown in the second row. In both cases, the NLO operator (<u>underlined</u>) gives the dominant contribution to DM absorption. Importantly, the dominant contribution in the scalar case is not directly related to the target material's conductivity/dielectric function. See Secs. 9.2 and 9.3 for details.	207
9.2	Material parameters for aluminum superconductor.	227
B.1	List of material properties used in DFT calculations. The calculated lattice parameters (a and c) are listed for both those used in the electronic (el.) and phonon (ph.) excitation calculations, along with reported experimental values (exp.). The space group and corresponding space group number are included for the crystal structures considered. The PBE-level calculated band gaps are also listed, with details explained in the text.	248
Q.1	Self-energies scaling with the DM and electron velocities in the absorption limit. Notice that each insertion of the identity operator induces a suppression of order $v_e v_\phi$ due to the wave-function orthogonality, and that parity odd self-energies receive an additional suppression of order q/k	306

Chapter 1

INTRODUCTION

Understanding the fundamental nature of dark matter (DM) continues to elude us. After nearly 80 years since the term itself was coined by Fritz Zwicky [66] we still do not know any more about its, if any, non-gravitational interactions. At the same time we continue to confirm its evidence on astrophysical and cosmological scales, which makes the problem more interesting than ever. Direct detection represents one class of experimental programs trying to understand more about DM. These experiments rely on a DM particle in the cosmic background interacting with a terrestrial detector strongly enough to be detected. The simplest experiment to understand is based on the principle of nuclear recoil. A DM particle flies in to the detector, kicks an atomic nucleus which is then detected at the boundary of the experiment. There are a wide variety detectors built on this principle, e.g., ANAIS [67], CRESST [15, 68, 69], DAMA/LIBRA [70], DAMIC [21, 71], DarkSide-50 [12], DM-Ice [72], KIMS [73], LUX [16, 74, 75], SABRE [76], SuperCDMS [23, 77–80], and XENON1T [13, 14], to name a few.

These experiments have been continually improving over the years, and are exceptionally sensitive machines. However they have an inherent limitation in the types of DM, discussed further in Sec. 1.3. Their main physics goal is to search for the prototypical DM candidate, the “weakly interacting massive particle”, or WIMP. This specific DM candidate is predicted to have a mass between $\mathcal{O}(\text{GeV})$ and $\mathcal{O}(\text{TeV})$. However DM with this mass is quickly being ruled out by the previously mentioned nuclear recoil experiments, as well as at collider experiments. This has led to an explosion of ideas both theoretically, and experimentally, for detection of lighter, sub-GeV DM.

This thesis explores a few different methods for searching for light DM via electronic, phononic, and magnonic excitations. These represent different ways a target material can respond to incoming DM. In an electronic excitation process the DM can cause an electron to transition across a band gap. Experiments based on this process, e.g., DAMIC [21, 71, 81], EDELWEISS [82–84], SENSEI [22, 85–87], SuperCDMS [23, 77–80, 88, 89]), are already underway. If the DM does not have enough energy to drive the electrons across the band gap, collective modes such as phonons, lattice vibrations, and magnons, spin waves, can become important. Experiments based on reading out phonon excitations are being built [90], while those based on magnon readout are a bit more futuristic [91–95]. Therefore to maximize the

amount of DM theory space these experiments can cover, it is crucial to have a first-principles understanding of how DM interacts with these excitations. These different excitations are well known in the condensed matter community, and this research has sparked new collaborations between the particle physics community and condensed matter/materials science communities. The wide range of other ideas is discussed in more detail in each chapter.

Chapters 2 and 10 are a collection of previously published manuscripts which build upon a large literature of results. Therefore the purpose of this introduction is to ease the reader in to these new results by providing context for these calculations, with minimal repetition. The outline of this introduction is as follows: Sec. 1.1 reviews the current evidence for DM and some model independent constraints on its particle nature. Sec. 1.2 discusses the theoretical motivations for light, sub-GeV, DM candidates and the “dark portals” paradigm as a useful intermediate between UV model building and lower energy phenomenology. Sec. 1.3 reviews some of the most relevant formulas in the direct detection literature which serves as the starting point of any excitation rate calculation. Lastly, Sec. 1.4 will connect the contents of each chapter to the discussion here and highlight how each of them furthers the field of direct detection of light DM. We will work in natural units throughout, where $\hbar = c = k_B = 1$.

1.1 The Evidence for Dark Matter

Understanding the fundamental nature of DM is one of the most important questions in all of physics for, mainly, one reason: we have evidence for its existence. This is in contrast to some of the other open problems in theoretical particle physics such as the hierarchy problem [96], cosmological constant problem [97], or Strong CP problem [98–100] which, while certainly unappealing features of the SM, are fundamentally fine-tuning problems. Our fundamental theory of nature must somehow contort to explain the absence of predicted features. The problem of DM is fascinating because we must understand how to change the fundamental theory to explain the DMs experimentally verified presence. In this section we review some of the most important pieces of evidence we have for the existence of DM. From these observations we also discuss the model independent statements we can make about DM. A fantastic review of some of these can be found in Ref. [101].

Galactic Rotation Curves

The earliest experimental evidence for DM came from “galactic rotation curves”, or the orbital velocity of galaxies, as a function of distance [66, 102–104]. These are typically measured by studying the Doppler shifted 21 cm radiation coming from a galaxy. The stars which are moving away emit red-shifted radiation, whereas those moving toward us, on the other side of the galactic center, emit blue-shifted radiation. The amount of frequency shift

can then be related to the orbital velocity of a star.

The predicted orbital velocity of the stars is directly related to the gravitational pull of the galactic mass density. For example, assuming a spherically symmetric galaxy, the orbital velocities, $v(r)$, as a function of distance from the galactic center, r are given by

$$v(r) = \sqrt{\frac{GM_{\text{enc}}(r)}{r}}, \quad (1.1)$$

where M_{enc} is the total amount of mass inside radius r .

Astronomers find that the predicted orbital velocities, based on the amount of luminous matter, are much smaller than the measured orbital velocities. This implies that M_{enc} must be composed of more than just luminous matter. This observation is the origin of “dark” matter in dark matter. While there are other explanations of this, such as Modified Newtonian Gravity [105, 106], interpretations other than DM typically have problems explaining the other phenomena we will discuss.

Cosmic Microwave Background Anisotropies

While galactic rotation curves provide astrophysical evidence for DM, these measurements can only probe relatively close galaxies, at small redshift. If DM has existed on cosmological time scales it would have a large influence on the cosmological evolution of the universe, and indeed this is what is observed.

The early universe was a hot plasma of particles, kept in thermal equilibrium via contact with photons. As the universe expanded and cooled the thermal bath-particle interaction strength became too small to compete with binding forces. Quarks bound into protons and neutrons at temperatures, $T \sim 100$ MeV, then Big Bang Nucleosynthesis (BBN) bound protons and neutrons into nuclei at $T \sim 100$ keV. Once hydrogen atoms started to form from the binding of nuclei and electrons in the plasma, at $T \sim$ eV, the plasma became neutral and photon interactions became ineffective. This allowed the photons to freely stream to us today and created the cosmic microwave background (CMB); a near perfect blackbody radiation spectrum with $T = 2.725$ K.

However not only is the temperature of the CMB measured, fluctuations in this temperature are as well. These are typically parameterized as,

$$\Theta(\hat{\mathbf{n}}) = \frac{T(\hat{\mathbf{n}}) - \bar{T}}{\bar{T}} = \sum_{\ell m} a_{\ell m} Y_{\ell m}(\hat{\mathbf{n}}), \quad (1.2)$$

where $\hat{\mathbf{n}}$ is some direction on the sky, \bar{T} is the average temperature, and $a_{\ell m}$ represent the coefficients in the spherical harmonic basis. Correlations in this quantity can be written

$$\langle \Theta(\hat{\mathbf{n}})\Theta(\hat{\mathbf{n}}') \rangle = \frac{1}{4\pi} \sum_l (2\ell + 1) C_\ell P_\ell(\hat{\mathbf{n}} \cdot \hat{\mathbf{n}}'), \quad (1.3)$$

where

$$C_\ell = \frac{1}{2\ell + 1} \sum_{m=-\ell}^{\ell} \langle |a_{\ell m}|^2 \rangle \quad (1.4)$$

is a power spectrum of the temperature fluctuations.

This temperature fluctuation power spectrum, C_ℓ , is highly sensitive to the matter-radiation content of the universe at the epoch of recombination (i.e., after production of bound atomic states), as well as the contents of the universe it passed through on its way to us. Therefore different cosmological models, i.e., with or without DM, will produce very different C_ℓ . Many experiments have measured C_ℓ (e.g., COBE [107], WMAP [108], Planck [109]) with exceptional precision and have found that the cosmological model which best fits the data, known as the Λ CDM model, has a DM component of,

$$\Omega_{\text{DM}} = \frac{\rho_{\text{DM}}}{\rho_c} = 0.265, \quad (1.5)$$

where $\rho_c = 3H_0^2/(8\pi G)$ is the critical density of the universe [101]. This is nearly five times larger than the baryonic matter density and very strong evidence for the cosmological existence of DM.

Structure Formation

The cosmological influence of DM can also be seen in the formation of galaxies. To understand this we will review a bit of cosmological perturbation theory [110, 111] which describes how small perturbations in the matter density lead to the structures we see today. Matter density perturbations can be written as,

$$\delta(\mathbf{x}) \equiv \frac{\rho(\mathbf{x}) - \bar{\rho}}{\bar{\rho}}, \quad (1.6)$$

where $\bar{\rho}$ is the average matter density. We will find it useful to work in Fourier space, and define the Fourier components of δ as $\delta_{\mathbf{k}}$. The evolution of these perturbations, assuming a single matter field, in an expanding universe can be shown to be determined by a relatively simple ODE,

$$\ddot{\delta}_{\mathbf{k}} + 2H\dot{\delta}_{\mathbf{k}} + \left(\frac{c_s^2 k^2}{a^2} - 4\pi G\bar{\rho} \right) \delta_{\mathbf{k}} = 0, \quad (1.7)$$

where H is the Hubble parameter, c_s is the speed of sound, and a is the scale factor. We can understand this equation in a few different limits by analogy with a damped oscillator. First, assume the universe is not expanding, or $H = 0, a = 1$. The equation simplifies to,

$$\ddot{\delta}_{\mathbf{k}} + c_s^2 k^2 \left(1 - \frac{k_J^2}{k^2}\right) \delta_{\mathbf{k}} = 0, \quad (1.8)$$

where we have defined the Jeans scale, $k_J^2 = 4\pi G\bar{\rho}/c_s^2$. This is exactly a simple harmonic oscillator. If $k < k_J$ then the sign on the second term is negative, corresponding to an oscillating solution, and if $k > k_J$ the perturbations grow. This Jeans factor can be thought of as the balance between gravitational forces and internal pressure. For $k > k_J$, or length scales smaller than $\sim 1/k_J$, the gravitational attraction overpowers the pressure and causes collapse.

Reintroducing the Hubble parameter damps the evolution and introduces some other complications, but much of the intuition gained in studying the simpler case transfers over. The evolution of the scale factor is determined by Friedmann equations, and depends on the cosmological content of the universe. One can show that the growing solutions satisfy

$$\delta_{\mathbf{k}} \propto \begin{cases} \ln a & \text{radiation domination} \\ a & \text{matter domination} \end{cases}, \quad (1.9)$$

when the universe is radiation dominated and matter dominated, respectively. In words, perturbations grow linearly in a matter dominated epoch, and only logarithmically in a radiation dominated epoch. Therefore we see why DM can affect structure formation so drastically; a large DM component can efficiently drive the evolution of density perturbations.

Today we can precisely measure the matter power spectrum, $P(k) \propto \langle |\delta_{\mathbf{k}}|^2 \rangle$, as well as the halo mass function (which is simply how many halos of a given mass we expect to see). These observables provide a wealth of information about the structures that form, and when they did. Again the Λ CDM model does exceptionally well in determining the features in both the matter power spectrum and the halo mass function piling on the evidence for the existence of DM.

In addition to further solidifying Λ CDM as the prominent cosmological model, these probes of structure formation also give us an important model independent feature of DM: it must be cold. That is $v_\chi \ll 1$, where v_χ is the velocity of DM. The reason for this is that if DM is relativistic, too much small scale structure is washed out. Put another way, if DM is relativistic it is not able to produce hierarchical structure formation from initial seeds of density perturbations. While the DM velocity will follow a specific distribution, as discussed

later in Sec. 1.3, the typical velocities are

$$v_\chi \sim 10^{-3}, \quad (1.10)$$

or about the same rotation speed as luminous matter. This is important for direct detection experiments whose kinematics crucially depend on the DM velocity. For $v_\chi \ll 1$ the DM can be treated as non-relativistic, and the classical, “billiard ball” kinematic intuition becomes useful.

However the Λ CDM model is not perfect, and there are some outstanding issues in its prediction of structure formation. For example, the missing satellites and core-cusp problems [112]. Put simply, on the smallest scales Λ CDM predicts more structure than experimentally seen, which can be seen as motivation for warm DM models, and might be able to wash out just enough structure to match observational constraints [112–121].

Gravitational Lensing of Galactic Mergers

Perhaps the most violent evidence that exists for DM comes from galactic mergers [122, 123]. The results in Sec. 1.1 imply that galaxies contain an abundant amount of DM, and sometimes two galaxies collide with one another. When this happens the luminous, Standard Model matter clumps at the center of the collision, due to relatively strong self-interactions. However if weakly interacting DM is inside the galaxies then it should just pass through; the central mass density should not be located at the same point which is emitting the majority of the radiation from the collision. The location of the mass density can be inferred from gravitational lensing. General relativity tells us that light will bend in gravitational fields, and by mapping the light paths near the merger we can locate the center of mass.

The measured result from the mergers is consistent with the DM hypothesis. Moreover we learn that DM cannot be too strongly self-interacting, otherwise the final center of masses of the galaxies would be closer together than seen. This bound is typically reported as a bound on the “self-interaction” cross section, [124, 125]

$$\frac{\sigma}{m_\chi} \lesssim 10^{-1} \frac{\text{cm}^2}{\text{g}}, \quad (1.11)$$

and gives us complimentary model independent information about DM.¹

Bounds on Dark Matter Mass

The majority of the properties of DM, discussed in the previous subsections, are inferred on astrophysical scales, and do not directly give any information about the particle content.

¹This bound only applies if the galaxies are made up of a single species of DM. Small DM subcomponents are still allowed to strongly interact, as long as the majority of the DM obeys Eq. 1.11.

However there are a couple model independent statements we can make about the DM mass which we will discuss here. If DM is composed of a single species of particle then

$$m_\chi \gtrsim \begin{cases} 10^{-24} \text{ eV} & \text{bosonic} \\ 100 \text{ eV} & \text{fermionic} \end{cases}, \quad (1.12)$$

where “bosonic” and “fermionic” represent the particles statistical type. As discussed in Sec. 1.1 DM is crucially needed for structures to form. However if DM is lighter than 10^{-24} eV then its de Broglie wavelength, $\lambda \sim (m_\chi v_\chi)^{-1}$, becomes larger than the size of galaxies. This dramatically changes the structures that begin forming, and would leave a measurable imprint on the CMB [113–115].

If DM is fermionic an even stronger constraint applies. Unlike bosonic DM, fermionic DM experiences a quantum Fermi pressure since fermions cannot occupy the same quantum state. This directly impacts the amount of fermionic matter which can be packed in to a portion of phase space. If fermionic matter is lighter than ~ 100 eV then the Fermi velocity can be greater than galactic escape velocities, limiting the amount of DM allowed in a galaxy. The first application of this principle led to the Tremaine-Gunn bound [126], and more recent studies have pushed this bound even further [127–129].²

1.2 Theoretical Motivation for Light Dark Matter Models

Even with the abundance of evidence for DM discussed in Sec. 1.1, we know almost nothing about its non-gravitational interactions with the Standard Model. This leaves a large playground for theorists to build DM models which can then be tested by comparing to experiment. A DM model must predict all of the experimentally observed properties: stable on cosmological time scales [131], $\Omega_{\text{DM}} = 0.265$, must be relatively cold ($v_\chi \sim 10^{-3}$), not interact too strongly with itself (Eq. (1.11)), and have a mass consistent with the discussion in Sec. 1.1.

The canonical DM candidate is the “weakly interacting massive particle”, or the WIMP motivated by electroweak scale supersymmetry [132]. See Ref. [133] for a recent review. This is a particle with $\text{GeV} \lesssim m_\chi \lesssim 100 \text{ TeV}$ whose production is set by the freeze-out mechanism, discussed further in Sec. 1.2. The lower bound on the mass is set by the observed DM density. If the DM was lighter then it would over populate the universe with DM, and much heavier than this requires cross sections which would contradict unitarity. As mentioned earlier, this DM candidate is being experimentally ruled out quickly, and therefore other DM candidates need to be identified.

²These bounds depend crucially on a single species of DM. If there are more species the bound relaxes [130].

In this section we will discuss some of those alternative ideas. This is in no way meant to be exhaustive, but to represent some of the theories which will be discussed in later chapters. We will begin by discussing some of the standard production mechanisms which generate the cosmic abundance of DM. We will then discuss a couple of standard, benchmark, light DM models which provide a good starting point to understanding some of the more complicated ones discussed in later chapters.

Production Mechanisms

Freeze Out

The most well known DM production mechanism is “Freeze Out” [111]. In the early universe all of the SM species were in thermal equilibrium mediated by the photon bath. Therefore it is reasonable to think that the DM was also in thermal equilibrium, and its number density was determined thermodynamically. However since DM is known to interact weakly, at some point the interaction rate, Γ , becomes smaller than the expansion rate of the universe, $\Gamma \lesssim H$. When this happens thermal equilibrium is no longer achieved, and the DM abundance stops tracking the thermal equilibrium. The evolution of the abundance is given by the Boltzmann equations,

$$\frac{dY}{dx} = -\frac{xs\langle\sigma v\rangle}{H} (Y^2 - Y_{\text{eq}}^2) , \quad (1.13)$$

where σ is the DM annihilation cross section, $x = m_\chi/T$, s is the entropy density of the universe, $Y = n_\chi/s$, and Y_{eq} is the equilibrium number density per entropy density. We see that as $\sigma/H \rightarrow 0$, Y stops changing, indicating that the particle species has frozen out. The final DM abundance is inversely proportional to σ ; a larger interaction cross section the longer DM stays in thermal equilibrium, and the lower the final abundance. The WIMP is an attractive DM candidate since for interaction cross section the size of the weak interaction, the DM abundance is set automatically. More generally, lets assume that the cross section scales as,

$$\sigma \sim \frac{g^4}{m_\chi^2} , \quad (1.14)$$

where g is some DM-SM coupling constant. For g smaller than typical weak interactions, m_χ can be light and still in agreement with the primordial abundance, set via σ . However since freeze out happens at $T \sim m_\chi$, if $m \lesssim \text{MeV}$ then DM will freeze out after neutrinos decouple, at $T \sim \text{MeV}$. This can influence N_{eff} , essentially the temperature ratio between neutrinos and photons, which is severely constrained experimentally [134, 135]. Therefore thermal freeze-out is only a valid production mechanism for $m_\chi > \text{MeV}$.

Freeze In

The freeze out mechanism discussed in Sec. 1.2 depends on the DM starting in thermal equilibrium with the Standard Model, i.e., for $x \ll 1$, $Y = Y_{\text{eq}}$. This need not be the case; the DM could have been absent initially: $Y = 0$ for $x \ll 1$. If the DM-SM coupling is strong enough then the SM would produce the DM efficiently enough to bring it to thermal equilibrium, and the universe is put back in the freeze out scenario. Therefore this difference in initial conditions is only important if the DM-SM coupling is small. In this scenario the SM will produce DM inefficiently, but over a long period of time, leading to the cosmic abundance seen today. This is known as the “Freeze In” mechanism [136, 137]. Such small couplings are naturally produced in Hidden Sector DM models, discussed in more detail in Sec. 1.2. DM which freezes in avoids the low mass constraints from BBN because the DM is never in thermal equilibrium.

Misalignment Mechanism

The previously discussed freeze out/in mechanisms rely on the thermal distribution of SM particles. These are natural guesses for DM production mechanisms by analogy with the SM thermal history. However DM production mechanisms do not have to be thermal. In fact, the existence of baryons over anti-baryons is an example of production via an asymmetry, somewhat distinct from a standard freeze out mechanism.³ Perhaps the most popular non-thermal production mechanism is the “misalignment mechanism” [145–147], used mainly in the context of axion DM, a model we will discuss further in Sec. 1.2.

To understand how the misalignment mechanism we will go through a simple exercise. Consider a complex scalar field with the Higgs-like potential,

$$V(\Phi) = -\mu^2 \Phi^* \cdot \Phi + \lambda (\Phi^* \cdot \Phi)^2. \quad (1.15)$$

By analogy with electroweak symmetry breaking we know that thermal effects at high temperatures keep the minimum at $\Phi = 0$. However as the temperature lowers, Φ develops a new minima at $v = \sqrt{2\mu^2/\lambda}$. After the symmetry breaking occurs we can describe the resultant Goldstone boson, which we will refer to as the “axion”, via a field redefinition,

$$\Phi = v e^{ia}, \quad (1.16)$$

where $a \in [0, 2\pi)$. Since the axion is a Goldstone boson, the field is massless. Conceptually the evolution of the axion field at this point is straightforward: it simply rolls around the

³There exist models of DM which use similar production methods and go by “asymmetric DM” [11, 136, 138–144]. This mechanism is appealing because it can be used to connect the DM density to the baryon density which are intriguingly only different by a factor of five.

bottom of the potential. However, imagine the U(1) symmetry is explicitly broken at a later stage, such that the potential contains a mass term for the axion.

$$V \supset \frac{m_a^2}{2} a^2. \quad (1.17)$$

This will tilt the axion potential, and push the axion to the new minimum. As the axion is pushed to the new minimum energy will be radiated which can set the primordial abundance. If the universe is in causal contact when the axion is generated, $T \sim v$, then the axion abundance will be set by the value of a when it started decaying to the new minima (created from the introduction of the mass term). This is not very attractive as a production mechanism for the DM abundance, since the value is precisely tuned to the initial condition of the axion field which was previously rolling around in the flat potential.

However this is not the end of the story. Imagine that the universe was *not* in causal contact when $T \sim v$. Then the axion field will essentially be a random value in different patches of the universe. In this scenario the DM abundance will then be set by the average value across all these patches. Therefore while different patches of the universe will have different DM densities, the average density can be used to generate a DM abundance which is not dependent on initial conditions. Moreover the axion relic density will be related to its mass, giving a concrete prediction for the DM mass.

The scenario discussed here is the standard misalignment case. Recently, there has been interest in expanding this idea by changing the initial conditions the axion field has before it starts to roll in the potential [148, 149]. Additionally there has been work on understanding whether this production mechanism is dominant. In a universe with many different patches there exist domain walls which can decay in to axions as well, which can also set the relic abundance [150].

Candidate Light Dark Matter Models

We now turn to discussing a couple specific light DM models, starting with the axion and then discussing hidden sector DM models.

Axion

As mentioned in Sec. 1.1, DM is not the only open problem particle physics faces. Another such problem is the ‘‘Strong CP’’ Problem [98–100]. SU(3) symmetry allows a term of the form,

$$\mathcal{L} \supset \theta G\tilde{G} \quad (1.18)$$

in the Lagrangian, where G is the $SU(3)$ field strength tensor. Naturally, one expects that all terms allowed by symmetry are present in the Lagrangian with $\mathcal{O}(1)$ coefficients. If a coefficient is unnaturally small then one might expect that there is a symmetry forbidding that term to exist. No such symmetry is known to forbid the term in Eq. (1.18), yet the experimentally measured value is bounded to

$$\theta \lesssim 10^{-10}, \quad (1.19)$$

an unnaturally small number indeed.

One solution is to introduce a new axial $U(1)$ symmetry to the Standard Model, typically referred to as a ‘‘Peccei-Quinn’’ symmetry for the creators of the mechanism. Imagine a new, heavy, field, Q , charged under this $U(1)_{PQ}$. Performing a field transformation, $Q \rightarrow e^{ia\gamma^5}Q$, where a is the axion, generates an anomalous coupling to $G\tilde{G}$. The theta term is then absorbed in to a field redefinition of a and vanishes, leaving a dynamic θ term. The minimum of the potential for this dynamic θ term is zero, thereby dynamically solving the Strong CP problem. An axion which does this is known as the QCD axion. The QCD axion can then be produced via the misalignment mechanism discussed in Sec. 1.2 and be a viable DM candidate. The ability to solve both the DM problem and Strong CP problem at once is powerful motivation for the QCD axion.

The mass of the QCD axion is generated by QCD effects and directly relates the $U(1)_{PQ}$ symmetry breaking scale, f_a (essentially v in Sec. 1.2),

$$m_a \propto \frac{m_\pi f_\pi}{f_a}, \quad (1.20)$$

where m_π is the pion mass, and f_π is the pion decay constant. The symmetry breaking scale, f_a , also sets the strength of interactions between the QCD axion and the SM. If f_a is too small the interaction strength will be too large and in conflict with stellar cooling bounds [30]. This constrains the mass of the QCD axion to $m_a \lesssim 100$ meV.

More generally one can consider axion-like particles (ALPs) whose mass is disconnected from the symmetry breaking scale and generates a mass, coupling parameter space for ALP DM. Searching for the QCD axion and ALPs experimentally is a large experimental program [91–93, 151–169], and in Ch. 6 we discuss in detail how to use phonons and magnons to probe these DM models for $\text{meV} \lesssim m_a \lesssim 100$ meV, a large chunk of previously unexplored model space below the stellar cooling limits.

Hidden Sector Dark Matter

Another class of light DM models is known as ‘‘Hidden Sector’’, or ‘‘dark portal’’ DM models. These are models in which the Standard Model and DM interact very weakly via a new force.

The new force acts as the “portal” between the Standard Model and the “hidden sector” of DM particles which are also charged under this new force. As an example we will discuss the light “dark photon” model [170] which has proven to be the most popular benchmark hidden sector model (at least within the context of direct detection) since it simply adds a new $U(1)'$ gauge group. Minimally the model adds two terms to the Standard Model Lagrangian,

$$\mathcal{L} \supset \frac{m_{A'}}{2} A'^2 + \frac{\kappa}{2} F^{\mu\nu} F'_{\mu\nu}, \quad (1.21)$$

where A' is the dark photon, $m_{A'}$ is its mass, and κ is known as a “kinetic mixing” parameter since it mixes the kinetic terms of the photon and dark photon. This κ can be radiatively generated through loops of heavy particles charged under $U(1) \times U(1)'$. To understand the phenomenology of this model it is typically useful to diagonalize the mass matrix of the A, A' system via the field transformation,

$$A_\mu \rightarrow A_\mu + \kappa A'_\mu. \quad (1.22)$$

Note that A'_μ cannot be rotated since that would generate a mass for the photon. In this rotated basis all of the Standard Model fermions which have an electromagnetic charge are now charged under A' and therefore the field acts like an additional photon field with rescaled couplings, $e \rightarrow \kappa e$.

The dark photon itself can be the DM [171, 172], typically one adds a particle χ which is charged under the $U(1)'$ and takes this to be the DM. This χ field then serves as the light DM candidate, and can give rise to a direct detection signal by scattering off a target via mediating an A' .

While the motivation for any given dark photon model is perhaps weaker than the motivation for the axion, this class of models, with an extra gauge group and a DM candidate is a very natural explanation for DM. The Standard Model is a collection of seemingly random gauge groups so it is not unfeasible to have one more gauge group. Moreover, extra gauge groups are a fairly generic prediction of Grand Unified Theories. The dark photon model serves as a useful benchmark for these more general cases since it is easier to calculate for than extensions with an extra $SU(N)$ group, or an MSSM-like model with many new parameters.

1.3 Direct Detection Preliminaries

We will now discuss computing the interaction rates between the cosmic background of DM and a target in direct detection experiments. While this formalism is reviewed, and extended, in many of the later chapters, we will take extra care here to discuss important details which are often taken for granted.

Light Dark Matter Kinematics

Before discussing the general interaction rate formalism it is useful to understand the kinematics, or how energy and momentum conservation are satisfied in interactions involving light DM. Since DM is cold, as discussed in Sec. 1.1, it can be treated as a non-relativistic particle, i.e.,

$$E_\chi \approx m_\chi + \frac{1}{2}m_\chi \mathbf{v}_\chi^2, \quad (1.23)$$

where χ is a DM particle, and $v_\chi \sim 10^{-3}$. There are two different processes we will focus on: scattering and absorption. In a scattering process a DM particle enters and leaves the detector, depositing some energy and momentum. Let \mathbf{p}_χ be the momentum of the incoming DM particle, and $\mathbf{p}'_\chi = \mathbf{p} - \mathbf{q}$ be the momentum of the outgoing DM particle,⁴ where \mathbf{q} is the momentum leaving the DM system (and entering the detector). In this scenario the energy deposited, ω , is determined by the momentum transfer,

$$\omega = E_\chi - E'_\chi = \frac{\mathbf{p}_\chi^2}{2m_\chi} - \frac{(m_\chi \mathbf{v}_\chi - \mathbf{q})^2}{2m_\chi} = \mathbf{q} \cdot \mathbf{v}_\chi - \frac{\mathbf{q}^2}{2m_\chi}, \quad (1.24)$$

where E_χ is the initial energy of the DM particle and E'_χ is the final energy of the DM particle.

From here, without any knowledge of the detector itself, we see that

$$q_{\max} = 2m_\chi v_{\chi, \max} \sim \text{keV} \left(\frac{m_\chi}{\text{MeV}} \right), \quad (1.25)$$

$$\omega_{\max} = \frac{1}{2}m_\chi v_{\chi, \max}^2 \sim \text{eV} \left(\frac{m_\chi}{\text{MeV}} \right), \quad (1.26)$$

where $v_{\chi, \max}$ is the maximum velocity of the incoming DM particle, q_{\max} is the maximum momentum transfer, and ω_{\max} is the maximum energy transfer. From this simple exercise we immediately understand the energy and momentum scales involved in DM scattering. Moreover the experimental energy resolution necessary to see these interactions is clear; if the threshold energy of an experiment is above ω_{\max} then these events will not be visible.

In addition to the kinematics on the DM side the detector must be able to respond. Consider the canonical direct detection experiment, i.e., DM scattering off a stationary nucleus of mass m_N . The final energy of the nucleus, $\mathbf{q}^2/2m_N$, must be equal to the energy deposited by the DM,

$$\frac{\mathbf{q}^2}{2m_N} = \mathbf{q} \cdot \mathbf{v}_\chi - \frac{\mathbf{q}^2}{2m_\chi}. \quad (1.27)$$

⁴Assuming that the outgoing particle is identical to the incoming one. If the DM is composite it can change its internal state, leaving a residual $\Delta E = m_\chi^{\text{in}} - m_\chi^{\text{out}}$ in Eq. (1.24). DM models with this behavior are sometimes referred to as “inelastic” DM [173] due to the inelastic nature of the collision.

Solving for \mathbf{q}, ω gives

$$\mathbf{q} = 2\mu_{N\chi}\mathbf{v}_\chi \quad (1.28)$$

$$\omega = 2\frac{\mu_{N\chi}^2}{m_N}\mathbf{v}_\chi^2, \quad (1.29)$$

where $\mu_{N\chi}$ is the reduced mass of the nucleus DM system. In the light DM limit, $m_\chi \ll m_N$, we can simplify the energy deposition,

$$\omega = 2\frac{m_\chi^2}{m_N}\mathbf{v}_\chi^2 \sim \text{meV} \left(\frac{m_\chi}{\text{MeV}} \right)^2, \quad (1.30)$$

where we have assumed a light nuclei $m_N \sim \text{GeV}$. For $m_\chi = \text{MeV}$ we see that nuclear recoil can only extract a thousandth of the energy available in a DM scattering event. Therefore we see that nuclear recoil is not well suited to search for light DM candidates, and that to maximize detector sensitivity we need excitations which can kinematically match the incoming DM. As we will discuss in detail, electronic, phononic, and magnonic excitations are ideal for this purpose.

The kinematics of DM absorption is even simpler than scattering. Since there is no outgoing DM state all of the energy and momentum of the initial DM state must be absorbed,

$$\mathbf{q} = m_\chi\mathbf{v}_\chi \quad (1.31)$$

$$\omega = m_\chi. \quad (1.32)$$

This can be thought of as the opposite limit of a scattering event since $q \ll \omega$, whereas in a scattering event $q \gg \omega$. Because q is so small an absorption event can be thought of as a vertical transition in the $q - \omega$ plane.

General Formalism

The calculation of DM-target interaction rates is typically treated with standard perturbation theory since the DM-target coupling is small. In the absence of DM-target interactions, the Hamiltonian governing the behavior of the DM and target is simply the sum of their individual Hamiltonians,

$$H^0 = H_{\text{DM}}^0 + H_{\text{target}}^0, \quad (1.33)$$

where H^0 has dimensions [eV]. Assuming the DM is a non-relativistic particle, H_{DM}^0 is simply

$$H_{\text{DM}}^0 = m_\chi + \frac{\mathbf{p}_\chi^2}{2m_\chi}. \quad (1.34)$$

and the eigensystem is then simply a set of plane wave states

$$H_{\text{DM}}^0|\mathbf{p}_\chi\rangle = E_\chi|\mathbf{p}_\chi\rangle, \quad (1.35)$$

$$E_\chi = m_\chi + \frac{\mathbf{p}_\chi^2}{2m_\chi}. \quad (1.36)$$

While this is a great approximation for the cosmic cold DM, we make no such assumptions for the target states. This is because these states will take a vastly different form depending on the excitation, e.g. electrons or phonons. To be as general as possible we take the eigensystem of H_{target}^0 to be,

$$H_{\text{target}}^0|I\rangle = \omega_I|I\rangle, \quad (1.37)$$

for some set of states labelled by I . Therefore a DM-target state is then just a product state,

$$|\mathcal{I}\rangle = |I\rangle \otimes |\mathbf{p}_\chi\rangle, \quad (1.38)$$

$$H^0|\mathcal{I}\rangle = \omega_{\mathcal{I}}|\mathcal{I}\rangle, \quad (1.39)$$

$$\omega_{\mathcal{I}} = \omega_I + E_\chi. \quad (1.40)$$

We now add a coupling between the DM and target system via an interaction Hamiltonian,

$$H = H^0 + \delta H. \quad (1.41)$$

Fermi's Golden rule then dictates the transition rate, or number of transitions per unit time. Assuming the initial (final) DM-target state is $|\mathcal{I}\rangle(|\mathcal{F}\rangle)$ the transition rate between the states, $\Gamma_{\mathcal{I}\rightarrow\mathcal{F}}$, is

$$\Gamma_{\mathcal{I}\rightarrow\mathcal{F}} = 2\pi \frac{|\langle\mathcal{F}|\delta H|\mathcal{I}\rangle|^2}{\langle\mathcal{F}|\mathcal{F}\rangle\langle\mathcal{I}|\mathcal{I}\rangle} \delta(\omega_{\mathcal{F}} - \omega_{\mathcal{I}}). \quad (1.42)$$

This formula should be familiar, except perhaps the denominator of state inner products. Fermi's Golden Rule is usually derived in the context of quantum mechanics where the states are implicitly unit normalized, and therefore the denominator is left out. However sometimes it is convenient to leave these factors in, since the DM states are sometimes normalized with QFT conventions. This formula simply generalizes Fermi's Golden rule to account for different state normalizations. Here we assume all states are unit normalized, i.e. $\langle I|I\rangle = \langle \mathbf{p}|\mathbf{p}\rangle = 1$.

Since the DM states are assumed to be plane waves, we can further simplify Eq. (1.42) by inserting an identity operator in the DM space,

$$1 = \frac{1}{V} \int d^3\mathbf{x} |\mathbf{x}\rangle\langle\mathbf{x}|, \quad (1.43)$$

where V is the target volume. Placing this inside of the matrix element gives

$$\langle \mathbf{p}_\chi | \delta H | \mathbf{p}'_\chi \rangle = \frac{1}{V^2} \int d^3\mathbf{x} d^3\mathbf{y} \langle \mathbf{p}'_\chi | \mathbf{x} \rangle \langle \mathbf{x} | \delta H | \mathbf{y} \rangle \langle \mathbf{y} | \mathbf{p}'_\chi \rangle, \quad (1.44)$$

$$= \frac{1}{V} \int d^3\mathbf{x} e^{i\mathbf{q}\cdot\mathbf{x}} \langle \mathbf{x} | \delta \hat{H} | \mathbf{x} \rangle, \quad (1.45)$$

$$\equiv \frac{1}{V} \tilde{\mathcal{V}}(-\mathbf{q}), \quad (1.46)$$

assuming the interaction Hamiltonian is local, $\langle \mathbf{x} | \delta \hat{H} | \mathbf{y} \rangle = \delta_{\mathbf{x}\mathbf{y}} \langle \mathbf{x} | \delta \hat{H} | \mathbf{x} \rangle = V \delta^{(3)}(\mathbf{x} - \mathbf{y}) \langle \mathbf{x} | \delta \hat{H} | \mathbf{x} \rangle$, $\langle \mathbf{x} | \mathbf{p} \rangle = e^{i\mathbf{p}\cdot\mathbf{x}}$, and $\mathbf{q} = \mathbf{p}_\chi - \mathbf{p}'_\chi$ is the momentum transferred to the target.⁵ We have introduced $\tilde{\mathcal{V}}$ which we will often refer to as the “scattering potential” which will depend on how the DM model couples to the target. Written in terms of the scattering potential, Eq. (1.42) is given by,

$$\Gamma_{\mathbf{p}_\chi, I \rightarrow \mathbf{p}'_\chi, F} = \frac{2\pi}{V^2} \left| \langle F | \tilde{\mathcal{V}}(-\mathbf{q}) | I \rangle \right|^2 \delta(\omega_F - \omega_I - \omega), \quad (1.47)$$

where $\omega \equiv E_\chi - E'_\chi$ is the amount of energy the DM deposits on the target.

The total interaction rate for an incoming DM particle of momentum \mathbf{p}_χ is found by simply summing over all the other states. However, instead of summing over all possible \mathbf{p}'_χ with $\sum_{\mathbf{p}'_\chi} \rightarrow V \int \frac{d^3\mathbf{p}'_\chi}{(2\pi)^3}$, it is convenient to shift variables to \mathbf{q} giving,

$$\Gamma_{\mathbf{p}_\chi} = \frac{2\pi}{V} \sum_I \sum_F \int \frac{d^3\mathbf{q}}{(2\pi)^3} \left| \langle F | \tilde{\mathcal{V}}(-\mathbf{q}) | I \rangle \right|^2 \delta(\omega_F - \omega_I - \omega). \quad (1.48)$$

This is the number of events per unit time assuming one incoming DM particle with momentum \mathbf{p}_χ . The average excitation rate per incoming DM particle, Γ , can then be computed once the momentum distribution of DM particles is known. Usually this is given in terms of the DM velocity, \mathbf{v}_χ since $\mathbf{p}_\chi = m_\chi \mathbf{v}_\chi$ in the nonrelativistic limit. We will discuss the standard choice of velocity distribution below. Assuming for now that the DM velocity distribution is $f_\chi(\mathbf{v}_\chi)$, the expected excitation rate per unit time, per incoming DM particle, is given by,

$$\Gamma = \frac{2\pi}{V} \int d^3\mathbf{v}_\chi f_\chi(\mathbf{v}_\chi) \sum_I \sum_F \int \frac{d^3\mathbf{q}}{(2\pi)^3} \left| \langle F | \tilde{\mathcal{V}}(-\mathbf{q}) | I \rangle \right|^2 \delta(\omega_F - \omega_I - \omega). \quad (1.49)$$

The total number of interactions per unit time per detector mass, M_T , is

$$R = \frac{N_\chi}{M_T} \Gamma = \frac{\rho_\chi V}{m_\chi \rho_T V} \Gamma = \frac{\rho_\chi}{m_\chi \rho_T} \Gamma, \quad (1.50)$$

$$= \frac{2\pi\rho_\chi}{m_\chi \rho_T V} \int d^3\mathbf{v}_\chi f_\chi(\mathbf{v}_\chi) \sum_I \sum_F \int \frac{d^3\mathbf{q}}{(2\pi)^3} \left| \langle F | \tilde{\mathcal{V}}(-\mathbf{q}) | I \rangle \right|^2 \delta(\omega_F - \omega_I - \omega), \quad (1.51)$$

⁵Another common choice for the definition of \mathbf{q} is $\mathbf{p}'_\chi - \mathbf{p}_\chi$, or simply the negative of the convention here. While this would remove the minus sign in the scattering potential, the momentum would now be “coming out” of the target, which is, arguably, less intuitive.

where N_χ is the number of DM particles in the detector, ρ_χ is the local DM density, taken throughout this thesis to be $\rho_\chi = 0.4 \text{ GeV cm}^{-3}$ [174], and ρ_T is the target density. This rate, R , is dimensionless (in natural units), but usually converted to units of $\text{kg}^{-1}\text{yr}^{-1}$ such that one simply needs to multiply by the exposure to find the total number of interactions. This is the central formula which will be used routinely in the coming chapters to compute the expected number of events in a detector.

A standard parameterization of the DM velocity distribution is a Maxwell-Boltzmann distribution [174–176] cutoff at the galactic escape velocity,

$$f_\chi(\mathbf{v}) = \frac{1}{N_0} e^{-\mathbf{v}^2/v_0^2} \Theta(v_{\text{esc}} - |\mathbf{v}|), \quad (1.52)$$

$$N_0 = \pi^{3/2} v_0^2 \left[v_0 \text{erf}(v_{\text{esc}}/v_0) - \frac{2v_{\text{esc}}}{\sqrt{\pi}} \exp(-v_{\text{esc}}^2/v_0^2) \right], \quad (1.53)$$

where our conventions throughout this thesis will be to use $v_0 = 230 \text{ km s}^{-1}$, $v_{\text{esc}} = 600 \text{ km s}^{-1}$ [177]. However this does not directly get substituted in to Eq. (1.51); this is the velocity distribution in the galactic frame. Since the Earth is also moving through the galaxy we need to boost the Maxwell-Boltzmann distribution to the Earth’s frame, i.e., $f_\chi(\mathbf{v}_\chi + \mathbf{v}_e)$ is the velocity distribution we use. The Earth velocity vector, \mathbf{v}_e , introduces interesting modulation effects which will be the subject of the next subsection.

Modulation Effects

Since the interactions between the DM and any given target are weak, it is crucial to find ways to differentiate a DM signal from any background sources. This way, even if only a tiny signal is observed, we can still claim the signal is significant. The key differentiating factor between DM and the majority of other backgrounds is that Earth is moving through a cosmic background of DM. This means that as the Earth velocity changes, in the Earth frame, the direction of the incoming DM is changing.

The two main modulation effects are “annual modulation” and “daily modulation”. Since the Sun is also moving around the galactic center, the Earth’s motion relative to it on a yearly basis changes the magnitude of the velocity relative to the incoming DM. We take the central value of the Earth velocity is $v_e = 240 \text{ km s}^{-1}$, and annual modulation causes $\mathcal{O}(10 \text{ km s}^{-1})$ fluctuations. While seemingly a relative small effect, remember from Sec. 1.3 that the maximum energy/momentum transfer is set by the maximum DM velocity, $v_{\text{max}} = v_{\text{esc}} + v_e$. As an example case where this might be important, consider an electronic transition across a band gap. If the DM mass is just barely kinematically able to drive the transition, then at different times of the year a transition may or may not be possible.

The other type of modulation effect, daily modulation, is the focus of Ch. 4, and discussed in Ch. 2. While the magnitude of the Earth’s velocity will change very slightly, the more important effect here is that the DM wind will hit the target from different directions. For a target with an isotropic response function this does not matter. However for targets which have an anisotropic response this effect can cause $\mathcal{O}(1)$ fluctuations in the DM rate. This spectacular signal, if observed, would be a “smoking gun” signature that the effect is due to DM.

Setting Constraints Assuming No Backgrounds

In the absence of any events seen in the detector, and assuming negligible background events, the rate in Eq. (1.51) can directly used to place constraints on the coupling constants which govern the strength of the potential. While different statistical procedures exist for placing limits, perhaps the simplest is to hypothesis test with the null hypothesis being a Poisson distribution with expected number of events, $\bar{N} = R \times M_T \times T$,

$$P(n, \bar{N}) = \frac{\bar{N}^n e^{-\bar{N}}}{n!}, \quad (1.54)$$

where T is the exposure time. The probability of seeing 0 events is then $e^{-\bar{N}}$. Therefore we can reject the null hypothesis at the $100 \times p$ th confidence level (C.L.) when $e^{-\bar{N}} = 1 - p$. Taking $p = 0.95$ implies $\bar{N} \approx 3$. This is commonly reported in the figure captions as, e.g., “the 95% C.L. constraints (3 events) assuming no background”.

1.4 Summary

We will now briefly summarize the contents in each of the following chapters, and connect the results to the previous discussion. The chapters are organized as follows: Chs. 2-3 discuss DM excitations in multiple channels: electron, phonons, and nuclear recoils. Chs. 4-7 are specific to single phonon and magnon excitations, and Chs. 8-10 are specific to electronic excitations.

- **Ch. 2: Multi-Channel Direct Detection of Light Dark Matter: Theoretical Framework**

Previously, calculations of electronic, phononic, and nuclear recoil signals from DM in direct detection experiments followed a variety of different formulas. While this is fine if one is only interested in a single excitation type, the response of any given target to incoming DM will depend on these multiple channels of excitations. Therefore it is useful to have a single theoretical framework from which each of the excitation rates can be

derived, and makes clear the assumptions being made in each calculation. Essentially, it is an extension of the general formalism discussed in Sec. 1.3 focused on general spin independent (SI) DM scattering. Using this general formalism we illustrated how daily modulation effects could arise in electronic transitions in anisotropic targets, showed that Umklapp processes are important for phonon excitations in models with a heavy mediator, and highlighted the kinematic regimes each channel is likely to dominate in.

- **Ch. 3: Multi-Channel Direct Detection of Light Dark Matter: Target Comparison**

Many different target materials have been utilized in direct detection experiments. From noble liquids, Xenon, and Argon in large chambers, to Si and Ge in detectors focusing on electronic excitations. Different target materials can have dramatically different properties, and an important question to ask is whether the optimal target material is being used. In this chapter we compare and contrast the effectiveness of 26 different target materials as light DM detectors. This chapter is a companion to Ch. 2 and relies heavily on the formalism developed there. Specifically, we compute the electronic, phononic, and nuclear recoil signals for a few benchmark DM models, including the light dark photon model discussed in Sec. 1.2, in all 26 targets. In addition we give simple analytic expressions in terms of macroscopic material properties which can be optimized to further search for optimal targets.

- **Ch. 4: Directional Detectability of Dark Matter With Single Phonon Excitations: Target Comparison**

While alluded to in the previous two chapters, anisotropic materials will not only have a daily modulation, discussed in Sec. 1.3, in electronic excitations, but also phonon excitations. Understanding the daily modulation pattern of a given target can be crucial in rejecting backgrounds. This chapter is a detailed study of daily modulation in single phonon excitations in the same 26 target materials, and benchmark DM models, discussed in Ch. 3. We find that a variety of anisotropic targets can have $\mathcal{O}(1)$ modulation fractions for a variety of DM model space.

- **Ch. 5: Detecting Light Dark Matter With Magnons**

Phonon excitations have been the collective excitation mode focused on so far, but they are not the only ones to appear in target materials. In targets with magnetic order-

ing the low energy excitations appearing are known as magnons. These are quantized spin waves arising from a Heisenberg-like Hamiltonian of spin interactions. Similar to phonons, the energy of these excitations are $\mathcal{O}(1 - 100 \text{ meV})$; guaranteeing kinematic matching between them and light DM candidates. Moreover these excitations are uniquely susceptible to DM models which couple to spin, and therefore offer a complementary probe of light DM model space. In this chapter we study the light DM-single magnon scattering rate for a few spin-dependent light DM models, in a yttrium iron garnet (YIG) target.

- **Ch. 6: Detectability of Axion Dark Matter With Phonon Polaritons and Magnons**

As discussed in Sec. 1.2, the QCD axion is a well motivated DM candidate with a unique production mechanism and ability to solve the Strong CP problem. Direct detection of the axion has a storied history, with many different detection ideas being utilized to search for it. Typically these rely on coupling the axion to an electromagnetic mode in a cavity and reading out the resultant electromagnetic field. While this is great for low, $m \lesssim \text{meV}$ scale axions, there quickly becomes a fundamental problem that the energy of these modes is inversely proportional to the cavity size, limiting exposure. Furthermore since stellar cooling constraints only limit the QCD axion to $m \lesssim 100 \text{ meV}$, there is open parameter space between $\mathcal{O}(1 - 100 \text{ meV})$. This is ideally matched to phonon and magnons modes, and we show that such experiments could reach the QCD axion line. Technically, the absorption occurs on phonon-polariton modes which come from the mixing between the photon and phonon near the level crossing, clearly an important regime for DM absorption kinematics. We also show that changing the direction of the external magnetic field can give rise to different phonon modes, allowing for modulation effects.

- **Ch. 7: Effective Field Theory of Dark Matter Direct Detection With Collective Excitations**

In Ch. 2 we discussed the general formalism for DM single phonon scattering via spin independent operators, and in Ch. 5 we discussed the formalism for DM single magnon scattering for operators depending on the electron spin. Here we unify and extend this formalism to account for general scattering potentials. The space of UV DM models is vast, and computing constraints for every single model is untenable. Thankfully this need not be done, there exists a basis of operators for which any UV DM model can be

mapped on to via an effective field theory (EFT) procedure. In this chapter we discuss the construction of this basis, and give examples of mapping some general DM model theories on to these scattering potentials. Moreover we show how this basis can be used for both DM-single phonon and single magnon scattering. We detail which response will be dominant in target materials which have both excitations. We also released an open source code, PhonoDark [178], which can compute the phonon excitation rate for any material and operator from density functional theory (DFT) input.

- **Ch. 8: Extended Calculation of Dark Matter Electron Scattering In Crystal Targets**

As discussed previously there are many ongoing experiments looking for electronic excitations. Therefore it is important to have accurate calculations of the DM induced electronic excitation rate. Central to this calculation is an accurate description of the electronic wave functions and energy levels. Previous calculations approximated these states with a variety of methods. Initially with the simplest analytic forms solving the Hydrogen Schrödinger equation, to semi-analytic forms working with these functions as a basis, to using density functional theory (DFT) techniques which solve for them numerically. In this chapter we combine the best aspects of the previous calculations, by using them when they are appropriate. For example, the states tightly bound to the ionic sites can be well approximated as “core” electronic states in which semi-analytic approaches work well, and the more free valence states can be computed with DFT. This allows for the first complete calculation to be performed which takes in to account all kinematically allowed transitions. We also take in to account “all-electron” reconstruction effects which correct the pseudo-potential calculated wave functions at small distances. We show that these effects can be important for heavy mediators, and more generally for transitions with $\omega \gtrsim 10$ eV. We packaged this calculation in to the open source program, EXCEED-DM [179].

- **Ch. 9: Dark Matter Absorption via Electronic Excitations**

In addition to the DM-electron scattering rate calculations performed in Ch. 8 absorption across the band gap can also take place. This ends up being a deceptively complex problem for kinematic reasons. In a perfectly vertical transition one needs to account for the fact that the energy eigenstates which the electron transitions between are orthogonal. Generally this leads to a suppression of the absorption rate, and since the DM momentum is smaller than the typical electron velocity, αm_e , electron veloc-

ity dependent effects can be important. To handle these subtleties we construct a non-relativistic EFT and carefully power count. This allows us to compute the DM absorption rate from first principles for any DM model. It has been previously shown that the vector DM and pseudoscalar DM absorption rates can be related to optical data, and we find good agreement between the data and our calculations. We also find that the scalar DM absorption rate cannot be related to optical data. Similar to Ch. 8 we add an absorption module to EXCEED-DM to numerically compute these absorption rates.

- **Ch. 10: Dark Matter Direct Detection In Materials With Spin-Orbit Coupling**

While Chs. 8 and 9 focused on DM scattering and absorption in the Si and Ge targets in use today, here we focus on more exotic targets, like ZrTe_5 , which have spin-orbit couplings. These targets can be special because they can have much smaller band gaps, $\mathcal{O}(\text{meV})$, than the standard semiconductors used today. This allows for more DM model parameter space to be covered in experiments which read out electrons, without having to resort to phonon or magnon mode readout. These targets are also theoretically interesting because the presence of spin-orbit coupling means that the electronic spin is no longer a good quantum number, and the wave functions become two component. We show that these effects can be important for states close to the band gap. We also discuss the differences in the calculation presented here and those done previously for Dirac materials which assume a perfectly linear dispersion relation.

Lastly in Ch. 11 we look to the future and discuss some important extensions of this work done in this thesis.

MULTI-CHANNEL DIRECT DETECTION OF LIGHT DARK MATTER: THEORETICAL FRAMEWORK

2.1 Introduction

Direct detection has been playing a central role in the quest for the particle nature of dark matter (DM). Over the past few decades, tremendous progress has been made at a range of experiments focused on nuclear recoil signals, including ANAIS [67], CRESST [15, 68, 69], DAMA/LIBRA [70], DAMIC [21, 71], DarkSide-50 [12], DM-Ice [72], KIMS [73], LUX [16, 74, 75], SABRE [76], SuperCDMS [23, 23, 77–80], and XENON1T [13, 14]. While these experiments have excluded much of the parameter space for DM heavier than roughly a GeV, much less is known about lighter DM. For sub-GeV DM, conventional nuclear recoil searches lose sensitivity due to kinematic mismatch, as only a small fraction of DM’s kinetic energy can be deposited on the heavier nuclei. Even with next generation detectors sensitive to sub-eV energy depositions, nuclear recoils can at best probe DM masses down to $\mathcal{O}(100 \text{ MeV})$.

To cover a broader mass range, electrons have been considered as an alternate pathway to detecting light DM. A variety of targets have been studied, including noble gas atoms which can be ionized with $\mathcal{O}(10 \text{ eV})$ energy deposition, semiconductors where electron transitions can happen across $\mathcal{O}(\text{eV})$ band gaps [19, 24, 25, 33–35, 39, 40, 177, 180], as well as systems with $\mathcal{O}(\text{meV})$ gaps like superconductors [41, 181, 182] and Dirac materials [29, 144, 183]. Electron transitions can potentially extract all of DM’s kinetic energy, and thus constitute a more efficient search channel than nuclear recoils. For example, semiconductor targets can probe DM masses down to $\mathcal{O}(\text{MeV})$.

When the energy deposition is below the band gap, electron transitions are kinematically forbidden. However, there are condensed matter systems with collective excitations that can couple to the DM. For example, collective excitations in superfluid helium (phonons and rotons) are sensitive to $\mathcal{O}(\text{meV})$ energy depositions, especially via phonon pair production [184–187]. In a crystal target, the active degrees of freedom below the electronic band gap are acoustic and optical phonons – quanta of collective oscillations of atoms/ions. Direct excitation of single phonons in crystals has been recently proposed as a new search channel for light DM [28, 64]. Optical phonons typically have energies of $\mathcal{O}(10\text{-}100 \text{ meV})$, and can be excited by DM as light as $\mathcal{O}(10 \text{ keV})$. Acoustic phonons are gapless and, assuming an $\mathcal{O}(\text{meV})$ detector threshold, can also probe DM down to $\mathcal{O}(10 \text{ keV})$.

All these detection channels do not exist in isolation. Depending on the DM mass and couplings to Standard Model (SM) particles, it may either cause nuclear recoils, or induce electron transitions, or excite phonons in the same target material. Thus, when designing direct detection experiments, an important consideration should be to search for DM across multiple channels in parallel. The kinematic interplay between several channels that we will discuss in detail is illustrated in Fig. 2.1.

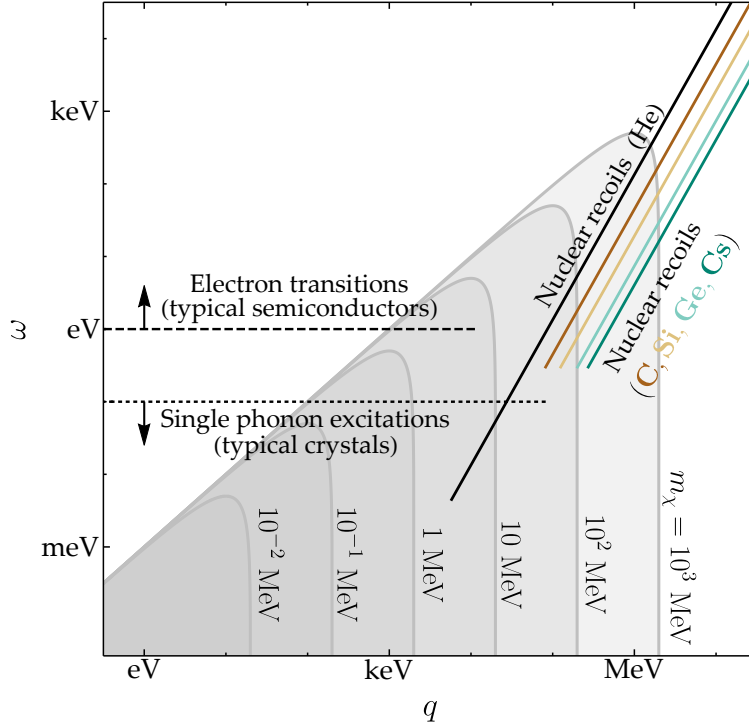


Figure 2.1: Illustration of kinematic regimes probed via the three detection channels considered in this paper. For an incoming DM particle with velocity $v = 10^{-3}$, the momentum transfer q and energy deposition ω are bounded by $\omega \leq qv - q^2/2m_\chi$, shown by the shaded regions for three DM masses. Nuclear recoils require $\omega = q^2/2m_N$ for a given type of nucleus, shown by the solid lines for helium and several elements in existing or proposed crystal targets. Standard calculations assuming scattering off individual nuclei break down below a few meV (a few hundred meV) for superfluid He (crystal targets), where we truncate the lines. Electron transitions can be triggered for ω above the band gap, which is $\mathcal{O}(\text{eV})$ for typical semiconductors, as shown by the dashed line. The end point at $q \sim 10 \text{ keV}$ corresponds to a few times αm_e , above which valence electron wavefunctions are suppressed, and only (semi-)core electrons can contribute (which requires ω to be much higher than the band gap). Single phonon excitations are relevant for $\omega \lesssim \mathcal{O}(100 \text{ meV})$ in typical crystals, as shown by the dotted line. The momentum transfer can be up to $q \sim \sqrt{m_N \omega_{\text{ph}}} \sim \mathcal{O}(100 \text{ keV})$ with ω_{ph} the phonon energies, above which the rate is suppressed by the Debye-Waller factor. We see that a GeV-mass DM can be probed by all three channels; a 10 MeV DM is out of reach in conventional nuclear recoil searches, but can be searched for via electron transitions in semiconductors and single phonon excitations in crystals; a sub-MeV DM cannot even trigger electron transitions in eV-gap materials, but can still be detected via single phonon excitations.

On the theory side, most of the basic ingredients for the rate calculation are known. However, they have been developed in separate contexts, and at first sight look very different for different detection channels. In our opinion, it would be much more convenient to have a common theoretical framework for all these calculations. This will not only facilitate the comparison of target materials across various existing and proposed search channels, but also provide the necessary calculation tools when new search channels are considered in the future.

It is the purpose of this paper to lay out such a formalism, focusing on spin-independent (SI) DM interactions.¹ As we will see, for each detection channel, the calculation is factorized into a particle physics model-specific part and a target response-specific part. The latter is encoded in a dynamic structure factor, to be computed by quantizing the particle number density operators in the Hilbert space of the excitations under study. We show how this is done in three cases – nuclear recoils, electron transitions and single phonon excitations. While the first two are relatively simple, and our calculation is mostly a formal rederivation of known results, the phonon calculation presented here contains new aspects. Our general framework allows us to derive single phonon excitation rates for arbitrary SI couplings from first principles, such as phonon excitation by coupling to electrons.

In addition to deriving general rate formulae in this unified framework, we also aim to clarify various conceptual and technical issues in direct detection calculations, and present new results that highlight some previously overlooked experimental prospects. For nuclear recoils, we clarify the range of validity of the standard calculation. For electron transitions, we go beyond the commonly made isotropic approximation. In fact, there exist simple materials with large anisotropies. As an example, we consider boron nitride (BN) with a hexagonal crystal structure, and $\mathcal{O}(\text{eV})$ band gap, and show that the expected rate can vary by $\pm(10-40)\%$ during a day as the DM wind enters from different directions. Such daily modulation signals have been pointed out previously for electron transitions in graphene [188], carbon nanotubes [189] and Dirac materials such as ZrTe_5 and BNQ-TTF [29, 183], and for single phonon excitations in sapphire [28] where they help distinguish signal from background. Here we show that also $\mathcal{O}(\text{eV})$ band gap three dimensional semiconductors, like BN, can exhibit daily modulation.² Finally, for single phonon excitations, we extend the rate calculation to DM heavier than an MeV, where the DM's de Broglie wavelength is shorter than the typical lattice spacing, and Umklapp processes can contribute significantly. We point

¹The idea of treating various detection channels in a common framework was previously advocated in Ref. [141], where the focus was on DM nuggets. Here we follow the same spirit and develop a formalism for calculating direct detection rates for general DM models, assuming a point-like DM particle.

²See also Refs. [190–192] for proposals that take advantage of direction-dependent threshold effects.

out an interesting interplay with nuclear recoils, and demonstrate the complementarity between the two channels. We also compute the phonon production rate for generic couplings to the proton, neutron and electron, extending previous results for dark photon mediated interactions.

We focus on the theoretical framework in the present work; in a companion paper [7], we apply the results presented here to carry out a comparative study of many candidate target materials, and discuss strategies to optimize the search across multiple channels. We also note that there are additional detection channels beyond those we discuss in detail here (e.g., excitation of molecular states [193–195], multi-excitation production in superfluid helium [184–187]), which have been pursued and can be studied in the same framework.

2.2 General Framework for Spin-Independent Dark Matter Scattering

In a direct detection event, a non-relativistic DM particle, χ , deposits a certain amount of energy, and triggers a transition $|i\rangle \rightarrow |f\rangle$ in the target system. We assume the target system is initially prepared in an energy eigenstate $|i\rangle$ (usually the ground state) and, as usual, treat the incoming and outgoing DM particles as momentum eigenstates $|\mathbf{p}\rangle$, $|\mathbf{p}'\rangle$, with $\mathbf{p} = m_\chi \mathbf{v}$, $\mathbf{p}' = \mathbf{p} - \mathbf{q}$. For a given incoming velocity \mathbf{v} and momentum transfer (from the DM to the target) \mathbf{q} , the energy deposition is

$$\omega_{\mathbf{q}} = \frac{1}{2} m_\chi v^2 - \frac{(m_\chi \mathbf{v} - \mathbf{q})^2}{2m_\chi} = \mathbf{q} \cdot \mathbf{v} - \frac{q^2}{2m_\chi}. \quad (2.1)$$

Here and in what follows, we denote $q \equiv |\mathbf{q}|$, where \mathbf{q} is the momentum 3-vector. Note that for given DM mass m_χ , the energy deposition is bounded by the parabola, $\omega_{\mathbf{q}} \leq qv_{\max} - q^2/2m_\chi$, as shown in Fig. 2.1. Applying Fermi's Golden Rule and summing over the final states, we obtain the rate:

$$\Gamma(\mathbf{v}) = \int \frac{d^3q}{(2\pi)^3} \sum_f |\langle \mathbf{p}', f | \delta \hat{H} | \mathbf{p}, i \rangle|^2 2\pi \delta(E_f - E_i - \omega_{\mathbf{q}}), \quad (2.2)$$

where $\delta \hat{H}$ is the interaction Hamiltonian, $|\mathbf{p}, i\rangle = |\mathbf{p}\rangle \otimes |i\rangle$, $|\mathbf{p}', f\rangle = |\mathbf{p}'\rangle \otimes |f\rangle$. We take the quantum states to be unit normalized unless specified otherwise, e.g., $\langle \mathbf{p} | \mathbf{p} \rangle = \langle i | i \rangle = 1$.

The DM part of the matrix element can be evaluated universally at the Born level:

$$\langle \mathbf{p}' | \delta \hat{H} | \mathbf{p} \rangle = \frac{1}{V} \int d^3x e^{i\mathbf{q} \cdot \mathbf{x}} \mathcal{V}(\mathbf{x}) = \frac{1}{V} \tilde{\mathcal{V}}(-\mathbf{q}), \quad (2.3)$$

where V is the total spatial volume, $\mathcal{V}(\mathbf{x})$ is the effective scattering potential felt by the DM, and $\tilde{\mathcal{V}}$ is its Fourier transform. We focus on SI couplings in the present work, in which case

the scattering potential takes the form³

$$\mathcal{V}(\mathbf{x}) = \int d^3x' [n_p(\mathbf{x}')\mathcal{V}_p(\mathbf{x} - \mathbf{x}') + n_n(\mathbf{x}')\mathcal{V}_n(\mathbf{x} - \mathbf{x}') + n_e(\mathbf{x}')\mathcal{V}_e(\mathbf{x} - \mathbf{x}')]. \quad (2.4)$$

Here n_p, n_n, n_e are the proton, neutron and electron number densities in the target, and $\mathcal{V}_p, \mathcal{V}_n, \mathcal{V}_e$ are the respective scattering potentials from a single particle located at the origin. We thus have

$$\tilde{\mathcal{V}}(-\mathbf{q}) = \tilde{n}_p(-\mathbf{q})\tilde{\mathcal{V}}_p(q) + \tilde{n}_n(-\mathbf{q})\tilde{\mathcal{V}}_n(q) + \tilde{n}_e(-\mathbf{q})\tilde{\mathcal{V}}_e(q). \quad (2.5)$$

Note that for SI interactions, $\tilde{\mathcal{V}}_\psi(-\mathbf{q}) = \tilde{\mathcal{V}}_\psi(q)$ ($\psi = p, n, e$) are functions of only the magnitude of \mathbf{q} . In vacuum, they simply coincide with $2 \rightarrow 2$ scattering matrix elements $\mathcal{M}_{\chi\psi}(q)$ familiar from standard quantum field theory calculations. In the target medium, however, they may receive corrections due to screening effects (see Sec. 2.2). We can define (momentum-dependent) effective in-medium couplings f_p, f_n, f_e to account for screening effects, while the corresponding couplings in the vacuum Lagrangian are denoted by f_p^0, f_n^0, f_e^0 . We can write

$$\tilde{\mathcal{V}}_\psi(-\mathbf{q}) = \frac{f_\psi(\mathbf{q})}{f_\psi^0} \mathcal{M}_{\chi\psi}(q) \equiv f_\psi(\mathbf{q}) \mathcal{M}_0(q), \quad (2.6)$$

where $\mathcal{M}_0 = \mathcal{M}_{\chi p}/f_p^0 = \mathcal{M}_{\chi n}/f_n^0 = \mathcal{M}_{\chi e}/f_e^0$ is the vacuum matrix element for DM scattering off any of the constituent particles (proton, neutron or electron) with unit coupling. The total scattering potential is then

$$\tilde{\mathcal{V}}(-\mathbf{q}) = [f_p(\mathbf{q})\tilde{n}_p(-\mathbf{q}) + f_n(\mathbf{q})\tilde{n}_n(-\mathbf{q}) + f_e(\mathbf{q})\tilde{n}_e(-\mathbf{q})] \mathcal{M}_0(q). \quad (2.7)$$

Let us rewrite this equation as follows:

$$\tilde{\mathcal{V}}(-\mathbf{q}) = \mathcal{M}_{\chi n}(q) \left[\frac{f_p(\mathbf{q})\tilde{n}_p(-\mathbf{q}) + f_n(\mathbf{q})\tilde{n}_n(-\mathbf{q}) + f_e(\mathbf{q})\tilde{n}_e(-\mathbf{q})}{f_n^0} \right] \quad (2.8)$$

$$= \mathcal{M}_{\chi e}(q) \left[\frac{f_p(\mathbf{q})\tilde{n}_p(-\mathbf{q}) + f_n(\mathbf{q})\tilde{n}_n(-\mathbf{q}) + f_e(\mathbf{q})\tilde{n}_e(-\mathbf{q})}{f_e^0} \right]. \quad (2.9)$$

Depending on the DM model and the process under consideration, we will factor out either $\mathcal{M}_{\chi n}$ or $\mathcal{M}_{\chi e}$, and define a target form factor, $\mathcal{F}_T(\mathbf{q})$, composed of contributions from protons, neutrons and electrons, as the quantity in brackets. In other words, we have

$$\tilde{\mathcal{V}}(-\mathbf{q}) = \mathcal{M}(q) \mathcal{F}_T(\mathbf{q}), \quad (2.10)$$

³More generally, DM interactions can be classified by nonrelativistic effective operators [55, 60, 196, 197]. The SI interaction we focus on here is the leading operator if generated without velocity suppression. Other operators result in spin and/or velocity dependence of the scattering potential $\mathcal{V}(\mathbf{x})$, and may be probed via additional detection channels beyond those considered in this work. For example, DM coupling to the electron spin can excite magnons in solid state systems with magnetic order [8]. We leave a general effective field theory study of light DM direct detection to future work.

where \mathcal{M} stands for $\mathcal{M}_{\chi n}$ or $\mathcal{M}_{\chi e}$. We can further factor out the q dependence of \mathcal{M} , which can only come from the mediator propagator for tree-level scattering:

$$\mathcal{M}(q) = \mathcal{M}(q_0) \mathcal{F}_{\text{med}}(q), \quad (2.11)$$

$$\mathcal{F}_{\text{med}}(q) = \begin{cases} 1 & \text{(heavy mediator),} \\ (q_0/q)^2 & \text{(light mediator).} \end{cases} \quad (2.12)$$

The reference momentum transfer is conventionally chosen to be $q_0 = m_\chi v_0$ (with v_0 the DM's velocity dispersion) for DM-neutron scattering, and $q_0 = \alpha m_e$ for DM-electron scattering.

The factorization in Eq. (2.10) is a key component of the formalism. From the target-independent particle-level matrix element \mathcal{M} , we define the reference cross sections:

$$\bar{\sigma}_n \equiv \frac{\mu_{\chi n}^2}{\pi} \overline{|\mathcal{M}_{\chi n}(q_0)|^2}_{q_0=m_\chi v_0}, \quad \bar{\sigma}_e \equiv \frac{\mu_{\chi e}^2}{\pi} \overline{|\mathcal{M}_{\chi e}(q_0)|^2}_{q_0=\alpha m_e}, \quad (2.13)$$

where μ denotes the reduced mass. These coincide with the total cross sections of DM-neutron and DM-electron scattering in the heavy mediator case. On the other hand, \mathcal{F}_T is target specific, from which we define the *dynamic structure factor*:⁴

$$S(\mathbf{q}, \omega) \equiv \frac{1}{V} \sum_f |\langle f | \mathcal{F}_T(\mathbf{q}) | i \rangle|^2 2\pi \delta(E_f - E_i - \omega), \quad (2.14)$$

which encapsulates response of the target to DM couplings to the proton, neutron and electron. Combining the two parts, we have

$$\Gamma(\mathbf{v}) = \frac{\pi \bar{\sigma}}{\mu^2} \int \frac{d^3 q}{(2\pi)^3} \mathcal{F}_{\text{med}}^2(q) S(\mathbf{q}, \omega_{\mathbf{q}}), \quad (2.15)$$

where $\bar{\sigma}$, μ , again, denote either $\bar{\sigma}_n, \mu_{\chi n}$ or $\bar{\sigma}_e, \mu_{\chi e}$.

Let us highlight the following regarding the dynamic structure factor $S(\mathbf{q}, \omega)$.

- $S(\mathbf{q}, \omega)$ captures the target's response to an energy-momentum deposition (\mathbf{q}, ω) .
- $S(\mathbf{q}, \omega)$ depends on the distribution of constituent particles p, n, e in the target system via $\tilde{n}_p, \tilde{n}_n, \tilde{n}_e$, which in turn depends on the nucleus types and electron wavefunctions. It is therefore *target material specific*.
- $S(\mathbf{q}, \omega)$ also depends on the active degrees of freedom in the target system via the choice of $|f\rangle$, which in turn determines how $\mathcal{F}_T(\mathbf{q})$ should be quantized. It is therefore *excitation (detection channel) specific*.

⁴Here we adopt a slightly different normalization convention compared to Ref. [141]. The right hand side of Eq. (2.14) here is identified with $\frac{2\pi}{\Omega} S(\mathbf{q}, \omega)$ in Ref. [141], where Ω is the primitive cell volume.

- If only one of the constituent particles p, n, e is responsible for the transitions $|i\rangle \rightarrow |f\rangle$, $S(\mathbf{q}, \omega)$ is DM model independent. Otherwise it depends on ratios (but not the overall strength) of the couplings f_p^0, f_n^0, f_e^0 .
- For any given DM mass m_χ and incoming velocity \mathbf{v} , only a slice in the (\mathbf{q}, ω) space, $\omega = \omega_{\mathbf{q}}$, is probed in the scattering process. The parabolic boundary of kinematic region for each m_χ in Fig. 2.1 is the envelope of these slices for all \mathbf{v} directions for fixed magnitude of \mathbf{v} .

Finally, to obtain the total rate per target mass, we average over the DM's initial velocity, multiply by the number of DM particles in the detector, and divide by the detector mass, giving

$$R = \frac{1}{\rho_T m_\chi} \int d^3v f_\chi(\mathbf{v}) \Gamma(\mathbf{v}), \quad (2.16)$$

where ρ_T is the target mass density, ρ_χ is the local DM energy density, and f_χ is the DM's velocity distribution in the target rest frame. A common choice for f_χ is a truncated Maxwell-Boltzmann (MB) distribution boosted by the Earth's velocity with respect to the galactic rest frame,

$$f_\chi^{\text{MB}}(\mathbf{v}) = \frac{1}{N_0} e^{-(\mathbf{v}+\mathbf{v}_e)^2/v_0^2} \Theta(v_{\text{esc}} - |\mathbf{v} + \mathbf{v}_e|), \quad (2.17)$$

$$N_0 = \pi^{3/2} v_0^2 \left[v_0 \text{erf}(v_{\text{esc}}/v_0) - \frac{2v_{\text{esc}}}{\sqrt{\pi}} \exp(-v_{\text{esc}}^2/v_0^2) \right]. \quad (2.18)$$

In the calculations presented in this paper, we take $\rho_\chi = 0.4 \text{ GeV/cm}^3$, $v_0 = 230 \text{ km/s}$, $v_{\text{esc}} = 600 \text{ km/s}$, $v_e = 240 \text{ km/s}$.

In addition to the total rate, it is often useful to know the differential rate with respect to the energy deposition onto the target ω . This simply requires inserting delta functions into the integrals to pick out the contributions with $\omega = \omega_{\mathbf{q}}$:

$$\frac{d\Gamma}{d\omega} = \frac{\pi\bar{\sigma}}{\mu^2} \int \frac{d^3q}{(2\pi)^3} \mathcal{F}_{\text{med}}^2(q) S(\mathbf{q}, \omega_{\mathbf{q}}) \delta(\omega - \omega_{\mathbf{q}}), \quad (2.19)$$

$$\frac{dR}{d\omega} = \frac{1}{\rho_T m_\chi} \int d^3v f_\chi(\mathbf{v}) \frac{d\Gamma}{d\omega}. \quad (2.20)$$

To summarize, we have the following algorithm for computing the rate for a given detection channel.

- First, identify the initial and final states $|i\rangle, |f\rangle$ according to the type of excitation.

- Next, quantize $\mathcal{F}_T(\mathbf{q})$ in terms of the relevant degrees of freedom such that it acts on the target Hilbert space to induce the transitions $|i\rangle \rightarrow |f\rangle$.
- Then, compute the transition matrix element $\langle f|\mathcal{F}_T(\mathbf{q})|i\rangle$, and thus the dynamic structure factor $S(\mathbf{q}, \omega)$ via Eq. (2.14).
- Finally, obtain the (differential) rate via Eqs. (2.15)-(2.20).

We will carry out this procedure for each detection channel in the next three sections. Before doing so, let us discuss some technical details regarding the phase space integration and in-medium effects.

Phase Space Integration

We see from Eqs. (2.15)-(2.20) that once the dynamic structure factor $S(\mathbf{q}, \omega)$ is known, we need to perform a six-dimensional integral over \mathbf{v} and \mathbf{q} to obtain the event rate R . The integration gives familiar results in the special case of isotropic target response, but is more complicated in the general anisotropic case. We now discuss the two cases in turn.

a) Special case: isotropic target response.

If $|\langle f|\mathcal{F}_T(\mathbf{q})|i\rangle|^2 = |\langle f|\mathcal{F}_T(q)|i\rangle|^2$, as is the case for nuclear recoils, the only dependence on the direction of \mathbf{q} is from the δ -function,

$$\delta(E_f - E_i - \omega_{\mathbf{q}}) = \frac{1}{qv} \delta\left(\cos\theta_{qv} - \frac{q}{2m_\chi v} - \frac{E_f - E_i}{qv}\right), \quad (2.21)$$

where θ_{qv} is the angle between \mathbf{q} and \mathbf{v} . Integrating over the angular variables, we have

$$\Gamma(\mathbf{v}) = \frac{\bar{\sigma}}{2\mu^2 v} \int q dq \mathcal{F}_{\text{med}}^2(q) \frac{1}{V} \sum_f |\langle f|\mathcal{F}_T(q)|i\rangle|^2 \Theta(v - v_{\min}(q, E_f - E_i)), \quad (2.22)$$

where

$$v_{\min}(q, \omega) = \frac{q}{2m_\chi} + \frac{\omega}{q}. \quad (2.23)$$

The velocity integral then gives

$$R = \frac{1}{\rho_T} \frac{\rho_\chi}{m_\chi} \frac{\bar{\sigma}}{2\mu^2} \int q dq \mathcal{F}_{\text{med}}^2(q) \frac{1}{V} \sum_f |\langle f|\mathcal{F}_T(q)|i\rangle|^2 \eta(v_{\min}(q, E_f - E_i)), \quad (2.24)$$

where

$$\eta(v_{\min}) = \int d^3v \frac{f_\chi(\mathbf{v})}{v} \Theta(v - v_{\min}). \quad (2.25)$$

These results are familiar from the standard nuclear recoil calculation [198], and have also been used in previous electron transition calculations, where the target response has been assumed to be isotropic. Note that they hold for any DM velocity distribution $f_\chi(\mathbf{v})$. In the case of the MB distribution in Eq. (2.17), the η function can be evaluated analytically, giving

$$\eta_{\text{MB}}(v_{\text{min}}) = \begin{cases} \frac{\pi v_0^2}{2N_0} \left\{ \sqrt{\pi} \frac{v_0}{v_e} \left[\text{erf}\left(\frac{v_{\text{min}}+v_e}{v_0}\right) - \text{erf}\left(\frac{v_{\text{min}}-v_e}{v_0}\right) \right] - 4 \exp\left(-\frac{v_{\text{esc}}^2}{v_0^2}\right) \right\} & \text{if } v_{\text{min}} < v_{\text{esc}} - v_e, \\ \frac{\pi v_0^2}{2N_0} \left\{ \sqrt{\pi} \frac{v_0}{v_e} \left[\text{erf}\left(\frac{v_{\text{esc}}}{v_0}\right) - \text{erf}\left(\frac{v_{\text{min}}-v_e}{v_0}\right) \right] - 2 \left(\frac{v_{\text{esc}}-v_{\text{min}}+v_e}{v_e}\right) \exp\left(-\frac{v_{\text{esc}}^2}{v_0^2}\right) \right\} & \text{if } v_{\text{esc}} - v_e < v_{\text{min}} < v_{\text{esc}} + v_e, \\ 0 & \text{if } v_{\text{min}} > v_{\text{esc}} + v_e. \end{cases} \quad (2.26)$$

We see that five of the six integrals have been done analytically, and we are left only with a one-dimensional integral over q (which can also be done analytically in the case of nuclear recoils).

b) General case: anisotropic target response. Generally, crystal targets are not fully isotropic, as the crystal structures break rotation symmetries. This implies that, for a terrestrial detector, since the DM wind comes in from different directions at different times of the day, there can be daily modulation in the detection rate. While the existence of this effect is well-known [19, 33, 64], it has been calculated only recently in the contexts of single phonon excitations [28] and electron transitions in Dirac materials [29, 183], where the energy deposition is $\mathcal{O}(\text{meV})$. In Sec. 2.4, we calculate this effect for the first time in electron transitions in an $\mathcal{O}(\text{eV})$ gap target.

When $|\langle f | \mathcal{F}_T(\mathbf{q}) | i \rangle|^2$ depends on the direction of \mathbf{q} , the six-dimensional integral generally does not admit a simple analytical solution. To proceed, we first evaluate the velocity integral and define [28, 199]

$$g(\mathbf{q}, \omega) \equiv \int d^3v f_\chi(\mathbf{v}) 2\pi\delta(\omega - \omega_{\mathbf{q}}). \quad (2.27)$$

The rate can then be written in terms of this $g(\mathbf{q}, \omega)$ function as

$$R = \frac{1}{\rho_T} \frac{\rho_\chi}{m_\chi} \frac{\pi\bar{\sigma}}{\mu^2} \int \frac{d^3q}{(2\pi)^3} \mathcal{F}_{\text{med}}^2(q) \frac{1}{V} \sum_f |\langle f | \mathcal{F}_T(\mathbf{q}) | i \rangle|^2 g(\mathbf{q}, E_f - E_i). \quad (2.28)$$

For general velocity distributions f_χ , we still have to evaluate a six-dimensional integral, which is a numerically intensive task. However, for the commonly assumed MB distribution,

Eq. (2.17), the $g(\mathbf{q}, \omega)$ function can be evaluated analytically, giving

$$g(\mathbf{q}, \omega) = \frac{2\pi^2 v_0^2}{N_0 q} \left[\exp(-v_-^2/v_0^2) - \exp(-v_{\text{esc}}^2/v_0^2) \right], \quad (2.29)$$

where

$$v_- = \min \left\{ \frac{1}{q} \left| \mathbf{q} \cdot \mathbf{v}_e + \frac{q^2}{2m_\chi} + \omega \right|, v_{\text{esc}} \right\}. \quad (2.30)$$

Thus, only the three-dimensional integral over \mathbf{q} needs to be done numerically (in addition to other integrals that may be encountered in the evaluation of the dynamic structure factor).

In-Medium Effects

In the case of a vector mediator, in-medium effects can cause screening and affect direct detection rates. They must be taken into account when deriving the target response $\mathcal{F}_T(\mathbf{q})$ (and hence the dynamical structure factor $S(\mathbf{q}, \omega)$) when present. While the treatment of in-medium effects has been discussed in various contexts [10, 29, 144, 182], we review it here for completeness. In particular, we derive the screening factors $f_\psi(\mathbf{q})/f_\psi^0$ ($\psi = p, n, e$) in this subsection.

For nonrelativistic systems relevant for direct detection that we focus on here, only electrons can contribute significantly to screening when the energy deposition is above phonon frequencies ($\omega \gtrsim \mathcal{O}(100 \text{ meV})$, corresponding to $m_\chi \gtrsim \mathcal{O}(100 \text{ keV})$), as nuclei are too heavy to respond. At lower frequencies that match energy depositions in phonon excitation processes, there is additional screening in an ionic (polar) crystal due to relative motion of ions. However, as we will see in Sec. 2.5, the ions' response should be included in the source term in Maxwell's equations in order to be quantized in terms of phonon modes. Thus, also in this case, we consider only electron contributions to in-medium effects.⁵

Consider a vector mediator A' , and suppose the vacuum Lagrangian takes the form

$$\begin{aligned} \mathcal{L} = & -\frac{1}{4} F_{\mu\nu} F^{\mu\nu} + e J_p^\mu A_\mu - e J_e^\mu A_\mu \\ & -\frac{1}{4} F'_{\mu\nu} F'^{\mu\nu} + \frac{1}{2} m_{A'}^2 A'_\mu A'^\mu + g_\chi J_\chi^\mu A'_\mu \\ & + (f_p^0 J_p^\mu + f_n^0 J_n^\mu + f_e^0 J_e^\mu) A'_\mu, \end{aligned} \quad (2.31)$$

where $J_\psi^\mu = \bar{\psi} \gamma^\mu \psi$ ($\psi = p, n, e$). Here the first line is standard electromagnetism, the second line is the dark sector Lagrangian, and the third line contains A' couplings to SM particles. We assume $|f_\psi^0| \ll 1$, and consistently keep terms only at linear order in these couplings. Because the electron current J_e^μ couples to the linear combination $A_\mu + \kappa A'_\mu$, with $\kappa = -f_e^0/e$,

⁵In-medium effects are also important when deriving astrophysical and cosmological constraints on vector mediators [10, 42, 46], where other SM particles may be relevant.

as opposed to just A_μ , the in-medium photon self-energy $\Pi^{\mu\nu}(\mathbf{q})$ implies the following terms in the momentum space quantum effective action,

$$\frac{1}{2} \Pi^{\mu\nu} (A_\mu + \kappa A'_\mu) (A_\nu + \kappa A'_\nu) = \frac{1}{2} \Pi^{\mu\nu} A_\mu A_\nu + \kappa \Pi^{\mu\nu} A_\mu A'_\nu + \mathcal{O}(\kappa^2). \quad (2.32)$$

As in Ref. [29], we can project $\Pi^{\mu\nu}$ onto the three polarizations,

$$\epsilon_L^\mu = \frac{1}{\sqrt{q^\alpha q_\alpha}} (q, \omega \hat{\mathbf{q}}), \quad \epsilon_\pm^\mu = \frac{1}{\sqrt{2}} (0, \hat{\mathbf{e}}_\perp \pm i(\hat{\mathbf{q}} \times \hat{\mathbf{e}}_\perp)), \quad (2.33)$$

(where $\hat{\mathbf{q}} = \mathbf{q}/|\mathbf{q}|$, and $\hat{\mathbf{e}}_\perp$ is a unit vector perpendicular to \mathbf{q}), and diagonalize the 3×3 matrix

$$\mathcal{K}_{\lambda\lambda'} \equiv -\epsilon_\lambda^{\mu*} \Pi_{\mu\nu} \epsilon_{\lambda'}^\nu, \quad (2.34)$$

to find the canonical modes. It is worth noting that the polarization vectors satisfy

$$g_{\mu\nu} \epsilon_\lambda^{\mu*} \epsilon_{\lambda'}^\nu = -\delta_{\lambda\lambda'}, \quad \sum_\lambda \epsilon_\lambda^\mu \epsilon_{\lambda'}^{\nu*} = -\left(g^{\mu\nu} - \frac{q^\mu q^\nu}{q^\alpha q_\alpha} \right). \quad (2.35)$$

As a result, in the vacuum limit where $\Pi_{\mu\nu} = (g_{\mu\nu} - q_\mu q_\nu / (q^\alpha q_\alpha)) \Pi$ and the photon propagator is proportional to $\frac{1}{q^\alpha q_\alpha - \Pi}$, we have $\mathcal{K}_{\lambda\lambda'} = \Pi \delta_{\lambda\lambda'}$. In an isotropic medium,

$$\Pi^{\mu\nu} = -\Pi_T \sum_{\lambda=\pm} \epsilon_\lambda^\mu \epsilon_{\lambda'}^{\nu*} - \Pi_L \epsilon_L^\mu \epsilon_L^{\nu*}, \quad \mathcal{K} = \text{diag}(\Pi_T, \Pi_T, \Pi_L), \quad (2.36)$$

and the photon propagators are proportional to $\frac{1}{q^\alpha q_\alpha - \Pi_{T,L}}$. Generically, for an anisotropic medium, we need to simultaneously rotate A and A' into a polarization basis where \mathcal{K} is diagonal. In this basis, the quadratic part of the effective action can be diagonalized for each polarization by

$$A_\mu = \tilde{A}_\mu + \kappa \frac{\Pi}{m_{A'}^2 - \Pi} \tilde{A}'_\mu, \quad A'_\mu = \tilde{A}'_\mu - \kappa \frac{\Pi}{m_{A'}^2 - \Pi} \tilde{A}_\mu, \quad (2.37)$$

where Π is an eigenvalue of \mathcal{K} . In the \tilde{A}, \tilde{A}' basis, the propagators are proportional to $\frac{1}{q^\alpha q_\alpha - \Pi}$ and $\frac{1}{q^\alpha q_\alpha - m_{A'}^2}$, respectively, and the interactions in Eq. (2.31) read

$$\begin{aligned} & \left[e(J_p^\mu - J_e^\mu) - \frac{\Pi}{m_{A'}^2 - \Pi} \kappa g_\chi J_\chi^\mu \right] \tilde{A}_\mu \\ & + \left[g_\chi J_\chi^\mu + \left(f_p^0 - \frac{\Pi}{m_{A'}^2 - \Pi} f_e^0 \right) J_p^\mu + f_n^0 J_n^\mu + \frac{m_{A'}^2}{m_{A'}^2 - \Pi} f_e^0 J_e^\mu \right] \tilde{A}'_\mu. \end{aligned} \quad (2.38)$$

Dark matter scattering is mediated by both \tilde{A} and \tilde{A}' . Taking both into account, we obtain the following effective interaction:

$$\begin{aligned}
& g_\chi J_{\chi\mu} \left\{ -\frac{1}{q^\alpha q_\alpha - \Pi} \frac{\Pi}{m_{A'}^2 - \Pi} \kappa e (J_p^\mu - J_e^\mu) \right. \\
& \quad \left. + \frac{1}{q^\alpha q_\alpha - m_{A'}^2} \left[\left(f_p^0 - \frac{\Pi}{m_{A'}^2 - \Pi} f_e^0 \right) J_p^\mu + f_n^0 J_n^\mu + \frac{m_{A'}^2}{m_{A'}^2 - \Pi} f_e^0 J_e^\mu \right] \right\} \\
&= \frac{1}{q^\alpha q_\alpha - m_{A'}^2} g_\chi J_{\chi\mu} \left\{ \left[f_p^0 + \left(1 - \frac{q^\alpha q_\alpha}{q^\alpha q_\alpha - \Pi} \right) f_e^0 \right] J_p^\mu \right. \\
& \quad \left. + f_n^0 J_n^\mu + \frac{q^\alpha q_\alpha}{q^\alpha q_\alpha - \Pi} f_e^0 J_e^\mu \right\} \tag{2.39}
\end{aligned}$$

$$= \frac{1}{q^\alpha q_\alpha - m_{A'}^2} g_\chi J_{\chi\mu} \left[\frac{q^\alpha q_\alpha}{q^\alpha q_\alpha - \Pi} f_e^0 (J_e^\mu - J_p^\mu) + (f_p^0 + f_e^0) J_p^\mu + f_n^0 J_n^\mu \right] \tag{2.40}$$

From the last equation, it is clear that the current A' couples to contains a screened component and an unscreened component: $f_p^0 J_p^\mu + f_n^0 J_n^\mu + f_e^0 J_e^\mu = f_e^0 (J_e^\mu - J_p^\mu) + [(f_p^0 + f_e^0) J_p^\mu + f_n^0 J_n^\mu]$. The first term, which is proportional to the electromagnetic current, gets screened by a factor of $\frac{q^\alpha q_\alpha}{q^\alpha q_\alpha - \Pi}$, whereas the second term is unaffected.

In the special case of a dark photon that kinetically mixes with the SM photon, Eq. (2.31) follows from diagonalizing the kinetic terms, and κ is equal to the kinetic mixing parameter. In this case, $f_p^0 = -f_e^0 = \kappa e$, $f_n^0 = 0$, and the DM interaction is maximally screened. In contrast, a $U(1)_{B-L}$ gauge boson has $f_p^0 = f_n^0 = -f_e^0$, and the coupling to neutrons is not screened. As a final example, a hadrophobic A' has $f_p^0 = f_n^0 = 0$, resulting in an unscreened DM coupling to protons (which originates from the A - A' mixing).

The screening factor $\frac{q^\alpha q_\alpha}{q^\alpha q_\alpha - \Pi}$ can be expressed in terms of the dielectric matrix $\boldsymbol{\varepsilon}(\mathbf{q}, \omega)$ by solving the following set of equations for $\Pi^{\mu\nu}$ [29, 182]:

$$J^\mu = -\Pi^{\mu\nu} A_\nu, \tag{2.41}$$

$$J^i = \sigma^i_j E^j = \sigma^i_j (i\omega A^j - iq^j A^0), \tag{2.42}$$

$$\boldsymbol{\sigma} = \boldsymbol{\sigma}^T = i\omega(\mathbb{1} - \boldsymbol{\varepsilon}). \tag{2.43}$$

Note that the three-dimensional quantities are defined by $\boldsymbol{\sigma} = \sigma^i_j$, $\mathbb{1} = \delta^i_j$, $\boldsymbol{\varepsilon} = \varepsilon^i_j$. We obtain the following solution:

$$\Pi^{\mu\nu} = \begin{pmatrix} \Pi_{00} & \boldsymbol{\Pi}_0 \\ \boldsymbol{\Pi}_0 & -\boldsymbol{\Pi} \end{pmatrix}, \tag{2.44}$$

$$\Pi_{00} = \frac{i}{\omega} \mathbf{q} \cdot \boldsymbol{\sigma} \cdot \mathbf{q}, \quad \boldsymbol{\Pi}_0 \equiv \Pi_0^i = i\boldsymbol{\sigma} \cdot \mathbf{q}, \quad \boldsymbol{\Pi} \equiv \Pi^i_j = -i\omega \boldsymbol{\sigma}. \tag{2.45}$$

Projecting $\Pi^{\mu\nu}$ onto polarization components, we obtain:

$$\mathcal{K}_{LL} = q^\alpha q_\alpha (1 - \hat{\mathbf{q}} \cdot \boldsymbol{\varepsilon} \cdot \hat{\mathbf{q}}), \quad \mathcal{K}_{L\pm} = \mathcal{K}_{L\mp} = -\omega \sqrt{q^\alpha q_\alpha} \hat{\mathbf{q}} \cdot \boldsymbol{\varepsilon} \cdot \boldsymbol{\epsilon}_\pm, \quad (2.46)$$

$$\mathcal{K}_{\pm\pm} = \omega^2 (1 - \boldsymbol{\epsilon}_\mp \cdot \boldsymbol{\varepsilon} \cdot \boldsymbol{\epsilon}_\pm), \quad \mathcal{K}_{\mp\pm} = -\omega^2 \boldsymbol{\epsilon}_\pm \cdot \boldsymbol{\varepsilon} \cdot \boldsymbol{\epsilon}_\pm. \quad (2.47)$$

We can see explicitly that in the isotropic limit, $\boldsymbol{\varepsilon} \propto \mathbb{1}$, so $\mathcal{K}_{L\pm} = \mathcal{K}_{\mp\pm} = 0$, and \mathcal{K}_{LL} , $\mathcal{K}_{\pm\pm}$ are identified as Π_L , Π_T , respectively. In this case, $\mathcal{K} = \text{diag}(\Pi_L, \Pi_T, \Pi_T)$, and the familiar relations

$$\Pi_L = q^\alpha q_\alpha (1 - \varepsilon), \quad \Pi_T = \omega^2 (1 - \varepsilon) \quad (2.48)$$

are reproduced. Beyond the isotropic limit, in general one has to diagonalize the \mathcal{K} matrix as discussed above. However, assuming anisotropies are not large, the calculation is simplified in the case of nonrelativistic scattering. Here, the currents involved (J_χ^μ , J_e^μ , etc.) have velocity suppressed spatial components, so the dominant contribution comes from the polarization that is almost longitudinal, for which $\Pi \simeq \mathcal{K}_{LL}$ up to small corrections. As a result, the screening factor in Eq. (2.40) becomes

$$\frac{q^\alpha q_\alpha}{q^\alpha q_\alpha - \Pi} \simeq \frac{q^2}{\mathbf{q} \cdot \boldsymbol{\varepsilon} \cdot \mathbf{q}}. \quad (2.49)$$

Now it is straightforward to read off the screening of DM couplings from Eq. (2.39):

$$f_p(\mathbf{q}) = f_p^0 + \left(1 - \frac{q^2}{\mathbf{q} \cdot \boldsymbol{\varepsilon} \cdot \mathbf{q}}\right) f_e^0, \quad f_n(\mathbf{q}) = f_n^0, \quad f_e(\mathbf{q}) = \frac{q^2}{\mathbf{q} \cdot \boldsymbol{\varepsilon} \cdot \mathbf{q}} f_e^0. \quad (2.50)$$

In what follows, we will often drop the argument \mathbf{q} and just write f_p, f_n, f_e for simplicity.

To close this subsection, we comment that in-medium screening affects different channels differently. Nuclear recoils happen at high enough momentum transfer where $\boldsymbol{\varepsilon}$ can be approximated as unity, so $f_\psi \simeq f_\psi^0$. For electron transitions, the situation depends on the band gap. For atoms, insulators and semiconductors with $\mathcal{O}(\text{eV})$ or larger band gaps, $\boldsymbol{\varepsilon}$ approaches unity when $q \gtrsim 2\pi/a \sim \mathcal{O}(\text{keV})$ [65], which is the range for DM scattering kinematics. For smaller q , the full $\boldsymbol{\varepsilon}(q)$ can be fitted to experimental measurements or calculated using advanced electronic structure techniques. For small-gap systems such as superconductors and Dirac semi-metals, it is important to keep the full energy-momentum dependence in $\boldsymbol{\varepsilon}(\mathbf{q}, \omega)$. For example, in a (super)conductor, $\boldsymbol{\varepsilon} \sim \lambda_{\text{TF}}^2/q^2$ at low q , where $\lambda_{\text{TF}} \sim \mathcal{O}(\text{keV})$ is the Thomas-Fermi screening parameter, resulting in significant screening [182]. In contrast, in a Dirac semi-metal, $\boldsymbol{\varepsilon}$ approaches a constant at low q , so sensitivity to dark photon mediated scattering (and also dark photon absorption) is much stronger [29, 144]. For phonon excitations, screening from electrons should also be accounted for, as we discuss in Sec. 2.5.

2.3 Nuclear Recoils

We now apply the general framework of the previous section to the case of nuclear recoils and reproduce familiar results. For simplicity we shall first assume only one type of nucleus is present, with proton number Z and atomic mass number A , and later generalize to the case of multiple nucleus types with non-degenerate $\{Z_N\}, \{A_N\}$.

To begin, we assume the nuclei do not interact with each other, so the Hilbert space of the target system, which contains $\rho_T V/m_N$ nuclei, is a direct product of $\rho_T V/m_N$ single nucleus Hilbert spaces. We will discuss the validity of this standard assumption in Sec. 2.3. The target system is prepared in the initial state

$$|i\rangle = \prod_{J=1}^{\rho_T V/m_N} |\mathbf{k}_i\rangle_J = |\mathbf{k}_i\rangle_1 \otimes |\mathbf{k}_i\rangle_2 \otimes \dots \quad (2.51)$$

with $\mathbf{k}_i = \mathbf{0}$. In the final state $|f\rangle$, one of the $|\mathbf{k}_i\rangle_J$'s is replaced by $|\mathbf{k}_f\rangle_J$ with $\mathbf{k}_f \neq \mathbf{0}$. We can write these states in terms of nucleus creation operators:

$$|\mathbf{k}_i\rangle_J = V^{-1/2} \hat{b}_{\mathbf{k}_i}^\dagger |0\rangle_J, \quad |\mathbf{k}_f\rangle_J = V^{-1/2} \hat{b}_{\mathbf{k}_f}^\dagger |0\rangle_J. \quad (2.52)$$

As usual, we have the canonical commutation relations $[\hat{b}_{\mathbf{k}}, \hat{b}_{\mathbf{k}'}^\dagger] = (2\pi)^3 \delta^3(\mathbf{k} - \mathbf{k}')$ or $\{\hat{b}_{\mathbf{k}}, \hat{b}_{\mathbf{k}'}^\dagger\} = (2\pi)^3 \delta^3(\mathbf{k} - \mathbf{k}')$, etc.

Now we need to quantize

$$\mathcal{F}_T(\mathbf{q}) = \frac{1}{f_n} [f_p \tilde{n}_p(-\mathbf{q}) + f_n \tilde{n}_n(-\mathbf{q}) + f_e \tilde{n}_e(-\mathbf{q})] \quad (2.53)$$

in terms of nucleus creation and annihilation operators \hat{b}^\dagger, \hat{b} . Obviously, the electron coupling does not contribute, so we drop the last term. The proton and neutron number densities, on the other hand, can be related to the nucleus number density n_N , if we assume elastic scattering (no transition between nuclear states):

$$n_{p,n}(\mathbf{x}') = \int d^3 x'' n_N(\mathbf{x}'') n_{p,n}^0(\mathbf{x}' - \mathbf{x}''), \quad (2.54)$$

where $n_{p,n}^0$ are the proton and neutron number densities around a single nucleus at the origin. Therefore,

$$\mathcal{F}_T(\mathbf{q}) = \frac{f_p \tilde{n}_p^0(-\mathbf{q}) + f_n \tilde{n}_n^0(-\mathbf{q})}{f_n} \tilde{n}_N(-\mathbf{q}) \equiv \frac{f_N}{f_n} F_N(\mathbf{q}) \tilde{n}_N(-\mathbf{q}), \quad (2.55)$$

where $f_N \equiv f_p Z + f_n (A - Z)$, the DM-nucleus coupling in the $q \rightarrow 0$ limit (where DM interacts with all nucleons coherently). $F_N(\mathbf{q})$ is a nuclear form factor that deviates from

unity only for q above the inverse nucleus radius. A commonly used form factor is the Helm form factor [200],

$$F_N(\mathbf{q}) = \frac{3j_1(qr_n)}{qr_n} e^{-(qs)^2/2} = 1 - \frac{(qr_n)^2}{10} - \frac{(qs)^2}{2} + \mathcal{O}(q^4), \quad (2.56)$$

where $r_n \simeq 1.14 A^{1/3}$ fm, $s \simeq 0.9$ fm. We can thus write $\mathcal{F}_T(\mathbf{q})$ in terms of \hat{b}^\dagger, \hat{b} via

$$\tilde{n}_N(-\mathbf{q}) = \int d^3x e^{i\mathbf{q}\cdot\mathbf{x}} \hat{b}_x^\dagger \hat{b}_x = \int \frac{d^3k'}{(2\pi)^3} \frac{d^3k}{(2\pi)^3} (2\pi)^3 \delta^3(\mathbf{k}' - \mathbf{k} - \mathbf{q}) \hat{b}_{\mathbf{k}'}^\dagger \hat{b}_{\mathbf{k}}. \quad (2.57)$$

To obtain the dynamic structure factor, we evaluate the matrix element,

$$\begin{aligned} {}_J\langle \mathbf{k}_f | \tilde{n}_N(-\mathbf{q}) | \mathbf{k}_i \rangle_J &= \frac{1}{V} \int \frac{d^3k'}{(2\pi)^3} \frac{d^3k}{(2\pi)^3} (2\pi)^3 \delta^3(\mathbf{k}' - \mathbf{k} - \mathbf{q}) \langle 0 | \hat{b}_{\mathbf{k}_f}^\dagger \hat{b}_{\mathbf{k}'}^\dagger \hat{b}_{\mathbf{k}} \hat{b}_{\mathbf{k}_i}^\dagger | 0 \rangle \\ &= \frac{(2\pi)^3}{V} \delta^3(\mathbf{k}_f - \mathbf{k}_i - \mathbf{q}), \end{aligned} \quad (2.58)$$

and sum over final states, which amounts to summing over the scattered nucleus J (simply multiplying by $\rho_T V / m_N$) and integrating over the final momentum $V \int d^3k_f / (2\pi)^3$. Therefore,

$$\begin{aligned} S(\mathbf{q}, \omega) &= 2\pi \frac{\rho_T}{m_N} \frac{f_N^2}{f_n^2} F_N^2(\mathbf{q}) \cdot V \int \frac{d^3k_f}{(2\pi)^3} \left[\frac{(2\pi)^3}{V} \delta^3(\mathbf{k}_f - \mathbf{k}_i - \mathbf{q}) \right]^2 \delta\left(\omega - \frac{q^2}{2m_N}\right) \\ &= 2\pi \frac{\rho_T}{m_N} \frac{f_N^2}{f_n^2} F_N^2(\mathbf{q}) \delta\left(\omega - \frac{q^2}{2m_N}\right), \end{aligned} \quad (2.59)$$

where we have regulated the delta function by $\frac{(2\pi)^3}{V} \delta^3(\mathbf{0}) = \frac{1}{V} \int d^3x e^{i\mathbf{0}\cdot\mathbf{x}} = 1$.

We can now reproduce the familiar results for the differential rate. Assuming the nuclear form factor is isotropic, $F_N(\mathbf{q}) = F_N(q)$, as is the case for the Helm form factor in Eq. (2.56), we can apply Eq. (2.24) and obtain

$$\frac{dR}{d\omega} = \frac{\rho_\chi}{m_\chi} \frac{\bar{\sigma}_n}{2\mu_{\chi n}^2} \frac{f_N^2}{f_n^2} \int dq F_N^2 \mathcal{F}_{\text{med}}^2 \eta(v_{\text{min}}) \frac{q}{m_N} \delta\left(\omega - \frac{q^2}{2m_N}\right) \quad (2.60)$$

$$= \frac{\rho_\chi}{m_\chi} \frac{\bar{\sigma}_n}{2\mu_{\chi n}^2} \frac{f_N^2}{f_n^2} F_N^2 \mathcal{F}_{\text{med}}^2 \eta(v_{\text{min}}) \Big|_{q^2=2m_N\omega}, \quad (2.61)$$

where $\eta(v_{\text{min}})$ is given by Eq. (2.25) and $v_{\text{min}} = \frac{q}{2\mu_{\chi N}}$ in the present case. It is now easy to generalize these results to the case of more than one nucleus type:

$$\frac{dR}{d\omega} = \frac{\rho_\chi}{m_\chi} \frac{\bar{\sigma}_n}{2\mu_{\chi n}^2} \frac{1}{\sum_N A_N} \left[\sum_N A_N \frac{f_N^2}{f_n^2} F_N^2 \mathcal{F}_{\text{med}}^2 \eta(v_{\text{min}}) \right]_{q^2=2m_N\omega}, \quad (2.62)$$

where N runs over the inequivalent nuclei in the target (e.g. $N = \text{Ga}, \text{As}$ for GaAs).

Validity of the Nuclear Recoil Calculation in Crystal Targets

A key assumption we have made in the derivation above is that the nuclei in the target do not interact with each other (hence the factorization of the Hilbert space). In a crystal target, however, the nuclei are not free, but interact with the neighboring nuclei in the crystal structure. The justification of treating the nuclei as free particles initially at rest lies in the fact that in the *classical* limit, the hard scattering process is instantaneous and local. In this case, the nuclei interactions affect only the subsequent secondary processes. For example, secondary phonons can be produced, which allows the energy deposition to be shared by many nuclei.

On the other hand, as detector thresholds are pushed to lower energies, at some point we would get into the *quantum* regime, where the finite duration and spatial extent of the scattering invalidate the free nuclei assumption. We can make a quick estimate on when this happens from the uncertainty principle. The time scale for the hard scattering to happen is $\sim 1/\omega$. This should be compared to the intrinsic time scale for atomic vibrations in a crystal, $1/\omega_{\text{ph}}$, with ω_{ph} the phonon energy. The instantaneous interaction approximation in the standard nuclear recoil calculation is valid when the energy deposition is much higher than the energies of all phonon modes, i.e.

$$\omega \gg \omega_{\text{ph}}^{\text{max}} \quad (\text{validity condition for nuclear recoils in crystals}). \quad (2.63)$$

An alternative way to reach the same conclusion is the following. Within the length scale $1/q$, the DM should see the nucleus as a plane wave for the nuclear recoil calculation to hold. Since the spatial extent of the nucleus wavefunction in a harmonic potential is $\sim (m_N \omega_{\text{ph}})^{-1/2}$, we need $q \gg (m_N \omega_{\text{ph}}^{\text{max}})^{1/2}$. Using the kinematic relation $\omega = \frac{q^2}{2m_N}$, we arrive at the same condition as Eq. (2.63).

To summarize, in crystal targets, the nuclear recoil calculation is valid for energy depositions much higher than the phonon energies, which are typically $\mathcal{O}(10 - 100)$ meV. This explains the truncation of the C, Si, Ge, Cs nuclear recoil lines at low ω in Fig. 2.1. At lower energy depositions, the target Hilbert space does not factorize into individual nuclei, but instead contains single phonon and multi-phonon states as energy eigenstates, and the direct detection rate calculation proceeds differently. We discuss single phonon excitations in Sec. 2.5, which will be the relevant processes when detector thresholds reach the 10-100 meV regime in the future. In the intermediate energy regime – above the single phonon energies yet below the validity range of nuclear recoils – direct multi-phonon production should be considered, which we plan to investigate in future work.

2.4 Electron Transitions

We next consider electron transitions. The initial state can be written as

$$|i\rangle = \prod_{I \in \text{occupied}} \hat{c}_I^\dagger |0\rangle, \quad (2.64)$$

where \hat{c}_I^\dagger are electron creation operators, with I running over all occupied electron states (energy eigenstates). Our normalization convention is such that $\{\hat{c}_I, \hat{c}_{I'}^\dagger\} = \delta_{II'}$, so the electron states are unit-normalized. The final states are labeled by I_1, I_2 , where one of the electrons has transitioned from I_1 to an unoccupied state I_2 :

$$|f\rangle = \hat{c}_{I_2}^\dagger \hat{c}_{I_1} |i\rangle. \quad (2.65)$$

The relevant piece in $\mathcal{F}_T(\mathbf{q})$ is simply

$$\mathcal{F}_T(\mathbf{q}) = \frac{f_e}{f_e^0} \tilde{n}_e(-\mathbf{q}) = \frac{f_e}{f_e^0} \int \frac{d^3 k'}{(2\pi)^3} \frac{d^3 k}{(2\pi)^3} (2\pi)^3 \delta^3(\mathbf{k}' - \mathbf{k} - \mathbf{q}) \hat{c}_{\mathbf{k}'}^\dagger \hat{c}_{\mathbf{k}}, \quad (2.66)$$

where the creation and annihilation operators are for momentum eigenstates, and satisfy $\{\hat{c}_{\mathbf{k}}, \hat{c}_{\mathbf{k}'}^\dagger\} = (2\pi)^3 \delta^3(\mathbf{k} - \mathbf{k}')$, etc. As discussed in Sec. 2.2, the screening factor is

$$\frac{f_e}{f_e^0} = \begin{cases} 1 & \text{(scalar mediator),} \\ q^2/(\mathbf{q} \cdot \boldsymbol{\varepsilon} \cdot \mathbf{q}) & \text{(vector mediator).} \end{cases} \quad (2.67)$$

The dynamic structure factor is therefore

$$\begin{aligned} S(\mathbf{q}, \omega) &= \frac{2\pi}{V} \left(\frac{f_e}{f_e^0} \right)^2 \sum_{I_1, I_2} \delta(E_{I_2} - E_{I_1} - \omega) \times \\ &\quad \left| \int \frac{d^3 k'}{(2\pi)^3} \frac{d^3 k}{(2\pi)^3} (2\pi)^3 \delta^3(\mathbf{k}' - \mathbf{k} - \mathbf{q}) \langle i | \hat{c}_{I_1}^\dagger \hat{c}_{I_2} \hat{c}_{\mathbf{k}'}^\dagger \hat{c}_{\mathbf{k}} | i \rangle \right|^2 \\ &= \frac{2\pi}{V} \left(\frac{f_e}{f_e^0} \right)^2 \sum_{I_1, I_2} \delta(E_{I_2} - E_{I_1} - \omega) \times \\ &\quad \left| \int \frac{d^3 k'}{(2\pi)^3} \frac{d^3 k}{(2\pi)^3} (2\pi)^3 \delta^3(\mathbf{k}' - \mathbf{k} - \mathbf{q}) \{ \hat{c}_{\mathbf{k}}, \hat{c}_{I_1}^\dagger \} \{ \hat{c}_{I_2}, \hat{c}_{\mathbf{k}'}^\dagger \} \right|^2, \end{aligned} \quad (2.68)$$

where we have used $\hat{c}_{I_1}^\dagger |i\rangle = \hat{c}_{I_2} |i\rangle = 0$, and that the anticommutators are just numbers. To evaluate the anticommutators, we expand the energy eigenstates in terms of momentum eigenstates:

$$\hat{c}_I^\dagger |0\rangle = \int \frac{d^3 k}{(2\pi)^3} \tilde{\psi}_I(\mathbf{k}) \hat{c}_{\mathbf{k}}^\dagger |0\rangle, \quad (2.69)$$

where $\tilde{\psi}_I(\mathbf{k})$ is the momentum space wavefunction, which satisfies the orthonormality condition $\int \frac{d^3k}{(2\pi)^3} \tilde{\psi}_{I'}^*(\mathbf{k}) \tilde{\psi}_I(\mathbf{k}) = \delta_{II'}$. We then obtain

$$S(\mathbf{q}, \omega) = \frac{2\pi}{V} \left(\frac{f_e}{f_e^0} \right)^2 \sum_{I_1, I_2} \delta(E_{I_2} - E_{I_1} - \omega) \cdot \left| \int \frac{d^3k'}{(2\pi)^3} \frac{d^3k}{(2\pi)^3} (2\pi)^3 \delta^3(\mathbf{k}' - \mathbf{k} - \mathbf{q}) \tilde{\psi}_{I_2}^*(\mathbf{k}') \tilde{\psi}_{I_1}(\mathbf{k}) \right|^2. \quad (2.70)$$

The dynamic structure factor in Eq. (2.70) applies for any target system where DM scattering can trigger electron transitions – atoms, crystals, superconductors, Dirac materials, etc. – once the energy levels and wavefunctions are known. In what follows, we examine the case of periodic crystals in more detail. Here, the energy eigenstates of an electron are Bloch waves labeled by a band index and a wavevector within the first Brillouin zone (1BZ), e.g.

$$\psi_{I_1}(\mathbf{x}) = \psi_{i_1 \mathbf{k}_1}(\mathbf{x}) = \frac{1}{\sqrt{V}} \sum_{\mathbf{G}_1} u_{i_1}(\mathbf{k}_1 + \mathbf{G}_1) e^{i(\mathbf{k}_1 + \mathbf{G}_1) \cdot \mathbf{x}}, \quad (2.71)$$

$$\begin{aligned} \tilde{\psi}_{i_1 \mathbf{k}_1}(\mathbf{k}) &= \int d^3x \psi_{i_1 \mathbf{k}_1}(\mathbf{x}) e^{-i\mathbf{k} \cdot \mathbf{x}} \\ &= \frac{1}{\sqrt{V}} \sum_{\mathbf{G}_1} u_{i_1}(\mathbf{k}_1 + \mathbf{G}_1) (2\pi)^3 \delta^3(\mathbf{k}_1 + \mathbf{G}_1 - \mathbf{k}), \end{aligned} \quad (2.72)$$

where \mathbf{G}_1 runs over all reciprocal lattice vectors. Note that the state labeled by i_1, \mathbf{k}_1 has Fourier components of \mathbf{k}_1 plus any reciprocal lattice vector. The coefficients $u_{i_1}(\mathbf{k}_1 + \mathbf{G}_1)$ are normalized as $\sum_{\mathbf{G}_1} |u_{i_1}(\mathbf{k}_1 + \mathbf{G}_1)|^2 = 1$. The dynamic structure factor now becomes

$$S(\mathbf{q}, \omega) = \frac{2}{V} \left(\frac{f_e}{f_e^0} \right)^2 \sum_{i_1, i_2} \int_{1\text{BZ}} \frac{d^3k_1}{(2\pi)^3} \frac{d^3k_2}{(2\pi)^3} 2\pi \delta(E_{i_2, \mathbf{k}_2} - E_{i_1, \mathbf{k}_1} - \omega) \times \left| \sum_{\mathbf{G}_1, \mathbf{G}_2} (2\pi)^3 \delta^3(\mathbf{k}_2 + \mathbf{G}_2 - \mathbf{k}_1 - \mathbf{G}_1 - \mathbf{q}) u_{i_2}^*(\mathbf{k}_2 + \mathbf{G}_2) u_{i_1}(\mathbf{k}_1 + \mathbf{G}_1) \right|^2, \quad (2.73)$$

where the prefactor 2 comes from summing over contributions from degenerate spin states, and the sums over the final state quantum numbers $\mathbf{k}_{1,2}$ have been replaced by integrals in the continuum limit. As in Ref. [33], we define a crystal form factor

$$f_{[i_1 \mathbf{k}_1, i_2 \mathbf{k}_2, \mathbf{G}]} \equiv \sum_{\mathbf{G}_1, \mathbf{G}_2} u_{i_2}^*(\mathbf{k}_2 + \mathbf{G}_2) u_{i_1}(\mathbf{k}_1 + \mathbf{G}_1) \delta_{\mathbf{G}_2 - \mathbf{G}_1, \mathbf{G}} \quad (2.74)$$

for the transition $i_1 \mathbf{k}_1 \rightarrow i_2 \mathbf{k}_2$ with an Umklapp \mathbf{G} . This simply encodes the wavefunction overlap, summed over all Fourier components consistent with momentum conservation. The

dynamic structure factor can now be written more concisely as

$$S(\mathbf{q}, \omega) = 2 \left(\frac{f_e}{f_e^0} \right)^2 \sum_{i_1, i_2} \int_{\text{1BZ}} \frac{d^3 k_1}{(2\pi)^3} \frac{d^3 k_2}{(2\pi)^3} 2\pi \delta(E_{i_2, \mathbf{k}_2} - E_{i_1, \mathbf{k}_1} - \omega) \times \sum_{\mathbf{G}} (2\pi)^3 \delta^3(\mathbf{k}_2 - \mathbf{k}_1 + \mathbf{G} - \mathbf{q}) |f_{[i_1 \mathbf{k}_1, i_2 \mathbf{k}_2, \mathbf{G}]}|^2. \quad (2.75)$$

Note that we have again used the identity $(2\pi)^3 \delta^3(\mathbf{0}) = \int d^3 x e^{i\mathbf{0}\cdot\mathbf{x}} = V$. The material-specific quantities appearing in $S(\mathbf{q}, \omega)$ are the electron band structures (energy eigenvalues $E_{i, \mathbf{k}}$) and Bloch wavefunction coefficients $u_i(\mathbf{k} + \mathbf{G})$. They can be computed by density functional theory (DFT) methods which we discuss more in our companion paper [7].

Finally, performing the phase space integration, we obtain the total rate per target mass:

$$R = \frac{2}{\rho_T} \frac{\rho_\chi}{m_\chi} \frac{\pi \bar{\sigma}_e}{\mu_{\chi e}^2} \sum_{i_1, i_2} \int_{\text{1BZ}} \frac{d^3 k_1}{(2\pi)^3} \frac{d^3 k_2}{(2\pi)^3} \sum_{\mathbf{G}} g(\mathbf{q}, \omega) \mathcal{F}_{\text{med}}^2(q) \left(\frac{f_e}{f_e^0} \right)^2 |f_{[i_1 \mathbf{k}_1, i_2 \mathbf{k}_2, \mathbf{G}]}|^2, \quad (2.76)$$

where

$$\mathbf{q} = \mathbf{k}_2 - \mathbf{k}_1 + \mathbf{G}, \quad \omega = E_{i_2, \mathbf{k}_2} - E_{i_1, \mathbf{k}_1}. \quad (2.77)$$

The $g(\mathbf{q}, \omega)$ function, the mediator form factor \mathcal{F}_{med} , the screening factor f_e/f_e^0 and the crystal form factor $f_{[i_1 \mathbf{k}_1, i_2 \mathbf{k}_2, \mathbf{G}]}$ are given by Eqs. (2.27), (2.12), (2.67) and (2.74), respectively. This generalizes the formula derived in Ref. [33] to account for possible anisotropies in the target response.

Target Anisotropies and Daily Modulation

The simplest crystal targets that have been considered for direct detection via electron transitions, like silicon and germanium, are quite isotropic. As a result, the rate is essentially independent of the direction of the incoming DM's velocity. However, this is not the case for materials with large anisotropies in the electron band structures or wavefunctions. For terrestrial experiments, as the target rotates with the Earth, the DM wind comes in from different directions at different times of the day, resulting in a *daily* modulation of the rate. This is on top of the *annual* modulation signal expected due to the variation of the average DM velocity as the Earth orbits around the Sun [33, 35]. If observed, it would be a smoking-gun signature of DM that is distinct from possible backgrounds. Our rate formula Eq. (2.76) incorporates directional information, and is well-suited for calculating the daily modulation signal.

As an example target, we consider hexagonal boron nitride (BN), shown in Fig. 2.2. The numerical calculation of electron band structures and wavefunction coefficients, as well as direct detection rates, proceeds in the same way as in our companion paper [7]. We include

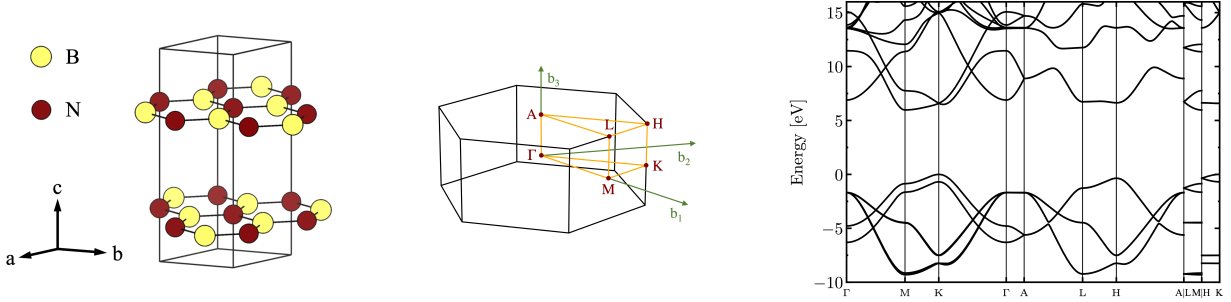


Figure 2.2: Crystal structure of hexagonal boron nitride (left), its corresponding first Brillouin zone (middle) and DFT-calculated electronic band structure (right) with the Fermi level set to zero. The letters shown in the Brillouin zone plot mark several of the high-symmetry points, and the orange lines mark Brillouin zone paths along which electronic band structure is plotted. The discontinuities in the band structure occur from taking a discontinuous path through the Brillouin zone, indicated by “|” on the horizontal axis.

the calculation details specific for BN in Appendix A. As a result of the layered crystal structure, the rate is strongly dependent on the angle between the DM wind and the layers. We note, however, that BN has a three-dimensional crystal structure with the layers of BN repeating in the out-of-plane direction, in contrast to single-layer graphene previously considered in Ref. [188].

To show this directional dependence, we consider the same experimental setup as in Refs. [28, 29], where the crystal c -axis is aligned with the Earth’s velocity \mathbf{v}_e at time $t = 0$. With this choice, daily modulation signal is independent of the location of the laboratory. In Fig. 2.3, we pick three DM masses $m_\chi = 5, 10, 100$ MeV to show how the expected detection rates – both total (left panel) and differential (right panel) – change during a sidereal day, assuming a light mediator and negligible in-medium effects. For all three masses, we see that the rate is maximized at $t = 12$ hours when the DM wind is roughly aligned with the crystal a - b plane, and minimized at $t = 0$ when the DM wind is aligned with the crystal c -axis. This can be understood from the fact that electron wavefunctions are more localized in the c direction and thus have smaller low-momentum components, whereas the DM scattering matrix element peaks at low q for a light mediator. We also observe that modulation is stronger for lighter DM. Generically, with a smaller energy deposition, the rate is more strongly affected by band structure anisotropies near the band gap; far from the band gap, the electron band structures and wavefunctions approach those for individual, isotropic ions. For DM heavier than 100 MeV, we find roughly the same amount of daily modulation as the $m_\chi = 100$ MeV case. This is again because the momentum integral is dominated by small q , which corresponds to the same kinematic region $\omega_{\mathbf{q}} \simeq \mathbf{q} \cdot \mathbf{v}$ in the large m_χ limit. On

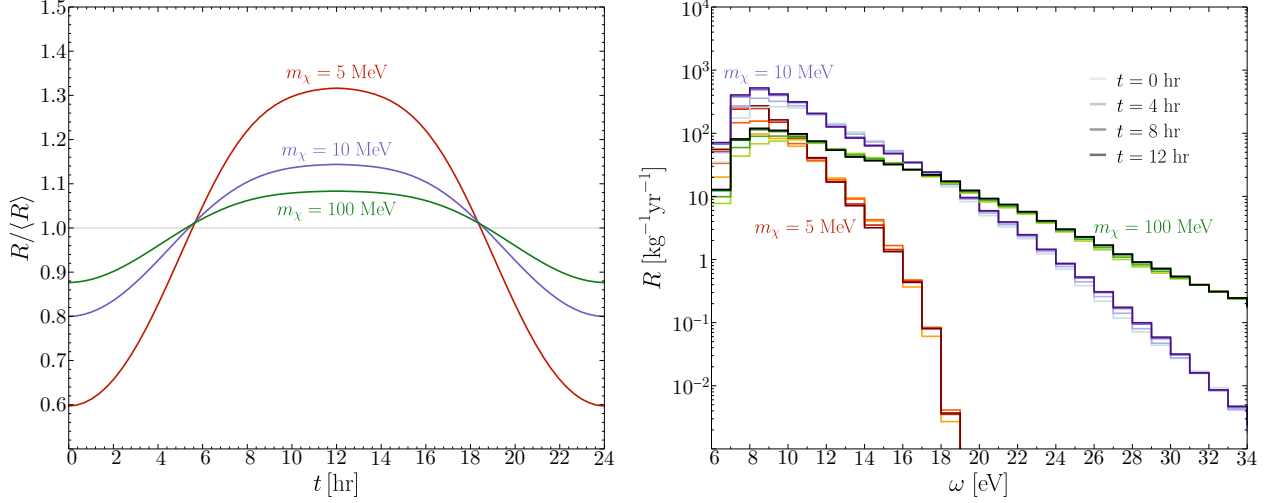


Figure 2.3: Total rate of electron transitions R in hexagonal BN, normalized to its daily average $\langle R \rangle$ as a function of time (left), and differential rates at several times of the day assuming $\bar{\sigma}_e = 10^{-37} \text{ cm}^2$ (right), for a 5, 10, 100 MeV DM scattering via a light mediator.

the other hand, once we go below $m_\chi = 5$ MeV, the total rate quickly approaches zero, as the DM does not carry sufficient kinetic energy to trigger a transition across the band gap, which is ~ 6 eV in BN.

2.5 Single Phonon Excitations

Finally, we derive single phonon production rates following the same procedure. Assuming zero temperature, the initial state is the ground state with no phonons, and the final state contains one phonon:

$$|i\rangle = |0\rangle, \quad |f\rangle = |\nu, \mathbf{k}\rangle = \hat{a}_{\nu, \mathbf{k}}^\dagger |0\rangle, \quad (2.78)$$

where the canonical commutation relations read $[\hat{a}_{\nu, \mathbf{k}}, \hat{a}_{\nu', \mathbf{k}'}^\dagger] = \delta_{\nu\nu'} \delta_{\mathbf{k}\mathbf{k}'}$, etc. Note that phonons are labeled by a branch index $\nu = 1, \dots, 3n$, where n is the number of atoms/ions in each primitive cell, and a momentum vector \mathbf{k} within the first Brillouin zone. For a crystal with N primitive unit cells, \mathbf{k} takes N discrete values. In the end we take the limit $N \rightarrow \infty$, where \mathbf{k} becomes continuous.

To see how $\mathcal{F}_T(\mathbf{q})$ should be quantized in the phonon Hilbert space, we note that phonons arise from atom/ion displacements:

$$\mathbf{u}_{lj} = \mathbf{x}_{lj} - \mathbf{x}_{lj}^0 = \sum_{\nu} \sum_{\mathbf{k} \in \text{1BZ}} \frac{1}{\sqrt{2Nm_j\omega_{\nu, \mathbf{k}}}} \left(\hat{a}_{\nu, \mathbf{k}} \boldsymbol{\epsilon}_{\nu, \mathbf{k}, j} e^{i\mathbf{k} \cdot \mathbf{x}_{lj}^0} + \hat{a}_{\nu, \mathbf{k}}^\dagger \boldsymbol{\epsilon}_{\nu, \mathbf{k}, j}^* e^{-i\mathbf{k} \cdot \mathbf{x}_{lj}^0} \right), \quad (2.79)$$

where \mathbf{x}_{lj} is the position of the j th atom/ion in the l th primitive cell, \mathbf{x}_{lj}^0 is the equilibrium position, m_j are the atom/ion masses, $\omega_{\nu, \mathbf{k}}$ are the phonon energies, and $\boldsymbol{\epsilon}_{\nu, \mathbf{k}, j}$ are the phonon

polarization vectors, normalized such that $\sum_j |\boldsymbol{\epsilon}_{\nu,\mathbf{k},j}|^2 = 1$. The task is thus to find how $\mathcal{F}_T(\mathbf{q})$ depends on the atom/ion positions \mathbf{x}_{lj} and displacements \mathbf{u}_{lj} .

To do so, let us revisit the scattering potential in Eq. (2.4). For a periodic crystal, it can be written as a sum over contributions from individual atoms/ions:

$$\begin{aligned} \mathcal{V}(\mathbf{x}) &= \sum_{l,j} \int_{\Omega_{lj}} d^3x' [n_p^{lj}(\mathbf{x}') \mathcal{V}_p(\mathbf{x} - \mathbf{x}') + n_n^{lj}(\mathbf{x}') \mathcal{V}_n(\mathbf{x} - \mathbf{x}') + n_e^{lj}(\mathbf{x}') \mathcal{V}_e(\mathbf{x} - \mathbf{x}')] \\ &= \sum_{l,j} \int_{\Omega_{lj}} d^3r [n_p^{lj}(\mathbf{r}) \mathcal{V}_p(\mathbf{x} - \mathbf{x}_{lj} - \mathbf{r}) \\ &\quad + n_n^{lj}(\mathbf{r}) \mathcal{V}_n(\mathbf{x} - \mathbf{x}_{lj} - \mathbf{r}) \\ &\quad + n_e^{lj}(\mathbf{r}) \mathcal{V}_e(\mathbf{x} - \mathbf{x}_{lj} - \mathbf{r})] \end{aligned} \quad (2.80)$$

where Ω_{lj} is a volume surrounding the lattice site l, j . Within each site volume, we have changed the integration variable to $\mathbf{r} = \mathbf{x}' - \mathbf{x}_{lj}$, the position relative to the center of the site, and defined $n_p^{lj}(\mathbf{r}) \equiv n_p(\mathbf{x}_{lj} + \mathbf{r})$, etc. For protons and neutrons, $n_{p,n}^{lj}$ here coincides with $n_{p,n}^0$ introduced in Sec. 2.3 for the nucleus at site l, j . Also, displacing an atom/ion does not change the nucleon distributions inside of a nucleus. Thus, we can write

$$n_{p,n}^{lj}(\mathbf{r}) = n_{p,n}^j(\mathbf{r}), \quad (2.81)$$

which makes it clear that nucleon number densities are the same in all primitive cells, and are not affected by atom/ion displacements in any particular primitive cell. For electrons, on the other hand, this is generally not true, since electron wavefunctions are distorted when displacing an atom/ion relative to the other atoms/ions in the crystal lattice. To account for this effect, we write

$$n_e^{lj}(\mathbf{r}) = n_e^j(\mathbf{r}) + \sum_{l',j'} \frac{\delta n_e^{lj}}{\delta \mathbf{u}_{l'j'}} \cdot \mathbf{u}_{l'j'} + \mathcal{O}(u^2) \simeq n_e^j(\mathbf{r}) + \frac{\delta n_e^{lj}}{\delta \mathbf{u}_{lj}} \cdot \mathbf{u}_{lj}, \quad (2.82)$$

where the last expression assumes the effect of electron redistribution following an atom/ion displacement is weak and local. This is usually a good approximation for ionic crystals such as gallium arsenide (GaAs), where electrons are semi-localized, and displacing an ion tends not to significantly affect the electron clouds of neighboring ions. For covalent crystals such as silicon, valence electron wavefunctions are more disperse, so more terms in the $l'j'$ sum should be included for an accurate calculation.

Assuming the approximation in Eq. (2.82) is valid, we can Fourier transform Eq. (2.80) and

obtain

$$\begin{aligned}\tilde{\mathcal{V}}(-\mathbf{q}) &= \mathcal{M}_0(\mathbf{q}) \sum_{l,j} e^{i\mathbf{q}\cdot\mathbf{x}_{lj}} \left[f_p \tilde{n}_p^j(-\mathbf{q}) + f_n \tilde{n}_n^j(-\mathbf{q}) + f_e \tilde{n}_e^j(-\mathbf{q}) + f_e \frac{\delta \tilde{n}_e^{lj}(-\mathbf{q})}{\delta \mathbf{u}_{lj}} \cdot \mathbf{u}_{lj} \right] \\ &= \mathcal{M}_0(\mathbf{q}) \sum_{l,j} e^{i\mathbf{q}\cdot\mathbf{x}_{lj}} \left[f_j F_{N_j}(\mathbf{q}) + f_e \tilde{n}_e^j(-\mathbf{q}) + f_e \frac{\delta \tilde{n}_e^{lj}(-\mathbf{q})}{\delta \mathbf{u}_{lj}} \cdot \mathbf{u}_{lj} \right],\end{aligned}\quad (2.83)$$

where $f_j = f_p Z_j + f_n (A_j - Z_j)$, and $F_{N_j}(\mathbf{q})$ is the nuclear form factor (introduced in Sec. 2.3) for the nucleus occupying site j in each primitive cell. We therefore obtain

$$\mathcal{F}_T(\mathbf{q}) = \sum_{l,j} [\mathcal{F}_j^0(\mathbf{q}) + \Delta_j(\mathbf{q}) \cdot \mathbf{u}_{lj}] e^{i\mathbf{q}\cdot\mathbf{x}_{lj}}, \quad (2.84)$$

with

$$\mathcal{F}_j^0(\mathbf{q}) \equiv \frac{1}{f_\psi^0} [f_j F_{N_j}(\mathbf{q}) + f_e \tilde{n}_e^j(-\mathbf{q})], \quad \Delta_j(\mathbf{q}) \equiv \frac{f_e}{f_\psi^0} \frac{\delta \tilde{n}_e^{lj}(-\mathbf{q})}{\delta \mathbf{u}_{lj}}, \quad (2.85)$$

where $f_\psi^0 = f_n^0 (f_e^0)$ if the rate is written in terms of $\bar{\sigma}_n$ ($\bar{\sigma}_e$). Note that Δ_j is independent of l due to lattice translation symmetries. From Eq. (2.84) we see that $\mathcal{F}_T(\mathbf{q})$ depends on \mathbf{u}_{lj} – which are quantized in terms of phonon modes as in Eq. (2.79) – via both the phase factor $e^{i\mathbf{q}\cdot\mathbf{x}_{lj}} = e^{i\mathbf{q}\cdot(\mathbf{x}_{lj}^0 + \mathbf{u}_{lj})}$ and the $\Delta_j(\mathbf{q}) \cdot \mathbf{u}_{lj}$ term.

With $\mathcal{F}_T(\mathbf{q})$ quantized in the phonon Hilbert space, we now move on to calculate the matrix element $\langle \nu, \mathbf{k} | \mathcal{F}_T(\mathbf{q}) | 0 \rangle$. We first apply the Baker-Campbell-Hausdorff (BCH) formula to the phase factor $e^{i\mathbf{q}\cdot\mathbf{x}_{lj}}$ to move annihilation operators to the right:

$$\begin{aligned}e^{i\mathbf{q}\cdot\mathbf{x}_{lj}} &= e^{i\mathbf{q}\cdot\mathbf{x}_{lj}^0} \prod_{\nu,\mathbf{k}} \exp \left[\frac{i(\mathbf{q} \cdot \boldsymbol{\epsilon}_{\nu,\mathbf{k},j}^*) e^{-i\mathbf{k}\cdot\mathbf{x}_{lj}^0}}{\sqrt{2Nm_j\omega_{\nu,\mathbf{k}}}} \hat{a}_{\nu,\mathbf{k}}^\dagger + \frac{i(\mathbf{q} \cdot \boldsymbol{\epsilon}_{\nu,\mathbf{k},j}) e^{i\mathbf{k}\cdot\mathbf{x}_{lj}^0}}{\sqrt{2Nm_j\omega_{\nu,\mathbf{k}}}} \hat{a}_{\nu,\mathbf{k}} \right] \\ &= e^{i\mathbf{q}\cdot\mathbf{x}_{lj}^0} \prod_{\nu,\mathbf{k}} \exp \left[\frac{i(\mathbf{q} \cdot \boldsymbol{\epsilon}_{\nu,\mathbf{k},j}^*) e^{-i\mathbf{k}\cdot\mathbf{x}_{lj}^0}}{\sqrt{2Nm_j\omega_{\nu,\mathbf{k}}}} \hat{a}_{\nu,\mathbf{k}}^\dagger \right] \cdot \exp \left[\frac{i(\mathbf{q} \cdot \boldsymbol{\epsilon}_{\nu,\mathbf{k},j}) e^{i\mathbf{k}\cdot\mathbf{x}_{lj}^0}}{\sqrt{2Nm_j\omega_{\nu,\mathbf{k}}}} \hat{a}_{\nu,\mathbf{k}} \right] \times \\ &\quad \exp \left(\frac{|\mathbf{q} \cdot \boldsymbol{\epsilon}_{\nu,\mathbf{k},j}|^2}{4Nm_j\omega_{\nu,\mathbf{k}}} [\hat{a}_{\nu,\mathbf{k}}^\dagger, \hat{a}_{\nu,\mathbf{k}}] \right) \\ &= e^{i\mathbf{q}\cdot\mathbf{x}_{lj}^0} e^{-W_j(\mathbf{q})} \exp \left[\sum_{\nu,\mathbf{k}} \frac{i(\mathbf{q} \cdot \boldsymbol{\epsilon}_{\nu,\mathbf{k},j}^*) e^{-i\mathbf{k}\cdot\mathbf{x}_{lj}^0}}{\sqrt{2Nm_j\omega_{\nu,\mathbf{k}}}} \hat{a}_{\nu,\mathbf{k}}^\dagger \right] \\ &\quad \times \exp \left[\sum_{\nu,\mathbf{k}} \frac{i(\mathbf{q} \cdot \boldsymbol{\epsilon}_{\nu,\mathbf{k},j}) e^{i\mathbf{k}\cdot\mathbf{x}_{lj}^0}}{\sqrt{2Nm_j\omega_{\nu,\mathbf{k}}}} \hat{a}_{\nu,\mathbf{k}} \right],\end{aligned}\quad (2.86)$$

where we have used the fact that the commutator between creation and annihilation operators is a classical number so the BCH series terminates. In the last equation,

$$W_j(\mathbf{q}) = \frac{1}{4Nm_j} \sum_{\nu} \sum_{\mathbf{k} \in 1\text{BZ}} \frac{|\mathbf{q} \cdot \boldsymbol{\epsilon}_{\nu,\mathbf{k},j}|^2}{\omega_{\nu,\mathbf{k}}} \rightarrow \frac{\Omega}{4m_j} \sum_{\nu} \int_{1\text{BZ}} \frac{d^3k}{(2\pi)^3} \frac{|\mathbf{q} \cdot \boldsymbol{\epsilon}_{\nu,\mathbf{k},j}|^2}{\omega_{\nu,\mathbf{k}}} \quad (2.87)$$

is the Debye-Waller factor (in the continuum limit $\sum_{\mathbf{k}} \rightarrow V \int \frac{d^3\mathbf{k}}{(2\pi)^3} = N\Omega \int \frac{d^3\mathbf{k}}{(2\pi)^3}$ with Ω the volume of the primitive cell). The physical meaning of this factor is that a transition $|i\rangle \rightarrow |f\rangle$ can be accompanied by additional phonons' creation out of the vacuum followed by their annihilation, and all these processes are resummed into the exponential. The matrix element thus becomes

$$\begin{aligned}
\langle \nu, \mathbf{k} | \mathcal{F}_T(\mathbf{q}) | 0 \rangle &= \sum_{l,j} e^{i\mathbf{q} \cdot \mathbf{x}_{lj}^0} e^{-W_j(\mathbf{q})} \times \\
&\quad \langle \nu, \mathbf{k} | [\mathcal{F}_j^0(\mathbf{q}) + \Delta_j(\mathbf{q}) \cdot \mathbf{u}_{lj}] \exp \left[\sum_{\nu', \mathbf{k}'} \frac{i(\mathbf{q} \cdot \boldsymbol{\epsilon}_{\nu', \mathbf{k}', j}^*) e^{-i\mathbf{k}' \cdot \mathbf{x}_{lj}^0}}{\sqrt{2Nm_j\omega_{\nu', \mathbf{k}'}}} \hat{a}_{\nu', \mathbf{k}'}^\dagger \right] | 0 \rangle \\
&= \sum_{l,j} e^{i(\mathbf{q}-\mathbf{k}) \cdot \mathbf{x}_{lj}^0} e^{-W_j(\mathbf{q})} \frac{i}{\sqrt{2Nm_j\omega_{\nu, \mathbf{k}}}} \times \\
&\quad \left[\mathcal{F}_j^0 \mathbf{q} - i \Delta_j + \frac{\mathbf{q}}{Nm_j} \sum_{\nu', \mathbf{k}'} \frac{(i\Delta_j \cdot \boldsymbol{\epsilon}_{\nu', \mathbf{k}', j})(\mathbf{q} \cdot \boldsymbol{\epsilon}_{\nu', \mathbf{k}', j}^*)}{2\omega_{\nu', \mathbf{k}'}} \right] \cdot \boldsymbol{\epsilon}_{\nu, \mathbf{k}, j}^*. \quad (2.88)
\end{aligned}$$

The l sum can be eliminated via the identity

$$\sum_l e^{i(\mathbf{q}-\mathbf{k}) \cdot \mathbf{x}_l} = N \sum_{\mathbf{G}} \delta_{\mathbf{q}-\mathbf{k}, \mathbf{G}}, \quad (2.89)$$

where $\mathbf{x}_{lj}^0 = \mathbf{x}_l + \mathbf{x}_j^0$ with \mathbf{x}_l being the position of the l th primitive cell and \mathbf{x}_j^0 being the equilibrium position of the j th atom/ion within the primitive cell, and \mathbf{G} runs over the reciprocal lattice vectors. In fact, at most one term in the \mathbf{G} sum is picked out for given \mathbf{q} and \mathbf{k} , since $\mathbf{k} \in 1\text{BZ}$. We will thus drop the \mathbf{G} sum in what follows. On each phonon branch, as we sum over \mathbf{k} , only the mode that satisfies $\mathbf{q} = \mathbf{k} + \mathbf{G}$ can give a nonzero contribution to the dynamic structure factor, as a result of lattice momentum conservation.

It is worth emphasizing that the notion of momentum conservation here differs from the one familiar in particle physics, due to the spontaneous breaking of continuous translation symmetries. While each phonon can be thought of as carrying a momentum \mathbf{k} within the 1BZ, it can be excited even when the momentum transfer \mathbf{q} is outside the 1BZ via Umklapp scattering, in which case $\mathbf{G} \neq \mathbf{0}$. For DM heavier than $\sim \text{MeV}$, the momentum transfer can exceed $\sim \text{keV}$, the typical size of the 1BZ. In this case, Umklapp processes can contribute significantly if the matrix element has support at high q (which is the case for a heavy mediator). We will see an example of this in Sec. 2.5. Note that momentum is still conserved at the fundamental level: the extra momentum \mathbf{G} leads to a recoil of the entire crystal, which becomes unobservable in the limit $N \rightarrow \infty$. On the other hand, the notion of energy conservation is the same, as continuous time translation symmetry remains unbroken. As a result, the energy deposition has to match the phonon energy for a phonon mode to be excited.

With the equations above, we obtain the dynamic structure factor:

$$\begin{aligned} S(\mathbf{q}, \omega) &= \frac{2\pi}{V} \sum_{\nu} \sum_{\mathbf{k} \in \text{1BZ}} |\langle \nu, \mathbf{k} | \mathcal{F}_T(\mathbf{q}) | 0 \rangle|^2 \delta(\omega - \omega_{\nu, \mathbf{k}}) \\ &= \frac{\pi}{\Omega} \sum_{\nu} \frac{1}{\omega_{\nu, \mathbf{k}}} \left| \sum_j \frac{e^{-W_j(\mathbf{q})}}{\sqrt{m_j}} e^{i\mathbf{G} \cdot \mathbf{x}_j^0} (\mathbf{Y}_j \cdot \boldsymbol{\epsilon}_{\nu, \mathbf{k}, j}^*) \right|^2 \delta(\omega - \omega_{\nu, \mathbf{k}}), \end{aligned} \quad (2.90)$$

where

$$\mathbf{Y}_j \equiv \mathcal{F}_j^0 \mathbf{q} - i \boldsymbol{\Delta}_j + \frac{\Omega}{m_j} \mathbf{q} \sum_{\nu'} \int_{\text{1BZ}} \frac{d^3 k'}{(2\pi)^3} \frac{(i \boldsymbol{\Delta}_j \cdot \boldsymbol{\epsilon}_{\nu', \mathbf{k}', j})(\mathbf{q} \cdot \boldsymbol{\epsilon}_{\nu', \mathbf{k}', j}^*)}{2\omega_{\nu', \mathbf{k}'}}. \quad (2.91)$$

We have made it implicit in the last line of Eq. (2.90) that the \mathbf{k} vector is the one inside the first Brillouin zone that satisfies $\mathbf{q} = \mathbf{k} + \mathbf{G}$.

Finally, integrating over the DM velocity distribution, we obtain the rate per target mass:

$$R = \frac{1}{m_{\text{cell}}} \frac{\rho_{\chi}}{m_{\chi}} \frac{\pi \bar{\sigma}}{2\mu^2} \int \frac{d^3 q}{(2\pi)^3} \mathcal{F}_{\text{med}}^2(q) \sum_{\nu} \frac{1}{\omega_{\nu, \mathbf{k}}} \left| \sum_j \frac{e^{-W_j(\mathbf{q})}}{\sqrt{m_j}} e^{i\mathbf{G} \cdot \mathbf{x}_j^0} (\mathbf{Y}_j \cdot \boldsymbol{\epsilon}_{\nu, \mathbf{k}, j}^*) \right|^2 g(\mathbf{q}, \omega_{\nu, \mathbf{k}}), \quad (2.92)$$

where $m_{\text{cell}} = \rho_T \Omega$ is the mass contained in a primitive cell. The mediator form factor \mathcal{F}_{med} , the Debye-Waller factor $W_j(\mathbf{q})$ and the $g(\mathbf{q}, \omega)$ function are given by Eqs. (2.12), (2.87) and (2.27), respectively. The DM couplings are encoded in the \mathbf{Y}_j vectors given in Eq. (2.91), with $\mathcal{F}_j^0, \boldsymbol{\Delta}_j$ defined in Eq. (2.85). Meanwhile, the material specific quantities – phonon dispersions $\omega_{\nu, \mathbf{k}}$ and polarization vectors $\boldsymbol{\epsilon}_{\nu, \mathbf{k}, j}$ – can be numerically computed using DFT methods detailed in our companion paper [7].

In the following subsections, we discuss the phonon excitation calculation in more detail. It is clear from the discussion above that \mathbf{Y}_j are the key quantities to compute for any specific DM model. In Sec. 2.5, we consider the simpler case where DM couples only to nucleons but not electrons, and point out an interesting complementarity with nuclear recoils. We also discuss the relevance of Umklapp processes for DM heavier than an MeV, for both heavy and light mediators. Including DM-electron couplings introduces complications, but we show in Sec. 2.5 that \mathbf{Y}_j take a simple form in the low q limit for general couplings $f_{p,n,e}$. Note that the dark photon mediator benchmark ($f_p^0 = f_e^0, f_n^0 = 0$) has been studied in Refs. [28, 64] based on the Fröhlich Hamiltonian. Our calculation here reproduces previous results, and helps clarify their range of validity.

Dark Matter Coupling Only to Nucleons

Setting $f_e = 0$ and $f_{\psi}^0 = f_n^0 = f_n$ in Eq. (2.85), we have

$$\mathcal{F}_j^0(\mathbf{q}) = \begin{pmatrix} f_j \\ f_n \end{pmatrix} F_{N_j}(q), \quad \boldsymbol{\Delta}_j(\mathbf{q}) = \mathbf{0}. \quad (2.93)$$

In this case, \mathbf{Y}_j is simply $\mathcal{F}_j^0 \mathbf{q}$, and the rate Eq. (2.92) becomes

$$R = \frac{1}{m_{\text{cell}}} \frac{\rho_\chi}{m_\chi} \frac{\pi \bar{\sigma}_n}{2\mu_{\chi n}^2} \int \frac{d^3 q}{(2\pi)^3} \mathcal{F}_{\text{med}}^2(q) \times \sum_{\nu} \frac{1}{\omega_{\nu, \mathbf{k}}} \left| \sum_j \frac{e^{-W_j(\mathbf{q})}}{\sqrt{m_j}} \frac{f_j}{f_n} F_{N_j}(q) e^{i\mathbf{G} \cdot \mathbf{x}_j^0} (\mathbf{q} \cdot \boldsymbol{\epsilon}_{\nu, \mathbf{k}, j}^*) \right|^2 g(\mathbf{q}, \omega_{\nu, \mathbf{k}}). \quad (2.94)$$

It is interesting to compare to the nuclear recoils case. If there is only one atom in the primitive cell, we have $m_{\text{cell}} = m_j = m_N$, and

$$R = \frac{\rho_\chi}{m_\chi} \frac{\pi \bar{\sigma}_n}{2\mu_{\chi n}^2} \int \frac{d^3 q}{(2\pi)^3} e^{-2W} \frac{f_N^2}{f_n^2} F_N^2 \mathcal{F}_{\text{med}}^2 \sum_{\nu} \frac{|\mathbf{q} \cdot \boldsymbol{\epsilon}_{\nu, \mathbf{k}}^*|^2}{m_N^2 \omega_{\nu, \mathbf{k}}} g(\mathbf{q}, \omega_{\nu, \mathbf{k}}). \quad (2.95)$$

The differential rate reads

$$\frac{dR}{d\omega} = \frac{\rho_\chi}{m_\chi} \frac{\pi \bar{\sigma}_n}{2\mu_{\chi n}^2} \int \frac{d^3 q}{(2\pi)^3} e^{-2W} \frac{f_N^2}{f_n^2} F_N^2 \mathcal{F}_{\text{med}}^2 g(\mathbf{q}, \omega) \sum_{\nu} \frac{|\mathbf{q} \cdot \boldsymbol{\epsilon}_{\nu, \mathbf{k}}^*|^2}{m_N^2 \omega} \delta(\omega - \omega_{\nu, \mathbf{k}}). \quad (2.96)$$

On the other hand, we can rewrite Eq. (2.60) for nuclear recoils in terms of the $g(\mathbf{q}, \omega)$ function via $\int q dq \eta(v_{\text{min}}) \rightarrow 2 \int \frac{d^3 q}{(2\pi)^3} g(\mathbf{q}, \omega)$, and multiply the integrand by $1 = \frac{q^2}{2m_N \omega}$:

$$\frac{dR}{d\omega} = \frac{\rho_\chi}{m_\chi} \frac{\pi \bar{\sigma}_n}{2\mu_{\chi n}^2} \int \frac{d^3 q}{(2\pi)^3} \frac{f_N^2}{f_n^2} F_N^2 \mathcal{F}_{\text{med}}^2 g(\mathbf{q}, \omega) \frac{q^2}{m_N^2 \omega} \delta\left(\omega - \frac{q^2}{2m_N}\right) \quad (\text{nuclear recoil}). \quad (2.97)$$

One can clearly see the similarity between Eqs. (2.96) and (2.97). However, a key difference between nuclear recoils and phonon excitations is the way in which contributions from different atoms add up in the case of more than one atoms in the primitive cell. Comparing Eq. (2.94) against Eq. (2.62), we see that, in contrast to the nuclear recoils case where we add up the *rates* from inequivalent nuclei, for phonon excitations the sum over j is taken at the *amplitude* level. It is worth noting, however, that this apparent coherence does not result in a more favorable scaling of the detection rate. In fact, the total rate per target mass scales with neither the number of nuclei in the primitive cell, nor the total number of atoms/ions in the crystal. The former can be seen from the fact that phonon polarization vectors scale as $\boldsymbol{\epsilon}_{\nu, \mathbf{k}, j} \sim \sqrt{m_j/m_{\text{cell}}}$, which, together with the prefactor, means the denominator of Eq. (2.94) scales as m_{cell}^2 . The latter is because of the $1/\sqrt{N}$ normalization factor when expanding \mathbf{u}_{ij} in terms of phonon creation and annihilation operators (see Eq. (2.79)). The intuition here is that, despite the collective nature of phonon excitations, we have to project the motion of each atom onto the phonon modes that match the energy-momentum transfer. As a result, coherence between more atoms comes with a price of a smaller overlap with phonon modes.

Another key difference between nuclear recoils and phonon excitations, alluded to in Fig. 2.1 and Sec. 2.3, is the kinematic regimes probed. In the phonon case, the Debye-Waller factor

e^{-W_j} cuts off the momentum integral for $q \gtrsim \sqrt{m_N \omega_{\text{ph}}}$, the inverse spatial extent of the nucleus wavefunction. The ω_{ph} here should be thought of as an average phonon energy over the entire 1BZ, which is of the same order as $\omega_{\text{ph}}^{\text{max}}$. As discussed in Sec. 2.3, this high q regime is exactly where the nuclear recoil calculation becomes valid. In addition, nuclear recoils happen at much higher energy depositions $\omega = q^2/2m_N \gg \omega_{\text{ph}}^{\text{max}}$ than phonon excitations.

A multi-channel search can exploit this complementarity between nuclear recoils and phonon excitations. Let us consider, as a benchmark model, a hadrophilic scalar mediator coupling identically to protons and neutrons ($f_p = f_n$, $f_e = 0$). In Fig. 2.4, we compare the reach of the two channels, using GaAs as an example target material. For a heavy mediator (left panel), we see that with sub-eV energy thresholds, nuclear recoils can probe DM masses above ~ 100 MeV — this is the mass regime where the single phonon excitation rate suffers from Debye-Waller suppression. Below ~ 100 MeV where nuclear recoils lose sensitivity, single phonon excitations can probe a few more orders of magnitude of m_χ , depending on the energy threshold. For a light mediator (right panel), on the other hand, single phonon excitations outperform nuclear recoils for all m_χ . This is because the momentum integral is dominated by the lowest q , which only depends on the energy threshold, $q_{\text{min}} \simeq \omega_{\text{min}}/v_{\text{max}}$. The mass scaling of the curves in Fig. 2.4 can be understood with a close examination of phase space integrals; we reserve a detailed discussion, including how the various features of the curves depend on material properties, for the companion paper [7].

It is also worth noting that while direct production of single phonons has been proposed mainly as a channel to search for sub-MeV DM, we see from Fig. 2.4 that its sensitivity extends well above MeV DM masses, which is important for covering the parameter space out of reach in nuclear recoils. A DM particle heavier than \sim MeV carries a momentum larger than the typical size of the 1BZ (or equivalently, the inverse lattice spacing). However, as explained below Eq. (2.89), a crystal target is able to absorb a momentum transfer beyond the 1BZ while still producing a phonon, provided the energy deposition matches that of the phonon energy. Such Umklapp processes can contribute significantly to the rate. In Fig. 2.5, we examine the role of Umklapp scattering by comparing the full rate (solid) vs. contributions from $q \in 1\text{BZ}$ (dashed), for three DM masses. We show the differential distribution up to 34 meV, the highest phonon energy in GaAs. For $m_\chi = 0.1$ MeV, the maximum momentum transfer $q_{\text{max}} \simeq 2m_\chi v_{\text{max}} \simeq 0.56$ keV is within the 1BZ, so the solid and dashed histograms coincide. Also, only acoustic phonons with energies below $c_s q_{\text{max}} \simeq 9$ meV (where c_s is the speed of sound) and optical phonons are kinematically accessible; contributions from optical phonons are suppressed at low q [201], so the total rate is dominated by the low energy

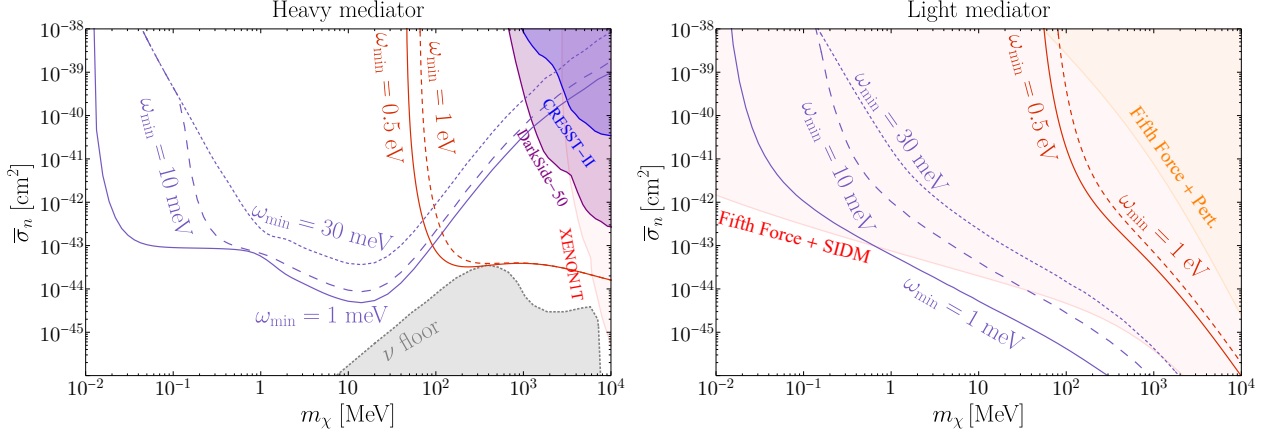


Figure 2.4: Projected reach for DM scattering via a heavy (left, $m_\phi \gtrsim 400$ MeV) or light (right, $m_\phi = 1$ eV) scalar mediator coupling to nucleons ($f_p = f_n$, $f_e = 0$), assuming 1 kg-yr exposure with a GaAs target, 3 signal events and no background. Both single phonon production (purple, assuming energy thresholds $\omega_{\min} = 1, 10, 30$ meV) and nuclear recoils (red, assuming $\omega_{\min} = 0.5, 1$ eV) are complementary in probing currently unconstrained parameter space. The heavy mediator case is free from stellar constraints for $m_\phi \gtrsim 400$ MeV [10], and the neutrino floor is taken from Ref. [11]. Currently, the best experimental nuclear recoil constraints in this region of parameter space are from DarkSide-50 [12] (assuming binomial fluctuations), and XENON1T (combined limits from [13, 14]). We also show the constraint from CRESST-II [15], which is stronger than the DarkSide-50 constraint at low masses assuming no fluctuation in energy quenching. A more complete collection of nuclear recoil constraints can be found in Refs. [12, 14, 16]. For a light mediator with $m_\phi = 1$ eV, fifth force experiments provide the dominant constraint on mediator-nucleon couplings [10]. Meanwhile, the mediator- χ coupling is constrained by DM self interactions (SIDM) if χ makes up all the DM [10], or just by perturbativity (Pert.) if χ is a DM subcomponent (in which case the projected reach can be easily rescaled).

acoustic phonons. For $m_\chi = 1$ MeV and 10 MeV, Umklapp processes dominate the rate in the heavy mediator case, since the momentum integral is dominated by large q . In the light mediator case, the matrix element peaks at small q , so the total rate is well approximated by the 1BZ contribution for sufficiently low energy thresholds (e.g. 1 meV). However, Umklapp scattering can still contribute significantly in the highest energy bins, and dominate the rate if the energy threshold is higher (e.g. 30 meV).

Dark Matter With Couplings to Electrons

In the presence of electron couplings $f_e \neq 0$, information about electron distributions is needed for the rate calculation. We focus on ionic crystals in this subsection, for which Eq. (2.82) is a good approximation, and the rate formula Eq. (2.92) directly applies. In this case, we need \tilde{n}_e^j and $\delta\tilde{n}_e^{lj}/\delta\mathbf{u}_{ij}$ as input. While \tilde{n}_e^j can be derived from the same

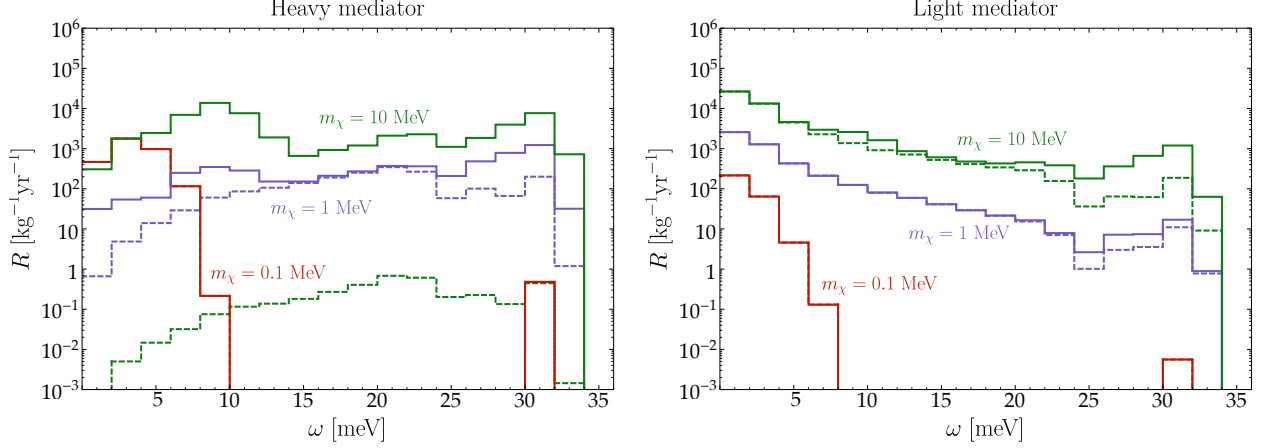


Figure 2.5: Differential rate of single phonon excitations in a GaAs target for $m_\chi = 0.1, 1, 10$ MeV, assuming a heavy (left) or light (right) scalar mediator coupling to nucleons ($f_p = f_n, f_e = 0$), with $\bar{\sigma}_n = 10^{-43}$ cm² and $\omega_{\min} = 1$ meV. Contributions from momentum transfer within the first Brillouin zone are shown in dash. Umklapp processes account for the differences between solid and dashed histograms.

electron wavefunctions as those used in electron transition calculations in Sec. 2.4, $\delta\tilde{n}_e^{lj}/\delta\mathbf{u}_{lj}$ is challenging to compute numerically for general \mathbf{q} and \mathbf{u}_{lj} .

However, the calculation simplifies in the limit $q \ll r_{\text{ion}}^{-1}$, the inverse ionic radii. As in classical electromagnetism, we can make a multipole expansion,

$$\tilde{n}_e^j(-\mathbf{q}) = \int_{\Omega_{lj}} d^3r e^{i\mathbf{q}\cdot\mathbf{r}} n_e^{lj}(\mathbf{r}) = N_{e,j} - i\mathbf{q} \cdot \mathbf{P}_{e,j} + \mathcal{O}(q^2), \quad (2.98)$$

where $N_{e,j}$ is the number of electrons associated with site l, j , and $\mathbf{P}_{e,j}$ is the electron contribution to the polarization in the volume Ω_{lj} . Consider the response of the total polarization of the volume to a lattice displacement \mathbf{u}_{lj} :

$$\delta\mathbf{P}_{lj} = Q_j \delta\mathbf{u}_{lj} + \delta\mathbf{P}_{e,j}, \quad (2.99)$$

where $Q_j = Z_j - N_{e,j}$ is the total charge. This defines the Born effective charge tensor:⁶

$$\mathbf{Z}_j^* \equiv \frac{\delta\mathbf{P}_{lj}}{\delta\mathbf{u}_{lj}} = Q_j \mathbb{1} + \frac{\delta\mathbf{P}_{e,j}}{\delta\mathbf{u}_{lj}}. \quad (2.100)$$

Thus,

$$\frac{\delta\tilde{n}_e^{lj}(-\mathbf{q})}{\delta\mathbf{u}_{lj}} = -i\mathbf{q} \cdot \frac{\delta\mathbf{P}_{e,j}}{\delta\mathbf{u}_{lj}} + \mathcal{O}(q^2) = -i\mathbf{q} \cdot (\mathbf{Z}_j^* - Q_j \mathbb{1}) + \mathcal{O}(q^2). \quad (2.101)$$

⁶More precisely, the Born effective charge \mathbf{Z}_j^* is defined as the change in macroscopic polarization caused by a uniform displacement of the entire sublattice j [202]. However, under the assumption we have made in Eq. (2.82) – that the electrons respond locally to the ionic displacements – the precise definition is equivalent to Eq. (2.100).

From Eqs. (2.98) and (2.101), we obtain (choosing $f^0 = f_e^0$ in the normalization):

$$\mathcal{F}_j^0(\mathbf{q}) = \frac{f_p}{f_e^0} Z_j + \frac{f_n}{f_e^0} (A_j - Z_j) + \frac{f_e}{f_e^0} N_{e,j} + \mathcal{O}(q), \quad (2.102)$$

$$\Delta_j(\mathbf{q}) = -\frac{f_e}{f_e^0} i\mathbf{q} \cdot (\mathbf{Z}_j^* - Q_j \mathbb{1}) + \mathcal{O}(q^2), \quad (2.103)$$

where we have set $F_{N,j}(\mathbf{q}) = 1$ since $q \ll r_{\text{ion}}^{-1}$ is much smaller than the inverse nucleus radius. We therefore obtain the following simple expression for \mathbf{Y}_j :

$$\mathbf{Y}_j = \mathbf{q} \cdot \left[\frac{f_p}{f_e^0} Z_j \mathbb{1} + \frac{f_n}{f_e^0} (A_j - Z_j) \mathbb{1} + \frac{f_e}{f_e^0} (Z_j \mathbb{1} - \mathbf{Z}_j^*) \right] + \mathcal{O}(q^2). \quad (2.104)$$

In the case of a vector mediator, the coupling ratios appearing in Eq. (2.104) should incorporate in-medium screening effects according to Eq. (2.50). As mentioned at the beginning of Sec. 2.2, while dielectric response of an ionic crystal comes from both electrons and ions at phonon frequencies, only the electron contribution is included in the derivation of Eq. (2.50). That this is the correct treatment should be clear from the calculation above. Polarization induced by lattice displacements has been treated as an effective charge density $\nabla \cdot \mathbf{P}$, since it can induce the transition $|0\rangle \rightarrow |\nu, \mathbf{k}\rangle$. As such, it enters the source term rather than the dielectric matrix $\boldsymbol{\varepsilon}$ in Maxwell's equations. In the low q limit, electron contributions to $\boldsymbol{\varepsilon}$ below the electronic band gap approach a constant $\boldsymbol{\varepsilon}_\infty$, referred to as the high-frequency dielectric constant.

In the special case of a dark photon mediator that kinetically mixes with the SM photon, $f_p^0 = -f_e^0$, $f_n^0 = 0$. Combining Eqs. (2.104) and (2.50), and setting $\boldsymbol{\varepsilon} \rightarrow \boldsymbol{\varepsilon}_\infty$, we obtain

$$\mathbf{Y}_j = -\frac{q^2}{\mathbf{q} \cdot \boldsymbol{\varepsilon}_\infty \cdot \mathbf{q}} (\mathbf{q} \cdot \mathbf{Z}_j^*). \quad (2.105)$$

By Eq. (2.92), the rate is therefore

$$R = \frac{1}{m_{\text{cell}}} \frac{\rho_\chi}{m_\chi} \frac{\pi \bar{\sigma}_e}{2\mu_{\chi e}^2} \int \frac{d^3q}{(2\pi)^3} \mathcal{F}_{\text{med}}^2(q) \frac{q^4}{(\mathbf{q} \cdot \boldsymbol{\varepsilon}_\infty \cdot \mathbf{q})^2} \times \sum_\nu \frac{1}{\omega_{\nu, \mathbf{k}}} \left| \sum_j \frac{e^{-W_j(q)}}{\sqrt{m_j}} e^{i\mathbf{G} \cdot \mathbf{x}_j^0} (\mathbf{q} \cdot \mathbf{Z}_j^* \cdot \boldsymbol{\epsilon}_{\nu, \mathbf{k}, j}^*) \right|^2 g(\mathbf{q}, \omega_{\nu, \mathbf{k}}). \quad (2.106)$$

Note that since Eq. (2.104) for \mathbf{Y}_j is derived in the limit $q \ll r_{\text{ion}}^{-1} \sim \mathcal{O}(\text{keV})$, Eq. (2.106) holds only when the integral is dominated by this region. This is the case for a light dark photon mediator for any DM mass, since the integrand peaks at small q . In this case, Eq. (2.106) is in agreement with the result obtain in Ref. [28] based on the Fröhlich Hamiltonian. For a heavy mediator, on the other hand, the integrand peaks at $q_{\text{max}} = 2m_\chi v_{\text{max}}$, so Eq. (2.106) holds only for $m_\chi \ll (2v_{\text{max}} r_{\text{ion}})^{-1} \sim \mathcal{O}(\text{MeV})$.

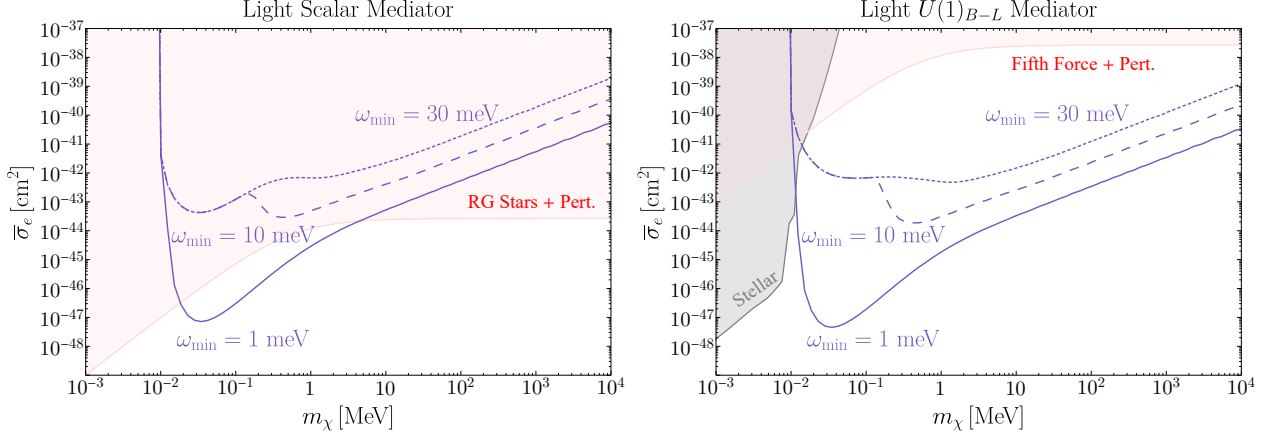


Figure 2.6: Projected reach for a 5% subcomponent of DM scattering via a light (1 eV) hadrophobic scalar (left) or $U(1)_{B-L}$ vector (right) mediator, assuming 1 kg-yr exposure with a GaAs target, 3 signal events and no background. Single phonon excitation reach is shown in purple, assuming energy thresholds $\omega_{\min} = 1, 10, 30$ meV. Pink regions are excluded when taking into account the strongest constraint on the mediator-SM coupling – red giant (RG) stars and fifth force experiments for the two models respectively [10] – together with perturbativity (Pert.) of the mediator- χ coupling. In the $U(1)_{B-L}$ case, the gray region is excluded by stellar production of χ [17].

Beyond the previously studied dark photon mediator case, our first-principle rate derivation here allows us to compute the reach for other DM models with couplings to electrons. As examples, we consider two benchmark models from Ref. [10] – a hadrophobic light scalar mediator and a light $U(1)_{B-L}$ vector mediator. In both cases, astrophysical constraints already rule out all of the parameter space within reach of proposed experiments if χ composes all the DM. We find similar results here: for a hadrophobic light scalar mediator, the astrophysical constraints extend past the reach of single phonon excitations in a GaAs target; for a light $U(1)_{B-L}$ vector mediator, for $m_\chi \gtrsim 100$ MeV and $\omega_{\min} = 1$ meV, the reach extends slightly past the astrophysical constraints, but the rest of the parameter space is constrained. Therefore, as in Ref. [10], we consider the case where χ is a 5% subcomponent of DM, in which case SIDM constraints are absent and single phonon excitations can probe currently unconstrained parameter space. The projected reach for both benchmark models is shown in Fig. 2.6, where a mediator mass of 1 eV is assumed for definiteness.

2.6 Conclusions

Dark matter direct detection has entered an era in which not only the mass coverage is extending beyond the classic WIMP window – especially into the sub-GeV regime – but also multi-channel target response is becoming an important consideration when designing new experiments. In this paper, we detailed a theoretical framework for calculating

spin-independent direct detection rates that can be applied across multiple search channels. Starting from generic DM couplings to the proton, neutron and electron, we factored out material and channel dependent target response into the dynamic structure factor, and derived a procedure to compute this factor which involves quantizing number density operators in the appropriate Hilbert space. We focused on $\mathcal{O}(\text{eV})$ -gap crystal targets where existing and proposed search channels include nuclear recoils, electron transitions and single phonon excitations, each probing a different kinematic regime (see Fig. 2.1). Despite the apparently very different physics involved, the calculation proceeds analogously for all three channels.

While part of this paper has been devoted to rederiving known results in this unified framework, we also obtained several new results, which we summarize in the following:

- We have clarified the range of validity of the standard nuclear recoils calculation (Sec. 2.3). For energy depositions lower than $\mathcal{O}(100 \text{ meV})$ in a crystal target, the picture of scattering off single nuclei breaks down. Collective motions of all nuclei have to be considered, with phonons being the appropriate degrees of freedom. The situation is analogous in fluids, though the energy cutoff can be lower (e.g. $\mathcal{O}(\text{meV})$ for superfluid helium).
- We have extended the electron transition calculation to account for anisotropic target response, and pointed out the resulting daily modulation can be significant (Sec. 2.4). As an example, we considered hexagonal boron nitride, a semiconductor with a 6 eV gap and layered crystal structure, and showed that $\pm(10-40)\%$ daily modulation can be expected, depending on the DM mass (Fig. 2.3).
- As a major new result, we have presented a first-principle derivation of single phonon excitation rates for generic SI couplings. The final result is Eq. (2.92), where dependence on the relative couplings to the proton, neutron, and electron is fully captured by the quantities \mathbf{Y}_j . Computing \mathbf{Y}_j is straightforward for DM coupling only to nucleons (Sec. 2.5), but nontrivial in the presence of coupling to electrons (Sec. 2.5). In the latter case, we have shown that \mathbf{Y}_j are related to the Born effective charges in an ionic crystal for a general light mediator (not necessarily a dark photon) – see Eq. (2.104). As examples, we computed the reach for DM scattering via a light hadrophobic scalar or $U(1)_{B-L}$ vector mediator (Fig. 2.6), where single phonon excitations offer a complementary search channel with competitive sensitivities to previous proposals [10].
- We have pointed out that sensitivity of the single phonon excitation channel is not restricted to sub-MeV DM. For heavier DM, Umklapp contribution can be significant

(Fig. 2.5), and single phonon excitations and nuclear recoils play complementary roles in probing the DM parameter space (Fig. 2.4).

In addition to shedding light on the connection and complementarity between various existing and proposed direct detection channels, the theoretical framework presented here also makes clear that there is a common algorithm one can follow to study yet unexplored novel detection channels in the future. Some of them will require extending our present formalism beyond SI interactions, a task we plan to take on in future work.

MULTI-CHANNEL DIRECT DETECTION OF LIGHT DARK MATTER: TARGET COMPARISON

3.1 Introduction

Direct detection experiments have traditionally focused on dark matter (DM) with mass near the weak scale. Cosmologically, however, thermal particle DM may inhabit a much broader mass range between a keV and 10 TeV. Recent years have seen bold advances in the efforts to probe DM in the range below 10 GeV, which was less explored previously. Here, despite the existence of well-motivated candidates – including MeV dark matter [203–205], WIMPless miracle DM [206], GeV hidden sector dark matter [207–209], asymmetric DM [142, 143], freeze-in DM [137], Strongly Interacting Massive Particles [210], and many others – conventional detection techniques based on nuclear recoils lose sensitivity as the energy deposition falls below detector thresholds. This has motivated an extensive exploration of novel detection channels using a variety of target systems. These include electron transitions in atoms and semiconductors [19, 24, 25, 33–35, 39, 40, 177, 180, 188, 190, 211, 212], superconductors [41, 181, 182], Dirac materials [29, 144, 183], via the Migdal effect [213–217], molecular dissociation or excitation [193–195], multi-excitation production in superfluid helium [184–187], defect production [191, 192], single phonon [28, 64] and magnon [8] excitations in crystals (see also Refs. [189, 218–224] for other recent proposals).

As new experiments are being planned and detection technologies are being discussed and improved, it is important to identify the most promising targets in order to prioritize the experimental program. There are two questions in this respect: *(i)* what types of excitations can be utilized as efficient detection paths with current and developing technologies, and *(ii)* what materials have the strongest response to DM scattering?

It is the purpose of this paper to initiate a discussion on these questions, and provide theory input to the optimization of experimental strategy. We consider several complementary detection channels:

- nuclear recoils, sensitive to the heaviest DM masses, down to $\mathcal{O}(100 \text{ MeV})$ at best;
- electron transitions across band gaps in crystals, covering DM masses down to $\mathcal{O}(100 \text{ keV})$;
- single phonon excitations in crystals, reaching the lightest DM masses, down to $\mathcal{O}(\text{keV})$.

The last two detection channels rely on collective properties of the target, which makes calculating the DM model reach more involved than the standard nuclear recoil calculation. While nuclear recoil was proposed long ago [225, 226], electron transitions in semiconductors (proposed in Refs. [19, 33, 177]) and phonon production from sub-MeV DM in crystals (put forth in Refs. [28, 39, 64]) have a much shorter history. Now that all these ideas are available, we hope to find materials which have a strong response in all channels, in order to cover a broad range of DM masses.

We begin in Sec. 3.2 with a brief review of each detection channel. A common framework to calculate the reach via all three channels is presented in a companion paper [227], which makes it clear that the detection rate factorizes into the particle-level scattering matrix element squared and a material specific dynamic structure factor that captures the target response. Here we summarize the main results of Ref. [227]. Our goal is to find materials with strong responses (a large dynamic structure factor) in each channel over the kinematically allowed mass region.

Toward this goal, in Secs. 3.3 and 3.4, we carry out a detailed comparison of target materials, focusing on two benchmark DM scenarios to illustrate how to optimize target choice for the best sensitivity. Our study covers a total of 24 crystal materials, whose key properties that determine sensitivity to DM scattering are summarized in Table 3.1. Six of the targets we consider are already used in existing nuclear recoil experiments, including Si (DAMIC [21, 71], SENSEI [22], SuperCDMS [23, 77–80, 88]), Ge (SuperCDMS), NaI (DAMA/LIBRA [70], KIMS [73], ANAIS [67], SABRE [76], DM-Ice [72]), CsI (KIMS [228]), Al_2O_3 (CRESST-I [68]), CaWO_4 (CRESST-II-III [15, 69]), but their responses over all channels have not been studied. Two other targets – GaAs and diamond – have been proposed for near-future experiments. We then choose a representative sample of well-known polar semiconductors comprising 16 materials. Our work utilizes state-of-the-art density functional theory (DFT) calculations of material properties. Technical aspects of these calculations are discussed in Appendix B, where we also present our calculated electron band structures and phonon dispersions for the target materials. In the main text, we will highlight a subset of these materials, chosen according to those currently (previously) in use in direct detection (Si, Ge, CsI, CaWO_4 , (Al_2O_3)), as well as one or two new materials which demonstrate particularly strong sensitivity to each benchmark model. In particular, for the dark photon mediator, we highlight SiO_2 and InSb. Results for the materials not presented in the main text can be found in Appendix C, along with other parameters assumed when calculating the reach.

3.2 Detection Channels

We begin by briefly reviewing the detection channels, which are discussed thoroughly in our companion paper [227]. Generally, for a DM particle χ , the event rate per unit target mass is given by

$$R = \frac{1}{\rho_T} \frac{\rho_\chi}{m_\chi} \int d^3v f_\chi(\mathbf{v}) \Gamma(\mathbf{v}), \quad (3.1)$$

where ρ_T is the target mass density, ρ_χ is the local DM energy density, m_χ is the DM mass, and $f_\chi(\mathbf{v})$ is the incoming DM's velocity distribution in the target rest frame. The event rate $\Gamma(\mathbf{v})$ for an incoming DM particle with velocity \mathbf{v} is usually normalized against a reference cross section, defined from the particle-level scattering matrix element \mathcal{M} (in the nonrelativistic normalization) evaluated at a reference momentum transfer q_0 . Here we adopt the following definitions,

$$\bar{\sigma}_n \equiv \frac{\mu_{\chi n}^2}{\pi} \overline{|\mathcal{M}_{\chi n}(q_0)|^2}_{q_0=m_\chi v_0}, \quad (3.2)$$

$$\bar{\sigma}_e \equiv \frac{\mu_{\chi e}^2}{\pi} \overline{|\mathcal{M}_{\chi e}(q_0)|^2}_{q_0=\alpha m_e}, \quad (3.3)$$

for DM-nucleon and DM-electron interactions, respectively, where $\mu_{\chi n}$, $\mu_{\chi e}$ are the reduced masses, and v_0 is the dispersion of the DM's velocity distribution. They coincide with the total particle-level scattering cross sections in the case of a heavy mediator. As we show in Ref. [227], for spin-independent (SI) scattering off a target material via tree-level exchange of a mediator, the matrix element factorizes into a DM component that is universal, and a target response component captured by a dynamic structure factor $S(\mathbf{q}, \omega)$ that is target and excitation specific, such that

$$\Gamma(\mathbf{v}) = \frac{\pi \bar{\sigma}}{\mu^2} \int \frac{d^3q}{(2\pi)^3} \mathcal{F}_{\text{med}}^2(q) S(\mathbf{q}, \omega_{\mathbf{q}}). \quad (3.4)$$

Here $\bar{\sigma}$, μ represent either $\bar{\sigma}_n$, $\mu_{\chi n}$ or $\bar{\sigma}_e$, $\mu_{\chi e}$, \mathbf{q} is the momentum transfer from the DM to the target, and

$$\omega_{\mathbf{q}} = \frac{1}{2} m_\chi v^2 - \frac{(m_\chi \mathbf{v} - \mathbf{q})^2}{2m_\chi} = \mathbf{q} \cdot \mathbf{v} - \frac{q^2}{2m_\chi} \quad (3.5)$$

is the corresponding energy deposition. The mediator form factor is given by¹

$$\mathcal{F}_{\text{med}}(q) = \begin{cases} 1 & \text{(heavy mediator),} \\ (q_0/q)^2 & \text{(light mediator).} \end{cases} \quad (3.6)$$

¹When present, in-medium screening effects are incorporated in the dynamic structure factor $S(\mathbf{q}, \omega)$ instead of the mediator form factor $\mathcal{F}_{\text{med}}(q)$.

The dynamic structure factor, which captures the target's response to a general energy-momentum transfer ω, \mathbf{q} , is given by

$$S(\mathbf{q}, \omega) \equiv \frac{1}{V} \sum_f |\langle f | \mathcal{F}_T(\mathbf{q}) | i \rangle|^2 2\pi \delta(E_f - E_i - \omega), \quad (3.7)$$

where V is the total volume, $|i\rangle, |f\rangle$ are the initial and final states of the target system, and \mathcal{F}_T is the quantum mechanical operator acting on the target Hilbert space that the DM couples to.

For an isotropic target, the dynamic structure factor depends only on the magnitude but not the direction of \mathbf{q} , so the velocity integral can be evaluated independently, giving

$$\eta(v_{\min}) \equiv \int d^3v \frac{f_\chi(\mathbf{v})}{v} \Theta(v - v_{\min}), \quad (3.8)$$

$$v_{\min} = \frac{q}{2m_\chi} + \frac{\Delta E}{q}, \quad (3.9)$$

for which analytic expressions can be obtained assuming a boosted truncated Maxwell-Boltzmann (MB) distribution. On the other hand, for the more general case of anisotropic target response, the dynamic structure factor depends on the direction of \mathbf{q} , and we can utilize the delta function in Eq. (3.7) to evaluate the velocity integral first, giving

$$g(\mathbf{q}, \omega) \equiv \int d^3v f_\chi(\mathbf{v}) 2\pi \delta(\omega - \omega_{\mathbf{q}}), \quad (3.10)$$

which can be computed analytically for the usually assumed boosted truncated MB distribution.

In the following subsections, we consider each detection channel in turn, summarizing the formalism presented in Ref. [227] on the dynamic structure factors and detection rates, building on the discussion in previous works (particularly [28, 33, 141]).

Nuclear Recoils

For each nucleus species,

$$S(\mathbf{q}, \omega) = 2\pi \frac{\rho_T}{m_N} \frac{f_N^2}{f_n^2} F_N^2(q) \delta\left(\frac{q^2}{2m_N} - \omega\right), \quad (3.11)$$

where m_N is the nucleus mass, f_n, f_p and $f_N = f_p Z + f_n(A - Z)$ are the DM-neutron, DM-proton and DM-nucleus couplings respectively, and $F_N(q)$ is the Helm form factor

$$F_N(q) = \frac{3j_1(qr_n)}{qr_n} e^{-(qs)^2/2}, \quad (3.12)$$

$$r_n \simeq 1.14 A_n^{1/3} \text{ fm}, \quad s \simeq 0.9 \text{ fm}, \quad (3.13)$$

which approaches 1 in the $q \rightarrow 0$ limit. The differential rate with respect to energy deposition, generalized to the case of multiple nucleus species, is

$$\frac{dR}{d\omega} = \frac{\rho_\chi \bar{\sigma}_n}{m_\chi 2\mu_{\chi n}^2 \sum_N A_N} \frac{1}{\left[\sum_N A_N \frac{f_N^2}{f_n^2} F_N^2 \mathcal{F}_{\text{med}}^2 \eta(v_{\text{min}}) \right]_{q^2=2m_N\omega}}, \quad (3.14)$$

where $v_{\text{min}} = \frac{q}{2\mu_{\chi N}}$.

The conventional nuclear recoil calculation is valid when each nucleus can be considered independent of the other nuclei. In a crystal target, this is true if the scattering happens at a timescale $1/\omega$ much shorter than the inverse phonon frequencies $1/\omega_{\text{ph}}$, i.e., if the energy deposition $\omega \gg \omega_{\text{ph}} \sim \mathcal{O}(100 \text{ meV})$, or equivalently, $q \gg \sqrt{m_N \omega_{\text{ph}}}$ (note that this momentum cutoff is essentially the inverse of the spatial extent of nucleus wavefunctions in a harmonic potential). For lower energy depositions, the scattering event proceeds by direct production of (single or multiple) phonons. We discuss single phonon excitations in Sec. 3.2. We will see that single phonon excitation rates are suppressed by the Debye-Waller factor for $q \gtrsim \sqrt{m_N \omega_{\text{ph}}}$, which shows the complementarity between the two channels.

Electron Transitions

In solids, electrons form band structures with energy eigenstates labeled by a band index i and a wave vector \mathbf{k} within the first Brillouin zone (1BZ). In an insulator or semiconductor, all electrons occupy the valence bands at low temperatures, and can be excited across the band gap to conduction bands. The dynamic structure factor encapsulates all such transitions from i_1, \mathbf{k}_1 to i_2, \mathbf{k}_2 :

$$S(\mathbf{q}, \omega) = 2 \sum_{i_1, i_2} \int_{\text{1BZ}} \frac{d^3 k_1 d^3 k_2}{(2\pi)^6} 2\pi \delta(E_{i_2, \mathbf{k}_2} - E_{i_1, \mathbf{k}_1} - \omega) \times \sum_{\mathbf{G}} (2\pi)^3 \delta^3(\mathbf{k}_2 - \mathbf{k}_1 + \mathbf{G} - \mathbf{q}) |f_{[i_1 \mathbf{k}_1, i_2 \mathbf{k}_2, \mathbf{G}]}|^2, \quad (3.15)$$

up to screening effects. Here $\mathbf{G} = n_1 \mathbf{b}_1 + n_2 \mathbf{b}_2 + n_3 \mathbf{b}_3$, with $n_1, n_2, n_3 \in \mathbb{Z}$ and $\mathbf{b}_{1,2,3}$ are reciprocal primitive vectors. The crystal form factor is defined by

$$f_{[i_1 \mathbf{k}_1, i_2 \mathbf{k}_2, \mathbf{G}]} \equiv \sum_{\mathbf{G}_1, \mathbf{G}_2} \delta_{\mathbf{G}_2 - \mathbf{G}_1, \mathbf{G}} u_{i_2}^*(\mathbf{k}_2 + \mathbf{G}_2) u_{i_1}(\mathbf{k}_1 + \mathbf{G}_1), \quad (3.16)$$

where $u_i(\mathbf{k} + \mathbf{G})$ are Bloch wavefunction coefficients computed from DFT (see Appendix B.1). We neglect possible spin dependence of the electron band structures, and simply sum over

contributions from the degenerate spin states. The total rate is given by

$$R = \frac{2}{\rho_T} \frac{\rho_\chi}{m_\chi} \frac{\pi \bar{\sigma}_e}{\mu_{\chi e}^2} \sum_{i_1, i_2} \int_{\text{1BZ}} \frac{d^3 k_1 d^3 k_2}{(2\pi)^6} \sum_{\mathbf{G}} g(\mathbf{q}, \omega) \mathcal{F}_{\text{med}}^2(q) |f_{[i_1 \mathbf{k}_1, i_2 \mathbf{k}_2, \mathbf{G}]}|^2, \quad (3.17)$$

where $\mathbf{q} = \mathbf{k}_2 - \mathbf{k}_1 + \mathbf{G}$ and $\omega = E_{i_2, \mathbf{k}_2} - E_{i_1, \mathbf{k}_1}$ are assumed. Note that unlike in nuclear recoils, the dynamic structure factor for electron transitions is generally not isotropic in \mathbf{q} for all energy-momentum depositions. When anisotropies are significant, the rate cannot be expressed in terms of $\eta(v_{\text{min}})$, and the g function in Eq. (3.10) should be used instead. The physical implication is that the rate depends on the direction of the DM wind and exhibits daily modulation. An example of this is discussed in Ref. [227].

Single Phonon Excitations

Phonons are quanta of lattice vibrations in crystals. For a three-dimensional crystal with n atoms/ions in the primitive cell, there are $3n$ phonon branches, with dispersions $\omega_{\nu, \mathbf{k}}$ ($\nu = 1, \dots, 3n$), where the wave vector \mathbf{k} is in the 1BZ. The dynamic structure factor has the general form

$$S(\mathbf{q}, \omega) = \frac{\pi}{\Omega} \sum_{\nu} \delta(\omega - \omega_{\nu, \mathbf{k}}) \times \frac{1}{\omega_{\nu, \mathbf{k}}} \left| \sum_j \frac{e^{-W_j(\mathbf{q})}}{\sqrt{m_j}} e^{i\mathbf{G} \cdot \mathbf{x}_j^0} (\mathbf{Y}_j \cdot \boldsymbol{\epsilon}_{\nu, \mathbf{k}, j}^*) \right|^2, \quad (3.18)$$

where Ω is the volume of the primitive cell, $j = 1, \dots, n$ runs over the atoms/ions in the primitive cell, \mathbf{x}_j^0 are their equilibrium positions, and m_j are their masses. \mathbf{Y}_j contains the DM-atom/ion couplings, whose general definition is given in Ref. [227]. We explicitly state the expression of \mathbf{Y}_j for each benchmark model below. $\boldsymbol{\epsilon}_{\nu, \mathbf{k}, j}$ are the phonon polarization vectors. \mathbf{k} is the momentum within the 1BZ that satisfies $\mathbf{q} = \mathbf{k} + \mathbf{G}$ for some reciprocal lattice vector \mathbf{G} — only those phonon modes that match the momentum transfer up to reciprocal lattice vectors can be excited, as a result of lattice momentum conservation. At large q , the dynamic structure factor is suppressed by the Debye-Waller factor, given by

$$W_j(\mathbf{q}) = \frac{\Omega}{4m_j} \sum_{\nu} \int_{\text{1BZ}} \frac{d^3 k}{(2\pi)^3} \frac{|\mathbf{q} \cdot \boldsymbol{\epsilon}_{\nu, \mathbf{k}, j}|^2}{\omega_{\nu, \mathbf{k}}}. \quad (3.19)$$

We obtain the total rate

$$R = \frac{1}{m_{\text{cell}}} \frac{\rho_\chi}{m_\chi} \frac{\pi \bar{\sigma}}{2\mu^2} \int \frac{d^3 q}{(2\pi)^3} \mathcal{F}_{\text{med}}^2(q) \sum_{\nu} g(\mathbf{q}, \omega_{\nu, \mathbf{k}}) \frac{1}{\omega_{\nu, \mathbf{k}}} \left| \sum_j \frac{e^{-W_j(\mathbf{q})}}{\sqrt{m_j}} e^{i\mathbf{G} \cdot \mathbf{x}_j^0} (\mathbf{Y}_j \cdot \boldsymbol{\epsilon}_{\nu, \mathbf{k}, j}^*) \right|^2, \quad (3.20)$$

where $m_{\text{cell}} = \rho_T \Omega$ is the mass contained in a primitive cell. The phonon dispersions $\omega_{\nu, \mathbf{k}}$ and polarization vectors $\epsilon_{\nu, \mathbf{k}, j}$ that enter this equation are obtained from DFT calculations (see Appendix B.2).

Acoustic vs. Optical Phonons

It is useful to distinguish acoustic and optical phonons, as they are sensitive to different types of DM interactions. Among the $3n$ phonon branches, three are gapless with linear dispersions $\omega_{\nu, \mathbf{k}} \sim c_s |\mathbf{k}|$ near $|\mathbf{k}| = 0$ (with c_s the sound speed), as a result of spontaneous breaking of translation symmetries; these are acoustic phonons that, in the long wavelength limit, correspond to in-phase oscillations of atoms/ions in the same primitive cell. The remaining $3(n - 1)$ branches are gapped “optical” phonons, corresponding to out-of-phase oscillations.

Due to the nature of in-phase oscillations, acoustic phonons can be efficiently excited if DM couples to different atoms/ions in a correlated way. An example is a DM particle coupling to nucleons via a scalar or vector mediator. In this case, \mathbf{Y}_j is proportional to a linear combination of A_j and Z_j , and can have the same sign and similar magnitudes for all j .

By contrast, the out-of-phase oscillations associated with gapped phonon modes have enhanced sensitivity to DM coupling to the atoms/ions in the same primitive cell differently. This is the case for dark-photon-mediated DM scattering with polar materials. The dark photon mediator kinetically mixes with the SM photon, and as a result, \mathbf{Y}_j point in opposite directions for oppositely charged ions. We follow convention and call all gapped phonon modes “optical,” though only in polar materials where there are both positively and negatively charged ions in the primitive cell (e.g., GaAs) do these modes couple strongly to the (dark) photon via the oscillating dipole. Diamond, Si and Ge, for example, all have gapped phonon modes, but none of these materials has a strong coupling to the dark photon as the primitive cell does not contain oppositely charged ions.

3.3 Target Comparison: Kinetically Mixed Light Dark Photon Mediator

A well motivated model of light dark matter involves interaction with the SM via a light dark photon A' that kinetically mixes with the photon:

$$\begin{aligned} \mathcal{L} = & -\frac{1}{4} F'^{\mu\nu} F'_{\mu\nu} + \frac{1}{2} \kappa F^{\mu\nu} F'_{\mu\nu} + \frac{1}{2} m_{A'}^2 A'^2 \\ & + (|D_\mu \chi|^2 - m_\chi^2 |\chi|^2) \quad \text{or} \quad (i\bar{\chi} \not{D} \chi - m_\chi \bar{\chi} \chi), \end{aligned} \quad (3.21)$$

where $D_\mu = \partial_\mu - ie' A'_\mu$, and the DM χ can be either a complex scalar or a Dirac fermion. The gauge boson kinetic terms can be diagonalized by redefining $A_\mu \rightarrow A_\mu + \kappa A'_\mu$, which

gives J_{EM}^μ a charge under the dark $U(1)$ of κe . The reference cross section, utilized in present results for this model, is given by

$$\bar{\sigma}_e = \frac{\mu_{\chi e}^2}{\pi} \frac{\kappa^2 e'^2 e^2}{(\alpha^2 m_e^2 + m_{A'}^2)^2}. \quad (3.22)$$

The projected 95% confidence level (C.L.) exclusion reach on $\bar{\sigma}_e$ assuming zero background (i.e., the cross section needed to obtain three events) from electron transitions and single phonon excitations are shown in Fig. 3.1, for $m_{A'} \rightarrow 0$ and an exposure of one kg-yr.² In the rest of this section, we describe in detail the features in this plot, and also discuss nuclear recoils.

Single Phonon Excitations

Optical phonon excitation is the dominant detection mode for dark photon mediated scattering. As shown in Ref. [227], in the low q limit (which dominates the momentum integral for a light mediator since $\mathcal{F}_{\text{med}}^2 \propto q^{-4}$), the interaction is described via the Born effective charges of the ions, \mathbf{Z}_j^* (which are generally 3×3 matrices),

$$\mathbf{Y}_j = -\frac{q^2}{\mathbf{q} \cdot \boldsymbol{\varepsilon}_\infty \cdot \mathbf{q}} (\mathbf{q} \cdot \mathbf{Z}_j^*) + \mathcal{O}(q^2), \quad (3.23)$$

where $\boldsymbol{\varepsilon}_\infty$ is the high-frequency dielectric matrix. The total rate is given by Eq. (3.20). Only *polar* materials, or those which have differently charged ions in the primitive cell, can couple phonon modes to the dark photon, which explains the absence of phonon reach curves for Si and Ge in Fig. 3.1.

As explained in the previous section, optical phonon modes involve out-of-phase oscillations and are gapped. Because the optical modes are the dominant contribution to the rate, the properties of the optical modes determine the shape of the phonon excitation curves in Fig. 3.1: when there are sharp changes in the reach as a function of mass, it is because there is a transition in the dominance of a particular optical mode. For low momentum transfer, the dispersion of the gapped modes is approximately a constant, such that the lowest DM mass reachable is determined by setting the maximum kinetic energy of the incoming DM,

² Changes in the constraint projections via single phonon excitations in Figs. 3.1, C.7-C.9, relative to previous versions, are due to a bug fix when using the Born effective charges, \mathbf{Z}_j^* . Targets with significant changes, at low m_χ , are SiO₂, CaWO₄ and MgF₂. The calculations have been updated using PhonoDark v1.1.0 [178].

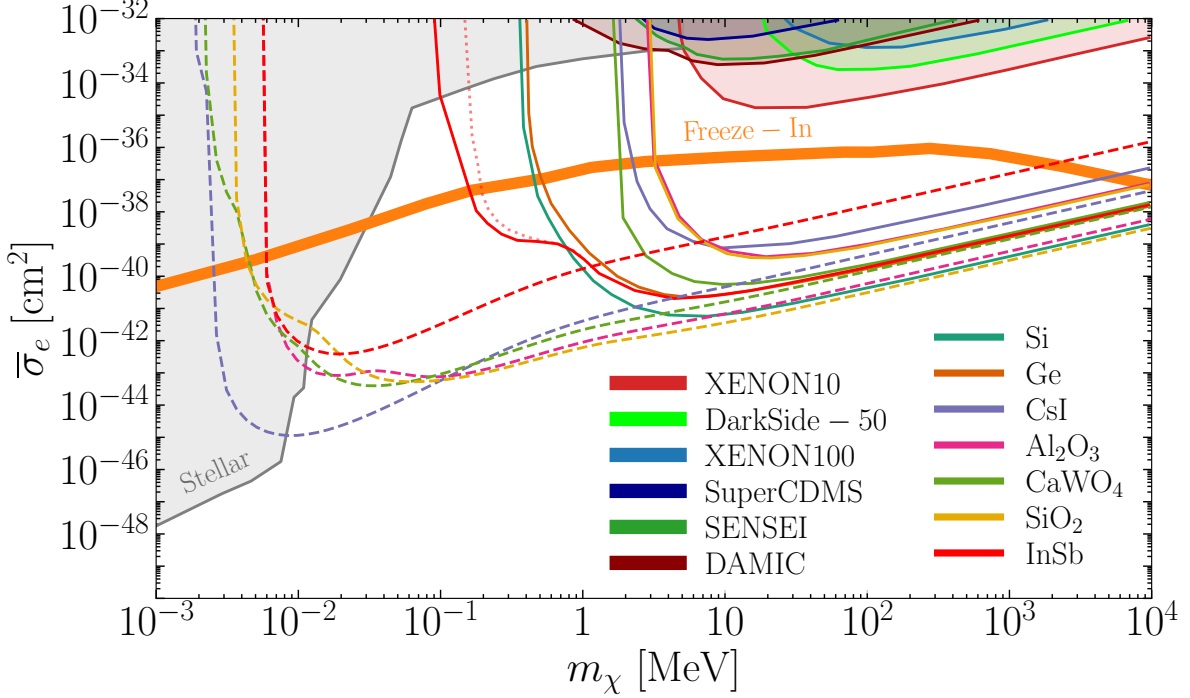


Figure 3.1: Projected reach from single phonon excitations (dashed) and electron transitions (solid) for DM scattering mediated by a kinetically mixed light dark photon (the smallest-gap target InSb suffers from slow convergence in the electronic transition calculation at $m_\chi < 1$ MeV, for which we show results of the two most accurate runs with solid and dotted curves, see Appendix B.1 for details). Nuclear recoils (not shown) can also probe this model, but the conclusion on which targets are superior is the same as for the light hadrophilic mediator model. A detector threshold of 1 meV is used for the phonon calculations, and all transitions with energy deposition greater than the band gaps are included in electron excitations. The freeze-in benchmark is taken from Refs. [18, 19], corrected by including plasmon decay for sub-MeV DM [20]. Stellar constraints are from Ref. [17] and direct detection constraints are from DAMIC [21], DarkSide-50 [12], SENSEI [22], SuperCDMS [23], XENON10 [24, 25], and XENON100 [12, 26].²

$m_\chi v_{\max}^2/2$, equal to the energy of the lowest optical mode,³

$$m_{\chi,\min} \sim 3 \text{ keV} \left(\frac{\omega_0}{10 \text{ meV}} \right). \quad (3.24)$$

Thus materials having low energy optical phonon modes are desirable to search for light dark matter; CsI, for example, has particularly low-lying optical phonon excitations, and its sensitivity to the lightest DM masses is seen in Fig. 3.1.

³One has to be careful with this estimate, as the lowest optical mode is generally not the dominant mode, rather it is the mode which is most “longitudinal,” or maximizes $\mathbf{q} \cdot \boldsymbol{\epsilon}$. For simple diatomic materials, there is one precisely longitudinal mode in the low q limit, but the same is not true for more complex materials such as Al₂O₃, as many gapped modes have a longitudinal component. A general rule of thumb is that the highest energy optical mode is the most longitudinal.

We can also see that at higher masses, single optical phonon production rates vary widely between materials. This can be understood analytically. Consider first the simplest case of a diatomic polar crystal (e.g., GaAs). The dominant contribution to the q integral in Eq. (3.20) is well within the 1BZ and therefore we can set $\mathbf{G} = \mathbf{0}$, $W_j \simeq 0$, and $g(\mathbf{q}, \omega) \propto q^{-1}$. Approximating $\mathbf{Z}_j^* \simeq Z_j^* \mathbb{1}$, and noting that $Z_1^* = -Z_2^* \equiv Z^*$, we see that the rate is dominated by the longitudinal optical (LO) mode, for which one can show $\epsilon_{\text{LO},\mathbf{k},1}$ and $\epsilon_{\text{LO},\mathbf{k},2}$ are anti-parallel, and $|\epsilon_{\text{LO},\mathbf{k},j}| = \sqrt{\mu_{12}/m_j}$ in the limit $k \rightarrow 0$, where μ_{12} is the reduced mass of the two ions. Further approximating the phonon dispersion as constant and $\epsilon_\infty \simeq \epsilon_\infty \mathbb{1}$, the rate simplifies to

$$\begin{aligned} R &\propto \frac{q_0^4}{m_{\text{cell}}} \frac{\rho_\chi}{m_\chi} \frac{\bar{\sigma}_e}{\epsilon_\infty^2 \omega_{\text{LO}}} \frac{Z^{*2}}{\mu_{\chi e}^2 \mu_{12}} \log\left(\frac{m_\chi v_0^2}{\omega_{\text{LO}}}\right) \\ &\propto \frac{Z^{*2}}{A_1 A_2 \epsilon_\infty^2} \left(\frac{\text{meV}}{\omega_{\text{LO}}}\right) \equiv Q. \end{aligned} \quad (3.25)$$

We call Q a quality factor, since it is the combination of material-specific quantities that determines the direct detection rate. A higher- Q material has a better reach in the high mass regime. More concretely, we find

$$\begin{aligned} R &\simeq \frac{1}{\text{kg yr}} \left(\frac{Q}{10^{-7}}\right) \left(\frac{m_e}{m_\chi}\right) \left(\frac{m_e^2}{\mu_{\chi e}^2}\right) \left(\frac{\bar{\sigma}_e}{10^{-39} \text{ cm}^2}\right) \\ &\quad \times \log\left(\frac{q_{\text{max}}}{q_{\text{min}}}\right). \end{aligned} \quad (3.26)$$

Note that although we have focused on the special case of diatomic polar crystals in order to derive analytic estimates, similar considerations apply for more complicated crystals. For example, it is not surprising that larger Born effective charges and lighter ions are helpful. When comparing the targets, we adopt the following prescription for the quality factor,

$$Q \equiv \frac{1}{\epsilon_\infty^2 \bar{\omega}_O} \prod_{j=1}^n \left(\frac{|Z_j^*|}{A_j}\right)^{\frac{2}{n}}, \quad (3.27)$$

where n is the total number of ions in the primitive cell, and $\bar{\omega}_O$ is the directionally averaged optical phonon energy of the highest mode near $\mathbf{k} = \mathbf{0}$, given in Table 3.1. In our list of materials LiF has the largest quality factor, with SiO₂ second. We choose to highlight SiO₂ in Fig. 3.1 because LiF is a less desirable experimental target due to large backgrounds [229].

A further consideration for optimizing Q given a fixed chemistry (atomic species) is to maximize the Born effective charges. For example, cubic tungsten trioxide (WO₃) has been reported to have anomalously high Born effective charges of up to +12.5 and -9.1 on W

and O respectively [230]. Materials with such high Born effective charges, a manifestation of highly covalent bonding character, provide a further route for maximizing Q .⁴

We comment in passing that also in the case of a heavy dark photon mediator, the rate is largely determined by the quality factor defined in Eq. (3.27) for sub-MeV DM; for heavier DM, couplings to ions cannot be simply captured by the Born effective charges at high momentum transfer, and the total rate is more challenging to compute [227].

Electron Transitions

The typical band gaps between valence and conduction bands, E_g , range from a fraction of an eV (InSb and Ge) to as high as 10 eV (e.g., SiO₂). This gap sets the lightest DM mass to which the experiment is sensitive, as kinematics requires that $m_\chi v_{\max}^2/2 > E_g$, implying

$$m_{\chi,\min} \sim 0.3 \text{ MeV} \left(\frac{E_g}{\text{eV}} \right). \quad (3.28)$$

Thus, small gap materials will generally have better reach. For example, InSb is superior to Si for $m_\chi \lesssim \text{MeV}$, as seen in Fig. 3.1; in fact, the sub-eV band gap of InSb allows for a significant $\mathbf{G} = \mathbf{0}$ contribution that is absent for larger gap materials, and this contribution dominates at $m_\chi \lesssim \text{MeV}$, greatly extending the reach. However, note that Ge, which has a smaller band gap than Si, does not have a better reach. The difference here is due to a direct vs indirect band gap.⁵ When depositing energy via a scattering process, there must be some momentum transfer, and therefore, strictly speaking, E_g in Eq. (3.28) should be replaced by the minimum kinematically allowed energy difference. For direct gap materials this means that $m_{\chi,\min}$ will increase, as it does in Ge, which is why Ge has worse reach than Si. Note that there is a complementarity between single phonon excitations and electron transitions. In the phonon case, materials with the best sensitivity tend to be insulators, as they have small values of ε_∞ . However, for electron transitions, one prefers materials with smaller band gaps, which generally have larger values of ε_∞ . This is because loop corrections to the in-medium photon propagator are larger for a smaller band-gap: virtual electrons can be more easily created because of the smaller energy difference.

For higher masses an analytic comparison is not tractable. The wavefunction coefficients in Eq. (3.17) cannot be modeled well analytically, and hence the reach must be computed numerically. Note that for Si, Ge, NaI, CsI, GaAs, and diamond, our results are roughly

⁴Cubic WO₃ is dynamically unstable giving imaginary frequencies in the phonon band structure. Therefore we do not include it in phonon comparison plots, and leave a study of other stable isomorphs for future work.

⁵The HSE06 exchange-correlation functional used in our DFT calculations slightly underestimates the direct band gap of Ge whilst being a close match to the indirect band gap [231]. This leads to the prediction of a direct band gap when optimized lattice parameters are used, contrary to experiment.

consistent with previous calculations in Refs. [33, 34, 180], where the DFT calculation is implemented differently. However, we find discrepancies in the semi-core electron contributions, which are subdominant for our light mediator benchmark, but become important for a heavy mediator. We will investigate this issue in detail in an upcoming publication. Another improvement of the calculation that we plan to address is the treatment of in-medium screening effects (see Ref. [227] for further discussion), which we have neglected in the present calculation. Such effects are expected to be weak for materials with band gaps larger than about 1 eV. However, for sub-eV gap targets such as InSb, for masses below ~ 1 MeV, the result here should be taken with caution, as the effects may not be negligible.

Nuclear Recoils

The dark photon mediator coupling in a target system is momentum dependent. At very small momentum transfers $q \rightarrow 0$, the coupling is negligible as the total target is assumed to have no net charge. For $q \lesssim r_{\text{ion}}^{-1}$, where r_{ion} is the size of an atom without the binding electrons, ionic charges, if present, can be coupled to. As the momentum transfer increases further, outer-shell electrons will respond incoherently, possibly transitioning to conduction bands independent of proton and inner-shell electron responses. On the other hand, in a nuclear recoil event, $q \gg \sqrt{m_N \omega_{\text{ph}}} \gg r_{\text{ion}}^{-1}$. In this regime, protons respond coherently as long as $F_N(q) \simeq 1$, since they are bound in the nucleus, whereas electron couplings are irrelevant since even the core electron wavefunctions do not have such high momentum components. Therefore, nuclear recoils can happen in an overall neutral crystal via coupling to the proton number of each nucleus without any atomic form factor suppression.

In order to compare against phonon and electron excitations, we express the reach in terms of $\bar{\sigma}_e$ instead of $\bar{\sigma}_n$. This corresponds to replacing $(f_N/f_n)^2 \rightarrow Z_N^2$ for each nucleus species, and $\mu_{\chi n} \rightarrow \mu_{\chi e}$, $q_0 \rightarrow \alpha m_e$, and lastly, $\bar{\sigma}_n \rightarrow \bar{\sigma}_e$ in Eq. (3.14). While we discuss material comparison in this subsection, nuclear recoil reach curves have been omitted in Fig. 3.1 in order not to further complicate the plot; they can be approximately rescaled from the reach curves in Fig. 3.2 below, and are straightforward to compute from Eq. (3.14).⁶

The low mass reach of nuclear recoils is material and threshold dependent, and can be understood from kinematics. The maximum momentum transfer is given by $q_{\text{max}} = 2\mu_{\chi N}v_{\text{max}}$, and therefore the maximum energy deposited is given by $\omega_{\text{max}} = 2\mu_{\chi N}^2v_{\text{max}}^2/m_N$. Requiring that this be larger than the threshold sets the minimum DM mass. For a threshold around 500 meV (which almost saturates the validity bound for some of the crystal targets as discussed

⁶ Changes in the constraint projections via single phonon excitations in Figs. 3.2-3.3, C.10-C.15, relative to previous versions, are due to a bug fix in computing F_{N_j} which altered the constraints by a factor of, approximately, 2.25. The calculations have been updated using PhonoDark v1.1.0 [178].

in Sec. 3.2), and $v_{\max} = 10^{-3}$, $m_\chi \ll m_N$, the minimum DM mass within reach is

$$m_{\chi,\min} \sim 100 \text{ MeV} \left(\frac{\omega_{\min}}{500 \text{ meV}} \right)^{\frac{1}{2}} \left(\frac{m_N}{10 \text{ GeV}} \right)^{\frac{1}{2}}, \quad (3.29)$$

Therefore, materials with lighter nuclei are more favorable for kinematic matching.

At higher masses, kinematics is not a limiting factor, and we can obtain an analytic approximation for the rate. Assuming a singular nuclear species, $A_N = A$, $Z_N = Z$ simplifies Eq. (3.14) to

$$\frac{dR}{d\omega} \propto \frac{\bar{\sigma}_e}{m_\chi \mu_{\chi e}^2} \frac{Z^2}{A^2} \frac{1}{\omega^2} \eta(v_{\min}), \quad (3.30)$$

and we see that the rate is dominated by small ω . At masses above a few hundred MeV and small ω , $\eta(v_{\min})$ approaches $\eta(0)$. The total rate then becomes

$$R \propto \frac{\bar{\sigma}_e}{m_\chi \mu_{\chi e}^2} \frac{Z^2}{A^2} \frac{1}{\omega_{\min}}, \quad (3.31)$$

and is approximately material independent. Note that if the dark photon mediator is heavy, the factor $A^2 \omega^2$ in the denominator of Eq. (3.30) would be absent, and heavier (larger Z) elements are advantageous.

3.4 Target Comparison: Hadrophilic Scalar Mediator

As a second benchmark model, we consider a real scalar mediator ϕ coupling to the proton and neutron,

$$\begin{aligned} \mathcal{L} &= \frac{1}{2}(\partial_\mu \phi)^2 - \frac{1}{2}m_\phi^2 \phi^2 + f_p \phi \bar{p}p + f_n \phi \bar{n}n \\ &+ \left(\frac{1}{2}(\partial_\mu \chi)^2 - \frac{1}{2}m_\chi^2 \chi^2 + \frac{1}{2}y_\chi m_\chi \phi \chi^2 \right) \\ &\text{or } (i\bar{\chi}\not{\partial}\chi - m_\chi \bar{\chi}\chi + y_\chi \phi \bar{\chi}\chi), \end{aligned} \quad (3.32)$$

where the DM χ is taken to be either a real scalar or a Dirac fermion. In the absence of electron couplings, the relevant search channels are single phonon excitations and nuclear recoils. We will quote the reach in terms of $\bar{\sigma}_n$, given by

$$\bar{\sigma}_n = \frac{\mu_{\chi n}^2}{4\pi} \frac{y_\chi^2 f_n^2}{(m_\chi^2 v_0^2 + m_\phi^2)^2}. \quad (3.33)$$

The 95% C.L. exclusion reach on $\bar{\sigma}_n$ for a light (effectively massless) and heavy mediator are shown in Figs. 3.2 and 3.3 respectively, assuming $f_p = f_n$, an exposure of one kg-yr, and zero background events. In the rest of this section we explain in detail the features in these plots.

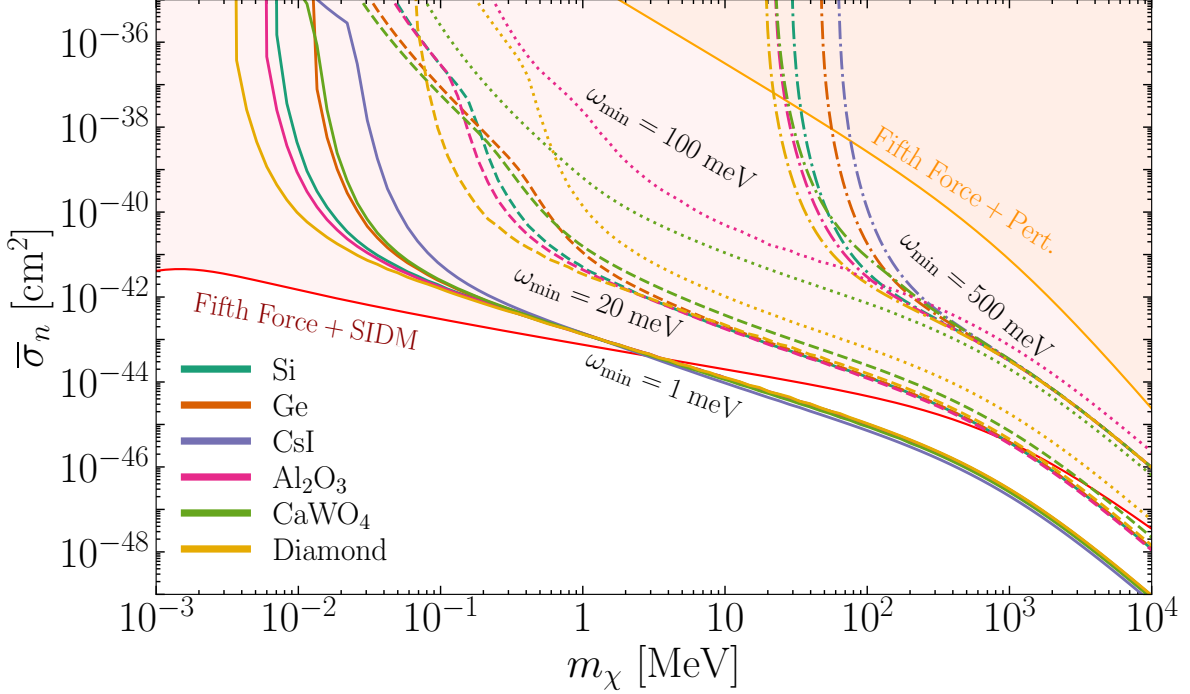


Figure 3.2: Single phonon and nuclear recoil reach for a light ($m_\phi = 1$ eV) hydrophilic scalar mediator. 1, 20, and 100 meV thresholds are shown for the single phonon reach (solid, dashed, and dotted respectively), and 500 meV threshold is assumed for the nuclear recoil reach (dot-dashed). For $m_\phi = 1$ eV the dominant constraint on f_n is from fifth force experiments [10]. If m_χ makes up all the DM then the dominant constraint on y_χ is from DM self-interactions (SIDM) [10]. If m_χ is only a subcomponent, we only require perturbativity $y_\chi < 1$ (Pert.); in this case the reach curves can be easily rescaled.⁶

Single Phonon Excitations

We first consider DM creating a single phonon via the nucleon coupling. As shown in Ref. [227],

$$\mathbf{Y}_j = \mathbf{q} \left(\frac{f_j}{f_n} \right) F_{N_j}(q), \quad (3.34)$$

where $f_j = f_p Z_j + f_n (A_j - Z_j)$ for the nucleus at site j in a primitive cell, and $F_{N_j}(q)$ is the nuclear form factor given by Eq. (3.13). As before, the total rate is calculated from Eq. (3.20). However, a major difference compared to the dark photon mediator model is that, if f_p and f_n have the same sign, the rate is dominated by acoustic and not optical phonons, assuming the energy threshold is low enough to access the acoustic phonons. This is because \mathbf{Y}_j points in the same direction for all j , resulting in stronger in-phase oscillations as discussed in Sec. 3.2.

We first discuss Fig. 3.2, for the light mediator case, when the energy threshold, ω_{\min} , is 1 meV. While such a low threshold is experimentally challenging, the curves are easier to

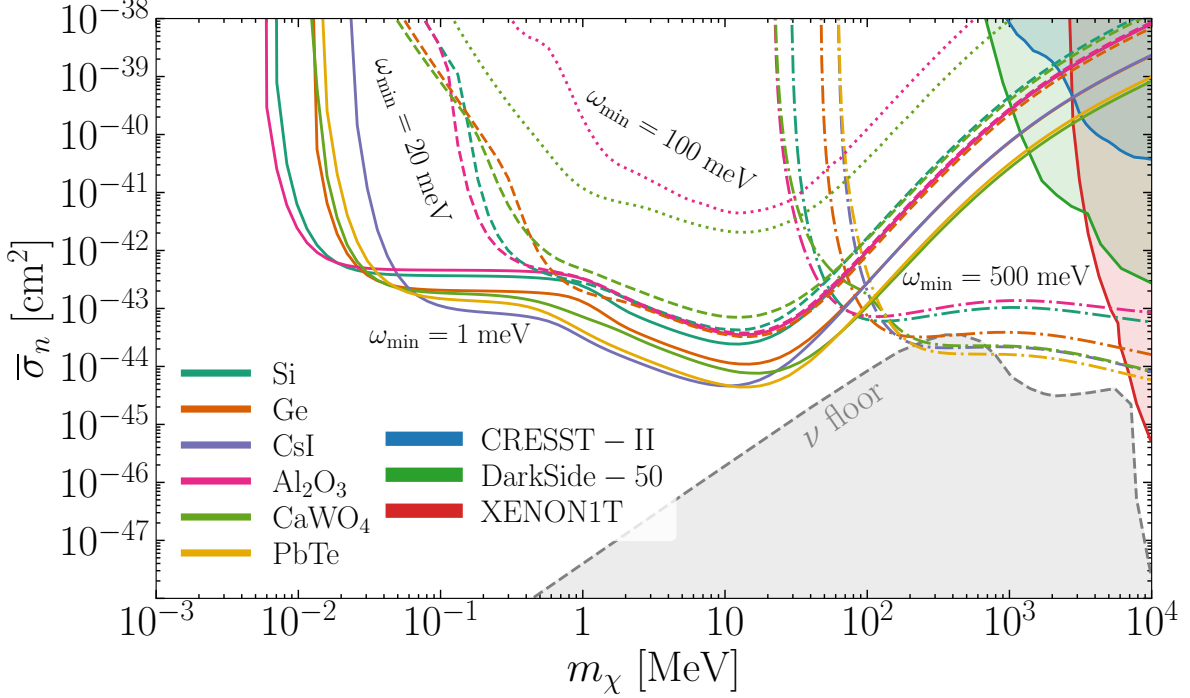


Figure 3.3: Single phonon and nuclear recoil reach for a massive ($m_\phi \gtrsim 400$ MeV) hadrophilic scalar mediator. 1, 20, and 100 meV thresholds are shown for the single phonon reach (solid, dashed, and dotted respectively), and 500 meV threshold is assumed for the nuclear recoil reach (dot-dashed). There are no stellar constraints for $m_\phi \gtrsim 400$ MeV [10]. Currently, the best experimental nuclear recoil constraints in this region of parameter space are from DarkSide-50 [12] (assuming binomial fluctuations), and XENON1T (combined limits from [13, 14]). We also show the constraint from CRESST-II [15], which is stronger than the DarkSide-50 constraint at low masses assuming no fluctuation in energy quenching. A more complete collection of nuclear recoil constraints can be found in Refs. [12, 16, 27]. The neutrino floor is taken from Ref. [11].⁶

understand conceptually compared to the higher ω_{\min} curves. In fact, over most of the mass range, for most materials, the rate is dominated by single longitudinal acoustic (LA) phonon production. At the high mass end, the reach is material-independent, understood analytically as follows. The mediator form factor $\mathcal{F}_{\text{med}} \propto 1/q^2$, and therefore the rate is dominated by the lowest detectable momentum transfer. In this case, we can set $\mathbf{G} = \mathbf{0}$ (or equivalently, $\mathbf{q} = \mathbf{k}$ in Eq. (3.20)), $W_j \simeq 0$, $\omega_{\text{LA}} = c_s^{\text{LA}} q$, $F_{N_j} \simeq 1$, and $g(q, \omega) \propto q^{-1}$. Lastly, in this limit $\mathbf{q} \cdot \boldsymbol{\epsilon}_{\text{LA},j,\mathbf{k}} \simeq q\sqrt{m_j/m_{\text{cell}}}$. Thus the rate

$$R \propto \frac{m_\chi^3}{m_{\text{cell}}^2} \frac{\bar{\sigma}_n}{\mu_{\chi n}^2} \left(\sum_j \frac{f_j}{f_n} \right)^2 \frac{1}{\omega_{\min}}. \quad (3.35)$$

For $f_p = f_n$, we have $f_j \propto A_j \propto m_{\text{cell}}/m_n$, and the dependence on the target properties drops out. The reference cross section $\bar{\sigma}_n$ corresponding to a given event rate R scales with

mass as $\mu_{\chi n}^2/m_\chi^3$, as we see in Fig. 3.2. Note that as we go to higher m_χ the reach on the couplings $f_n^2 y_\chi^2$ gets worse as $\mu_{\chi n}^2 m_\chi$; the apparent better reach at higher mass in Fig. 3.2 is due to the definition of $\bar{\sigma}_n \propto m_\chi^{-4}$.

For DM masses below ~ 0.1 MeV in Fig. 3.2, kinematics causes the reach to diminish: the maximum momentum transfer, $2m_\chi v_{\max}$, must be large enough to reach the minimum momentum transfer set by the detector threshold, $\omega_{\min}/c_s^{\text{LA}}$. This sets the minimum reachable DM mass

$$m_{\chi,\min} \sim 20 \text{ keV} \left(\frac{\omega_{\min}}{\text{meV}} \right) \left(\frac{10^{-5}}{c_s^{\text{LA}}} \right). \quad (3.36)$$

To reach the lightest dark matter particle at low thresholds, an ideal material is then diamond, as it has the highest speed of sound. AlN and SiO₂ are the next best candidates from our search.

As we move on to the curves with higher energy thresholds, $\omega_{\min} = 20$ meV and 100 meV, the materials with lower sound speed lose reach altogether. (The $\omega_{\min} = 500$ meV curves are derived from nuclear recoil; this is discussed in the next subsection.) The reason is that acoustic phonons are accessible only when $\omega_{\min} \lesssim c_s^{\text{LA}}/a$, where a is the lattice spacing. For materials with lower sound speed, the energy threshold may simply never be low enough to have any reach with an acoustic phonon. In addition, one can see where optical phonons start to play a role, as the slope of the reach curve changes at lower masses, e.g., Si with an energy threshold of 20 meV. This feature will be present for all materials if the lowest kinematically reachable DM mass from optical phonon excitations, given in Eq. (3.24), is smaller than the lowest kinematically reachable DM mass from acoustic phonon excitations, given in Eq. (3.36).

Next we turn our attention to Fig. 3.3, for the same hadrophilic scalar mediator benchmark, but with a heavy mediator. Again, we first focus on the case of a 1 meV threshold, as here the acoustic phonon contributions dominate and analytic simplifications can be made since the integrals are dominated by the high momentum behavior. There are four distinct regions in mass and we now discuss the mass and material parameters dependence of each of them.

In the lowest mass regime, $m_\chi \lesssim 10^{-1}$ MeV, the reach ends when the acoustic modes are no longer kinematically available, just as in the massless mediator case, with minimum reachable mass again set by Eq. (3.36). Between 10^{-1} and 1 MeV, the reach curves flatten and the order of the curves reverses: materials with a higher speed of sound have worse reach, which can be understood analytically starting with Eq. (3.20). For $m_\chi \lesssim 1$ MeV the momentum transfer is within the 1BZ, so we can take $\mathbf{q} = \mathbf{k}$, $W_j \simeq 0$, $\omega = c_s q$ and $g(q, \omega) \propto 1/q$ as in the light mediator case. For simplicity we ignore angular dependence, assume the ions are

the same, $A_j \equiv A$, $m_j \equiv m$, set $f_n = f_p$, and consider only the longitudinal mode so that $\mathbf{q} \cdot \boldsymbol{\varepsilon} \propto q$. Then we have

$$R \propto \frac{\bar{\sigma}_n}{m_{\text{cell}} m_\chi^3 c_s} \int^{2m_\chi v} d^3k \frac{1}{k^2} \left(\frac{kA}{\sqrt{m}} \right)^2 \propto \frac{\bar{\sigma}_n}{c_s}, \quad (3.37)$$

where the upper cutoff is due to kinematics and manifests in the g function, which goes to zero as k reaches the maximum allowed momentum transfer.

A similar derivation applies to the mass dependence in the next two regimes. For $1 \text{ MeV} \lesssim m_X \lesssim 10 \text{ MeV}$, the dominant momentum transfer is outside of the 1BZ, which means that ω can no longer be approximated by $c_s q$. In fact, since ω is only a function of the phonon momentum in the 1BZ, it will vary rapidly as q increases. We therefore exchange ω with a q independent quantity, roughly thought of as the average of ω over the whole 1BZ, $\langle \omega \rangle$. The rate becomes

$$R \propto \frac{\bar{\sigma}_n}{m_{\text{cell}} m_\chi^3 \langle \omega \rangle} \int^{2m_\chi v} d^3k \frac{1}{k} \left(\frac{kA}{\sqrt{m}} \right)^2 \propto \frac{\bar{\sigma}_n m_\chi}{\langle \omega \rangle}. \quad (3.38)$$

Since the rate scales inversely with $\langle \omega \rangle$, materials with lower energy phonon modes are preferred. As $\langle \omega \rangle$ is usually correlated with c_s , the ordering of the curves is the same as in the previous regime. We have neglected the Debye-Waller factor in the analytic estimates above, because the momentum transfer is on the order of $m_\chi v$, and is less than the Debye-Waller cut-off around $\sqrt{m_N \langle \omega \rangle}$. However, for the last mass regime, above $\sim 10 \text{ MeV}$, this is no longer the case, and the momentum integral is cut-off by the Debye-Waller factor,

$$R \propto \frac{\bar{\sigma}_n}{m_{\text{cell}} m_\chi \mu_{\chi n}^2 \langle \omega \rangle} \int_0^{\sqrt{m_N \langle \omega \rangle}} d^3k \frac{1}{k} \left(\frac{kA}{\sqrt{m}} \right)^2 \propto \frac{\bar{\sigma}_n A^2 \langle \omega \rangle^2}{m_\chi \mu_{\chi n}^2}. \quad (3.39)$$

Therefore, materials with heavier elements and higher phonon energies are preferred. In our search, CaWO_4 has the highest factor of $A \langle \omega \rangle$, with PbTe following, which is the reason we choose to highlight PbTe in Fig. 3.3.

For higher thresholds, the optical phonon modes contribute to a greater degree, so the scaling arguments given above for the first two mass regimes no longer hold, but for the last two they do, which is why the curves are almost parallel.

Nuclear Recoils

For DM heavier than $\mathcal{O}(100 \text{ MeV})$, nuclear recoils offer a complementary detection channel to phonon excitations. The low mass behavior of the reach curves is understood in the same

way as in Sec. 3.3 (see Eq. (3.29)), and lighter elements are advantageous. At higher masses, the $\bar{\sigma}_n$ reach depends on the mediator mass. To show this analytically we again consider a single nucleus species, $A_N = A$, and $f_n = f_p$. In the case of a light mediator the differential rate in Eq. (3.14) becomes

$$\frac{dR}{d\omega} \propto \frac{\bar{\sigma}_n m_\chi^3}{\mu_{\chi n}^2} \frac{1}{\omega^2} \eta(v_{\min}). \quad (3.40)$$

For DM heavier than a few hundred MeV, the m_N dependence via $\eta(v_{\min})$ is weak, as in the dark photon mediator case. The rate is then

$$R \propto \frac{\bar{\sigma}_n m_\chi^3}{\mu_{\chi n}^2} \frac{1}{\omega_{\min}}, \quad (3.41)$$

which is material independent. This is why all the reach curves coincide for large DM masses. We also see that as in the case of acoustic phonons, achieving lower energy thresholds is crucial for improving the reach.

If the mediator is heavy, we have

$$\frac{dR}{d\omega} \propto \frac{\bar{\sigma}_n A^2}{m_\chi \mu_{\chi n}^2} \eta(v_{\min}), \quad (3.42)$$

$$R \propto \frac{\bar{\sigma}_n A^2}{m_\chi \mu_{\chi n}^2} \omega_{\max} \propto \frac{\bar{\sigma}_n A \mu_{\chi N}^2}{m_\chi \mu_{\chi n}^2}, \quad (3.43)$$

where for simplicity we take the η function to decrease sharply at the kinematic bound. We reach the conclusion that heavier nuclei are preferred, similar to the case of single phonon excitations with a heavy mediator. Note also that there is no threshold dependence for larger masses. Therefore a lower threshold only helps to reach lower DM masses, as opposed to the case of the light mediator.

Target	E_g [eV]	\bar{c}_s^{LA} [10^{-5}]	A_j	\bar{Z}^*	$\bar{\epsilon}_\infty$	$\bar{\omega}_O$ [meV]	Q [10^{-7}]
Si	1.11	2.84	28.1	-	-	62.3	-
Ge	0.67	1.61	72.6	-	-	34.8	-
NaI	5.8	0.90	23.0, 127	1.20	3.27	12.4 - 20.0	23
CsI	6.14	0.46	133, 127	1.22	2.70	6.9 - 10.0	12
CaWO ₄	5.2	1.42	40, 184, 16	2.84, 4.67	3.84	8.48 - 106	45
GaAs	1.42	1.57	69.7, 74.9	2.27	10.9	31.8 - 34.9	2.4
Al ₂ O ₃	8.8	3.51	27.0, 16.0	2.97	3.26	35.6 - 104	130
Diamond	5.47*	5.98	12.0	-	-	161	-
SiO ₂	9.2	5.76	28.1, 16.0	3.38	2.41	13.7 - 149	200
PbTe	0.19*	1.17	207, 128	5.69	26.3	3.91 - 13.5	1.3
InSb	0.24*	1.13	115, 122	2.40	23.7	20.5 - 21.5	0.34
AlN	6.20	5.70	27.0, 14.0	2.57	4.54	29.4 - 109	78
CaF ₂	11.81	2.15	40, 19.0	2.36	2.26	28.4 - 55.6	130
GaN	3.43*	4.17	69.7, 14.0	2.74	6.10	16.7 - 88.9	23
GaSb	0.720	1.32	69.7, 122	1.92	21.6	26.4 - 27.3	0.33
LiF	14.2	2.17	6.9, 19.0	1.05	2.02	33.5 - 77.2	270
MgF ₂	12.4	2.43	24.3, 19.0	2.00	1.97	12.1 - 73.7	130
MgO	7.83	3.11	24.3, 16.0	1.97	3.38	46.3 - 82.6	110
NaCl	8.75	1.19	23.0, 35.5	1.09	2.44	19.1 - 30.6	80
NaF	11.5	1.78	23.0, 19.0	0.98	1.78	29.6 - 49.9	140
PbS	0.29*	1.41	207, 32.1	4.45	15.0	7.27 - 26.9	4.9
PbSe	0.17*	1.27	207, 79.0	4.86	19.5	4.86 - 17.1	2.2
ZnO	3.3	4.18	65.4, 16.0	2.17	6.13	11.1 - 63.4	19
ZnS	3.80*	1.53	65.4, 32.1	2.03	5.91	32.8 - 41.0	14

Table 3.1: Target materials studied in this work and their key parameters. The four blocks contain materials currently in use in nuclear recoil experiments, those considered for proposed near-future experiments, those with superior properties for some specific DM models discussed in this paper, and the remaining ones in alphabetical order, respectively. Sensitivity of electron transitions relies heavily on the band gap E_g , for which experimental values are shown (those with asterisks are measured at low temperature). Nuclear recoils and acoustic phonon excitations in the nucleon-coupling benchmark model are largely determined by the speed of sound of longitudinal acoustic phonons \bar{c}_s^{LA} and atomic mass numbers A_j . For optical phonon excitations in the light dark photon mediated model, relevant parameters are the Born effective charges \bar{Z}^* , high-frequency dielectric constant $\bar{\epsilon}_\infty$, optical phonon energies $\bar{\omega}_O$ as well as A_j , all of which combine into a quality factor Q , defined in Eq. (3.27), which determines the reach at high mass. Barred quantities are properly averaged values; see Appendix B.3 for details.

Light dark photon mediator (Sec. 3.3, Fig. 3.1)			
Detection channel	Quantity to maximize to reach ...		Best materials
	... lower m_χ	... lower $\bar{\sigma}_e$	
(Optical) phonons	ω_O^{-1} (Eq. (3.24))	quality factor Q defined in Eq. (3.27)	SiO ₂ , Al ₂ O ₃ , CaWO ₄
Electron transitions	E_g^{-1} (Eq. (3.28))	depends on details of electron wavefunctions	InSb, Si
Nuclear recoils	$(A\omega_{\min})^{-1}$ (Eq. (3.29))	$(Z/A)^2 \omega_{\min}^{-1}$ (Eq. (3.31))	diamond, LiF
Hadrophilic scalar mediator (Sec. 3.4, Figs. 3.2, 3.3)			
Detection channel	Quantity to maximize to reach ...		Best materials
	... lower m_χ	... lower $\bar{\sigma}_n$	
(Acoustic) phonons	c_s/ω_{\min} (Eq. (3.36))	Light mediator: ω_{\min}^{-1} (Eq. (3.35))	diamond, SiO ₂
		Heavy mediator: c_s^{-1} or ω_{ph}^{-1} or $A\omega_{\text{ph}}$ depending on m_χ (Eqs. (3.37), (3.38), (3.39))	all complementary
Nuclear recoils	$(A\omega_{\min})^{-1}$ (Eq. (3.29))	Light mediator: ω_{\min}^{-1} (Eq. (3.40))	diamond, LiF
		Heavy mediator: A (Eq. (3.43))	CsI, Pb compounds

Table 3.2: Summary of our results. The material properties relevant for the optimization of target are: atomic mass number A , proton number Z , electronic band gap E_g , speed of sound c_s , optical phonon energy ω_O , average phonon energy ω_{ph} , as well as Born effective charges and the high-frequency dielectric constant that enter the quality factor Q . Achieving lower detector energy thresholds ω_{\min} is also crucial in several cases.

3.5 Conclusions

We considered spin independent DM direct detection through three channels – single phonon excitations, electron transitions, and nuclear recoils – in a wide variety of crystal target materials, and two well motivated DM models. Many of these materials are already being discussed for DM detection, but we have presented some new targets for consideration.

For each type of interaction, we specified the target material parameters which should be optimized in order to maximize the reach, and we found complementarity between targets depending on *(i)* the experimental threshold, *(ii)* the mass range, and *(iii)* the model. The experimental threshold dictates which modes are available: at higher recoil energies, only electron transitions and nuclear recoils are possible; as the threshold drops, optical and acoustic phonons become accessible. The phonon modes in materials with high sound speed become kinematically available at higher thresholds than in materials with lower sound speeds. Also, for a given threshold, materials with higher sound speeds have reach to lighter dark matter. Regarding the mass range, the smallest detectable masses are always set by a kinematic constraint, and the dependence on material parameters, and detection threshold, can be found in Eqs. (3.24), (3.28), (3.36), (3.29) for optical phonon, electron, acoustic phonon excitations, and nuclear recoils respectively. As for the model, we defined a quality factor (in Eq. (3.27)) for single optical phonon excitations from dark photon mediated scattering to indicate which targets will have the best sensitivity. On the other hand, for a hadrophilic mediator, target optimization for acoustic phonon excitations depends on the mediator and DM masses. We summarize our results in Table 3.2.

An attractive feature of phonon and electron excitations is the possible daily modulation of event rates, as the dynamic structure factors in Eqs. (3.15) and (3.18) are generically anisotropic. In the context of phonon excitations, Al_2O_3 has been considered in Ref. [28], and in our companion paper [227] we have discussed hexagonal boron nitride as an example of an $\mathcal{O}(\text{eV})$ -gap target which exhibits daily modulation in electron transitions. We plan on identifying other promising targets for daily modulation in the future.

Part I

Collective Excitations

DIRECTIONAL DETECTABILITY OF DARK MATTER WITH SINGLE PHONON EXCITATIONS: TARGET COMPARISON

4.1 Introduction

If the cold dark matter (DM) in the universe consists of new particles, they must interact very weakly with the Standard Model. Directly detecting these feeble interactions in a laboratory requires extraordinarily sensitive devices. Traditional direct detection experiments (e.g., ANAIS [232], CRESST [233–235], DAMA/LIBRA [236], DAMIC [237], DarkSide-50 [12], DM-Ice [72], KIMS [73], LUX [16, 238], SABRE [239], SuperCDMS [80, 240], and Xenon1T [14]), based on nuclear recoil, are gradually improving their sensitivity and closing the open parameter space before reaching the irreducible solar and atmospheric neutrino background. However, these experiments are fundamentally limited in the DM mass, m_χ , they can probe. When the DM scatters off a nucleus at rest, the energy deposited, ω , is limited by $\omega \lesssim m_\chi^2 v^2 / m_N$, with $v \sim 10^{-3}$, and vanishes quickly as the DM mass decreases below the nucleus mass m_N .

This limitation in DM mass is typically not problematic in the search for the prototypical weakly interacting massive particle (WIMP) which produces the DM abundance through freeze-out, as $m_\chi \lesssim \text{GeV}$ would both be overabundant and be in tension with indirect detection bounds on DM annihilation rates. However, many other theoretically motivated explanations of the origin of DM such as freeze-in [136, 137], hidden sector DM [207–209, 241], asymmetric DM [138, 139, 142, 143], and strong self interactions [210, 242], allow for DM lighter than a GeV and therefore should be searched for by means other than nuclear recoil.

In the pursuit of sub-GeV DM, several new experimental concepts have been proposed. These include electron excitations in a variety of target systems [19, 24, 33–35, 81, 87, 89, 177, 180, 188, 243, 244] for DM with mass above an MeV, while single (primary) phonon excitations [4, 6, 7, 28, 64, 184–187, 245–250], with energies up to $\mathcal{O}(100)$ meV, have been shown to be especially sensitive to a wide range of DM models with masses down to a keV. This coupled with the fact that detector energy thresholds are approaching the $\mathcal{O}(100)$ meV range [251–255] makes single phonon excitations an exciting avenue for DM direct detection. Phonons are quasiparticle vibration quanta which can exist in multiple states of matter, e.g., as sound waves in liquids or superfluids and lattice vibrations in crystalline solids. Superfluid helium has been proposed [184] and studied as a light DM detector [185–187, 245, 246] and

an experiment is currently in the R&D phase [90]. Crystal targets have also been proposed [64] and studied extensively. Initial studies focused on GaAs and Al_2O_3 (sapphire) targets [28], and more recently this analysis has been extended to account for more general DM interactions [4, 7] and applied to a broader set of target materials [6]. Other targets have also been proposed individually, e.g., SiC [248], and there has been work on understanding the signal from multi-phonon excitations [247, 249, 250]. Similar to superfluid helium, a DM detector using a crystal target with single phonon readout is also in the R&D phase of development [90].

Most of the previous work has focused on calculating the theoretically predicted DM-phonon interaction strength. Equally important is to minimize the experimental background [256]. This becomes easier when the DM scattering signal has unique properties which can distinguish it from backgrounds. For example, in experiments sensitive to nuclear recoil or electron excitations, the rate modulates annually due to the change in the DM velocity distribution in the Earth frame, as the Earth orbits around the Sun [33, 35, 226].

In an experiment based on primary phonon readout, the DM scattering rate can have a larger and more unique signature: *daily* modulation. As the Earth rotates about its own axis, the orientation of the detector relative to the DM wind changes. In a nuclear recoil experiment this does not have an effect since the interaction matrix element is independent of the direction of the DM velocity relative to the detector orientation — an (unpolarized) nucleus is isotropic in its response. However, crystal targets can be highly anisotropic, which means that the amplitude of the response depends not only on the magnitude of the momentum transfer but also on its direction. This can lead to a significant daily modulation. Moreover, since the modulation pattern depends on the crystal orientation, running an experiment with multiple detectors simultaneously with different orientations can further enhance the signal-to-noise ratio. This effect was studied for sapphire in Ref. [28] (see also Refs. [7, 29, 183, 188] for discussions of daily modulation in electron excitations). In this work, we expand the understanding of the daily modulation effect in single phonon excitations to a broader range of materials, including those targeted in Ref. [6].

In particular, we highlight the following targets in the main text: Al_2O_3 (sapphire) and CaWO_4 , which were already utilized for DM detection and have a significant daily modulation; SiO_2 , which was shown to have a strong reach to several benchmark models; SiC, which was proposed in Ref. [248] (for which we choose the commercially available 4H polytype); and h-BN (hexagonal boron nitride), which is a highly anisotropic material. Among them, Al_2O_3 and CaWO_4 have the best prospects overall in terms of daily modulation reach and experimental feasibility.

Of the additional materials considered in Ref. [6], results for those with daily modulation larger than 1% (for at least some DM masses where the material has substantial reach) are presented in an appendix. We make available our code for the phonon rate calculation [257], and also publish an interactive webpage [258] where results for all the materials presented in Ref. [6] and in this paper, including reach curves, differential rates and daily modulation patterns, can be generated from our calculations. Twenty-six materials are initially included on the interactive webpage [258]: Al₂O₃, AlN, h-BN, CaF₂, CaWO₄, CsI, C (diamond), GaAs, Ge, GaN, GaSb, InSb, LiF, MgF₂, MgO, NaCl, NaF, NaI, PbS, PbSe, PbTe, Si, 4H-SiC, SiO₂, ZnO, and ZnS. This diverse set of materials (with some currently in use in nuclear recoil experiments, some proposed for light dark matter detection, and some others being promising polar crystals from theoretical considerations) aims to explore a wide range of possibilities with the hope of identifying broad theoretical features that could be implemented in a more practical experimental setup. Materials shown in-text (Al₂O₃, SiO₂, SiC, CaWO₄ and h-BN) are the ones with the highest daily modulation in this list.

4.2 Directional Detection With Single Phonon Excitations

Excitation Rate

We begin by summarizing the formulae for single phonon excitation rates; see Refs. [7, 28, 64] for more details. For the scattering of a DM particle χ with mass m_χ and general spin-independent interactions, the rate per unit target mass takes the form

$$R(t) = \frac{1}{\rho_T} \frac{\rho_\chi}{m_\chi} \frac{\pi \bar{\sigma}_\psi}{\mu_{\chi\psi}^2} \int d^3v f_\chi(\mathbf{v}, t) \times \int \frac{d^3q}{(2\pi)^3} \mathcal{F}_{\text{med}}^2(q) S(\mathbf{q}, \omega_q), \quad (4.1)$$

where \mathbf{v} is the incoming DM's velocity, \mathbf{q} is the momentum transferred to the target, ρ_T is the target's mass density, and $\rho_\chi = 0.4 \text{ GeV}/\text{cm}^3$ is the local DM density. $\bar{\sigma}_\psi$, with $\psi = n$ or e (neutron or electron), is a reference cross section defined as

$$\bar{\sigma}_\psi \equiv \frac{\mu_{\chi\psi}^2}{\pi} |\mathcal{M}_{\chi\psi}(q = q_0)|^2, \quad (4.2)$$

where $\mu_{\chi\psi}$ is the reduced mass, $\mathcal{M}_{\chi\psi}$ is the vacuum matrix element for $\chi\psi \rightarrow \chi\psi$ scattering, and q_0 is a reference momentum transfer. We present the reach in terms of $\bar{\sigma}_\psi$, with $q_0 = m_\chi v_0$ (where $v_0 = 230 \text{ km/s}$, the dispersion of DM's velocity distribution) for $\psi = n$ and $q_0 = \alpha m_e$ for $\psi = e$. $f_\chi(\mathbf{v}, t)$ is the DM's velocity distribution in the lab frame, taken to be a truncated Maxwell-Boltzmann distribution, boosted by the time-dependent Earth velocity $\mathbf{v}_e(t)$, as will be discussed in more detail in the next subsection. $\mathcal{F}_{\text{med}}(q)$ is the mediator form factor, which

captures the q dependence of the mediator propagator:

$$\mathcal{F}_{\text{med}}(q) = \begin{cases} 1 & \text{(heavy mediator),} \\ (q_0/q)^2 & \text{(light mediator).} \end{cases} \quad (4.3)$$

Finally, $S(\mathbf{q}, \omega)$ is the dynamic structure factor that encodes target response to DM scattering with momentum transfer \mathbf{q} and energy transfer ω , constrained by energy-momentum conservation to be

$$\omega_{\mathbf{q}} = \mathbf{q} \cdot \mathbf{v} - \frac{q^2}{2m_{\chi}}. \quad (4.4)$$

Generally, one sums over a set of final states f with energies ω_f , and $S(\mathbf{q}, \omega)$ takes the form

$$S(\mathbf{q}, \omega) = \sum_f 2\pi \delta(\omega - \omega_f) S'_f(\mathbf{q}). \quad (4.5)$$

For single phonon excitations, we assume the target system is initially prepared in the ground state at zero temperature with no phonons, and sum over single phonon states labeled by branch ν and momentum \mathbf{k} inside the first Brillouin zone (1BZ). Lattice momentum conservation dictates that $\mathbf{q} = \mathbf{k} + \mathbf{G}$, with \mathbf{G} a reciprocal lattice vector. To find \mathbf{k} and \mathbf{G} from a given \mathbf{q} , we first find the reduced coordinates (q_1, q_2, q_3) (i.e., $\mathbf{q} = \sum_{i=1}^3 q_i \mathbf{b}_i$ with \mathbf{b}_i the basis vectors of the reciprocal lattice), and then find the nearest point (G_1, G_2, G_3) with $G_i \in \mathbb{Z}$. In this way, any \mathbf{q} outside of the 1BZ is mapped to a \mathbf{k} inside the 1BZ and a \mathbf{G} vector. The sum over final states therefore only runs over the phonon branches, indexed by ν ,

$$S(\mathbf{q}, \omega) = \sum_{\nu} 2\pi \delta(\omega - \omega_{\nu, \mathbf{k}}) S'_{\nu}(\mathbf{q}). \quad (4.6)$$

As was shown in Refs. [7, 28, 64], S'_{ν} can be written in terms of the phonon energies $\omega_{\nu, \mathbf{k}}$, eigenvectors $\boldsymbol{\epsilon}_{\nu, \mathbf{k}, j}$ and an effective DM-ion couplings \mathbf{Y}_j (with j labeling the ions in the primitive cell):

$$S'_{\nu}(\mathbf{q}) = \frac{1}{2\Omega \omega_{\nu, \mathbf{k}}} \left| \sum_j \frac{e^{-W_j(\mathbf{q})}}{\sqrt{m_j}} e^{i\mathbf{G} \cdot \mathbf{x}_j^0} (\mathbf{Y}_j \cdot \boldsymbol{\epsilon}_{\nu, \mathbf{k}, j}^*) \right|^2, \quad (4.7)$$

where Ω is the volume of the primitive cell, and m_j , \mathbf{x}_j^0 , and $W_j(\mathbf{q}) \equiv \frac{\Omega}{4m_j} \sum_{\nu} \int \frac{d^3k}{(2\pi)^3} \frac{|\mathbf{q} \cdot \boldsymbol{\epsilon}_{\nu, \mathbf{k}, j}|^2}{\omega_{\nu, \mathbf{k}}}$ are the masses, equilibrium positions, and Debye-Waller factors of the ions, respectively. We obtain the material-specific force constants in the quadratic crystal potential and the equilibrium positions from density functional theory (DFT) calculations [6, 28, 259], and use the open-source phonon eigensystem solver `phonopy` [50] to derive the values of $\omega_{\nu, \mathbf{k}}$, $\boldsymbol{\epsilon}_{\nu, \mathbf{k}, j}$ for each material.

The DM-ion coupling vectors \mathbf{Y}_j are DM model dependent. In our target comparison study in Sec. 4.3, we will focus on two sets of benchmark models, with a light dark photon mediator

and a heavy or light hadrophilic scalar mediator, respectively. These are the same models considered in Ref. [6], for which \mathbf{Y}_j are given by

$$\mathbf{Y}_j = \begin{cases} -\frac{\mathbf{q} \cdot \mathbf{Z}_j^*}{\hat{\mathbf{q}} \cdot \boldsymbol{\varepsilon}_\infty \cdot \hat{\mathbf{q}}} & \text{(dark photon med.)}, \\ \mathbf{q} A_j F_{N_j}(q) & \text{(hadrophilic scalar med.)}. \end{cases} \quad (4.8)$$

Here \mathbf{Z}_j^* is the Born effective charge tensor of the j^{th} ion, $\boldsymbol{\varepsilon}_\infty$ is the high-frequency dielectric tensor that captures the electronic contribution to in-medium screening, A_j is the atomic mass number, and $F_{N_j}(q) = \frac{3j_1(qr_j)}{qr_j} e^{-(qs)^2/2}$ (with $r_j = 1.14 A_j^{1/3}$ fm, $s = 0.9$ fm) is the Helm nuclear form factor [200] (which is close to unity for the DM masses considered in this work).

These benchmark models have highly complementary features. In a polar crystal, the dark photon couples to the Born effective charges of the ions, which have opposite signs within the primitive cell, and therefore dominantly induces out-of-phase oscillations corresponding to gapped optical phonon modes in the long-wavelength limit. By contrast, the hadrophilic scalar mediator couples to all ions with the same sign, and therefore dominantly excites gapless acoustic phonons that correspond to in-phase oscillations in the long-wavelength limit. There is also a difference between a light and heavy mediator due to the mediator form factor in Eq. (4.3). Noting that \mathbf{Y}_j scales with q and the energy conserving delta function contributes a factor of q^{-1} (see Eq. (4.11) below), we see that for a heavy mediator, the integral scales as $\int dq q^3 \omega^{-1}$ and so is always dominated by large q . For a light mediator, on the other hand, the integral scales as $\int dq q^{-1} \omega^{-1}$. So for optical phonons with $\omega \sim q^0$, it receives similar contributions from all q , whereas for acoustic phonons, it is dominated by small q where $\omega \sim q$.

Daily Modulation

In the rate formula Eq. (4.1), the time dependence comes from the DM's velocity distribution $f_\chi(\mathbf{v}, t)$, specifically via the Earth's velocity $\mathbf{v}_e(t)$ that boosts the distribution. Concretely, we take

$$f_\chi(\mathbf{v}, t) = \frac{1}{N_0} \exp\left[-\frac{(\mathbf{v} + \mathbf{v}_e(t))^2}{v_0^2}\right] \Theta(v_{\text{esc}} - |\mathbf{v} + \mathbf{v}_e(t)|), \quad (4.9)$$

where N_0 is a normalization constant such that $\int d^3v f_\chi(\mathbf{v}) = 1$, $v_{\text{esc}} = 600$ km/s is the galactic escape velocity, and $v_0 = 230$ km/s as mentioned above. Assuming the detector is fixed on the Earth, in the lab frame \mathbf{v}_e becomes a function of time that is approximately periodic over a sidereal day as a result of the Earth's rotation. As a default setup, we adopt

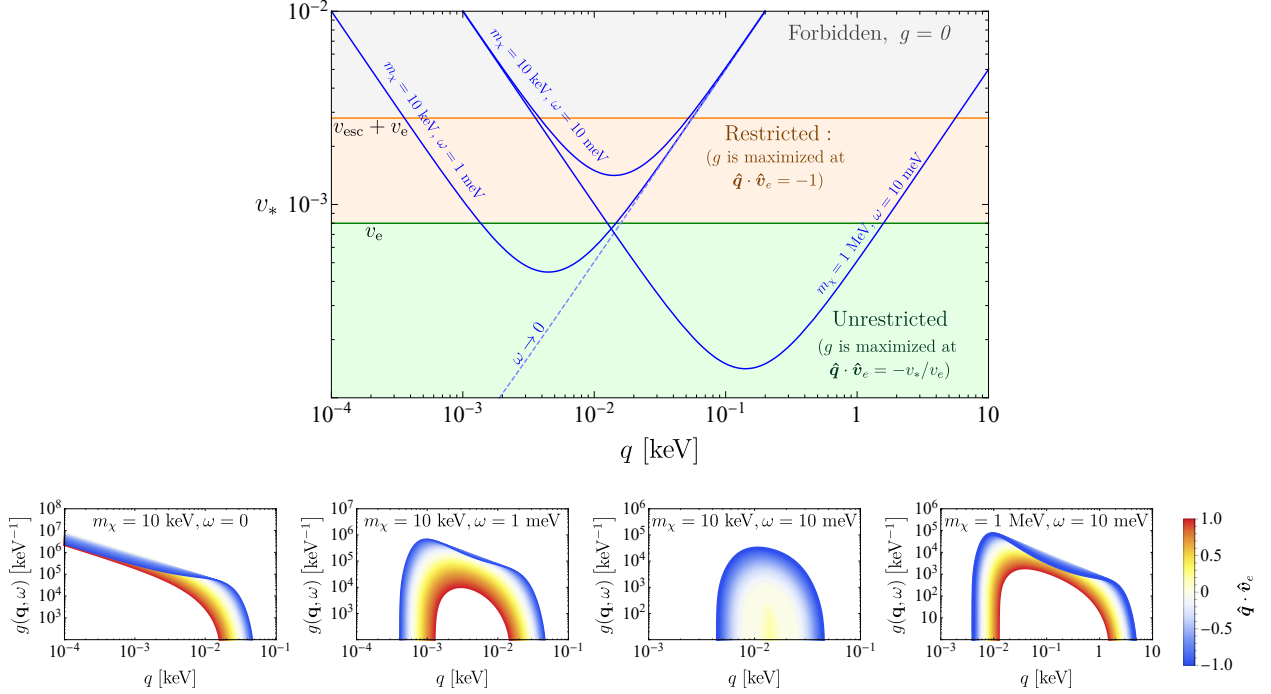


Figure 4.1: **Top:** To understand the kinematic function, $g(\mathbf{q}, \omega)$, defined in Eq. (4.11), we plot $v_* \equiv \frac{q}{2m_\chi} + \frac{\omega}{q}$ as a function of q (blue) for various m_χ and ω values. Comparing v_* to v_e and $v_e + v_{\text{esc}}$ we can qualitatively reconstruct the shape of $g(\mathbf{q}, \omega)$, as discussed in the text. **Bottom:** $g(\mathbf{q}, \omega)$ vs. q for several fixed m_χ, ω values, with varying $\hat{\mathbf{q}} \cdot \hat{\mathbf{v}}_e$. The kinematic function weights different $\hat{\mathbf{q}}$ directions according to their angle with respect to $\mathbf{v}_e(t)$, which ultimately leads to a daily modulating rate.

the detector orientation in Refs. [7, 28, 29], for which, independent of the detector's location,

$$\mathbf{v}_e(t) = v_e \begin{pmatrix} \sin \theta_e \sin \phi(t) \\ \sin \theta_e \cos \theta_e (\cos \phi(t) - 1) \\ \cos^2 \theta_e + \sin^2 \theta_e \cos \phi(t) \end{pmatrix}, \quad (4.10)$$

where $v_e = 240$ km/s, $\theta = 42^\circ$, and $\phi(t) = 2\pi(\frac{t}{24\text{hr}})$. It is this periodicity of the *direction* of $\mathbf{v}_e(t)$ that induces the daily modulation in $R(t)$ we study in this work.¹

With the specific form of f_χ in Eq. (4.9), the velocity integral in Eq. (4.1) can be done

¹Annual modulation is also present, due to the change of the *magnitude* of \mathbf{v}_e , as in any terrestrial direct detection experiment. Here we fix $v_e = 240$ km/s and focus on the daily modulation signal, which is unique to anisotropic (crystal) targets.

analytically [7, 28, 29]. We define

$$\begin{aligned} g(\mathbf{q}, \omega, t) &\equiv \int d^3v f_\chi(\mathbf{v}, t) 2\pi\delta(\omega - \omega_{\mathbf{q}}) \\ &= \frac{2\pi^2 v_0^2}{N_0 q} \left\{ \exp\left[-\frac{(v_-(\mathbf{q}, \omega, t))^2}{v_0^2}\right] - \exp\left[-\frac{v_{\text{esc}}^2}{v_0^2}\right] \right\}, \end{aligned} \quad (4.11)$$

where

$$v_-(\mathbf{q}, \omega, t) = \min\left(\left|\hat{\mathbf{q}} \cdot \mathbf{v}_e(t) + \frac{q}{2m_\chi} + \frac{\omega}{q}\right|, v_{\text{esc}}\right). \quad (4.12)$$

We will refer to $g(\mathbf{q}, \omega, t)$ as the *kinematic function*. The rate formula Eq. (4.1) then becomes

$$\begin{aligned} R(t) &= \frac{1}{\rho_T} \frac{\rho_\chi}{m_\chi} \frac{\pi \bar{\sigma}_\psi}{\mu_{\chi\psi}^2} \int \frac{d^3q}{(2\pi)^3} \mathcal{F}_{\text{med}}^2(q) \\ &\quad \sum_\nu S'_\nu(\mathbf{q}) g(\mathbf{q}, \omega_{\nu, \mathbf{k}}, t). \end{aligned} \quad (4.13)$$

With the rate written in this form, the time dependence now comes from the v_- function contained in $g(\mathbf{q}, \omega, t)$. As we will discuss in detail in the rest of this subsection, the origin of daily modulation is as follows. First, the kinematic function $g(\mathbf{q}, \omega, t)$ selects a region of \mathbf{q} space at each time of the day that is strongly correlated with $\mathbf{v}_e(t)$. For anisotropic targets, this then results in a modulating rate after the \mathbf{q} integral in Eq. (4.13). Intuitively, the DM wind hits the target from different directions throughout the day, some of which may induce a stronger response than others.

Kinematic Function

The kinematic function $g(\mathbf{q}, \omega_{\nu, \mathbf{k}}, t)$ can be viewed as a weight function: for each phonon branch ν , the integrand in Eq. (4.13), $\mathcal{F}_{\text{med}}^2(q) S'_\nu(\mathbf{q})$, is weighted toward momentum transfers \mathbf{q} that maximize the g function or, equivalently, minimize v_- defined in Eq. (4.12). To visualize this minimization, we plot

$$v_* \equiv \frac{q}{2m_\chi} + \frac{\omega}{q} \quad (4.14)$$

as a function of q in the top panel of Fig. 4.1. Setting ω to a constant approximates the case of optical phonons, which have relatively flat dispersions, whereas $\omega \rightarrow 0$ corresponds to the case of acoustic phonons, for which ω/q is bounded by the sound speed, which is typically much smaller than the DM's velocity. We can identify three distinct regions (as shown with different colors in the plot):

- For $v_* \geq v_{\text{esc}} + v_e$, we have $v_- = v_{\text{esc}}$ and therefore $g = 0$ for all $\hat{\mathbf{q}}$ directions. This is the kinematically forbidden region.

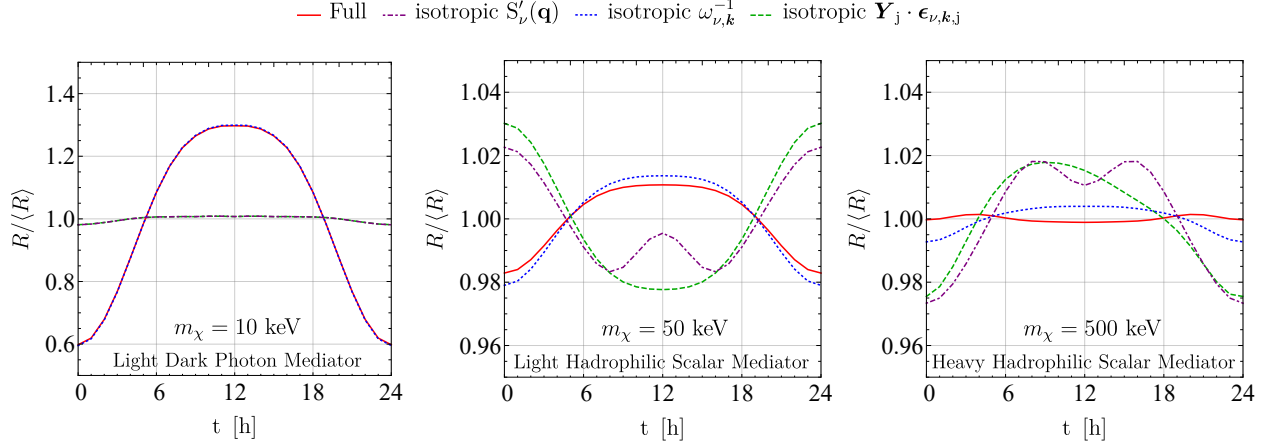


Figure 4.2: Comparison between the various sources of anisotropy a in SiO_2 target, for an example DM mass for each benchmark model. A 1 meV energy threshold is assumed in all cases. As discussed in the text, anisotropy in the $\mathbf{Y}_j \cdot \boldsymbol{\epsilon}_{\nu,k,j}$ factor in Eq. (4.7) is the dominant factor in determining the daily modulation pattern.

- For $v_e \leq v_* < v_{\text{esc}} + v_e$, the g function is maximized at $\hat{\mathbf{q}} \cdot \hat{\mathbf{v}}_e = -1$.
- For $v_* \leq v_e$, the g function is nonzero for all $\hat{\mathbf{q}}$ directions, and is maximized at $\hat{\mathbf{q}} \cdot \hat{\mathbf{v}}_e = -v_*/v_e$. In the large m_χ , small ω limit, $v_* \rightarrow 0$, and therefore the g function is maximized when $\hat{\mathbf{q}} \cdot \hat{\mathbf{v}}_e = 0$.

These behaviors are seen in the lower panels of Fig. 4.1 (see also Ref. [29]), where we plot $g(\mathbf{q}, \omega)$ as a function of q for fixed m_χ , ω , and with varying $\hat{\mathbf{q}} \cdot \hat{\mathbf{v}}_e$. Note that in the $\omega \rightarrow 0$ case, the g function has support down to $q = 0$, but the phase space integral for acoustic phonons is cut off at $q_{\text{min}} \simeq \frac{\omega_{\text{min}}}{c_s} = 2 \times 10^{-2} \text{ keV} \left(\frac{\omega_{\text{min}}}{1 \text{ meV}} \right) \left(\frac{5 \times 10^{-5}}{c_s} \right)$, where ω_{min} is the detector's energy threshold, and c_s is the sound speed (slope of the linear dispersion). From these plots we see that the kinematically favored region of \mathbf{q} is strongly correlated with $\hat{\mathbf{v}}_e(t)$ and, therefore, rotates with it throughout the day. This rotation then translates any target anisotropy into a detection rate that modulates daily.

Sources of Anisotropy

There are a number of possible sources of anisotropy, as we can infer from Eq. (4.13) and Eq. (4.7). First of all, the phonon energies $\omega_{\nu,k}$ generically depend on the direction of $\mathbf{q} = \mathbf{k} + \mathbf{G}$. This means that the region selected by the kinematic function, as discussed above, does not preserve its shape as it rotates in \mathbf{q} space. Also, the $\omega_{\nu,k}^{-1}$ factor in Eq. (4.7)

is different in the dominating kinematic region at different times of the day, which adds to the daily modulation signal.

The anisotropy in $\omega_{\nu,\mathbf{k}}$ has two contributing factors. First, phonon dispersions can be anisotropic as a result of crystal structures. For example, in h-BN, the sound speed of the longitudinal acoustic phonons differs by more than a factor of two between different \mathbf{k} directions. Second, by the prescription explained above Eq. (4.6), a sphere of constant q outside the 1BZ does not map to a sphere of constant k inside the 1BZ. Since the size of the 1BZ is typically $\mathcal{O}(\text{keV})$, and the DM velocity is $\mathcal{O}(10^{-3})$, this is relevant for $m_\chi \gtrsim \text{MeV}$. Another related source of anisotropy is the $e^{i\mathbf{G}\cdot\mathbf{x}_j^0}$ factor in Eq. (4.7): a constant- q sphere outside the 1BZ does not map onto a unique \mathbf{G} vector.

In addition to $\omega_{\nu,\mathbf{k}}$ and $e^{i\mathbf{G}\cdot\mathbf{x}_j^0}$ discussed above, the scalar product of the DM-ion coupling and phonon eigenvectors, $\mathbf{Y}_j \cdot \boldsymbol{\epsilon}_{\nu,\mathbf{k},j}$, can also be anisotropic for a variety of reasons, depending on the DM model. For the hadrophilic scalar mediator model, $\mathbf{Y}_j \cdot \boldsymbol{\epsilon}_{\nu,\mathbf{k},j}$ are simply proportional to the longitudinal components of phonon eigenvectors $\hat{\mathbf{q}} \cdot \boldsymbol{\epsilon}_{\nu,\mathbf{k},j}$, so the anisotropy is determined by the extent to which the phonon eigenvectors deviate from transverse and longitudinal in different $\hat{\mathbf{q}}$ directions. For the dark photon mediator model, $\mathbf{Y}_j \cdot \boldsymbol{\epsilon}_{\nu,\mathbf{k},j}$ are instead proportional to $\frac{\hat{\mathbf{q}} \cdot \mathbf{Z}_j^* \cdot \boldsymbol{\epsilon}_{\nu,\mathbf{k},j}}{\hat{\mathbf{q}} \cdot \boldsymbol{\epsilon}_\infty \cdot \hat{\mathbf{q}}}$, so there are additional anisotropies if the Born effective charges \mathbf{Z}_j^* and dielectric tensor $\boldsymbol{\epsilon}_\infty$ are not proportional to the identity. All these anisotropies are ultimately determined by the crystal structure.

We can carry out a simple exercise to see how the various sources of anisotropy discussed above contribute to the full daily modulation signal. As an example, we consider a SiO₂ target, and pick one m_χ value for each benchmark model, as shown in the three panels of Fig. 4.2. We obtain the full rate normalized to its daily average, $R/\langle R \rangle$, as a function of time, as shown by the solid red curves labeled by “full.” We then artificially make the various factors in the rate formula isotropic and see how the modulation pattern changes.

First, we make $S'_\nu(\mathbf{q})$ isotropic by setting $\omega_{\nu,\mathbf{k}}$ and $\mathbf{Y}_j \cdot \boldsymbol{\epsilon}_{\nu,\mathbf{k},j}$ to their values at a specific direction ($\hat{\mathbf{q}} = \hat{\mathbf{z}}$), and setting $e^{i\mathbf{G}\cdot\mathbf{x}_j^0} \rightarrow 1$. This isolates the effect of the kinematic function $g(\mathbf{q}, \omega_{\nu,\mathbf{k}}, t)$ on daily modulation. The results are shown by the dot-dashed purple curves in Fig. 4.2, labeled “isotropic $S'_\nu(\mathbf{q})$.” In all three panels, we see that the “isotropic $S'_\nu(\mathbf{q})$ ” curves are far from the full results (solid red curves), meaning that the anisotropy in $S'_\nu(\mathbf{q})$ plays an important role in determining the total modulation pattern. We find the same conclusion for the other materials and for other m_χ, ω_{\min} values.

We can further dissect the anisotropy in $S'_\nu(\mathbf{q})$ by computing the daily modulation with $\omega_{\nu,\mathbf{k}}^{-1}$ or $\mathbf{Y}_j \cdot \boldsymbol{\epsilon}_{\nu,\mathbf{k},j}$ made isotropic by the same prescription as above; these are labeled “isotropic

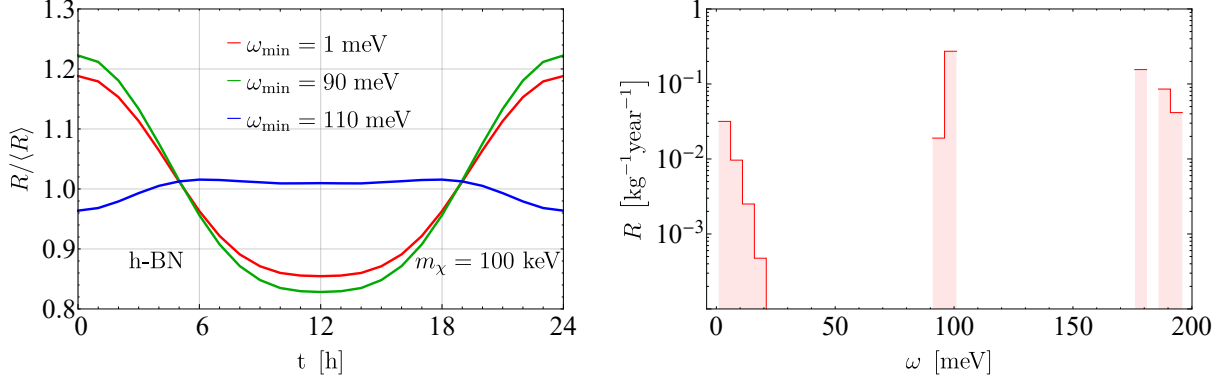


Figure 4.3: **Left:** Daily modulation for a h-BN target with various experimental thresholds, ω_{\min} , assuming dark photon mediated scattering and $m_\chi = 100$ keV. **Right:** Differential rate at $t = 0$ for the same process assuming $\bar{\sigma}_e = 10^{-43}$ cm². The daily modulation pattern is drastically different depending on whether the optical phonon modes just below 100 meV are included or excluded.

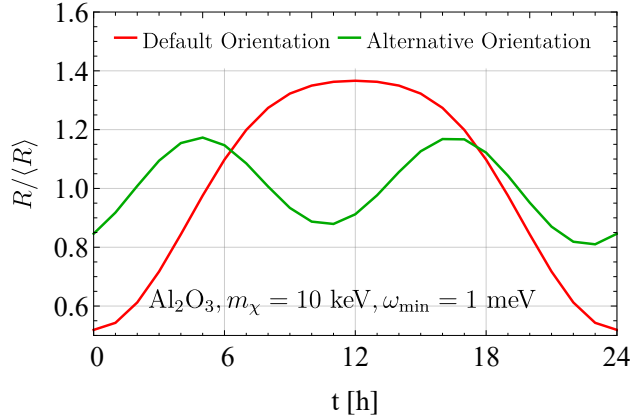


Figure 4.4: Effect of the crystal target orientation on the daily modulation pattern, for a sapphire target and the light dark photon mediator model as an example. The default orientation is the one adopted in Refs. [7, 28, 29] for which $\mathbf{v}_e(t)$ is given by Eq. (4.10), and the alternative orientation is achieved by rotating the crystal z axis by 60° clockwise around $\hat{\mathbf{n}} = (\hat{\mathbf{x}} + \hat{\mathbf{y}} + \hat{\mathbf{z}})/\sqrt{3}$ (or equivalently, a -60° right-handed rotation around $\hat{\mathbf{n}}$.)

$\omega_{\nu,\mathbf{k}}^{-1}$ ” (dotted blue curves) and “isotropic $\mathbf{Y}_j \cdot \boldsymbol{\epsilon}_{\nu,\mathbf{k},j}$ ” (dashed green curves) in Fig. 4.2, respectively. We see that the anisotropy in the $\mathbf{Y}_j \cdot \boldsymbol{\epsilon}_{\nu,\mathbf{k},j}$ factor contributes the most to daily modulation, as making it isotropic leads to the most significant deviations from the full results. We find the same is true for other materials.

We have also examined the effect of setting $e^{i\mathbf{G}\cdot\mathbf{x}_j^0} \rightarrow 1$ in $S'_\nu(\mathbf{q})$ while leaving both $\omega_{\nu,\mathbf{k}}^{-1}$ and

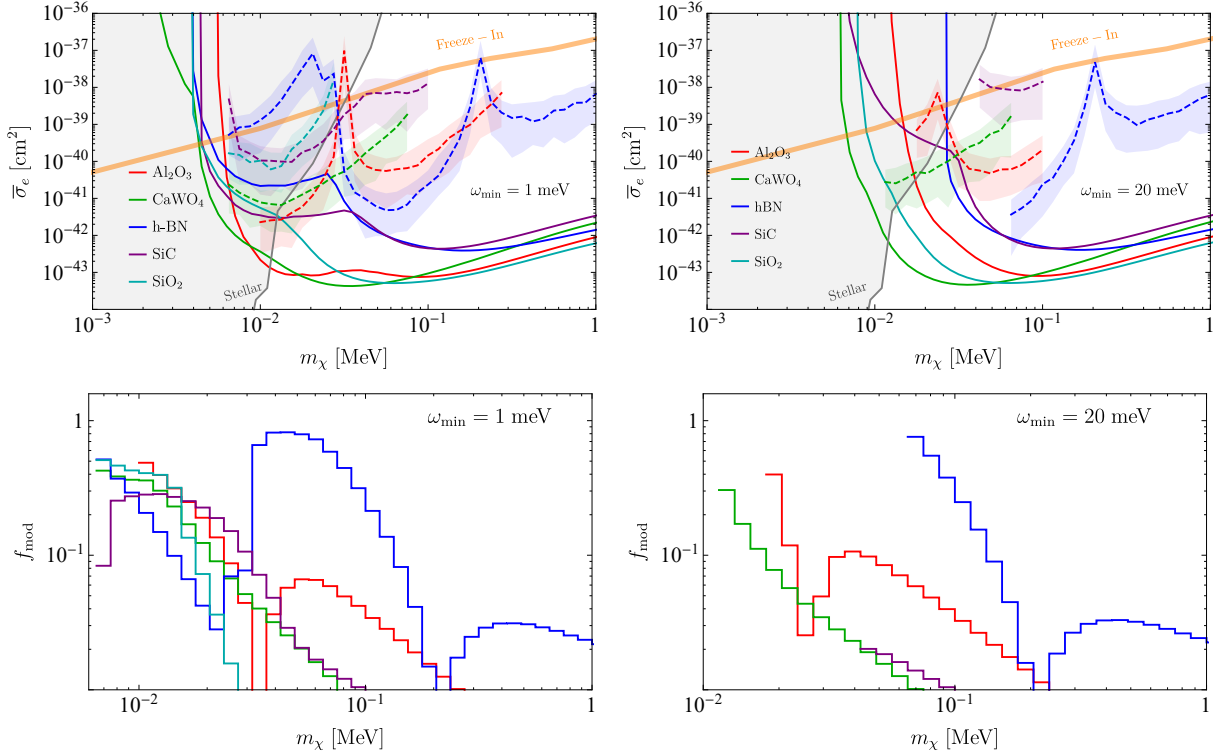


Figure 4.5: **Top:** Projected reach for the dark photon mediator model assuming 1 meV and 20 meV detector energy thresholds and one kg-year exposure. Solid curves show the 95% confidence level (CL) exclusion limits in the case of zero observed events, assuming no background. Dashed curves and the associated $\pm 1\sigma$ bands show the modulation reach for DM masses with more than 1% daily modulation, i.e., cross sections for which we can reject the non-modulating hypothesis and establish the statistical significance of a modulating signal, as explained in App. E. **Bottom:** Daily modulation amplitudes f_{mod} , defined in Eq. (4.15), for the same energy thresholds. Results are shown only for m_χ values where a material has substantial reach and $f_{\text{mod}} > 10^{-2}$. The exact DM mass corresponding to a specific bar can be read off from the left edge of that bar.

$\mathbf{Y}_j \cdot \boldsymbol{\epsilon}_{\nu,k,j}$ intact. This has a visible impact only when the region of \mathbf{q} space just outside the 1BZ has a significant contribution to the rate; as \mathbf{q} moves farther away from the 1BZ, summing over contributions from many different \mathbf{G} vectors mitigates the effect. For the dark photon mediator model, this explains the enhanced daily modulation at $m_\chi \gtrsim \text{MeV}$ (see Fig. 4.5 below). For the light hadrophilic scalar mediator model, there is no significant effect since the \mathbf{q} integral is dominated by small q . For the heavy hadrophilic scalar mediator model, in contrast, the \mathbf{q} integral is dominated by large q , so the enhancement happens in a window around $m_\chi \sim \text{MeV}$ (see Fig. 4.7 below).

Effects of Experimental Setup

The daily modulation pattern can also be significantly affected by experimental factors, including in particular the detector’s energy threshold and the orientation of the target crystal. The energy threshold ω_{\min} can be important if phonon modes at different energies have different modulation patterns. As an example, we show in the left panel of Fig. 4.3 the daily modulation in h-BN for several different values of ω_{\min} , for the dark photon mediator model with $m_\chi = 100$ keV. The distinct daily modulation curves can be understood from the differential rate plot in the right panel of Fig. 4.3. We see that the phonon modes just below 100 meV dominate the total rate, so long as ω_{\min} is below this, and they drive the daily modulation pattern. On the other hand, if $\omega_{\min} > 100$ meV, these modes are no longer accessible, and the daily modulation is instead induced by phonon modes at energies higher than about 175 meV, for which the rate has a very different time dependence.

Meanwhile, the orientation of the crystal determines the function $\mathbf{v}_e(t)$, and hence the daily modulation pattern. As an example, Fig. 4.4 compares the daily modulation patterns between our default setup, given in Eq. (4.10), and an (arbitrarily chosen) alternative orientation where the crystal z axis is rotated by 60° clockwise around $\hat{\mathbf{n}} = (\hat{\mathbf{x}} + \hat{\mathbf{y}} + \hat{\mathbf{z}})/\sqrt{3}$ (or equivalently, a -60° right-handed rotation around $\hat{\mathbf{n}}$.)

4.3 Target Comparison

Having discussed the physics underlying daily modulation, we now consider concrete target materials. Among the 26 materials studied [258], 19 are observed to have more than 1% daily modulation for some DM masses in at least one of the benchmark models considered. In this section, we focus on the following five which are observed to have the highest daily modulation amplitudes: Al_2O_3 , SiO_2 , SiC, CaWO_4 and h-BN. Among them, Al_2O_3 , SiO_2 and SiC have been proposed and recommended for near-future phonon-based experiments, while Al_2O_3 and CaWO_4 are in use in the CRESST experiment. Meanwhile, h-BN is a highly anisotropic target with layered crystal structure that we have found to have exceptionally large daily modulation; while its experimental prospects have not been assessed, it serves as a useful benchmark for our theoretical study. We supplement this analysis with the remaining 14 materials with more than 1% daily modulation (AlN, CaF_2 , GaN, GaSb, InSb, LiF, MgF_2 , MgO, NaF, PbS, PbSe, PbTe, ZnO, ZnS) in App. D.

Our main results are shown in Figs. 4.5, 4.6 and 4.7, for the dark photon mediator model and the light and heavy hadrophilic scalar mediator models, respectively. In the top panels of each figure, we show both the projected exclusion limits (solid) and the cross sections needed to distinguish the modulating signal and a non-modulating hypothesis in the event of discovery

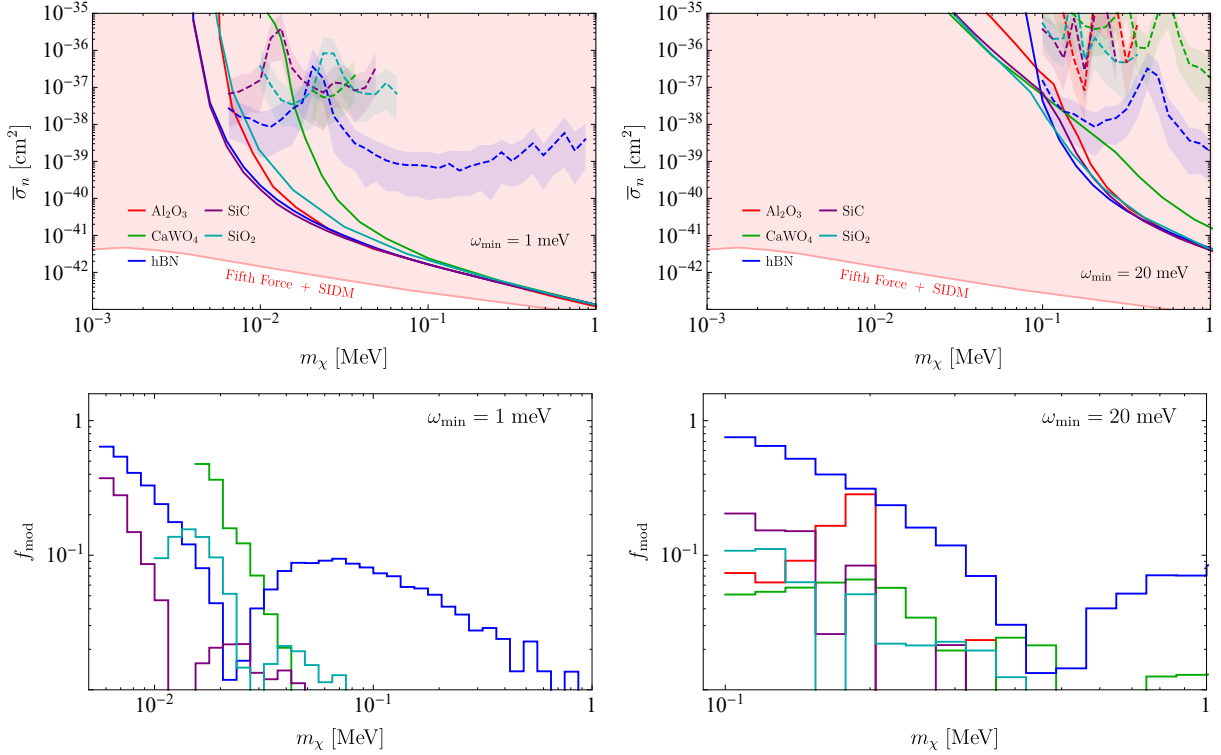


Figure 4.6: Same as Fig. 4.5, for the light hydrophilic scalar mediator model.

(dashed and shaded $\pm 1\sigma$ bands), assuming 1 and 20 meV detector energy thresholds. These energy thresholds have been envisioned with near-future advances in detector technology, and the primary motivation for these specific values is to differentiate the effects of acoustic and optical phonon dominated scattering. For the solid curves, we set $t = 0$ when computing the rates for concreteness, and assume 3 events per kilogram-year exposure, corresponding to 95% confidence level (CL) exclusion in a background-free experiment. The results for Al_2O_3 , CaWO_4 and SiO_2 were computed previously in Ref. [6] (numerical errors in some of the materials in early versions of that reference have been corrected here and on the interactive webpage [258]), and here we perform the calculation also for SiC and h-BN. For the dashed curves and the shaded bands for the modulation reach, we compute the number of events needed to reject the constant rate hypothesis at the 95% confidence level by a prescription discussed in App. E; they are truncated where the daily modulation falls below 1%.

In the lower panels of Figs. 4.5, 4.6 and 4.7, we quantify the amount of daily modulation for several representative DM masses by

$$f_{\text{mod}} \equiv \frac{\max(|R - \langle R \rangle|)}{\langle R \rangle}, \quad (4.15)$$

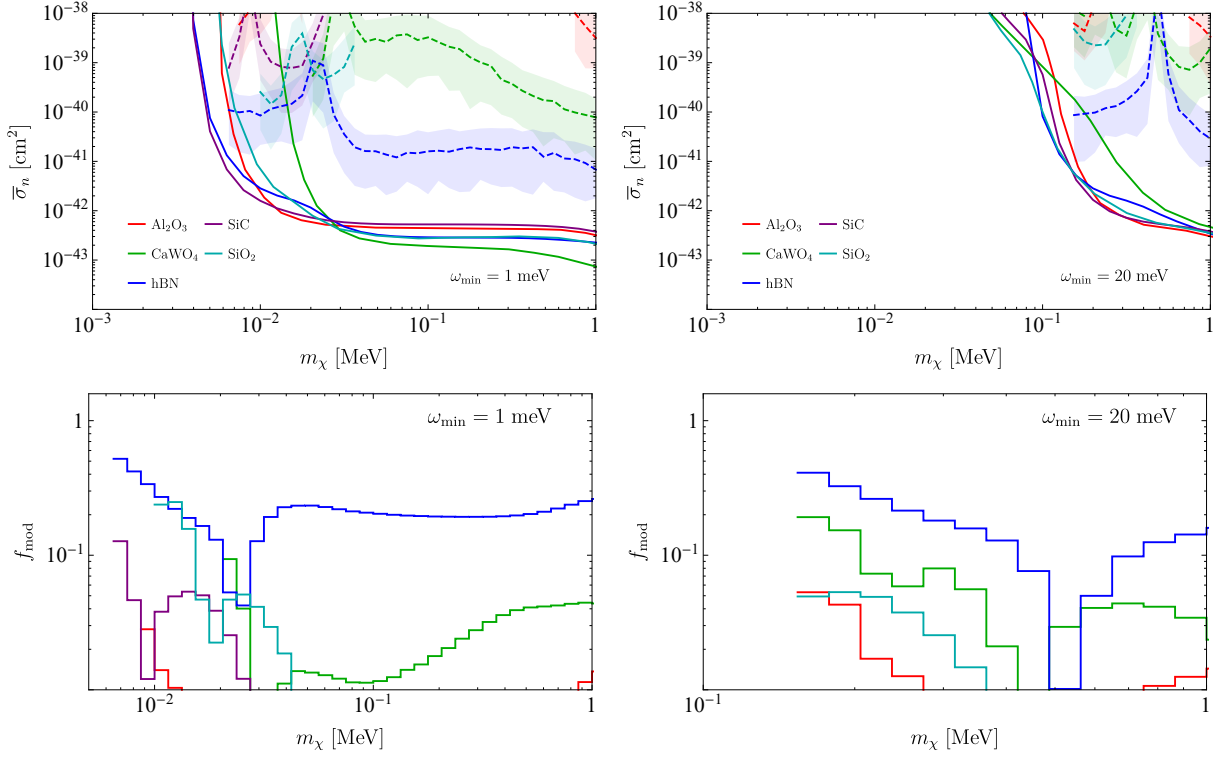


Figure 4.7: Same as Fig. 4.5, for the heavy hydrophilic scalar mediator model.

which characterizes the maximum deviation of detection rate throughout the day from the daily average $\langle R \rangle$. We shall refer to f_{mod} as the daily modulation amplitude. The f_{mod} plots give us an overview of the amount of daily modulation to expect. More detailed information on the daily modulation signal can be gained by plotting $R(t)/\langle R \rangle$, as in Figs. 4.2, 4.3 and 4.4, for each DM mass and energy threshold; we provide these plots on the interactive webpage [258].

We have considered detector energy thresholds $\omega_{\min} = 1$ meV and 20 meV. For the dark photon mediator model (Fig. 4.5), the energy threshold does not have a significant impact on either the reach or the daily modulation amplitude, except at the lowest m_χ values. This is because gapped optical phonons dominate the rate as long as they are above ω_{\min} and the DM is heavy enough to excite them. For the hydrophilic scalar mediator models (Figs. 4.6 and 4.7), on the other hand, gapless acoustic phonons dominate and, as a result, both the reach and the daily modulation amplitude are sensitive to ω_{\min} . Generally, a higher energy threshold tends to amplify the daily modulation since the kinematically accessible phase space becomes limited, as discussed in detail in Sec. 4.2. Similarly, the daily modulation amplitude tends to increase at the lowest m_χ considered because of phase space restrictions. The enhanced daily modulation in these cases comes at the price of a lower total rate, so

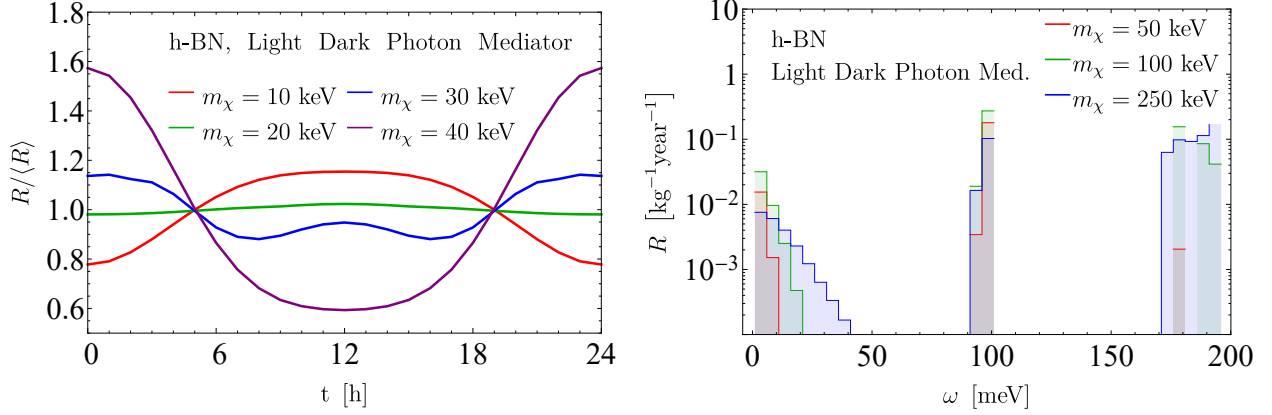


Figure 4.8: **Left:** Daily modulation for an h-BN target with various DM masses, assuming dark photon mediated scattering and $\omega_{\min} = 1$ meV. The change in modulation pattern is a result of the kinematically favored $\hat{\mathbf{q}} \cdot \hat{\mathbf{v}}_e$ increasing from -1 toward 0 as m_χ increases. During the transition between different modulation patterns, an intermediate mass value around 20 keV features a reduced modulation amplitude, which explains the peak in the modulation reach curve in the top-left panel of Fig. 4.5. A similar effect is also observed for the hadrophilic scalar mediator models in Figs. 4.6 and 4.7. **Right:** Differential rates at $t = 0$ for several higher m_χ assuming $\bar{\sigma}_e = 10^{-43}$ cm². Another transition between modulation patterns occurs when new phonon modes become dominant as m_χ increases, resulting in a second reduced modulation mass point, around 200 keV, in Fig. 4.5.

there is a trade-off between better overall sensitivity and a higher daily modulation signal. This is reflected by the dashed modulation reach curves in the top panels of each figure, which ascend at lower masses since the rate also vanishes.

From Figs. 4.5, 4.6 and 4.7, we see that h-BN consistently outperforms all other materials in terms of the daily modulation amplitude, which reaches $\mathcal{O}(1)$ for some m_χ and ω_{\min} values. This is due to the layered crystal structure which means that the momentum transfers perpendicular and parallel to the layers lead to very different target responses. Among the other materials, Al_2O_3 , CaWO_4 and SiC are also competitive targets for the dark photon mediator model at $m_\chi \lesssim 100$ keV, and CaWO_4 shows percent level daily modulation across a wide range of DM masses for the heavy scalar mediator model.

It is also worth noting that the modulation reach curves and f_{mod} often exhibit a nontrivial dependence on m_χ . In particular, for given target material and ω_{\min} , there can be m_χ values where the modulation signal diminishes. For example, for dark photon mediated scattering, h-BN with $\omega_{\min} = 1$ meV has two such low- f_{mod} mass points at around 20 keV and 200 keV, corresponding to the peaks of the modulation reach curve in the top-left panel of Fig. 4.5.

Generally, low- f_{mod} points at low m_χ result from the change in $\hat{\mathbf{q}} \cdot \hat{\mathbf{v}}_e$ favored by the kinematic

function. As discussed in Sec. 4.2, as m_χ increases, the favored $\hat{\mathbf{q}} \cdot \hat{\mathbf{v}}_e$ increases from -1 toward 0 . As $\hat{\mathbf{v}}_e$ changes with time (e.g., as in Eq. (4.10)), a given $\hat{\mathbf{q}} \cdot \hat{\mathbf{v}}_e$ probes the crystal's $S'_\nu(\mathbf{q})$ along a set of $\hat{\mathbf{q}}$ directions that modulates, and the modulation pattern depends on the kinematically favored $\hat{\mathbf{q}} \cdot \hat{\mathbf{v}}_e$ value. We verify this expectation in the left panel of Fig. 4.8 for h-BN. In this case, the modulation pattern flips as m_χ increases from 10 keV to 40 keV, and an approximate cancelation occurs around 20 keV. Note, however, that the daily modulation sensitivity may be recovered by analyzing the differential rates $\frac{dR(t)}{d\omega}$.

The low- f_{mod} points at higher m_χ , on the other hand, are explained by new phonon modes with different modulation patterns becoming kinematically accessible as m_χ increases. Again focusing on h-BN as an example, we see from the right panel of Fig. 4.8 that while the dominant phonon modes are the ~ 100 meV modes for $m_\chi = 50$ keV and 100 keV, the modes above 150 meV take over as m_χ increases to 250 keV. The reduced modulation sensitivity at $m_\chi \simeq 200$ keV results from the transition between the two regimes.

4.4 Conclusions

As new experiments focused on light DM detection with single optical and acoustic phonons begin an R&D phase [90], it is important and timely to understand which target crystals have the optimal sensitivity to well-motivated DM models. This includes not only the sensitivity to the smallest interaction cross section for a given DM model, but also the ability to extract a smoking gun signature for DM that can be distinguished from background. Daily modulation provides such a unique fingerprint. In this work, we have carried out a comparative study of daily modulation signals for several benchmark models, where DM scattering is mediated by a dark photon or hadrophilic scalar mediator. Our results supplement the information on the cross section reach obtained previously in Ref. [6], and provide further theoretical guidance to the optimization of near future phonon-based experiments.

Based on our analysis of 26 crystals, we observe that there is often a trade-off between detection rate, modulation amplitude, and experimental feasibility. For example, for dark photon mediated scattering, Al_2O_3 (sapphire), CaWO_4 and SiO_2 (α -quartz) outperform h-BN in terms of their sensitivities to the total rate; h-BN's daily modulation signal, however, is significantly stronger. Still, despite having the largest daily modulation amplitude, h-BN will likely be difficult to fabricate as a large ultra-pure single crystal target. Overall, Al_2O_3 and CaWO_4 provide perhaps the optimal balance between the overall reach and the daily modulation signal, and have both already been used in direct detection experiments.

Beyond the results presented in this paper, we also publish an interactive webpage [258], where additional results can be generated from our calculations of single phonon excitation

rates and their daily modulation.

DETECTING LIGHT DARK MATTER WITH MAGNONS

5.1 Introduction

Direct detection of dark matter (DM) has undergone a dramatic expansion of scope in recent years. Well-motivated theories where sub-GeV DM arises in a hidden sector/hidden valley, with new weakly or strongly coupled dynamics (see e.g., Refs. [140, 203–205, 210, 241, 260, 261] for early examples), have given impetus to new ideas to search for light DM. Conventional nuclear recoils, well-matched kinematically to search for weak-scale DM, are not effective for light DM — once the DM mass drops below the target nucleus mass, the fraction of the DM’s kinetic energy that can be deposited on the target falls. Beyond nuclear recoils, better DM-target kinematic matching allows us to probe qualitatively new parameter space, through lighter targets (e.g., electrons) with \sim eV (as in semiconductors and atoms [19, 24, 25, 33–35, 39, 40, 177, 180] as well as molecules [193–195]) or \sim meV (as in superconductors [41, 181, 182] and Dirac materials [188]) energy gaps. Reading out such small energy depositions is achieved through improvements to cryogenic superconducting calorimeters, such as transition edge sensors (TES) and microwave kinetic inductance devices (MKIDs). *Collective* excitations, such as phonons in superfluid helium [184–187] and crystals [28, 64], open new avenues for good kinematic matching. For example, the presence of $\mathcal{O}(10\text{--}100)$ meV gapped optical phonons in some systems facilitates the extraction of a large fraction of DM’s kinetic energy for DM as light as ~ 10 keV.

Beyond kinematics, there is also a *dynamics* aspect of the problem — depending on how the DM couples to Standard Model (SM) particles, different target responses are relevant. A familiar example from nuclear recoils is the presence of several nuclear responses – spin-independent (SI), spin-dependent (SD), *etc.* – which can probe different DM-SM interactions [55, 60, 196, 197]. Together they provide broad coverage of the DM theory space, with various target nuclei offering complementary information. Another example is dark photon mediated DM: a material with a strong optical response, such as a superconductor, has weak reach since the effective coupling of the dark photon is suppressed due to in-medium effects, while Dirac materials and polar crystals, which have weaker optical response, have excellent reach [28, 64, 188]. Similarly, collective excitations can arise from different degrees of freedom, such as charge or spin, and some excitations may be advantageous over others for certain types of DM couplings. Therefore, in order to identify the broadest DM detection strategy,

it is important to consider collective excitations of all types.

From this perspective, previous proposals via phonon excitations are aimed at probing SI responses. While they cover many simple DM models, including those with a dark photon or scalar mediator, there are other scenarios that are equally plausible, where the leading DM-SM interactions lead to stronger SD responses. For example, in dark photon mediated models, the DM may in fact be charge neutral, but couple to the dark photon via a higher multipole, e.g., magnetic dipole or anapole [52–63]. Also, a spin-0 mediator may dominantly couple to the pseudoscalar (rather than scalar) current of SM fermions. In these scenarios, summarized in Table 5.1, SI responses are suppressed compared to the previously considered cases, and ideas of detecting SD responses are needed. More generally, SI and SD couplings can coexist, so it is desirable to pursue detection channels for both in order to have a more complete picture of DM interactions.

Magnetic dipole DM	$\mathcal{L} = \frac{g_\chi}{\Lambda_\chi} \bar{\chi} \sigma^{\mu\nu} \chi V_{\mu\nu} + g_e \bar{e} \gamma^\mu e V_\mu$	$\hat{O}_\chi^\alpha = \frac{4g_\chi g_e}{\Lambda_\chi m_e} (\delta^{\alpha\beta} - \frac{q^\alpha q^\beta}{q^2}) \hat{S}_\chi^\beta$	$\bar{\sigma}_e = \frac{g_\chi^2 g_e^2}{\pi} \frac{6m_\chi^2 + m_e^2}{\Lambda_\chi^2 (m_\chi + m_e)^2}$
Anapole DM	$\mathcal{L} = \frac{g_\chi}{\Lambda_\chi^2} \bar{\chi} \gamma^\mu \gamma^5 \chi \partial^\nu V_{\mu\nu} + g_e \bar{e} \gamma^\mu e V_\mu$	$\hat{O}_\chi^\alpha = \frac{2g_\chi g_e}{\Lambda_\chi^2 m_e} \epsilon^{\alpha\beta\gamma} i q^\beta \hat{S}_\chi^\gamma$	$\bar{\sigma}_e = \frac{g_\chi^2 g_e^2}{\pi} \frac{3\alpha^2 \mu_\chi^2}{2\Lambda_\chi^4}$
Pseudo-mediated DM	$\mathcal{L} = g_\chi \bar{\chi} \chi \phi + g_e \bar{e} i \gamma^5 e \phi$	$\hat{O}_\chi^\alpha = -\frac{g_\chi g_e}{q^2 m_e} i q^\alpha \mathbb{1}_\chi$	$\bar{\sigma}_e = \frac{g_\chi^2 g_e^2}{4\pi} \frac{\mu_\chi^2}{\alpha^2 m_e^2}$

Table 5.1: Dark matter models, having Lagrangian \mathcal{L} , with SD interactions considered in this work; these models are particularly well-motivated when DM does not carry a charge of any type, see e.g., Refs. [52–63]. χ is a spin-1/2 DM particle, and V , ϕ are ultralight (typically \ll eV) spin-0 mediators, respectively. g_χ , g_e are dimensionless couplings, and Λ_χ is the effective theory cutoff. In the non-relativistic limit, these Lagrangians reduce to the operators \hat{O}_χ^α (with Cartesian coordinates $\alpha = 1, 2, 3$), as in Eq. (5.4). $q \equiv |\mathbf{q}|$ is the momentum transfer, and $\hat{S}_\chi^\alpha = \sigma^\alpha/2$ is the DM spin operator. $\bar{\sigma}_e$ is the reference cross section defined in Eq. (5.11) that we will use to present the reach.

In this *Letter*, we propose a novel detection path for spin-dependent light DM-electron interactions via magnon excitations. Magnons are quanta of collective spin wave excitations in condensed matter systems that exhibit magnetic dipole order in the ground state. They can be thought of as the SD counterpart of phonons for DM detection with similar kinematics. We demonstrate as a proof of principle that single magnon excitations can probe interesting DM scenarios through scattering, thus broadening the coverage of the DM theory space. In future work we will pursue DM (in particular axion DM) absorption through magnon excitations.

5.2 Magnons In Magnetically Ordered Materials

Magnetic order can arise in solid state systems due to the interplay between electron-electron interactions, electron kinetic energy and Pauli exclusion (see e.g., Refs. [262, 263]). Such systems are usually described by a spin lattice model, e.g., the Heisenberg model,

$$H = \frac{1}{2} \sum_{l,l'=1}^N \sum_{j,j'=1}^n J_{ll'jj'} \mathbf{S}_{lj} \cdot \mathbf{S}_{l'j'}. \quad (5.1)$$

Here l, l' label the magnetic unit cells, and j, j' label the magnetic atoms/ions inside the unit cell. Depending on the sign of the exchange coupling $J_{ll'jj'}$, the spins \mathbf{S}_{lj} and $\mathbf{S}_{l'j'}$ tend to align or anti-align. The low energy excitations are obtained by applying the Holstein-Primakoff transformation to expand the spins around the ordered ground state in terms of bosonic creation and annihilation operators \hat{a}^\dagger, \hat{a} . The quadratic part of the Hamiltonian can then be diagonalized via a Bogoliubov transformation (see Supplemental Material for details),

$$\begin{pmatrix} \hat{a}_{j,\mathbf{k}} \\ \hat{a}_{j,-\mathbf{k}}^\dagger \end{pmatrix} = \begin{pmatrix} U_{j\nu,\mathbf{k}} & V_{j\nu,\mathbf{k}} \\ V_{j\nu,-\mathbf{k}}^* & U_{j\nu,-\mathbf{k}}^* \end{pmatrix} \begin{pmatrix} \hat{b}_{\nu,\mathbf{k}} \\ \hat{b}_{\nu,-\mathbf{k}}^\dagger \end{pmatrix}, \quad (5.2)$$

$$H = \sum_{\nu=1}^n \sum_{\mathbf{k} \in 1\text{BZ}} \omega_{\nu,\mathbf{k}} \hat{b}_{\nu,\mathbf{k}}^\dagger \hat{b}_{\nu,\mathbf{k}}, \quad (5.3)$$

so that \hat{b}^\dagger, \hat{b} are creation and annihilation operators of the canonical magnon modes, which are collective excitations of the spins. For a system with N magnetic unit cells and n magnetic atoms/ions in the unit cell, there are n magnon branches, labeled by ν , with N modes on each branch, labeled by momentum vectors \mathbf{k} within the first (magnetic) Brillouin zone (1BZ). The $n \times n$ matrices U, V can be calculated for each \mathbf{k} .

5.3 Magnon Excitation From Dark Matter Scattering

If the DM couples to the electron spin, it can scatter off the target material and create magnon excitations.¹ Suppose the nonrelativistic effective Lagrangian takes the form

$$\mathcal{L} = - \sum_{\alpha=1}^3 \hat{\mathcal{O}}_{\chi}^{\alpha}(\mathbf{q}) \hat{S}_e^{\alpha}, \quad (5.4)$$

where α denotes the Cartesian coordinates, and \mathbf{q} is the momentum transfer from the DM to the target. The operators $\hat{\mathcal{O}}_{\chi}$ that follow from the three Lagrangians we consider are listed in Table 5.1. Focusing on transitions from the ground state to single magnon states $|\nu, \mathbf{k}\rangle$, we obtain the matrix element as (see Supplemental Material for details)

$$\mathcal{M}_{\nu, \mathbf{k}}^{s_i s_f}(\mathbf{q}) = \delta_{\mathbf{q}, \mathbf{k} + \mathbf{G}} \frac{1}{\sqrt{N\Omega}} \sum_{\alpha=1}^3 \langle s_f | \hat{\mathcal{O}}_{\chi}^{\alpha}(\mathbf{q}) | s_i \rangle \epsilon_{\nu, \mathbf{k}, \mathbf{G}}^{\alpha}, \quad (5.5)$$

where Ω is the volume of the magnetic unit cell, \mathbf{G} denotes a reciprocal lattice vector, and $|s_{i,f}\rangle$ are the initial and final DM spin states. $\epsilon_{\nu, \mathbf{k}, \mathbf{G}}$ is the analog of polarization vectors for the magnon modes,

$$\epsilon_{\nu, \mathbf{k}, \mathbf{G}} = \sum_{j=1}^n \sqrt{\frac{S_j}{2}} (V_{j\nu, -\mathbf{k}} \mathbf{r}_j^* + U_{j\nu, \mathbf{k}}^* \mathbf{r}_j) e^{i\mathbf{G} \cdot \mathbf{x}_j}, \quad (5.6)$$

where $r_j^{\alpha} \equiv R_j^{\alpha 1} + iR_j^{\alpha 2}$ parameterize the spin orientations in the ground state,

$$S_{l_j}^{\alpha} = \sum_{\beta} R_j^{\alpha\beta} S_{l_j}^{\prime\beta}, \quad \{\langle S_{l_j}^{\prime 1} \rangle, \langle S_{l_j}^{\prime 2} \rangle, \langle S_{l_j}^{\prime 3} \rangle\} = \{0, 0, S_j\}, \quad (5.7)$$

and $\mathbf{x}_j \equiv \mathbf{x}_{l_j} - \mathbf{x}_l$ is the position of the j th site within a magnetic unit cell. As a simple example, a ferromagnet with one magnetic ion per unit cell ($n = 1$) has $\mathbf{r} = (1, i, 0)$, $U = 1$, $V = 0$, and thus, $\epsilon = \sqrt{S/2}(1, i, 0)$ for all \mathbf{k} and \mathbf{G} , reminiscent of a photon polarization vector.

From Eq. (5.5) we see that for given \mathbf{q} , only the magnon modes with $\mathbf{k} \in 1\text{BZ}$ satisfying $\mathbf{q} = \mathbf{k} + \mathbf{G}$ for some \mathbf{G} can be excited, due to lattice momentum conservation. Summing over s_f and averaging over s_i , we obtain

$$\overline{|\mathcal{M}_{\nu, \mathbf{k}}(\mathbf{q})|^2} = \frac{\delta_{\mathbf{q}, \mathbf{k} + \mathbf{G}}}{N\Omega^2} \text{tr}(\hat{\rho}_{\chi} \hat{\mathcal{O}}_{\chi}^{\alpha}(\mathbf{q}) \hat{\mathcal{O}}_{\chi}^{\dagger\beta}(\mathbf{q})) \epsilon_{\nu, \mathbf{k}, \mathbf{G}}^{\alpha} \epsilon_{\nu, \mathbf{k}, \mathbf{G}}^{*\beta}, \quad (5.8)$$

¹Magnons can also be excited via couplings to orbital angular momenta. Here we assume negligible orbital angular momenta for simplicity, noting that this is the case for many familiar materials where 3d electrons are responsible for the magnetic order.

where $\hat{\rho}_\chi = \frac{1}{2S_\chi+1} \mathbb{1}_{2S_\chi+1}$ is the density matrix for the spin of the incoming DM. The total event rate per unit target mass is then obtained as

$$R = \frac{1}{\rho_T} \frac{\rho_\chi}{m_\chi} \int d^3v_\chi f(\mathbf{v}_\chi) \sum_\nu \sum_{\mathbf{k} \in \text{1BZ}} \Gamma_{\nu, \mathbf{k}}(\mathbf{v}_\chi), \quad (5.9)$$

$$\Gamma_{\nu, \mathbf{k}}(\mathbf{v}_\chi) = 2\pi \sum_{\mathbf{q}=\mathbf{k}+\mathbf{G}} \overline{|\mathcal{M}_{\nu, \mathbf{k}}(\mathbf{q})|^2} \delta(E_{\chi_i} - E_{\chi_f} - \omega_{\nu, \mathbf{k}}), \quad (5.10)$$

where ρ_T is the target mass density, $\rho_\chi = 0.3 \text{ GeV/cm}^3$ is the local DM energy density, $E_{\chi_i} = \frac{1}{2} m_\chi v_\chi^2$, $E_{\chi_f} = (m_\chi \mathbf{v}_\chi - \mathbf{q})^2 / (2m_\chi)$. We assume the DM velocity distribution $f(\mathbf{v}_\chi)$ is Maxwell-Boltzmann, with dispersion 220 km/s, truncated by the galactic escape velocity 500 km/s, and boosted to the target rest frame by the Earth's velocity in the galactic rest frame, 240 km/s. We take the continuum limit $\sum_{\mathbf{k} \in \text{1BZ}} \rightarrow N \Omega \int \frac{d^3k}{(2\pi)^3}$, where R becomes N -independent.

5.4 Projected Reach

As a first demonstration of the detection concept, we consider a yttrium iron garnet (YIG, $\text{Y}_3\text{Fe}_5\text{O}_{12}$) target. YIG is a classic ferrimagnetic material that has been extensively studied and well-characterized, and can be readily synthesized with high quality [264, 265]. It has been exploited for axion DM detection via absorption in an external magnetic field [93, 164, 266]. Here we focus on DM scattering for which external fields are not necessary for producing a signal. Particular detection schemes will be explored in future work.

YIG has 20 magnetic ions Fe^{3+} per unit cell, with effective spins $S_j = 5/2$ ($j = 1, \dots, 20$) coming from five 3d electrons with quenched orbital angular momentum. The ground state has the 12 tetrahedral-site and 8 octahedral-site spins pointing in opposite directions. Taking the crystal parameters from Ref. [267] and Heisenberg model parameters from Ref. [264], we diagonalize the magnon Hamiltonian using the algorithm of Ref. [268] to obtain the magnon spectrum $\omega_{\nu, \mathbf{k}}$ and the U, V matrices that enter the rate formulae. For simplicity, we fix the direction of the DM wind to be parallel (perpendicular) to the ground state spins for the magnetic dipole and anapole (pseudo-mediated) models, which maximizes the event rate. For fixed target orientation, we find a daily modulation of $\mathcal{O}(10\%)$, which could be utilized for distinguishing DM signals from backgrounds. Following common practice, we present the projected reach in terms of a reference cross section $\bar{\sigma}_e$ defined from DM-free electron scattering. Here we generalize the definition in Ref. [19] beyond SI interactions by defining

$$\bar{\sigma}_e \equiv \frac{\mu_{\chi e}^2}{16\pi m_\chi^2 m_e^2} \overline{|\mathcal{M}_{\text{free}}|^2} (q = \alpha m_e, v^\perp = \alpha), \quad (5.11)$$

where $\mu_{\chi e}$ is the DM-electron reduced mass, $\alpha = 1/137$ is the fine structure constant, and v^\perp is the component of the relative velocity perpendicular to \mathbf{q} . The reference cross-section for each model is given in Table 5.1.

Our results are shown in Fig. 5.1 for m_χ up to 10 MeV, assuming 3 events on a YIG target (colored solid curves) with kilogram-year exposure and, following convention for easy comparison to other experiments, no background.² Beyond 10 MeV, the simple Heisenberg model description breaks down in part of the kinematic integration region where q exceeds the inverse ionic radius of Fe^{3+} ; however, electron excitations are expected to have sensitivity in this mass regime [19, 24, 25, 33–35, 177, 180] (though precise results are not currently available for the SD models considered here). We consider several detector thresholds ω_{\min} corresponding to capabilities of TESs expected within the next few years (40 meV) and further into the future (10 meV, 1 meV). Also shown in the plots are contours of model parameters in the magnon sensitivity region (gray).

For each benchmark DM model, magnons can probe currently unconstrained parameter space. For the vector mediator models, assuming the mediator V couples to SM particles only via kinetic mixing with the photon, V production in stellar media and in the early universe is suppressed when $m_V \rightarrow 0$, so the only astrophysical and cosmological constraints are from DM production. The latter, however, depend on whether Λ_χ is above or below the energies involved and, if below, the ultraviolet (UV) completion of the effective operators. For example, if $\Lambda_\chi \sim m_\chi$ and the UV completion involves millicharged particles [17, 270] with couplings $\sim g_\chi$, we find that magnetic dipole DM with $g_\chi g_e \lesssim 10^{-10}$ satisfies all existing constraints, but can be probed by magnons. On the other hand, if $\Lambda_\chi \gtrsim \mathcal{O}(100 \text{ MeV})$, we can map the constraints derived in Ref. [271] onto the gray contours in Fig. 5.1, e.g., excluding $g_\chi g_e m_\chi / \Lambda_\chi \in (10^{-12}, 10^{-10}) m_\chi / m_e$ for magnetic dipole DM from SN1987A — in this case, there is a large region of unconstrained parameter space above this band (even after imposing Big Bang Nucleosynthesis constraints) [271], which can be fully covered by our projected magnon reach. The anapole model is more challenging to discover via magnons due to the high power of momentum suppression, but the magnon sensitivity region still accommodates viable UV models, such as those involving two dark photons [272] which evade astrophysical and cosmological bounds altogether. Finally, for the pseudo-mediated DM model, the mediator-electron coupling is constrained by white dwarf cooling to be $g_e \lesssim 2 \times 10^{-13}$, so that g_χ has to be $\mathcal{O}(1)$ to produce a detectable signal. Given the existing

²For calorimetric readout, the backgrounds are expected to be similar to other experiments reading out meV-eV energy depositions: radiogenic backgrounds are not expected to be problematic at such low energies, while coherent scattering from high-energy photons can be suppressed with an active veto, leaving pp solar neutrinos the main irreducible background. We expect the latter to be at most a few events per kilogram-year, as estimated from neutrino-nucleus scattering (see e.g., Refs. [182, 269]).

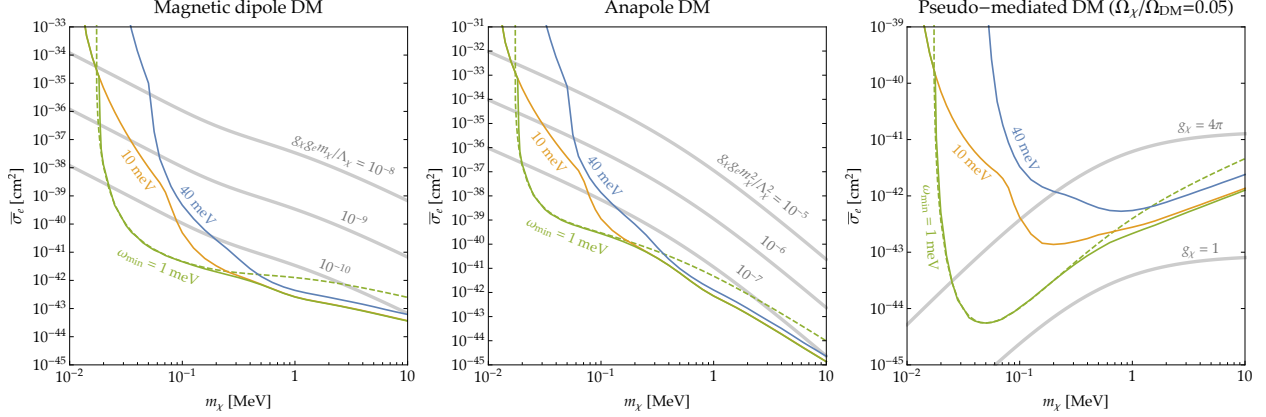


Figure 5.1: Projected reach for the DM models in Table 5.1 for a YIG target, assuming three events with kilogram-year exposure, for several magnon detection thresholds ω_{\min} (solid). Also shown are the results of a Heisenberg ferromagnet with the same mass and spin densities as YIG, and the same magnon dispersion as the low-energy gapless modes of YIG, for $\omega_{\min} = 1$ meV (dashed); they coincide with the YIG curves for $0.02 \text{ MeV} \lesssim m_\chi \lesssim 0.1 \text{ MeV}$, which can be understood from the effective theory argument in the text. The gray contours show the model parameters in the magnon sensitivity regions, which astrophysical and cosmological constraints on specified UV completions can be mapped onto (see text). For the pseudo-mediated model, we consider a DM subcomponent to evade SIDM constraints, and let g_e saturate the white dwarf cooling bound.

self-interacting dark matter constraints, we consider χ to be a 5% subcomponent of DM as a viable scenario, and show contours of g_χ in Fig. 5.1 with g_e saturating its upper bound.

To gain some analytical intuition, we note that for momentum transfer well within the 1BZ, corresponding to $m_\chi \lesssim 0.1 \text{ MeV}$ for a YIG target, the rate can be estimated via an effective $n = 1$ ferromagnetic model. This is because in the $q \rightarrow 0$ limit, the external probe $\hat{\mathcal{O}}_\chi^\alpha$ acts like a uniform magnetic field. In a semiclassical picture, this causes all the spins in the target to precess in phase, so the angle between them, and thus the total energy of the Heisenberg model, stays the same. As a result, only the *gapless* mode(s), i.e., Goldstone mode(s) of the broken rotational symmetry, can be excited. Even for finite q , gapped magnon contributions are suppressed by powers of aq , where a is the lattice spacing, and thus subdominant for $q \ll a^{-1}$ ($\simeq 0.2 \text{ keV}$ for YIG). For a ferrimagnet like YIG, we can integrate out the gapped modes to arrive at an effective theory, where the only relevant degree of freedom is the total spin density n_s . There is only one magnon branch in this effective $n = 1$ ferromagnetic theory, which matches the gapless branch of the original ferrimagnet for $k \ll a^{-1}$. For YIG, the total spin density is $S_{\text{cell}} = (12 - 8) \times 5/2 = 10$ per unit cell volume $\Omega = a^3/2$, with $a \simeq 12.56 \text{ \AA}$, i.e., $n_s = 20/a^3 \simeq (4.6 \text{ \AA})^{-3}$. The effective exchange coupling can be shown to be $J_{\text{eff}} \simeq -4 \text{ K} = -0.35 \text{ meV}$ [264], resulting in a quadratic magnon dispersion

$\omega = |J_{\text{eff}}|S_{\text{cell}}(ak)^2 \simeq k^2/(7 \text{ MeV})$ at small k . For this $n = 1$ ferromagnetic theory, we obtain (see Supplemental Material for details),

$$\begin{aligned}
R &\simeq \frac{n_s \rho_\chi}{\rho_T m_\chi} \int d^3 v_\chi f(\mathbf{v}_\chi) \cdot \\
&\quad \int \frac{d^3 q}{8\pi^2} \text{tr}(\hat{\rho}_\chi \hat{\mathcal{O}}_\chi^+(\mathbf{q}) \hat{\mathcal{O}}_\chi^{+-}(\mathbf{q})) \delta(E_{\chi_i} - E_{\chi_f} - \omega), \\
&\simeq 3 (\text{kg} \cdot \text{yr})^{-1} \left(\frac{n_s}{(4.6 \text{ \AA})^{-3}} \right) \left(\frac{4.95 \text{ g/cm}^3}{\rho_T} \right) \left(\frac{0.1 \text{ MeV}}{m_\chi} \right) \\
&\quad \int d^3 v_\chi f(\mathbf{v}_\chi) \left(\frac{10^{-3}}{v_\chi} \right) \left(\frac{\hat{R}}{4 \times 10^{-27}} \right), \tag{5.12}
\end{aligned}$$

where $\hat{\mathcal{O}}_\chi^\pm \equiv \hat{\mathcal{O}}_\chi^1 \pm i\hat{\mathcal{O}}_\chi^2$, and

$$\begin{aligned}
\hat{R} &= m_e^2 \int \frac{d^3 q}{2\pi q} \text{tr}(\hat{\rho}_\chi \hat{\mathcal{O}}_\chi^+ \hat{\mathcal{O}}_\chi^{+-}) \delta\left(\cos\theta - \frac{q}{2m_\chi v_\chi} - \frac{\omega}{v_\chi q}\right) \\
&= \begin{cases} \frac{2g_\chi^2 g_e^2 (1+\langle c^2 \rangle)}{\Lambda_\chi^2} (q_{\text{max}}^2 - q_{\text{min}}^2) & \text{(magnetic dipole),} \\ \frac{g_\chi^2 g_e^2 (1+\langle c^2 \rangle)}{4\Lambda_\chi^4} (q_{\text{max}}^4 - q_{\text{min}}^4) & \text{(anapole),} \\ g_\chi^2 g_e^2 \langle s^2 \rangle \log(q_{\text{max}}/q_{\text{min}}) & \text{(pseudo-mediated).} \end{cases} \tag{5.13}
\end{aligned}$$

Here θ is the angle between \mathbf{q} and \mathbf{v}_χ , $\langle c^2 \rangle$ and $\langle s^2 \rangle$ are properly averaged values of cosine and sine squared of the angle between \mathbf{q} and the ground state spin direction over accessible scattering kinematics, $q_{\text{max}} \simeq 2m_\chi v_\chi$, and q_{min} is the magnon momentum for which $\omega_{\mathbf{q}} = \omega_{\text{min}}$. The q dependence in Eq. (5.13) is indicative of dipole-dipole, quadrupole-dipole and charge-dipole type interactions, respectively, for the three DM models.

The projected reach for this $n = 1$ Heisenberg ferromagnet is shown by the dashed curves in Fig. 5.1 in the $\omega_{\text{min}} = 1 \text{ meV}$ case, with $\langle c^2 \rangle$ set to $1/3$. We see that the full YIG results are almost exactly reproduced for $0.02 \text{ MeV} \lesssim m_\chi \lesssim 0.1 \text{ MeV}$. For $m_\chi \lesssim 0.02 \text{ MeV}$, the gapless branch becomes kinematically inaccessible, and the reach is dominated by the gapped magnons. For $m_\chi \gtrsim 0.1 \text{ MeV}$, YIG beats the $n = 1$ ferromagnet due to contributions from the gapped magnons, which are no longer suppressed as the typical momentum transfer approaches (and goes beyond) the boundaries of the 1BZ. For higher ω_{min} , effective theory predictions (not shown) are off because the lowest-energy magnon modes on the gapless branch become inaccessible.

5.5 Discussion

While we have chosen three specific DM models for illustration, we note that there are other scenarios with SD interactions that can be probed via magnon excitation. Examples include

models with a spin-1 mediator coupling to $\bar{e}\gamma^\mu\gamma^5e$ or nonminimally to the electron. Generally, \hat{O}_χ^α is the mediator propagator multiplied by a function that is at least linear in q , so the rate is at least logarithmic (as in the pseudo-mediated model). Given the strong astrophysical and cosmological constraints on light DM and mediator scenarios [10, 135, 182], magnon excitations are most relevant for probing subcomponents of DM with SD interactions, if not mediated by a dark photon.

Beyond scattering, a magnon signal can also arise from absorption of bosonic DM. A prime example is an axion a interacting via $(\partial_\mu a)\bar{e}\gamma^\mu\gamma^5e \rightarrow \nabla a \cdot \mathbf{S}_e$. However, Heisenberg-type materials with 3d electrons, such as YIG, have very limited sensitivity to DM absorption, because gapped modes with $k \simeq 0$, which match the kinematics, have strongly suppressed matrix elements as explained above. Here we identify three possible solutions to pursue in future work. First, in materials with nondegenerate Landé g -factors (due to different orbital angular momentum admixtures in the effective spins), magnetic atoms/ions within the same unit cell can respond differently in the $q \rightarrow 0$ limit, allowing excitation of gapped magnons. Second, anisotropic spin-spin interactions can lift the otherwise gapless Goldstone modes, enabling them to match DM absorption kinematics. Finally, the gapless modes can also be lifted by an external magnetic field, which can be tuned to scan the DM mass, as considered in Refs. [93, 164, 266] (see also Ref. [221]) in the context of axion absorption.

5.6 Conclusions

Collective excitations in condensed matter systems offer a novel detection path for light DM because of favorable kinematics. Given our ignorance of how the DM may interact with SM particles, it is important to explore different types of collective excitations in various materials in order to cover the broadest range of possibilities. In this *Letter*, we proposed using magnon excitations to detect DM in the 10 keV-10 MeV mass range that couples to the electron spin. This complements previous proposals of detecting spin-independent DM interactions via phonon excitation. For a concrete demonstration of the discovery potential, we calculated the rate for three benchmark DM models, and found that currently unconstrained parameter space can be probed via magnon excitation in a YIG target.

To move forward and realize our proposed DM detection concept, a pressing question is an experimental scheme to detect magnon quanta. One possibility is calorimetric readout similar to phonon detection [28, 64], in which case magnon propagation and decay, as well as magnon-TES/MKID interactions, need to be understood. Besides, recent research in quantum magnonics has taken on the challenge of resolving single magnons [273, 274], and may find application in DM detection. We plan to investigate these possibilities in future

work.

DETECTABILITY OF AXION DARK MATTER WITH PHONON POLARITONS AND MAGNONS

6.1 Introduction

The QCD axion [98, 99, 275, 276] remains one of the best-motivated and predictive models of dark matter (DM) [145–147]. The search for the axion has a decades long history, and is still ongoing. At the moment, only the Axion Dark Matter Experiment (ADMX) [151, 152] has sensitivity to the QCD axion in a narrow mass range around 2-3 μeV . The HAYSTAC [153] and ORGAN [154] experiments are seeking to extend these results to higher frequencies. The ABRACADABRA [155] and CASPER [156] experiments have also recently achieved their first limits for very light masses (though with sensitivity still far above that needed to reach the QCD axion). The CERN Axion Solar Telescope (CAST) [157] is searching for axions emitted by the Sun, and can constrain the QCD axion for masses above $\sim 1 \text{ eV}$. Many more experiments plan to join this search. These include the MAgnetized Disk and Mirror Axion eXperiment (MADMAX) [158, 159], which uses a layered dielectric in an external magnetic field, and the QUaere AXion (QUAX) experiment [91–93], which searches for axion-induced classical spin waves inside a magnetic target. See also Ref. [160–169] for recent axion DM search proposals.

The QCD axion mass window $m_a \sim \mathcal{O}(1-100) \text{ meV}$ remains, however, unconstrained.¹ The current best limits are provided by CAST, but this could be outperformed in the future by fourth generation helioscopes like IAXO [291], and dish antennas [292] or multilayer films [293] (both of which are related to MADMAX in concept but can reach higher axion masses). These are limited by current single photon detection technology, which is rapidly improving. Recently the use of axionic topological antiferromagnets has been proposed to detect axions in this region [221], although such materials have not been fabricated yet in the lab, and even then, this proposal is limited to $m_a \lesssim 10 \text{ meV}$.

Collective excitations, such as phonons and magnons, have resonance energies in the $\mathcal{O}(1-100) \text{ meV}$ range, as shown in Fig. 6.1. They have been proposed as an excellent way to detect light dark matter through scattering (if the dark matter is heavier than a keV) or absorption (if the dark matter is in the $\mathcal{O}(1-100) \text{ meV}$ mass window) [6–8, 28, 39, 41, 64, 184–187, 245].

¹There are many well-motivated models that accommodate a QCD axion in this mass window — see e.g., Refs. [149, 277–290].

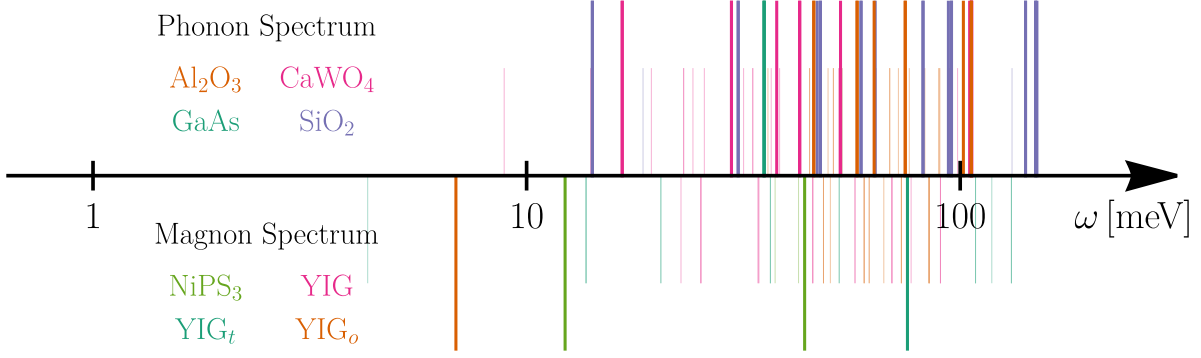


Figure 6.1: Spectra of gapped phonon polaritons and magnons at zero momentum for several representative targets considered in this work. These collective excitations have typical energies of $\mathcal{O}(1-100)$ meV, and can be utilized to search for axion DM in the mass window $m_a \sim \mathcal{O}(1-100)$ meV. Longer lines with darker colors correspond to the resonances in Figs. 6.3, 6.4 and 6.5, while the shorter ones with lighter colors represent modes with suppressed couplings to axion DM due to selection rules.

While previous work has shown the reach to dark photon absorption, an open question is whether phonon and magnon excitations possess a sufficiently strong coupling to reach the QCD axion.

In this paper, we investigate axion absorption onto phonons and magnons, and demonstrate the potential of these processes to cover the $m_a \sim \mathcal{O}(1-100)$ meV QCD axion mass window. The particle-level axion interactions of interest are:

$$\mathcal{L} = -\frac{1}{4}g_{a\gamma\gamma}a F_{\mu\nu}\tilde{F}^{\mu\nu} + \sum_{f=e,p,n} \frac{g_{aff}}{2m_f}(\partial_\mu a)(\bar{f}\gamma^\mu\gamma^5 f) - \sum_{f=p,n} \frac{g_{af\gamma}}{4}a F_{\mu\nu}(\bar{f}i\sigma^{\mu\nu}\gamma^5 f), \quad (6.1)$$

where the three terms are the axion's electromagnetic, wind and electric dipole moment (EDM) couplings, respectively. In the nonrelativistic limit, the effective interaction Hamiltonian is²

$$\delta\hat{H} = -g_{a\gamma\gamma} \int d^3x a \mathbf{E} \cdot \mathbf{B} - \sum_{f=e,p,n} \frac{g_{aff}}{m_f} \nabla a \cdot \mathbf{s}_f - \sum_{f=p,n} g_{af\gamma} a \mathbf{E} \cdot \mathbf{s}_f. \quad (6.2)$$

These couplings can be further matched onto axion couplings to low energy degrees of freedom in a crystal. In particular, phonon excitation results from couplings to atomic displacements $\mathbf{u}_{lj} = \mathbf{x}_{lj} - \mathbf{x}_{lj}^0$, where l labels the primitive cell, j labels the atoms within each cell, and \mathbf{x}_{lj}^0 are the equilibrium positions, while magnons can be excited via couplings to the

²The coupling to the axial current also generates a term proportional to $m_a \mathbf{s}_f \cdot \mathbf{v}_f$, we neglect this term since its coupling to collective spin excitations is suppressed compared to the one generated by the $\nabla a \cdot \mathbf{s}_f$ term.

(effective) spins of magnetic ions \mathbf{S}_{lj} . An axion field oscillating with frequency $\omega = m_a$ and wavenumber $\mathbf{p} = m_a \mathbf{v}_a$ is represented by

$$a(\mathbf{x}, t) = a_0 \cos(\mathbf{p} \cdot \mathbf{x} - \omega t), \quad (6.3)$$

where the field amplitude is related to the energy density via $\rho_a = m_a^2 a_0^2 / 2$. The resulting effective Hamiltonian relevant for phonon and magnon production takes the general form

$$\delta \hat{H} = \delta \hat{H}_0 e^{-i\omega t} + \text{c.c.}, \quad \delta \hat{H}_0 = \begin{cases} \sum_{lj} e^{i\mathbf{p} \cdot \mathbf{x}_{lj}^0} \mathbf{f}_j \cdot \mathbf{u}_{lj} & \Rightarrow \text{phonons}, \\ \sum_{lj} e^{i\mathbf{p} \cdot \mathbf{x}_{lj}^0} \mathbf{f}_j \cdot \mathbf{S}_{lj} & \Rightarrow \text{magnons}, \end{cases} \quad (6.4)$$

with the effective couplings, \mathbf{f}_j , proportional to a_0 and the relevant axion coupling. While our focus here is axion DM, the same equations hold for general field-like DM candidates.

In Sec. 6.2, we derive rate formulae for single phonon and magnon excitations starting from the general form of couplings in Eq. (6.4).³ In the case of phonon excitation, the true energy eigenmodes in a polar crystal, at the low momentum transfers relevant for dark matter absorption, are phonon polaritons due to the mixing between the photon and phonons. We take this mixing into account while still often referring to the gapped polaritons as phonons since their phonon components are much larger. The final results for phonon and magnon excitation rates are Eqs. (6.18) and (6.27). Depending on the couplings \mathbf{f}_j and symmetries of the target system, it often happens that excitation of some of the phonon or magnon modes is suppressed, reducing the sensitivity to DM. We discuss this problem and possible ways to alleviate it in Sec. 6.3.

Then it remains to determine the effective couplings \mathbf{f}_j in terms of particle physics parameters – $g_{a\gamma\gamma}$, g_{aff} , etc. – in the case of axion DM. The effective couplings can receive multiple contributions, some of which rely on the presence of an external field. We discuss the various possibilities for axion-induced single phonon or magnon production in Sec. 6.4. Among them, two are particularly promising: the coupling of the gradient of the axion field to the electron spin, g_{aee} , allows for magnon excitation, while the axion-induced electric field in the presence of an external magnetic field, due to the axion-photon coupling $g_{a\gamma\gamma}$, can excite phonon polaritons. These processes are summarized in Table 6.1. It is in fact not difficult to roughly estimate the rates based on simple considerations about the physical quantities that should enter each process. We show these estimates in the last column of the table, which will allow us to quickly assess the projected sensitivity in Eqs. (6.40) and (6.36).

³Previous calculations of DM absorption rates often rely on rescaling of optical data. While this is in principle possible for some of the processes discussed in this paper, the full set of data needed to capture general anisotropic target responses are hard to come by. Therefore, we take a first-principle approach and explicitly compute the DM absorption rates starting from the Hamiltonian.

We present our full numerical results for the projected reach via these processes in Sec. 6.5. We find that, consistent with the parametric estimates, when the axion mass is well-matched to phonon polariton or magnon resonances in the target material, the QCD axion can be easily within reach. The sensitivity is inherently narrow-band for any specific target material, with the axion masses covered limited by the resonance widths. However, combining the reach of a set of judiciously chosen materials with different phonon and magnon frequencies can offer a broader coverage. Finally, we conclude in Sec. 6.6 and discuss future interdisciplinary work needed to better understand and realize the potential of the ideas presented in this work.

Process	Fundamental interaction	\mathbf{f}_j in Eq. (6.4)	Rate formula	Rate estimate (on resonance)
Axion + B field \rightarrow phonon	$a\mathbf{E} \cdot \mathbf{B}$	$\frac{1}{\sqrt{2}} g_{a\gamma\gamma} \frac{e\sqrt{\rho_a}}{m_a} \mathbf{B} \cdot \boldsymbol{\varepsilon}_\infty^{-1} \cdot \mathbf{Z}_j^*$	Eq. (6.18)	$\frac{g_{a\gamma\gamma}^2 \rho_a}{m_a^3} \frac{Z^{*2} e^2 B^2}{\varepsilon_\infty^2 m_{\text{ion}}^2 \gamma}$ (Eq. (6.40))
Axion \rightarrow magnon	$\nabla a \cdot \mathbf{s}_e$	$-\frac{i}{\sqrt{2}} g_{aee} (g_j - 1) \frac{\sqrt{\rho_a}}{m_e} \mathbf{v}_a$	Eq. (6.27)	$\frac{g_{aee}^2 \rho_a v_a^2}{m_e^2} \frac{n_a}{\rho_T \gamma}$ (Eq. (6.36))

Table 6.1: Summary of the potentially detectable channels identified in Sec. 6.4. The axion field a is given by Eq. (6.3), ρ_a is its energy density, and \mathbf{v}_a is its velocity. The axion couplings $g_{a\gamma\gamma}$ and g_{aee} are defined in Eqs. (6.1) and (6.2), and given by Eqs. (6.31) and (6.32) for the QCD axion. ε_∞ is the high-frequency dielectric constant due to electronic screening, \mathbf{Z}_j^* is the Born effective charge tensor of the ion, g_j is the Landé g -factor, ρ_T is the target's mass density, and γ is the resonance width.

6.2 General Formalism For Absorption Rate Calculations

In this section, we adapt the DM scattering calculations in Refs. [7, 8] to the present case of bosonic DM absorption. Unlike the scattering case, light bosonic DM (denoted by a in what follows) should be treated as a classical field. Within the coherence time $\tau_a = (m_a v_a^2)^{-1} \sim 10^{-7} \text{ s}$ ($10 \text{ meV}/m_a$), its effect can be modeled as a harmonic perturbation on the target system as in Eq. (6.4). In this work, we focus on configurations with no external AC electromagnetic fields, so that $\omega = m_a$. An AC external field with frequency ω_e would generate perturbations with $\omega = |m_a \pm \omega_e|$, for which the calculations in this section also apply.

Phonons and magnons arise from quantizing crystal lattice degrees of freedom, displacements \mathbf{u}_{lj} and effective spins \mathbf{S}_{lj} respectively, which DM can couple to, as mentioned in the Introduction — see Eq. (6.4). The effective couplings \mathbf{f}_j depend on the atom/ion types, hence the subscript j . We will keep \mathbf{f}_j general in this section, and derive their expressions for the case of axion DM in Sec. 6.4.

We assume the target system is prepared in its ground state $|0\rangle$ at zero temperature. The transition rate from standard time-dependent perturbation theory reads

$$\Gamma = \sum_f |\langle f | \delta \hat{H}_0 | 0 \rangle|^2 2\pi \delta(\omega - \omega_f). \quad (6.5)$$

Strictly speaking, since phonons and magnons are unstable particles, the sum over final states f should include multi-particle states resulting from their decays. In practice, however, when ω is close to a phonon/magnon resonance, we can simply smear the delta function to the Breit-Wigner function and sum over single phonon/magnon states:⁴

$$\Gamma = \sum_{\nu, \mathbf{k}} |\langle \nu, \mathbf{k} | \delta \hat{H}_0 | 0 \rangle|^2 \frac{4\omega \omega_{\nu, \mathbf{k}} \gamma_{\nu, \mathbf{k}}}{(\omega^2 - \omega_{\nu, \mathbf{k}}^2)^2 + (\omega \gamma_{\nu, \mathbf{k}})^2}, \quad (6.6)$$

where $|\nu, \mathbf{k}\rangle$ is the single phonon/magnon state on branch ν with momentum \mathbf{k} , and $\gamma_{\nu, \mathbf{k}}$ is its decay width. Away from a resonance, the lineshape deviates from Breit-Wigner, and depends on the details of phonon/magnon interactions. Since we are interested in sub-eV DM candidates, the momentum deposited is limited to $m_a v_a \lesssim \text{meV}$ — the DM field drives phonon/magnon modes close to the center of the first Brillouin zone (1BZ). Finally, averaging over the DM velocity distribution $f(\mathbf{v})$, we obtain the expected total rate:

$$\langle \Gamma \rangle = \int d^3v f(\mathbf{v}) \Gamma(\mathbf{v}). \quad (6.7)$$

⁴In deriving Eq. (6.6) we have assumed the observation time $t \gtrsim \gamma_{\nu, \mathbf{k}}^{-1}$, for which the transition rate Γ is time-independent. We also assume that the line width of the axion, $\Delta\omega \sim m_a v_a^2 \sim 10^{-8} \text{ eV}$ ($m_a/10 \text{ meV}$) is smaller than excitation linewidth, $\gamma_{\nu, \mathbf{k}}$, which is true as long as $\gamma_{\nu, \mathbf{k}}$ is greater than $\sim 10^{-6}$ times the resonance frequency.

We take $f(\mathbf{v})$ to be a boosted Maxwell-Boltzmann distribution,

$$f_x^{\text{MB}}(\mathbf{v}) = \frac{1}{N_0} e^{-(\mathbf{v}+\mathbf{v}_e)^2/v_0^2} \Theta(v_{\text{esc}} - |\mathbf{v} + \mathbf{v}_e|), \quad (6.8)$$

$$N_0 = \pi^{3/2} v_0^2 \left[v_0 \operatorname{erf}(v_{\text{esc}}/v_0) - \frac{2v_{\text{esc}}}{\sqrt{\pi}} \exp(-v_{\text{esc}}^2/v_0^2) \right]. \quad (6.9)$$

with parameters $v_0 = 230$ km/s, $v_e = 240$ km/s, $v_{\text{esc}} = 600$ km/s. The local axion DM density ρ_a , which enters the effective couplings \mathbf{f}_j (see Table 6.1), is assumed to be 0.3 GeV/cm³.

In the following subsections, we derive the rate formulae for single phonon and magnon excitations, respectively. For easy comparison, we present both derivations in as similar ways as possible.

Phonon excitations

We begin by calculating the absorption rate from couplings to phonons. The target Hamiltonian results from expanding the potential energy of the crystal around equilibrium positions of atoms:

$$\hat{H} = \sum_{lj} \frac{\mathbf{p}_{lj}^2}{2m_j} + \frac{1}{2} \sum_{l'j'j''} \mathbf{u}_{lj} \cdot \mathbf{V}_{l'j'j''} \cdot \mathbf{u}_{l'j''} + \mathcal{O}(\mathbf{u}^3), \quad (6.10)$$

where $\mathbf{p}_{lj} = m_j \dot{\mathbf{u}}_{lj}$, and the force constant matrices, $\mathbf{V}_{l'j'j''}$, can be calculated from *ab initio* density functional theory (DFT) methods [294–297].

To diagonalize the Hamiltonian, we expand the atomic displacements and their conjugate momenta in terms of canonical phonon modes:

$$\mathbf{u}_{lj} = \sum_{\nu=1}^{3n} \sum_{\mathbf{k}} \frac{1}{\sqrt{2Nm_j\omega_{\nu,\mathbf{k}}}} (\hat{a}_{\nu,\mathbf{k}} + \hat{a}_{\nu,-\mathbf{k}}^\dagger) e^{i\mathbf{k}\cdot\mathbf{x}_{lj}^0} \boldsymbol{\epsilon}_{\nu,\mathbf{k},j}, \quad (6.11)$$

$$\mathbf{p}_{lj} = i \sum_{\nu=1}^{3n} \sum_{\mathbf{k}} \sqrt{\frac{m_j\omega_{\nu,\mathbf{k}}}{2N}} (\hat{a}_{\nu,-\mathbf{k}}^\dagger - \hat{a}_{\nu,\mathbf{k}}) e^{i\mathbf{k}\cdot\mathbf{x}_{lj}^0} \boldsymbol{\epsilon}_{\nu,\mathbf{k},j}, \quad (6.12)$$

where ν labels the phonon branch (of which there are $3n$ for a three-dimensional crystal with n atoms per primitive cell), \mathbf{k} labels the phonon momentum within the 1BZ, N is the total number of primitive cells, m_j is the mass of the j th atom in the primitive cell, and $\hat{a}_{\nu,\mathbf{k}}^\dagger, \hat{a}_{\nu,\mathbf{k}}$ are the phonon creation and annihilation operators. The phonon energies $\omega_{\nu,\mathbf{k}}$ and eigenvectors $\boldsymbol{\epsilon}_{\nu,\mathbf{k},j} = \boldsymbol{\epsilon}_{\nu,-\mathbf{k},j}^*$ are obtained by solving the eigensystem of $\mathbf{V}_{l'j'j''}$, for which we use the open-source code **phonopy** [50]. The target Hamiltonian then reads

$$\hat{H} = \sum_{\nu=1}^{3n} \sum_{\mathbf{k}} \omega_{\nu,\mathbf{k}} \hat{a}_{\nu,\mathbf{k}}^\dagger \hat{a}_{\nu,\mathbf{k}} + \mathcal{O}(\hat{a}^3). \quad (6.13)$$

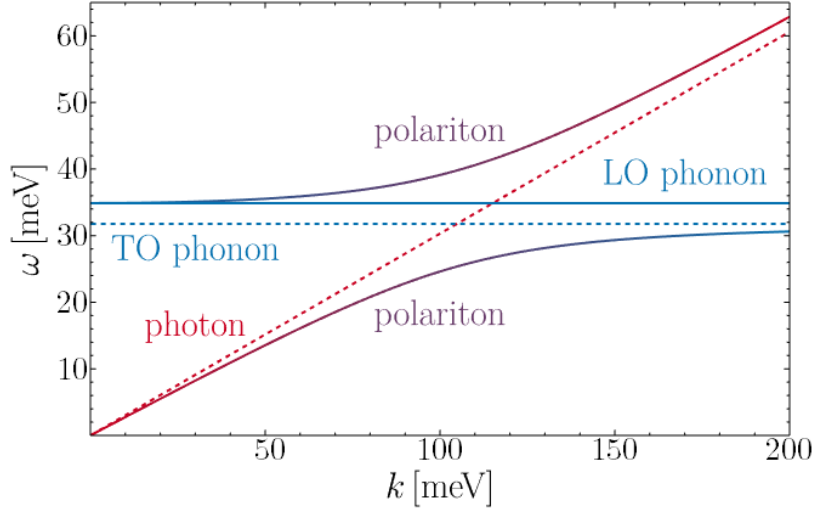


Figure 6.2: Dispersion of phonon polaritons in GaAs near the center of the 1BZ, $k \sim \omega$. The mixing between the photon and TO phonons is maximal at $\omega \sim k$. At $k \ll \omega$, the TO phonon-like modes are degenerate with the LO phonon mode (blue line), while at $\omega \gg k$ they approach their unperturbed value (dotted blue line), and an LO-TO splitting is present.

For a polar crystal, since the ions are electrically charged, some of the phonon modes mix with the photon. This mixing has a negligible impact in most of the 1BZ where $k \gg \omega$, and in particular does not affect the DM scattering calculations in Refs. [6, 7, 28, 64]. However, near the center of the 1BZ where $k \lesssim \omega$ – relevant for DM absorption – the photon-phonon mixing modifies the dispersions to avoid a level crossing. The true energy eigenstates are linear combinations of photon and phonon modes, known as phonon polaritons. This is shown in Fig. 6.2 for gallium arsenide (GaAs) as a simple example. For an isotropic diatomic crystal like GaAs, the two degenerate, (mostly) transverse optical (TO) phonon modes at $k \gg \omega$ continue to photon-like modes at $k \ll \omega$, and vice versa. The phonon-like modes at $k \ll \omega$ do not have the same energies as away from the polariton regime: the TO phonon-like modes become degenerate with the longitudinal optical (LO) phonon mode at ω_{LO} as $k \rightarrow 0$, whereas there is an LO-TO splitting, $\omega_{\text{TO}} \neq \omega_{\text{LO}}$, at $k \gg \omega$. For more complex crystals like sapphire (Al_2O_3), quartz (SiO_2) and calcium tungstate (CaWO_4), the mixing involves more phonon modes, and in general shift all their energies with respect to the eigenvalues $\omega_{\nu, k}$ computed from diagonalizing just the lattice Hamiltonian.

To account for the photon-phonon mixing, we write the total Hamiltonian of electromagnetic fields coupling to the ions in the target crystal, and diagonalize its quadratic part via a Bogoliubov transformation. We explain this procedure in detail in Appendix G. The resulting

diagonal Hamiltonian is

$$\hat{H} = \sum_{\nu=1}^{3n+2} \sum_{\mathbf{k}} \omega'_{\nu,\mathbf{k}} \hat{a}'_{\nu,\mathbf{k}} \hat{a}'_{\nu,\mathbf{k}} + \mathcal{O}(\hat{a}'^3). \quad (6.14)$$

At each \mathbf{k} , there are $(3n + 2)$ modes, created (annihilated) by $\hat{a}'_{\nu,\mathbf{k}}$ ($\hat{a}'_{\nu,\mathbf{k}}$), which are linear combinations of $3n$ phonon modes and 2 photon polarizations. Among them, 5 are gapless at $k = 0$, including 3 acoustic phonons and 2 photon-like polaritons. The number of gapped modes, $3n - 3$, is the same as in the phonon-only theory, but their energy spectrum is shifted, $\{\omega'_{\nu=(6,\dots,3n+2),\mathbf{k}}\} \neq \{\omega_{\nu=(4,\dots,3n),\mathbf{k}}\}$. The original phonon modes are linear combinations of the phonon polariton eigenmodes:

$$\hat{a}_{\nu,\mathbf{k}} = \sum_{\nu'=1}^{3n+2} (\mathbb{U}_{\nu\nu',\mathbf{k}} \hat{a}'_{\nu',\mathbf{k}} + \mathbb{V}_{\nu\nu',\mathbf{k}} \hat{a}'_{\nu',-\mathbf{k}}). \quad (6.15)$$

For DM coupling to the atomic displacements \mathbf{u}_{lj} , the perturbing potential is given by Eq. (6.4) and therefore

$$\begin{aligned} \delta \hat{H}_0 |0\rangle &= \sum_{lj} \sum_{\nu=1}^{3n} \sum_{\mathbf{k}} e^{i(\mathbf{p}-\mathbf{k})\cdot\mathbf{x}_{lj}^0} \frac{1}{\sqrt{2Nm_j\omega_{\nu,\mathbf{k}}}} \mathbf{f}_j \cdot \boldsymbol{\epsilon}_{\nu,\mathbf{k},j}^* (\hat{a}_{\nu,-\mathbf{k}} + \hat{a}'_{\nu,\mathbf{k}}) |0\rangle \\ &= \sqrt{\frac{N}{2}} \sum_{\nu=1}^{3n} \sum_j \frac{1}{\sqrt{m_j\omega_{\nu,\mathbf{p}}}} \mathbf{f}_j \cdot \boldsymbol{\epsilon}_{\nu,\mathbf{p},j}^* (\hat{a}_{\nu,-\mathbf{p}} + \hat{a}'_{\nu,\mathbf{p}}) |0\rangle \\ &= \sqrt{\frac{N}{2}} \sum_{\nu=1}^{3n} \sum_{\nu'=1}^{3n+2} \sum_j \frac{1}{\sqrt{m_j\omega_{\nu,\mathbf{p}}}} \mathbf{f}_j \cdot \boldsymbol{\epsilon}_{\nu,\mathbf{p},j}^* (\mathbb{U}_{\nu\nu',\mathbf{p}}^* + \mathbb{V}_{\nu\nu',-\mathbf{p}}) |\nu',\mathbf{p}\rangle, \end{aligned} \quad (6.16)$$

where $|\nu',\mathbf{p}\rangle = \hat{a}'_{\nu',\mathbf{p}} |0\rangle$. To arrive at the second equation, we have used the identity $\sum_l e^{i(\mathbf{p}-\mathbf{k})\cdot\mathbf{x}_{lj}^0} = N\delta_{\mathbf{k},\mathbf{p}}$ (for $\mathbf{k}, \mathbf{p} \in 1\text{BZ}$). It follows that

$$\langle \nu, \mathbf{k} | \delta \hat{H}_0 |0\rangle = \delta_{\mathbf{k},\mathbf{p}} \sqrt{\frac{N}{2}} \sum_{\nu'=1}^{3n} \sum_j \frac{1}{\sqrt{m_j\omega_{\nu',\mathbf{p}}}} \mathbf{f}_j \cdot \boldsymbol{\epsilon}_{\nu',\mathbf{p},j}^* (\mathbb{U}_{\nu'\nu,\mathbf{p}}^* + \mathbb{V}_{\nu'\nu,-\mathbf{p}}), \quad (6.17)$$

where we have swapped the dummy indices ν and ν' . The DM absorption rate per unit target mass, $R = \langle \Gamma \rangle / (Nm_{\text{cell}})$, is therefore

$$\begin{aligned} R &= \frac{2\omega}{m_{\text{cell}}} \int d^3v_a f(\mathbf{v}_a) \\ &\times \sum_{\nu=6}^{3n+2} \frac{\omega'_{\nu,\mathbf{p}} \gamma_{\nu,\mathbf{p}}}{(\omega^2 - \omega'_{\nu,\mathbf{p}})^2 + (\omega \gamma_{\nu,\mathbf{p}})^2} \left| \sum_j \sum_{\nu'=1}^{3n} \frac{1}{\sqrt{m_j\omega_{\nu',\mathbf{p}}}} \mathbf{f}_j \cdot \boldsymbol{\epsilon}_{\nu',\mathbf{p},j}^* (\mathbb{U}_{\nu'\nu,\mathbf{p}}^* + \mathbb{V}_{\nu'\nu,-\mathbf{p}}) \right|^2, \end{aligned} \quad (6.18)$$

where $\omega = m_a$, $\mathbf{p} = m_a \mathbf{v}_a$, and m_{cell} is the total mass of the atoms in a primitive cell. For our numerical calculations, we use the `phonopy` code [50] to process DFT output [6, 7, 28]

to obtain the unmixed phonon energies and eigenvectors $\omega_{\nu',\mathbf{p}}$, $\boldsymbol{\epsilon}_{\nu',\mathbf{p},j}$ as mentioned above, and then compute the polariton-corrected energy eigenvalues $\omega'_{\nu,\mathbf{p}}$ and mixing matrices \mathbb{U} , \mathbb{V} via the algorithm of Refs. [268, 298]. We relegate the technical details to Appendix G, and review the diagonalization algorithm [268, 298] in Appendix I.

Magnon excitations

We now move to the case of magnons. The target Hamiltonian is a spin lattice model, with the following general form:

$$\hat{H} = \sum_{ll'} \mathbf{S}_{lj} \cdot \mathbf{J}_{ll'} \cdot \mathbf{S}_{l'j'} + \mu_B \mathbf{B} \cdot \sum_{lj} g_j \mathbf{S}_{lj}, \quad (6.19)$$

where l , l' label the magnetic unit cells and j , j' the magnetic ions inside the unit cell, $\mu_B = \frac{e}{2m_e}$ is the Bohr magneton, \mathbf{B} is an external uniform magnetic field, and g_j are the magnetic ions' Landé g -factors. In the simplest case of the Heisenberg model, $\mathbf{J}_{ll'} \propto \mathbf{1}$ for pairs of lj and $l'j'$ on (nearest, next-to-nearest, etc.) neighboring sites. One material which is well described by this simple model is yttrium ion garnet (YIG) [264, 265], which has already been considered for DM detection [8, 32, 91–93, 164]. However, as we will see below, materials with spin-spin interactions beyond the simplest Heisenberg type can be useful for enhancing DM-magnon couplings.

The spin-spin interactions in Eq. (6.19) can result in a ground state with magnetic order. Here we focus on the simplest case of commensurate magnetic dipole orders, for which a rotation on each sublattice can take \mathbf{S}_{lj} to a local coordinate system where each spin points in the $+\hat{z}$ direction:

$$\mathbf{S}_{lj} = \mathbf{R}_j \cdot \mathbf{S}'_{lj}, \quad \langle \mathbf{S}'_{lj} \rangle = (0, 0, S_j). \quad (6.20)$$

YIG and many other magnetic insulators have commensurate magnetic order. The calculation can be easily generalized to single- Q incommensurate orders, as we discuss in Appendix H.

For a magnetically ordered system, the lowest energy excitations are magnons. To obtain the canonical magnon modes, we first apply the Holstein-Primakoff transformation to write the Hamiltonian in terms of bosonic creation and annihilation operators:

$$S_{lj}^{'+} = (2S_j - \hat{a}_{lj}^\dagger \hat{a}_{lj})^{1/2} \hat{a}_{lj}, \quad S_{lj}^{\prime-} = \hat{a}_{lj}^\dagger (2S_j - \hat{a}_{lj}^\dagger \hat{a}_{lj})^{1/2}, \quad S_{lj}^{\prime z} = S_j - \hat{a}_{lj}^\dagger \hat{a}_{lj}, \quad (6.21)$$

where $S_{lj}^{\prime\pm} = S_{lj}^{\prime x} \pm i S_{lj}^{\prime y}$. The Holstein-Primakoff transformation ensures that the spin commutation relations $[S_{lj}^{\prime\alpha}, S_{l'j'}^{\prime\beta}] = \delta_{ll'} \delta_{jj'} i \epsilon^{\alpha\beta\gamma} S_{lj}^{\prime\gamma}$ are preserved when the usual canonical commutation relations $[\hat{a}_{lj}, \hat{a}_{l'j'}^\dagger] = \delta_{ll'} \delta_{jj'}$ are imposed. As in the phonon case, translation symmetry

instructs us to go to momentum space:

$$\hat{a}_{lj} = \frac{1}{\sqrt{N}} \sum_{\mathbf{k}} \hat{a}_{j,\mathbf{k}} e^{i\mathbf{k}\cdot\mathbf{x}_{lj}^0}, \quad (6.22)$$

where $\mathbf{k} \in 1\text{BZ}$. The quadratic Hamiltonian, whose detailed form can be found in Appendix H, only couples modes with the same momentum, i.e. $\hat{a}_{j,\mathbf{k}}$ and $\hat{a}'_{j',\mathbf{k}}, \hat{a}'_{j',-\mathbf{k}}$. A Bogoliubov transformation takes the quadratic Hamiltonian to the desired diagonal form:

$$\hat{H} = \sum_{\nu=1}^n \sum_{\mathbf{k}} \omega_{\nu,\mathbf{k}} \hat{a}'_{\nu,\mathbf{k}} \hat{a}'_{\nu,\mathbf{k}} + \mathcal{O}(\hat{a}'^3). \quad (6.23)$$

At each \mathbf{k} , there are n magnon modes with n the number of spins per magnetic unit cell. These energy eigenmodes are created (annihilated) by $\hat{a}'_{\nu,\mathbf{k}}$ ($\hat{a}'_{\nu,\mathbf{k}}$), which are related to the unprimed creation and annihilation operators by

$$\hat{a}_{j,\mathbf{k}} = \sum_{\nu=1}^n (\mathbb{U}_{j\nu,\mathbf{k}} \hat{a}'_{\nu,\mathbf{k}} + \mathbb{V}_{j\nu,\mathbf{k}} \hat{a}'_{\nu,-\mathbf{k}}). \quad (6.24)$$

For DM coupling to the effective spins \mathbf{S}_{lj} , the interaction is given by Eq. (6.4), and we find, in complete analogy with Eq. (6.16),

$$\begin{aligned} \delta\hat{H}_0|0\rangle &= \sum_{lj} \sum_{\mathbf{k}} e^{i(\mathbf{p}-\mathbf{k})\cdot\mathbf{x}_{lj}^0} \sqrt{\frac{S_j}{2N}} \mathbf{f}_j \cdot (\mathbf{r}_j^* \hat{a}_{j,-\mathbf{k}} + \mathbf{r}_j \hat{a}_{j,\mathbf{k}}^\dagger) |0\rangle \\ &= \delta_{\mathbf{k},\mathbf{p}} \sqrt{\frac{N}{2}} \sum_j \sqrt{S_j} \mathbf{f}_j \cdot (\mathbf{r}_j^* \hat{a}_{j,-\mathbf{k}} + \mathbf{r}_j \hat{a}_{j,\mathbf{k}}^\dagger) |0\rangle \\ &= \delta_{\mathbf{k},\mathbf{p}} \sqrt{\frac{N}{2}} \sum_{\nu=1}^n \sum_j \sqrt{S_j} \mathbf{f}_j \cdot (\mathbb{U}_{j\nu,\mathbf{p}}^* \mathbf{r}_j + \mathbb{V}_{j\nu,-\mathbf{p}} \mathbf{r}_j^*) |\nu, \mathbf{p}\rangle, \end{aligned} \quad (6.25)$$

where $\mathbf{r}_j \equiv (\mathbf{R}_j^{xx}, \mathbf{R}_j^{yx}, \mathbf{R}_j^{zx}) + i(\mathbf{R}_j^{xy}, \mathbf{R}_j^{yy}, \mathbf{R}_j^{zy})$, and $|\nu, \mathbf{p}\rangle = \hat{a}'_{\nu,\mathbf{p}}^\dagger |0\rangle$. Therefore,

$$\langle\nu, \mathbf{k}|\delta\hat{H}_0|0\rangle = \delta_{\mathbf{k},\mathbf{p}} \sqrt{\frac{N}{2}} \sum_{\nu=1}^n \sum_j \sqrt{S_j} \mathbf{f}_j \cdot (\mathbb{U}_{j\nu,\mathbf{p}}^* \mathbf{r}_j + \mathbb{V}_{j\nu,-\mathbf{p}} \mathbf{r}_j^*). \quad (6.26)$$

We can now obtain the DM absorption rate per unit target mass:

$$R = \frac{2\omega}{m_{\text{cell}}} \int d^3v_a f(\mathbf{v}_a) \sum_{\nu=n_0+1}^n \frac{\omega_{\nu,\mathbf{p}} \gamma_{\nu,\mathbf{p}}}{(\omega^2 - \omega_{\nu,\mathbf{p}}^2)^2 + (\omega \gamma_{\nu,\mathbf{p}})^2} \left| \sum_j \sqrt{S_j} \mathbf{f}_j \cdot (\mathbb{U}_{j\nu,\mathbf{p}}^* \mathbf{r}_j + \mathbb{V}_{j\nu,-\mathbf{p}} \mathbf{r}_j^*) \right|^2, \quad (6.27)$$

where n_0 is the number of gapless modes, which depends on the material (in particular, on the symmetry breaking pattern). Similarity to the phonon formula Eq. (6.18) is apparent. We again use the algorithm of Refs. [268, 298], reviewed in Appendix I, to solve the diagonalization problem to obtain the magnon energies $\omega_{\nu,\mathbf{p}}$ and mixing matrices \mathbb{U}, \mathbb{V} .

6.3 Selection Rules And Ways Around Them

Depending on the DM couplings \mathbf{f}_j , excitation rates for some of the phonon or magnon modes can be suppressed. In the context of DM scattering, it has been known that acoustic and optical phonons are sensitive to different types of DM couplings [6, 7]: if DM couples to the inequivalent atoms/ions with the same sign (different signs), the single phonon excitation rate is dominated by acoustic (optical) phonons, corresponding to in-phase (out-of-phase) oscillations of the atoms/ions.

The same considerations apply to absorption of DM, though here the gapless acoustic phonons are kinematically inaccessible, and therefore only gapped optical phonons can be excited. Thus, the rate is suppressed if all \mathbf{f}_j point in the same direction. As an extreme example, consider $\mathbf{f}_j = m_j \mathbf{f}$, with \mathbf{f} a constant vector. Up to the photon-phonon mixing (which mostly shifts the energy eigenvalues while leaving the factor $(U_{\nu'\nu, \mathbf{p}}^* + V_{\nu'\nu, -\mathbf{p}})$ close to $\delta_{\nu'\nu}$), the rate in Eq. (6.18) is proportional to $|\sum_j \sqrt{m_j} \mathbf{f} \cdot \boldsymbol{\epsilon}_{\nu, \mathbf{p}, j}^*|^2$. However, one can show from translation symmetry that $\sqrt{m_j} \mathbf{f}$ can be written as a linear combination of the polarization vectors $\boldsymbol{\epsilon}_{\nu, \mathbf{p} \rightarrow \mathbf{0}, j}$ with $\nu \in \text{acoustic}$ — see for example the explicit discussion of [201], consistent with the earlier results in Refs. [28, 64]. This is not surprising since gapless acoustic phonons are Goldstone modes of the broken translation symmetries. Thus, by the orthogonality of the phonon polarization vectors, optical phonons do not contribute to the rate in the $\mathbf{p} \rightarrow \mathbf{0}$ limit, and only higher order terms in the DM velocity can give a nonzero contribution. In the next section, in the context of axion DM, we will encounter both cases where the suppression due to the \mathbf{f}_j 's being aligned is present and absent, and will identify a process free of the suppression as a viable detection channel.

Additional selection rules may be present among the optical phonons. For example, sapphire has 27 optical phonon branches, but we find that near the 1BZ center, only 10 of them couple to the axion-induced electric field (in the presence of an external magnetic field). Furthermore, 8 of the 10 modes are degenerate in pairs, reducing the total number of distinct resonances to 6, as seen in Fig. 6.1. This is consistent with the well-known fact that, due to crystalline symmetries, sapphire has 6 infrared-active phonon modes [299–301]. Thus, despite the existence of many optical phonon modes, sapphire does not really offer broadband coverage of the axion mass. The same observation, that only a subset of gapped phonon modes couple to axion DM, also holds for the other targets considered: SiO₂ and CaWO₄ — see Fig. 6.1 (GaAs has only 3 optical phonon modes which are all degenerate and can couple to axion DM). To broaden the mass coverage, it is therefore necessary to run experiments with several target materials with distinct phonon frequencies.

There are also selection rules in the case of magnon excitations. It has been pointed out

that, assuming the absence of an external magnetic field, for a target system described by the Heisenberg model with quenched orbital angular momentum, such as YIG, only gapless magnons can be excited in the zero momentum transfer limit [8, 302]. To understand why, let us review and quantify the semiclassical argument given in Ref. [8]. Within a coherence length, the DM field couples to the spins as a uniform magnetic field, causing all the spins to precess. As a result, the rate of change in the Heisenberg interaction energy between any pair of spins is proportional to

$$\begin{aligned} \frac{d}{dt}(\mathbf{S}_{lj} \cdot \mathbf{S}_{\nu j'}) &= \frac{d\mathbf{S}_{lj}}{dt} \cdot \mathbf{S}_{\nu j'} + \mathbf{S}_{lj} \cdot \frac{d\mathbf{S}_{\nu j'}}{dt} = (\mathbf{f}_j \times \mathbf{S}_{lj}) \cdot \mathbf{S}_{\nu j'} + \mathbf{S}_{lj} \cdot (\mathbf{f}_{j'} \times \mathbf{S}_{\nu j'}) \\ &= (\mathbf{f}_j - \mathbf{f}_{j'}) \cdot (\mathbf{S}_{lj} \times \mathbf{S}_{\nu j'}), \end{aligned} \quad (6.28)$$

which vanishes for $\mathbf{f}_j = \mathbf{f}_{j'}$. Therefore, if the target system is described by the Heisenberg Hamiltonian, and all \mathbf{f}_j are equal (which is quite generic since they all originate from DM-electron spin coupling), the total energy cannot change in response to the DM field, and no gapped magnons can be excited. In other words, the DM field only couples to gapless magnons. In the case of scattering, the rate is not severely suppressed by this fact since the scattering kinematics allows access to finite momentum magnons, and hence sufficient energy deposition to be detected.

The situation is much worse in the case of absorption, because the momentum transfer is small in comparison to the DM mass due to its small velocity $v \sim 10^{-3}$. Therefore, gapless modes cannot be excited due to kinematics. As a result, the detection rate is severely suppressed by powers of DM velocity. We have checked this explicitly for several target materials. In what follows, let us expand on the two examples.

YIG ($\text{Y}_3\text{Fe}_5\text{O}_{12}$). The crystal primitive cell of YIG consists of four copies of $\text{Y}_3\text{Fe}_5\text{O}_{12}$. The magnetic ions are Fe^{3+} , each of which has spin 5/2. The magnetic unit cell coincides with the crystal primitive cell, and contains 20 magnetic ions. The spin Hamiltonian has antiferromagnetic Heisenberg interactions, which we include up to third nearest neighbors [265]. The ground state has ferrimagnetic order, where the 12 magnetic ions on the tetrahedral sites and the 8 magnetic ions on the octahedral sites have spins pointing in opposite directions [264], taken to be $\pm\hat{z}$. The symmetry breaking pattern is $\text{SO}(3) \rightarrow \text{SO}(2)$, and hence there are two broken generators S_x, S_y . There is however just one Goldstone mode (with quadratic dispersion) due to the nonvanishing expectation value of the commutator between the broken generators, $\langle [S_x, S_y] \rangle = (i/2)\langle S_z \rangle \neq 0$ [303–306]. Thus, among the 20 magnon branches, only one is gapless. We find that at zero momentum, the j sum in the rate formula Eq. (6.27), $\sum_j \sqrt{S_j} \cdot (\mathbb{U}_{j\nu, \mathbf{0}}^* \mathbf{r}_j + \mathbb{V}_{j\nu, \mathbf{0}} \mathbf{r}_j^*)$, indeed vanishes for all but the gapless mode ($\nu = 1$), confirming the argument above that the DM field only couples to gapless magnons.

Ba₃NbFe₃Si₂O₁₄. This is an example of materials with incommensurate magnetic order. We discuss the generalization needed in the rate calculation in Appendix H, with the final result given in Eq. (H.11). The magnetic unit cell contains three magnetic ions Fe³⁺ with spin 5/2, which form a triangle in the x - y plane. The crystal consists of layers stacked in the z direction. The antiferromagnetic Heisenberg interactions result in a frustrated order with 120° between the three spins that are nearest neighbors. Further, the chiral structure of inter-layer Heisenberg exchange couplings results in a rotation of the order in the z direction, with a wavevector that is irrational, $\mathbf{Q} \simeq 0.1429 (2\pi/c) \hat{z}$ where $c \simeq 5.32 \text{ \AA}$ is the inter-layer lattice spacing [268]. This is known as a single- Q incommensurate order. All 3 generators of SO(3) are broken while the ground state has zero total magnetization, so there are 3 Goldstone modes. These appear at $\mathbf{k} = \mathbf{0}, \pm\mathbf{Q}$, which are also the momenta near which the axion coupling is nonzero due to (generalized) momentum conservation. We find that at all three momenta, the j sum in the generalized rate formula Eq. (H.11) is nonzero only for $\nu = 1$, *i.e.* the gapless modes, again confirming the argument above that the DM field only couples to gapless magnons.

Nevertheless, there are several possibilities to alleviate the problem. First, one can consider targets involving additional, non-Heisenberg interactions. These additional terms can explicitly break the rotational symmetries, causing the otherwise gapless Goldstone modes to become gapped, and match the DM absorption kinematics. Concretely, we can identify two ways of implementing this idea:

- An *external magnetic field* $\mathbf{B} \neq 0$ can generate a gap for the lowest magnon branch equal to the Larmor frequency,

$$\omega_L = 2\mu_B B = 0.12 \text{ meV} \left(\frac{B}{\text{T}} \right), \quad (6.29)$$

assuming $g_j = 2$ for all j . The QUAX experiment [91–93] makes use of this to search for axion DM with $m_a \sim \mathcal{O}(0.1 \text{ meV})$, currently in the regime where the magnon number is large and a classical description can be used. Recently, a calculation to exploit this effect in the quantum regime, similar to the derivation in Sec. 6.2, was carried out in Ref. [32]. However, sensitivity of such a setup is limited to sub-meV DM by the achievable magnetic field strengths, and only the lowest magnon mode(s) can be excited.

- There are materials with *anisotropic interactions* where the number of gapless Goldstone modes is reduced. In Sec. 6.5, we consider a concrete example, NiPS₃, where the $\mathbf{J}_{ll'}$ matrices in the spin Hamiltonian Eq. (6.19) have unequal diagonal entries [307].

In this case, two gapped magnon modes at 12 meV and 44 meV can couple to axions. There are also materials with nonzero off-diagonal entries in $\mathbf{J}_{ll'jj'}$, arising from *e.g.* Dzyaloshinskii-Moriya interactions, that could be used to achieve the same result.

An orthogonal route to solve the problem is to use targets where the DM-spin couplings \mathbf{f}_j are nondegenerate.

- For materials with *nondegenerate Landé g -factors*, even a uniform magnetic field can drive the magnetic ions differently and excite gapped magnon modes; the same is true for a uniform DM field. The basic reason for this is the presence of spin-orbit couplings that break the degeneracy between the DM couplings to the magnetic ions' total effective spins. Concretely, the Landé g -factors are given by

$$g_j = \frac{3}{2} + \frac{1}{2} \frac{s_j(s_j + 1) - \ell_j(\ell_j + 1)}{S_j(S_j + 1)}, \quad (6.30)$$

where s_j and ℓ_j are respectively the spin and orbital angular momentum components of the total effective spin \mathbf{S}_{lj} . In the simplest and most common case of magnetic ions with quenched orbital angular momenta (*i.e.* $\ell_j \simeq 0$), we recover the usual result $g_j = 2$. Breaking the degeneracy requires the magnetic ions to have different spin and orbital angular momentum compositions. We demonstrate how this allows for axion couplings to gapped magnons in Sec. 6.5.

As in the case of phonons, there are usually additional selection rules due to crystalline symmetries. As a result, the strategies discussed above usually generate axion couplings to only a subset of gapped magnon modes – see Fig. 6.1. Therefore, multiple target materials which cover complementary ranges of magnon frequencies are desirable.

6.4 Axion Couplings And Detection Channels

The derivation and discussion in the previous two sections apply to general field-like DM candidates. We now specialize to the case of axion DM. Our goal in the present section is to identify the most promising detection channels involving phonon or magnon excitation via order-of-magnitude estimates. We then examine these processes quantitatively in the next section.

The axion couplings of interest are already given in Eqs. (6.1) and (6.2). For the QCD axion,

we have [43]

$$g_{a\gamma\gamma} = C_\gamma \frac{\alpha}{2\pi f_a} = 2.03 \times 10^{-12} C_\gamma \left(\frac{m_a}{10 \text{ meV}} \right) \text{GeV}^{-1}, \quad (6.31)$$

$$g_{aff} = C_f \frac{m_f}{f_a} = 1.18 \times 10^{-13} C_f \left(\frac{m_f}{\text{MeV}} \right) \left(\frac{m_a}{\text{meV}} \right), \quad (6.32)$$

$$\begin{aligned} g_{an\gamma} &= -g_{ap\gamma} = (3.7 \pm 1.5) \times 10^{-3} \frac{1}{f_a} \frac{1}{\text{GeV}} \\ &= (6.5 \pm 2.6) \times 10^{-12} \left(\frac{m_a}{10 \text{ meV}} \right) \text{GeV}^{-2}, \end{aligned} \quad (6.33)$$

where we have denoted $C_\gamma \equiv E/N - 1.92(4)$ with $E/N = 0$ (8/3) in the KSVZ (DFSZ) model. The axion-fermion couplings C_f are also model dependent. In particular, the axion-electron coupling is $C_e = \sin^2 \beta/3$ in the DFSZ model, where $\tan \beta$ is the ratio of the vacuum expectation values of the two Higgs doublets giving masses to the up and down-type quarks. In the KSVZ model, on the other hand, C_e is $\mathcal{O}(\alpha^2)$ suppressed.

In the following subsections we consider axion couplings independent of external fields and in the presence of a magnetic field.⁵ In each case, we discuss the phonon and magnon excitation processes that are allowed, and identify those with potentially detectable rates. The results of this exercise are summarized in Table 6.1.

Axion couplings independent of external fields

The axion wind coupling to electron spin leads to a coupling to the spin component of \mathbf{S}_{lj} . From $\mathbf{s}_{lj} + \boldsymbol{\ell}_{lj} = \mathbf{S}_{lj}$ and $2\mathbf{s}_{lj} + \boldsymbol{\ell}_{lj} = g_j \mathbf{S}_{lj}$, we see that the axion wind couples to $\mathbf{s}_{lj} = (g_j - 1) \mathbf{S}_{lj}$. Thus,

$$\delta \hat{H} = -\frac{g_{aee}}{m_e} \nabla a \cdot \sum_{lj} (g_j - 1) \mathbf{S}_{lj} = -\frac{g_{aee}}{m_e} (i m_a \mathbf{v}_a) \frac{a_0}{2} \cdot \sum_{lj} (g_j - 1) \mathbf{S}_{lj} e^{i\mathbf{p} \cdot \mathbf{x}_{lj}^0 - i\omega t} + \text{h.c.} \quad (6.34)$$

In the notation of Eq (6.4), we thus have

$$\mathbf{f}_j = -\frac{i}{\sqrt{2}} g_{aee} (g_j - 1) \frac{\sqrt{\rho_a}}{m_e} \mathbf{v}_a. \quad (6.35)$$

For an order of magnitude estimate of the rate, let us note that the mixing matrices \mathbb{U}, \mathbb{V} in Eq. (6.27) generically scale as $1/\sqrt{n}$ with n the number of magnetic ions in a primitive cell. The maximum rate is obtained on resonance, which is parametrically given by

$$R \sim \frac{g_{aee}^2 \rho_a v_a^2 n_s}{m_e^2 \rho_T \gamma} \sim (\text{kg}\cdot\text{yr})^{-1} \left(\frac{g_{aee}}{10^{-15}} \right)^2 \left(\frac{\mu\text{eV}}{\gamma} \right). \quad (6.36)$$

⁵An external electric field shifts the equilibrium positions of the ions such that there is no net electric field at the new equilibrium positions, so it does not generate new axion couplings at leading order.

where n_s and ρ_T are the spin and mass densities of the target, taken to be $(5 \text{ \AA})^{-3}$ and 5 g/cm^3 , respectively (close to the values for YIG), in the estimate. We see that, with single magnon sensitivity, interesting values of g_{aee} may be reached with less than a kilogram-year exposure.

The axion wind also couples to nucleon spins. However, these couplings do not excite magnons, since magnetic order originates from electron-electron interactions, meaning that the effective spins of magnetic ions that appear in the spin Hamiltonian Eq. (6.19) come from electrons. On the other hand, if the nuclear spins \mathbf{S}_N are ordered (*e.g.* by applying an external magnetic field which does not affect the axion-nucleon couplings) and form a periodic structure, the axion wind couplings could excite phonons. However, the rate suffers from multiple suppressions. First, coupling to atomic displacements relies on the spatial variation of $\nabla a \cdot \mathbf{S}_N$, which brings in an additional factor of v_a on top of the gradient: $\mathbf{f}_j \sim (C_f/f_a) m_a^2 a (\mathbf{v}_a \cdot \mathbf{S}_{N,j}) \mathbf{v}_a$. Second, there is a further suppression for exciting optical phonons since \mathbf{f}_j are approximately aligned with acoustic phonon polarizations if all $\mathbf{S}_{N,j}$ point in the same direction (see discussion in Sec. 6.3). Even without taking into account the second suppression, the estimated on-resonance rate using Eq. (6.18),

$$R \sim \frac{C_f^2 \rho_a m_a v_a^4}{f_a^2} \frac{n_s^2}{\rho_T^2 \gamma_\nu} \sim (\text{kg}\cdot\text{yr})^{-1} C_f^2 \left(\frac{100 \text{ GeV}}{f_a} \right)^2 \left(\frac{m_a}{10 \text{ meV}} \right) \left(\frac{\mu\text{eV}}{\gamma_\nu} \right), \quad (6.37)$$

can be sizable only for uninterestingly low f_a . Therefore, we conclude that axion wind couplings to nucleon spins do not offer a viable detection channel.

Beyond the axion wind couplings, the axion field also turns magnetic dipole moments from \mathbf{s}_f into oscillating EDMs, and one may consider phonon and magnon excitation by the resulting electromagnetic radiation fields. In the case of the electron, since the EDM coupling is perturbatively generated by the $aF\tilde{F}$ coupling, the process mentioned above is essentially converting the crystal magnetic field into electromagnetic radiation, and should be less efficient than applying an external magnetic field (discussed below in Sec. 6.4). In the case of nucleons, the EDM coupling in Eq. (6.1) is not much larger than the perturbative contribution from $aF\tilde{F}$, so the same conclusion applies.

In sum, for axion couplings independent of external fields, we have identified *magnon excitation via the axion wind coupling to electrons* as the only viable detection channel.

Axion couplings in a magnetic field

In the presence of a DC magnetic field \mathbf{B} , the axion field induces oscillating electromagnetic fields via the $aF\tilde{F}$ coupling. Solving the modified Maxwell equations (see *e.g.* Ref. [308, 309]), we find the induced electric field is $\mathbf{E}_a = -g_{a\gamma} a \boldsymbol{\varepsilon}_\infty^{-1} \cdot \mathbf{B}$. Note that the high frequency

dielectric constant, ϵ_∞ , which takes into account screening effects from the fast-responding electrons while excluding ionic contributions, should be used when solving the macroscopic Maxwell equations — essentially, since we are concerned with how the axion induced electric field acts on the ions, the ion charges should appear in the source term rather than being coarse grained into a macroscopic electric polarization. In the long-wavelength limit, the axion-induced electric field \mathbf{E}_a couples to charged ions via an effective dipole coupling:

$$\delta\hat{H} = -e \sum_{lj} \mathbf{E}_a \cdot \mathbf{Z}_j^* \cdot \mathbf{u}_{lj} = e g_{a\gamma\gamma} a \sum_{lj} \mathbf{B}_a \cdot \epsilon_\infty^{-1} \cdot \mathbf{Z}_j^* \cdot \mathbf{u}_{lj}, \quad (6.38)$$

where \mathbf{Z}_j^* is the Born effective charge tensor of the j th ion in the primitive cell — it captures the change in macroscopic polarization due to a lattice displacement, $\delta\mathbf{P} = e \mathbf{Z}_j^* \cdot \delta\mathbf{u}_{lj}/\Omega$, and is numerically close to the ionic charge, $\mathbf{Z}_j^* \simeq Q_j \mathbb{1}$ (where Ω is the primitive cell volume). It follows that

$$\mathbf{f}_j = \frac{1}{\sqrt{2}} g_{a\gamma\gamma} \frac{e\sqrt{\rho_a}}{m_a} \mathbf{B} \cdot \epsilon_\infty^{-1} \cdot \mathbf{Z}_j^*. \quad (6.39)$$

Noting that the phonon polarization vectors scale as $1/\sqrt{n}$ with n the number of ions in the primitive cell, and assuming photon-phonon mixing gives just a small correction, we can estimate the on-resonance rate from Eq. (6.18) as follows:

$$R \sim \frac{g_{a\gamma\gamma}^2 \rho_a}{m_a^3} \frac{Z^{*2} e^2 B^2}{\epsilon_\infty^2 m_{\text{ion}}^2 \gamma} \sim (\text{kg}\cdot\text{yr})^{-1} \left(\frac{g_{a\gamma\gamma}}{10^{-13} \text{ GeV}^{-1}} \right)^2 \left(\frac{100 \text{ meV}}{m_a} \right)^3 \left(\frac{B}{10 \text{ T}} \right)^2 \left(\frac{\text{meV}}{\gamma} \right), \quad (6.40)$$

where we have taken $Z^*/\epsilon_\infty \sim 1$ and $m_{\text{ion}} \sim 20 \text{ GeV}$. We see that, with single phonon sensitivity, there is excellent potential for reaching the QCD axion coupling if the axion mass is close to a phonon resonance.

The axion-induced magnetic field is much smaller, $B_a \sim E_a v_a$. An order of magnitude estimate tells us that the magnon excitation rate by B_a is much smaller than the phonon excitation rate by E_a : $\frac{R_{\text{magnon}}}{R_{\text{phonon}}} \sim \left(\frac{\mu_B B_a S_{lj}}{e Z^* E_a u_{lj}} \right)^2 \sim \frac{m_j m_a v_a^2}{m_e^2} \sim 10^{-8}$ for a 100 meV axion.

In sum, we have identified *phonon excitation via the axion-photon coupling in a magnetic field* as the only novel viable detection channel when considering an external DC magnetic field.

6.5 Projected Sensitivity

We now compute the projected sensitivity for the two detection channels identified in the previous section (see Table 6.1). In both phonon and magnon calculations, an important but elusive parameter is the resonance width, $\gamma_{\nu, \mathbf{p}}$, of each mode. While all other material parameters entering the rate calculation (equilibrium positions, phonon energies and eigenvectors, magnon energies and mixing matrices) can be computed within the quadratic

Hamiltonian, the widths involve anharmonic interactions and are not always readily available. In what follows, we present the reach with reasonable assumptions for $\gamma_{\nu,\mathbf{p}}$. Our goal here is to demonstrate the viability of phonons and magnons for detecting axion DM, and motivate further study in the condensed matter and materials science community on phonon and magnon interactions. This will be crucial both for having more accurate inputs to the DM detection rate calculation, and for designing detectors to read out these excitations.

Phonon excitation via the axion-photon coupling

When axion absorption excites a phonon polariton, it cascade decays to a collection of lower energy phonons and photons on a timescale of $\gamma^{-1} \sim \text{ps} (\text{meV}/\gamma)$. Since the polariton is a phonon-like state which decays via anharmonic phonon couplings, theoretically it is most efficient to read out phonons (heat) in the final state. However, phonon readout (*e.g.* through a transistor edge sensor) is complicated by the strong external magnetic field needed for the axion absorption process. One possibility is to detect the phonon via evaporation of helium atoms deposited on the surface of the crystal. The helium atoms are then detected well away from the crystal, such that the magnetic field is isolated from the sensor.⁶ Alternatively, if a target material can be found in which the photon yield from phonon polariton decays is substantial, photon readout becomes a viable option. In this case, the photons may be focused by a mirror and lens and directed by a waveguide onto a single photon detector (*e.g.* a superconducting nanowire) placed in a region of zero magnetic field. Both the phonon and photon readout possibilities sketched above will be studied in future work. In what follows, we simply assume 3 single phonon polariton excitation events per kilogram-year exposure (corresponding to 90% C.L. for a background-free counting experiment) when presenting the reach.

To compute the projected sensitivity to the axion-photon coupling, we use the rate formula Eq. (6.18), with the effective couplings \mathbf{f}_j given in Eq. (6.39). We consider several example target materials and different orientations of the external magnetic field. The results are shown in Figs. 6.3 and 6.4. As we discussed in Sec. 6.3, materials with different phonon frequencies play important complementary roles in covering a broader axion mass range. In these plots, we have taken the resonance widths to be $\gamma/\omega = 10^{-2}$, consistent with the order of magnitude of the measured numbers in sapphire. As predicted by Eq. (6.40), the on-resonance phonon production rate scales as $R \propto \gamma^{-1}$. From this follows that near-resonance constraints on $g_{a\gamma\gamma}$ scales like $\gamma^{1/2}$ making them stronger (weaker) for smaller (larger) value of the width, while at the same time narrowing (broadening) the peak structure. We should also note that our projected constraints are derived assuming a Breit-Wigner lineshape, which is

⁶We thank Stephen Lyon and Thomas Schenkel for discussions on this experimental avenue.

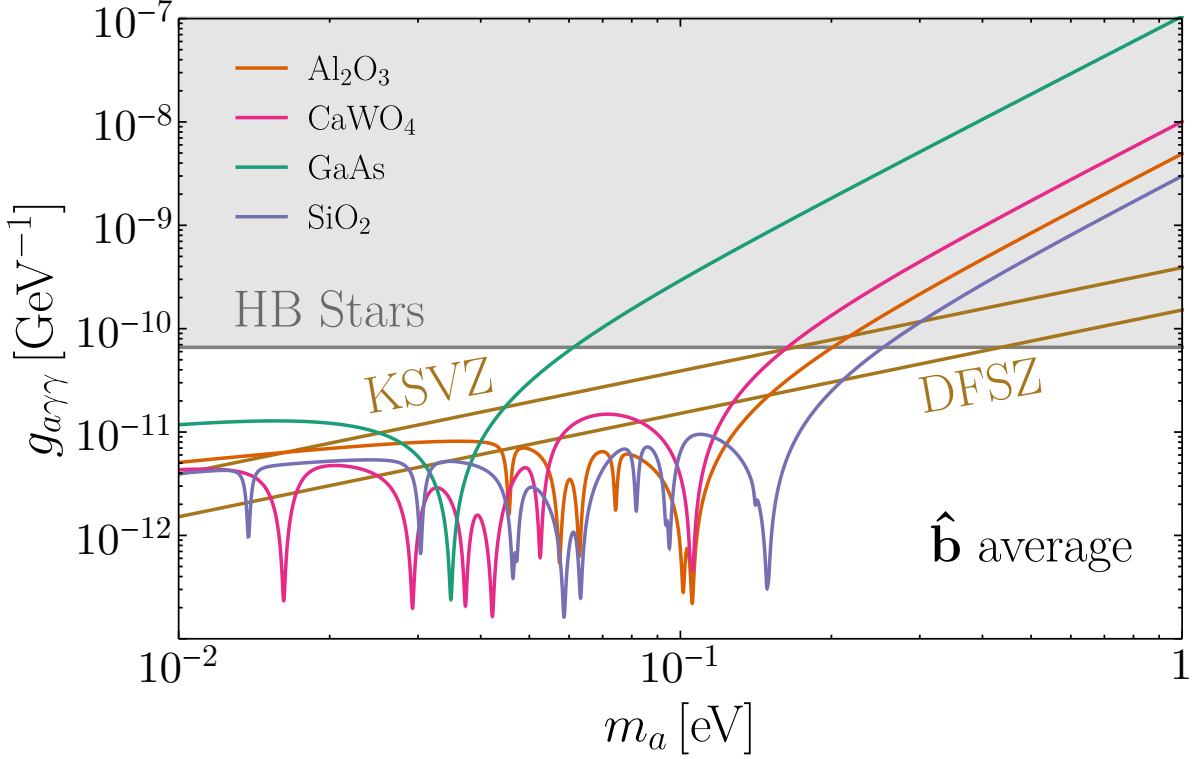


Figure 6.3: Projected reach on $g_{a\gamma\gamma}$ from axion absorption onto phonon polaritons in Al_2O_3 , CaWO_4 , GaAs and SiO_2 , in an external 10 T magnetic field, averaged over the magnetic field directions, assuming 3 events per kilogram-year. Also shown are predictions of the KSVZ and DFSZ QCD axion models, and horizontal branch (HB) star cooling constraints [30].

expected to be a good approximation near resonance; details of phonon self-interactions are needed to obtain more accurate results away from resonance.

It is also worth noting that, since the effective couplings \mathbf{f}_j depend on the direction of the magnetic field $\hat{\mathbf{b}}$, the strengths of the resonances vary as $\hat{\mathbf{b}}$ is changed, as we can see in Fig. 6.4. For example, for a sapphire target, when $\hat{\mathbf{b}}$ is parallel (perpendicular) to the crystal c -axis, chosen to coincide with the z -axis here, only 2 (4) out of the 6 resonances appear. This observation provides a useful handle to confirm a discovery by running the same experiment with the magnetic field applied in different directions.

Magnon excitation via the axion wind coupling

To compute the magnon excitation rate, we substitute the coupling \mathbf{f}_j in Eq. (6.35), into the rate formula Eq. (6.27). In Sec. 6.3, we discussed three strategies to alleviate the suppression of axion-magnon couplings due to selection rules: external magnetic fields, anisotropic interactions, and nondegenerate g -factors. In this subsection, we show the projected reach for each of these strategies. The results are summarized in Fig. 6.5, assuming 3 single magnon

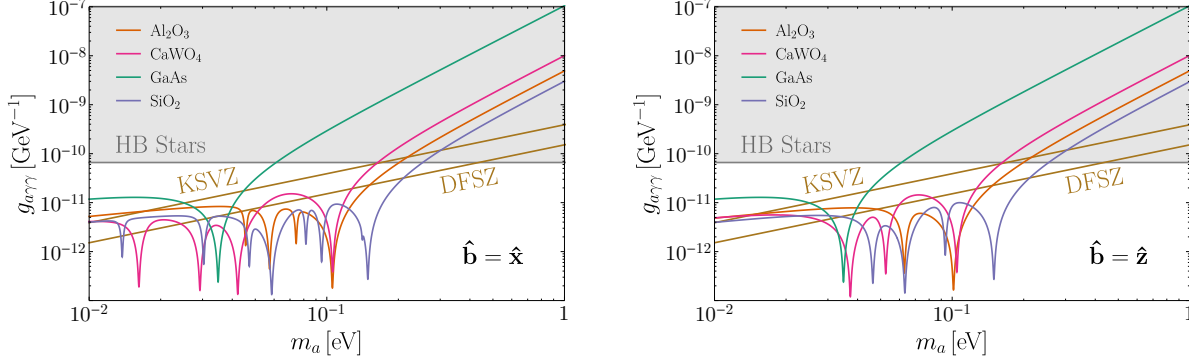


Figure 6.4: Similar to Fig. 6.3, but with the external magnetic field oriented in the \hat{x} (\hat{z}) direction in the left (right) panel. The strength of axion-photon couplings depends on the orientation of the magnetic field, and different resonances can be selected by changing the magnetic field direction.

events per kilogram-year exposure. Absent a detailed study of anharmonic magnon interactions, we take the resonance widths to be a free parameter, and show results for $\gamma/\omega = 10^{-2}$ and 10^{-5} , consistent with measured phonon width values on the high end and YIG’s Kittel magnon width on the low end. We see that, on resonance, all methods could reach axion-electron couplings predicted by QCD axion models. In the following, we expand on the calculation for each strategy.

External magnetic field. The idea of using an external magnetic field to lift the gapless mode is the one adopted in the QUAX experiment [91–93]. In Ref. [92], a classical calculation was used to estimate the axion absorption rate. Our formalism allows to compute the same rate in the quantum regime, and agrees with the recent computation carried out in Ref. [32]. The projected reach we obtain for a YIG sample in a 1 T field is shown in Fig. 6.5, where the resonance is at 0.12 meV (see Eq. (6.29)). For comparison, we also overlay the projection in Ref. [32] based on scanning the resonance frequency by changing the magnetic field, with an observation time of 10^4 s per frequency interval and a total integration time of 10 years. In deriving their constraints, the authors of Ref. [32] also include an estimate for the expected background noise. This, together with the smaller observation time per resonant frequency, is the origin of the difference between their constraints and our predicted peak sensitivity.

Anisotropic interactions. As another way to lift the gapless magnon modes, so that the absorption kinematics are satisfied, we may use materials with anisotropic exchange couplings. As an example, we consider NiPS₃, which has a layered crystal structure [310]. The magnetic ions are spin-1 Ni²⁺. Following Ref. [307], we model the system as having

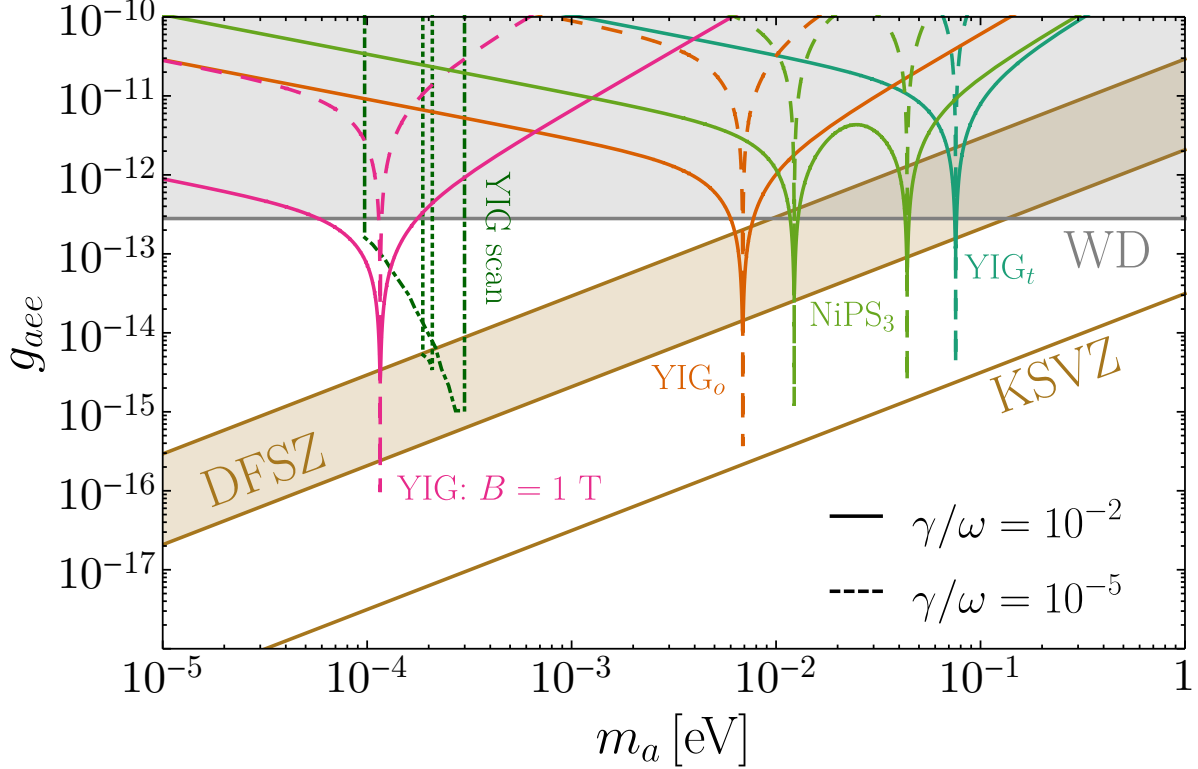


Figure 6.5: Projected reach on g_{aee} from axion-to-magnon conversion, compared with DFSZ (assuming $0.28 \leq \tan \beta \leq 140$) and KSVZ model predictions, as well as white dwarf (WD) constraints from Ref. [31]. The suppression of axion-magnon couplings is alleviated by using the three strategies discussed in the main text: lifting gapless magnon modes by an external magnetic field (YIG target in a 1 T magnetic field, compared to the scanning scheme of Ref. [32]), anisotropic interactions (NiPS₃ target), and using targets with nondegenerate g -factors (hypothetical toy models based on YIG, referred to as YIG_o and YIG_t). For all the cases considered we assume 3 events per kilogram-year exposure, and take the magnon width to frequency ratio γ/ω to be 10^{-2} (solid) or 10^{-5} (dashed).

intralayer anisotropic exchange couplings up to third nearest neighbors, as well as single-ion anisotropies. All four magnon branches are gapped, two of which are found to have nonzero couplings to the axion wind. These correspond to the resonances at 12 meV and 44 meV in Fig. 6.5.

Nondegenerate g -factors. Finally, we consider coupling the axion to gapped magnon modes in the presence of nondegenerate g -factors. We are not aware of a well-characterized material with nondegenerate g -factors so, as a proof of principle, we entertain a few toy models, where a nondegenerate ℓ component is added to the effective spins S in YIG. In reality, all the magnetic ions Fe³⁺ in YIG have $(\ell, s, S) = (0, 5/2, 5/2)$; the orbital angular momenta of 3d electrons are quenched. In Fig. 6.5, we show the reach for two toy models, with

either the octahedral sites or the tetrahedral sites modified to have $(\ell, s, S) = (1, 5/2, 7/2)$. In each case, only one of the 19 gapped magnon modes, at 7 meV and 76 meV respectively, is found to contribute to axion absorption. This is because, to preserve the lattice symmetries, we have modified all the effective spin compositions on tetrahedral or octahedral sites in the same way. The sole gapped mode that couples to axion DM corresponds to out-of-phase precessions of the tetrahedral and octahedral spins.

6.6 Conclusions

In this paper we showed multiple ways collective excitations in crystal targets are, in principle, sensitive to QCD axion DM. Specifically, we identified two novel detection possibilities: axion-induced phonon polariton excitation in an external magnetic field, and axion-induced magnon excitation in the absence of external fields. These paths are complementary as each probes a different axion coupling, $g_{a\gamma\gamma}$ and g_{aee} in the phonon case and magnon case respectively.

In the phonon polariton case, we considered several example targets – Al_2O_3 , CaWO_4 , GaAs and SiO_2 – and showed that on resonance, per kilogram-year exposure, they can reach $g_{a\gamma\gamma} \sim 10^{-12} \text{ GeV}^{-1}$, as shown in Figs. 6.3 and 6.4. This outperforms the leading constraint in this mass window from stellar cooling, and reaches below the QCD axion band. Carefully choosing a set of target materials with different phonon frequencies is key to covering a broad range of axion masses.

Previous proposals for probing g_{aee} via absorption onto magnons, which underlies the QUAX experiment, considered targets in an external magnetic field, which would lift the lowest magnon mode and kinematically allow sub-meV axion absorption [32, 91–93, 164]. In contrast, we focused on the $\mathcal{O}(1\text{-}100)$ meV axion mass window, and showed that without an external magnetic field, materials with anisotropic exchange interactions, *e.g.* NiPS_3 , and materials with nondegenerate g -factors can host gapped magnons coupling to the axion. On resonance and with kilogram-year exposure, they can have sensitivity to the DFSZ model and down to $g_{aee} \sim 10^{-15}$, shown in Fig. 6.5.

Realizing the exciting potential of discovering $\mathcal{O}(1\text{-}100)$ meV axion DM via phonons and magnons hinges upon the ongoing effort to achieve low threshold single quanta detection. One possibility is to evaporate helium atoms from phonon interactions at the surface of the crystal and then detect the evaporated helium atoms in a region separated from the magnetic field region; R&D is underway for this direction. Another route is to read out photons produced from the decay of a phonon polariton. Single photon detectors (*e.g.* superconducting nanowires) may operate in a field-free region, away from the crystal target

and connected to it via a waveguide. Finally, magnons are read out in a resonant cavity in the QUAX setup in the classical regime [91–93, 164, 311, 312]. Work is underway to detect single magnons in YIG by coupling cavity modes to a superconducting qubit [274], though as in other resonant cavity searches, axion masses are best produced near the inverse cavity size; for larger axion masses the virtual cavity modes will be off-shell and readout efficiency is suppressed. On the materials side, we would like to make more accurate predictions for the detection rates via an improved understanding of phonon and magnon resonance lineshapes, and explore the possibility of scanning the resonance frequencies by engineering material properties, in order to fully exploit the discovery potential of an axion DM search experiment based on phonon and magnon excitations.

EFFECTIVE FIELD THEORY OF DARK MATTER DIRECT DETECTION WITH COLLECTIVE EXCITATIONS

7.1 Introduction

Light dark matter (DM) with sub-GeV mass is theoretically well-motivated [137, 142, 143, 203–210] but difficult to detect in traditional WIMP-focused experiments [12, 14, 75, 80, 313]. This can be understood from simple scattering kinematics: if the DM mass $m_\chi \lesssim \text{GeV}$, the amount of energy deposited in a nuclear recoil process, $\omega = \frac{q^2}{2m_N}$, is suppressed by the heavy target nucleus mass m_N and limited by the possible momentum transfer $q \lesssim 2m_\chi v$. This, along with a steady improvement to the energy sensitivity of detectors [251–255], has motivated the study of excitation channels far outside the scope of standard nuclear recoil. Perhaps the most studied alternative is electronic excitations, in a variety of different targets, e.g., individual atoms [19, 24, 33, 35, 177, 244], semiconductors and scintillators [6, 7, 19, 22, 23, 33–35, 87, 177, 180, 237, 314], superconductors [181, 182], aromatic organic targets [243], graphene [188] and Dirac materials [29, 144, 183]. The smallest DM mass that can be probed is limited by the band gap in these materials, typically $\mathcal{O}(\text{eV})$ corresponding to DM masses $\gtrsim \text{MeV}$ (the exceptions being superconductors and Dirac materials which typically have $\mathcal{O}(\text{meV})$ gaps and sensitivity to keV scale DM).

For sensitivity to smaller energy deposits, and optimal reach to light DM and mediating particles, we look toward excitations at sub-eV energies. Such excitations exist and are derived from collective behaviors of atoms, ions or electrons in condensed matter systems. Phonons were proposed in Ref. [184] and further studied in Refs. [185–187, 245, 315] for direct detection in superfluid helium (where maxon and roton excitations also contribute), and were also discussed in the context of bosonic DM absorption in superconductors [41] and semiconductors [39], though ultimately, acoustic and optical phonons in (polar) crystals were advanced [64] and shown to have the best experimental prospects and sensitivity to light dark matter [6, 7, 28, 247, 248]. Magnons – quanta of collective spin excitations – were also proposed in Ref. [8]. Both phonons and magnons in crystal targets have typical energies up to $\mathcal{O}(100 \text{ meV})$. To date, the work in the literature has focused on demonstrating the sensitivity of phonons and magnons to simple DM models. Only spin-independent (SI) interactions, via couplings to linear combinations of the proton, neutron and electron numbers, have been considered for phonon excitations, while a few benchmark models have been studied for


magnon excitations.

The goal of this paper is to extend these results to general types of DM interactions. Effective field theory (EFT) is well-suited for this purpose: we can match a general relativistic theory of DM onto a nonrelativistic (NR) EFT, and then compute the target response to the EFT operators. Within this framework, starting from a UV model consisting of relativistic operators coupling the DM to the proton, neutron, and/or electron, we can systematically compute direct detection rates via single phonon and magnon excitations in various target materials. The idea is along the lines of previous works on EFT calculations of nuclear recoils [60, 197, 316–319] (which extend earlier studies focused on standard SI and spin-dependent (SD) DM-nucleon interactions), and, more recently, of electron excitations in atoms [244] (which extends earlier studies focused on SI DM-electron interactions), but technically there are important differences. Specifically, our EFT approach to DM-induced single phonon and magnon excitations consists of the following steps:

- i) Matching of a relativistic theory of DM interactions onto the NR EFT (DM model-specific).
- ii) Matching of NR operators onto DM couplings to lattice degrees of freedom (universal).
- iii) Calculation of phonon or magnon excitation matrix elements (target- and excitation-specific).

We explain each of these steps in the three subsections of Sec. 7.2. The first step – matching relativistic DM theories to the NR EFT – largely follows previous works [60, 197, 244, 316–319], and we review the procedure for completeness. For nuclear recoils, one then derives the nuclear responses to the EFT operators. Analogously, the key quantities in the present case are *crystal responses* which determines how DM couples to the collective excitations (we emphasize, however, that despite the similar choice of terminology, collective excitations are associated with a different kinematic regime and degrees of freedom than nuclear recoils and therefore require a distinct EFT calculation). Technically, for both phonon and magnon excitations in crystal targets, the second step listed above involves matching the NR EFT of DM-nucleon and DM-electron interactions onto an effective scattering potential that involves ionic degrees of freedom in the crystal lattice — in the long wavelength (low momentum transfer) limit relevant for light DM scattering, these (as we will **highlight** throughout) are quantities that characterize an ion as a whole, including the total particle numbers $\langle N_\psi \rangle$ for the proton, neutron and electron ($\psi = p, n, e$), total spins $\langle \mathbf{S}_\psi \rangle$, orbital angular momenta $\langle \mathbf{L}_\psi \rangle$, as well as spin-orbit couplings $\langle \mathbf{L}_\psi \otimes \mathbf{S}_\psi \rangle$ (a tensor with components $\langle L_\psi^i S_\psi^k \rangle$ summed

over the constituent nucleons/electrons). Finally, in the third step, we quantize the scattering potential to obtain the phonon and magnon modes in a specific target material and compute the matrix elements for exciting them. All four types of crystal responses highlighted above can lead to phonon excitation in appropriately chosen targets, while $\langle \mathbf{S}_e \rangle$ and $\langle \mathbf{L}_e \rangle$ can also lead to magnon excitation.

Our new results significantly extend the searchable DM model space via phonon and magnon excitations, which we showcase in Sec. 7.3 with a variety of well-motivated benchmark models. We present full numerical calculations for several representative target materials, and apply simple analytic estimates to understand the results. We compare for which operators and interactions one expects phonon versus magnon excitations to dominate the rate, quantifying and generalizing the discussion in Ref. [8]. These calculations highlight the complementarity between phonon and magnon excitations, and between different targets, in probing the light DM theory space. We make the code for computing single phonon excitation rates publicly available on GitHub  [257]; it integrates the open-source phonon eigensystem solver `phonopy` [50], and takes general NR EFT operator coefficients, together with density functional theory (DFT) calculations of material properties, as input. Our magnon code, based on the Toth-Lake algorithm [268] for solving the magnon eigensystem, is also available upon request.

7.2 Effective Field Theory Calculation of Dark Matter Induced Collective Excitations

Our goal is to present a framework for computing direct detection rates for general DM models, for the process where a DM particle scatters off a crystal target and induces a quasiparticle excitation in the crystal. This quantum mechanical process follows Fermi's golden rule which, when the incoming and outgoing DM particles are momentum eigenstates in free space, takes the form

$$\Gamma(\mathbf{v}) = \frac{1}{V} \int \frac{d^3q}{(2\pi)^3} \sum_f |\langle f | \tilde{\mathcal{V}}(-\mathbf{q}, \mathbf{v}) | i \rangle|^2 2\pi \delta(E_f - E_i - \omega_{\mathbf{q}}), \quad (7.1)$$

where \mathbf{v} is the incoming DM's velocity, V is the total target volume, $|i\rangle$ and $|f\rangle$ are the initial and final states of the target system (defined with NR normalization: $\langle i|i\rangle = \langle f|f\rangle = 1$), and $\tilde{\mathcal{V}}$ is the Fourier transform of the scattering potential. The momentum transfer from the DM to the target, \mathbf{q} , is integrated over, while the energy deposition onto the target is constrained to be

$$\omega_{\mathbf{q}} = \frac{1}{2} m_{\chi} v^2 - \frac{(m_{\chi} \mathbf{v} - \mathbf{q})^2}{2m_{\chi}} = \mathbf{q} \cdot \mathbf{v} - \frac{q^2}{2m_{\chi}}. \quad (7.2)$$

See Ref. [7] for a review of the general formalism.

We now need to specify the type of transitions $|i\rangle \rightarrow |f\rangle$ in the target system to calculate the matrix element $\langle f | \tilde{\mathcal{V}}(-\mathbf{q}, \mathbf{v}) | i \rangle$. Here we focus on excitation of single phonon or magnon in a crystal target at zero temperature. We therefore take $|i\rangle$ to be the ground state $|0\rangle$, and $|f\rangle$ to be the one-phonon or one-magnon states $|\nu, \mathbf{k}\rangle$, labeled by branch ν and momentum \mathbf{k} within the first Brillouin zone (1BZ). For a crystal target, we write the scattering potential as a sum of contributions from individual ions:¹

$$\mathcal{V}(\mathbf{x}, \mathbf{v}) = \sum_{lj} \mathcal{V}_{lj}(\mathbf{x} - \mathbf{x}_{lj}, \mathbf{v}), \quad (7.3)$$

where $l = 1, \dots, N$ labels the primitive cells, $j = 1, \dots, n$ labels the ions within each primitive cell, and \mathbf{x}_{lj} is the position of the ion labeled by l, j . Therefore,

$$\tilde{\mathcal{V}}(-\mathbf{q}, \mathbf{v}) = \int d^3x e^{i\mathbf{q}\cdot\mathbf{x}} \mathcal{V}(\mathbf{x}, \mathbf{v}) = \sum_{lj} e^{i\mathbf{q}\cdot\mathbf{x}_{lj}} \tilde{\mathcal{V}}_{lj}(-\mathbf{q}, \mathbf{v}), \quad (7.4)$$

and we obtain

$$\Gamma(\mathbf{v}) = \frac{1}{V} \int \frac{d^3q}{(2\pi)^3} \sum_{\nu, \mathbf{k}} \left| \sum_{lj} \langle \nu, \mathbf{k} | e^{i\mathbf{q}\cdot\mathbf{x}_{lj}} \tilde{\mathcal{V}}_{lj}(-\mathbf{q}, \mathbf{v}) | 0 \rangle \right|^2 2\pi \delta(\omega_{\nu, \mathbf{k}} - \omega_{\mathbf{q}}). \quad (7.5)$$

The central quantity for the rate calculation is then the lattice potential $\tilde{\mathcal{V}}_{lj}$ which the DM senses. This will depend on both the specific DM model and on the lattice degrees of freedom (e.g., the nucleon/electron number or total electronic spin of the ions) available to scatter from. We will determine the lattice potential $\tilde{\mathcal{V}}_{lj}$ in two steps previously mentioned in the introduction: first, in Sec. 7.2, we review the procedure of matching relativistic DM models onto NR effective operators; next, in Sec. 7.2, we further reduce these effective operators to DM couplings to the lattice degrees of freedom. In the simplest case of SI interactions, there is only one effective operator, $\mathcal{O}_1 = \mathbb{1}$, and $\tilde{\mathcal{V}}_{lj}$ is a linear combination of $\langle N_p \rangle_{lj}$, $\langle N_n \rangle_{lj}$ and $\langle N_e \rangle_{lj}$ (proton, neutron and electron numbers of the ions, respectively) [7]. More generally, a DM model can generate a larger set of effective operators that involve the spins, momentum transfer, and the relative velocity. The resulting lattice potential $\tilde{\mathcal{V}}_{lj}$ depends on lattice degrees of freedom that include, in addition to the particle numbers $\langle N_\psi \rangle_{lj}$ ($\psi = p, n, e$), also their spins $\langle \mathbf{S}_\psi \rangle_{lj}$, orbital angular momenta $\langle \mathbf{L}_\psi \rangle_{lj}$, as well as spin-orbit couplings $\langle \mathbf{L}_\psi \otimes \mathbf{S}_\psi \rangle_{lj}$ (a tensor with components $\langle L_\psi^i S_\psi^k \rangle_{lj}$, see Eq. (7.27) below). The last step in computing the scattering rate is to quantize $\tilde{\mathcal{V}}_{lj}$ in terms of phonon/magnon creation and annihilation operators; we carry out this exercise in Sec. 7.2. The framework in this section will provide the basis for concrete calculations of direct detection rates via single phonon and magnon excitations, and will be applied to a set of benchmark models in Sec. 7.3.

¹For simplicity, we will refer to either atoms or ions on lattice sites as ions.

From Dark Matter Models to Nonrelativistic Effective Operators

In this subsection, we take a top-down approach in deriving the EFT, focusing on how the effective operators arise from NR matching of well-motivated relativistic models. While one can also take a bottom-up approach as in e.g., Ref. [197], and construct the EFT by enumerating operators consistent with Galilean and translation invariance, we find it useful to have a set of benchmark UV models to develop intuition on how realistic theories of DM, which often predict correlations between EFT operators [55, 60], can be probed by experiment.

Let us start from a relativistic model of a DM particle χ interacting with the proton (p), neutron (n) and electron (e);² we denote these Standard Model (SM) particles collectively by ψ in the following. To compute the NR EFT, we take the NR limit of the relativistic theory and map it on to the appropriate NR degrees of freedom. The EFT consists of the NR fields χ^\pm , ψ^\pm , generally defined by (using the SM fermion ψ for example):

$$\psi^+(\mathbf{x}, t) \equiv \sum_I e^{-i\varepsilon_I t} \Psi_I(\mathbf{x}) \hat{b}_I, \quad \psi^- \equiv (\psi^+)^\dagger. \quad (7.6)$$

Here the sum is over energy eigenstates, $\varepsilon_I = E_I - m_\psi$ are the energy eigenvalues minus the rest mass, $\Psi_I(\mathbf{x})$ are the wavefunctions (which are two-component for spin- $\frac{1}{2}$ fermions) and \hat{b}_I are the annihilation operators. In the familiar case of a fermion in free space, the energy eigenstates are labeled by momentum \mathbf{k} and spin $s = \pm$, with eigenvalues $\varepsilon_{\mathbf{k},s} = \varepsilon_{\mathbf{k}} = \sqrt{\mathbf{k}^2 + m_\psi^2} - m_\psi \simeq \frac{\mathbf{k}^2}{2m_\psi}$, and therefore³

$$\psi_{\text{free}}^+(\mathbf{x}, t) = \int \frac{d^3k}{(2\pi)^3} e^{-i\varepsilon_{\mathbf{k}} t} e^{i\mathbf{k}\cdot\mathbf{x}} \xi_s \hat{b}_{\mathbf{k},s}, \quad (7.7)$$

where $\xi_+ = \begin{pmatrix} 1 \\ 0 \end{pmatrix}$, $\xi_- = \begin{pmatrix} 0 \\ 1 \end{pmatrix}$.

For a spin- $\frac{1}{2}$ fermion, the relation between the relativistic field ψ and NR field ψ^+ is (see Appendix J)

$$\psi(\mathbf{x}, t) = e^{-im_\psi t} \frac{1}{\sqrt{2}} \left(\begin{pmatrix} 1 - \frac{\boldsymbol{\sigma}\cdot\mathbf{k}}{2m_\psi + \varepsilon} \\ 1 + \frac{\boldsymbol{\sigma}\cdot\mathbf{k}}{2m_\psi + \varepsilon} \end{pmatrix} \psi^+(\mathbf{x}, t) \right), \quad (7.8)$$

at leading order in m_ψ^{-1} , where \mathbf{k} , ε are operators acting on ψ^+ . For a fermion in free space, we have $\mathbf{k} = -i\nabla$, $\varepsilon = i\partial_t$, which become simply numbers in momentum space.

²The DM-proton and DM-neutron couplings follow from the DM-quark and DM-gluon couplings in the fundamental Lagrangian by standard methods, see e.g., Ref. [316].

³In this and the next subsection, we shall use \mathbf{k} to denote a SM fermion's momentum while deriving the lattice potential, which should not be confused with the phonon momentum in Eq. (7.5). Afterward, starting from Sec. 7.2, we will no longer need to deal with fermion momenta, and the notation \mathbf{k} will be recycled for phonon momentum.

In the presence of an external potential (Φ, \mathbf{A}) (e.g., electromagnetic fields from the ions), $\mathbf{k} = -i\nabla - \mathbf{A}$ is the kinematical momentum, while $\varepsilon = i\partial_t - \Phi$. Eq. (7.8) applies for the SM fermions $\psi = p, n, e$. If the DM χ is a spin- $\frac{1}{2}$ fermion, it also applies for the DM, with ψ replaced by χ . For a spin-0 DM, on the other hand, $\chi = e^{-im_\chi t}\chi^+$, with χ^+ given by Eq. (7.7) without the ξ_s factor.

To demonstrate the procedure of matching a relativistic model onto the NR EFT, we focus on tree level DM scattering mediated by a spin-0 or abelian spin-1 particle, denoted by ϕ and V_μ respectively. While it should be kept in mind that the EFT is capable of describing a broader class of models, including e.g. loop-mediated scattering, we find it useful to organize our thinking by categorizing mediator couplings to fermion bilinears. In Table 7.1, we list the commonly considered types of couplings at the level of the relativistic Lagrangian, and their NR limits. We explain the table in detail in the following two paragraphs.

Lagrangian Term	Coupling Type	(Effective) Current \rightarrow NR Limit
$g_S \phi \bar{\psi} \psi$	Scalar	$J_S = \bar{\psi} \psi \rightarrow \mathbb{1}$
$g_P \phi \bar{\psi} i \gamma^5 \psi$	Pseudoscalar	$J_P = \bar{\psi} i \gamma^5 \psi \rightarrow -\frac{i\mathbf{q} \cdot \mathbf{S}_\psi}{m_\psi}$
$g_V V_\mu \bar{\psi} \gamma^\mu \psi$	Vector	$J_V^\mu = \bar{\psi} \gamma^\mu \psi \rightarrow \left(\mathbb{1}, \frac{\mathbf{K}}{2m_\psi} - \frac{i\mathbf{q}}{m_\psi} \times \mathbf{S}_\psi \right)$
$g_A V_\mu \bar{\psi} \gamma^\mu \gamma^5 \psi$	Axial vector	$J_A^\mu = \bar{\psi} \gamma^\mu \gamma^5 \psi \rightarrow \left(\frac{\mathbf{K} \cdot \mathbf{S}_\psi}{m_\psi}, 2\mathbf{S}_\psi \right)$
$\frac{g_{\text{edm}}}{4m_\psi} V_{\mu\nu} \bar{\psi} \sigma^{\mu\nu} i \gamma^5 \psi$	Electric dipole	$J_{\text{edm}}^\mu = \frac{1}{2m_\psi} \partial_\nu (\bar{\psi} \sigma^{\mu\nu} i \gamma^5 \psi) \rightarrow \left(-\frac{i\mathbf{q}}{m_\psi} \cdot \mathbf{S}_\psi, \frac{i\omega}{m_\psi} \mathbf{S}_\psi + \frac{i\mathbf{q}}{m_\psi} \times \left(\frac{\mathbf{K}}{2m_\psi} \times \mathbf{S}_\psi \right) \right)$
$\frac{g_{\text{mdm}}}{4m_\psi} V_{\mu\nu} \bar{\psi} \sigma^{\mu\nu} \psi$	Magnetic dipole	$J_{\text{mdm}}^\mu = \frac{1}{2m_\psi} \partial_\nu (\bar{\psi} \sigma^{\mu\nu} \psi) \rightarrow \left(\frac{i\mathbf{q}}{m_\psi} \cdot \left(\frac{\mathbf{K}}{2m_\psi} \times \mathbf{S}_\psi \right) - \frac{q^2}{4m_\psi^2}, -\frac{i\mathbf{q}}{m_\psi} \times \mathbf{S}_\psi \right)$
$\frac{g_{\text{ana}}}{4m_\psi^2} (\partial^\nu V_{\mu\nu}) (\bar{\psi} \gamma^\mu \gamma^5 \psi)$	Anapole	$J_{\text{ana}}^\mu = -\frac{1}{4m_\psi^2} (g^{\mu\nu} \partial^2 - \partial^\mu \partial^\nu) (\bar{\psi} \gamma_\nu \gamma^5 \psi) \rightarrow -\frac{q^2}{4m_\psi^2} J_A^\mu + \left(\frac{\mathbf{q}}{m_\psi} \cdot \mathbf{S}_\psi \right) \frac{q^\mu}{2m_\psi}$
$\frac{g_{V2}}{4m_\psi^2} (\partial^\nu V_{\mu\nu}) (\bar{\psi} \gamma^\mu \psi)$	Vector ($\mathcal{O}(q^2)$)	$J_{V2}^\mu = -\frac{1}{4m_\psi^2} \partial^2 (\bar{\psi} \gamma^\mu \psi) \rightarrow -\frac{q^2}{4m_\psi^2} J_V^\mu$

Table 7.1: Types of couplings between a spin- $\frac{1}{2}$ fermion ψ and a scalar (vector) mediator ϕ (V_μ). The (effective) currents are defined by $\mathcal{L} \supset g_X \phi J_X$ ($X = S, P$) or $g_X V_\mu J_X^\mu$ ($X = V, A, \text{edm}, \text{mdm}, \text{ana}, V2$), upon integration by parts in the last four cases. The expressions following the arrows are the leading operators in the NR reduction of the currents (assuming scattering kinematics), which appear between the nonrelativistic fields ψ^- and ψ^+ — see e.g., Eq. (7.9). These will be used to derive the NR operators generated by specific DM models involving tree-level exchange of a scalar or vector mediator in Table 7.2.

For a spin-0 mediator ϕ , we consider its couplings to the scalar and pseudoscalar currents J_S , J_P . For a spin-1 mediator V_μ , we consider both minimal coupling to the vector and axial-vector currents J_V^μ , J_A^μ , and non-minimal couplings to the field strength $V_{\mu\nu}$.⁴ The latter include a series of higher dimensional operators. At dimension five, we have the electric dipole moment (edm) and magnetic dipole moment (mdm) couplings. Upon integration by parts, they can be cast in the same form, $V_\mu J^\mu$, as the minimal coupling case, with effective currents J_{edm}^μ , J_{mdm}^μ listed in the last column of Table 7.1. Next, at dimension six, we consider $\partial^\nu V_{\mu\nu}$ coupling to the axial-vector and vector currents. The former represents a new type of coupling known as the anapole [52, 55, 59], and the corresponding effective current is denoted by J_{ana}^μ . On the other hand, $\partial^\nu V_{\mu\nu}$ coupling to the vector current gives an $\mathcal{O}(q^2)$ contribution to the same form factors that J_V^μ induces (i.e., the familiar charge and magnetic dipole in quantum electrodynamics), so we denote the effective current by J_{V2}^μ . It is useful to note that all the (effective) currents that couple to a spin-1 mediator, except J_A^μ , are conserved: $q_\mu J_X^\mu = 0$ ($X = V, \text{edm}, \text{mdm}, \text{ana}, V2$).

In the NR limit, we can substitute Eq. (7.8) for the relativistic fermion field ψ into the expressions for the (effective) currents in Table 7.1, and expand in powers of $\frac{\mathbf{k}}{m_\psi}$ and $\frac{\varepsilon}{m_\psi}$. For example, for $J_V^\mu = (J_V^0, \mathbf{J}_V)$, we find, at leading order,

$$J_V^0 = \bar{\psi}\gamma^0\psi \rightarrow \psi^-\psi^+, \quad \mathbf{J}_V = \bar{\psi}\boldsymbol{\gamma}\psi \rightarrow \psi^-\left(\frac{\mathbf{K}}{2m_\psi} - \frac{i\mathbf{q}}{m_\psi} \times \mathbf{S}_\psi\right)\psi^+. \quad (7.9)$$

where $\mathbf{S}_\psi = \frac{\boldsymbol{\sigma}}{2}$ is the spin operator, and

$$\mathbf{K} \equiv \mathbf{k}' + \mathbf{k}, \quad \mathbf{q} \equiv \mathbf{k}' - \mathbf{k}, \quad (7.10)$$

with \mathbf{k}' defined as acting on the ψ^- field on the left, $\mathbf{k}' = i\overleftarrow{\nabla} - \mathbf{A}$, giving the kinematical momentum of the final state ψ . We can carry out the same exercise for the other (effective) currents. The results, up to the first nonvanishing order, are listed after the arrows in the last column of Table 7.1, with ψ^- on the left and ψ^+ on the right implicit. We see that all currents reduce to operators involving \mathbf{S}_ψ , \mathbf{K} and $i\mathbf{q}$; in the case of the electric dipole coupling, $\omega \equiv \varepsilon' - \varepsilon$ also appears, with ε' defined as acting on ψ^- on the left.

With Table 7.1, it is straightforward to derive the NR effective operators generated by tree-level exchange of a spin-0 or spin-1 mediator between a DM current and a SM current. Concretely, let us consider a set of benchmark models of spin- $\frac{1}{2}$ DM [60], listed in Table 7.2. In each model, the DM χ and a SM fermion ψ each couple to the mediator via a linear combination of the currents in the last column of Table 7.1, whose NR limits can be directly

⁴Other operators, such as those with derivatives acting on ψ and those involving the dual field strength $\tilde{V}_{\mu\nu}$, are not independent — see e.g., Ref. [320].

read off. Integrating out the mediator at tree level, we then arrive at a NR EFT for DM scattering of the form

$$\mathcal{L}_{\text{eff}} = \chi^- \left[\varepsilon - \frac{\mathbf{p}^2}{2m_\chi} + \mathcal{O}(m_\chi^{-2}) \right] \chi^+ + \psi^- \left[\varepsilon - \frac{\mathbf{k}^2}{2m_\psi} + \mathcal{O}(m_\psi^{-2}) \right] \psi^+ + \sum_i \sum_{\psi=p,n,e} c_i^{(\psi)} \mathcal{O}_i^{(\psi)} \chi^- \chi^+ \psi^- \psi^+. \quad (7.11)$$

For convenience, we reserve \mathbf{k} and \mathbf{k}' for the momentum operators acting on ψ^\pm , and write the same operators as \mathbf{p} and \mathbf{p}' when they act on χ^\pm . We normalize the operators by powers of m_ψ so that $\mathcal{O}_i^{(\psi)}$ are dimensionless and $c_i^{(\psi)}$ have dimension -2 .

Model	UV Lagrangian	NR EFT	Responses
Standard SI	$\phi(g_\chi J_{S,\chi} + g_\psi J_{S,\psi})$ or $V_\mu(g_\chi J_{V,\chi}^\mu - g_\psi J_{V,\psi}^\mu)$	$c_1^{(\psi)} = \frac{g_\chi g_\psi}{q^2 + m_\phi^2}$	N
Standard SD ⁵	$V_\mu(g_\chi J_{A,\chi}^\mu + g_\psi J_{A,\psi}^\mu)$	$c_4^{(\psi)} = \frac{4g_\chi g_\psi}{q^2 + m_V^2}$	S
Other scalar mediators	$P \times S$ $\phi(g_\chi J_{P,\chi} + g_\psi J_{S,\psi})$	$c_{11}^{(\psi)} = \frac{m_\psi}{m_\chi} \frac{g_\chi g_\psi}{q^2 + m_\phi^2}$	N
	$S \times P$ $\phi(g_\chi J_{S,\chi} + g_\psi J_{P,\psi})$	$c_{10}^{(\psi)} = -\frac{g_\chi g_\psi}{q^2 + m_\phi^2}$	S
	$P \times P$ $\phi(g_\chi J_{P,\chi} + g_\psi J_{P,\psi})$	$c_6^{(\psi)} = \frac{m_\psi}{m_\chi} \frac{g_\chi g_\psi}{q^2 + m_\phi^2}$	S
Multi-pole DM models	Electric dipole $V_\mu(g_\chi J_{\text{edm},\chi}^\mu + g_\psi(J_{V,\psi}^\mu + \delta\tilde{\mu}_\psi J_{\text{mdm},\psi}^\mu))$	$c_{11}^{(\psi)} = -\frac{m_\psi}{m_\chi} \frac{g_\chi g_\psi}{q^2 + m_V^2}$	N
	Magnetic dipole $V_\mu(g_\chi J_{\text{mdm},\chi}^\mu + g_\psi(J_{V,\psi}^\mu + \delta\tilde{\mu}_\psi J_{\text{mdm},\psi}^\mu))$	$c_1^{(\psi)} = \frac{q^2}{4m_\chi^2} \frac{g_\chi g_\psi}{q^2 + m_V^2}$ $c_4^{(\psi)} = \tilde{\mu}_\psi \frac{q^2}{m_\chi m_\psi} \frac{g_\chi g_\psi}{q^2 + m_V^2}$ $c_5^{(\psi)} = \frac{m_\psi}{m_\chi} \frac{g_\chi g_\psi}{q^2 + m_V^2}$ $c_6^{(\psi)} = -\tilde{\mu}_\psi \frac{m_\psi}{m_\chi} \frac{g_\chi g_\psi}{q^2 + m_V^2}$	N, S, L
	Anapole $V_\mu(g_\chi J_{\text{ana},\chi}^\mu + g_\psi(J_{V,\psi}^\mu + \delta\tilde{\mu}_\psi J_{\text{mdm},\psi}^\mu))$	$c_8^{(\psi)} = \frac{q^2}{2m_\chi^2} \frac{g_\chi g_\psi}{q^2 + m_V^2}$ $c_9^{(\psi)} = -\tilde{\mu}_\psi \frac{q^2}{2m_\chi^2} \frac{g_\chi g_\psi}{q^2 + m_V^2}$	N, S, L
$(\mathbf{L} \cdot \mathbf{S})$ -interacting	$V_\mu(g_\chi J_{V,\chi}^\mu + g_\psi(J_{\text{mdm},\psi}^\mu + \kappa J_{V2,\psi}^\mu))$	$c_1^{(\psi)} = (1 + \kappa) \frac{q^2}{4m_\phi^2} \frac{g_\chi g_\psi}{q^2 + m_V^2}$ $c_3^{(\psi)} = \frac{g_\chi g_\psi}{q^2 + m_V^2}$ $c_4^{(\psi)} = \frac{q^2}{m_\chi m_\psi} \frac{g_\chi g_\psi}{q^2 + m_V^2}$ $c_6^{(\psi)} = -\frac{m_\psi}{m_\chi} \frac{g_\chi g_\psi}{q^2 + m_V^2}$	$N, S, L \otimes S$

Table 7.2: Benchmark models of spin- $\frac{1}{2}$ DM χ coupling to SM fermions $\psi = p, n, e$. Each model is matched onto the NR EFT by multiplying the currents $J_\chi J_\psi$ (defined in Table 7.1) and the mediator propagator, and accounting for in-medium effects (if present) according to Eq. (7.14). The leading order nonvanishing coefficients $c_i^{(\psi)}$ for the operators $\mathcal{O}_i^{(\psi)}$ (defined in Table 7.3) are listed in the second to last column. For the multipole DM models, $\delta\tilde{\mu}_\psi \equiv \tilde{\mu}_\psi - 1$ where $\tilde{\mu}_\psi$ is half the Landé g -factor of ψ ($\tilde{\mu}_p \simeq 2.8$, $\tilde{\mu}_n \simeq -1.9$, $\tilde{\mu}_e \simeq 1$). The last column lists the lattice degrees of freedom which enter the scattering potential, Eq. (7.30). All models can excite phonons, and models with S or L response generated by DM-electron coupling can also excite magnons.

For each UV model, the coefficients $c_i^{(\psi)}$ of the NR operators generated at leading order are given in Table 7.2. These coefficients contain all the information for constructing the lattice potential $\tilde{\mathcal{V}}_{ij}$ for a given DM model, and will be exploited below for computing the DM detection rate. The list of NR operators $\mathcal{O}_i^{(\psi)}$ is already familiar from previous works on the EFT for direct detection via nuclear recoils [60, 197, 316–319]. We list the operators up to linear order in \mathbf{v}^\perp (defined below in Eq. (7.13)) in Table 7.3 (grouped into four categories to be explained below), adopting the basis of Ref. [319]. These encompass all the operators generated at leading order in the benchmark models we consider here. The standard SI and SD interactions correspond to \mathcal{O}_1 and \mathcal{O}_4 , respectively.⁶ Other types of scalar mediators generate \mathcal{O}_6 , \mathcal{O}_{10} and \mathcal{O}_{11} . A well-motivated class of (hidden sector) models contain DM particles coupling to a vector mediator via a multipole moment, which in turn kinetically mixes with the photon (see e.g., Refs. [52–55, 58–60, 321]). We consider the electric dipole, magnetic dipole and anapole DM models, which generate \mathcal{O}_{11} , $\mathcal{O}_{1,4,5,6}$ and $\mathcal{O}_{8,9}$, respectively. Finally, Table 7.2 includes a model where a vector mediator couples to the SM fermion’s magnetic dipole moment J_{mdm}^μ , and as a result generates \mathcal{O}_3 . Among other things, this leads to a coupling to the SM fermion’s spin-orbit coupling, which can be the leading interaction if one simultaneously introduces a coupling to the “ $\mathcal{O}(q^2)$ vector current” J_{V2}^μ (see Table 7.1), with a coefficient (relative to J_{mdm}^μ) tuned to $\kappa = -1$ to cancel the standard SI interaction \mathcal{O}_1 .

⁶Note that the standard SD interaction cannot be realized with a light mediator. In that case the leading interaction is induced by longitudinal vector exchange, and is proportional to $J_{P,\chi} J_{P,\psi}$ rather than $J_{A,\chi}^\mu J_{A,\psi\mu}$.

Interaction Type	NR Operators	Point-like Response	Composite Response
Coupling to charge, \mathbf{v}^\perp - independent	$\mathcal{O}_1^{(\psi)} = \mathbb{1}$ $\mathcal{O}_{11}^{(\psi)} = \mathbf{S}_\chi \cdot \frac{i\mathbf{q}}{m_\psi}$	N	-
Coupling to charge, \mathbf{v}^\perp - dependent	$\mathcal{O}_5^{(\psi)} = \mathbf{S}_\chi \cdot \left(\frac{i\mathbf{q}}{m_\psi} \times \mathbf{v}^\perp \right)$ $\mathcal{O}_8^{(\psi)} = \mathbf{S}_\chi \cdot \mathbf{v}^\perp$	N	L
Coupling to spin, \mathbf{v}^\perp - independent	$\mathcal{O}_4^{(\psi)} = \mathbf{S}_\chi \cdot \mathbf{S}_\psi$ $\mathcal{O}_6^{(\psi)} = \left(\mathbf{S}_\chi \cdot \frac{\mathbf{q}}{m_\psi} \right) \left(\mathbf{S}_\psi \cdot \frac{\mathbf{q}}{m_\psi} \right)$ $\mathcal{O}_9^{(\psi)} = \mathbf{S}_\chi \cdot \left(\mathbf{S}_\psi \times \frac{i\mathbf{q}}{m_\psi} \right)$ $\mathcal{O}_{10}^{(\psi)} = \mathbf{S}_\psi \cdot \frac{i\mathbf{q}}{m_\psi}$	S	-
Coupling to spin, \mathbf{v}^\perp - dependent	$\mathcal{O}_3^{(\psi)} = \mathbf{S}_\psi \cdot \left(\frac{i\mathbf{q}}{m_\psi} \times \mathbf{v}^\perp \right)$ $\mathcal{O}_7^{(\psi)} = \mathbf{S}_\psi \cdot \mathbf{v}^\perp$ $\mathcal{O}_{12}^{(\psi)} = \mathbf{S}_\chi \cdot \left(\mathbf{S}_\psi \times \mathbf{v}^\perp \right)$ $\mathcal{O}_{13}^{(\psi)} = \left(\mathbf{S}_\chi \cdot \mathbf{v}^\perp \right) \left(\mathbf{S}_\psi \cdot \frac{i\mathbf{q}}{m_\psi} \right)$ $\mathcal{O}_{14}^{(\psi)} = \left(\mathbf{S}_\psi \cdot \mathbf{v}^\perp \right) \left(\mathbf{S}_\chi \cdot \frac{i\mathbf{q}}{m_\psi} \right)$ $\mathcal{O}_{15}^{(\psi)} = \left(\mathbf{S}_\chi \cdot \left(\frac{i\mathbf{q}}{m_\psi} \times \mathbf{v}^\perp \right) \right) \left(\mathbf{S}_\psi \cdot \frac{i\mathbf{q}}{m_\psi} \right)$	S	$L \otimes S$

Table 7.3: NR effective operators relevant for DM scattering defined in Eq. (7.11), organized into four categories, and the (point-like and composite) crystal responses generated. Here χ is the DM and ψ is a SM particle that can be the proton, neutron or electron. \mathbf{q} is the momentum transfer from the DM to the SM target. $\mathbf{v}^\perp \equiv \frac{\mathbf{P}}{2m_\chi} - \frac{\mathbf{K}}{2m_\psi}$, defined in Eq. (7.13), is the component of the relative velocity perpendicular to \mathbf{q} . Previous calculations [6–8, 28, 64] focused on phonon and magnon excitations via \mathbf{v}^\perp -independent couplings to charge and spin, corresponding to the first and third categories listed here. In this work we extend the calculations to all operators.

For kinematic conventions, we take

$$\mathbf{q} \equiv \mathbf{k}' - \mathbf{k} = \mathbf{p} - \mathbf{p}' \quad (7.12)$$

to denote the momentum transfer from the DM to the target, which agrees with Refs. [316, 319] but has an opposite sign compared to the definitions in Refs. [60, 197, 317, 318]. The other independent combination of momenta is

$$\mathbf{v}^\perp \equiv \frac{\mathbf{P}}{2m_\chi} - \frac{\mathbf{K}}{2m_\psi} = \mathbf{v} - \frac{\mathbf{k}}{m_\psi} - \frac{\mathbf{q}}{2\mu_{\chi\psi}}, \quad (7.13)$$

where $\mathbf{P} = \mathbf{p}' + \mathbf{p}$, $\mathbf{K} = \mathbf{k}' + \mathbf{k}$, and $\mu_{\chi\psi}$ is the reduced mass. Recall from the beginning of this section that we use $\mathbf{v} = \frac{\mathbf{p}}{m_\chi}$ for the incoming DM's velocity. So $\mathbf{v} - \frac{\mathbf{k}}{m_\psi}$ in Eq. (7.13) is the relative velocity, and \mathbf{v}^\perp is the component of the relative velocity perpendicular to the momentum transfer, $\mathbf{q} \cdot \mathbf{v}^\perp = 0$. Note that Eq. (7.13) reduces to the familiar relation with $\mathbf{k} = \mathbf{0}$ for DM scattering off a target particle at rest; the term proportional to \mathbf{k} accounts for motions of the initial state $\psi = p, n, e$, and will be important for deriving DM-ion scattering potentials below.

We also note that, in the case of a vector mediator coupling to the electron's vector current $J_{V,e}^\mu$, in-medium screening effects modify the effective couplings to the proton and electron [7, 10, 29, 144, 182]. For NR scattering via the N response, e.g., standard SI interactions, this amounts to replacing

$$g_p \rightarrow g_p^{\text{eff}} = g_p + \left(1 - \frac{\mathbf{q}^2}{\mathbf{q} \cdot \boldsymbol{\varepsilon} \cdot \mathbf{q}}\right) g_e, \quad g_e \rightarrow g_e^{\text{eff}} = \frac{\mathbf{q}^2}{\mathbf{q} \cdot \boldsymbol{\varepsilon} \cdot \mathbf{q}} g_e, \quad (7.14)$$

where $\boldsymbol{\varepsilon}$ is the dielectric tensor, and $g_{p,e}$ are the tree-level (unscreened) couplings, as shown in Refs. [7, 10]. The same is true for a scalar mediator coupling to the electron's scalar current $J_{S,e}$ [44]. For single phonon and magnon excitations below the electronic band gap that we focus on in this work, one can use the high-frequency dielectric $\boldsymbol{\varepsilon}_\infty$, which captures the screening due to fast electron responses [7, 28, 322].

We will study the reach phonon and magnon detectors have to these benchmark models in Sec. 7.3, after developing the formalism of rate calculations within the EFT in the rest of this section.

Matching Effective Operators Onto Lattice Degrees of Freedom

We now match the effective operators $\mathcal{O}_i^{(\psi)}$ onto lattice degrees of freedom (highlighted for clarity) that appear in the DM-ion scattering potentials $\tilde{\mathcal{V}}_{lj}$. In Table 7.3, we have organized the operators into four categories, according to whether $\mathcal{O}_i^{(\psi)} \propto \mathbb{1}_\psi$ (“coupling to charge”)

or $\mathcal{O}_i^{(\psi)} \propto \mathbf{S}_\psi$ (“coupling to spin”), and whether the operator involves \mathbf{v}^\perp . Since our focus is light DM that evades conventional searches via nuclear recoils and electronic excitations, we will work in the long wavelength limit, where the momentum transfer is small compared to the inverse ionic radius (corresponding to $m_\chi \lesssim 10$ MeV), so at leading order, the only relevant degrees of freedom are those that characterize the ion as a whole. Intuitively, we expect couplings to charge and spin of a constituent particle $\psi = p, n, e$ to match onto couplings to the total number $\langle N_\psi \rangle$ and spin $\langle \mathbf{S}_\psi \rangle$ of that particle, respectively. These are point-like degrees of freedom that do not involve the internal motions of the ion constituents; they are the only degrees of freedom to which DM couples if the operator is velocity-independent. On the other hand, velocity-dependent operators are expected to couple DM to the motion of ψ particles inside an ion, manifest as the total orbital angular momenta $\langle \mathbf{L}_\psi \rangle$ and spin-orbit couplings $\langle \mathbf{L}_\psi \otimes \mathbf{S}_\psi \rangle$, which are “composite” degrees of freedom. In the rest of this subsection, we will see concretely how these intuitive expectations are borne out. The final result of this calculation is the lattice potential in terms of the NR EFT operator coefficients $c_i^{(\psi)}$, given below in Eq. (7.30).

Since the calculation proceeds in much the same way for all operators in the same category, to avoid tedious repetition we pick one operator from each category to explain the procedure: $\mathcal{O}_1^{(\psi)}$, $\mathcal{O}_8^{(\psi)}$, $\mathcal{O}_4^{(\psi)}$ and $\mathcal{O}_3^{(\psi)}$, with ψ taken to be one of p, n, e . To obtain the DM-ion scattering potentials $\tilde{\mathcal{V}}_{lj}$, we need to compute the matrix elements of these operators between the incoming and outgoing states of the DM-ion system. Since the initial and final DM states are plane waves, the DM part of the matrix element simply yields a phase factor, so

$$\begin{aligned} \tilde{\mathcal{V}}_{lj}(-\mathbf{q}, \mathbf{v}) \supset \sum_{\alpha} \left[c_1^{(\psi)} \langle e^{i\mathbf{q}\cdot\mathbf{x}_\alpha} \rangle_{lj} + c_4^{(\psi)} \mathbf{S}_\chi \cdot \langle e^{i\mathbf{q}\cdot\mathbf{x}_\alpha} \mathbf{S}_{\psi,\alpha} \rangle_{lj} \right. \\ \left. + c_8^{(\psi)} \mathbf{S}_\chi \cdot \langle e^{i\mathbf{q}\cdot\mathbf{x}_\alpha} \mathbf{v}_\alpha^\perp \rangle_{lj} + c_3^{(\psi)} \frac{i\mathbf{q}}{m_\psi} \cdot \langle e^{i\mathbf{q}\cdot\mathbf{x}_\alpha} \mathbf{v}_\alpha^\perp \times \mathbf{S}_{\psi,\alpha} \rangle_{lj} \right], \end{aligned} \quad (7.15)$$

where α runs over all the ψ fermions associated with the ion labeled by l, j , and $\langle \cdot \rangle$ represents the ionic expectation value (assuming the ionic state is unchanged for the low energy depositions of interest). Computing these expectation values in full generality is a tedious task that involves numerical integration over nuclear and electronic wavefunctions. However, the calculation is dramatically simplified in the long wavelength limit of interest here, where we can expand $e^{i\mathbf{q}\cdot\mathbf{x}_\alpha} = 1 + i\mathbf{q}\cdot\mathbf{x}_\alpha + \dots$ and keep just the leading nonvanishing terms. In the following two paragraphs, we discuss in turn the \mathbf{v}^\perp -independent operators $\mathcal{O}_1^{(\psi)}$, $\mathcal{O}_4^{(\psi)}$ (first line of Eq. (7.15)) and the \mathbf{v}^\perp -dependent operators $\mathcal{O}_8^{(\psi)}$, $\mathcal{O}_3^{(\psi)}$ (second line of Eq. (7.15)).

a) **\mathbf{v}^\perp -independent operators:** $\mathcal{O}_1^{(\psi)}, \mathcal{O}_4^{(\psi)}$. For these, it is sufficient to set $e^{i\mathbf{q}\cdot\mathbf{x}_\alpha} \rightarrow 1$:

$$c_1^{(\psi)} \sum_{\alpha} \langle e^{i\mathbf{q}\cdot\mathbf{x}_\alpha} \rangle_{lj} \simeq c_1^{(\psi)} \sum_{\alpha} \langle 1 \rangle_{lj} = c_1^{(\psi)} \langle N_\psi \rangle_{lj}, \quad (7.16)$$

$$c_4^{(\psi)} \mathbf{S}_\chi \cdot \sum_{\alpha} \langle e^{i\mathbf{q}\cdot\mathbf{x}_\alpha} \mathbf{S}_{\psi,\alpha} \rangle_{lj} \simeq c_4^{(\psi)} \mathbf{S}_\chi \cdot \sum_{\alpha} \langle \mathbf{S}_{\psi,\alpha} \rangle_{lj} = c_4^{(\psi)} \mathbf{S}_\chi \cdot \langle \mathbf{S}_\psi \rangle_{lj}. \quad (7.17)$$

So we obtain, respectively, the expectation values of the number and total spin of ψ particles for ion l, j , as one would expect for the lowest order ‘‘coupling to charge’’ ($\mathcal{O}_1^{(\psi)}$) and ‘‘coupling to spin’’ ($\mathcal{O}_4^{(\psi)}$) operators. Note that $\langle \mathbf{S}_\psi \rangle_{lj}$ should not be confused with the total nuclear or ionic spin, which may also contain orbital angular momentum components. We will see in the next subsection that the total ionic spin (from electrons) is relevant for magnon excitations, and we will need to work out its decomposition into spin and orbital components (see Eq. (7.36) below); the total nuclear spin, on the other hand, does not enter the calculation of phonon or magnon excitations.

b) **\mathbf{v}^\perp -dependent operators:** $\mathcal{O}_8^{(\psi)}, \mathcal{O}_3^{(\psi)}$. We can write \mathbf{v}_α^\perp as

$$\mathbf{v}_\alpha^\perp = \mathbf{v} - \frac{\mathbf{q}}{2m_\chi} - \frac{(\mathbf{k} + \mathbf{k}')_\alpha}{2m_\psi} = \mathbf{v} - \frac{\mathbf{q}}{2m_\chi} + \frac{i}{2m_\psi} \overleftrightarrow{\nabla}_\alpha, \quad (7.18)$$

where $\mathbf{v} = \frac{\mathbf{p}}{m_\chi}$ is the incoming DM’s velocity. The first two terms do not act on the ψ wavefunctions, so just as in the \mathbf{v}^\perp -independent case,

$$\sum_{\alpha} \left\langle e^{i\mathbf{q}\cdot\mathbf{x}_\alpha} \left(\mathbf{v} - \frac{\mathbf{q}}{2m_\chi} \right) \right\rangle_{lj} \simeq \left(\mathbf{v} - \frac{\mathbf{q}}{2m_\chi} \right) \sum_{\alpha} \langle 1 \rangle_{lj} = \left(\mathbf{v} - \frac{\mathbf{q}}{2m_\chi} \right) \langle N_\psi \rangle_{lj}, \quad (7.19)$$

$$\begin{aligned} \sum_{\alpha} \left\langle e^{i\mathbf{q}\cdot\mathbf{x}_\alpha} \left(\mathbf{v} - \frac{\mathbf{q}}{2m_\chi} \right) \times \mathbf{S}_{\psi,\alpha} \right\rangle_{lj} &\simeq \left(\mathbf{v} - \frac{\mathbf{q}}{2m_\chi} \right) \times \sum_{\alpha} \langle \mathbf{S}_{\psi,\alpha} \rangle_{lj} \\ &= \left(\mathbf{v} - \frac{\mathbf{q}}{2m_\chi} \right) \times \langle \mathbf{S}_\psi \rangle_{lj}. \end{aligned} \quad (7.20)$$

The last term in Eq. (7.18), on the other hand, is the probability current operator, $\mathbf{j}_\alpha = \frac{i}{2m_\psi} \overleftrightarrow{\nabla}_\alpha$. The treatment of this term is analogous to the nuclear recoil calculation [197]. First, we note that the expectation value of \mathbf{j}_α is zero; assuming the ionic states are energy eigenstates implies that the probability density is constant in time, and therefore by the continuity equation, $\partial_i \langle j_\alpha^i \rangle_{lj} = 0$. This means that j_α^i can be written as a total derivative, $j_\alpha^i = \partial_k (x_\alpha^i j_\alpha^k)$, and therefore has vanishing expectation value. The leading contribution then comes from expanding the $e^{i\mathbf{q}\cdot\mathbf{x}_\alpha}$ to the next order in \mathbf{q} :

$$\sum_{\alpha} \langle e^{i\mathbf{q}\cdot\mathbf{x}_\alpha} \mathbf{j}_\alpha \rangle_{lj} \simeq i \sum_{\alpha} \langle (\mathbf{q} \cdot \mathbf{x}_\alpha) \mathbf{j}_\alpha \rangle_{lj}, \quad (7.21)$$

$$\sum_{\alpha} \langle e^{i\mathbf{q}\cdot\mathbf{x}_\alpha} \mathbf{j}_\alpha \times \mathbf{S}_{\psi,\alpha} \rangle_{lj} \simeq i \sum_{\alpha} \langle (\mathbf{q} \cdot \mathbf{x}_\alpha) \mathbf{j}_\alpha \times \mathbf{S}_{\psi,\alpha} \rangle_{lj}. \quad (7.22)$$

To go further, we note that $\langle x_\alpha^i j_\alpha^k \rangle_{lj}$ is anti-symmetric in $i \leftrightarrow k$ since the symmetric part can be written as a total derivative, $x_\alpha^i j_\alpha^k + x_\alpha^k j_\alpha^i = \partial_{i'}(x_\alpha^i x_\alpha^k j_\alpha^{i'})$ and therefore has vanishing expectation value. Expanding the anti-symmetric part gives

$$\langle x_\alpha^i j_\alpha^k \rangle_{lj} = \frac{1}{2} \langle x_\alpha^i j_\alpha^k - x_\alpha^k j_\alpha^i \rangle_{lj} = \frac{i}{4m_\psi} \left(\langle x_\alpha^i \vec{\nabla}_\alpha^k \rangle_{lj} - \langle x_\alpha^i \overleftarrow{\nabla}_\alpha^k \rangle_{lj} - \langle x_\alpha^k \vec{\nabla}_\alpha^i \rangle_{lj} + \langle x_\alpha^k \overleftarrow{\nabla}_\alpha^i \rangle_{lj} \right), \quad (7.23)$$

which after integration by parts can be simplified to

$$\langle x_\alpha^i j_\alpha^k \rangle_{lj} = \frac{i}{2m_\psi} \langle x^i \vec{\nabla}_\alpha^k - x^k \vec{\nabla}_\alpha^i \rangle_{lj} = -\frac{1}{2m_\psi} \epsilon_{ikk'} \langle L_\alpha^{k'} \rangle_{lj}, \quad (7.24)$$

where \mathbf{L}_α is the angular momentum operator. We therefore have

$$\begin{aligned} \sum_\alpha \langle e^{i\mathbf{q}\cdot\mathbf{x}_\alpha} \mathbf{j}_\alpha \rangle_{lj} &\simeq \frac{i\mathbf{q}}{2m_\psi} \times \sum_\alpha \langle \mathbf{L}_{\psi,\alpha} \rangle_{lj} = \frac{i\mathbf{q}}{2m_\psi} \times \langle \mathbf{L}_\psi \rangle_{lj}, \quad (7.25) \\ \sum_\alpha \langle e^{i\mathbf{q}\cdot\mathbf{x}_\alpha} \mathbf{j}_\alpha \times \mathbf{S}_{\psi,\alpha} \rangle_{lj} &\simeq \frac{i}{2m_\psi} \sum_\alpha \langle (\mathbf{q} \times \mathbf{L}_{\psi,\alpha}) \times \mathbf{S}_{\psi,\alpha} \rangle_{lj} \\ &= \frac{i}{2m_\psi} \left(\sum_\alpha \langle \mathbf{L}_{\psi,\alpha} \otimes \mathbf{S}_{\psi,\alpha} \rangle_{lj} \cdot \mathbf{q} - \sum_\alpha \langle \mathbf{L}_{\psi,\alpha} \cdot \mathbf{S}_{\psi,\alpha} \rangle_{lj} \mathbf{q} \right) \\ &= \frac{i}{2m_\psi} \left(\langle \mathbf{L}_\psi \otimes \mathbf{S}_\psi \rangle_{lj} \cdot \mathbf{q} - \langle \mathbf{L}_\psi \cdot \mathbf{S}_\psi \rangle_{lj} \mathbf{q} \right) \\ &= \frac{i}{2m_\psi} \left[\langle \mathbf{L}_\psi \otimes \mathbf{S}_\psi \rangle_{lj} \cdot \mathbf{q} - \text{tr}(\langle \mathbf{L}_\psi \otimes \mathbf{S}_\psi \rangle_{lj}) \mathbf{q} \right]. \quad (7.26) \end{aligned}$$

where

$$\langle \langle \mathbf{L}_\psi \otimes \mathbf{S}_\psi \rangle_{lj} \rangle^{ik} = \langle L_\psi^i S_\psi^k \rangle_{lj} \equiv \sum_\alpha \langle L_{\psi,\alpha}^i S_{\psi,\alpha}^k \rangle_{lj} \quad (7.27)$$

are Cartesian components of the spin-orbit coupling tensor. Combining these with Eqs. (7.19) and (7.20), we finally obtain

$$c_8^{(\psi)} \mathbf{S}_\chi \cdot \sum_\alpha \langle e^{i\mathbf{q}\cdot\mathbf{x}_\alpha} \mathbf{v}_\alpha^\perp \rangle_{lj} = c_8^{(\psi)} \mathbf{S}_\chi \cdot \left[\left(\mathbf{v} - \frac{\mathbf{q}}{2m_\chi} \right) \langle \mathbf{N}_\psi \rangle_{lj} + \frac{i\mathbf{q}}{2m_\psi} \times \langle \mathbf{L}_\psi \rangle_{lj} \right], \quad (7.28)$$

$$\begin{aligned} c_3^{(\psi)} \frac{i\mathbf{q}}{m_\psi} \cdot \sum_\alpha \langle e^{i\mathbf{q}\cdot\mathbf{x}_\alpha} \mathbf{v}_\alpha^\perp \times \mathbf{S}_{\psi,\alpha} \rangle_{lj} \\ = c_3^{(\psi)} \left[\left(\frac{i\mathbf{q}}{m_\psi} \times \mathbf{v} \right) \cdot \langle \mathbf{S}_\psi \rangle_{lj} + \frac{1}{2m_\psi^2} (\mathbf{q}^2 \delta^{ik} - q^i q^k) \langle \langle \mathbf{L}_\psi \otimes \mathbf{S}_\psi \rangle_{lj} \rangle^{ik} \right]. \quad (7.29) \end{aligned}$$

As alluded to previously, the \mathbf{v}^\perp -dependent operators $\mathcal{O}_8^{(\psi)}$ and $\mathcal{O}_3^{(\psi)}$ induce DM couplings to not only the number and total spin of ψ particles, but also their total orbital angular momentum and spin-orbit coupling.

We can carry out the same calculation for the other operators in Table 7.3. The result is

$$\begin{aligned}
\tilde{\mathcal{V}}_{lj}(-\mathbf{q}, \mathbf{v}) = & \sum_{\psi=p,n,e} c_1^{(\psi)} \langle N_\psi \rangle_{lj} \\
& + c_3^{(\psi)} \left[-\frac{i\mathbf{q}}{m_\psi} \mathbf{v}' \cdot (\hat{\mathbf{q}} \times \langle \mathbf{S}_\psi \rangle_{lj}) + \frac{q^2}{2m_\psi^2} (\delta^{ik} - \hat{q}^i \hat{q}^k) (\langle \mathbf{L}_\psi \otimes \mathbf{S}_\psi \rangle_{lj})^{ik} \right] \\
& + c_4^{(\psi)} \mathbf{S}_\chi \cdot \langle \mathbf{S}_\psi \rangle_{lj} \\
& + c_5^{(\psi)} \left[\frac{i\mathbf{q}}{m_\psi} \cdot (\mathbf{v}' \times \mathbf{S}_\chi) \langle N_\psi \rangle_{lj} + \frac{q^2}{2m_\psi^2} \mathbf{S}_\chi \cdot (\mathbb{1} - \hat{\mathbf{q}}\hat{\mathbf{q}}) \cdot \langle \mathbf{L}_\psi \rangle_{lj} \right] \\
& + c_6^{(\psi)} \frac{q^2}{m_\psi^2} (\hat{\mathbf{q}} \cdot \mathbf{S}_\chi) (\hat{\mathbf{q}} \cdot \langle \mathbf{S}_\psi \rangle_{lj}) \\
& + c_7^{(\psi)} \left[\mathbf{v}' \cdot \langle \mathbf{S}_\psi \rangle_{lj} + \epsilon^{ikk'} \frac{iq^{k'}}{2m_\chi} (\langle \mathbf{L}_\psi \otimes \mathbf{S}_\psi \rangle_{lj})^{ik} \right] \\
& + c_8^{(\psi)} \left[(\mathbf{v}' \cdot \mathbf{S}_\chi) \langle N_\psi \rangle_{lj} + \frac{i\mathbf{q}}{2m_\psi} \mathbf{S}_\chi \cdot (\hat{\mathbf{q}} \times \langle \mathbf{L}_\psi \rangle_{lj}) \right] \\
& + c_9^{(\psi)} \frac{i\mathbf{q}}{m_\psi} \mathbf{S}_\chi \cdot (\langle \mathbf{S}_\psi \rangle_{lj} \times \hat{\mathbf{q}}) \\
& + c_{10}^{(\psi)} \frac{i\mathbf{q}}{m_\psi} \cdot \langle \mathbf{S}_\psi \rangle_{lj} \\
& + c_{11}^{(\psi)} \frac{i\mathbf{q}}{m_\psi} \cdot \mathbf{S}_\chi \langle N_\psi \rangle_{lj} \\
& + c_{12}^{(\psi)} \left[(\mathbf{v}' \times \mathbf{S}_\chi) \cdot \langle \mathbf{S}_\psi \rangle_{lj} + \frac{i\mathbf{q}}{2m_\psi} ((\hat{\mathbf{q}} \cdot \mathbf{S}_\chi) \delta^{ik} - \hat{q}^k S_\chi^i) (\langle \mathbf{L}_\psi \otimes \mathbf{S}_\psi \rangle_{lj})^{ik} \right] \\
& + c_{13}^{(\psi)} \left[\frac{i\mathbf{q}}{m_\psi} (\mathbf{v}' \cdot \mathbf{S}_\chi) (\hat{\mathbf{q}} \cdot \langle \mathbf{S}_\psi \rangle_{lj}) + \frac{q^2}{2m_\psi^2} (\hat{\mathbf{q}} \times \mathbf{S}_\chi) \cdot \langle \mathbf{L}_\psi \otimes \mathbf{S}_\psi \rangle_{lj} \cdot \hat{\mathbf{q}} \right] \\
& + c_{14}^{(\psi)} \left[\frac{i\mathbf{q}}{m_\psi} (\hat{\mathbf{q}} \cdot \mathbf{S}_\chi) (\mathbf{v}' \cdot \langle \mathbf{S}_\psi \rangle_{lj}) - \epsilon^{ikk'} \frac{q^2}{2m_\psi^2} \hat{q}^{k'} (\hat{\mathbf{q}} \cdot \mathbf{S}_\chi) (\langle \mathbf{L}_\psi \otimes \mathbf{S}_\psi \rangle_{lj})^{ik} \right] \\
& + c_{15}^{(\psi)} \left[-\frac{q^2}{m_\psi^2} (\hat{\mathbf{q}} \cdot (\mathbf{v}' \times \mathbf{S}_\chi)) (\hat{\mathbf{q}} \cdot \langle \mathbf{S}_\psi \rangle_{lj}) \right. \\
& \quad \left. + \frac{iq^3}{2m_\psi^3} \mathbf{S}_\chi \cdot (\mathbb{1} - \hat{\mathbf{q}}\hat{\mathbf{q}}) \cdot \langle \mathbf{L}_\psi \otimes \mathbf{S}_\psi \rangle_{lj} \cdot \hat{\mathbf{q}} \right], \tag{7.30}
\end{aligned}$$

where

$$\mathbf{v}' \equiv \mathbf{v} - \frac{\mathbf{q}}{2m_\chi}. \tag{7.31}$$

and summation over repeated Cartesian indices is implicit. Here and in what follows, we denote $q \equiv |\mathbf{q}|$ (so that $q^2 \equiv \mathbf{q}^2 \neq q^\mu q_\mu$), and $\hat{\mathbf{q}} \equiv \mathbf{q}/q$.

To summarize, in the long wavelength limit, the DM-ion scattering potential $\tilde{\mathcal{V}}_{lj}$ involves a set of quantities that characterize properties of the ion: the total numbers $\langle N_\psi \rangle$, spins $\langle \mathbf{S}_\psi \rangle$ and orbital angular momenta $\langle \mathbf{L}_\psi \rangle$ of the constituent particles $\psi = p, n, e$, as well as the spin-orbit coupling tensors $\langle \mathbf{L}_\psi \otimes \mathbf{S}_\psi \rangle$. We will refer to these as different types of *crystal responses*, as DM couplings to these quantities drive collective excitations in the crystal; they play a similar role to the nuclear responses in nuclear recoil calculations (which similarly reduce to the total nucleon numbers, spins, etc. in the long wavelength limit [60, 197, 317, 318]). We emphasize, however, that in contrast to standard nuclear recoil where nuclei are treated as free – a valid approximation at energy depositions $\gtrsim 500$ meV [7] – collective excitations arise in a lower energy regime where inter-ionic interactions become important; the EFT therefore involves different degrees of freedom and the calculation proceeds differently.⁷ We will sometimes abbreviate the crystal responses introduced above as N , S , L , $L \otimes S$, or simply N , S , L , $L \otimes S$, when there is no confusion. The crystal responses generated by each NR operator and in each benchmark DM model have been summarized in Tables 7.3 and 7.2, respectively.

We reiterate that, among the four types of crystal responses, $\langle N_\psi \rangle$ and $\langle \mathbf{S}_\psi \rangle$ are induced by DM couplings to point-like ionic degrees of freedom (which do not involve internal motions of nucleons or electrons inside an ion), while $\langle \mathbf{L}_\psi \rangle$ and $\langle \mathbf{L}_\psi \otimes \mathbf{S}_\psi \rangle$ are induced by DM couplings to composite degrees of freedom. We therefore refer to them as point-like and composite responses respectively. Velocity-independent operators (first and third categories in Table 7.3) generate only point-like responses, while velocity-dependent operators (second and fourth categories in Table 7.3) can also generate the corresponding composite responses. It is worth noting that for the velocity-dependent operators that generate both point-like and composite responses – \mathcal{O}_3 , \mathcal{O}_5 , \mathcal{O}_8 , $\mathcal{O}_{12,\dots,15}$ – the ratio of composite versus point-like responses (i.e., coefficients of $\langle \mathbf{L}_\psi \rangle$ versus $\langle N_\psi \rangle$, or $\langle \mathbf{L}_\psi \otimes \mathbf{S}_\psi \rangle$ versus $\langle \mathbf{S}_\psi \rangle$ in Eq. (7.30)) is, parametrically, $\frac{q}{m_\psi v}$. This is generic, as point-like and composite responses result from the leading two terms in the expansion $e^{i\mathbf{q}\cdot\mathbf{x}_\alpha} = 1 + i\mathbf{q}\cdot\mathbf{x}_\alpha + \dots$, and $qx \sim \frac{q}{m_\psi v}L$, with $L \sim \mathcal{O}(1)$. For nuclear recoils, $\frac{q}{m_\psi v} \sim \frac{\mu_{\chi N}}{m_{p,n}}$ with $\mu_{\chi N}$ the reduced mass of the DM and the target nucleus, so composite responses can be significant, as emphasized in Refs. [60, 317]. In contrast, in the present case of collective excitations induced by light DM, we have $\frac{q}{m_\psi v} \lesssim \frac{m_\chi}{m_\psi}$. For couplings to nucleons, $\psi = p, n$, this ratio is always smaller than one for sub-GeV DM, so for a given

⁷Technically, Refs. [197, 317] defined a few “nuclear response functions,” $W_M^{\tau\tau'}$, $W_{\Sigma'}^{\tau\tau'}$ etc., which the nuclear recoil rate is proportional to, from the unpolarized average of nuclear matrix element squared. No such averaging is involved in the calculation of collective excitations, and the rate formulae derived below do not depend on the same functions $W_M^{\tau\tau'}$, $W_{\Sigma'}^{\tau\tau'}$ etc. even in the absence of coupling to electrons. Here we are simply borrowing the terminology “response” in the sense that it refers to a type of coupling, just as M , Σ' , etc., usually called “nuclear responses,” are different types of couplings to the nucleus.

type of excitation, point-like responses tend to dominate; for couplings to electrons, $\psi = e$, both point-like and composite responses, if present, can be important. From the bottom-up point of view, it is useful to keep in mind this interplay between point-like and composite responses for the purpose of organizing the effects of various operators, although from the top-down point of view, it seems difficult to construct well-motivated simple models that dominantly generate a composite response (L or $L \otimes S$) without being accompanied by a point-like response (N or S) of at least comparable size, similar to the case of nuclear recoil as highlighted in Ref. [60]. We will elaborate on this in Sec. 7.3.

Quantization of Lattice Potential for Phonons and Magnons

Now that we have obtained $\tilde{\mathcal{V}}_{lj}$ in terms of the lattice degrees of freedom, Eq. (7.30), it remains to compute the matrix elements

$$\langle \nu, \mathbf{k} | \tilde{\mathcal{V}}(-\mathbf{q}, \mathbf{v}) | 0 \rangle = \sum_{l,j} \langle \nu, \mathbf{k} | e^{i\mathbf{q} \cdot \mathbf{x}_{lj}} \tilde{\mathcal{V}}_{lj}(-\mathbf{q}, \mathbf{v}) | 0 \rangle \quad (7.32)$$

by quantizing the lattice potential in terms of phonon or magnon modes. The simplest cases, where phonon excitations in a crystal proceed through $\langle N_\psi \rangle$ (via the SI operator $\mathcal{O}_1 = \mathbb{1}$) and magnon excitations proceed through $\langle S_e \rangle$ were considered previously in Refs. [6, 7, 28, 64] and Ref. [8], respectively. Here we extend those calculations to include all four crystal responses ($\langle N_\psi \rangle$, $\langle S_\psi \rangle$, $\langle L_\psi \rangle$, $\langle L_\psi \otimes S_\psi \rangle$) identified in the previous subsection, which can be generated by the full set of effective operators.

Phonons arise from the ions' displacements with respect to their equilibrium positions \mathbf{x}_{lj}^0 :

$$\mathbf{u}_{lj} = \mathbf{x}_{lj} - \mathbf{x}_{lj}^0 = \sum_{\nu=1}^{3n} \sum_{\mathbf{k} \in \text{1BZ}} \frac{1}{\sqrt{2Nm_j\omega_{\nu,\mathbf{k}}}} \left(\hat{a}_{\nu,\mathbf{k}} \boldsymbol{\epsilon}_{\nu,\mathbf{k},j} e^{i\mathbf{k} \cdot \mathbf{x}_{lj}^0} + \hat{a}_{\nu,\mathbf{k}}^\dagger \boldsymbol{\epsilon}_{\nu,\mathbf{k},j}^* e^{-i\mathbf{k} \cdot \mathbf{x}_{lj}^0} \right). \quad (7.33)$$

Recall that N (without subscript, not to be confused with $\langle N_\psi \rangle$) is the total number of primitive cells in the crystal lattice, to be sent to infinity at the end of the calculation. The phonon creation and annihilation operators satisfy the canonical commutation relations, $[\hat{a}_{\nu,\mathbf{k}}, \hat{a}_{\nu',\mathbf{k}'}^\dagger] = \delta_{\nu\nu'} \delta_{\mathbf{k},\mathbf{k}'}$ with all others vanishing. The eigenenergies $\omega_{\nu,\mathbf{k}}$ and eigenvectors $\boldsymbol{\epsilon}_{\nu,\mathbf{k},j}$ (normalized such that $\sum_j |\boldsymbol{\epsilon}_{\nu,\mathbf{k},j}|^2 = 1$) are solved for by diagonalizing the quadratic crystal potential. The quadratic crystal potential, and equilibrium positions, are computed with DFT [294] (see Refs. [6, 28] for details) and the diagonalization is performed with phonopy [50]. At leading order, dependence of the matrix element in Eq. (7.32) on \mathbf{u}_{lj} comes only from the phase factor $e^{i\mathbf{q} \cdot \mathbf{x}_{lj}}$; we assume the DM-ion scattering potentials $\tilde{\mathcal{V}}_{lj}(-\mathbf{q}, \mathbf{v})$ are not significantly affected by ionic displacements and can thus be pulled out of the matrix

element.⁸ Then, evaluating the matrix element of the phase factor, $\langle \nu, \mathbf{k} | e^{i\mathbf{q} \cdot \mathbf{x}_{lj}} | 0 \rangle$, follows the standard procedure of expanding \mathbf{x}_{lj} as in Eq. (7.33) and applying the Baker-Campbell-Hausdorff formula to normal-order the phonon creation and annihilation operators [7]. As a result,

$$\langle \nu, \mathbf{k} | \tilde{\mathcal{V}}(-\mathbf{q}, \mathbf{v}) | 0 \rangle = \frac{1}{\sqrt{N}} \sum_{\nu, \mathbf{k}, j} \left[\sum_l \tilde{\mathcal{V}}_{lj}(-\mathbf{q}, \mathbf{v}) e^{i(\mathbf{q}-\mathbf{k}) \cdot \mathbf{x}_{lj}^0} \right] e^{-W_j(\mathbf{q})} \frac{i(\mathbf{q} \cdot \boldsymbol{\epsilon}_{\nu, \mathbf{k}, j}^*)}{\sqrt{2m_j \omega_{\nu, \mathbf{k}}}}, \quad (7.34)$$

where $W_j(\mathbf{q}) = \frac{1}{4Nm_j} \sum_{\nu, \mathbf{k}} \frac{|\mathbf{q} \cdot \boldsymbol{\epsilon}_{\nu, \mathbf{k}, j}|^2}{\omega_{\nu, \mathbf{k}}}$ is the Debye-Waller factor. Crucially, the $\frac{1}{\sqrt{N}}$ factor (which originates from Eq. (7.33) and is to be squared when computing the rate), together with the prefactor $\frac{1}{\sqrt{V}}$ in the rate formula Eq. (7.5), indicates that the rate Γ would scale as $\frac{1}{N^2} \rightarrow 0$ *unless* the l sum in Eq. (7.34) scales with N . This in turn requires the N terms in the l sum to add up coherently, which is possible only when *i*) the phonon momentum \mathbf{k} matches the momentum transfer \mathbf{q} up to reciprocal lattice vectors, which is the statement of lattice momentum conservation, and *ii*) $\sum_l \tilde{\mathcal{V}}_{lj} \sim N$, i.e., the DM couples coherently across the crystal lattice. The second requirement is trivially satisfied for DM couplings to the scalar quantities $\langle N_\psi \rangle$, $\text{tr}(\langle \mathbf{L}_\psi \otimes \mathbf{S}_\psi \rangle)$. For couplings to the vector and tensor quantities $\langle \mathbf{S}_\psi \rangle$, $\langle \mathbf{L}_\psi \rangle$, $\langle \mathbf{L}_\psi \otimes \mathbf{S}_\psi \rangle$ (modulo the trace part), on the other hand, coherence is possible only when they are ordered (or polarized), so that they point in the same directions in all primitive cells; in the case of $\langle \mathbf{S}_\psi \rangle$, this can be achieved by spontaneous magnetic ordering for $\psi = e$, or by applying an external magnetic field for $\psi = p, n$.

Up to possible small corrections due to the presence of different isotopes, we can set $\tilde{\mathcal{V}}_{lj} = \tilde{\mathcal{V}}_j$, which is independent of l . We then obtain the single phonon excitation rate:

$$\Gamma(\mathbf{v}) = \frac{1}{\Omega} \int \frac{d^3q}{(2\pi)^3} \sum_{\nu=1}^{3n} 2\pi \delta(\omega_{\nu, \mathbf{k}} - \omega_{\mathbf{q}}) \frac{1}{2\omega_{\nu, \mathbf{k}}} \left| \sum_j e^{-W_j(\mathbf{q})} e^{i\mathbf{G} \cdot \mathbf{x}_j^0} \frac{\mathbf{q} \cdot \boldsymbol{\epsilon}_{\nu, \mathbf{k}, j}^*}{\sqrt{m_j}} \tilde{\mathcal{V}}_j(-\mathbf{q}, \mathbf{v}) \right|^2, \quad (7.35)$$

where Ω is the volume of the primitive cell, \mathbf{x}_j^0 is the equilibrium position of the j th ion with respect to the cell center, and it is implicit that $\mathbf{q} = \mathbf{k} + \mathbf{G}$ where \mathbf{G} is a reciprocal lattice vector. To map \mathbf{q} to a vector \mathbf{k} within the 1BZ, we first write $\mathbf{q} = \sum_{i=1}^3 a_i \mathbf{b}_i$, with \mathbf{b}_i the basis vectors of the reciprocal lattice, then construct a set of eight candidate \mathbf{G} vectors whose components in reduced coordinates take the floor and ceiling integer values of a_i , and finally choose the correct \mathbf{G} vector to be the one that minimizes $|\mathbf{q} - \mathbf{G}|$.

The DM-ion scattering potential $\tilde{\mathcal{V}}_j$ that enters Eq. (7.35) is simply given by Eq. (7.30) above, with the l subscripts dropped, assuming $\langle \mathbf{S}_\psi \rangle$, $\langle \mathbf{L}_\psi \rangle$, $\langle \mathbf{L}_\psi \otimes \mathbf{S}_\psi \rangle$ are ordered, as

⁸If $\tilde{\mathcal{V}}_{lj}$ receives contributions from DM-electron couplings, the scattering potential can depend on \mathbf{u}_{lj} directly, as ionic displacements distort the electron wavefunctions. This correction can be taken into account via the Born effective charges in the case of SI interactions in the long wavelength limit, as discussed in Ref. [7].

explained above; in the absence of ordering, the corresponding terms should be dropped (with $\langle \mathbf{L}_\psi \otimes \mathbf{S}_\psi \rangle$ set to its scalar component $\frac{1}{3} \text{tr}(\langle \mathbf{L}_\psi \otimes \mathbf{S}_\psi \rangle) \mathbb{1} = \frac{1}{3} \langle \mathbf{L}_\psi \cdot \mathbf{S}_\psi \rangle \mathbb{1}$). In the special case of SI interactions, one has only $c_1^{(\psi)}$, so $\tilde{V}_j = \sum_\psi c_1^{(\psi)} \langle N_\psi \rangle_j$, reproducing the results in Ref. [7], whereas in the full EFT, all four crystal responses can contribute to phonon excitations.

Next we move on to magnons. They are collective spin excitations in a magnetically ordered phase, and can thus respond to DM scattering only if the potentials \tilde{V}_{lj} depend on the magnetic ions' effective spins \mathbf{S}_{lj} . Generally, \mathbf{S}_{lj} can come from the electrons' spin and orbital angular momenta, $\langle \mathbf{S}_e \rangle_{lj}$ and $\langle \mathbf{L}_e \rangle_{lj}$, respectively. When projected onto the Hilbert space spanned by \mathbf{S}_{lj} , they become

$$\langle \mathbf{S}_e \rangle_{lj} \rightarrow \lambda_{S,j} \mathbf{S}_{lj}, \quad \langle \mathbf{L}_e \rangle_{lj} \rightarrow \lambda_{L,j} \mathbf{S}_{lj}, \quad (7.36)$$

where $\lambda_{S,j}$, $\lambda_{L,j}$ are numbers (which we will say more about shortly). Therefore, from Eq. (7.30) we obtain the matrix element for exciting a magnon mode $|\nu, \mathbf{k}\rangle$:

$$\langle \nu, \mathbf{k} | \tilde{\mathcal{V}}(-\mathbf{q}, \mathbf{v}) | 0 \rangle = \sum_{l,j} e^{i\mathbf{q} \cdot \mathbf{x}_{lj}} \mathbf{f}_j(-\mathbf{q}, \mathbf{v}) \cdot \langle \nu, \mathbf{k} | \mathbf{S}_{lj} | 0 \rangle, \quad (7.37)$$

where

$$\begin{aligned} \mathbf{f}_j(-\mathbf{q}, \mathbf{v}) = & \\ & \lambda_{S,j} \left[c_3^{(e)} \frac{i\mathbf{q}}{m_e} (\hat{\mathbf{q}} \times \mathbf{v}') + c_4^{(e)} \mathbf{S}_\chi + c_6^{(e)} \frac{q^2}{m_e^2} (\hat{\mathbf{q}} \cdot \mathbf{S}_\chi) \hat{\mathbf{q}} + c_7^{(e)} \mathbf{v}' + c_9^{(e)} \frac{i\mathbf{q}}{m_e} (\hat{\mathbf{q}} \times \mathbf{S}_\chi) + c_{10}^{(e)} \frac{i\mathbf{q}}{m_e} \right. \\ & \left. + c_{12}^{(e)} (\mathbf{v}' \times \mathbf{S}_\chi) + c_{13}^{(e)} \frac{i\mathbf{q}}{m_e} (\mathbf{v}' \cdot \mathbf{S}_\chi) + c_{14}^{(e)} \frac{i\mathbf{q}}{m_e} (\hat{\mathbf{q}} \cdot \mathbf{S}_\chi) \mathbf{v}' - c_{15}^{(e)} \frac{q^2}{m_e^2} (\hat{\mathbf{q}} \cdot (\mathbf{v}' \times \mathbf{S}_\chi)) \hat{\mathbf{q}} \right] \\ & + \frac{\lambda_{L,j}}{2} \left[c_5^{(e)} \frac{q^2}{m_e^2} (\mathbb{1} - \hat{\mathbf{q}}\hat{\mathbf{q}}) \cdot \mathbf{S}_\chi - c_8^{(e)} \frac{i\mathbf{q}}{m_e} (\hat{\mathbf{q}} \times \mathbf{S}_\chi) \right]. \end{aligned} \quad (7.38)$$

As in Eq. (7.30), we have defined $q \equiv |\mathbf{q}|$, $\hat{\mathbf{q}} \equiv \mathbf{q}/q$, and $\mathbf{v}' \equiv \mathbf{v} - \frac{\mathbf{q}}{2m_\chi}$.

Now we need to compute $\langle \nu, \mathbf{k} | \mathbf{S}_{lj} | 0 \rangle$. The calculation follows Ref. [8], which we encourage the reader to consult for more details. The magnetic order is captured by a set of rotation matrices \mathbf{R}_j that take each \mathbf{S}_{lj} to a local coordinate system where it points in the $+z$ direction:

$$\mathbf{S}_{lj} = \mathbf{R}_j \cdot \mathbf{S}'_{lj}, \quad \langle \mathbf{S}'_{lj} \rangle = (\langle S'^x_{lj} \rangle, \langle S'^y_{lj} \rangle, \langle S'^z_{lj} \rangle) = (0, 0, S_j). \quad (7.39)$$

We restrict ourselves to commensurate orders, in which case the rotation matrices \mathbf{R}_j do not depend on the primitive cell label l . We then apply the Holstein-Primakoff transformation and expand \mathbf{S}_{lj} around the ground state in terms of bosonic creation and annihilation operators:

$$S'^x_{lj} = (2S_j - \hat{a}_{lj}^\dagger \hat{a}_{lj})^{1/2} \hat{a}_{lj}, \quad S'^y_{lj} = \hat{a}_{lj}^\dagger (2S_j - \hat{a}_{lj}^\dagger \hat{a}_{lj})^{1/2}, \quad S'^z_{lj} = S_j - \hat{a}_{lj}^\dagger \hat{a}_{lj}. \quad (7.40)$$

Magnon eigenstates are obtained by diagonalizing the spin Hamiltonian, which is specific to the target material; in the simplest cases, the target can be modeled by Heisenberg exchange interactions $\mathbf{S}_{lj} \cdot \mathbf{S}_{l'j'}$ between neighboring sites, while more complicated model descriptions are needed in other cases. For a general spin Hamiltonian, the diagonalization can be achieved by a Bogoliubov transformation in momentum space:

$$\hat{a}_{lj} = \frac{1}{\sqrt{N}} \sum_{\mathbf{k} \in \text{1BZ}} \hat{a}_{j,\mathbf{k}} e^{i\mathbf{k} \cdot \mathbf{x}_{lj}}, \quad \begin{pmatrix} \hat{a}_{j,\mathbf{k}} \\ \hat{a}_{j,-\mathbf{k}}^\dagger \end{pmatrix} = \begin{pmatrix} \mathbb{U}_{j\nu,\mathbf{k}} & \mathbb{V}_{j\nu,\mathbf{k}} \\ \mathbb{V}_{j\nu,-\mathbf{k}}^* & \mathbb{U}_{j\nu,-\mathbf{k}}^* \end{pmatrix} \begin{pmatrix} \hat{b}_{j,\mathbf{k}} \\ \hat{b}_{j,-\mathbf{k}}^\dagger \end{pmatrix}, \quad (7.41)$$

where \mathbb{U}, \mathbb{V} are $n \times n$ matrices (with n the number of magnetic ions per cell), and $\hat{b}_{j,\mathbf{k}}, \hat{b}_{j,\mathbf{k}}^\dagger$ are the creation and annihilation operators for the magnon eigenstates satisfying canonical commutation relations, $[\hat{b}_{\nu,\mathbf{k}}, \hat{b}_{\nu',\mathbf{k}'}^\dagger] = \delta_{\nu\nu'} \delta_{\mathbf{k},\mathbf{k}'}$ with all others vanishing. An efficient algorithm for the diagonalization can be found in Ref. [268] (see also Refs. [5, 8]). Now computing the magnon excitation matrix element $\langle \nu, \mathbf{k} | \mathbf{S}_{lj} | 0 \rangle$, and hence the DM scattering rate, is reduced to standard algebra. We obtain [5, 8]

$$\Gamma(\mathbf{v}) = \frac{1}{\Omega} \int \frac{d^3q}{(2\pi)^3} \sum_{\nu=1}^n 2\pi \delta(\omega_{\nu,\mathbf{k}} - \omega_{\mathbf{q}}) \frac{1}{2} \left| \sum_j e^{i\mathbf{G} \cdot \mathbf{x}_j^0} \sqrt{S_j} (\mathbb{U}_{j\nu,\mathbf{k}}^* \mathbf{r}_j + \mathbb{V}_{j\nu,-\mathbf{k}} \mathbf{r}_j^*) \cdot \mathbf{f}_j(-\mathbf{q}, \mathbf{v}) \right|^2, \quad (7.42)$$

where $\mathbf{r}_j = (R_j^{xx}, R_j^{yx}, R_j^{zx}) + i(R_j^{xy}, R_j^{yy}, R_j^{zy})$. As in the phonon case, it is implicit that \mathbf{k} matches \mathbf{q} up to a reciprocal lattice vector, $\mathbf{q} = \mathbf{k} + \mathbf{G}$, due to lattice momentum conservation.

A comment is in order about the target choice. In the case where the total \mathbf{S}_{lj} involve only spin degrees of freedom (as is the case for yttrium iron garnet (YIG) discussed in Ref. [8]), $\lambda_{S,j} = 1$, $\lambda_{L,j} = 0$, and only the first two lines of Eq. (7.38) are relevant. Targets for which $\lambda_{L,j} \neq 0$ are more exotic. One class of materials with $\lambda_{L,j} \neq 0$ is spin-orbit-entangled Mott insulators [323–325], where the combined effect of crystal fields and spin-orbit coupling results in effective spins $S_j = \frac{1}{2}$, and we can show that $\lambda_{S,j} = -\frac{1}{3}$, $\lambda_{L,j} = -\frac{4}{3}$ (see Appendix K for details, and Refs. [324–327] for related discussion), so the magnetic ions' effective spins are in fact dominated by their orbital components. Perovskite irridates such as Sr_2IrO_4 [323, 326] and Kitaev materials Na_2IrO_3 , $\alpha\text{-RuCl}_3$ [325, 327–329] are among the materials with this feature that have been actively studied recently by the condensed matter physics community. While perhaps futuristic as DM detectors, such materials have the novel feature of being sensitive to DM couplings with electrons' orbital angular momenta.

As a final remark, we note from the derivation above that when the same crystal response, $\langle \mathbf{S}_e \rangle$ or $\langle \mathbf{L}_e \rangle$, excites both phonons and magnons, the phonon excitation rate is parametrically suppressed by $\frac{q^2}{m_{\text{ion}} \omega} \sim 10^{-2} \left(\frac{q}{\text{keV}} \right)^2 \left(\frac{10 \text{ GeV}}{m_{\text{ion}}} \right) \left(\frac{10 \text{ meV}}{\omega} \right)$. Thus, for example, for the third group of operators in Table 7.3 with $\psi = e$, which generates only $\langle \mathbf{S}_e \rangle$ response, single magnon

excitation is expected to achieve better sensitivity than single phonon excitation for the same exposure and detector efficiency. On the other hand, since phonons can be excited also by other crystal responses, they have a broader coverage of the DM theory space. We will investigate the interplay between single phonon and magnon excitations in the context of our benchmark models in the next section.

7.3 Application to Benchmark Models

We now apply the general results of the previous section to the set of benchmark models in Table 7.2. The first step of the calculation – matching the relativistic model onto the NR EFT – was already done in Sec. 7.2. The results are the operator coefficients $c_i^{(\psi)}$ listed in the second to last column of Table 7.2. We then need to substitute these operator coefficients into the formulae derived in Secs. 7.2 and 7.2 to compute direct detection rates $\Gamma(\mathbf{v})$ — Eq. (7.35) together with Eq. (7.30) for single phonon excitations, and Eq. (7.42) together with Eq. (7.38) for single magnon excitations.

In order to present the results in a concise way, let us introduce the following definitions. For single phonon excitation, we define (cf. Eq. (7.35))

$$F_{X,\nu}^{(\psi)}(\mathbf{q}) \equiv \sum_j e^{-W_j(\mathbf{q})} e^{i\mathbf{G}\cdot\mathbf{x}_j^0} \frac{\mathbf{q} \cdot \boldsymbol{\epsilon}_{\nu,\mathbf{k},j}^*}{\sqrt{2m_j\omega_{\nu,\mathbf{k}}}} \langle X_\psi \rangle_j, \quad (7.43)$$

where X represents one of the crystal responses, $X = N, S, L, L \otimes S$; note that $F_{X,\nu}^{(\psi)}$ are vector (tensor) quantities when $X = S, L$ ($X = L \otimes S$), and will be written as $\mathbf{F}_{X,\nu}^{(\psi)}$ ($\mathbf{F}_{X,\nu}^{(\psi)}$). These $F_{X,\nu}^{(\psi)}$ play the role of form factors for exciting a single phonon via a certain type of response. For single magnon excitation, we define (cf. Eq. (7.42))

$$\mathbf{E}_{X,\nu}(\mathbf{q}) \equiv \sum_j e^{i\mathbf{G}\cdot\mathbf{x}_j^0} \sqrt{\frac{S_j}{2}} (\mathbb{U}_{j\nu,\mathbf{k}}^* \mathbf{r}_j + \mathbb{V}_{j\nu,-\mathbf{k}} \mathbf{r}_j^*) \lambda_{X,j}, \quad (7.44)$$

where $X = S, L$. These are formally analogous to polarization vectors of a vector field. In both Eqs. (7.43) and (7.44), \mathbf{k} is the phonon momentum inside the 1BZ that satisfies $\mathbf{q} = \mathbf{k} + \mathbf{G}$ for some reciprocal lattice vector \mathbf{G} ; as emphasized below Eq. (7.35), \mathbf{k} is uniquely determined by mapping \mathbf{q} into the 1BZ through reciprocal lattice vectors. We further define a set of quantities $\Sigma_\nu(\mathbf{q})$, for both single phonon and single magnon excitations, by (cf. Eq. (7.5))

$$\Gamma(\mathbf{v}) \equiv \frac{1}{\Omega} \int \frac{d^3q}{(2\pi)^3} \sum_\nu 2\pi \delta(\omega_{\nu,\mathbf{k}} - \omega_{\mathbf{q}}) \Sigma_\nu(\mathbf{q}). \quad (7.45)$$

We will refer to $\Sigma_\nu(\mathbf{q})$, which have mass dimension -4 , as “differential rates.” Practically, $\Sigma_\nu(\mathbf{q})$ are obtained simply by taking $\tilde{\mathcal{V}}_{lj}$ in Eq. (7.30), substituting $\langle X_\psi \rangle_{lj}$ by $F_{X,\nu}^{(\psi)}$ (for

$\psi = p, n, e$ and $X = N, S, L, L \otimes S$ or $\mathbf{E}_{X,\nu}$ (for $\psi = e$ only, and $X = S, L$), squaring it and averaging over the DM's spin (which amounts to replacing $S_\chi^i S_\chi^k \rightarrow \frac{1}{4} \delta^{ik}$). As we will see, written in terms of the dimensionless quantities $F_{X,\nu}^{(\psi)}$ and $\mathbf{E}_{X,\nu}$ defined above, $\Sigma_\nu(\mathbf{q})$ can be expressed in a concise form for each benchmark model. This will be convenient when we compare the rates between different models, and between phonon and magnon excitations.

Our final results will be presented in terms of the rate per unit target mass,

$$R = \frac{1}{\rho_T} \frac{\rho_\chi}{m_\chi} \int d^3v f_\chi(\mathbf{v}) \Gamma(\mathbf{v}), \quad (7.46)$$

where ρ_T is the target's mass density that we take from Ref. [267], $\rho_\chi = 0.4 \text{ GeV/cm}^3$ is the local DM mass density, and $f_\chi(\mathbf{v})$ is the DM's velocity distribution, taken to be a boosted and truncated Maxwell-Boltzmann distribution — see Appendix L for technical details of evaluating the velocity integrals. For the projected reach, we assume 3 events per kilogram-year exposure, corresponding to 95% C.L. exclusion in a background-free counting experiment, and assume a detector energy threshold of 1 meV. While we will present full numerical results, the main features can usually be understood by simple parametric estimates. Generally, noting that the velocity integral over the energy conserving delta function $\delta(\omega_{\nu,\mathbf{k}} - \omega_{\mathbf{q}})$ yields a function that scales as q^{-1} (see Appendix L), we have from Eqs. (7.45) and (7.46), parametrically,

$$R \sim \frac{\rho_\chi}{m_\chi} \frac{1}{m_{\text{cell}}} \int dq q \Sigma, \quad (7.47)$$

where $m_{\text{cell}} = \rho_T \Omega$ is the mass of the primitive cell, and as before, $q = |\mathbf{q}|$. Then, from the formulas for $\Sigma_\nu(\mathbf{q})$ presented below for each model in terms of $F_{X,\nu}^{(\psi)}$ and $\mathbf{E}_{X,\nu}$ defined in Eqs. (7.43) and (7.44), we can estimate the rate R by

$$F_{X,\nu}^{(\psi)} \sim \frac{q}{\sqrt{m_{\text{ion}} \omega}} \langle X_\psi \rangle, \quad \mathbf{E}_{X,\nu} \sim \sqrt{S_{\text{ion}}}. \quad (7.48)$$

In the case of single phonon excitations, we should further note that ω , which appears in $F_{X,\nu}^{(\psi)}$ above, can scale differently with q for different models and DM masses. Typically, either acoustic phonons (associated with in-phase oscillations) or optical phonons (associated with out-of-phase oscillations) dominate the total rate, depending on whether the DM model couples to different ions in a correlated or anti-correlated way. For acoustic phonons, and for q within the 1BZ, $\omega \sim c_s q$ (with c_s the sound speed that is typically $\mathcal{O}(10^{-5})$), whereas for optical phonons or for q beyond the 1BZ, $\omega \sim q^0$. The size of the 1BZ is set by the inverse lattice spacing a^{-1} , and is typically $\mathcal{O}(\text{keV})$. Since $v \sim \mathcal{O}(10^{-3})$, contributions from outside the 1BZ are possible for DM masses above around an MeV. We will see below that in several cases, the curves scale differently for $m_\chi \lesssim \text{MeV}$ and $m_\chi \gtrsim \text{MeV}$ for this reason.

On the target side, we will consider the following representative set of materials:

- **GaAs** [phonons, subject of R&D]. As the first-studied target for DM detection via phonons, GaAs is already in R&D as a target for both electron excitations and phonon excitations [90]. Phonons in GaAs form 3 acoustic and 3 optical branches, and have energies up to ~ 35 meV.
- **SiO₂** (quartz) [phonons, optimal sensitivity]. Based on our previous theoretical study comparing the phonon reach of a variety of target materials [6], we have advocated quartz as having good sensitivity to DM couplings to both acoustic and optical phonons. Also, quartz has complementary features compared to GaAs: while GaAs has a simple crystal structure and relatively low phonon energies, quartz has a large number of phonon branches (3 acoustic, 24 optical), with energies up to ~ 150 meV.
- **Y₃Fe₅O₁₂** (**YIG**) [mostly magnons, also phonons for comparison]. YIG is a well studied material with ferrimagnetic order, and is already used in an axion DM detection experiment QUAX [91–95]. The effective spin Hamiltonian is a Heisenberg model, with $S_j = \frac{5}{2}$ for the magnetic Fe³⁺ ions coming entirely from electron spins $\langle \mathbf{S}_e \rangle$ (i.e., $\lambda_{S,j} = 1$, $\lambda_{L,j} = 0$ in Eq. (7.44)). We take the antiferromagnetic exchange coupling parameters from Ref. [264], together with the crystal parameters from Ref. [267], to compute the magnon spectrum and rotation matrices. YIG has 20 magnon branches, one of which is gapless and has a quadratic dispersion at small k . The gapped magnons have energies up to ~ 90 meV. We will mostly consider YIG as a candidate material for DM detection via magnon excitations, but will also consider phonon excitations in YIG via DM couplings to the ordered electron spins in Sec. 7.3 for comparison; in this case the scattering potential is determined by $\langle \mathbf{S}_e \rangle_{lj}$ of the Fe³⁺ ions, which have magnitude $\frac{5}{2}$ and directions set by the ferrimagnetic order. YIG has 80 ions in total in the primitive cell and therefore 240 phonon branches (3 acoustic, 237 optical), with energies up to ~ 120 meV.
- **α -RuCl₃** [small-gap magnons with orbital component]. As discussed below Eq. (7.38), α -RuCl₃ is one of the materials where the effective ionic spins involve orbital degrees of freedom, and is therefore sensitive to DM couplings to the electrons' orbital angular momenta. The magnetic ions Ru³⁺ have $S_{lj} = \frac{1}{2}$, coming from both $\langle \mathbf{S}_e \rangle$ and $\langle \mathbf{L}_e \rangle$ with $\lambda_{S,j} = -\frac{1}{3}$, $\lambda_{L,j} = -\frac{4}{3}$, as discussed in Appendix K. The effective spin Hamiltonian features Kitaev-type bond-directional exchange couplings. We use the Hamiltonian parameters derived from neutron scattering data in Ref. [330], which also includes an antiferromagnetic Heisenberg exchange; see Ref. [329] for a summary of some alternative model parameterizations derived from a variety of experimental and numerical techniques. The resulting magnetic order is zig-zag antiferromagnetic. Magnons in

α -RuCl₃, of which there are 4 branches, are at very low energy, below 7 meV, and can thus probe lighter DM than YIG. Also, since all magnon branches are gapped at zero momentum, the sensitivity is not significantly affected by the finite detector threshold. This is in contrast with YIG, where the assumed 1 meV energy threshold limits the momentum transfer to be greater than ~ 80 eV in order to excite magnons on the gapless branch. Therefore, even though the experimental prospects of α -RuCl₃ itself are unclear, it can be regarded as a useful benchmark which highlights the generic advantage of small-gap targets.

Our main results are Figs. 7.1-7.4. We give a brief summary here and discuss them in more detail in the following subsections. A major issue of interest is the comparison of sensitivity to various types of DM interactions, via single phonon and magnon excitations induced by various crystal responses. First, we consider the standard SD interaction in Fig. 7.1, where we see that magnons outperform phonons, typically, by more than an order of magnitude in terms of the coupling reach. Next, in Fig. 7.2, we compare the phonon and magnon rates for the four combinations of scalar mediator couplings; the phonon production rate is larger, if the scalar and pseudoscalar couplings are of the same order, while magnons allow access to the models where the mediator dominantly couples to the pseudoscalar currents of SM fermions. Next, we compare the reach of phonons and magnons to multipole models in Fig. 7.3; for the magnetic dipole and anapole models we expect the magnon reach to be better, and indeed it is. However, the phonon reach from quartz is sufficiently strong that, given the greater experimental challenges currently associated with magnon read-out, quartz should be considered a competitor for these models. Lastly, in Fig. 7.4, we compare theoretical reach in the $(\mathbf{L} \cdot \mathbf{S})$ -interacting model, where magnons outperform phonons for sub-MeV DM with the same exposure; however, the $(\mathbf{L} \cdot \mathbf{S})$ -interacting model is difficult to UV complete, and our calculation is perhaps somewhat an academic exercise that demonstrate aspects of the EFT.

We now discuss each benchmark model in turn.

Standard Spin-Dependent Interaction

For the standard SD interaction there is only one operator, \mathcal{O}_4 , which generates the S response, and can excite both phonons and magnons in a magnetically ordered target. Here, only couplings to electrons (whose spins are ordered) are relevant, and we obtain, for the

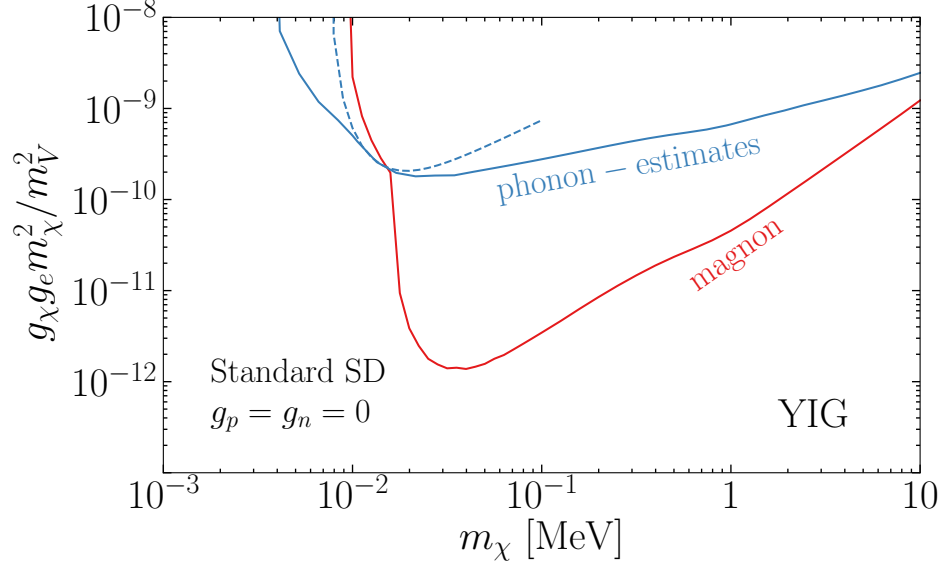


Figure 7.1: Projected reach on the standard SD model listed in Table 7.2 from single magnon (red) and phonon (blue) excitations in YIG. The phonon rate is estimated in two ways, as discussed in the text, which lead to the solid and dashed curves, respectively. Since this model generates only the S response, magnons are seen to have better sensitivity than phonons.

differential rates,

$$\Sigma_\nu(\mathbf{q})_{\text{phonon}} = \frac{4g_\chi^2 g_e^2}{m_V^4} |\mathbf{F}_{S,\nu}^{(e)}|^2, \quad (7.49)$$

$$\Sigma_\nu(\mathbf{q})_{\text{magnon}} = \frac{4g_\chi^2 g_e^2}{m_V^4} |\mathbf{E}_{S,\nu}|^2. \quad (7.50)$$

In Fig. 7.1, we compare the phonon and magnon reach with YIG. As a technical note, in the absence of a DFT calculation for the crystal potential in YIG which is necessary for computing the phonon eigenmodes, we estimate the rate in two ways. First, we carry out an approximate analytic calculation taking into account long-wavelength acoustic phonons, as explained in Appendix M. This results in the dashed reach curve in Fig. 7.1, which is truncated at the DM mass for which the maximum momentum transfer reaches the edge of the 1BZ, so that the approximations we make cease to hold. Second, we borrow the crystal potential of $\text{Y}_3\text{Ga}_5\text{O}_{12}$ (YGG) which is publicly available [259]. YGG has the same crystal structure as YIG, with Fe replaced by Ga, and the phonon dispersions we obtain for YGG are very similar to those of YIG [331]. The resulting reach is shown by the solid blue curve in Fig. 7.1. We see from the figure that both estimates are in good agreement near $m_\chi \sim 10^{-2}$ MeV, where acoustic phonons dominate, while including optical phonon contributions in the second approach improves the reach at lower and higher m_χ .

We can understand these curves by estimating the rates using Eqs. (7.47) and (7.48). The q integrals are dominated by $q_{\max} \sim m_\chi v$. As a result,

$$R_{\text{phonon}} \sim \frac{\rho_\chi}{m_\chi} \frac{1}{m_{\text{cell}}} \frac{g_\chi^2 g_e^2}{m_V^4} \frac{S_{\text{ion}}^2}{m_{\text{ion}}} \int dq \frac{q^3}{\omega} \sim \begin{cases} \frac{g_\chi^2 g_e^2}{m_V^4} \frac{\rho_\chi}{m_\chi} \frac{S_{\text{ion}}^2}{m_{\text{cell}} m_{\text{ion}} c_s} (m_\chi v)^3 & (\text{acoustic, } m_\chi v \lesssim a^{-1}), \\ \frac{g_\chi^2 g_e^2}{m_V^4} \frac{\rho_\chi}{m_\chi} \frac{S_{\text{ion}}^2}{m_{\text{cell}} m_{\text{ion}} \langle \omega \rangle} (m_\chi v)^4 & (\text{otherwise}), \end{cases} \quad (7.51)$$

$$R_{\text{magnon}} \sim \frac{\rho_\chi}{m_\chi} \frac{1}{m_{\text{cell}}} \frac{g_\chi^2 g_e^2}{m_V^4} S_{\text{ion}} \int dq q \sim \frac{g_\chi^2 g_e^2}{m_V^4} \frac{\rho_\chi}{m_\chi} \frac{S_{\text{ion}}}{m_{\text{cell}}} (m_\chi v)^2. \quad (7.52)$$

Fixing R , the coupling plotted in Fig. 7.1, $g_\chi g_e \frac{m_\chi}{m_V^2}$ scales as m_χ , $m_\chi^{1/2}$ and $m_\chi^{3/2}$, respectively, in the three cases, in agreement with the high- m_χ behaviors of the dashed blue, solid blue and red curves in Fig. 7.1, respectively. Also, magnons have better sensitivity than phonons to the SD coupling by a factor of $\sqrt{\frac{R_{\text{magnon}}}{R_{\text{phonon}}}} \sim \frac{\sqrt{m_{\text{ion}} \omega / S_{\text{ion}}}}{m_\chi v}$, and the advantage becomes more significant at smaller m_χ (though the magnon curve hits the kinematic threshold at higher m_χ due to the dispersion being quadratic).

Scalar Mediator Models

We next consider scalar mediator models with both scalar and pseudoscalar couplings. We take the mediator couplings to SM fermions to be proportional to their masses, $g_\psi \propto m_\psi$ (motivated by Higgs-portal hidden sector theories, see Ref. [332] for a recent review), and consider each of the four combinations of currents, which we denote by $S \times S$, $P \times S$, $S \times P$ and $P \times P$. Among them, $S \times S$ (i.e., standard SI considered previously in Refs. [6, 7, 28, 64]) and $P \times S$ can excite phonons via the N response,⁹ while $S \times P$ and $P \times P$ can excite both phonons and magnons in a magnetically ordered target via the S response. However, similar to the standard SD interaction in Sec. 7.3, the phonon excitation rate will be suppressed relative to the magnon excitation rate, so we focus on the latter here. We obtain the following

⁹These models generate additional operators when matched onto the NR EFT beyond leading order, which could excite magnons. We do not consider magnon excitation here due to the severely suppressed rate. The same applies to the SI and electric dipole DM models in Sec. 7.3.

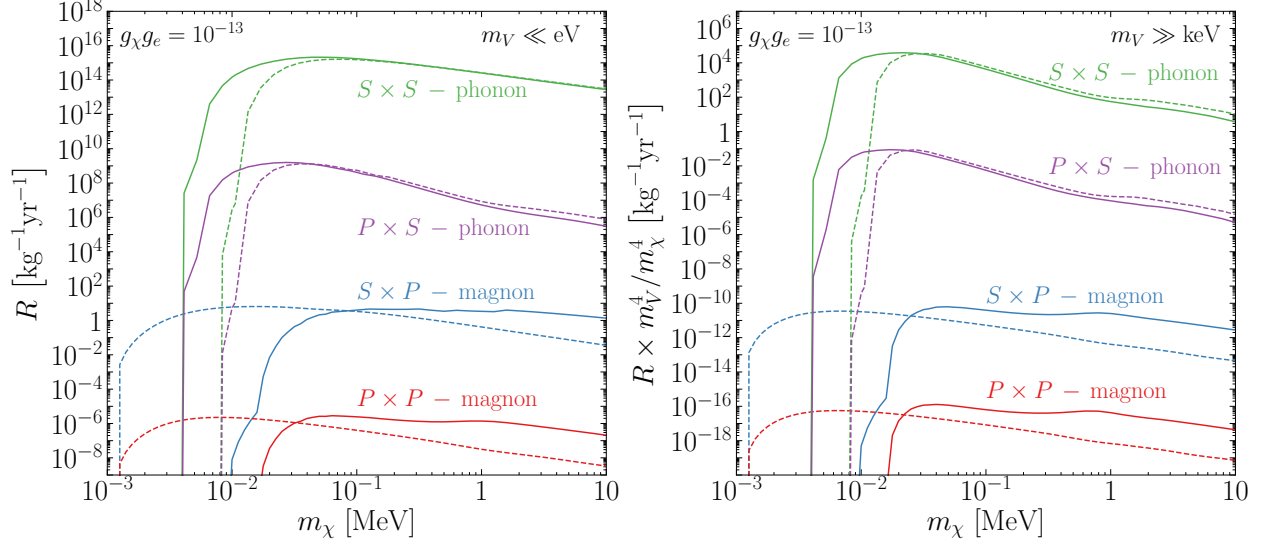


Figure 7.2: Comparison of the total detection rate in models with a light (left panel) or heavy (right panel) scalar mediator. The couplings to SM fermions are taken proportional to their masses, $g_p = g_n = \frac{m_p}{m_e} g_e$, and we fix $g_\chi g_e = 10^{-13}$. Each curve is labeled with the model type as in Table 7.2 and the excitation type (phonon or magnon) that can probe each model. The phonon curves assume SiO₂ (solid) and GaAs (dashed) targets, and the magnon curves assume YIG (solid) and α -RuCl₃ (dashed) targets.

expressions for the differential rates defined in Eq. (7.45):

$$\Sigma_\nu(\mathbf{q})_{\text{phonon}}^{S \times S} = \frac{g_\chi^2}{(q^2 + m_\phi^2)^2} \left| \sum_\psi g_\psi^{\text{eff}} F_{N,\nu}^{(\psi)} \right|^2, \quad (7.53)$$

$$\Sigma_\nu(\mathbf{q})_{\text{phonon}}^{P \times S} = \frac{g_\chi^2}{(q^2 + m_\phi^2)^2} \frac{q^2}{4m_\chi^2} \left| \sum_\psi g_\psi^{\text{eff}} F_{N,\nu}^{(\psi)} \right|^2, \quad (7.54)$$

$$\Sigma_\nu(\mathbf{q})_{\text{magnon}}^{S \times P} = \frac{g_\chi^2 g_e^2}{(q^2 + m_\phi^2)^2} \frac{q^2}{m_e^2} \left| \hat{\mathbf{q}} \cdot \mathbf{E}_{S,\nu} \right|^2, \quad (7.55)$$

$$\Sigma_\nu(\mathbf{q})_{\text{magnon}}^{P \times P} = \frac{g_\chi^2 g_e^2}{(q^2 + m_\phi^2)^2} \frac{q^4}{4m_\chi^2 m_e^2} \left| \hat{\mathbf{q}} \cdot \mathbf{E}_{S,\nu} \right|^2. \quad (7.56)$$

Note that for the $S \times S$ and $P \times S$ models, screening effects have been taken into account by using g_ψ^{eff} in place of g_ψ , as discussed around Eq. (7.14); the dielectric tensors ϵ_∞ of the phonon targets GaAs and SiO₂ are obtained from DFT calculations [248].

In Fig. 7.2, we plot the expected rate for each of the four coupling combinations, for a common value for the product of couplings, to illustrate the hierarchy between the rate from the different interactions. We have chosen to show the rate instead of projected reach here so that the general case where more than one types of interactions are present, it would be straightforward to rescale the curves to see which one is dominant. For example, if

$g_\chi^{(S)} \sim g_\chi^{(P)}$, $g_\psi^{(S)} \sim g_\psi^{(P)}$, we have the highest rate from phonon excitations via the $S \times S$ coupling, i.e., the standard SI interaction, as expected. On the other hand, if the couplings to SM fermions are dominantly pseudoscalar, $g_\psi^{(P)}/g_\psi^{(S)} \gtrsim 10^7$, magnon excitations have better sensitivity than phonon excitations for the same exposure; this is one of the benchmark models considered previously in Ref. [8]. The hierarchy seen in Fig. 7.2, and also some main features of the curves, can be understood following Eqs. (7.47) and (7.48), as we now explain.

First consider the light mediator case, $m_V \ll q$ (left panel of Fig. 7.2). For phonon excitations in the $S \times S$ and $P \times S$ models, since the couplings to all ions have the same sign, the rate is dominated by acoustic phonons. For q within the 1BZ, setting $\omega \sim c_s q$, we obtain

$$R_{\text{phonon}}^{S \times S} \sim \frac{\rho_\chi}{m_\chi} \frac{1}{m_{\text{cell}}} g_\chi^2 g_p^2 \frac{\langle N_{p,n} \rangle^2}{m_{\text{ion}}} \int dq \frac{1}{q\omega} \sim g_\chi^2 g_p^2 \frac{\rho_\chi}{m_\chi} \frac{\langle N_{p,n} \rangle^2}{m_{\text{cell}} m_{\text{ion}} \omega_{\text{min}}}, \quad (7.57)$$

$$R_{\text{phonon}}^{P \times S} \sim \frac{\rho_\chi}{m_\chi} \frac{1}{m_{\text{cell}}} g_\chi^2 g_p^2 \frac{\langle N_{p,n} \rangle^2}{m_{\text{ion}} m_\chi^2} \int dq \frac{q}{\omega} \sim g_\chi^2 g_p^2 \frac{\rho_\chi}{m_\chi} \frac{\langle N_{p,n} \rangle^2}{m_{\text{cell}} m_{\text{ion}} m_\chi c_s}, \quad (7.58)$$

where $\omega_{\text{min}} = c_s q_{\text{min}}$. These are consistent with the m_χ^{-1} and m_χ^{-2} scaling of the green and purple curves for m_χ up to $\sim \text{MeV}$. Also, consistent with the figure, the ratio between them is $\frac{R_{\text{phonon}}^{P \times S}}{R_{\text{phonon}}^{S \times S}} \sim \frac{\omega_{\text{min}}}{m_\chi} \frac{v}{c_s} \sim 10^{-6} \frac{\omega_{\text{min}}}{1 \text{ meV}} \frac{10^{-1} \text{ MeV}}{m_\chi} \frac{v}{10^{-3}} \frac{10^{-5}}{c_s}$ for couplings of the same size. For heavier DM, on the other hand, momentum transfers beyond the 1BZ are allowed. For the $S \times S$ model, this is irrelevant since the integral is dominated by small q , so the m_χ^{-1} trend continues past MeV. For the $P \times S$ model, since the integral is dominated by high q where ω no longer scales with q , we have $\frac{v^2}{\omega}$ in place of $\frac{v}{m_\chi c_s}$ in Eq. (7.58). This explains the m_χ^{-1} scaling of the purple curves past $m_\chi \sim \text{MeV}$ in the left panel of Fig. 7.2.

For magnon excitations in the $S \times P$ and $P \times P$ models, we have

$$R_{\text{magnon}}^{S \times P} \sim \frac{\rho_\chi}{m_\chi} \frac{1}{m_{\text{cell}}} g_\chi^2 g_e^2 \frac{S_{\text{ion}}}{m_e^2} \int dq \frac{1}{q} \sim g_\chi^2 g_e^2 \frac{\rho_\chi}{m_\chi} \frac{S_{\text{ion}}}{m_{\text{cell}} m_e^2}, \quad (7.59)$$

$$R_{\text{magnon}}^{P \times P} \sim \frac{\rho_\chi}{m_\chi} \frac{1}{m_{\text{cell}}} g_\chi^2 g_e^2 \frac{S_{\text{ion}}}{m_e^2 m_\chi^2} \int dq q \sim g_\chi^2 g_e^2 \frac{\rho_\chi}{m_\chi} \frac{S_{\text{ion}}}{m_{\text{cell}} m_e^2} v^2, \quad (7.60)$$

again consistent with the m_χ^{-1} scaling of the corresponding curves in Fig. 7.2 (though the YIG curves have a bump near MeV due to the gapped magnons starting to contribute, as discussed in Ref. [8], which slightly obscures the overall scaling with m_χ). Comparing the two models, we see that $\frac{R_{\text{magnon}}^{P \times P}}{R_{\text{magnon}}^{S \times P}} \sim v^2$. Also, comparing with phonon excitation in the $S \times S$ model, we have $\frac{R_{\text{magnon}}^{S \times P}}{R_{\text{phonon}}^{S \times S}} \sim \frac{g_e^2}{g_p^2} \frac{S_{\text{ion}} m_{\text{ion}} \omega_{\text{min}}}{\langle N_{p,n} \rangle^2 m_e^2} \sim \frac{\omega_{\text{min}}}{m_{\text{ion}}} \sim 10^{-14} \frac{\omega_{\text{min}}}{1 \text{ meV}} \frac{100 \text{ GeV}}{m_{\text{ion}}}$, assuming similar values of m_{cell} , m_{ion} for the targets and $S_{\text{ion}} \sim \mathcal{O}(1)$, and noting that $g_p^{\text{eff}} \simeq g_p$ and $g_e/g_p = m_e/m_p$. This is consistent with what we see in Fig. 7.2.

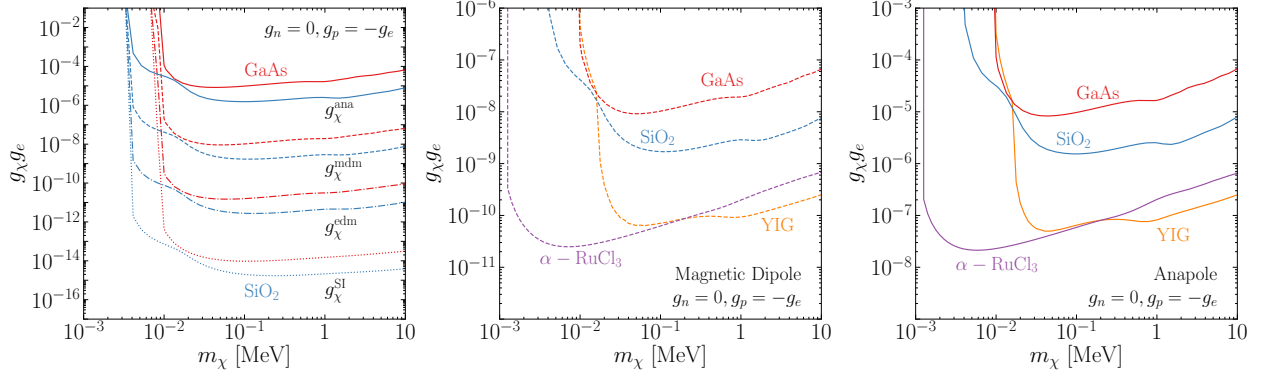


Figure 7.3: Projected reach on the multipole DM models listed in Table 7.2, assuming dark photon-like couplings to SM particles: $g_p = -g_e, g_n = 0$. The left panel shows the hierarchy of sensitivities of single phonon excitations, in GaAs and in SiO₂, to the three multipole DM models, together with the SI interaction model for comparison. The center and right panels focus on the magnetic dipole and anapole DM models, respectively, and compare the phonon reach of GaAs and SiO₂ (via the N response), and the magnon reach of YIG (via the S response) and α -RuCl₃ (via both S and L responses); these models are best probed by magnons, though the phonon sensitivity with an optimal target like SiO₂ may be competitive.

The heavy mediator case, $m_V \gg q$ (right panel of Fig. 7.2), follows a similar analysis. All the q integrals are now peaked at $q_{\max} \sim m_\chi v$, and we find

$$R_{\text{phonon}}^{S \times S} \sim \frac{\rho_\chi}{m_\chi} \frac{1}{m_{\text{cell}}} \frac{g_\chi^2 g_p^2}{m_V^4} \frac{\langle N_{p,n} \rangle^2}{m_{\text{ion}}} \int dq \frac{q^3}{\omega} \sim \begin{cases} \frac{g_\chi^2 g_p^2}{m_V^4} \frac{\rho_\chi}{m_\chi} \frac{\langle N_{p,n} \rangle^2}{m_{\text{cell}} m_{\text{ion}} c_s} (m_\chi v)^3 & (m_\chi v \lesssim a^{-1}) \\ \frac{g_\chi^2 g_p^2}{m_V^4} \frac{\rho_\chi}{m_\chi} \frac{\langle N_{p,n} \rangle^2}{m_{\text{cell}} m_{\text{ion}} \langle \omega \rangle} (m_\chi v)^4 & (m_\chi v \gtrsim a^{-1}), \end{cases} \quad (7.61)$$

$$R_{\text{phonon}}^{P \times S} \sim v^2 R_{\text{phonon}}^{S \times S}, \quad (7.62)$$

$$R_{\text{magnon}}^{S \times P} \sim \frac{\rho_\chi}{m_\chi} \frac{1}{m_{\text{cell}}} \frac{g_\chi^2 g_p^2}{m_V^4} \frac{S_{\text{ion}}}{m_e^2} \int dq q^3 \sim \frac{g_\chi^2 g_e^2}{m_V^4} \frac{\rho_\chi}{m_\chi} \frac{S_{\text{ion}}}{m_{\text{cell}} m_e^2} (m_\chi v)^4, \quad (7.63)$$

$$R_{\text{magnon}}^{P \times P} \sim v^2 R_{\text{magnon}}^{S \times P}. \quad (7.64)$$

These equations explain both the hierarchy of the rates for the four models, and the m_χ scaling: in all cases, $R \frac{m_V^4}{m_\chi^4} \sim m_\chi^{-1}$ at large m_χ , while the phonon curves switch to m_χ^{-2} scaling below $\sim \text{MeV}$.

Multipole Dark Matter Models

We now turn to the electric dipole, magnetic dipole, and anapole DM models in Table 7.2. For comparison, we also include the SI interaction model with a vector mediator. Motivated by the kinetic mixing benchmark, we assume the mediator couples to electric charge, $g_p = -g_e$, $g_n = 0$, and is much lighter than the smallest momentum transfer, $m_V \ll \text{eV}$. The SI and electric dipole DM models generate \mathcal{O}_1 and \mathcal{O}_{11} at leading order, respectively, both of

which induce only the N response, which can be probed by single phonon excitation. The differential rates are

$$\Sigma_\nu(\mathbf{q})_{\text{phonon}}^{\text{SI}} = \frac{g_\chi^2 g_e^2}{(\mathbf{q} \cdot \boldsymbol{\varepsilon}_\infty \cdot \mathbf{q})^2} \left| F_{N,\nu}^{(p)} - F_{N,\nu}^{(e)} \right|^2, \quad (7.65)$$

$$\Sigma_\nu(\mathbf{q})_{\text{phonon}}^{\text{edm}} = \frac{g_\chi^2 g_e^2}{(\mathbf{q} \cdot \boldsymbol{\varepsilon}_\infty \cdot \mathbf{q})^2} \frac{q^2}{4m_\chi^2} \left| F_{N,\nu}^{(p)} - F_{N,\nu}^{(e)} \right|^2. \quad (7.66)$$

Eq. (7.65) is in agreement with previous results in Refs. [6, 7, 28]. The magnetic dipole and the anapole DM models generate, in addition to N , also S and L responses, and can therefore be probed by both phonons and magnons. For single phonon excitation, we have

$$\begin{aligned} \Sigma_\nu(\mathbf{q})_{\text{phonon}}^{\text{mdm}} = & \frac{g_\chi^2 g_e^2}{4m_\chi^2 q^2} \left\{ \frac{q^4}{(\mathbf{q} \cdot \boldsymbol{\varepsilon}_\infty \cdot \mathbf{q})^2} \frac{q^2}{4m_\chi^2} \left| F_{N,\nu}^{(p)} - F_{N,\nu}^{(e)} \right|^2 \right. \\ & + \left| \frac{q^4}{(\mathbf{q} \cdot \boldsymbol{\varepsilon}_\infty \cdot \mathbf{q})^2} (\hat{\mathbf{q}} \times \mathbf{v}) \left(F_{N,\nu}^{(p)} - F_{N,\nu}^{(e)} \right) \right. \\ & \left. \left. - (\mathbb{1} - \hat{\mathbf{q}}\hat{\mathbf{q}}) \cdot \left[\frac{i\mathbf{q}}{2m_p} \left(2\tilde{\mu}_p \mathbf{F}_{S,\nu}^{(p)} + \mathbf{F}_{L,\nu}^{(p)} \right) - \frac{i\mathbf{q}}{2m_e} \left(2\tilde{\mu}_e \mathbf{F}_{S,\nu}^{(e)} + \mathbf{F}_{L,\nu}^{(e)} \right) \right] \right|^2 \right\}, \end{aligned} \quad (7.67)$$

$$\begin{aligned} \Sigma_\nu(\mathbf{q})_{\text{phonon}}^{\text{ana}} = & \frac{g_\chi^2 g_e^2}{16m_\chi^4} \left| \frac{q^4}{(\mathbf{q} \cdot \boldsymbol{\varepsilon}_\infty \cdot \mathbf{q})^2} \left(\mathbf{v} - \frac{\mathbf{q}}{2m_\chi} \right) \left(F_{N,\nu}^{(p)} - F_{N,\nu}^{(e)} \right) \right. \\ & \left. + \frac{i\mathbf{q}}{2m_p} \times \left(2\tilde{\mu}_p \mathbf{F}_{S,\nu}^{(p)} + \mathbf{F}_{L,\nu}^{(p)} \right) - \frac{i\mathbf{q}}{2m_e} \times \left(2\tilde{\mu}_e \mathbf{F}_{S,\nu}^{(e)} + \mathbf{F}_{L,\nu}^{(e)} \right) \right|^2. \end{aligned} \quad (7.68)$$

Note that for an unorderd/unpolarized target, $\mathbf{F}_{S,\nu}^{(\psi)} = \mathbf{F}_{L,\nu}^{(\psi)} = \mathbf{0}$. For single magnon excitation, we have

$$\Sigma_\nu(\mathbf{q})_{\text{magnon}}^{\text{mdm}} = \frac{g_\chi^2 g_e^2}{16m_\chi^2 m_e^2} \left| (\mathbb{1} - \hat{\mathbf{q}}\hat{\mathbf{q}}) \cdot (2\tilde{\mu}_e \mathbf{E}_{S,\nu} + \mathbf{E}_{L,\nu}) \right|^2, \quad (7.69)$$

$$\Sigma_\nu(\mathbf{q})_{\text{magnon}}^{\text{ana}} = \frac{g_\chi^2 g_e^2}{64m_\chi^4 m_e^2} \left| \mathbf{q} \times (2\tilde{\mu}_e \mathbf{E}_{S,\nu} + \mathbf{E}_{L,\nu}) \right|^2, \quad (7.70)$$

which extend the results in Ref. [8].

A comparison of the phonon reach in these models is shown in the left panel of Fig. 7.3. The center and right panels of Fig. 7.3 zoom in on the magnetic dipole and anapole DM models, respectively, and compare the reach of phonon and magnon excitations.

We can carry out a similar analysis as in the previous subsections to understand the main features in Fig. 7.3. For single phonon excitation in GaAs and SiO₂, we keep only the $F_{N,\nu}^{(\psi)}$ terms in the $\Sigma_\nu(\mathbf{q})$ formulae above, and note that, as in the SI case discussed previously in

Refs. [6, 7, 28, 64], the DM-ion couplings, being proportional to $\langle N_p \rangle - \langle N_e \rangle = Q_{\text{ion}}$, have opposite signs for oppositely charged ions, so the optical phonon modes with $\omega \sim q^0$ give the dominant contributions. Using Eqs. (7.47) and (7.48), we obtain the following parametric estimates:

$$R_{\text{phonon}}^{\text{SI}} \sim \frac{\rho_\chi}{m_\chi} \frac{1}{m_{\text{cell}}} \frac{g_\chi^2 g_e^2}{\varepsilon_\infty^2} \frac{Q_{\text{ion}}^2}{m_{\text{ion}} \omega} \int dq \frac{1}{q} \sim g_\chi^2 g_e^2 \frac{\rho_\chi}{m_\chi} \left(\frac{Q_{\text{ion}}^2}{\varepsilon_\infty^2 m_{\text{cell}} m_{\text{ion}} \omega} \right), \quad (7.71)$$

$$\frac{R_{\text{phonon}}^{\text{edm}}}{R_{\text{phonon}}^{\text{SI}}} \sim \frac{R_{\text{phonon}}^{\text{mdm}}}{R_{\text{phonon}}^{\text{edm}}} \sim \frac{R_{\text{phonon}}^{\text{ana}}}{R_{\text{phonon}}^{\text{mdm}}} \sim v^2, \quad (7.72)$$

$$R_{\text{magnon}}^{\text{mdm}} \sim \frac{\rho_\chi}{m_\chi} \frac{S_{\text{ion}}}{m_{\text{cell}}} \frac{g_\chi^2 g_e^2}{m_\chi^2 m_e^2} \int dq q \sim g_\chi^2 g_e^2 \frac{\rho_\chi}{m_\chi} \frac{S_{\text{ion}} v^2}{m_{\text{cell}} m_e^2}, \quad (7.73)$$

$$\frac{R_{\text{magnon}}^{\text{ana}}}{R_{\text{magnon}}^{\text{mdm}}} \sim v^2. \quad (7.74)$$

Several comments are in order. First, Eq. (7.72) explains the hierarchy of sensitivity of phonon excitations to the four models in the left panel of Fig. 7.3, while Eq. (7.74) shows a similar hierarchy of sensitivity of magnon excitations to the magnetic dipole and anapole DM models. Also, note that in all cases, $R \sim m_\chi^{-1}$, so the reach on $g_\chi g_e$ scales as $m_\chi^{1/2}$, as seen in Fig. 7.3.

Next, let us compare the reach of different target materials, and via phonons versus magnons. For phonon excitations, the factor in parentheses in Eq. (7.71) reproduces the ‘‘quality factor’’ identified in Ref. [6], up to $\mathcal{O}(1)$ factors we have dropped here. It captures the material properties that determine the sensitivity to the SI model with a dark photon mediator, and is the quantity to maximize in order to optimize target choice. For example, SiO₂ has a quality factor that is about 80 times that of GaAs, which explains its significantly better reach, by almost an order of magnitude on the coupling $g_\chi g_e$, as seen in Fig. 7.3 (and also previously in Ref. [6]).

For magnon excitations for the magnetic dipole and anapole DM models, we have considered YIG, which probes only the S response, and α -RuCl₃, which probes both S and L . Since for these models, DM couples to the linear combination $2\mathbf{S}_e + \mathbf{L}_e$ – the spin of an elementary particle has a Landé g -factor of 2 – the additional L response that α -RuCl₃ has does not qualitatively improve the sensitivity. Indeed, we see from Fig. 7.3 that YIG and α -RuCl₃ have very similar reach around $m_\chi \sim 0.1$ MeV. At higher m_χ , YIG performs better due to additional contributions from the large number of gapped magnon modes. On the other hand, α -RuCl₃ extends the reach down to much lower $m_\chi \sim$ keV. As discussed previously, this is because the magnon modes at zero momentum are gapped at a few meV (in contrast

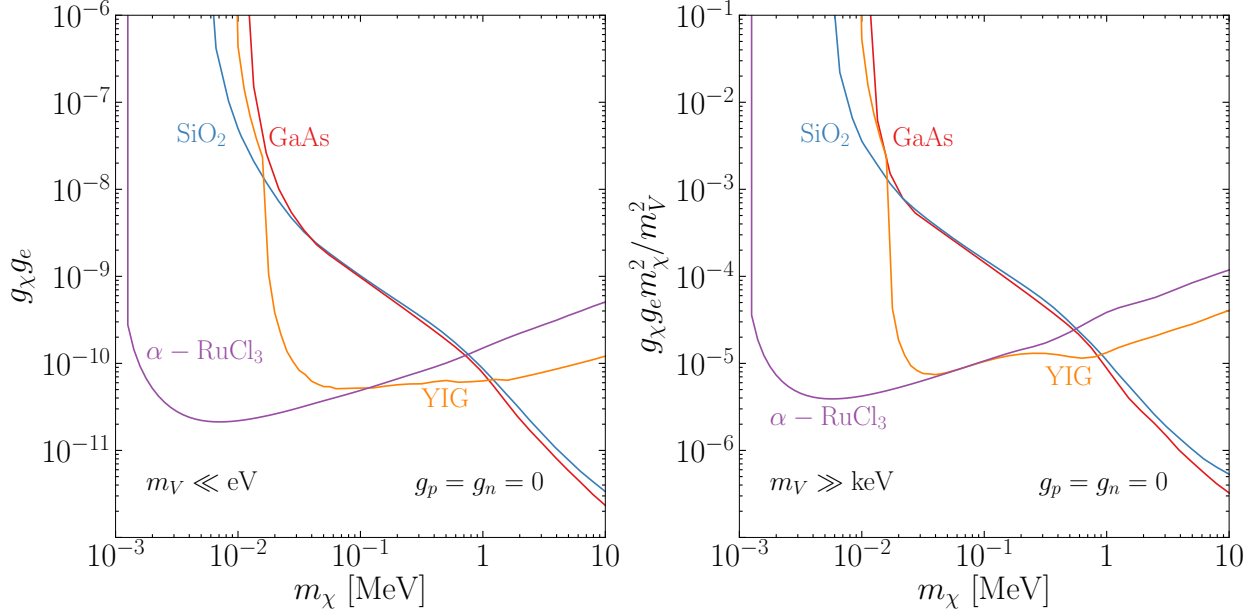


Figure 7.4: Projected reach on the $(\mathbf{L} \cdot \mathbf{S})$ -interacting DM model in Table 7.2, assuming coupling only to electrons, and $\kappa = 0$. Single phonon excitations in GaAs and SiO₂ targets (via the N response) and single magnon excitations in YIG and α -RuCl₃ targets (via the S response) are seen to cover complementary regions of parameter space.

to YIG which has a gapless magnon branch that dominates the coupling to DM in the low momentum transfer limit).

Finally, we can compare the magnon and phonon excitation rates for the two models (magnetic dipole and anapole DM) where both are available. Let us denote $\mathcal{Q} \equiv \frac{Q_{\text{ion}}^2}{\epsilon_{\infty}^2} \frac{m_p^2}{m_{\text{cell}} m_{\text{ion}}} \frac{1 \text{ meV}}{\omega}$, which is the phonon quality factor with the dimensionful parameters normalized in a way close to Ref. [6]. Its values are typically $\mathcal{O}(10^{-7}-10^{-5})$, with GaAs and SiO₂ residing on the lower and higher ends of the interval, respectively. We find

$$\frac{R_{\text{phonon}}^{\text{mdm}}}{R_{\text{magnon}}^{\text{mdm}}} \sim \frac{R_{\text{phonon}}^{\text{ana}}}{R_{\text{magnon}}^{\text{ana}}} \sim \frac{\mathcal{Q} m_{\text{cell}} m_e^2 v^2}{S_{\text{ion}} m_p^2 \cdot 1 \text{ meV}} \sim 10^{-4} \left(\frac{\mathcal{Q}}{1.4 \times 10^{-7}} \right), \quad (7.75)$$

where m_{cell} is for the target for magnon excitations, and we have substituted the numbers for YIG in the last equation. We see that, for the magnetic dipole and anapole DM models, magnons are indeed more sensitive than phonons, though choosing high phonon quality factor targets, such as SiO₂ with $\mathcal{Q} \sim 10^{-5}$ can approach the magnon sensitivity. Up to $\mathcal{O}(1)$ factors, this is consistent with the center and right panels of Fig. 7.3.

$(\mathbf{L} \cdot \mathbf{S})$ -Interacting Dark Matter

We finally consider the $(\mathbf{L} \cdot \mathbf{S})$ -interacting DM model, which induces N , S and $L \otimes S$ responses. Taking the mediator to couple only to electrons for simplicity, we obtain the differential rates:

$$\begin{aligned} \Sigma_\nu(\mathbf{q})_{\text{phonon}} = & \frac{g_\chi^2 g_e^2}{(q^2 + m_V^2)^2} \left\{ \left| \frac{q^2}{4m_e^2} \left[(1 + \kappa) F_{N,\nu}^{(e)} \right. \right. \right. \\ & \left. \left. + 2 \operatorname{tr}((\mathbb{1} - \hat{\mathbf{q}}\hat{\mathbf{q}}) \cdot \mathbf{F}_{L \otimes S, \nu}^{(e)}) \right] + \left(\frac{i\mathbf{q}}{m_e} \times \mathbf{v} \right) \cdot \mathbf{F}_{S,\nu}^{(e)} \right|^2 \\ & \left. + \frac{q^4}{4m_\chi^2 m_e^2} \left| (\mathbb{1} - \hat{\mathbf{q}}\hat{\mathbf{q}}) \cdot \mathbf{F}_{S,\nu}^{(e)} \right|^2 \right\}, \end{aligned} \quad (7.76)$$

$$\Sigma_\nu(\mathbf{q})_{\text{magnon}} = \frac{g_\chi^2 g_e^2}{(q^2 + m_V^2)^2} \frac{q^2}{m_e^2} \left[\frac{q^2}{4m_\chi^2} \left| (\mathbb{1} - \hat{\mathbf{q}}\hat{\mathbf{q}}) \cdot \mathbf{E}_{S,\nu} \right|^2 + \left| (\hat{\mathbf{q}} \times \mathbf{v}) \cdot \mathbf{E}_{S,\nu} \right|^2 \right]. \quad (7.77)$$

In the absence of magnetic order, $\mathbf{F}_{S,\nu}^{(e)} = 0$. Also, unless κ is tuned to be very close to -1 , we do not expect the $\mathbf{F}_{L \otimes S, \nu}^{(e)}$ term in Eq. (7.76) to dominate — the total spin-orbit coupling vanishes for full shells, and is otherwise often suppressed by crystal fields, especially for lighter elements. Thus, while an interesting feature of this model, the coupling to $\mathbf{L} \cdot \mathbf{S}$ does not suggest a better probe than searching for phonon excitations via the N response with already proposed target materials. In Fig. 7.4, we include only the $F_{N,\nu}^{(e)}$ term when computing phonon reach for GaAs and SiO₂, and for concreteness set $\kappa = 0$. Since the total electron numbers of ions are all positive, the rate is dominated by acoustic phonons, with $\omega \sim c_s q$. Again using Eqs. (7.47) and (7.48), we can estimate

$$R_{\text{phonon}} \sim \frac{\rho_\chi}{m_\chi} \frac{1}{m_{\text{cell}}} g_\chi^2 g_e^2 \frac{\langle N_e \rangle^2}{m_{\text{ion}} m_e^4} \int dq \frac{q^3}{\omega} \sim \begin{cases} g_\chi^2 g_e^2 \frac{\rho_\chi}{m_\chi} \frac{\langle N_e \rangle^2 (m_\chi v)^3}{m_{\text{cell}} m_{\text{ion}} m_e^4 c_s} & (m_\chi v \lesssim a^{-1}), \\ g_\chi^2 g_e^2 \frac{\rho_\chi}{m_\chi} \frac{\langle N_e \rangle^2 (m_\chi v)^4}{m_{\text{cell}} m_{\text{ion}} m_e^4(\omega)} & (m_\chi v \gtrsim a^{-1}), \end{cases} \quad (7.78)$$

for a light mediator ($m_V \ll q$), and

$$R_{\text{phonon}} \sim \frac{\rho_\chi}{m_\chi} \frac{1}{m_{\text{cell}}} \frac{g_\chi^2 g_e^2}{m_V^4} \frac{\langle N_e \rangle^2}{m_{\text{ion}} m_e^4} \int dq \frac{q^7}{\omega} \sim \begin{cases} \frac{g_\chi^2 g_e^2}{m_V^4} \frac{\rho_\chi}{m_\chi} \frac{\langle N_e \rangle^2 (m_\chi v)^7}{m_{\text{cell}} m_{\text{ion}} m_e^4 c_s} & (m_\chi v \lesssim a^{-1}), \\ \frac{g_\chi^2 g_e^2}{m_V^4} \frac{\rho_\chi}{m_\chi} \frac{\langle N_e \rangle^2 (m_\chi v)^8}{m_{\text{cell}} m_{\text{ion}} m_e^4(\omega)} & (m_\chi v \gtrsim a^{-1}), \end{cases} \quad (7.79)$$

for a heavy mediator ($m_V \gg q$). These equations explain the scaling of the phonon curves in Fig. 7.4: fixing R , we obtain $g_\chi g_e \sim m_\chi^{-1} (m_\chi^{-3/2})$ for m_χ below (above) about an MeV in the light mediator case, and the same for $g_\chi g_e \frac{m_\chi^2}{m_V^2}$ in the heavy mediator case.

The magnon reach curves for YIG and α -RuCl₃ can be understood in a similar way. We have

$$R_{\text{magnon}} \sim \frac{\rho_\chi}{m_\chi} \frac{1}{m_{\text{cell}}} g_\chi^2 g_e^2 \frac{S_{\text{ion}}}{m_e^2 m_\chi^2} \int dq q \sim g_\chi^2 g_e^2 \frac{\rho_\chi}{m_\chi} \frac{S_{\text{ion}} v^2}{m_{\text{cell}} m_e^2} \quad (7.80)$$

for a light mediator ($m_V \ll q$), and

$$R_{\text{magnon}} \sim \frac{\rho_\chi}{m_\chi} \frac{1}{m_{\text{cell}}} \frac{g_\chi^2 g_e^2}{m_V^4} \frac{S_{\text{ion}}}{m_e^2 m_\chi^2} \int dq q^5 \sim \frac{g_\chi^2 g_e^2}{m_V^4} \frac{\rho_\chi}{m_\chi} \frac{S_{\text{ion}} m_\chi^4 v^6}{m_{\text{cell}} m_e^2} \quad (7.81)$$

for a heavy mediator ($m_V \gg q$). In contrast to the phonon case, the reach on $g_\chi g_e$ ($g_\chi g_e \frac{m_\chi^2}{m_V^2}$) in the light (heavy) mediator case scales as $m_\chi^{1/2}$. So the magnon reach becomes better at lower m_χ , as we can see in Fig. 7.4. In particular, magnons outperform phonons for m_χ below about an MeV, which we can understand from the estimate: $\frac{R_{\text{phonon}}}{R_{\text{magnon}}} \sim \frac{\langle N_e \rangle^2 m_\chi^3 v}{S_{\text{ion}} m_{\text{ion}} m_e^2 c_s} \sim \left(\frac{m_\chi}{\text{MeV}}\right)^3 \left(\frac{\langle N_e \rangle}{10}\right)^2 \frac{10 \text{ GeV}}{m_{\text{ion}}} \frac{v}{10^{-3}} \frac{10^{-5}}{c_s}$, assuming similar m_{cell} and m_{ion} for the targets and $S_{\text{ion}} \sim \mathcal{O}(1)$.

7.4 Conclusions

We have formulated an EFT framework for computing direct detection rates via single phonon and magnon excitations for general DM interactions, and illustrated its application with a set of benchmark models, listed in Table 7.2, that cover a wide range of possibilities for a spin- $\frac{1}{2}$ DM particle interacting with SM fermions $\psi = p, n, e$ (proton, neutron and electron). The procedure consists of first matching a relativistic DM model onto the standard set of NR effective operators, listed in Table 7.3, and then matching these operators onto lattice degrees of freedom, including particle numbers $\langle N_\psi \rangle$, spins $\langle \mathbf{S}_\psi \rangle$, orbital angular momenta $\langle \mathbf{L}_\psi \rangle$ and spin-orbit couplings $\langle \mathbf{L}_\psi \otimes \mathbf{S}_\psi \rangle$ for the $\psi = p, n, e$ particles in an ion. These define the four types of *crystal responses* and enter the rate formula for single phonon excitation, while a subset of them – $\langle \mathbf{S}_e \rangle$ and $\langle \mathbf{L}_e \rangle$ – also enter the rate formula for single magnon excitation.

A practical prescription for computing direct detection rates, as explained around Eq. (7.45), utilizes the central formula, Eq. (7.30), which gives the lattice scattering potential in terms of the effective operator coefficients $c_i^{(\psi)}$. Upon plugging in the $c_i^{(\psi)}$'s generated by a relativistic theory of DM (listed in Table 7.2 for our benchmark models), one simply replaces the ionic expectation values $\langle X_\psi \rangle_{lj}$ by $F_{X,\nu}^{(\psi)}$ defined in Eq. (7.43) (for $\psi = p, n, e$ and $X = N, S, L, L \otimes S$) or $\mathbf{E}_{X,\nu}$ defined in Eq. (7.44) (for $\psi = e$ and $X = S, L$), squares the expression and takes the DM spin average. This gives the differential rates $\Sigma_\nu(\mathbf{q})$, which are then substituted into Eqs. (7.45) and (7.46) for the total rate of single phonon or magnon excitation.

The set of crystal responses that we have identified point to various possibilities of optimizing detector target choice. However, a general observation from our calculations in Sec. 7.3 is that, among the four types of crystal responses, $\langle N_\psi \rangle$ and $\langle \mathbf{S}_\psi \rangle$, which are associated with point-like degrees of freedom, tend to dominate the rate, compared to the composite responses $\langle \mathbf{L}_\psi \rangle$ and $\langle \mathbf{L}_\psi \otimes \mathbf{S}_\psi \rangle$. This implies that, purely from the point of view of maxi-

mizing the rate, exotic materials with orbital orders or strong spin-orbit couplings are not necessary for improving the reach to a broad class of DM models.

Meanwhile, as phonon DM experiments focused on crystal targets, such as SPICE (Sub-eV Polar Interactions Cryogenic Experiment), which is part of the TESSERACT (Transition Edge Sensors with Sub-EV Resolution And Cryogenic Targets) project [90], move into R&D, it is important to note that their discovery potential extends well beyond the simplest models with spin-independent interactions studied previously. As we showed in Sec. 7.3, with the exception of a pure spin-dependent interaction, phonon excitations have broad sensitivity to light DM models. Perhaps surprisingly, with judicious choice of target material, phonon excitations may even be competitive with magnon excitations for some DM models where the latter is expected to have a parametrically higher rate, such as the magnetic dipole and anapole DM models. Given the greater challenges associated with single magnon detection relative to phonons, this is encouraging for phonon-based experiments in the near term.

Part II

Electronic Excitations

EXTENDED CALCULATION OF DARK MATTER ELECTRON SCATTERING IN CRYSTAL TARGETS

8.1 Introduction

Electronic excitations have been established as an alternative to nuclear recoils in direct detection of sub-GeV dark matter (DM). Nuclear recoil searches lose sensitivity at lower DM masses due to kinematic mismatch between the DM and heavier nuclei, whereas electronic transitions can potentially extract all of the DM kinetic energy during a DM-electron scattering event by excitation across an energy gap. Proposed targets, including noble gas atoms with $\mathcal{O}(10\text{ eV})$ ionization energies [14, 19, 24, 35, 177, 244, 333, 334], semiconductors with $\mathcal{O}(\text{eV})$ electronic band gaps [6, 7, 19, 25, 33–35, 39, 40, 177, 180, 248, 256], and superconductors and Dirac materials with $\mathcal{O}(\text{meV})$ band gaps [29, 41, 144, 181–183, 335], extend the reach on DM mass well below the limit of nuclear recoil. Experimental searches using dielectric crystal targets are currently underway, specifically with Si (DAMIC [21, 71, 81], SENSEI [22, 85–87], SuperCDMS [23, 77–80, 88, 89]) and Ge (EDELWEISS [82–84], as well as SuperCDMS) which have been predicted to have excellent sensitivity down to $\mathcal{O}(\text{MeV})$ DM masses based on their $\mathcal{O}(\text{eV})$ band gaps.

Reliable theoretical predictions of target-specific transition rates are important not only for current experiments, but also for planning the next generation of detectors. Compared to the DM-induced electron ionization rate in noble gases like xenon [14, 19, 24, 35, 177, 244, 333, 334], calculations for the DM-electron scattering rate in a crystal are more complicated. Ionization rates for noble gases can be calculated by considering each noble gas atom as an individual target, where the calculation simplifies to finding the ionization rate from an isolated atom, for which the wave functions and energy levels are well tabulated [336]. However, for crystal targets the atoms are not isolated and more involved techniques are required to obtain an accurate characterization of DM-electron interactions in a many-body system.

There have been a variety of approaches taken to compute the DM-electron scattering rate in crystals. One of the first attempts, Ref. [177], computed the rate with semi-analytic approximations for the initial and final state wave functions, and used the density of states to incorporate the electronic band structure. Later, Ref. [35] continued in this direction and used improved semi-analytic approximations for the initial state wave functions. Mean-

while, a fully numerical approach was advanced in Refs. [19, 33, 34] where density functional theory (DFT) was employed to calculate the valence and conduction electronic band structures and wave functions. The latter approach, as implemented in the `QEdark` program and embedded in the `QUANTUM ESPRESSO` package [337–339], has become the standard for first-principles calculations of DM detection rates. Recently, in Refs. [6, 7] we used a similar DFT approach as implemented in our own program for a study of DM-electron scattering in a variety of target materials. More recently there has been work utilizing the relation between the dielectric function and the spin-independent scattering rate [36, 48, 49], which also properly incorporates screening effects.

The goal of this work is to further extend the DM-electron scattering calculation in several key aspects, and present state-of-the-art predictions for Si and Ge detectors using a combination of DFT and semi-analytic methods. As we will elaborate on shortly, the time- and resource-consuming nature of DFT calculations presents an intrinsic difficulty that has limited the scope of previous work in this direction to a restricted region of phase space; typically only bands within a few tens of eV above and below the band gap were included and electronic wave functions were cut off at a finite momentum. We overcome this difficulty by implementing all-electron (AE) reconstruction (whose importance was previously emphasized in Ref. [340]) to recover higher momentum components of DFT-computed wave functions, and by extending the calculation to bands farther away from the band gap using semi-analytic approximations along the lines of Refs. [35, 177]. As we will see, the new contributions computed here have a significant impact on detection prospects in cases where higher energy and/or momentum regions of phase space dominate the rate, including scattering via a heavy mediator, and experiments with $\mathcal{O}(10\text{ eV})$ or higher energy thresholds. We also stress that in contrast to the recent work emphasizing the relation between spin-independent DM-electron scattering rates and the dielectric function [36, 48, 49], our calculation can be straightforwardly extended to DM models beyond the standard spin-independent coupling. Furthermore, we do not make assumptions about isotropy for the majority of our calculation, and our framework is capable of treating anisotropic targets which exhibit smoking-gun daily modulation signatures [7, 29, 183] (see also Refs. [28, 341] for discussions of daily modulation for phonon excitations).

Our calculation is implemented in an open-source program `EXCEED-DM` (EXtended Calculation of Electronic Excitations for Direct detection of Dark Matter), to be released in an upcoming publication. Currently a beta version of the program is available [here](#) [342]. We also make available our DFT-computed wave functions [343] and the output of `EXCEED-DM` [344] for Si and Ge.

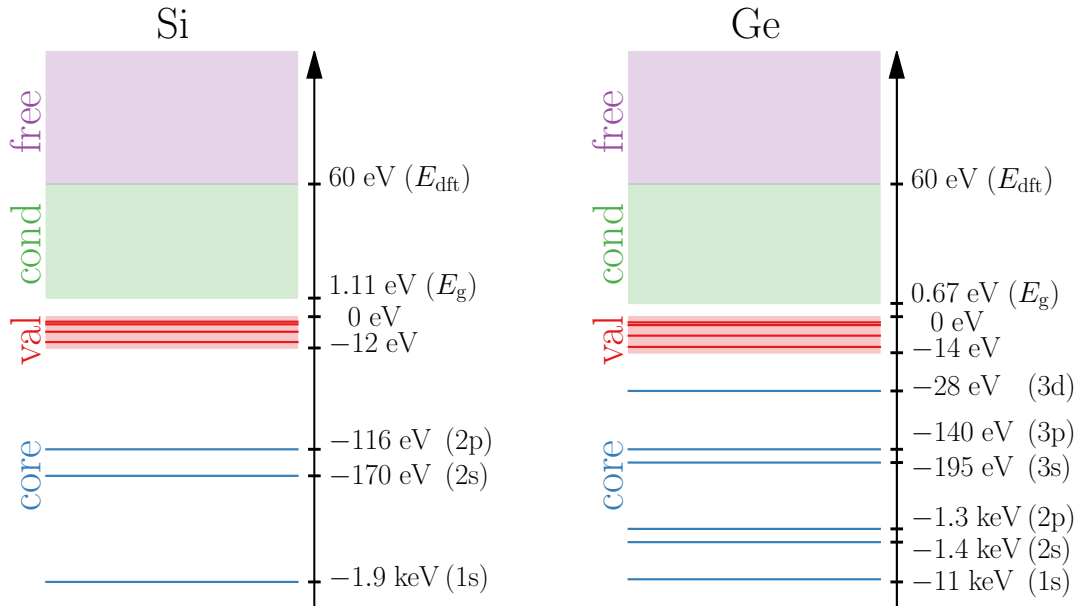


Figure 8.1: Schematic representation of electronic states in Si (left) and Ge (right), divided into core, valence (“val”), conduction (“cond”) and free. Shaded regions indicate the range of energies for each type of electronic states. In a scattering process, electrons transition from either core or valence states, below the Fermi surface at $E = 0$, to conduction or free states above the band gap E_g . As outlined in Sec. 8.1 and explained in detail in Sec. 8.2, we compute the valence and conduction states numerically using DFT (including all-electron reconstruction), model the core states semi-analytically with RHF wave functions, and treat the free states as plane waves.

Overview of the Calculation and Key Results

Before delving into the technical details, let us give a brief overview of the calculation and highlight some key results. We divide the electronic states in a (pure) crystal into four categories: core, valence, conduction and free, as illustrated in Fig. 8.1 for Si and Ge and discussed in more detail in Sec. 8.2. At zero temperature, electrons occupy states up to the Fermi energy, defined as the maximum of the valence bands and denoted by $E = 0$. The band gap E_g , i.e., the energy gap between the occupied valence bands and unoccupied conduction bands, is typically $\mathcal{O}(\text{eV})$ for semiconductors, e.g., 1.11 eV for Si and 0.67 eV for Ge; this sets a lower limit on the energy deposition needed for an electron transition to happen.

The electronic states near the band gap deviate significantly from atomic orbitals and need to be computed numerically. We apply DFT methods (including AE reconstruction) for this calculation, and refer to the DFT-computed states as valence and conduction. Specifically, for both Si and Ge, we take the first four bands below the gap to be valence, which span an energy range of -12 eV to 0 and -14 eV to 0 , respectively, and take bands above the gap up

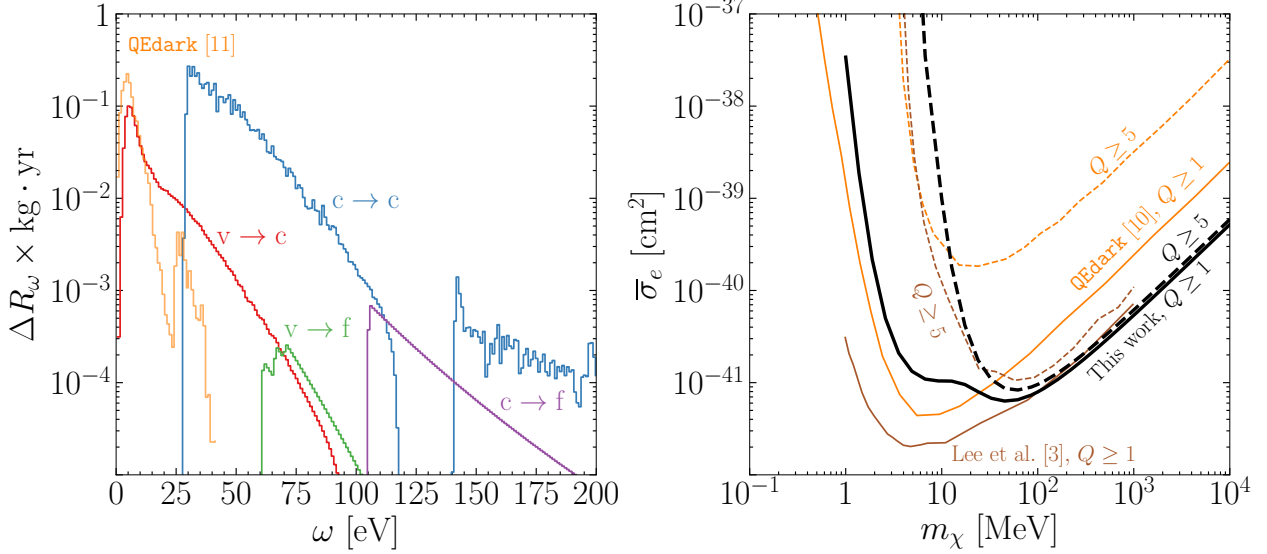


Figure 8.2: Selection of results from Sec. 8.4, for DM-electron scattering via a heavy mediator in a Ge target. **Left:** Contribution from each of the four transition types, valence to conduction ($v \rightarrow c$), valence to free ($v \rightarrow f$), core to conduction ($c \rightarrow c$), and core to free ($c \rightarrow f$) to the scattering rate binned in energy deposition (with $\Delta\omega = 1$ eV) for a 1 GeV DM at a given reference cross section $\bar{\sigma}_e = 10^{-40}$ cm². **Right:** 95% C.L. projected limit (3 events) on $\bar{\sigma}_e$ assuming 1 kg-year exposure, for energy thresholds corresponding to 1 and 5 electron-hole pairs. We compare our results with QEdark calculations in Refs. [33, 34] and the semi-analytic model of Lee et al [35]; see text for details.

to $E_{\text{dft}} = 60$ eV to be conduction.

With more computing power we can in principle include more states, both below and above the band gap, in the DFT calculation. However, since the states far from the band gap can be modeled semi-analytically with reasonable accuracy, computing them with DFT is inefficient. Below the valence bands, electrons are tightly bound to the atomic nuclei. We model them using semi-analytic atomic wave functions and refer to them as core states. These include the 1s, 2s, 2p states in Si and 1s, 2s, 2p, 3s, 3p, 3d states in Ge (the 3d states in Ge are sometimes referred to as semi-core, and we will compare the DFT and semi-analytic treatment of them in Secs. 8.2 and 8.3). Finally, above $E_{\text{dft}} = 60$ eV, we model the states as free electrons as they are less perturbed by the crystal environment.

With the electronic states modeled this way, we compute the rate for valence to conduction ($v \rightarrow c$), valence to free ($v \rightarrow f$), core to conduction ($c \rightarrow c$) and core to free ($c \rightarrow f$) transitions induced by DM scattering, as discussed in detail in Sec. 8.3. The total rate is the sum of all four contributions. We then use our calculation to update the projected reach of direct detection experiments in Sec. 8.4, and compare our results with previous literature.

Figure 8.2 gives a glimpse of some of our key results. Here we consider the case of DM scattering via a heavy mediator in a Ge target. The impact of core (3d) to conduction contributions is clearly visible from both the differential rate (left panel, for $m_\chi = 1$ GeV) and the projected reach (right panel). They dominate the total rate for $m_\chi \gtrsim 10$ MeV, and, as we can see from the right panel of Fig. 8.2, lead to significantly more optimistic reach compared to previous DFT calculations implemented in `QEdark` [33, 34]; this is especially true for higher detector thresholds (corresponding to higher Q values). Note that while Refs. [33, 34] included the 3d states in their DFT calculation, their contributions were significantly underestimated due to the absence of AE reconstruction. The importance of AE reconstruction is also seen from the valence to conduction differential rate in the left panel of Fig. 8.2, where our calculation predicts a much higher rate at $\omega \gtrsim 15$ eV compared to the `QEdark` calculation in Ref. [34]. Meanwhile, accounting for in-medium screening (see Sec. 8.3) we find, consistent with Ref. [36], a lower rate at energy depositions just above the band gap, and as a result, weaker reach at low m_χ , compared to Refs. [33, 34]. On the other hand, our modeling of the core (3d) states is similar to the semi-analytic approach of Ref. [35], and indeed we find very similar reach at large m_χ ; however, the approach of Ref. [35] overestimates the rate at smaller m_χ due to reduced accuracy in the modeling of the valence and conduction states. We reserve a more detailed comparison with the literature for Sec. 8.4.

8.2 Electronic States

To compute the DM-electron scattering rate one must understand the electronic states of the target. In targets with a periodic potential, Bloch's theorem states that the energy eigenstates can be indexed by a momentum, \mathbf{k} , which lies within the first Brillouin zone (1BZ). These Bloch states, $\psi_{i,\mathbf{k}}$, where i represents additional quantum numbers, are eigenstates of the discrete translation operator such that $\psi_{i,\mathbf{k}}(\mathbf{x} + \mathbf{r}) = e^{i\mathbf{k}\cdot\mathbf{r}}\psi_{i,\mathbf{k}}(\mathbf{x})$, which means the electronic wave functions can be written as

$$\psi_{i,\mathbf{k}}(\mathbf{x}) = \frac{1}{\sqrt{V}} e^{i\mathbf{k}\cdot\mathbf{x}} u_{i,\mathbf{k}}(\mathbf{x}), \quad (8.1)$$

where $u_{i,\mathbf{k}}(\mathbf{x} + \mathbf{r}) = u_{i,\mathbf{k}}(\mathbf{x})$ and V is the target volume. For every \mathbf{k} there exists a tower of eigenstates (labeled by i) of the target Hamiltonian which constitutes the complete set of states in the target. Unfortunately this complete set is not known for a general material and therefore a combination of approximations must be used to calculate them. As discussed in Sec. 8.1 and illustrated in Fig. 8.1, we divide the states into core, valence, conduction and free, and use a combination of numerical calculations and semi-analytic modeling. In this section, we expand on the treatment of each type of electronic states.

We first discuss the DFT calculation for valence and conduction states in Sec. 8.2, and then

move on to explain the semi-analytic treatment of core states in Sec. 8.2. Our main results are contained in Fig. 8.3 where we compare the average magnitude of electronic wave functions, binned in momentum (see Eq. (8.7)), computed with and without AE reconstruction, discussed further in Sec. 8.2, and, for the highest energy core states (2p in Si and 3d in Ge), those computed using the core approximation discussed in Sec. 8.2. We find that the AE reconstruction includes a significant contribution from wave functions at large momentum as expected, and that for the core states, the semi-analytic approach reproduces the large momentum components of these AE reconstructed DFT wave functions. Lastly we will discuss the analytic treatment of the free states in Sec. 8.2.

DFT Wave Functions and Band Structures

In principle, DFT provides an exact solution to the many-electron Schrödinger equation by the Hohenberg-Kohn theorems that treat all properties of a quantum many-body system as unique functionals of the ground state density. They further show that the exact ground state density and energy can be found by minimizing the total energy of the system [294, 345]. This becomes tractable by the Kohn-Sham (KS) equations that reduce the many-body problem to non-interacting electrons moving in an effective potential, V_{eff} ,

$$\left(\frac{p^2}{2m_e} + V_{\text{eff}} - \epsilon_i \right) \psi_i = 0, \quad V_{\text{eff}} = V_{\text{ext}} + V_{\text{H}} + V_{\text{xc}}, \quad (8.2)$$

where ϵ_i is the orbital energy of the KS orbital ψ_i [346]. The external potential V_{ext} and Hartree potential V_{H} , are known, while the exchange-correlation (xc) potential V_{xc} , which contains the many-body interactions, must be approximated. Herein lies the deviation from the exact solution, and although various formulations of xc-energy functionals have been successful, the choice of xc-functional will affect the predicted electronic states and hence calculated transition rates. For Si, we use PBE [347], a type of generalized gradient approximation (GGA) xc-functional which is one of the most popular and low-cost choices. Local and semi-local based xc-functionals, such as PBE, suffer from a self-interaction error and band gap underestimation, which we modify with a “scissor correction” where the bands are shifted to match the experimentally determined values of band gap. For Ge, this underestimation results in zero band gap with PBE, therefore we instead use a hybrid functional, which mixes a parameterized amount of exact exchange into the xc-functional, correcting band gaps and band widths by error cancellation at the cost of increased computation time. We use the range-separated hybrid functional HSE06 [348, 349], which applies a screened Coulomb potential to correct the long-range behavior of the xc-potential, giving high accuracy at a mid-level computational cost. Our computed band structures for Si and Ge are shown in Fig. 8.4.

The periodic Bloch wave functions, $u_{i,\mathbf{k}}(\mathbf{x})$, Eq. (8.1), for band i and Bloch wave vector \mathbf{k} are computed by finding the Fourier coefficients, $\tilde{u}_{i,\mathbf{k},\mathbf{G}}$ (which satisfy the normalization condition, $\sum_{\mathbf{G}} |\tilde{u}_{i,\mathbf{k},\mathbf{G}}|^2 = 1$):

$$u_{i,\mathbf{k}}(\mathbf{x}) = \sum_{\mathbf{G}} \tilde{u}_{i,\mathbf{k},\mathbf{G}} e^{i\mathbf{G}\cdot\mathbf{x}}. \quad (8.3)$$

The number of reciprocal lattice vectors \mathbf{G} kept in the sum is conventionally set by an energy cutoff, E_{cut} , such that $|\mathbf{k} + \mathbf{G}|^2 < 2m_e E_{\text{cut}}$. These Bloch wave function coefficients $\tilde{u}_{i,\mathbf{k},\mathbf{G}}$ for both Si and Ge are computed with the projector augmented wave (PAW) method [350, 351] within VASP [295–297, 352] up to $E_{\text{cut}} = 1$ keV on a $10 \times 10 \times 10$ uniform \mathbf{k} mesh over the 1BZ. We then include AE reconstruction effects up to a higher energy cutoff, $E_{\text{AE}} = 2$ keV, which recovers higher momentum components of the wave functions up to $|\mathbf{k} + \mathbf{G}|^2 < 2m_e E_{\text{AE}}$, as discussed in more detail in Sec. 8.2. The Bloch wave function coefficients, $\tilde{u}_{i,\mathbf{k},\mathbf{G}}$, for Si and Ge used for this work can be found here [343].

A final consideration of using DFT wave functions is that DFT is fundamentally a ground state method, and the KS conduction band states are only approximations to excited states. Excited state methodologies are much more computationally expensive than ground state KS-DFT. Furthermore, since excited state quasiparticles, such as excitons, have been argued to have a negligible effect on the calculation of DM scattering rates [34], they are neglected in our calculations.

All-Electron Reconstruction

There are many different approaches to find the eigenstates of Eq. (8.2). The PAW method [350] is one such standard approach. The main idea of the PAW method is to split up the calculation of the eigenstates: near the ionic centers the wave functions resemble the eigenstates of an isolated atom, while further away they can be computed numerically with a pseudopotential. This greatly simplifies the numeric calculation since the focus is then on large distance (small momentum), and the small distance (high momentum) pieces can be self-consistently reintroduced after the main part of the DFT calculation. The large distance components of the wave function are known as “pseudo wave functions” (PS wave functions) and the total wave functions are known as the “all-electron wave functions” (AE wave functions), indicating that all of the wave function components are included. We will now give a brief overview of how the AE wave functions can be reconstructed from the PS wave functions, computed with PAW-based DFT codes, and refer the reader to Refs. [350, 351, 353, 354] for more detailed information.¹

¹It is possible to calculate all electronic eigenstates, including the core, self-consistently by other more complex methods such as the full-potential linearized augmented plane wave (FP-LAPW) method or the

The AE wave functions, $|\Psi^{\text{AE}}\rangle$ are built from two components. Near the ionic core, or inside an “augmentation sphere,” $|\Psi^{\text{AE}}\rangle$ is expanded in a set of basis functions, $|\phi_j^{\text{AE}}\rangle$, which are simply taken to be the wave functions of an isolated atom,

$$|\Psi^{\text{AE}}\rangle = \sum_j c_j |\phi_j^{\text{AE}}\rangle. \quad (8.4)$$

Outside of the augmentation sphere, $|\Psi^{\text{AE}}\rangle = |\Psi^{\text{PS}}\rangle$. Near the ionic core the PS wave functions $|\Psi^{\text{PS}}\rangle$ are expanded in a set of basis functions $|\phi_j^{\text{PS}}\rangle$ that are computationally more convenient than the $|\phi_j^{\text{AE}}\rangle$. Therefore,

$$|\Psi^{\text{AE}}\rangle = |\Psi^{\text{PS}}\rangle - \sum_j c'_j |\phi_j^{\text{PS}}\rangle + \sum_j c_j |\phi_j^{\text{AE}}\rangle, \quad (8.5)$$

which simply replaces the components in $|\Psi^{\text{PS}}\rangle$ within the augmentation sphere with the AE wave function. To find the c coefficients we insert an identity, $1 = \sum_j |\phi_j^{\text{AE}}\rangle \langle p_j^{\text{AE}}| = \sum_j |\phi_j^{\text{PS}}\rangle \langle p_j^{\text{PS}}|$, where $|p_j^{\text{AE/PS}}\rangle$ are projector functions, defined to satisfy this identity within the augmentation sphere. Therefore, $c_j = \langle p_j^{\text{AE}} | \Psi^{\text{AE}} \rangle$, $c'_j = \langle p_j^{\text{PS}} | \Psi^{\text{PS}} \rangle$. The last ingredient to compute $|\Psi^{\text{AE}}\rangle$ from $|\Psi^{\text{PS}}\rangle$ is to require that $|\phi_j^{\text{AE}}\rangle$ is related to $|\phi_j^{\text{PS}}\rangle$ via a transformation, $|\phi_j^{\text{AE}}\rangle = \mathcal{T} |\phi_j^{\text{PS}}\rangle$. This implies that all the PS states are related to AE states by this transformation \mathcal{T} , such that $c_j = c'_j$ and the AE reconstruction can be written as

$$|\Psi^{\text{AE}}\rangle = |\Psi^{\text{PS}}\rangle + \sum_j (|\phi_j^{\text{AE}}\rangle - |\phi_j^{\text{PS}}\rangle) \langle p_j^{\text{PS}} | \Psi^{\text{PS}} \rangle. \quad (8.6)$$

In practice, we implement the AE reconstruction with `pawpyseed` [354], and the plane wave expansion cutoff of $|\Psi^{\text{AE}}\rangle$, E_{AE} , can be increased from the initial E_{cut} . We use $E_{\text{AE}} = 2$ keV.

To visualize the effect of AE reconstruction, we plot in Fig. 8.3 the average magnitude of the Bloch wave functions, binned in q ,

$$\langle |\tilde{u}_i|^2 \rangle (q; \Delta q) \equiv \frac{1}{N_q} \sum_{\mathbf{k}} \sum_{\mathbf{G}} |\tilde{u}_{i,\mathbf{k},\mathbf{G}}|^2 \theta(q + \Delta q - |\mathbf{k} + \mathbf{G}|) \theta(|\mathbf{k} + \mathbf{G}| - q), \quad (8.7)$$

where $\tilde{u}_{i,\mathbf{k},\mathbf{G}}$ are the Fourier components of the Bloch wave functions, defined in Eq. (8.3). Each bin in momentum space extends from q to $q + \Delta q$ with $\Delta q = 1$ keV, and N_q is a normalization factor equal to the number of points in a bin, $N_q = \sum_{\mathbf{k}} \sum_{\mathbf{G}} \theta(q + \Delta q - |\mathbf{k} + \mathbf{G}|) \theta(|\mathbf{k} + \mathbf{G}| - q)$. We see that AE reconstruction recovers the high momentum components, which as we will see can significantly affect the DM-induced transition rate for processes which favor large momentum transfers (such as processes mediated by heavy particles), or processes limited to larger ω (e.g., higher experimental thresholds where large

q processes are the only kinematically allowed transitions). Previous DFT calculations of DM-induced electron transition rates, with the exceptions of Ref. [6, 7, 340], used only the pseudo wave functions, $|\Psi^{\text{PS}}\rangle$ as opposed to the AE wave functions, $|\Psi^{\text{AE}}\rangle$, and have therefore underestimated detection rates in several cases.

Atomic Wave Functions

If one could reconstruct the AE wave functions arbitrarily deep into the band structure, and to arbitrarily high momentum, one could calculate an accurate representation of the complete set of electronic states with a DFT calculation. In practice, however, this is neither feasible nor necessary. States deep in the band structure are more isolated from the influence of the crystal environment, and so an isolated atomic approximation becomes valid. We refer to these inner, tightly bound electrons as core electrons. In Si, we will show that the 2p states and below can be treated as core, while in Ge, the 3d states and below can, as alluded to in Fig. 8.1. The purpose of this subsection is to expand on the atomic approximation for core electrons and discuss its accuracy.

More precisely, the initial states of a transition should be taken as a linear combination of isolated atomic wave functions that is in Bloch form (known as Wannier states):

$$\psi_{\kappa nlm, \mathbf{k}}(\mathbf{x}) = \frac{1}{\sqrt{N}} \sum_{\mathbf{r}} e^{i\mathbf{k} \cdot (\mathbf{r} + \mathbf{x}_{\kappa})} \psi_{\kappa nlm}^{\text{atom}}(\mathbf{x} - \mathbf{r} - \mathbf{x}_{\kappa}), \quad (8.8)$$

where κ labels the atom in the primitive cell, n, l, m are the standard atomic quantum numbers, \mathbf{x}_{κ} is the equilibrium position of the κ^{th} atom, $\sum_{\mathbf{r}}$ sums over all primitive cells in the lattice, and N is the total number of cells. In contrast to the valence and conduction states discussed in the previous subsection, the core states are labeled by (κnlm) rather than band index i . The corresponding periodic (dimensionless) u functions can be easily obtained via Eq. (8.1):

$$u_{\kappa nlm, \mathbf{k}}(\mathbf{x}) = \sqrt{\Omega} \sum_{\mathbf{r}} e^{-i\mathbf{k} \cdot (\mathbf{x} - \mathbf{r} - \mathbf{x}_{\kappa})} \psi_{\kappa nlm}^{\text{atom}}(\mathbf{x} - \mathbf{r} - \mathbf{x}_{\kappa}), \quad (8.9)$$

where $\Omega = V/N$ is the primitive cell volume.

In general, the atomic wave functions $\psi_{\kappa nlm}^{\text{atom}}$ are not known analytically, but are expanded in a basis of well-motivated analytic functions. The basis coefficients are then fit by solving the isolated atomic Hamiltonian, giving a semi-analytic expression for $\psi_{\kappa nlm}^{\text{atom}}$. We use a basis of Slater type orbital (STO) wave functions whose radial component is

$$R_{\text{STO}}(r; Z, n) = a_0^{-3/2} \frac{(2Z)^{n+\frac{1}{2}}}{\sqrt{(2n)!}} \left(\frac{r}{a_0}\right)^{n-1} e^{-Zr/a_0}, \quad (8.10)$$

where $a_0 = 0.53 \text{ \AA} = (3.7 \text{ keV})^{-1}$ is the Bohr radius, and Z is an effective charge of the ionic potential. Including the angular part, the atomic wave functions are then

$$\psi_{\kappa n l m}^{\text{atom}}(\mathbf{x}) = \sum_j C_{j l n, \kappa} R_{\text{STO}}(x; Z_{j l, \kappa}, n_{j l, \kappa}) Y_l^m(\hat{\mathbf{x}}), \quad (8.11)$$

where $C_{j l n, \kappa}$, $Z_{j l, \kappa}$, $n_{j l, \kappa}$ are tabulated in Ref. [336], and $Y_l^m(\hat{\mathbf{x}})$ are the spherical harmonics with the Condon-Shortley phase convention [355].

To assess the accuracy of the atomic wave function approximation, we temporarily push the DFT calculation beyond its default regime (valence and conduction), to the highest core states – 2p states in Si and 3d states in Ge, where it is still computationally feasible – and compare the numerical wave functions to the semi-analytic ones discussed above. The results, in terms of the average magnitude of Bloch wave functions defined in Eq. (8.7), are shown in the right panels of Fig. 8.3.² We see that the atomic approximation accurately reproduces the numerical wave functions up to the momentum cutoff $\sqrt{2m_e E_{\text{AE}}} \simeq 50 \text{ keV}$ for $E_{\text{AE}} = 2 \text{ keV}$. These plots also show the limitation of DFT calculations. While AE reconstruction recovers higher-momentum components of electronic wave functions, it is not feasible to expand the plane wave basis set to arbitrarily high cutoff. However, having verified the atomic approximation for the highest core states, we can use it for all core states with confidence, allowing us to more easily include the high momentum components beyond the DFT cutoff.

Plane Wave Approximation

With the inclusion of the semi-analytic core states, all of the states below the band gap have been modeled. States above the band gap can also be computed with DFT methods, as described in Sec. 8.2. Similar to valence bands, there are practical limitations to how many conduction bands can be included. To remedy this in the simplest way possible, we model states far above the band gap as plane waves,

$$\psi_{\mathbf{G}, \mathbf{k}}(\mathbf{x}) = \frac{1}{\sqrt{V}} e^{i(\mathbf{k} + \mathbf{G}) \cdot \mathbf{x}}, \quad E_{\mathbf{G}, \mathbf{k}} = \frac{|\mathbf{k} + \mathbf{G}|^2}{2m_e}, \quad (8.12)$$

where \mathbf{G} is a reciprocal lattice vector, and plays the role of a band index. (To understand this, simply note that every momentum can be decomposed into a \mathbf{k} vector inside the 1BZ and a reciprocal lattice vector. Integrating over the momentum of plane wave states amounts to a \mathbf{k} integral within the 1BZ and a \mathbf{G} sum.) From Eq. (8.1) we see that the corresponding

²The flatness of band structures offers a complementary check of the validity of the atomic approximation. We have verified that the DFT computed energy eigenvalues indeed have a small variance for the highest core states, as expected.

periodic u functions are simply

$$u_{\mathbf{G},\mathbf{k}}(\mathbf{x}) = e^{i\mathbf{G}\cdot\mathbf{x}}. \quad (8.13)$$

The plane wave approximation is often used in atomic ionization rate calculations, with the inclusion of a *Fermi factor*, $F(\nu)$,

$$F(\nu) = \frac{\nu}{1 - e^{-\nu}}, \quad \nu(Z_{\text{eff}}, E) = 2\pi Z_{\text{eff}} \frac{\alpha m_e}{\sqrt{2m_e E}}, \quad (8.14)$$

where E is the final state electron energy, and Z_{eff} is an effective charge parameter, which enhances the transition rate at low E to account for the long range behavior of the Coulomb potential. See Refs. [19, 35, 177, 333] for more details. In atomic ionization calculations one usually takes Z_{eff} to be related to the binding energy of the initial state, E_B ,

$$Z_{\text{eff}} = n \sqrt{\frac{E_B}{13.6 \text{ eV}}}, \quad (8.15)$$

where n is the principal quantum number. Since the rate is proportional to the Fermi factor, $Z_{\text{eff}} = 1$ is seen as the conservative choice. Later in Secs. 8.3 and 8.3 we quantify how much of an effect this has on the transition rate. This uncertainty is only important for very high experimental thresholds, and generally we find that $Z_{\text{eff}} = 1$ leads to a smoother match (within an $\mathcal{O}(1)$ factor) to conduction band contributions from DFT calculations.

8.3 Electronic Transition Rates

We now present the DM-induced electron transition rate calculation. We begin with a general discussion and then in Secs. 8.3-8.3 consider the four different transition types in turn: valence to conduction ($v \rightarrow c$), valence to free ($v \rightarrow f$), core to conduction ($c \rightarrow c$) and core to free ($c \rightarrow f$). Finally, in Sec. 8.3 we discuss the treatment of in-medium screening.

The general derivation has been discussed previously (see, e.g., Refs. [7, 33, 177, 244, 340]), and we repeat it here for completeness and clarity, as a variety of conventions have been used. Beginning with Fermi's Golden Rule, the transition rate between electronic states $|i, s\rangle$ and $|f, s'\rangle$ due to scattering with an incoming non-relativistic DM particle, χ , with mass m_χ , velocity \mathbf{v} , and spin σ is given by

$$\Gamma_{i,s,\sigma \rightarrow f,s',\sigma'}(\mathbf{v}) = 2\pi V \int \frac{d^3q}{(2\pi)^3} |\langle \mathbf{p}', \sigma'; f, s' | \delta \hat{H} | \mathbf{p}, \sigma; i, s \rangle|^2 \delta(E_{f,s'} - E_{i,s} - \omega_{\mathbf{q}}), \quad (8.16)$$

where $|\mathbf{p}, \sigma; i, s\rangle = |\mathbf{p}, \sigma\rangle \otimes |i, s\rangle$, \mathbf{q} is the momentum deposited onto the target, $\mathbf{p} = m_\chi \mathbf{v}$, $\mathbf{p}' = \mathbf{p} - \mathbf{q}$, $\delta \hat{H}$ is the interaction Hamiltonian, V is total volume of the target, and $\omega_{\mathbf{q}}$ is the energy deposition:

$$\omega_{\mathbf{q}} = \frac{1}{2} m_\chi v^2 - \frac{(m_\chi \mathbf{v} - \mathbf{q})^2}{2m_\chi} = \mathbf{q} \cdot \mathbf{v} - \frac{q^2}{2m_\chi}. \quad (8.17)$$

We assume that all quantum states are unit normalized. Modulo in-medium screening effects, discussed below in Sec. 8.3, we can write Eq. (8.16) in terms of the standard QFT matrix element, defined with plane wave incoming and outgoing states, by inserting $\mathbb{1} = V \sum_s \int \frac{d^3k}{(2\pi)^3} |\mathbf{k}, s\rangle \langle \mathbf{k}, s|$ and using

$$\langle \mathbf{p}', \sigma'; \mathbf{k}', s' | \delta \hat{H} | \mathbf{p}, \sigma; \mathbf{k}, s \rangle \equiv \frac{(2\pi)^3}{V^2} \frac{\mathcal{M}_{\sigma' s' \sigma s}(\mathbf{p}', \mathbf{k}', \mathbf{p}, \mathbf{k})}{4m_e m_\chi} \delta^{(3)}(\mathbf{p}' + \mathbf{k}' - \mathbf{p} - \mathbf{k}). \quad (8.18)$$

We find

$$\begin{aligned} \Gamma_{i,s,\sigma \rightarrow f,s',\sigma'}(\mathbf{v}) &= \frac{2\pi}{16V m_e^2 m_\chi^2} \int \frac{d^3q}{(2\pi)^3} \delta(E_{f,s'} - E_{i,s} - \omega_{\mathbf{q}}) \\ &\times \left| \int \frac{d^3k}{(2\pi)^3} \mathcal{M}_{\sigma' s' \sigma s}(\mathbf{p} - \mathbf{q}, \mathbf{k} + \mathbf{q}, \mathbf{p}, \mathbf{k}) \tilde{\psi}_f^*(\mathbf{k} + \mathbf{q}) \tilde{\psi}_i(\mathbf{k}) \right|^2, \end{aligned} \quad (8.19)$$

where $\tilde{\psi}_i(\mathbf{k}) = \sqrt{V} \langle \mathbf{k} | i \rangle$.

We will limit our analysis to matrix elements which only depend on \mathbf{q} , and assume that the electron energy levels are also spin independent, which allows the spin sums to be easily computed:

$$\begin{aligned} \bar{\Gamma}_{i \rightarrow f} &\equiv \frac{1}{2} \sum_{\sigma, \sigma'} \sum_{s, s'} \Gamma_{i,s,\sigma \rightarrow f,s',\sigma'} \\ &= \frac{4\pi}{16V m_e^2 m_\chi^2} \int \frac{d^3q}{(2\pi)^3} \overline{|\mathcal{M}(\mathbf{q})|^2} |f_{i \rightarrow f}|^2 \delta(E_f - E_i - \omega_{\mathbf{q}}), \end{aligned} \quad (8.20)$$

$$f_{i \rightarrow f} \equiv \int \frac{d^3k}{(2\pi)^3} \tilde{\psi}_f^*(\mathbf{k} + \mathbf{q}) \tilde{\psi}_i(\mathbf{k}) = \int d^3x e^{i\mathbf{q} \cdot \mathbf{x}} \psi_f^*(\mathbf{x}) \psi_i(\mathbf{x}), \quad (8.21)$$

where $\overline{|\mathcal{M}|^2}$ is the spin averaged matrix element squared and we have defined a crystal form factor $f_{i \rightarrow f}$, written in terms of both momentum and position space representations of the wave functions.

The transition rate per target mass, $R_{i \rightarrow f}$, is then given by

$$R_{i \rightarrow f} = \frac{1}{\rho_T} \frac{\rho_\chi}{m_\chi} \int d^3v f_\chi(\mathbf{v}) \bar{\Gamma}_{i \rightarrow f}, \quad (8.22)$$

where ρ_T is the target density, $\rho_\chi = 0.4 \text{ GeV}/\text{cm}^3$ is the local DM density, and f_χ is taken to be a boosted Maxwell-Boltzmann distribution. The total rate, R , is then simply the sum over all possible transitions from initial to final states. Since the only \mathbf{v} dependence in Eq. (8.22) comes from the energy conserving delta function, we perform the \mathbf{v} integral first and define $g(\mathbf{q}, \omega) = 2\pi \int d^3v f_\chi(v) \delta(\omega - \omega_{\mathbf{q}})$. This integral can be evaluated analytically (see

e.g., Refs. [7, 29, 341]):

$$g(\mathbf{q}, \omega) = \frac{2\pi^2 v_0^2}{N_0} \frac{1}{q} \left(e^{-v_-^2/v_0^2} - e^{-v_{\text{esc}}^2/v_0^2} \right), \quad (8.23)$$

$$v_- = \min \left\{ \frac{1}{q} \left| \omega + \frac{q^2}{2m_\chi} + \mathbf{q} \cdot \mathbf{v}_e \right|, v_{\text{esc}} \right\}, \quad (8.24)$$

where $\omega = E_f - E_i$ is the deposited energy, and N_0 is a normalization factor such that $\int d^3\mathbf{v} f_\chi(\mathbf{v}) = 1$. We take the DM velocity distribution parameters to be $v_0 = 230$ km/s, $v_{\text{esc}} = 600$ km/s, and $v_e = 240$ km/s. The total rate then becomes

$$R = \frac{2}{16V m_e^2 m_\chi^3 \rho_T} \sum_{i,f} \int \frac{d^3q}{(2\pi)^3} \overline{|\mathcal{M}(\mathbf{q})|^2} g(\mathbf{q}, \omega) |f_{i \rightarrow f}(\mathbf{q})|^2. \quad (8.25)$$

Here we focus on simple DM models, such as the kinetically mixed dark photon or leptophilic scalar mediator models. In these models $\mathcal{M}(\mathbf{q})$ can be factorized as $\mathcal{M}(q) = \mathcal{M}(q_0) \mathcal{F}_{\text{med}}(q_0/q) (f_e/f_e^0)$, where $\mathcal{F}_{\text{med}}(q_0/q) = 1$ for a heavy mediator and $\mathcal{F}_{\text{med}}(q_0/q) = (q_0/q)^2$ for a light mediator, and f_e/f_e^0 is a screening factor discussed in more detail in Sec. 8.3. As in previous works, we choose the reference momentum transfer to be $q_0 = \alpha m_e$. We can then finally write the rate in terms of a reference cross section,

$$\bar{\sigma}_e = \frac{\mu_{\chi e}^2}{16\pi m_\chi^2 m_e^2} \overline{|\mathcal{M}(q_0)|^2}, \quad (8.26)$$

and find

$$R = \frac{2\pi \bar{\sigma}_e}{V \mu_{\chi e}^2 m_\chi \rho_T} \sum_{i,f} \int \frac{d^3q}{(2\pi)^3} \left(\frac{f_e}{f_e^0} \right)^2 \mathcal{F}_{\text{med}}^2 g(\mathbf{q}, \omega) |f_{i \rightarrow f}(\mathbf{q})|^2. \quad (8.27)$$

Another useful quantity is the *binned* rate (the rate for energy deposition between ω and $\omega + \Delta\omega$), ΔR_ω , defined as

$$\begin{aligned} \Delta R_\omega &= \frac{2\pi \bar{\sigma}_e}{V \mu_{\chi e}^2 m_\chi \rho_T} \sum_{i,f} \theta(\omega + \Delta\omega - E_f + E_i) \theta(\omega - E_f + E_i) \\ &\quad \times \int \frac{d^3q}{(2\pi)^3} \left(\frac{f_e}{f_e^0} \right)^2 \mathcal{F}_{\text{med}}^2 g(\mathbf{q}, \omega) |f_{i \rightarrow f}(\mathbf{q})|^2. \end{aligned} \quad (8.28)$$

Valence to Conduction

We begin with valence to conduction band transitions. The initial (final) states are indexed by band number, $i(f)$, and Bloch momentum, $\mathbf{k}_i(\mathbf{k}_f)$ inside the 1BZ. The wave functions in Eq. (8.1) can be substituted into the crystal form factor in Eq. (8.21),

$$\begin{aligned} f_{i, \mathbf{k}_i \rightarrow f, \mathbf{k}_f} &= \frac{1}{V} \int d^3x e^{i(\mathbf{k}_i - \mathbf{k}_f + \mathbf{q}) \cdot \mathbf{x}} u_{f, \mathbf{k}_f}^*(\mathbf{x}) u_{i, \mathbf{k}_i}(\mathbf{x}) \\ &= \sum_{\mathbf{G}} \delta_{\mathbf{q}, \mathbf{k}_f - \mathbf{k}_i + \mathbf{G}} \frac{1}{\Omega} \int_{\text{cell}} d^3x e^{i\mathbf{G} \cdot \mathbf{x}} u_{f, \mathbf{k}_f}^*(\mathbf{x}) u_{i, \mathbf{k}_i}(\mathbf{x}), \end{aligned} \quad (8.29)$$

where the integral is over the primitive cell with volume Ω , and we have used the identity $\sum_{\mathbf{r}} e^{i\mathbf{q}\cdot\mathbf{r}} = N \sum_{\mathbf{G}} \delta_{\mathbf{q},\mathbf{G}}$. The total rate in Eq. (8.27) is then

$$R = \frac{2\pi\bar{\sigma}_e}{\mu_\chi^2 m_\chi} \frac{\rho_\chi}{\rho_T} \sum_{i=1}^{N_v} \sum_{f=1}^{N_c} \int_{\text{1BZ}} \frac{d^3k_i}{(2\pi)^3} \frac{d^3k_f}{(2\pi)^3} \sum_{\mathbf{G}} \left(\frac{f_e}{f_e^0} \right)^2 \mathcal{F}_{\text{med}}^2 g(\mathbf{q}, \omega) \times \left| \frac{1}{\Omega} \int_{\text{cell}} d^3x e^{i\mathbf{G}\cdot\mathbf{x}} u_{f,\mathbf{k}_f}^*(\mathbf{x}) u_{i,\mathbf{k}_i}(\mathbf{x}) \right|^2, \quad (8.30)$$

where $\mathbf{q} = \mathbf{k}_f - \mathbf{k}_i + \mathbf{G}$, $N_{v(c)}$ is the number of valence (conduction) bands. This is identical to the rate formulae derived in [6, 7, 33] but written in terms of the periodic Bloch functions, $u_{i,\mathbf{k}}(\mathbf{x})$, instead of their Fourier transformed components, $\tilde{u}_{i,\mathbf{k},\mathbf{G}}$, similar to Ref. [340]. Numerically the position space form is superior since the integral over the primitive cell can be computed by Fast Fourier Transform. This reduces the computational complexity from $\mathcal{O}(N_G^2)$ to $\mathcal{O}(N_G \log N_G)$, where N_G is the number of \mathbf{G} points, i.e., the number of Fourier components in the expansion of $\tilde{u}_{i,\mathbf{k}}$ in Eq. (8.3).

In Fig. 8.5 we show the scattering rate from valence to conduction transitions binned in energy deposition, defined in Eq. (8.28), for a 1 GeV DM. The main difference between the calculation performed here and in previous works is the effect of the AE reconstruction, as discussed in Sec. 8.2. For the case of DM with a heavy mediator, the rate, even with experimental thresholds as low as ~ 10 eV, is significantly enhanced relative to previous work. The AE reconstruction plays less of a role in the light mediator case since the transition rate is dominated by small momentum transfers. However, at high thresholds, where only larger momentum components can contribute, the AE reconstruction can still significantly boost the scattering rate by fully including the contributions neglected in the pseudo wave functions.

Since most earlier works computing DM-electron scattering include only valence to conduction transitions, it is useful to understand for which DM masses these are the only kinematically allowed transitions. If $\omega < E_g - E_{\text{max}}^{\text{core}}$, where $E_{\text{max}}^{\text{core}}$ is the maximum energy of the core states, then the core states cannot contribute; if $\omega < E_{\text{dft}}$ the free states are not available. Therefore if $\omega < \min\{E_{\text{dft}}, E_g - E_{\text{max}}^{\text{core}}\}$ only the valence to conduction transitions are allowed, which can be related to a DM mass via $\omega_{\text{max}}(m_\chi) < \min\{E_{\text{dft}}, E_g - E_{\text{max}}^{\text{core}}\}$, where

$$\omega_{\text{max}}(m_\chi) = \frac{1}{2} m_\chi v_{\text{max}}^2 = 3.9 \text{ eV} \left(\frac{m_\chi}{\text{MeV}} \right) \left(\frac{v_{\text{max}}}{840 \text{ km/s}} \right)^2, \quad (8.31)$$

with $v_{\text{max}} = v_e + v_{\text{esc}}$, the maximum incoming DM velocity. For Si (Ge), $E_{\text{max}}^{\text{core}} = -116$ eV

(−28 eV), this corresponds to

$$m_\chi < \begin{cases} 15.2 \text{ MeV} & (\text{Si}), \\ 7.8 \text{ MeV} & (\text{Ge}). \end{cases} \quad (8.32)$$

Requiring that $\omega_{\max} > E_g$, where E_g is the band gap, sets a lower bound on the minimum detectable mass, m_χ^{\min} ,

$$m_\chi^{\min} = \frac{2E_g}{v_{\max}^2} = 0.25 \text{ MeV} \left(\frac{E_g}{\text{eV}} \right) \left(\frac{840 \text{ km/s}}{v_{\max}} \right)^2. \quad (8.33)$$

For Si (Ge), with a band gap of 1.11 (0.67) eV, m_χ^{\min} is 0.28 (0.17) MeV. Lastly, we remark that for DM interactions characterized by higher-dimensional operators (not considered in this work), the scattering rate scales with higher powers of q and therefore is even more sensitive to AE reconstruction (and also $c \rightarrow c$ contributions discussed below in Sec. 8.3), which must be included in the analysis.

Valence to Free

For valence to free transitions the initial states are identical to those from Sec. 8.3, labeled by band number i and Bloch momentum, \mathbf{k}_i . The final state wave functions are simple plane waves given by Eq. (8.12), labeled by a momentum \mathbf{k}_f in the 1BZ with the bands labeled by \mathbf{G} . We can therefore directly substitute Eq. (8.13) into Eq. (8.29) derived in the previous subsection, and obtain the crystal form factor:

$$\begin{aligned} f_{i,\mathbf{k}_i \rightarrow \mathbf{G}_f, \mathbf{k}_f} &= \sum_{\mathbf{G}} \delta_{\mathbf{q}, \mathbf{k}_f - \mathbf{k}_i + \mathbf{G}} \frac{1}{\Omega} \int_{\text{cell}} d^3x e^{i(\mathbf{G} - \mathbf{G}_f) \cdot \mathbf{x}} u_{i,\mathbf{k}_i}(\mathbf{x}) \\ &= \sum_{\mathbf{G}} \delta_{\mathbf{q}, \mathbf{k}_f - \mathbf{k}_i + \mathbf{G}} \tilde{u}_{i,\mathbf{k}_i, \mathbf{G}_f - \mathbf{G}}, \end{aligned} \quad (8.34)$$

where $\tilde{u}_{i,\mathbf{k}_i, \mathbf{G}}$ are the Fourier components of the Bloch wave functions defined in Eq. (8.3). Incorporating the Fermi factor correction discussed in Sec. 8.2, we find the rate in Eq. (8.27) is given by

$$R = \frac{2\pi \bar{\sigma}_e \rho_\chi}{\mu_{\chi e}^2 m_\chi \rho_T} \sum_{i=1}^{N_v} \sum_{\mathbf{G}_f} \int_{1\text{BZ}} \frac{d^3k_i}{(2\pi)^3} \frac{d^3k_f}{(2\pi)^3} F(\nu_{i,\mathbf{k}_i}) \sum_{\mathbf{G}} \left(\frac{f_e}{f_e^0} \right)^2 \mathcal{F}_{\text{med}}^2 g(\mathbf{q}, \omega) |\tilde{u}_{i,\mathbf{k}_i, \mathbf{G}_f - \mathbf{G}}|^2, \quad (8.35)$$

where

$$\omega \equiv \frac{|\mathbf{k}_f + \mathbf{G}_f|^2}{2m_e} - E_{i,\mathbf{k}_i}, \quad \nu_{i,\mathbf{k}_i} = \nu(Z_{\text{eff}}^{i,\mathbf{k}_i}, \omega + E_{i,\mathbf{k}_i}). \quad (8.36)$$

With a change of variables, $\mathbf{G}' = \mathbf{G}_f - \mathbf{G}$ and defining $\mathbf{k}' \equiv \mathbf{k}_f + \mathbf{G}_f$ (and then dropping the prime for simplicity), the rate becomes

$$R = \frac{2\pi\bar{\sigma}_e}{\mu_{\chi e}^2 m_\chi} \frac{\rho_\chi}{\rho_T} \sum_{i=1}^{N_v} \int_{\text{1BZ}} \frac{d^3 k_i}{(2\pi)^3} F(\nu_{i,\mathbf{k}_i}) \sum_{\mathbf{G}} |\tilde{u}_{i,\mathbf{k}_i,\mathbf{G}}|^2 \int \frac{d^3 k}{(2\pi)^3} \left(\frac{f_e}{f_e^0}\right)^2 \mathcal{F}_{\text{med}}^2 g(\mathbf{q}, \omega). \quad (8.37)$$

where $\mathbf{q} = \mathbf{k} - \mathbf{k}_i - \mathbf{G}$.

In Fig. 8.6 we compare the binned rate from the valence to conduction (v→c) calculation in the previous subsection to the valence to free (v→f) one performed here, again for a 1 GeV DM. We see that for large ω , where the v→c calculation is limited by the number of conduction bands included, the v→f calculation extrapolates the results to higher ω as expected. There is some uncertainty due to the choice of the effective charge parameters, which is why the results are shown in bands. The lower edge corresponds to the conservative choice of $Z_{\text{eff}}^{i,\mathbf{k}_i} = 1$ for all i, \mathbf{k}_i , and the upper edge corresponds to the value set by the binding energy, Eq. (8.15) with $E_B = -E_{i,\mathbf{k}_i}$. We find that the conservative choice $Z_{\text{eff}}^{i,\mathbf{k}_i} = 1$ is a better match to the edge for the v→c calculation, and will use this in our final projections in Sec. 8.4. Note that as the threshold increases, the effect of v→f transitions becomes more important, and for a heavy mediator non-negligible constraints can be placed even with $\mathcal{O}(100)$ eV energy thresholds.

Core to Conduction

We now turn to core to conduction transitions. The initial core states are indexed by κ , the atom in the primitive cell, the usual atomic quantum numbers, n, l, m , and the Bloch momentum, \mathbf{k}_i . The final states are the DFT computed conduction states. The crystal form factor is simply obtained from Eq. (8.29) by substituting $u_{i,\mathbf{k}_i} \rightarrow u_{\kappa nlm,\mathbf{k}_i}$:

$$f_{\kappa nlm,\mathbf{k}_i \rightarrow f,\mathbf{k}_f} = \sum_{\mathbf{G}} \delta_{\mathbf{q}, \mathbf{k}_f - \mathbf{k}_i + \mathbf{G}} \frac{1}{\Omega} \int_{\text{cell}} d^3 x e^{i\mathbf{G}\cdot\mathbf{x}} u_{f,\mathbf{k}_f}^*(\mathbf{x}) u_{\kappa nlm,\mathbf{k}_i}(\mathbf{x}), \quad (8.38)$$

The total scattering rate is then

$$R = \frac{2\pi\bar{\sigma}_e}{\mu_{\chi e}^2 m_\chi} \frac{\rho_\chi}{\rho_T} \sum_{\kappa=1}^{N_a} \sum_{n=1}^{N_p^\kappa} \sum_{l=0}^{n-1} \sum_{m=-l}^l \sum_{f=1}^{N_c} \int_{\text{1BZ}} \frac{d^3 k_i}{(2\pi)^3} \frac{d^3 k_f}{(2\pi)^3} \sum_{\mathbf{G}} \left(\frac{f_e}{f_e^0}\right)^2 \mathcal{F}_{\text{med}}^2 g(\mathbf{q}, \omega) \times \left| \frac{1}{\Omega} \int_{\text{cell}} d^3 x e^{i\mathbf{G}\cdot\mathbf{x}} u_{f,\mathbf{k}_f}^*(\mathbf{x}) u_{\kappa nlm,\mathbf{k}_i}(\mathbf{x}) \right|^2, \quad (8.39)$$

where N_a is the number of atoms in the primitive cell, N_p^κ is the largest principal quantum number for atom κ , and $\omega = E_{f,\mathbf{k}_f} - E_{\kappa nl}$. The core wave functions $u_{\kappa nlm,\mathbf{k}_i}(\mathbf{x})$ are given by Eq. (8.9), and involves a sum over primitive cells. Since the integral in Eq. (8.38) is just

over one primitive cell, only the atoms in this and neighboring cells can have a significant contribution. In other words, the sum over \mathbf{r} converges very quickly due to the localized nature of atomic wave functions. We therefore restrict \mathbf{r} to be summed over only the $3 \times 3 \times 3$ nearest cells.

The contribution of core to conduction ($c \rightarrow c$) transitions to the binned rate, for $m_\chi = 1$ GeV, can be seen in Fig. 8.7. In most cases the $v \rightarrow c$ transitions are dominant compared to the $c \rightarrow c$, but there are two main scenarios where this is not true. First, when the experimental threshold is raised; this excludes the $v \rightarrow c$ transitions and causes the $c \rightarrow c$ contribution to be dominant. For example, consider a Si detector and a DM model with a heavy mediator (bottom left panel of Fig. 8.7). If the experimental threshold is ~ 50 eV the $c \rightarrow c$ contribution from the 2p states in Si gives the dominant contribution. Second, for a Ge target, and a DM model with a heavy mediator, the 3d states dominate the rate even at the lowest experimental threshold. To understand this in more detail we present Fig. 8.8 which compares the binned rate taking different modeling approaches for the 3d states in Ge. We see that the large momentum components of the wave function, recovered only after AE reconstruction in the DFT calculation, dominate the rate, which explains why previous works have underestimated the importance of 3d electrons. Meanwhile, we see explicitly at the scattering rate level that the semi-analytic approach accurately reproduces the DFT calculation at low ω , and extends the latter beyond its cutoff at high ω , consistent with the observation at the wave function level in Fig. 8.3.

Core to Free

The last transition type we consider involves a core electron initial state and a free electron final state. The crystal form factor is most easily obtained by substituting Eqs. (8.8) and (8.12) into its definition, Eq. (8.21):

$$\begin{aligned}
 f_{\kappa n l m, \mathbf{k}_i \rightarrow \mathbf{G}_f, \mathbf{k}_f} &= \frac{1}{\sqrt{NV}} \sum_{\mathbf{r}} e^{i\mathbf{k}_i \cdot (\mathbf{r} + \mathbf{x}_\kappa)} \int d^3x e^{i(\mathbf{q} - \mathbf{k}_f - \mathbf{G}_f) \cdot \mathbf{x}} \psi_{\kappa n l m}^{\text{atom}}(\mathbf{x} - \mathbf{r} - \mathbf{x}_\kappa) \\
 &= \frac{1}{\sqrt{NV}} e^{i(\mathbf{k}_i + \mathbf{q} - \mathbf{k}_f - \mathbf{G}_f) \cdot \mathbf{x}_\kappa} \sum_{\mathbf{r}} e^{i(\mathbf{q} - \mathbf{k}_f + \mathbf{k}_i) \cdot \mathbf{r}} \int d^3x e^{i(\mathbf{q} - \mathbf{k}_f - \mathbf{G}_f) \cdot \mathbf{x}} \psi_{\kappa n l m}^{\text{atom}}(\mathbf{x}) \\
 &= \frac{1}{\sqrt{\Omega}} e^{i(\mathbf{k}_i + \mathbf{q} - \mathbf{k}_f - \mathbf{G}_f) \cdot \mathbf{x}_\kappa} \sum_{\mathbf{G}} \delta_{\mathbf{q} - \mathbf{k}_f + \mathbf{k}_i, \mathbf{G}} \tilde{\psi}_{\kappa n l m}^{\text{atom}}(-\mathbf{k}_i + \mathbf{G} - \mathbf{G}_f), \quad (8.40)
 \end{aligned}$$

where the Fourier transform of the RHF Slater type orbital (STO) core wave functions, given in Eq. (8.10), are known analytically [356]:

$$\tilde{\psi}_{\text{STO}}(\mathbf{q}; Z, n, l, m) = \int d^3x e^{i\mathbf{q}\cdot\mathbf{x}} R_{\text{STO}}(x; Z, n) Y_l^m(\hat{\mathbf{x}}) \equiv \chi_{\text{STO}}(q; Z, n, l) Y_l^m(\hat{\mathbf{q}}), \quad (8.41)$$

$$\chi_{\text{STO}}(q; Z, n) = 4\pi N(n-l)!(2Z)^n \left(\frac{ia_0q}{Z}\right)^{l \lfloor (n-l)/2 \rfloor} \sum_{s=0}^{\lfloor (n-l)/2 \rfloor} \frac{\omega_s^{nl}}{((a_0q)^2 + Z^2)^{n-s+1}}, \quad (8.42)$$

$$\omega_s^{nl} = (-4Z^2)^{-s} \frac{(n-s)!}{s!(n-l-2s)!}. \quad (8.43)$$

The direct detection rate is then

$$R = \frac{2\pi\bar{\sigma}_e}{\mu_{\chi e}^2 m_{\chi}} \frac{\rho_{\chi}}{\rho_T \Omega} \sum_{\kappa=1}^{N_a} \sum_{n=1}^{N_p^{\kappa}} \sum_{l=0}^{n-1} \sum_{m=-l}^l \int_{\text{1BZ}} \frac{d^3k_i}{(2\pi)^3} \frac{d^3k_f}{(2\pi)^3} \\ \times \sum_{\mathbf{G}_f} \sum_{\mathbf{G}} F(\nu_{\kappa nl}) \left(\frac{f_e}{f_e^0}\right)^2 \mathcal{F}_{\text{med}}^2 g(\mathbf{q}, \omega) \left| \tilde{\psi}_{\kappa n l m}^{\text{atom}}(-\mathbf{k}_i + \mathbf{G} - \mathbf{G}_f) \right|^2, \quad (8.44)$$

where $\mathbf{q} = \mathbf{k}_f - \mathbf{k}_i + \mathbf{G}$, and $\nu_{\kappa nl} = \nu(Z_{\text{eff}}^{\kappa nl}, \omega + E_{\kappa nl})$. We can now shift the \mathbf{G}_f variable, $\mathbf{G}' \equiv \mathbf{G}_f - \mathbf{G}$ and define $\mathbf{k} = \mathbf{k}_i + \mathbf{G}'$ and $\mathbf{k}' = \mathbf{k}_f + \mathbf{G}$. Therefore, $\mathbf{q} = \mathbf{k}' - \mathbf{k}$ and

$$R = \frac{2\pi\bar{\sigma}_e}{\mu_{\chi e}^2 m_{\chi}} \frac{\rho_{\chi}}{\rho_T \Omega} \sum_{\kappa=1}^{N_a} \sum_{n=1}^{N_p^{\kappa}} \sum_{l=0}^{n-1} \sum_{m=-l}^l \int \frac{d^3k}{(2\pi)^3} \frac{d^3k'}{(2\pi)^3} F(\nu_{\kappa nl}) \left(\frac{f_e}{f_e^0}\right)^2 \mathcal{F}_{\text{med}}^2 g(\mathbf{q}, \omega) \left| \tilde{\psi}_{\kappa n l m}^{\text{atom}}(\mathbf{k}) \right|^2, \quad (8.45)$$

which is the closest expression to the vacuum matrix element, with just the inclusion of the core wave functions acting as a form factor.

In Fig. 8.9, we compare the binned rate from the core to conduction (c→c) calculation to the core to free (c→f) calculation and see a reasonable extrapolation to higher ω . As with the transition region between v→c and v→f shown in Fig. 8.6, we find $Z_{\text{eff}} = 1$ gives a better match between c→c and c→f. While the total number of electrons from these transitions is expected to be much less than lower energy transitions, this is the best available calculation for thresholds up to the kinematic limit of ω_{max} .

In-Medium Screening

DM-electron interactions mediated by a dark photon or scalar are screened due to the in-medium mixing between the mediator and the photon. The relevance of screening has been recently emphasized in Ref. [36]. The screening factor, f_e/f_e^0 , is related to the longitudinal dielectric, $f_e/f_e^0 = (\hat{\mathbf{q}} \cdot \boldsymbol{\epsilon} \cdot \hat{\mathbf{q}})^{-1}$, where $\boldsymbol{\epsilon}$ is the dielectric tensor. It can be computed from

Target	ϵ_0	α	ω_p [eV]	q_{TF} [keV]
Si	11.3	1.563	16.6	4.13
Ge	14	1.563	15.2	3.99

Table 8.1: Parameters used in the model of dielectric function, Eq. (8.46), of Si and Ge from Ref. [65], which accounts for in-medium screening effects on the transition rate.

in-medium loop diagrams or extracted from optical data. Here we model the dielectric of Si and Ge following Ref. [65]:

$$\epsilon(q, \omega) = 1 + \left[\frac{1}{\epsilon_0 - 1} + \alpha \left(\frac{q}{q_{\text{TF}}} \right)^2 + \frac{q^4}{4m_e^2 \omega_p^2} - \left(\frac{\omega}{\omega_p} \right)^2 \right]^{-1}, \quad (8.46)$$

and $\epsilon_{ij} = \epsilon(q, \omega) \delta_{ij}$. Here, $\epsilon_0 \equiv \epsilon(0, 0)$ is the static dielectric, α is a fitting parameter, q_{TF} is the Thomas-Fermi momentum, and ω_p is the plasma frequency. The parameters used for Si and Ge are listed in Table 8.1, and we plot the dielectric as a function of q, ω in Fig. 8.10.

Naively one might expect that the effect of the dielectric is to screen the rate by an $\mathcal{O}(100)$ factor due to the fact that the static dielectric, ϵ_0 , is $\mathcal{O}(10)$. However, this is only the value of the dielectric function at $q = \omega = 0$, while as $q \rightarrow \infty$ and $\omega \rightarrow \infty$ the dielectric approaches unity. Therefore, the effect of the dielectric crucially depends on the region of the kinematic phase space being probed. For a given energy deposition, ω , the momentum transfer is limited to $q \gtrsim \omega/v$ where $v \sim 10^{-3}$ is the DM velocity. Therefore, the absolute minimum momentum transfer is $q_{\text{min}} \sim E_g/v \sim \mathcal{O}(\text{keV})$, for $\mathcal{O}(\text{eV})$ band gap targets. This is parametrically the same size as the Thomas-Fermi momentum q_{TF} , so the dielectric is expected to slightly deviate from one, which causes only an $\mathcal{O}(1)$ shift to the scattering rate, as seen in Fig. 8.11.

8.4 Projected Sensitivity

We now compile the results from the previous sections to compute the projected sensitivity. We also compare the relative importance of each transition type, and discuss differences between our results and previous calculations in the literature. When there are large differences, it is typically because of the inclusion of AE reconstruction and core states in the calculation. Since AE reconstruction and core states contribute predominantly at higher momentum transfer and energy deposition, we will find the largest differences typically occur for a massive mediator and higher detector threshold, where the effects in some cases can be more than an order of magnitude (especially for Ge). For the case of a massless mediator and lower detection threshold, the differences with previous literature are much smaller and

mostly due to the inclusion of in-medium effects.

In Fig. 8.12 we show the contribution to the binned rate from each of the four transition types, for a 1 GeV DM. We see that valence to conduction ($v \rightarrow c$) has a higher peak than the other three transition types, except for the Ge, heavy mediator case, where core to conduction ($c \rightarrow c$) has the highest peak. For comparison, Refs. [33, 34] compute the valence to conduction rates with DFT, including also the 3d states in Ge, but without AE reconstruction. As expected, we find a lower rate at the lowest energy depositions due to the inclusion of in-medium screening, and a much higher rate at high ω due to AE reconstruction and inclusion of core states.

The impact of these observations on the reach depends on the energy threshold. Assuming charge readout (e.g., via a CCD), the relevant quantity is the number of electron-hole pairs, Q , produced in an event. For an energy deposition ω , this is given by

$$Q = 1 + \left\lfloor \frac{\omega - E_g}{\varepsilon} \right\rfloor, \quad (8.47)$$

where the values for ε are 3.6 eV and 2.9 eV for Si and Ge respectively. In Fig. 8.13, we show the total rate as a function of the DM mass, for $Q \geq 1, 5, 10$. The threshold only affects the $v \rightarrow c$ rate, as the other three transition types involve energy depositions corresponding to $Q > 10$, and are therefore always fully included. We see that for $Q \geq 1$, the valence to conduction ($v \rightarrow c$) contribution dominates the total rate with the exception of the Ge, heavy mediator scenario, where core to conduction ($c \rightarrow c$) is dominant for $m_\chi \gtrsim 30$ MeV. Higher thresholds significantly cut out $v \rightarrow c$ contributions in all cases, and render $c \rightarrow c$ more important for Ge, even in the light mediator scenario. For Si, on the other hand, the total rate is still dominated by $v \rightarrow c$ because the core states are much deeper and contribute a lower rate. We also see that $v \rightarrow f$ and $c \rightarrow f$ contributions are subdominant in all cases.

Finally, we present the projected reach on the DM-electron reference cross section $\bar{\sigma}_e$ in Figs. 8.14 and 8.15, for $Q \geq 1$ and $Q \geq 10$, respectively. Our new calculation yields several important differences compared to the previous literature, and we discuss them in detail in the following subsection.

Comparison With Previous Results

We begin by comparing to our previous work, Ref. [6], shown in brown in Fig. 8.14. We previously restricted our analysis to the light mediator scenario, and $Q \geq 1$, which is relatively unaffected by AE reconstruction effects since the rate is peaked at small energy/momentum transfers, as seen in Fig. 8.5. The main reason the reach here is weaker is the inclusion of in-medium screening discussed in Sec. 8.3.

Next we compare to Ref. [33], shown in red in Figs. 8.14 and 8.15. Those results were computed solely from valence to conduction ($v \rightarrow c$) transitions. The largest discrepancy is in the high m_χ regime scattering off a Ge target via a heavy mediator. This is due to high momentum contributions to the 3d wave functions in Ge. Ref. [33] computed the 3d states with DFT without AE reconstruction, which as we saw in Fig. 8.3 is crucial for recovering the dominant part of the 3d wave functions at high momentum. As discussed in Sec. 8.2, our modeling of 3d electrons in Ge as core states reproduces their DFT-computed wave functions up to the AE reconstruction cutoff, and provides a robust parameterization of higher momentum components. Since the valence states in Ge also contribute an appreciable amount, the $Q \geq 1$ results in Fig. 8.14 only differ by about an order of magnitude. However, the difference is more stark when going to higher Q thresholds in Fig. 8.15, which essentially isolates the 3d electrons' contribution. In the low mass regime the difference is less significant, and primarily due to the inclusion of screening effects. Another difference that is important here is sampling of the 1BZ. Ref. [33] used a uniform $6 \times 6 \times 6$ mesh with extra 27 points chosen by hand close to the center of the 1BZ, whereas here (as well as in Ref. [6]) we use a uniform $10 \times 10 \times 10$ grid. While checking convergence we found our (unscreened) results using a $6 \times 6 \times 6$ uniform mesh were a closer match to Ref. [33]; generally, increasing the number of \mathbf{k} points reduces the rate toward convergence, i.e., $R_{10 \times 10 \times 10} < R_{9 \times 9 \times 9} < R_{8 \times 8 \times 8}$. This can be seen more directly in the difference between the brown and red lines in the light mediator scenario (as both are computed without screening), and it affects Ge more than Si, as is expected due to the smaller band gap and greater dispersions of nearby bands requiring denser \mathbf{k} point sampling for convergence.

Ref. [35] also computed DM-electron scattering rates in semiconductors, focusing on Ge. The approach taken in that paper was to semi-analytically model the Ge wave functions with the core wave functions (with the same set of RHF STO wave function coefficients tabulated in Ref. [336]) and treat the final states as free with a Fermi factor, analogous to the core to free calculation performed here. As we can see from Fig. 8.14, while for most of the mass range and mediators the estimates are too optimistic due to incorrect modeling of the valence and conduction states, in the high mass region with a heavy mediator (bottom-right panel), where 3d states dominate, their estimates are in good agreement with ours presented here, as expected.

Finally, we discuss the comparison with the most recent work, Ref. [36], which was limited to valence to conduction transitions. To show the effect of screening, we show their projected reach with (purple) and without (green) screening in Fig. 8.14. Again the largest discrepancy is in the heavy mediator scenario with a Ge target, primarily due to the neglect of the 3d

states in Ref. [36]. When these are not important, i.e., the low mass regime or a light mediator, we generally find good agreement, with our reach being a bit stronger. Notably this does not seem due to a mis-model of the dielectric, since the effect of screening relative to our previous results, Ref. [6], is consistent with their result. We also find that screening has a smaller effect at high masses in the heavy mediator scenario for Si. These small differences are harder to disentangle since they could be due to: 1) different xc-functionals used (PBE and HSE vs. TB09); 2) local field effects which are only partially included here since we assume the screening factor is isotropic; 3) the plane wave expansion parameter, E_{cut} , taken to be 500 eV without AE reconstruction in Ref. [36], vs. 1 keV, AE corrected to 2 keV taken here; 4) DM velocity distribution parameters, studied in detail in Refs. [357, 358], for which Ref. [36] assumed $v_{\text{esc}} = 500$ km/s as opposed to $v_{\text{esc}} = 600$ km/s chosen here; and 5) Ref. [36] took a directionally averaged dielectric, whereas here we only assume isotropy in the screening factor but not the matrix element itself.

8.5 Conclusions

Dark matter-electron scattering in dielectric crystal targets, especially semiconductors like Si and Ge, are at the forefront of DM direct detection experiments. It is therefore imperative to have accurate theoretical predictions for the excitation rates. In this work, we extended the scattering rate calculation in several key aspects. Much of the focus of previous calculations has been on transitions from valence to conduction bands just across the band gap, which will be accessible to near-future experiments. We performed state-of-the-art DFT calculations for these states, and highlighted the importance of all-electron reconstruction which has been neglected in most previous works. Along with this, we extended the transition rate calculation by explicitly including the contributions from core electrons and additional states more than 60 eV above the band gap using analytic approximations.

We updated the projected reach with our new calculation and found important differences compared to previous results. In particular, we found that in the heavy mediator scenario, 3d electrons in Ge give a dominant contribution to the detection rate for DM heavier than about 30 MeV. Relative to previous works the increased importance of the 3d electrons is due to more accurate modelling of the high momentum components of their electronic wave functions, as seen in Fig. 8.3. Intuitively, the more accurate model here stems from a more accurate model of the short distance potential (a pseudo-potential versus the all-electron reconstructed potential, discussed in Sec. 8.2) which dominantly affects the high momentum components of the wave functions. Also, the rate can be significantly higher than predicted previously for higher experimental thresholds. This is exciting because new DM parameter space will be within reach even before detectors reach the single electron ionization threshold.

We also release a beta version of EXCEED-DM (available [here](#) [342]) that implements our DM-electron scattering calculation for general crystal targets, and make the electronic wave function data for Si and Ge [343], as well as the EXCEED-DM output [344], publicly available so our present analysis can be reproduced. We have previously used EXCEED-DM for a target comparison study [6], and to study the daily modulation signals that can arise in anisotropic materials [7]. The generality of EXCEED-DM means that potential applications are vast. It can be used to compute detection rates for other target materials (assuming DFT calculations of valence and conduction states are available), and can also be adapted to include additional DM interactions such as in an effective field theory framework similar to the study of atomic ionizations in Ref. [244] (see Ref. [359] for a recent effort in this direction). For momentum-suppressed effective operators, a full calculation in our framework is even more important, as the effects of all-electron reconstruction and core states (overlooked in Ref. [359]) are generally amplified. Moreover, the differential information that can be obtained from our program facilitates further studies including realistic backgrounds. Details of EXCEED-DM and additional example calculations will be presented in an upcoming publication.

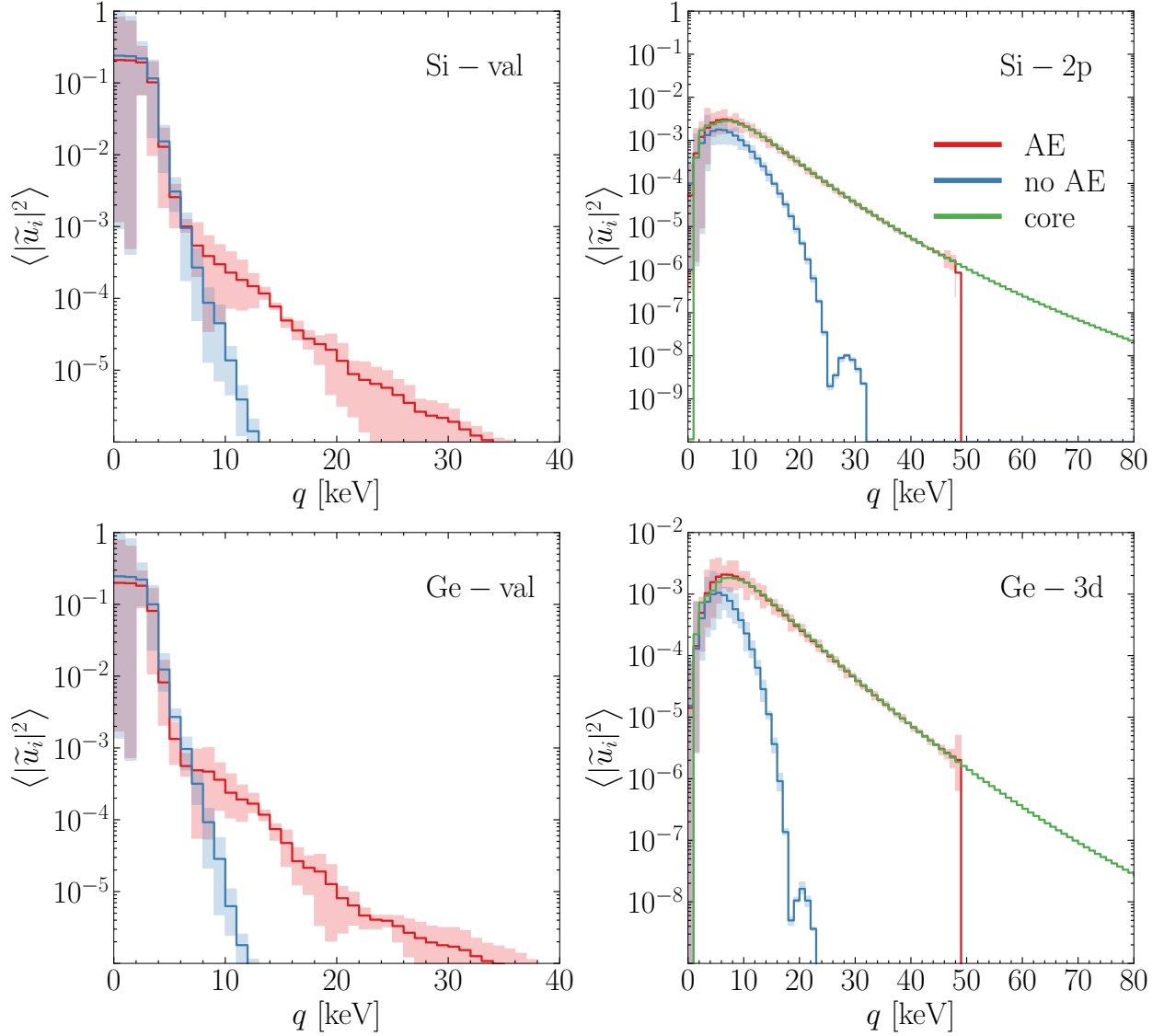


Figure 8.3: Comparison of the Bloch wave function magnitudes, defined in Eq. (8.7), computed with DFT with (red, “AE”) and without (blue, “no AE”) AE reconstruction, and the semi-analytic core approximation of Eq. (8.9) (green, “core”). Shaded bands indicate the maximum and minimum values across all the bands belonging to the state type indicated in the upper right corner of each panel. AE reconstruction, discussed in Sec. 8.2, recovers the large momentum behavior of the electronic wave functions. Core electronic states, such as those shown in the right panels and discussed in Sec. 8.2, can be well modeled semi-analytically with atomic wave functions, as seen by the good agreement between the “core” and “AE” curves. When applicable, the semi-analytic parameterization is advantageous since the electronic wave functions are then known to arbitrarily large momentum.

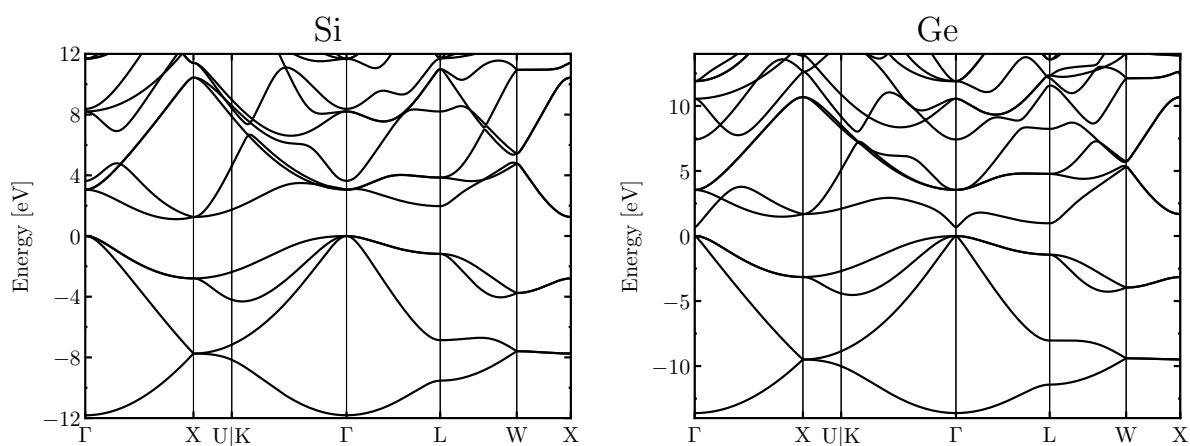


Figure 8.4: Calculated band structures of Si (left) using a PBE xc-functional within DFT and Ge (right) using a hybrid functional HSE06. The band gaps have been scissor corrected to their measured values near zero temperature, 1.11 eV and 0.67 eV for Si and Ge, respectively. The Fermi level is set to 0 eV in both panels.

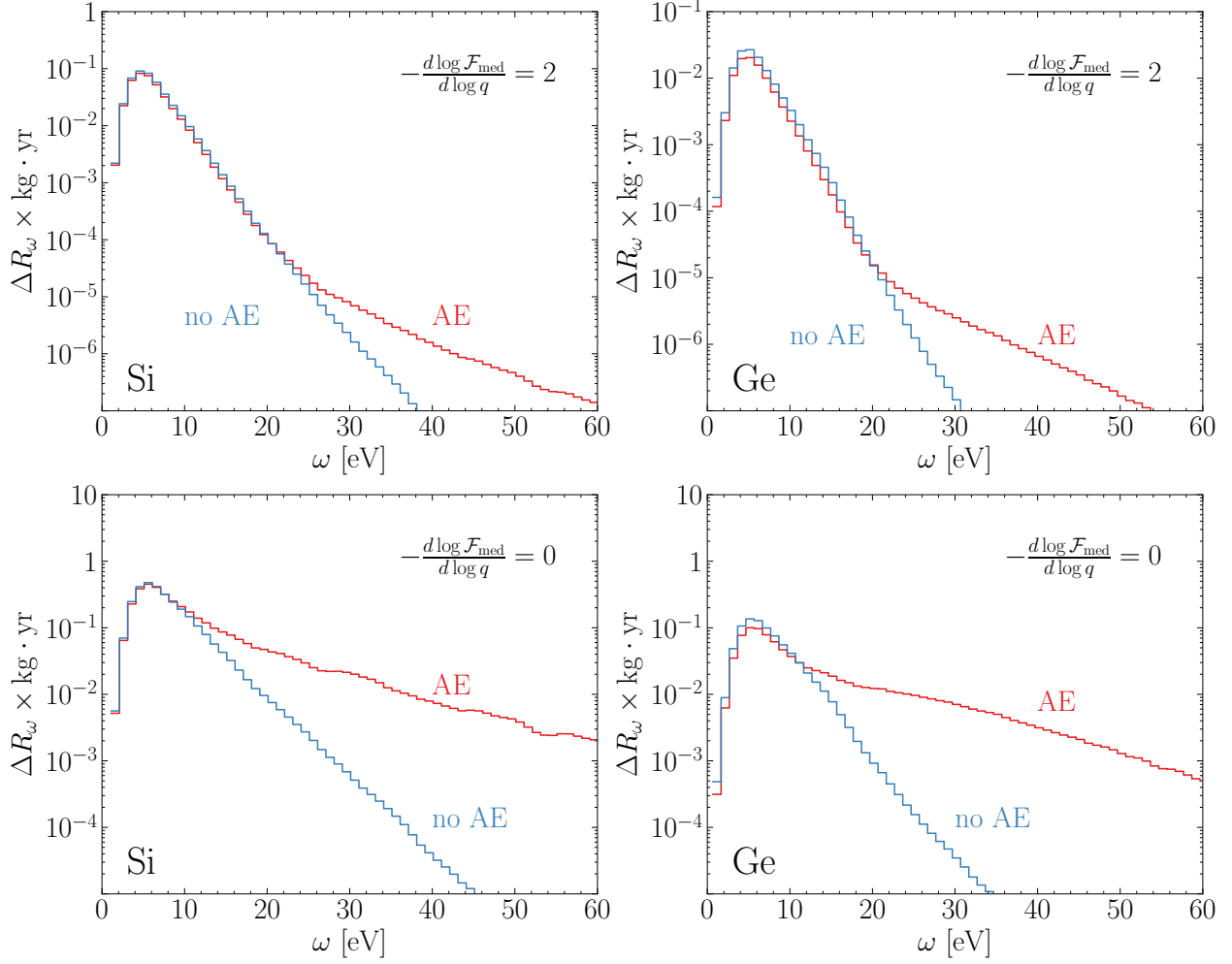


Figure 8.5: DM-electron scattering rate from valence to conduction bands binned in energy deposition (with $\Delta\omega = 1$ eV) for 1 GeV DM, light (top row) and heavy (bottom row) mediators, assuming $\bar{\sigma}_e = 10^{-40}$ cm², computed with vs. without AE reconstruction. Valence states included are the first four bands below the band gap, and conduction states included are all bands up to $E_{\text{dft}} = 60$ eV.

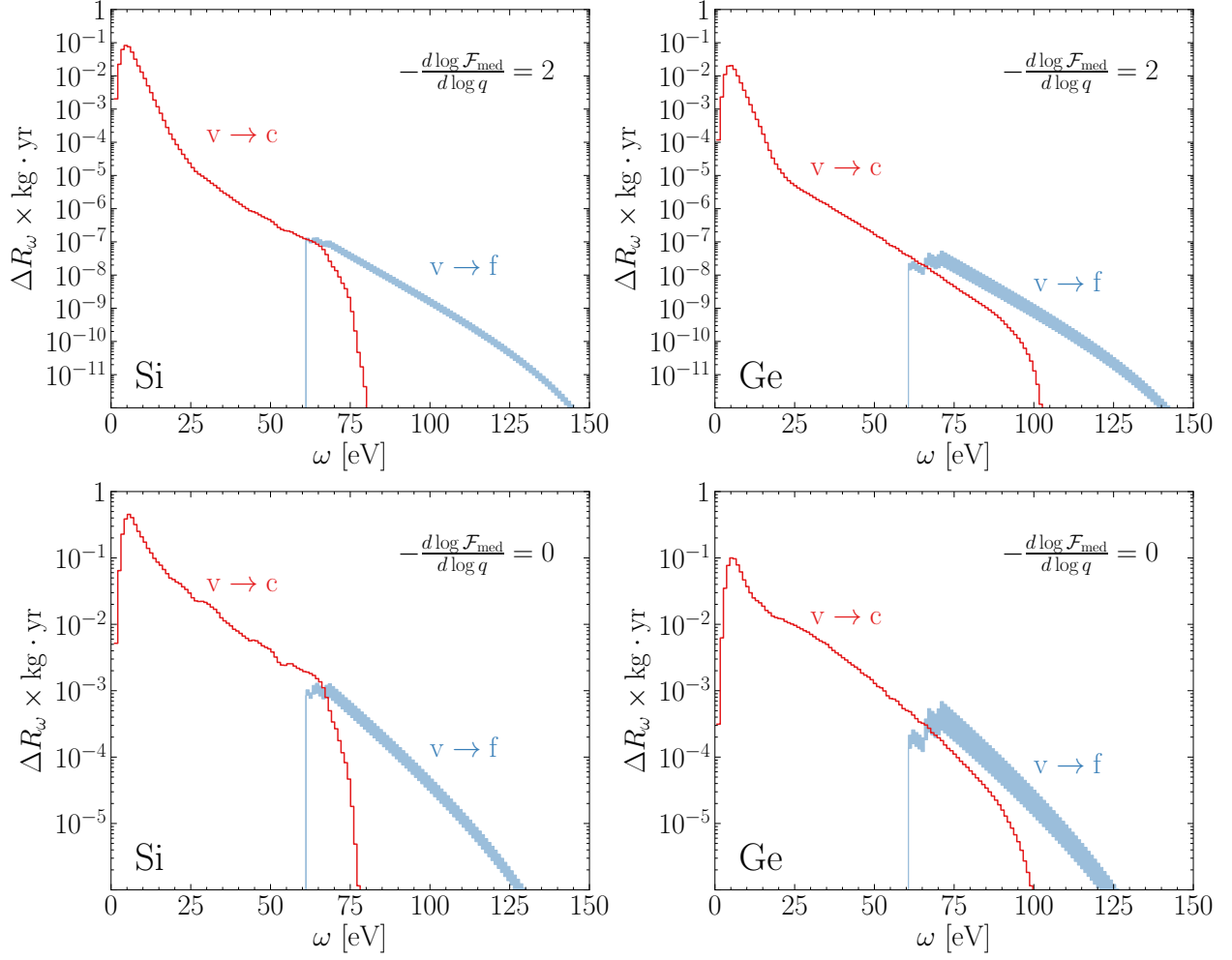


Figure 8.6: DM-electron scattering rate from valence to conduction ($v \rightarrow c$) bands and from valence bands to free states ($v \rightarrow f$) binned in energy deposition (with $\Delta\omega = 1$ eV) for 1 GeV DM, light (top row) and heavy (bottom row) mediators, assuming $\bar{\sigma}_e = 10^{-40}$ cm². The upper edge of the shaded region corresponds to using Z_{eff} from Eq. (8.15), while the bottom edge corresponds to $Z_{\text{eff}} = 1$.

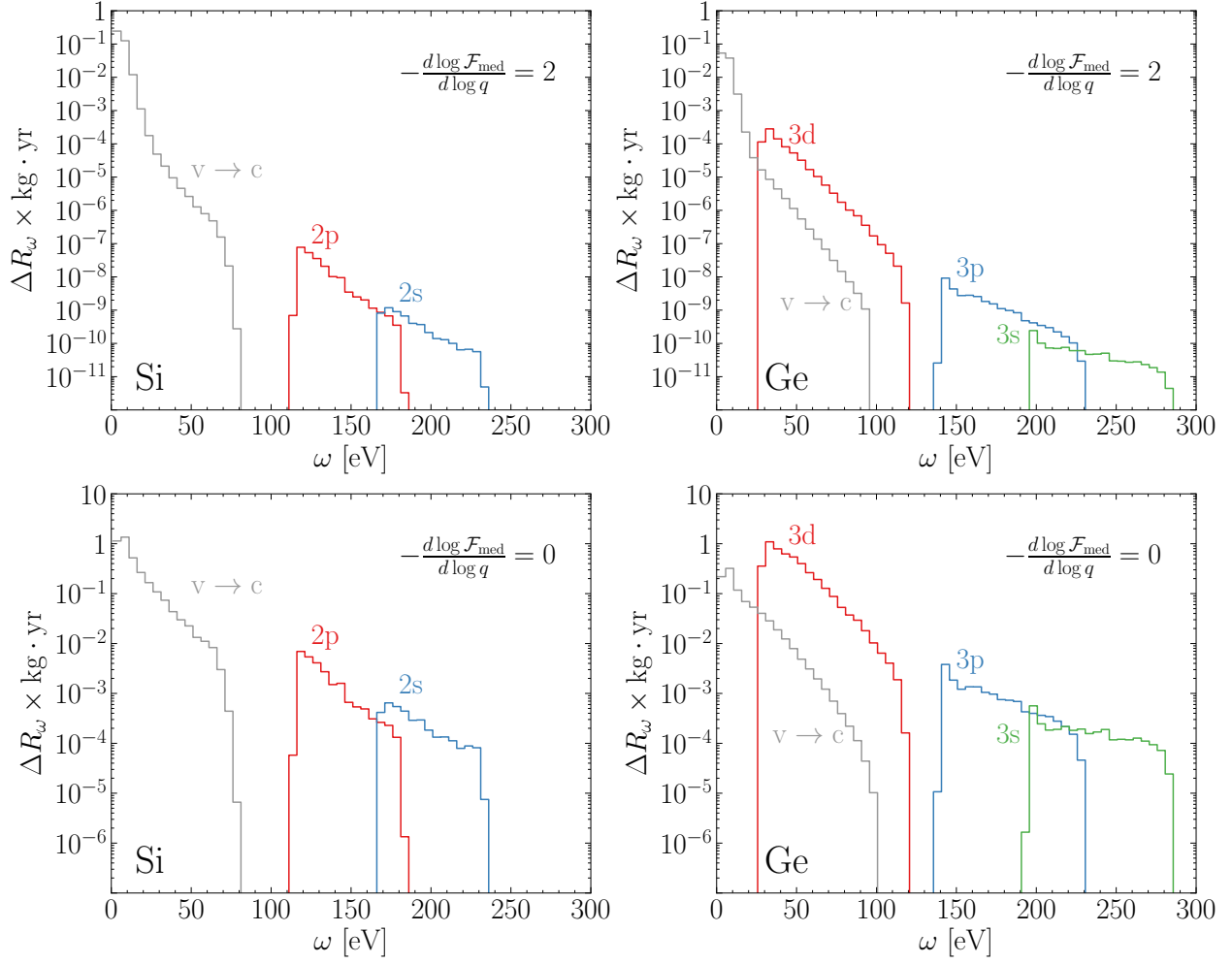


Figure 8.7: DM-electron scattering rate from core states to conduction bands binned in energy deposition (with $\Delta\omega = 5$ eV) for 1 GeV DM, light (top row) and heavy (bottom row) mediators, assuming $\bar{\sigma}_e = 10^{-40}$ cm². The core states are labelled by the corresponding atomic orbitals, and the conduction states up to $E_{\text{dft}} = 60$ eV are included. For comparison we also show the $\nu \rightarrow c$ contribution (after AE reconstruction) from Fig. 8.5 in gray.

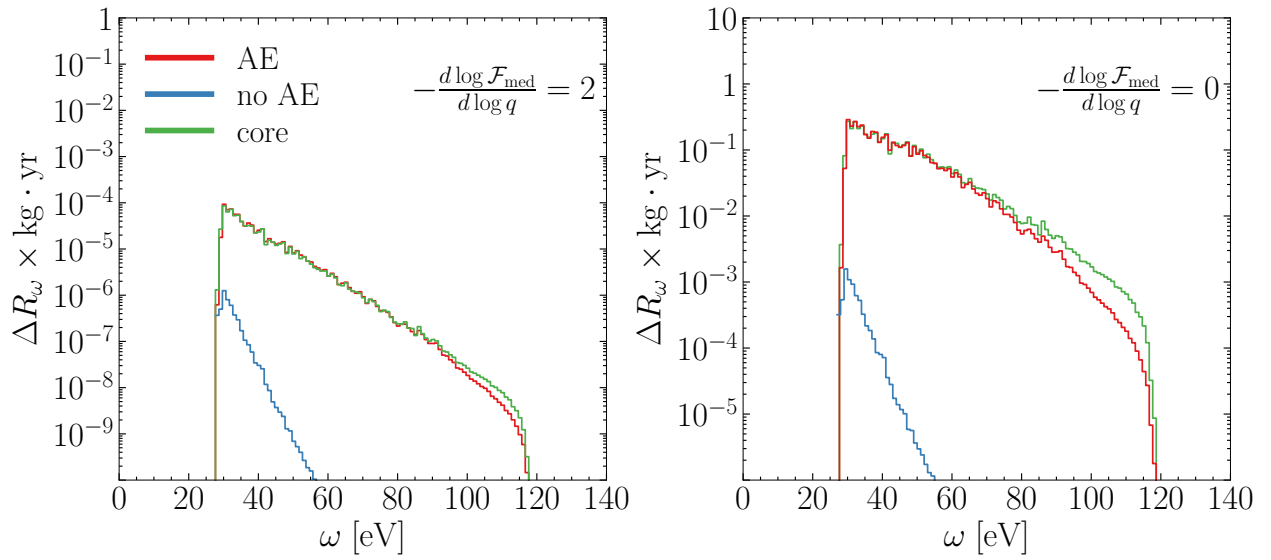


Figure 8.8: Contribution to the DM-electron scattering rate binned in energy deposition (with $\Delta\omega = 1$ eV) from 3d electrons to conduction bands in Ge, for 1 GeV DM, light (left) and heavy (right) mediators, assuming $\bar{\sigma}_e = 10^{-40}$ cm². The three curves in each panel are computed using DFT with and without AE reconstruction, and using the semi-analytic core wave functions.

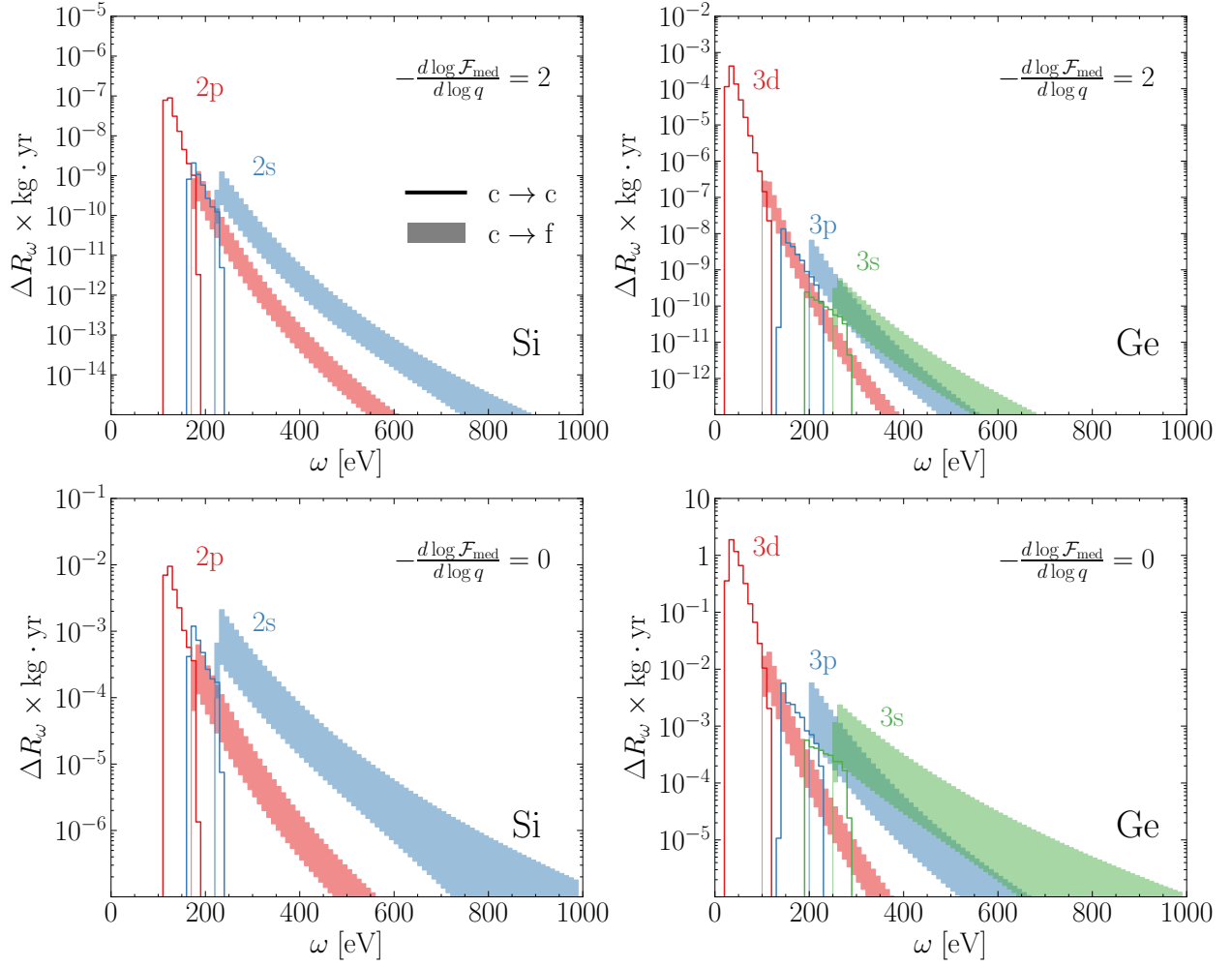


Figure 8.9: DM-electron scattering rate from core states to conduction bands ($c \rightarrow c$) and to free states ($c \rightarrow f$) binned in energy deposition (with $\Delta\omega = 10$ eV) for 1 GeV DM, light (top row) and heavy (bottom row) mediators, assuming $\bar{\sigma}_e = 10^{-40}$ cm². As in the $\nu \rightarrow f$ calculation in Fig. 8.6, the upper edge of the shaded bands corresponds to Z_{eff} from Eq. (8.15), and the lower edge corresponds to $Z_{\text{eff}} = 1$.

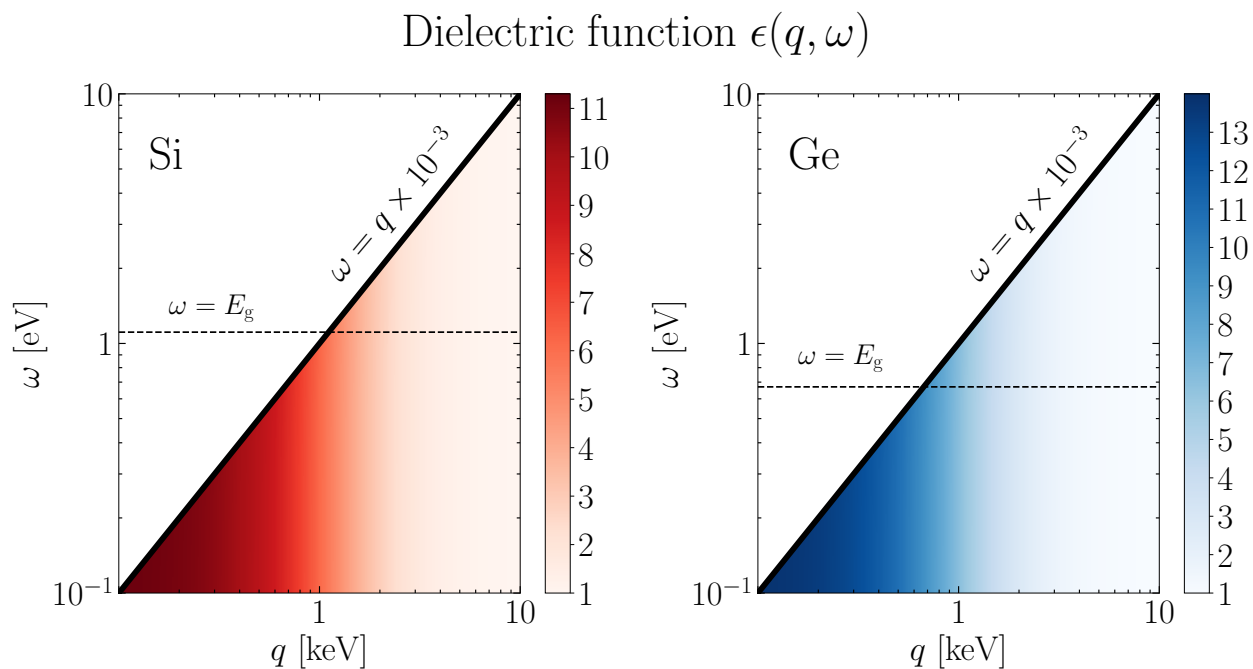


Figure 8.10: Dielectric function $\epsilon(q, \omega)$, given by Eq. (8.46) with the parameters in Table 8.1, of Si (left) and Ge (right) used to incorporate screening effects. The solid line indicates the edge of the kinematically accessible region $\omega \lesssim qv$. The dashed line is the band gap of the target. While the static dielectric can be $\mathcal{O}(10)$, in the kinematically allowed region $\epsilon(q, \omega)$ is an $\mathcal{O}(1)$ number, leading to an $\mathcal{O}(1)$ effect on the scattering rates when the latter are dominated by small q, ω transitions.

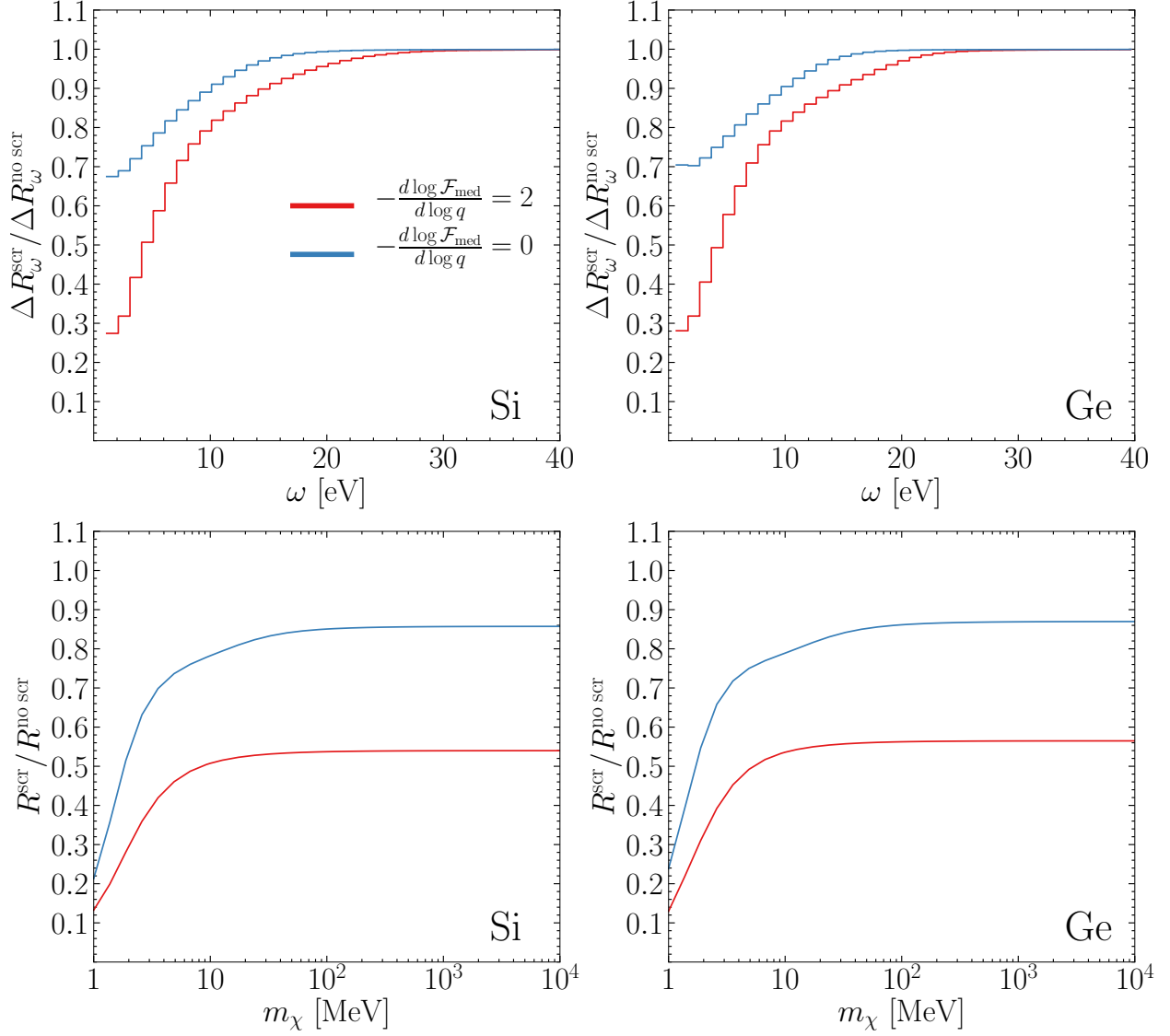


Figure 8.11: Effect of screening on the binned rate (top row, for 1 GeV DM) and total rate (bottom row, as a function of m_{χ}) from $v \rightarrow c$ transitions for DM models with a light (red) and heavy (blue) mediator. The unscreened rate $R^{\text{no scr}}$ is obtained with $\epsilon = 1$, and the screened rate R^{scr} is obtained with the model of the dielectric function given in Eq. (8.46).

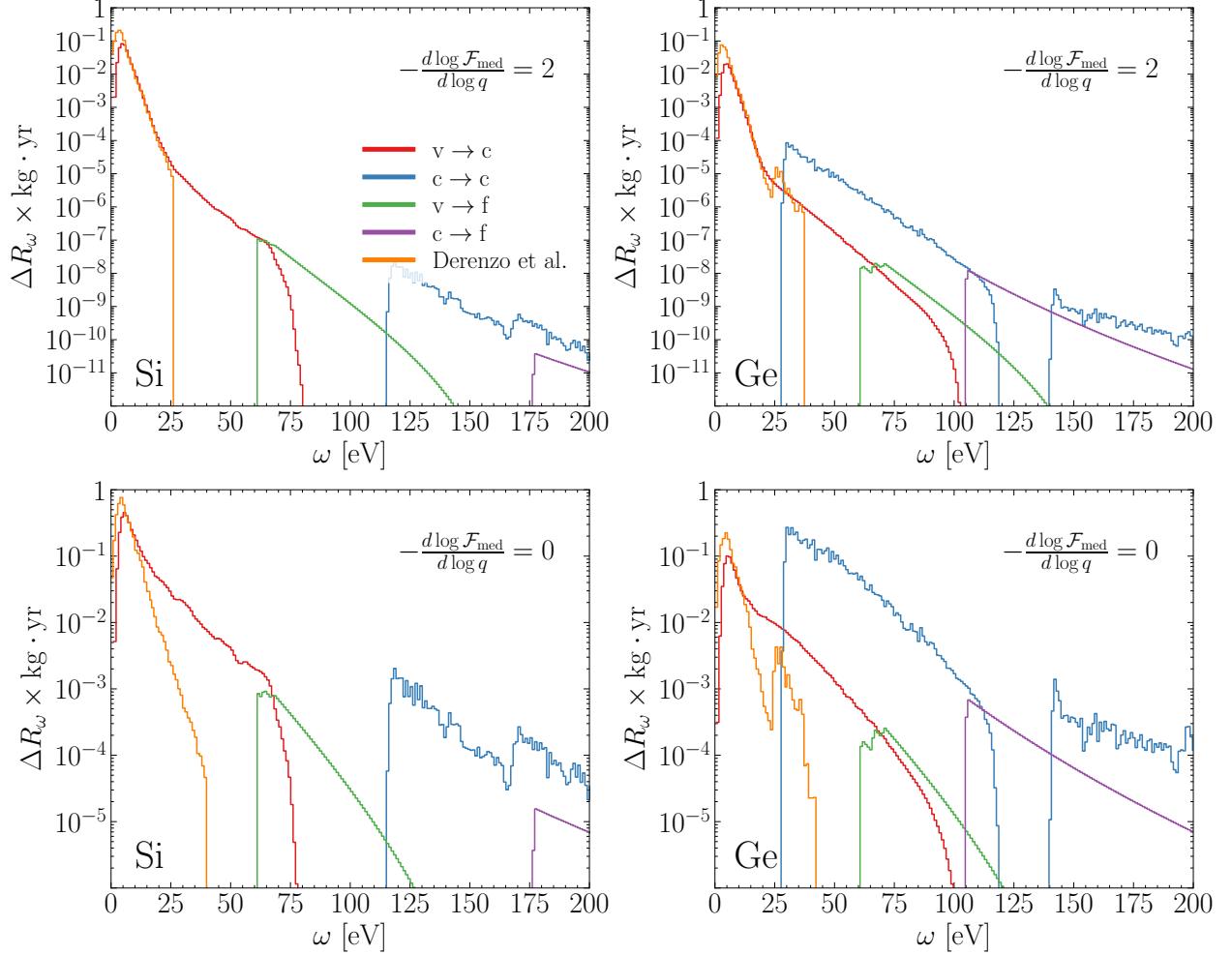


Figure 8.12: DM-electron scattering rate binned in energy deposition (with $\Delta\omega = 1$ eV) for 1 GeV DM, light (top row) and heavy (bottom row) mediators, from all four transition types: valence to conduction ($v \rightarrow c$), valence to free ($v \rightarrow f$), core to conduction ($c \rightarrow c$), and core to free ($c \rightarrow f$). We assume $\bar{\sigma}_e = 10^{-40}$ cm², and take $Z_{\text{eff}} = 1$ for all effective charges in the Fermi factor. Note that the $c \rightarrow c$ and $c \rightarrow f$ transitions involve semi-analytic treatment of 2p (3d) states and below in Si (Ge), which has been validated with DFT calculations including AE reconstruction; see Fig. 8.3. We also overlay the binned rate from Ref. [34] which computed the $v \rightarrow c$ contribution using QEdark (treating 3d states in Ge as valence, without including AE reconstruction effects).

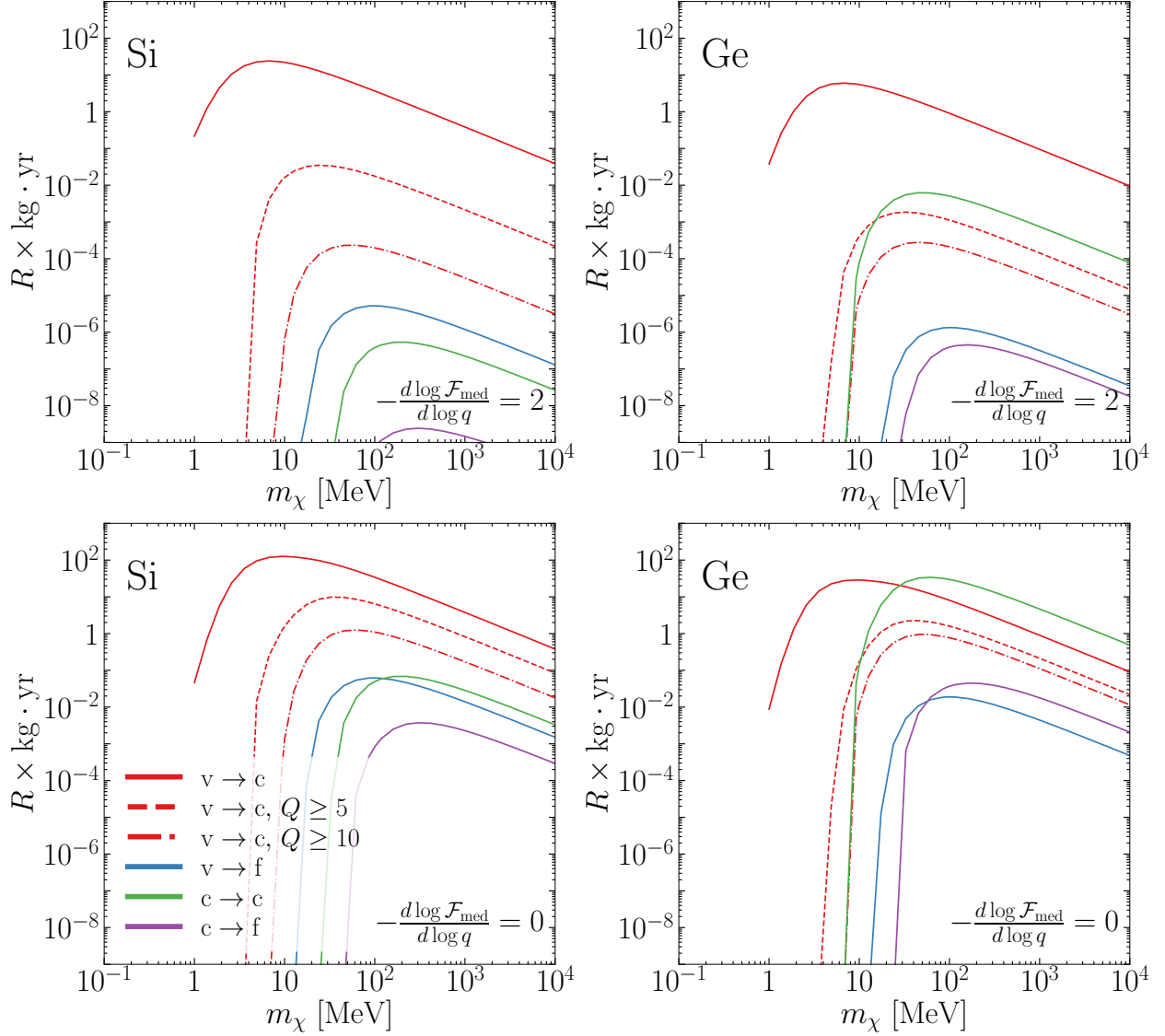


Figure 8.13: DM-electron scattering rate as a function of the DM mass, for light (top row) and heavy (bottom row) mediators, from all four transition types: valence to conduction ($v \rightarrow c$), valence to free ($v \rightarrow f$), core to conduction ($c \rightarrow c$), and core to free ($c \rightarrow f$). We assume $\bar{\sigma}_e = 10^{-40} \text{ cm}^2$, take $Z_{\text{eff}} = 1$ for all effective charges in the Fermi factor, and show results for several threshold Q values which significantly impact the $v \rightarrow c$ contribution.

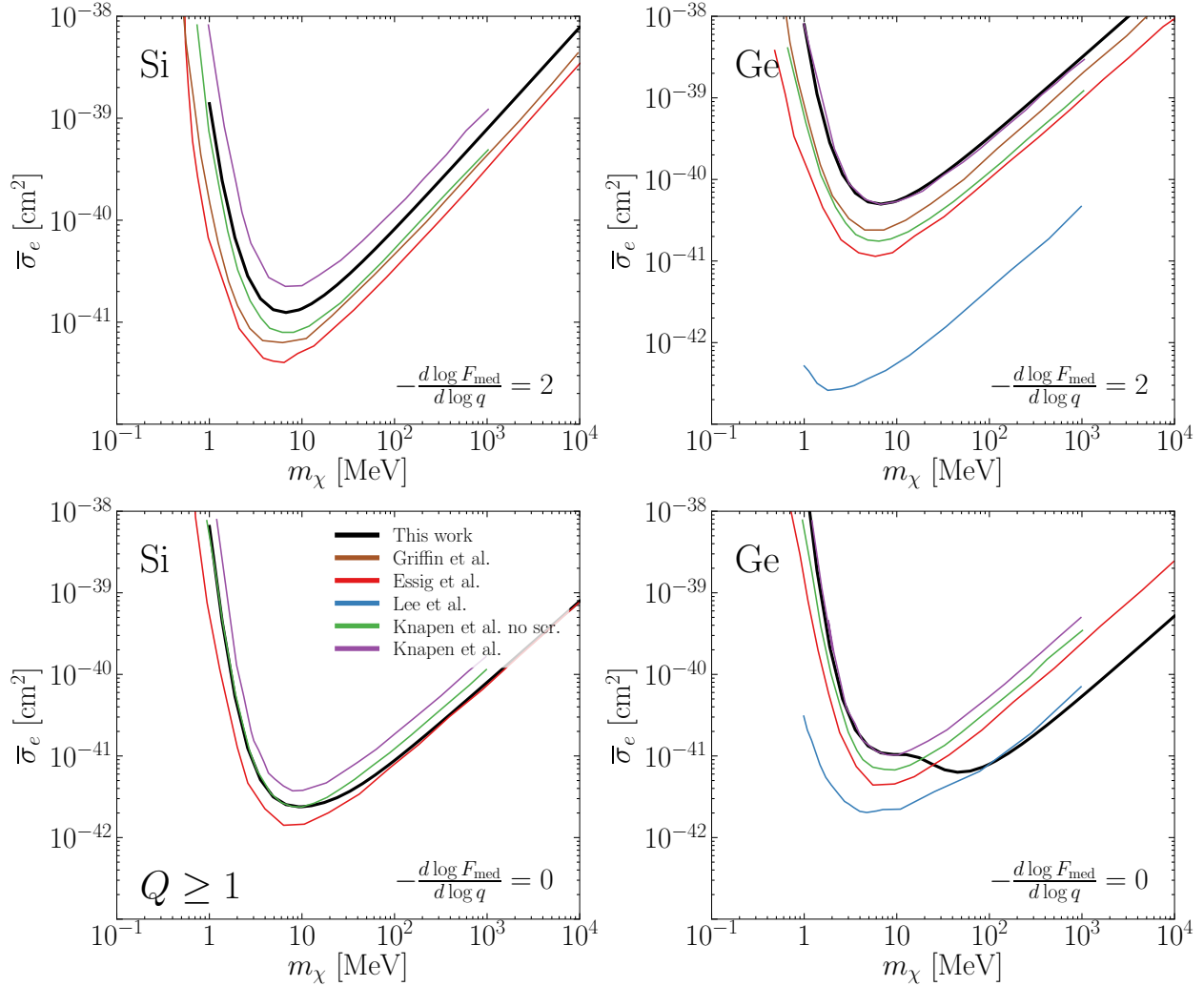


Figure 8.14: 95% C.L. exclusion reach (3 events) assuming 1 kg-year exposure, $Q \geq 1$, for light (top row) and heavy (bottom row) mediators. The results shown are from this work, Griffin et al. [6], Essig et al. [33], Lee et al. [35], and Knapen et al. [36] (with and without screening). See Sec. 8.4 for detailed comparison.

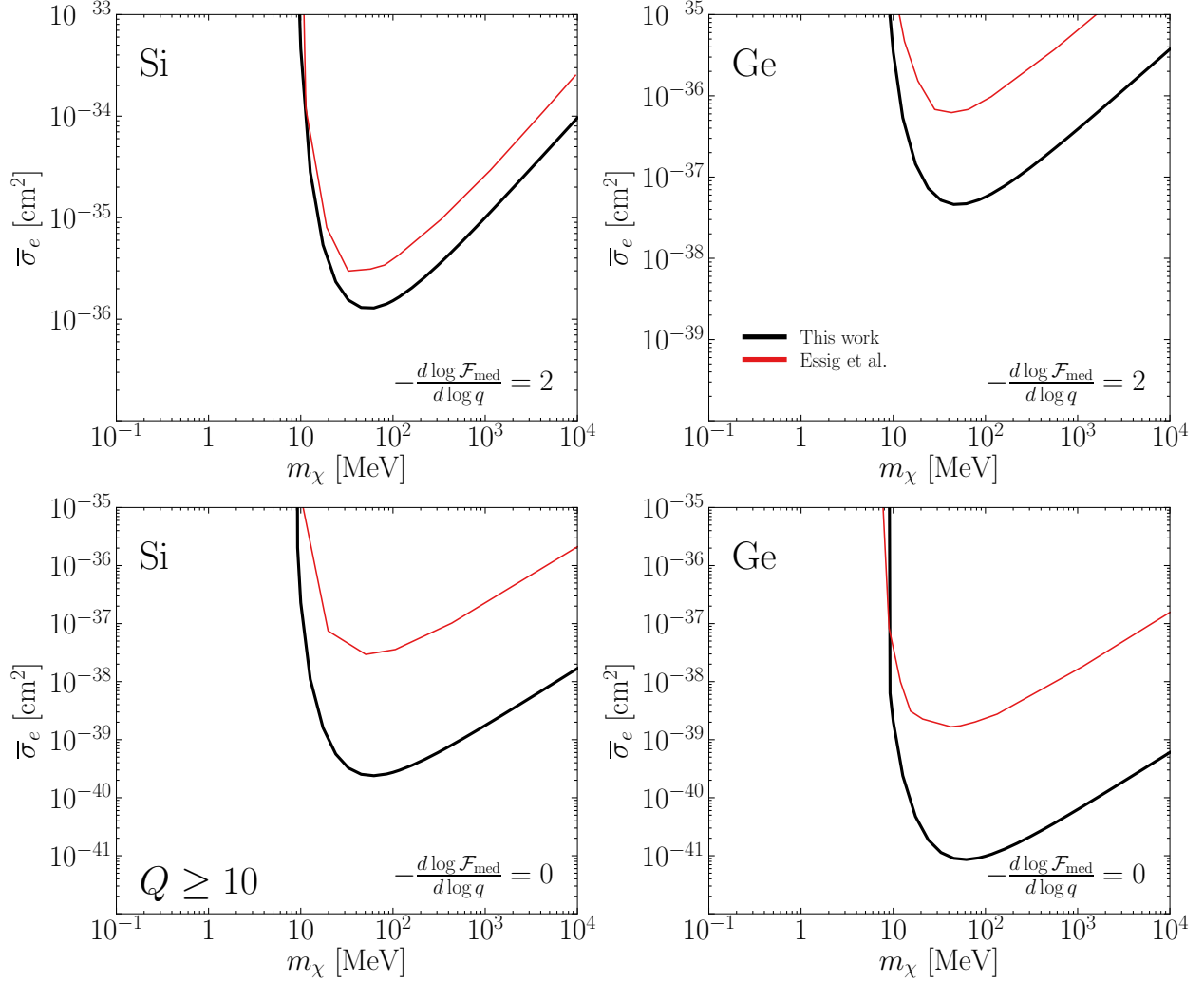


Figure 8.15: 95% C.L. exclusion reach (3 events) assuming 1 kg-year exposure, $Q \geq 10$, for light (top row) and heavy (bottom row) mediators. The results shown are from this work and Essig et al. [33]. See Sec. 8.4 for detailed comparison.

DARK MATTER ABSORPTION VIA ELECTRONIC EXCITATIONS

9.1 Introduction

Uncovering the nature of cosmic dark matter (DM) remains one of the major goals in particle physics. Recent advances in low-threshold detectors (e.g., skipper charge-coupled devices [85], transition edge sensors [90, 251, 253, 255], microwave kinetic inductance detectors [254] and quantum evaporation of helium atoms [252]) coupled with new theoretical investigations of various small-gap materials (e.g., $\mathcal{O}(\text{eV})$ -gap semiconductor crystals [6, 7, 9, 19, 25, 33–35, 39, 40, 177, 180, 248, 256], $\mathcal{O}(\text{meV})$ -gap superconductors [41, 181, 182] and Dirac materials [29, 144, 183, 335]) have opened up new possibilities in the pursuit of this goal, well beyond the scope of conventional searches based on nuclear recoils. In a direct detection experiment, DM may leave its trace not only via scattering off the target ions or electrons, but also via absorption if it is bosonic and has a mass that matches the difference between energy levels in the target system [28, 29, 39–41, 44, 64, 144, 166, 180, 183, 185, 194, 360–365]. In this work, we focus on processes where the absorption of a bosonic DM drives electronic excitations, i.e. transitions between electronic states.

It has been widely appreciated that, for several well-motivated bosonic DM models, the absorption process is closely related to that of photon absorption, and the rate can be expressed in terms of the target material’s optical properties, i.e. the (complex) conductivity or dielectric function. In fact, most studies on DM absorption so far have utilized this feature to make rate predictions by simply rescaling optical data. This approach is obviously attractive because it saves the labor of first-principles calculations, which can be technically challenging or resource-intensive, and because one can often make quick comparisons between target materials based on existing data.

Nevertheless, this data-driven approach has important limitations. First of all, conductivity/dielectric data are not always readily available, especially for newly proposed, more exotic materials, in which case one has to resort to first-principles calculations and/or semi-analytic modeling (this is the case, e.g., for Dirac materials studied in several recent works [29, 144, 183, 335]). Meanwhile, and more importantly, the question of whether DM absorption for a particular model can be simply related to photon absorption is a nontrivial one, and explicit calculations are needed to establish the answer.

It is the purpose of this work to revisit the calculation of DM absorption via electronic

excitations. We critically examine the question above by carefully working out the matching between relativistic Lagrangians for DM-electron interactions and non-relativistic (NR) effective field theories (EFTs) (Sec. 9.2), and computing in-medium self-energies to fully account for mixing and screening effects (Sec. 9.3). This is a slightly different strategy than several previous calculations: by matching onto a NR EFT from the beginning instead of taking the NR limit of a relativistic calculation in the end, the power counting relevant for the absorption process becomes more transparent; also, the cryogenic nature of direct detection experiments allows us to perform the in-medium calculation in the zero-temperature limit and avoid the complications of thermal field theory. We will carry out the calculation for three widely-studied bosonic DM candidates:

- Vector (e.g., dark photon) DM, which can be produced, for example, by inflationary fluctuations [172], by parent particle decays or coherent oscillations after reheating [171, 366–368], or from a network of cosmic strings [369]. In this case, since the DM couples to electrons via the same vector current $\bar{\psi}\gamma^\mu\psi$ as the photon does, its absorption rate is trivially a rescaling of the photon absorption rate.
- Pseudoscalar (e.g., axion-like particle) DM, which can be produced, for example, via the misalignment mechanism [145–147], from the decays of topological defects [370–372], or by a variety of other mechanisms (see e.g., Refs. [278, 280, 287, 290, 367]). While not immediately obvious (since the DM couples to a different current, $\bar{\psi}i\gamma^5\psi$, than the photon does), it has been well-known that also in this case, there is a simple relation between DM and photon absorption [360]. We will recover this result in the NR EFT calculation. It is worth noting that the dominant contribution to NR pseudoscalar DM absorption actually comes from an operator generated at the next-to-leading order (NLO) in the $1/m_e$ expansion, because the leading order (LO) operator suffers a suppression by the DM’s momentum q .
- Scalar DM, which can be produced via mechanisms similar to pseudoscalar DM mentioned above. It couples to the scalar current $\bar{\psi}\psi$, which at LO coincides with the temporal component of the vector current $\bar{\psi}\gamma^0\psi$. However, as we will see, the LO operator gives a q -suppressed contribution and, as in the pseudoscalar case, the rate is dominated by a NLO operator. Importantly, this NLO operator has a different structure than the photon coupling, and its contribution cannot be simply related to photon absorption, invalidating the data-driven approach.

We make the statements above on the scalar and pseudoscalar DM more concrete in Table 9.1.

DM type	Scalar ($\phi \bar{\psi} \psi$)	Pseudoscalar ($\phi \bar{\psi} i \gamma^5 \psi$)
NR operators	$\phi \psi_+^\dagger \psi_+ + \frac{1}{8m_e^2} \phi \psi_+^\dagger \overleftrightarrow{\nabla}^2 \psi_+$	$-\frac{1}{2m_e} (\nabla \phi) \cdot (\psi_+^\dagger \Sigma \psi_+) + \frac{i}{4m_e^2} (\partial_t \phi) (\psi_+^\dagger \Sigma \cdot \overleftrightarrow{\nabla} \psi_+)$
Related to dielectric?	✓	✓

Table 9.1: Summary of results for scalar and pseudoscalar DM ϕ coupling to electron ψ . The effective operators at LO and NLO in the NR ($1/m_e$) expansion are shown in the second row. In both cases, the NLO operator (underlined) gives the dominant contribution to DM absorption. Importantly, the dominant contribution in the scalar case is not directly related to the target material's conductivity/dielectric function. See Secs. 9.2 and 9.3 for details.

The fact that the DM absorption rate is not always relatable to the target material’s optical properties highlights the necessity to go beyond the conventional data-driven approach. (The same can be said for DM scattering, for which the data-driven approach based on the dielectric function that has been advocated recently [36, 48, 49] covers only a limited set of DM interactions.) In this work, we consider two types of targets:

- Semiconductor crystals with $\mathcal{O}(\text{eV})$ gaps (Sec. 9.4), focusing on silicon (Si) and germanium (Ge) that are in use in current experiments (DAMIC [71, 81, 237], EDELWEISS [82–84], SENSEI [22, 86, 87], SuperCDMS [23, 77–80, 88, 89]). We compute DM absorption rates using first-principles density functional theory (DFT) calculations of electronic band structures and wave functions, which are now publicly available [343]. The numerical calculation builds upon the EXCEED-DM framework [9] and we publish the “absorption” module of the program together with this work [179].
- Conventional (BCS) superconductors with $\mathcal{O}(\text{meV})$ gaps (Sec. 9.5), focusing on aluminum (Al) that has been proposed for direct detection [41, 181, 182]. We compute DM absorption rates by semi-analytically modeling the electronic states near the Fermi surface, largely following Refs. [41, 181, 182].

For all the materials under study, we find good agreement between our theoretical calculation and the data-driven approach for the DM models where both are valid, i.e. vector and pseudoscalar DM. This serves as an important validation of our calculations. In the case of scalar DM, we show explicitly how the data-driven approach fails to reproduce the leading contribution, and present our calculated sensitivity projections. In particular, for Al superconductor, our revised projected reach is much more optimistic than that found in Ref. [44], although somewhat weaker than the original estimate in Ref. [41].

9.2 Dark Matter Couplings to Non-relativistic Electrons

Since electrons in a detector are non-relativistic, it is convenient to perform the DM absorption calculation in the framework of NR EFT (see e.g., Refs. [373, 374] for reviews). In this section, we work through the procedure of matching a relativistic theory of DM-electron interactions onto effective operators involving the NR electron field. The total Lagrangian of interest is

$$\mathcal{L} = \mathcal{L}_\psi + \mathcal{L}_\phi + \mathcal{L}_{\text{int}}. \quad (9.1)$$

Here \mathcal{L}_ψ is the Standard Model part that includes the electron ψ coupling to electromagnetism,

$$\mathcal{L}_\psi = \bar{\psi} \left[i\gamma^\mu (\partial_\mu + ieA_\mu) - m_e \right] \psi, \quad (9.2)$$

\mathcal{L}_ϕ contains the standard kinetic and mass terms of the DM field ϕ , and we consider the following DM-electron interactions:

$$\mathcal{L}_{\text{int}} = \begin{cases} g\phi\bar{\psi}\psi & (\text{scalar DM, } g = d_{\phi ee} \frac{\sqrt{4\pi} m_e}{M_{\text{Pl}}}), \\ g\phi\bar{\psi}i\gamma^5\psi \simeq -\frac{g}{2m_e}(\partial_\mu\phi)(\bar{\psi}\gamma^\mu\gamma^5\psi) & (\text{pseudoscalar DM, } g = g_{aee}), \\ g\phi_\mu\bar{\psi}\gamma^\mu\psi & (\text{vector DM, } g = \kappa e), \end{cases} \quad (9.3)$$

where we have also indicated the relation between the coupling g and commonly adopted parameters $d_{\phi ee}$, g_{aee} , κ in the literature. Note that there are two equivalent ways of writing the pseudoscalar coupling that are related by a field redefinition and integration by parts (IBP).

Let us first consider \mathcal{L}_ψ . Writing the electron field in the relativistic theory as

$$\psi(\mathbf{x}, t) = e^{-im_e t} \psi_{\text{NR}}(\mathbf{x}, t). \quad (9.4)$$

We obtain

$$\mathcal{L}_\psi = \psi_{\text{NR}}^\dagger \left[i\partial_t - eA_0 + i\gamma^0\boldsymbol{\gamma} \cdot (\nabla - ie\mathbf{A}) + (1 - \gamma^0) m_e \right] \psi_{\text{NR}}. \quad (9.5)$$

We now define projection operators

$$P_\pm \equiv \frac{1}{2} (1 \pm \gamma^0), \quad (9.6)$$

which satisfy $P_\pm^2 = P_\pm$, $P_+P_- = P_-P_+ = 0$ and $(P_\pm)^\dagger = P_\pm$. By using $P_\pm\gamma^0 = \gamma^0P_\pm = \pm P_\pm$ and $P_\pm\gamma^i = \gamma^iP_\mp$, we can rewrite Eq. (9.5) as

$$\mathcal{L}_\psi = \psi_+^\dagger (i\partial_t - eA_0) \psi_+ + \psi_-^\dagger (i\partial_t - eA_0 + 2m_e) \psi_- + \psi_+^\dagger i\boldsymbol{\gamma} \cdot (\nabla - ie\mathbf{A}) \psi_- - \psi_-^\dagger i\boldsymbol{\gamma} \cdot (\nabla - ie\mathbf{A}) \psi_+, \quad (9.7)$$

where $\psi_\pm \equiv P_\pm\psi_{\text{NR}}$ (thus $\psi_{\text{NR}} = \psi_+ + \psi_-$). Integrating out the heavy field ψ_- at tree level by solving its equation of motion (EOM),

$$\psi_- = \frac{1}{2m_e + i\partial_t - eA_0} i\boldsymbol{\gamma} \cdot (\nabla - ie\mathbf{A}) \psi_+, \quad (9.8)$$

we arrive at the EFT for ψ_+ :

$$\begin{aligned} \mathcal{L}_\psi^{\text{eff}} &= \psi_+^\dagger \left[i\partial_t - eA_0 - \boldsymbol{\gamma} \cdot (\nabla - ie\mathbf{A}) \frac{1}{2m_e + i\partial_t - eA_0} \boldsymbol{\gamma} \cdot (\nabla - ie\mathbf{A}) \right] \psi_+ \\ &= \psi_+^\dagger \left[i\partial_t - eA_0 + \frac{(\nabla - ie\mathbf{A})^2}{2m_e} + (\nabla \times \mathbf{A}) \cdot \frac{e\boldsymbol{\Sigma}}{2m_e} \right. \\ &\quad \left. - \frac{i}{4m_e^2} (\nabla - ie\mathbf{A}) \cdot \partial_t (\nabla - ie\mathbf{A}) + \dots \right] \psi_+ \end{aligned} \quad (9.9)$$

where we have used

$$\gamma^i \gamma^j = -\delta^{ij} - i\epsilon^{ijk} \Sigma^k, \quad \Sigma \equiv \begin{pmatrix} \boldsymbol{\sigma} & 0 \\ 0 & \boldsymbol{\sigma} \end{pmatrix}. \quad (9.10)$$

We can readily identify the first four terms in Eq. (9.9), which come from LO in the $1/m_e$ expansion, as the familiar electromagnetic interactions as in NR quantum mechanics. There are several operators at NLO in the $1/m_e$ expansion, of which we have only written out the one involving ∂_t . This is the last term in Eq. (9.9), and is the only NLO term that will be relevant in what follows. Importantly, it gives a tree-level contribution to the wave function renormalization of the ψ_+ field. In NR EFT calculations, it is often convenient to adopt an operator basis where temporal derivatives in the quadratic part of the Lagrangian have been traded for spatial derivatives, so as to eliminate any non-trivial wave function renormalization factors at tree level. The field redefinition needed to go into this basis, at the order we are working here, is

$$\psi_+ = \left[1 - \frac{1}{8m_e^2} (\boldsymbol{\gamma} \cdot (\nabla - ie\mathbf{A}))^2 \right] \hat{\psi}_+. \quad (9.11)$$

This field redefinition does not change the LO Lagrangian (the first four terms in Eq. (9.9)), but replaces the last term in Eq. (9.9) by NLO operators that do not contain ∂_t (and hence do not contribute to the wave function renormalization of $\hat{\psi}_+$). We will not need the NLO operators for electron couplings to vector fields (photon and dark photon),¹ but the field redefinition in Eq. (9.11) that modifies the NLO Lagrangian will be important in the cases of scalar and pseudoscalar DM.

We are interested in the case where the photon field A^μ consists of an electrostatic background Φ and quantum fluctuations \mathcal{A}^μ :

$$A_0(\mathbf{x}, t) = \Phi(\mathbf{x}) + \mathcal{A}_0(\mathbf{x}, t), \quad \mathbf{A}(\mathbf{x}, t) = \mathcal{A}(\mathbf{x}, t). \quad (9.12)$$

The normalized NR field $\hat{\psi}_+$ can be expanded in energy eigenstates of the NR Schrödinger equation:

$$\hat{\psi}_+(\mathbf{x}, t) = \sum_{I,s} \hat{c}_{I,s} e^{-i\varepsilon_I t} \Psi_I(\mathbf{x}) \frac{1}{\sqrt{2}} \begin{pmatrix} \xi_s \\ \xi_s \end{pmatrix}, \quad (9.13)$$

where $\hat{c}_{I,s}$ are annihilation operators for NR electrons, and

$$\left(-\frac{\nabla^2}{2m_e} - e\Phi(\mathbf{x}) \right) \Psi_I(\mathbf{x}) = \varepsilon_I \Psi_I(\mathbf{x}), \quad \xi_+ = \begin{pmatrix} 1 \\ 0 \end{pmatrix}, \quad \xi_- = \begin{pmatrix} 0 \\ 1 \end{pmatrix}. \quad (9.14)$$

¹As a side remark, in the special case of an electrostatic potential, $A_0 = \Phi(\mathbf{x})$, $\mathbf{A} = \mathbf{0}$, one can check that keeping all the NLO terms reproduces the familiar fine structure correction in NR quantum mechanics: $\mathcal{L}_\psi^{\text{eff,NLO}} = \hat{\psi}_+^\dagger \frac{\nabla^4}{8m_e^3} \hat{\psi}_+ - \frac{e}{8m_e^2} (\nabla^2 \Phi) \hat{\psi}_+^\dagger \hat{\psi}_+ - \frac{ie}{8m_e^2} (\nabla \Phi) \cdot (\hat{\psi}_+^\dagger \boldsymbol{\Sigma} \times \overleftrightarrow{\nabla} \hat{\psi}_+)$, where the three terms are the relativistic kinetic energy correction, the Darwin term and spin-orbit coupling, respectively.

Note that the form of the background field in Eq. (9.12) assumes negligible spin-orbit coupling, in which case the two spin states $s = \pm$ for a given I are degenerate. From Eqs. (9.9) and (9.12), we can also deduce the electron's coupling to photon quanta \mathcal{A}^μ at LO in the NR EFT:

$$\mathcal{L}_{\psi\mathcal{A}}^{\text{eff}} = -e\mathcal{A}_0\hat{\psi}_+^\dagger\hat{\psi}_+ - \frac{ie}{2m_e}\mathcal{A}\cdot\left(\hat{\psi}_+^\dagger\overleftrightarrow{\nabla}\hat{\psi}_+\right) + \frac{e}{2m_e}(\nabla\times\mathcal{A})\cdot\left(\hat{\psi}_+^\dagger\Sigma\hat{\psi}_+\right) - \frac{e^2}{2m_e}\mathcal{A}^2\hat{\psi}_+^\dagger\hat{\psi}_+, \quad (9.15)$$

where $\hat{\psi}_+^\dagger\overleftrightarrow{\nabla}\hat{\psi}_+ \equiv \hat{\psi}_+^\dagger(\nabla\hat{\psi}_+) - (\nabla\hat{\psi}_+^\dagger)\hat{\psi}_+$.

Let us now move on to the DM-electron interaction \mathcal{L}_{int} . For vector DM, we can simply replace $e\mathcal{A}^\mu \rightarrow e\mathcal{A}^\mu - g\phi^\mu$ in the derivation above, and obtain:

$$\begin{aligned} \mathcal{L}_{\text{int}}^{\text{eff}} &= g\phi_0\hat{\psi}_+^\dagger\hat{\psi}_+ + \frac{ig}{2m_e}\phi\cdot\left(\hat{\psi}_+^\dagger\overleftrightarrow{\nabla}\hat{\psi}_+\right) - \frac{g}{2m_e}(\nabla\times\phi)\cdot\left(\hat{\psi}_+^\dagger\Sigma\hat{\psi}_+\right) \\ &\quad + \frac{ge}{m_e}\phi\cdot\mathcal{A}\hat{\psi}_+^\dagger\hat{\psi}_+ - \frac{g^2}{2m_e}\phi^2\hat{\psi}_+^\dagger\hat{\psi}_+ \end{aligned} \quad (\text{vector DM}). \quad (9.16)$$

For the scalar and pseudoscalar cases, since \mathcal{L}_{int} contains an operator that has a different structure than all the operators in \mathcal{L}_ψ , there is no such simple replacement. In principle, we should have included \mathcal{L}_{int} when solving the EOM for ψ_- in Eq. (9.8). However, if we are working at leading order in the DM-electron coupling g , it is sufficient to simply substitute Eq. (9.8) into \mathcal{L}_{int} . We therefore obtain, at LO in the NR expansion:

$$\mathcal{L}_{\text{int}}^{\text{eff,LO}} = \begin{cases} g\phi\hat{\psi}_+^\dagger\hat{\psi}_+ & (\text{scalar DM}), \\ -\frac{g}{2m_e}(\nabla\phi)\cdot\hat{\psi}_+^\dagger\Sigma\hat{\psi}_+ & (\text{pseudoscalar DM}). \end{cases} \quad (9.17)$$

We now show that these LO terms are not sufficient to capture the dominant contributions to DM absorption. The point is that our NR EFT is an expansion in $\frac{\nabla}{m_e} \sim v_e$, and the power counting is such that momenta (and spatial derivatives) count as $m_e v_e$ and energies (and time derivatives) count as $m_e v_e^2$. For NR absorption, the energy deposition is $\omega \simeq m_\phi \sim m_e v_e^2$. Meanwhile although the momentum transfer formally counts as $m_e v_e$, it is in fact much smaller: $q = m_\phi v_\phi \sim m_e v_e^2 v_\phi \ll m_e v_e$, with $v_\phi \sim \mathcal{O}(10^{-3})$. Therefore, when the LO result contains factors of q , we need to work out the NLO terms and see if they may in fact dominate.

From Eq. (9.17) it is clear that such q suppression is indeed present in the pseudoscalar case. It is perhaps less obvious that the scalar case also suffers a q suppression, and its origin can be understood from charge conservation: the LO operator couples the scalar DM ϕ to the electron number density $\hat{\psi}_+^\dagger\hat{\psi}_+ = -\rho_e/e$ (with ρ_e the charge density carried by the electron),

whose matrix elements vanish in the $q \rightarrow 0$ limit because $\rho_e = \mathbf{q} \cdot \mathbf{J}_e/\omega$; technically this is manifest via the orthogonality of initial and final state electron wave functions, as we will see later in the paper.² Therefore, in both scalar and pseudoscalar cases, we need to expand \mathcal{L}_{int} up to NLO where there are several operators. Many of them will not be needed, though, because they are also q suppressed or involve too many fields to contribute to the in-medium self-energies to be computed in the next section. Including only the unsuppressed operators at NLO that contain up to four fields, we have

$$\mathcal{L}_{\text{int}}^{\text{eff}} = \begin{cases} g \phi \hat{\psi}_+^\dagger \hat{\psi}_+ + \frac{g}{8m_e^2} \phi \left(\hat{\psi}_+^\dagger \overleftrightarrow{\nabla}^2 \hat{\psi}_+ \right) - \frac{ig_e}{2m_e^2} \phi \mathcal{A} \cdot \left(\hat{\psi}_+^\dagger \overleftrightarrow{\nabla} \hat{\psi}_+ \right) & \text{(scalar DM)}, \\ -\frac{g}{2m_e} (\nabla \phi) \cdot \hat{\psi}_+^\dagger \Sigma \hat{\psi}_+ + \frac{ig}{4m_e^2} (\partial_t \phi) \left(\hat{\psi}_+^\dagger \Sigma \cdot \overleftrightarrow{\nabla} \hat{\psi}_+ \right) & \text{(pseudoscalar DM)}. \end{cases} \quad (9.18)$$

These results were already summarized in Table 9.1 (for brevity we dropped the hat on $\hat{\psi}_+$ and omitted the last operator in the scalar case in that table — we will see that it gives vanishing contribution to DM absorption in an isotropic medium). The second term in the scalar case, where the DM ϕ couples to $\hat{\psi}_+^\dagger \overleftrightarrow{\nabla}^2 \hat{\psi}_+ \equiv \hat{\psi}_+^\dagger (\nabla^2 \hat{\psi}_+) + (\nabla^2 \hat{\psi}_+) \hat{\psi}_+ - 2(\nabla \hat{\psi}_+^\dagger) \cdot (\nabla \hat{\psi}_+)$, is obtained by combining the $\psi_-^\dagger \psi_-$ term from $\bar{\psi} \psi = \psi_+^\dagger \psi_+ - \psi_-^\dagger \psi_-$ (with ψ_- replaced by its EOM solution Eq. (9.8)) and additional terms from the field redefinition in Eq. (9.11). We will see in the next section that this operator gives the dominant contribution to scalar DM absorption. Pseudoscalar DM absorption is likewise dominated by the NLO operator $(\partial_t \phi) (\hat{\psi}_+^\dagger \Sigma \cdot \overleftrightarrow{\nabla} \hat{\psi}_+)$.³

9.3 In-medium Self-energies and Absorption Rates

We now use the NR EFT derived in the previous section to compute DM absorption rates. Generally, the absorption rate of a state can be derived from the imaginary part of its self-energy. In a medium, care must be taken because of mixing effects. If the DM ϕ mixes with a SM state A in the medium (generalization to the case of mixing with multiple states is straightforward) then the self-energy matrix has to be diagonalized to find the in-medium

²The same can be said for the ϕ_0 component in the vector DM case. However, since ϕ_0 couples exactly to the charge density even beyond LO, retaining higher order terms in the NR expansion does not remove the q suppression.

³Technically, the electron fields in the two equivalent expressions of the pseudoscalar coupling, $g\phi\bar{\psi}i\gamma^5\psi$ and $-\frac{g}{2m_e}(\partial_\mu\phi)(\bar{\psi}\gamma^\mu\gamma^5\psi)$, are not the same, but are related by a field redefinition. If one derives the NR EFT starting from $-\frac{g}{2m_e}(\partial_\mu\phi)(\bar{\psi}\gamma^\mu\gamma^5\psi)$, this NLO operator is obtained directly from its $\mu = 0$ component. On the other hand, if one derives the NR EFT from $g\phi\bar{\psi}i\gamma^5\psi$, a further field redefinition is needed to eliminate operators involving the background electrostatic potential Φ and arrive at the same operator coefficient shown in Eq. (9.18).

eigenstates:

$$\begin{pmatrix} m_\phi^2 + \Pi_{\phi\phi} & \Pi_{\phi A} \\ \Pi_{A\phi} & \Pi_{AA} \end{pmatrix} \rightarrow \begin{pmatrix} m_\phi^2 + \Pi_{\hat{\phi}\hat{\phi}} & 0 \\ 0 & \Pi_{\hat{A}\hat{A}} \end{pmatrix}, \quad (9.19)$$

where $\Pi_{\phi\phi} \sim \mathcal{O}(g^2)$, $\Pi_{\phi A}, \Pi_{A\phi} \sim \mathcal{O}(g)$. For a 4-momentum $Q^\mu = (\omega, \mathbf{q})$, we have $\Pi_{\phi A}(Q) = \Pi_{A\phi}(-Q)$. Simple algebra shows that to $\mathcal{O}(g^2)$,

$$\Pi_{\hat{\phi}\hat{\phi}} \simeq \Pi_{\phi\phi} + \frac{\Pi_{\phi A}\Pi_{A\phi}}{m_\phi^2 - \Pi_{AA}}. \quad (9.20)$$

The DM absorption rate is then derived from the imaginary part of the eigenvalue corresponding to the DM-like state, $\hat{\phi}$:

$$\Gamma_{\text{abs}}^\phi = -\frac{Z_{\hat{\phi}}}{\omega} \text{Im} \Pi_{\hat{\phi}\hat{\phi}} \simeq -\frac{1}{\omega} \text{Im} \left(\Pi_{\phi\phi} + \frac{\Pi_{\phi A}\Pi_{A\phi}}{m_\phi^2 - \Pi_{AA}} \right), \quad (9.21)$$

where the wave function renormalization $Z_{\hat{\phi}} = \left(1 - \frac{d\text{Re}\Pi_{\hat{\phi}\hat{\phi}}}{d\omega^2}\right)^{-1} = 1 + \mathcal{O}(g^2)$ has been approximated as unity. The total rate per unit target mass is given by

$$R = \frac{\rho_\phi}{\rho_T} \frac{1}{\omega} \Gamma_{\text{abs}}^\phi = -\frac{\rho_\phi}{\rho_T} \frac{1}{\omega^2} \text{Im} \left(\Pi_{\phi\phi} + \frac{\Pi_{\phi A}\Pi_{A\phi}}{m_\phi^2 - \Pi_{AA}} \right), \quad (9.22)$$

where ρ_T is the target's mass density, and $\rho_\phi = 0.4 \text{ GeV}/\text{cm}^3$ is the local DM energy density. For non-relativistic DM, $\omega \simeq m_\phi$, and $\rho_\phi \simeq \frac{1}{2}m_\phi^2\phi_0^2$ with the DM field amplitude defined by $\phi(\mathbf{x}, t) = \phi_0 \cos(\mathbf{q} \cdot \mathbf{x} - \omega t)$.

The calculation of self-energies generally involves two graph topologies:

$$\begin{array}{c} \text{---} \xrightarrow{Q} \text{---} \text{---} \text{---} \text{---} \text{---} \\ \text{---} \text{---} \text{---} \text{---} \text{---} \text{---} \text{---} \text{---} \text{---} \text{---} \\ \text{---} \text{---} \text{---} \text{---} \text{---} \text{---} \text{---} \text{---} \text{---} \text{---} \end{array} \equiv -i \Pi_{\mathcal{O}_1, \mathcal{O}_2}(Q) = -i \Pi_{\mathcal{O}_2, \mathcal{O}_1}(-Q), \quad (9.23)$$

$$\begin{array}{c} \text{---} \xrightarrow{Q} \text{---} \text{---} \text{---} \text{---} \text{---} \\ \text{---} \text{---} \text{---} \text{---} \text{---} \text{---} \text{---} \text{---} \text{---} \end{array} \equiv -i \Pi'_{\mathcal{O}}(Q), \quad (9.24)$$

where a blob represents the sum of one-particle-irreducible (1PI) graphs. While we have drawn curly external lines for concreteness, they can each represent a scalar, pseudoscalar or vector. The operators $\mathcal{O}_1, \mathcal{O}_2, \mathcal{O}$ that the external fields couple to may carry Lorentz indices, in which case Π and Π' inherit these indices. We discuss the calculation of these self-energy diagrams in App. N.

In the cases of interest here, A represents one of the polarizations of the SM photon, and Π_{AA} is directly related to the target's complex conductivity/dielectric function, as discussed further below. Since Π_{AA} enters the absorption rate formula (Eq. (9.22)) as long as there is a nonzero mixing $\Pi_{\phi A}$, let us examine this quantity in more detail before specializing to each DM model. The photon self-energy tensor $\Pi^{\mu\nu}$ is defined such that the effective action contains

$$\begin{aligned} \mathcal{S}_{\text{eff}} &\supset \frac{1}{2} \int d^4Q \Pi^{\mu\nu}(Q) \mathcal{A}_\mu(Q) \mathcal{A}_\nu(-Q) \\ &= \frac{1}{2} \int d^4Q \left[\Pi^{00}(Q) \mathcal{A}_0(Q) \mathcal{A}_0(-Q) - 2 \Pi^{0j}(Q) \mathcal{A}_0(Q) \mathcal{A}^j(-Q) + \Pi^{ij}(Q) \mathcal{A}^i(Q) \mathcal{A}^j(-Q) \right], \end{aligned} \quad (9.25)$$

where \mathcal{A}^j ($j = 1, 2, 3$) represent the three components of \mathcal{A} . As usual, we compute $\Pi^{\mu\nu}$ from the sum of 1PI graphs. From Eq. (9.25) it is clear that the sign convention here is such that $i\Pi^{00}$, $-i\Pi^{0j}$ and $i\Pi^{ij}$ are given by the sum of two-point 1PI graphs between $\mathcal{A}_0\mathcal{A}_0$, $\mathcal{A}_0\mathcal{A}^j$ and $\mathcal{A}^i\mathcal{A}^j$, respectively. From the photon-electron couplings in Eq. (9.15), we obtain $\Pi^{\mu\nu}$ in terms of $\Pi_{\mathcal{O}_1, \mathcal{O}_2}$ and $\Pi'_{\mathcal{O}}$ defined in Eq. (9.23) and (9.24):

$$\begin{aligned} \Pi^{00} &= -e^2 \Pi_{\mathbb{1}, \mathbb{1}}, & \Pi^{0j} &= -e^2 \Pi_{\mathbb{1}, v^j}, \\ \Pi^{ij} &= -e^2 \Pi_{v^i, v^j} - \frac{e^2}{4m_e^2} (q^2 \delta^{ij} - q^i q^j) \Pi_{\mathbb{1}, \mathbb{1}} + \frac{e^2}{m_e} \delta^{ij} \Pi'_{\mathbb{1}}, \end{aligned} \quad (9.26)$$

where the velocity operator v^j is defined by

$$v^j \equiv -\frac{i \overleftrightarrow{\nabla}^j}{2m_e}. \quad (9.27)$$

Here and in what follows, we suppress the arguments $Q^\mu = (\omega, \mathbf{q})$ of self-energy functions where there is no confusion. To arrive at the expression of Π^{ij} in Eq. (9.26), we have simplified the spin trace assuming the electron loop does not involve non-trivial spin structures; for example,

$$\Pi_{\Sigma^i, \Sigma^j} = \frac{\text{tr}(\sigma^i \sigma^j)}{\text{tr} \mathbb{1}} \Pi_{\mathbb{1}, \mathbb{1}} = \delta^{ij} \Pi_{\mathbb{1}, \mathbb{1}}. \quad (9.28)$$

This assumption is obviously valid for one-loop self-energy diagrams. In the superconductor calculation in Sec. 9.5, we will need two-loop self-energies with an internal phonon line; in that case the electron-phonon coupling is spin-independent, so the same simplification applies.

The photon self-energy satisfies the Ward identity $Q_\mu \Pi^{\mu\nu} = Q_\nu \Pi^{\mu\nu} = 0$. From Eq. (9.26) we see that this implies the following relations between $\Pi_{\mathbb{1}, \mathbb{1}}$, $\Pi_{\mathbb{1}, v^j}$, Π_{v^i, v^j} and $\Pi'_{\mathbb{1}}$:

$$\omega \Pi_{\mathbb{1}, \mathbb{1}} = q^j \Pi_{\mathbb{1}, v^j}, \quad \omega \Pi_{\mathbb{1}, v^j} = q^i \Pi_{v^i, v^j} - \frac{q^j}{m_e} \Pi'_{\mathbb{1}}. \quad (9.29)$$

These relations can be explicitly checked with the one-loop-level expressions in Eqs. (N.7) and (N.8).

We can write $\Pi^{\mu\nu}$ in terms of its polarization components as follows:

$$\Pi^{\mu\nu} = - \sum_{\lambda, \lambda' = \pm, L} \Pi_{\lambda\lambda'} e_{\lambda}^{\mu} e_{\lambda'}^{\nu*}, \quad (9.30)$$

where

$$e_{\pm}^{\mu} = \frac{1}{\sqrt{2}} (0, \hat{\mathbf{x}} \pm i\hat{\mathbf{y}}), \quad e_L^{\mu} = \frac{1}{\sqrt{Q^2}} (q, \omega\hat{\mathbf{z}}) \quad (9.31)$$

for $Q^{\mu} = (\omega, \mathbf{q}) = (\omega, q\hat{\mathbf{z}})$. These are the three photon polarizations in Lorenz gauge $Q_{\mu}e_{\lambda}^{\mu} = 0$, and coincide with the three physical polarizations of a massive vector with $m^2 = Q^2$.

We will mostly focus on isotropic target materials in this work, and leave a discussion of the anisotropic case to App. O. For an isotropic medium, the 3×3 matrix $\Pi_{\lambda\lambda'}$ is diagonal:

$$\begin{pmatrix} \Pi_{++} & \Pi_{+-} & \Pi_{+L} \\ \Pi_{-+} & \Pi_{--} & \Pi_{-L} \\ \Pi_{L+} & \Pi_{L-} & \Pi_{LL} \end{pmatrix} \xrightarrow{\text{isotropic}} \begin{pmatrix} \Pi_T & 0 & 0 \\ 0 & \Pi_T & 0 \\ 0 & 0 & \Pi_L \end{pmatrix} \quad (9.32)$$

where Π_T and Π_L are the transverse and longitudinal photon self-energies, respectively. The photon self-energy tensor $\Pi^{\mu\nu}$ therefore has the following form:

$$\Pi^{\mu\nu} \xrightarrow{\text{isotropic}} -\Pi_T (e_{+}^{\mu} e_{+}^{\nu*} + e_{-}^{\mu} e_{-}^{\nu*}) - \Pi_L e_L^{\mu} e_L^{\nu*} = - \begin{pmatrix} \frac{q^2}{Q^2} \Pi_L & 0 & 0 & \frac{\omega q}{Q^2} \Pi_L \\ 0 & \Pi_T & 0 & 0 \\ 0 & 0 & \Pi_T & 0 \\ \frac{\omega q}{Q^2} \Pi_L & 0 & 0 & \frac{\omega^2}{Q^2} \Pi_L \end{pmatrix}. \quad (9.33)$$

From the linear response relation $J^{\mu} = -\Pi^{\mu\nu} A_{\nu}$ ⁴ and Ohm's law $\mathbf{J} = \sigma \mathbf{E} = \sigma(i\omega \mathbf{A} - i\mathbf{q} A_0)$ we can relate Π_T and Π_L to the complex conductivity σ , which in turn is related to the complex dielectric ε via $\sigma = i\omega(1 - \varepsilon)$ [7, 29, 182]:

$$\Pi_T = -i\omega\sigma = \omega^2(1 - \varepsilon), \quad \Pi_L = -i\omega Z_L^{-1}\sigma = Q^2(1 - \varepsilon), \quad (9.34)$$

where $Z_L = \omega^2/Q^2$. The real part of the conductivity $\sigma_1 \equiv \text{Re } \sigma$ (the imaginary part of the dielectric) gives the photon absorption rate in medium:

$$\sigma_1 = \omega \text{Im } \varepsilon = -\frac{1}{\omega} \text{Im } \Pi_T = -\frac{Z_L}{\omega} \text{Im } \Pi_L. \quad (9.35)$$

⁴Strictly speaking, linear response theory relates J^{μ} and A_{ν} via the retarded Green's function $R^{\mu\nu}$, which differs from the time-ordered self-energy $\Pi^{\mu\nu}$ by the sign of the imaginary part at negative frequencies. This difference is however irrelevant for our calculations.

We finally note that all the quantities introduced above – the complex conductivity σ and dielectric ε , and photon self-energies Π_T, Π_L can be simply computed from $\Pi_{\mathbb{1},\mathbb{1}}$:

$$\varepsilon - 1 = \frac{i\sigma}{\omega} = -\frac{\Pi_L}{Q^2} = -\frac{\Pi_T}{\omega^2} = -\frac{e^2}{q^2} \Pi_{\mathbb{1},\mathbb{1}}. \quad (9.36)$$

With the photon part of the self-energy calculation completed, we now move on to consider self-energies involving the DM and compute DM absorption rates.

Vector Absorption

Since a vector DM couples to electrons in the same way as the photon, albeit with a coupling rescaled by $-g/e = -\kappa$, we have

$$\Pi_{\phi\phi}^{\mu\nu} = -\kappa \Pi_{\phi A}^{\mu\nu} = -\kappa \Pi_{A\phi}^{\mu\nu} = \kappa^2 \Pi^{\mu\nu}. \quad (9.37)$$

Each of the three polarizations of ϕ mixes with the corresponding polarization of the photon. Therefore, for the transverse (longitudinal) polarization, we simply set $\Pi_{\phi\phi} = -\kappa \Pi_{\phi A} = -\kappa \Pi_{A\phi} = \kappa^2 \Pi_{AA}$ in Eq. (9.22), with $\Pi_{AA} = \Pi_T$ (Π_L). As a result,

$$R_{T,L} = -\kappa^2 \frac{\rho_\phi}{\rho_T} \text{Im} \left(\frac{\Pi_{T,L}}{m_\phi^2 - \Pi_{T,L}} \right) = -\kappa^2 \frac{\rho_\phi}{\rho_T} m_\phi^2 \text{Im} \left(\frac{1}{m_\phi^2 - \Pi_{T,L}} \right). \quad (9.38)$$

The total absorption rate for an unpolarized vector DM is obtained by averaging over the three polarizations, $R = (2R_T + R_L)/3$. For NR absorption, we have $\omega^2 \simeq Q^2 = m_\phi^2$, and $\Pi_T \simeq \Pi_L = m_\phi^2 \frac{e^2}{q^2} \Pi_{\mathbb{1},\mathbb{1}}$ (see Eq. (9.36)), so

$$R_{\text{vector}} = -\kappa^2 \frac{\rho_\phi}{\rho_T} \text{Im} \left(\frac{1}{1 - \frac{e^2}{q^2} \Pi_{\mathbb{1},\mathbb{1}}} \right). \quad (9.39)$$

The rate is semi-independent of the momentum transfer (and hence the DM velocity) since $\Pi_{\mathbb{1},\mathbb{1}}$ generically scales as q^2 .

The result can also be written in terms of the material's complex conductivity/dielectric:

$$R_{\text{vector}} = -\kappa^2 \frac{\rho_\phi}{\rho_T} \text{Im} \left(\frac{1}{\varepsilon} \right) = \kappa^2 \frac{\rho_\phi}{\rho_T} \frac{1}{|\varepsilon|^2} \frac{\sigma_1}{m_\phi}, \quad (9.40)$$

with ε, σ_1 evaluated at $\omega = m_\phi, q = 0$. One may think of

$$\frac{1}{|\varepsilon|^2} = \frac{m_\phi^4}{(m_\phi^2 - \text{Re} \Pi_L)^2 + (\text{Im} \Pi_L)^2} \quad (9.41)$$

as an in-medium screening factor, which suppresses the absorption rate compared to the obvious rescaling of photon absorption by κ^2 [39, 41, 362, 375].

Pseudoscalar Absorption

A pseudoscalar does not mix with the photon due to parity mismatch,⁵ and we simply have $R = -\frac{\rho_\phi}{\rho_T} \frac{1}{\omega^2} \text{Im} \Pi_{\phi\phi}$. The pseudoscalar self-energy $\Pi_{\phi\phi}$ is defined such that the effective action contains

$$\mathcal{S}_{\text{eff}} \supset -\frac{1}{2} \int d^4Q [m_\phi^2 + \Pi_{\phi\phi}(Q)] \phi(Q) \phi(-Q). \quad (9.42)$$

Therefore, $-i\Pi_{\phi\phi}$ is given by the sum of two-point 1PI graphs. From the pseudoscalar coupling in Eq. (9.18), we find, again after simplifying the spin trace as in Eq. (9.28):

$$\text{Im} \Pi_{\phi\phi} = \frac{g^2}{4m_e^2} \text{Im} \left[q^2 \Pi_{\mathbb{1},\mathbb{1}} - \omega q^j (\Pi_{\mathbb{1},vj} + \Pi_{vj,\mathbb{1}}) + \omega^2 \Pi_{vj,vj} \right] \quad (9.43)$$

Comparing with Eq. (9.26), we see that $\text{Im} \Pi_{\phi\phi}$ for a pseudoscalar is closely related to the photon polarization $\Pi^{\mu\nu}$:

$$\text{Im} \Pi_{\phi\phi} = -\frac{g^2}{e^2} \frac{1}{4m_e^2} \text{Im} \left[q^2 \Pi^{00} - \omega q^j (\Pi^{0j} + \Pi^{j0}) + \omega^2 \Pi^{jj} - q^2 \frac{\omega^2}{2m_e^2} \Pi^{00} \right]. \quad (9.44)$$

Note that the $\Pi_{\mathbb{1}}^{jj}$ term in Π^{jj} is purely real and thus does not appear in the equation above. Also, since $\omega \ll m_e$, we can drop the last term. Writing $\Pi^{\mu\nu}$ in terms of Π_T and Π_L as in Eq. (9.33) and setting $g = g_{aee}$, we find

$$R_{\text{pseudoscalar}} = -g_{aee}^2 \frac{\rho_\phi}{\rho_T} \frac{1}{4m_e^2 \omega^2} \frac{1}{e^2} (2\omega^2 \text{Im} \Pi_T + m_\phi^2 \text{Im} \Pi_L). \quad (9.45)$$

For NR absorption, $\omega^2 \simeq Q^2 = m_\phi^2$, and $\Pi_T \simeq \Pi_L = e^2 \frac{m_\phi^2}{q^2} \Pi_{\mathbb{1},\mathbb{1}}$ (see Eq. (9.36)), and therefore,

$$R_{\text{pseudoscalar}} = -g_{aee}^2 \frac{\rho_\phi}{\rho_T} \frac{3m_\phi^2}{4m_e^2} \frac{1}{q^2} \text{Im} \Pi_{\mathbb{1},\mathbb{1}}. \quad (9.46)$$

As in the vector DM case, the absorption rate can be written solely in terms of $\Pi_{\mathbb{1},\mathbb{1}}$; the other self-energies that appear in Eq. (9.43) have been traded for $\Pi_{\mathbb{1},\mathbb{1}}$ via the Ward identity. Also, analogous to the vector DM case, the rate is semi-independent of the DM velocity as $\Pi_{\mathbb{1},\mathbb{1}} \sim q^2$. Note that the dominant contribution to pseudoscalar DM absorption comes from the last term in Eq. (9.43) that is proportional to $\omega^2 \Pi_{vj,vj}$, which originates from the second (formally NLO) operator in Eq. (9.18) (as underlined in Table 9.1).

We can further recast the pseudoscalar DM absorption rate in terms of the photon absorption rate $\sigma_1 = \text{Re} \sigma = \omega \text{Im} \varepsilon$ and reproduce the standard result [39–41, 360]:

$$R_{\text{pseudoscalar}} = \frac{g_{aee}^2}{e^2} \frac{\rho_\phi}{\rho_T} \frac{3m_\phi \sigma_1}{4m_e^2}. \quad (9.47)$$

⁵The mixed self-energy $\Pi_{\phi A}^0$ ($\Pi_{\phi A}^j$) between ϕ and A_0 (A^j) has to be parity odd (even). For an isotropic target one must have $\Pi_{\phi A}^j \propto q^j$ while $\Pi_{\phi A}^0$ is a scalar function of q^2 , so neither has the right parity if nonzero.

We remark in passing that pseudoscalar absorption has also been studied in the context of solar axion detection; in that case, the relativistic kinematics $\omega \gg m_\phi$ means that the $\text{Im } \Pi_L$ term in Eq. (9.45) is negligible, so the proportionality factor in Eq. (9.47) is $\frac{1}{2}$ instead of $\frac{3}{4}$ [39, 360, 376].

Scalar Absorption

For scalar DM, we need to compute explicitly both $\text{Im } \Pi_{\phi\phi}$ and its mixing with the photon $\Pi_{\phi A}^\mu(Q) = \Pi_{A\phi}^\mu(-Q)$. These self-energies are defined such that

$$\begin{aligned} \mathcal{S}_{\text{eff}} &\supset \int d^4Q \left[-\frac{1}{2}(m_\phi^2 + \Pi_{\phi\phi}(Q)) \phi(Q) \phi(-Q) - \Pi_{\phi A}^\mu(Q) \phi(Q) \mathcal{A}_\mu(-Q) \right] \\ &= \int d^4Q \left[-\frac{1}{2}(m_\phi^2 + \Pi_{\phi\phi}(Q)) \phi(Q) \phi(-Q) \right. \\ &\quad \left. - \Pi_{\phi A}^0(Q) \phi(Q) \mathcal{A}_0(-Q) + \Pi_{\phi A}^j(Q) \phi(Q) \mathcal{A}^j(-Q) \right]. \end{aligned} \quad (9.48)$$

Therefore, $-i \Pi_{\phi\phi}$, $-i \Pi_{\phi A}^0$ and $i \Pi_{\phi A}^j$ are given by the sum of two-point 1PI graphs between $\phi\phi$, $\phi\mathcal{A}_0$ and $\phi\mathcal{A}^j$, respectively. From the scalar coupling in Eq. (9.18) and photon coupling in Eq. (9.15), we find:

$$\text{Im } \Pi_{\phi\phi} = g^2 \text{Im} \left(\Pi_{\mathbb{1},\mathbb{1}} - \Pi_{\mathbb{1},\bar{v}^2} - \Pi_{\bar{v}^2,\mathbb{1}} + \Pi_{\bar{v}^2,\bar{v}^2} \right), \quad (9.49)$$

$$\Pi_{\phi A}^0 = -ge \left(\Pi_{\mathbb{1},\mathbb{1}} - \Pi_{\bar{v}^2,\mathbb{1}} \right), \quad (9.50)$$

$$\Pi_{\phi A}^j = -ge \left(\Pi_{\mathbb{1},v^j} - \Pi_{\bar{v}^2,v^j} + \frac{1}{m_e} \Pi'_{v^j} \right), \quad (9.51)$$

where

$$\bar{v}^2 \equiv \frac{1}{2} v^j v^j = -\frac{\overleftrightarrow{\nabla}^2}{8m_e^2}. \quad (9.52)$$

As in the photon case, the self-energies are related by the Ward identity $Q_\mu \Pi_{\phi A}^\mu = 0$:

$$\omega \Pi_{\bar{v}^2,\mathbb{1}} = q^j \Pi_{\bar{v}^2,v^j} - \frac{q^j}{m_e} \Pi'_{v^j}, \quad (9.53)$$

where we have used the first relation in Eq. (9.29). One can explicitly check that Eq. (9.53) holds between the one-loop-level expressions for the self-energies in Eqs. (N.7) and (N.8).

For an isotropic medium, we must have $\Pi_{\phi A}^j \propto q^j$ because there is no special direction other than \mathbf{q} .⁶ So the mixing only involves the photon's longitudinal component. Therefore, Π_{AA}

⁶We note in passing that the Π'_{v^j} term in $\Pi_{\phi A}^j$ is \mathbf{q} independent and must therefore vanish in an isotropic medium. This is why we have omitted the $\phi \mathcal{A} \cdot (\hat{\psi}_+^\dagger \overleftrightarrow{\nabla} \hat{\psi}_+)$ operator in Eq. (9.18), which only contributes to this term, from Table 9.1.

in the rate formula Eq. (9.22) should be set to $\Pi_L = m_\phi^2 \frac{e^2}{q^2} \Pi_{\mathbb{1},\mathbb{1}}$ (see Eq. (9.36)), and $\Pi_{\phi A}$ should be set to

$$\Pi_{\phi L} = \Pi_{\phi A}^\mu e_{L\mu} = \frac{1}{q\sqrt{Q^2}} (q^2 \Pi_{\phi A}^0 - \omega q^j \Pi_{\phi A}^j) = -\frac{\sqrt{Q^2}}{q} \Pi_{\phi A}^0 = ge \frac{\sqrt{Q^2}}{q} (\Pi_{\mathbb{1},\mathbb{1}} - \Pi_{\bar{v}^2,\mathbb{1}}), \quad (9.54)$$

where we have used the Ward identity to trade $q^j \Pi_{\phi A}^j$ for $\omega \Pi_{\phi A}^0$. Substituting the expressions for $\text{Im} \Pi_{\phi\phi}$, $\Pi_{\phi L}$ and Π_L above into Eq. (9.22), and applying the NR absorption kinematics $\omega^2 \simeq Q^2 = m_\phi^2$, we find

$$R_{\text{scalar}} = -d_{\phi ee}^2 \frac{4\pi m_e^2}{M_{\text{Pl}}^2} \frac{\rho_\phi}{\rho_T} \frac{1}{m_\phi^2} \text{Im} \left[\Pi_{\bar{v}^2,\bar{v}^2} + \frac{q^2}{e^2} \frac{(1 - \frac{e^2}{q^2} \Pi_{\bar{v}^2,\mathbb{1}})(1 - \frac{e^2}{q^2} \Pi_{\mathbb{1},\bar{v}^2})}{1 - \frac{e^2}{q^2} \Pi_{\mathbb{1},\mathbb{1}}} \right], \quad (9.55)$$

where we have used $\Pi_{L\phi}(Q) = \Pi_{\phi L}(-Q)$, $\Pi_{\bar{v}^2,\mathbb{1}}(-Q) = \Pi_{\mathbb{1},\bar{v}^2}(Q)$, and $g = d_{\phi ee} \frac{\sqrt{4\pi} m_e}{M_{\text{Pl}}}$.

We see that the result for scalar absorption, Eq. (9.55), depends on $\Pi_{\bar{v}^2,\bar{v}^2}$, $\Pi_{\bar{v}^2,\mathbb{1}}$, $\Pi_{\mathbb{1},\bar{v}^2}$ in addition to $\Pi_{\mathbb{1},\mathbb{1}}$. If we had kept only the LO operator $\phi \hat{\psi}_+^\dagger \hat{\psi}_+$ in the calculation above, we would obtain Eq. (9.55) with $\Pi_{\bar{v}^2,\bar{v}^2}$, $\Pi_{\bar{v}^2,\mathbb{1}}$, $\Pi_{\mathbb{1},\bar{v}^2}$ set to zero, which coincides with $\frac{q^2}{m_\phi^2}$ times the vector DM absorption rate in Eq. (9.39). Just as in the vector DM case, the contribution of the LO operator $\phi \hat{\psi}_+^\dagger \hat{\psi}_+$ to scalar DM absorption is screened due to in-medium mixing [44]. However, the formally NLO operator $\phi (\hat{\psi}_+^\dagger \overleftrightarrow{\nabla}^2 \hat{\psi}_+)$ introduces additional contributions via $\Pi_{\bar{v}^2,\bar{v}^2}$, $\Pi_{\bar{v}^2,\mathbb{1}}$, $\Pi_{\mathbb{1},\bar{v}^2}$. As we will see in the next two sections, generically $\Pi_{\mathbb{1},\mathbb{1}}$, $\Pi_{\bar{v}^2,\mathbb{1}} \sim q^2$ while $\Pi_{\bar{v}^2,\bar{v}^2} \sim q^0$. It is thus clear from Eq. (9.55) that the absorption rate of a NR scalar DM is in fact dominated by the $\Pi_{\bar{v}^2,\bar{v}^2}$ term:

$$R_{\text{scalar}} \simeq -d_{\phi ee}^2 \frac{4\pi m_e^2}{M_{\text{Pl}}^2} \frac{\rho_\phi}{\rho_T} \frac{1}{m_\phi^2} \text{Im} \Pi_{\bar{v}^2,\bar{v}^2}. \quad (9.56)$$

Importantly, this term (overlooked in several previous calculations of scalar DM absorption [44, 364, 365]) is not directly proportional to the photon absorption rate and is un-screened. We emphasize that the suppression of LO operator's contribution is specific to the case of non-relativistic DM absorption, where $q \ll \omega$; for absorption of a relativistic scalar ($q \simeq \omega$) or scalar-mediated scattering ($q \gg \omega$), the LO operator $\phi \hat{\psi}_+^\dagger \hat{\psi}_+$ indeed gives the dominant contribution.

To summarize, in this section we have derived DM absorption rates in terms of in-medium self-energies of the form $\Pi_{\mathcal{O}_1,\mathcal{O}_2}$, as defined in Eq. (9.23). (Contributions from the other graph topology, Eq. (9.24), have been eliminated using the Ward identity.) Both vector and pseudoscalar absorption involve a single self-energy function $\Pi_{\mathbb{1},\mathbb{1}} \propto \Pi_L$ (see Eqs. (9.39) and (9.46)), and the rates can be simply related to the (complex) conductivity/dielectric (see

Eqs. (9.40) and (9.47)). In these cases, the data-driven approach based on the measured conductivity/dielectric is viable, and we can also use optical data to calibrate our theoretical calculations based on DFT or analytic modeling. On the other hand, for scalar DM absorption, additional self-energy functions $\Pi_{\bar{v}^2, \bar{v}^2}$, $\Pi_{\bar{v}^2, \mathbb{1}}$, $\Pi_{\mathbb{1}, \bar{v}^2}$ enter (see Eq. (9.55)), and the rate is not directly related to photon absorption. In this case, the data-driven approach fails and theoretical calculations are needed.

In the next two sections, we compute the self-energies $\Pi_{\mathbb{1}, \mathbb{1}}$, $\Pi_{\bar{v}^2, \bar{v}^2}$, $\Pi_{\bar{v}^2, \mathbb{1}}$, $\Pi_{\mathbb{1}, \bar{v}^2}$ in crystal and superconductor targets, respectively, which then allow us to derive the absorption rates of vector, pseudoscalar and scalar DM in these targets. Our main results for Si, Ge and Al-superconductor (Al-SC) targets are collected in Figs. 9.1, 9.2 and 9.3. First, Fig. 9.1 confirms the dominance of the $\Pi_{\bar{v}^2, \bar{v}^2}$ term in the scalar DM absorption rate (i.e. that Eq. (9.55) indeed simplifies to Eq. (9.56)) by rewriting Eq. (9.55) as

$$R_{\text{scalar}} = d_{\phi ee}^2 \frac{4\pi m_e^2}{M_{\text{Pl}}^2} \frac{\rho_\phi}{\rho_T} (\mathcal{R}_{\bar{v}^2, \bar{v}^2} + \mathcal{R}_{\mathbb{1}, \mathbb{1}} + \mathcal{R}_{\bar{v}^2, \mathbb{1}}), \quad (9.57)$$

and comparing the sizes of the terms. Here $\mathcal{R}_{\bar{v}^2, \bar{v}^2} \equiv -\frac{1}{m_\phi^2} \text{Im} \Pi_{\bar{v}^2, \bar{v}^2}$, $\mathcal{R}_{\mathbb{1}, \mathbb{1}} \equiv -\frac{1}{m_\phi^2} \frac{q^2}{e^2} \text{Im} \left(\frac{1}{1 - \frac{e^2}{q^2} \Pi_{\mathbb{1}, \mathbb{1}}} \right)$, while the remaining terms define $\mathcal{R}_{\bar{v}^2, \mathbb{1}}$. Next, Fig. 9.2 shows the projected reach for the pseudoscalar and vector DM models, where we see good agreement between our theoretical calculations (solid curves) and rescaled optical data (dashed curves). Lastly, Fig. 9.3 shows our calculated reach for scalar DM and compares the Al-SC results with previous work [39, 44]. These results will be discussed in detail in the following sections.

9.4 Dark Matter Absorption in Crystals

In this section, we specialize to the case of crystal targets that are described by band theory. It suffices to compute the self-energies $\Pi_{\mathcal{O}_1, \mathcal{O}_2}$ at one-loop level, with $\mathcal{O}_{1,2} = \mathbb{1}, \bar{v}^2$. The result for general $\mathcal{O}_1, \mathcal{O}_2$ is given in Eq. (N.7) in Appendix N, and involves a sum over electronic states I, I' that run in the loop. Since we assume the target is at zero temperature the occupation numbers $f_I, f_{I'}$ take values of either 1 or 0. Only pairs of states for which $f_{I'} - f_I \neq 0$, i.e. one is occupied and the other is unoccupied, contribute to the sum — it is between these pairs of states that electronic transitions can happen.

In the present case, the states are labeled by a band index i and momentum \mathbf{k} within the first Brillouin zone (1BZ), so we write $I = i, \mathbf{k}$, and $I' = i', \mathbf{k}'$. The wave functions have the Bloch form, which in real and momentum space read, respectively:

$$\Psi_{i, \mathbf{k}}(\mathbf{x}) = \frac{1}{\sqrt{V}} \sum_{\mathbf{G}} u_{i, \mathbf{k}, \mathbf{G}} e^{i(\mathbf{k} + \mathbf{G}) \cdot \mathbf{x}}, \quad \tilde{\Psi}_{i, \mathbf{k}}(\mathbf{p}) = \sqrt{V} \sum_{\mathbf{G}} u_{i, \mathbf{k}, \mathbf{G}} \delta_{\mathbf{p}, \mathbf{k} + \mathbf{G}}, \quad (9.58)$$

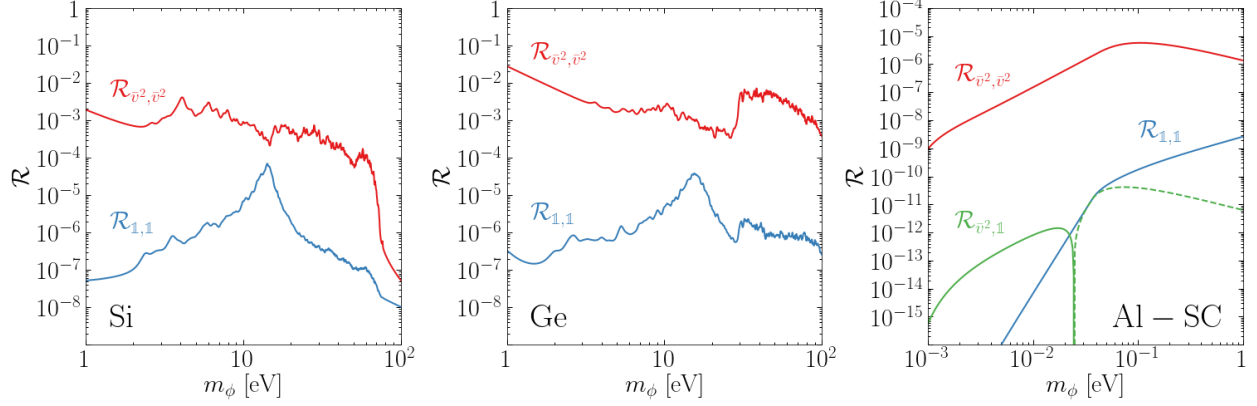


Figure 9.1: Comparison between different terms contributing to the scalar DM absorption rate, defined in Eq. (9.57), for Si, Ge and Al-SC targets assuming $q = 10^{-3}m_\phi$. Dashed curves indicate negative values. In all three targets we see that $\mathcal{R}_{\bar{v}^2, \bar{v}^2}$ dominates over the entire DM mass range considered. This term comes from an NLO operator in the NR EFT (underlined in Table 9.1) and cannot be directly related to the target’s optical properties (i.e. the complex conductivity/dielectric function). For Si and Ge, the calculation of $\mathcal{R}_{\bar{v}^2, \mathbb{1}}$ is technically challenging as explained in Sec. 9.4; however, it is parameterically the same order in q as $\mathcal{R}_{\mathbb{1}, \mathbb{1}}$ and therefore expected to be also subdominant compared to $\mathcal{R}_{\bar{v}^2, \bar{v}^2}$.

where the sum runs over all reciprocal lattice vectors \mathbf{G} . These are related by

$$\Psi_{i, \mathbf{k}}(\mathbf{x}) = \int \frac{d^3 p}{(2\pi)^3} \tilde{\Psi}_{i, \mathbf{k}}(\mathbf{p}) e^{i\mathbf{p}\cdot\mathbf{x}}, \quad \tilde{\Psi}_{i, \mathbf{k}}(\mathbf{p}) = \int d^3 x \Psi_{i, \mathbf{k}}(\mathbf{x}) e^{-i\mathbf{p}\cdot\mathbf{x}} \quad (9.59)$$

upon applying the standard dictionary between discrete and continuum expressions:

$$\sum_{\mathbf{p}} = V \int \frac{d^3 p}{(2\pi)^3}, \quad \delta_{\mathbf{p}_1, \mathbf{p}_2} = \frac{(2\pi)^3}{V} \delta^3(\mathbf{p}_1 - \mathbf{p}_2). \quad (9.60)$$

We now examine the matrix element $\langle i', \mathbf{k}' | \mathcal{O}_1 e^{i\mathbf{q}\cdot\mathbf{x}} | i, \mathbf{k} \rangle$ involved in Eq. (N.7) for the \bar{v}^2 and $\mathbb{1}$ operators; $\langle i, \mathbf{k} | \mathcal{O}_2 e^{-i\mathbf{q}\cdot\mathbf{x}} | i', \mathbf{k}' \rangle$ is completely analogous. For the \bar{v}^2 operator, we simply obtain

$$\begin{aligned} \langle i', \mathbf{k}' | \bar{v}^2 e^{i\mathbf{q}\cdot\mathbf{x}} | i, \mathbf{k} \rangle &= -\frac{1}{8m_e^2} \int d^3 x (\Psi_{i', \mathbf{k}'}^* \overleftrightarrow{\nabla}^2 \Psi_{i, \mathbf{k}}) e^{i\mathbf{q}\cdot\mathbf{x}} \\ &= \frac{1}{8m_e^2} \sum_{\mathbf{G}', \mathbf{G}} (\mathbf{k}' + \mathbf{G}' + \mathbf{k} + \mathbf{G})^2 u_{i', \mathbf{k}', \mathbf{G}'}^* u_{i, \mathbf{k}, \mathbf{G}} \delta_{\mathbf{k}' + \mathbf{G}', \mathbf{k} + \mathbf{G} + \mathbf{q}}. \end{aligned} \quad (9.61)$$

For NR absorption in the mass range of interest here, $m_\phi \lesssim 100$ eV, the momentum transfer $q \sim 10^{-3}m_\phi \sim \text{meV} (\frac{m_\phi}{\text{eV}})$ is well within the 1BZ ($\mathcal{O}(\text{keV})$). This implies that Umklapp processes where $\mathbf{G}' \neq \mathbf{G}$ do not contribute, so (lattice) momentum conservation simply

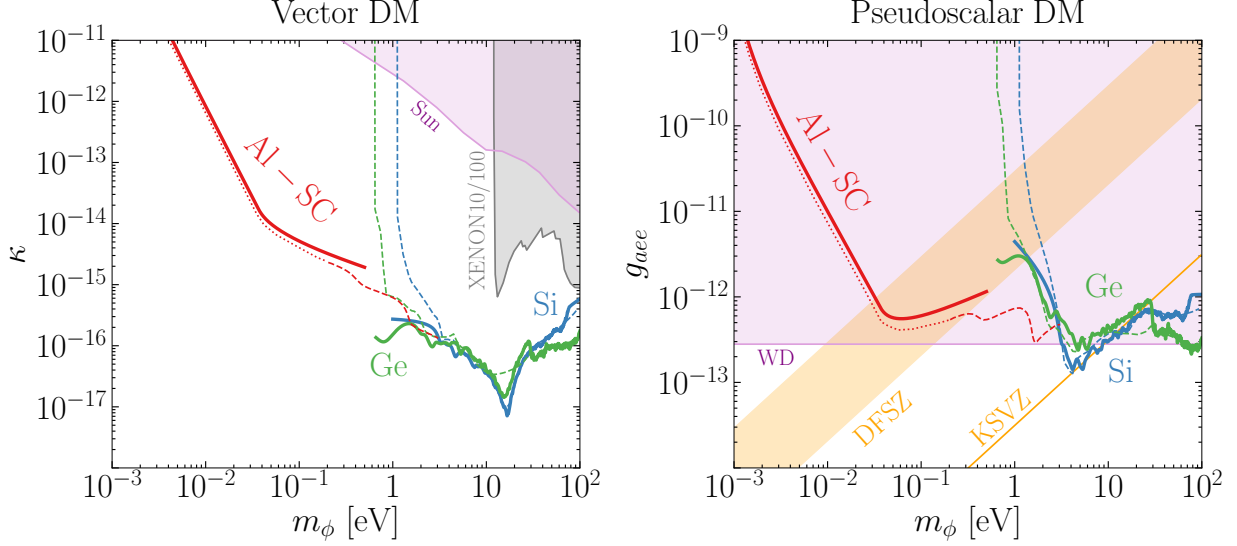


Figure 9.2: Projected 95% C.L. reach (3 events with no background) with semiconductor crystal (Si, Ge) and superconductor (Al-SC) targets for the vector and pseudoscalar DM models defined in Eq. (9.3), assuming 1 kg-yr exposure. We compare our theoretically calculated reach (solid) against the data-driven approach utilizing the target material’s measured conductivity/dielectric [37, 38] (dashed). For Si and Ge, the data-driven approach was taken in previous works [39, 40], with which we find good agreement. For Al-SC, our theoretical calculation reproduces the results in Ref. [41] (dotted) up to the choice of overall normalization factor. Also shown are existing direct detection limits from XENON10/100 [40], stellar cooling constraints from the Sun (assuming Stückelberg mass for vector DM) [42] and white dwarfs (WD) [31], and pseudoscalar couplings corresponding to the QCD axion in KSVZ and DFSZ (for $0.28 \leq \tan \beta \leq 140$) models [43].

dictates $\mathbf{k}' = \mathbf{k} + \mathbf{q}$. At leading order in q we can set $\mathbf{k}' = \mathbf{k}$, and Eq. (9.61) simplifies to

$$\langle i', \mathbf{k}' | \bar{v}^2 e^{i\mathbf{q}\cdot\mathbf{x}} | i, \mathbf{k} \rangle = \delta_{\mathbf{k}', \mathbf{k}} \frac{1}{2m_e^2} \sum_{\mathbf{G}} (\mathbf{k} + \mathbf{G})^2 u_{i', \mathbf{k}, \mathbf{G}}^* u_{i, \mathbf{k}, \mathbf{G}} + \mathcal{O}(q). \quad (9.62)$$

For the $\mathbb{1}$ operator, additional care is needed since $\langle i', \mathbf{k}' | e^{i\mathbf{q}\cdot\mathbf{x}} | i, \mathbf{k} \rangle$ vanishes in the $q \rightarrow 0$ limit: $|i', \mathbf{k}'\rangle$ and $|i, \mathbf{k}\rangle$ are distinct energy eigenstates and therefore orthogonal. At $\mathcal{O}(q)$, we have $\langle i', \mathbf{k}' | e^{i\mathbf{q}\cdot\mathbf{x}} | i, \mathbf{k} \rangle \simeq i\mathbf{q} \cdot \langle i', \mathbf{k}' | \mathbf{x} | i, \mathbf{k} \rangle$. A numerically efficient way to compute this matrix element is to trade the position operator for the momentum operator via its commutator with the Hamiltonian $H = \frac{\mathbf{p}^2}{2m_e} + V(\mathbf{x})$:

$$\langle i', \mathbf{k}' | \mathbf{x} | i, \mathbf{k} \rangle = -\frac{1}{\varepsilon_{i', \mathbf{k}'} - \varepsilon_{i, \mathbf{k}}} \langle i', \mathbf{k}' | [\mathbf{x}, H] | i, \mathbf{k} \rangle = -\frac{i}{m_e(\varepsilon_{i', \mathbf{k}'} - \varepsilon_{i, \mathbf{k}})} \langle i', \mathbf{k}' | \mathbf{p} | i, \mathbf{k} \rangle. \quad (9.63)$$

Substituting in the wave functions, we find:

$$\langle i', \mathbf{k}' | e^{i\mathbf{q}\cdot\mathbf{x}} | i, \mathbf{k} \rangle = \delta_{\mathbf{k}', \mathbf{k}} \frac{\mathbf{q}}{m_e \omega_{i', \mathbf{k}}} \cdot \sum_{\mathbf{G}} (\mathbf{k} + \mathbf{G}) u_{i', \mathbf{k}, \mathbf{G}}^* u_{i, \mathbf{k}, \mathbf{G}} + \mathcal{O}(q^2). \quad (9.64)$$

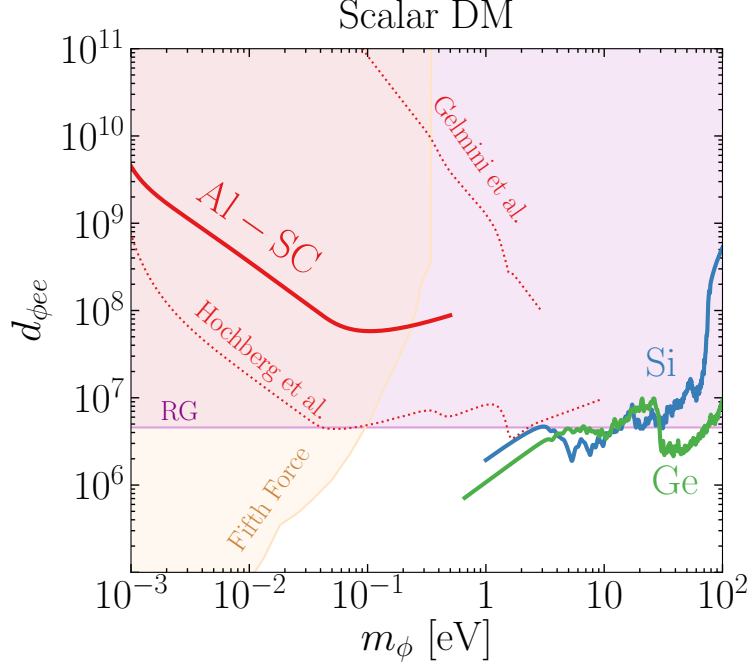


Figure 9.3: Projected 95% C.L. reach (3 events with no background) with semiconductor crystal (Si, Ge) and superconductor (Al-SC) targets, for the scalar DM model defined in Eq. (9.3), assuming 1 kg-yr exposure. In contrast to the vector and pseudoscalar cases shown in Fig. 9.2, the projections here cannot be derived from the target’s optical properties. Differences compared to Hochberg et al. [41] and Gelmini et al. [44] in the Al-SC case are discussed in detail in Sec. 9.5. Also shown are existing constraints from fifth force [45] and red giant (RG) cooling [46].

where $\omega_{i'i, \mathbf{k}} \equiv \varepsilon_{i', \mathbf{k}} - \varepsilon_{i, \mathbf{k}}$.

It is convenient to define the following crystal form factors, via which the Bloch wave functions enter DM absorption rates (at leading order in q):

$$f_{i'i, \mathbf{k}} \equiv \frac{1}{2m_e^2} \sum_{\mathbf{G}} (\mathbf{k} + \mathbf{G})^2 u_{i', \mathbf{k}, \mathbf{G}}^* u_{i, \mathbf{k}, \mathbf{G}}, \quad (9.65)$$

$$\mathbf{f}_{i'i, \mathbf{k}} \equiv \frac{1}{\omega_{i'i, \mathbf{k}}} \sum_{\mathbf{G}} (\mathbf{k} + \mathbf{G}) u_{i', \mathbf{k}, \mathbf{G}}^* u_{i, \mathbf{k}, \mathbf{G}}. \quad (9.66)$$

Note that they differ from the crystal form factor used in spin-independent DM scattering [7, 9, 33]: $f_{[i' \mathbf{k}', i \mathbf{k}, \mathbf{G}]} = \sum_{\mathbf{G}'} u_{i', \mathbf{k}', \mathbf{G}'+\mathbf{G}}^* u_{i, \mathbf{k}, \mathbf{G}'}$. The absorption kinematics simply set the \mathbf{k} and \mathbf{G} vectors of the initial and final states to be the same; also, powers of $(\mathbf{k} + \mathbf{G})$ appear as follows from the effective operators.

The crystal form factors defined above allow us to write the self-energies in a concise form. For the operators $\mathbb{1}$ and \bar{v}^2 , the spin trace is trivial and simply yields a factor of two. Each

pair of valence/conduction states between which a transition can happen contributes to two terms in the sum over electronic states, because either i, \mathbf{k} or i', \mathbf{k}' can be a valence or conduction state. Combining the two terms for each pair, we obtain

$$\Pi_{\mathbb{1},\mathbb{1}} = \frac{2}{V} \sum_{\substack{i' \in \text{cond.} \\ i \in \text{val.}}} \sum_{\mathbf{k} \in \text{1BZ}} \left(\frac{1}{\omega - \omega_{i',\mathbf{k}} + i\delta} - \frac{1}{\omega + \omega_{i',\mathbf{k}} - i\delta} \right) \left| \frac{\mathbf{q}}{m_e} \cdot \mathbf{f}_{i',\mathbf{k}} \right|^2, \quad (9.67)$$

$$\Pi_{\bar{v}^2, \bar{v}^2} = \frac{2}{V} \sum_{\substack{i' \in \text{cond.} \\ i \in \text{val.}}} \sum_{\mathbf{k} \in \text{1BZ}} \left(\frac{1}{\omega - \omega_{i',\mathbf{k}} + i\delta} - \frac{1}{\omega + \omega_{i',\mathbf{k}} - i\delta} \right) |f_{i',\mathbf{k}}|^2, \quad (9.68)$$

where $\delta \rightarrow 0^+$. We see explicitly that $\Pi_{\mathbb{1},\mathbb{1}} \sim q^2$ and $\Pi_{\bar{v}^2, \bar{v}^2} \sim q^0$, as already alluded to in Sec. 9.3. The other two self-energies, $\Pi_{\bar{v}^2, \mathbb{1}}$ and $\Pi_{\mathbb{1}, \bar{v}^2}$, take the form of $\mathbf{q} \cdot \mathcal{F} + \mathcal{O}(q^2)$, where \mathcal{F} is a target-dependent function that involves $f_{i',\mathbf{k}}$ and $\mathbf{f}_{i',\mathbf{k}}$. In the absence of a special direction, we must have $\mathcal{F} = \mathbf{0}$ and therefore, $\Pi_{\bar{v}^2, \mathbb{1}}, \Pi_{\mathbb{1}, \bar{v}^2} \sim \mathcal{O}(q^2)$. Working out the leading $\mathcal{O}(q^2)$ contribution to these self-energies would require the $\mathcal{O}(q^2)$ term in $\langle i', \mathbf{k}' | e^{i\mathbf{q} \cdot \mathbf{x}} | i, \mathbf{k} \rangle$, which however does not admit a simple expression in terms of just the momentum operator as in Eq. (9.63). Nevertheless, $\Pi_{\bar{v}^2, \mathbb{1}}$ and $\Pi_{\mathbb{1}, \bar{v}^2}$ only enter the absorption rate in the scalar DM case and we expect $\mathcal{R}_{\bar{v}^2, \mathbb{1}} \sim \mathcal{R}_{\mathbb{1}, \mathbb{1}}$ since $\Pi_{\bar{v}^2, \mathbb{1}}, \Pi_{\mathbb{1}, \bar{v}^2}$ and $\Pi_{\mathbb{1}, \mathbb{1}}$ all scale as q^2 . So as long as $\mathcal{R}_{\mathbb{1}, \mathbb{1}} \ll \mathcal{R}_{\bar{v}^2, \bar{v}^2}$, it is justified to neglect the second term in Eq. (9.55) altogether and use Eq. (9.56) for the rate; computing $\Pi_{\bar{v}^2, \mathbb{1}}, \Pi_{\mathbb{1}, \bar{v}^2}$ then becomes unnecessary. We see from Fig. 9.1 that this is indeed the case for Si and Ge.

To calculate the DM absorption rates and make sensitivity projections, we use DFT-computed electronic band structures and wave functions for Si and Ge [343], including all-electron reconstruction up to a cutoff of 2 keV; see Ref. [9] for details. We adopt the same numerical setup as the ‘‘valence to conduction’’ calculation in Ref. [9], and include also the 3d states in Ge as valence (treating them as core states gives similar results). The finite resolution of the \mathbf{k} -grid means we need to apply some kind of smearing to the delta functions coming from the imaginary part of Eqs. (9.67) and (9.68). This is done in practice by setting δ in Eqs. (9.67) and (9.68) to a finite constant 0.2 eV, which we find appropriate for a $10 \times 10 \times 10$ \mathbf{k} -grid for the majority of the DM mass range. We implement our numerical calculation as a new module ‘‘absorption’’ of the EXCEED-DM program [179].

We present the projected reach for the three DM models in Figs. 9.2 and 9.3, assuming 3 events (corresponding to 95% CL) for 1 kg-yr exposure without including background, together with existing constraints on these models for reference. The solid curves are our theoretical predictions; they are obtained using the rate formulae Eqs. (9.39), (9.46) and (9.56) for vector, pseudoscalar and scalar DM, respectively, with the self-energies $\Pi_{\mathbb{1},\mathbb{1}}, \Pi_{\bar{v}^2, \bar{v}^2}$ computed numerically for Si and Ge according to Eqs. (9.67) and (9.68) as explained above.

For pseudoscalar and scalar DM, the reach curves are essentially the sum of Lorentzians coming from the smearing of delta functions in $\text{Im } \Pi_{\mathbb{1},\mathbb{1}}$ and $\text{Im } \Pi_{\bar{v}^2,\bar{v}^2}$, respectively; there is no screening in these cases. For vector DM, in-medium mixing with the photon results in the plasmon peak (dip in the reach curves) between 10 and 20 eV for both Si and Ge; the rate is screened below the plasmon peak.

For vector and pseudoscalar DM, we can alternatively take the data-driven approach, using Eqs. (9.40) and (9.47), respectively, to derive the rate from the measured conductivity/dielectric. As in Ref. [39, 40], we use the measured optical data from Ref. [37]. Results from this data-driven approach are shown by the dashed curves; they are the same as in Ref. [39, 40] upon inclusion of backgrounds. For Si, the solid and dashed curves are very close to each other for $m_\phi \gtrsim 3$ eV; the theoretical calculation (solid curves) systematically overestimates the rate as m_ϕ approaches the band gap (1.2 eV) because of the smearing procedure discussed above. For Ge, we see the same systematic discrepancy close to the band gap (0.67 eV); also, the theoretical calculation predicts a sharper plasmon peak (corresponding to a smaller $\text{Im } \Pi_{\mathbb{1},\mathbb{1}}$ near the plasmon frequency) compared to data. Aside from these issues, we view the overall good agreement between the solid and dashed curves in the vector and pseudoscalar cases as a validation of our DFT-based theoretical calculation in the majority of DM mass range. Importantly, this gives credence to the reach curves we have calculated in the scalar DM case, where the data-driven approach does not apply, though one has to keep in mind that our calculation systematically overestimates the rate for DM masses below about 3 eV because of the smearing issue.

9.5 Dark Matter Absorption in Superconductors

We now turn to the case of conventional superconductors described by BCS theory. For the majority of the calculation, we are concerned with electronic states with energies ε satisfying $|\varepsilon - \varepsilon_F| \gg \Delta$, where ε_F is the Fermi energy and $2\Delta \sim \mathcal{O}(\text{meV})$ is the gap, and the description of a superconductor approaches that of a normal metal; corrections due to Cooper pairing only become relevant within $\mathcal{O}(\Delta)$ of the Fermi surface.

Following Refs. [41, 181, 182], we model the electrons near the Fermi surface with a free-electron dispersion $\varepsilon_{\mathbf{k}} = \frac{k^2}{m_*}$ and wave function $\Psi_{\mathbf{k}}(\mathbf{x}) = \frac{1}{\sqrt{V}} e^{i\mathbf{k}\cdot\mathbf{x}}$, where the effective mass m_* is generally an $\mathcal{O}(1)$ number times the electron's vacuum mass m_e . At zero temperature, electrons occupy states up to the Fermi surface, a sphere of radius $k_F = \sqrt{2m_*\varepsilon_F}$. The volume of the Fermi sphere gives the density of free electrons, $n_e = \frac{2}{(2\pi)^3} \frac{4}{3} \pi k_F^3$, where the twofold spin degeneracy has been taken into account. We expect this simple effective description to hold up to a UV cutoff ω_{max} (~ 0.5 eV for Al), above which interband transitions

become important and one may instead perform a DFT calculation (as in the case of crystals discussed in Sec. 9.4).

Within this simple free-electron model, the self-energies $\Pi_{\mathcal{O}_1, \mathcal{O}_2}$ are real at one-loop level; it is easy to see that two electronic states differing by energy ω and momentum \mathbf{q} cannot be both on-shell when $\omega \gg q$. Therefore, the leading contribution to the imaginary part arises at two loops, and we have

$$\Pi_{\mathcal{O}_1, \mathcal{O}_2} \simeq \text{Re} \Pi_{\mathcal{O}_1, \mathcal{O}_2}^{(1\text{-loop})} + i \text{Im} \Pi_{\mathcal{O}_1, \mathcal{O}_2}^{(2\text{-loop})}. \quad (9.69)$$

For the real part $\text{Re} \Pi_{\mathcal{O}_1, \mathcal{O}_2} = \text{Re} \Pi_{\mathcal{O}_1, \mathcal{O}_2}^{(1\text{-loop})}$, we apply the general formula Eq. (N.7) to the free-electron model in the limit $\omega \gg q$, as explained in detail in App. N.2. The results are:

$$\text{Re} \Pi_{\mathbb{1}, \mathbb{1}} = \frac{q^2}{\omega^2} \frac{n_e}{m_*}, \quad \text{Re} \Pi_{\bar{v}^2, \mathbb{1}} = \text{Re} \Pi_{\mathbb{1}, \bar{v}^2} = \frac{k_F^2}{2m_e^2} \frac{q^2}{\omega^2} \frac{n_e}{m_*}. \quad (9.70)$$

While these are derived for normal conductors, we expect them to carry over to the superconductor case; proportionality to n_e (the total number of electronic states within the Fermi sphere) implies insensitivity to deformations within $\mathcal{O}(\Delta)$ of the Fermi surface. We also note in passing that, via Eq. (9.36), we obtain the familiar result for the photon self-energies [377, 378]: $\text{Re} \Pi_T = \omega_p^2$, $\text{Re} \Pi_L = \frac{Q^2}{\omega^2} \omega_p^2$, where $\omega_p^2 \equiv \frac{e^2 n_e}{m_*}$ is the plasma frequency squared.

For the imaginary part $\text{Im} \Pi_{\mathcal{O}_1, \mathcal{O}_2} = \text{Im} \Pi_{\mathcal{O}_1, \mathcal{O}_2}^{(2\text{-loop})}$, we expect the dominant contribution to come from two-loop diagrams with an internal phonon line for a high-purity sample (otherwise impurity scattering may also contribute). These are associated with ϕ (or γ) + $e^- \rightarrow e^-$ + phonon processes by the optical theorem, and can be computed by the standard cutting rules, as we detail in App. N.3. We model the (acoustic) phonons with a linear dispersion, $\omega_{\mathbf{q}'} = c_s q'$ where c_s is the sound speed, and neglect Umklapp processes which amounts to imposing a cutoff on the phonon momentum, $q'_{\text{max}} = q_D \equiv \omega_D/c_s$ with ω_D the Debye frequency. The electron-phonon coupling, in our normalization convention, is given by $\frac{C_{e\text{-ph}} q'}{\sqrt{2\omega_{\mathbf{q}'} \rho_T}}$ [41, 379, 380], with $C_{e\text{-ph}} \sim \mathcal{O}(\varepsilon_F)$ a constant with mass dimension one. Accounting

Fermi energy	$\varepsilon_F = 11.7 \text{ eV}$
Plasma frequency	$\omega_p = 12.2 \text{ eV}$
Electron effective mass	$m_* = \frac{9\pi^2\omega_p^4}{128\alpha^2\varepsilon_F^3} = 0.35 m_e$
Fermi momentum	$k_F = \sqrt{2m_*\varepsilon_F} = 2.1 \text{ keV}$
Superconducting gap	$2\Delta = 0.6 \text{ meV}$
Debye frequency	$\omega_D = 37 \text{ meV}$
Sound speed	$c_s = 2.1 \times 10^{-5}$
Maximum phonon momentum	$q_D = \frac{\omega_D}{c_s} = 1.8 \text{ keV}$
Electron-phonon coupling	$C_{\text{e-ph}} = 56 \text{ eV}$
Mass density	$\rho_T = 2.7 \text{ g/cm}^3$

Table 9.2: Material parameters for aluminum superconductor.

for the superconducting gap, we obtain, for $\omega \gg q$:

$$\text{Im } \Pi_{\mathbb{1},\mathbb{1}} = -\frac{C_{\text{e-ph}}^2 \omega^2 q^2}{3(2\pi)^3 \rho_T c_s^6} \int_0^{\min(1-\frac{2\Delta}{\omega}, \frac{\omega_D}{\omega})} dx x^4 (1-x) E\left(\sqrt{1 - \frac{(2\Delta/\omega)^2}{(1-x)^2}}\right), \quad (9.71)$$

$$\text{Im } \Pi_{\bar{v}^2, \bar{v}^2} = -\frac{C_{\text{e-ph}}^2 \omega^4}{(2\pi)^3 \rho_T c_s^4} \frac{m_*^4}{m_e^4} \int_0^{\min(1-\frac{2\Delta}{\omega}, \frac{\omega_D}{\omega})} dx x^2 (1-x)^3 E\left(\sqrt{1 - \frac{(2\Delta/\omega)^2}{(1-x)^2}}\right), \quad (9.72)$$

$$\text{Im } \Pi_{\bar{v}^2, \mathbb{1}} = \text{Im } \Pi_{\mathbb{1}, \bar{v}^2} = \frac{C_{\text{e-ph}}^2 \omega^2 q^2}{3(2\pi)^3 \rho_T c_s^4} \frac{m_*^4}{m_e^4} \int_0^{\min(1-\frac{2\Delta}{\omega}, \frac{\omega_D}{\omega})} dx x^2 (1-x)^2 E\left(\sqrt{1 - \frac{(2\Delta/\omega)^2}{(1-x)^2}}\right), \quad (9.73)$$

where $E(z) = \int_0^1 dt \sqrt{\frac{1-z^2t^2}{1-t^2}}$ is the complete elliptic integral of the second kind. For energy depositions much higher than the gap, $\omega \gg 2\Delta$, the elliptic integral $E(1) = 1$ drops out and we reproduce the results for a normal conductor; see App. N.3 for details.

With the expressions of self-energies above, we can use Eqs. (9.39), (9.46) and (9.55) to calculate the absorption rates for vector, pseudoscalar and scalar DM. We consider an aluminum superconductor (Al-SC) target, for which the relevant material parameters are listed in Table 9.2. We use the same numerical values as in Ref. [41] for ε_F , ω_p , Δ , ω_D , c_s , and determine the electron-phonon coupling $C_{\text{e-ph}}$ from resistivity measurements [381, 382] as explained in App. N.3. For scalar DM, we again confirm the dominance of the $\mathcal{R}_{\bar{v}^2\bar{v}^2}$ term in Eq. (9.57), as seen in Fig. 9.1, so the rate formula Eq. (9.55) simplifies to Eq. (9.56) as in the cases of Si and Ge discussed in Sec. 9.4.

Figs. 9.2 and 9.3 show the projected reach, assuming 3 events per kg-yr exposure without

including background. We see that Al-SC, with its $\mathcal{O}(\text{meV})$ gap, significantly extends the reach with respect to Si and Ge to lower m_ϕ . The solid red curves are obtained from the self-energy calculations discussed above; the underlying model has a UV cutoff $\omega_{\text{max}} \sim 0.5 \text{ eV}$ where we truncate the curves. Low-temperature conductivity data are available between 0.2 eV and 3 eV [38]. For the vector and pseudoscalar DM models, we also present the reach following the data-driven approach in this mass range (dashed curves), obtained by using Eqs. (9.40) and (9.47) with $\sigma_1 (= \text{Re } \sigma = \omega \text{ Im } \varepsilon)$ taken from Ref. [38] and $\text{Re } \varepsilon$ set to $1 - \frac{\omega_p^2}{\omega^2}$. Between 0.2 eV and 0.5 eV where both theoretical (solid) and data-driven (dashed) predictions are shown, they are in reasonable agreement, with the latter stronger by about 40% for both κ and g_{aee} at 0.2 eV. The difference is presumably a result of approaching the UV cutoff of the theoretical calculation, and possibly also the neglect of Umklapp contributions. For scalar DM, the data-driven approach is not viable, and we present our theoretical prediction up to 0.5 eV. We also show the reach curves obtained in the previous literature [41, 44] for comparison, and discuss the differences in what follows.

Comparison with previous calculations. The calculation of DM absorption in superconductors was first carried out in Ref. [41], where the $2 \rightarrow 2$ matrix element for $\phi + e^- \rightarrow e^- + \text{phonon}$ was evaluated at leading order in q . For vector and pseudoscalar DM, our results agree with Ref. [41] as seen in Fig. 9.2, up to a minor numerical prefactor understood as follows. Ref. [41] chose the value of the electron-phonon coupling $C_{e\text{-ph}}$ such that the photon absorption rate (i.e. conductivity σ_1) matches the experimentally measured value at $\omega = 0.2 \text{ eV}$. In this work, we instead determine $C_{e\text{-ph}}$ via the λ_{tr} parameter following Refs. [381, 382], which results in a slightly lower value and hence the slight mismatch observed in Fig. 9.2.

The more significant numerical difference in the scalar case between our results and Ref. [41], as seen in Fig. 9.3, can be traced to two sources. First, the numerically dominant effect is that Ref. [41] did not distinguish m_* and m_e , while we have kept the vacuum mass m_e in the operator coefficients and used the effective mass m_* for the electron's dispersion and phase space; the two masses differ by about a factor of three in Al-SC. Note that the difference between m_e and m_* does not affect the vector and pseudoscalar absorption rates as they only depend on $\Pi_{\mathbf{1},\mathbf{1}}$, which is independent of m_*/m_e . Second, Ref. [41] dropped a factor of $(1-x)^2$ in the scalar absorption matrix element when taking the soft phonon limit; this results in an $\mathcal{O}(1)$ difference on the projected reach that is numerically subdominant. One can easily verify these two points by evaluating the integral in Eq. (N.38) using $x^2(1-x)$ in place of $\frac{m_*^4}{m_e^4} x^2(1-x)^3$ in the last line; this would reproduce the analytic relation presented in Ref. [41] between scalar and photon absorption rates in the limit $\omega \gg 2\Delta$.

More recently, Ref. [44] revisited scalar DM absorption and claimed that in-medium effects lead to a significantly weaker reach. We reiterate that while in-medium mixing with the photon screens the contribution from the LO operator $\mathbb{1}$, the leading contribution to scalar absorption comes instead from the NLO operator \bar{v}^2 that is not screened. In fact, the screening factor in Ref. [44] was (correctly) derived for the $\mathbb{1}$ operator but inconsistently applied to the dominant contribution coming from the \bar{v}^2 operator as obtained in Ref. [41]. As a result, Ref. [44] significantly underestimated the reach as we can see from Fig. 9.3.

9.6 Conclusions

In this paper we revisited the calculation of electronic excitations induced by absorption of bosonic DM. Specifically, we focused on $\mathcal{O}(1-100)$ eV mass DM for Si and Ge targets that are in use in current experiments, and sub-eV mass DM that a proposed Al superconductor detector will be sensitive to. We utilized an NR EFT framework, where couplings between the DM and electron in a relativistic theory are matched onto NR effective operators in a $1/m_e$ expansion. We then computed absorption rates from in-medium self-energies, carefully accounting for mixing between the DM and the photon. For crystal targets like Si and Ge, we used first-principles calculations of electronic band structures and wave functions based on density functional theory, and implemented the numerical rate calculation as a new module “absorption” of the EXCEED-DM program [9, 179]. For BCS superconductors, we adopted an analytic model as in Refs. [41, 181, 182] treating electrons near the Fermi surface as free quasiparticles and including corrections due to the $\mathcal{O}(\text{meV})$ superconducting gap. The projected reach is presented in Figs. 9.2 and 9.3 for vector, pseudoscalar and scalar DM.

Most of previous calculations of DM absorption relied upon relating the process to photon absorption, and hence to the target’s optical properties, i.e. the complex conductivity/dielectric. For vector and pseudoscalar DM, this is a valid approach. Our theoretical calculations reproduced the results of this data-driven approach in the majority of mass range, which we view as a validation of our methodology and numerical implementation.

For scalar DM, however, we showed that the dominant contribution is not directly related to photon absorption. One therefore cannot simply rescale optical data to derive the DM absorption rate. Importantly, the familiar coincidence between scalar and vector couplings, $\bar{\psi}\psi \simeq \bar{\psi}\gamma^0\psi$, holds only at leading order in the NR EFT. For non-relativistic scalar DM ϕ , matrix elements of the leading order operator are severely suppressed by the momentum transfer $q \sim 10^{-3}m_\phi$. The dominant contribution comes instead from a different operator that is formally next-to-leading-order in the NR EFT expansion, and does not suffer from in-medium screening. We presented reach projections for scalar DM based on our theoretical

calculations. Notably, for Al superconductor, the reach we found is much more optimistic than the recent estimate in Ref. [44].


It is straightforward to extend the calculation presented here to anisotropic targets and materials with spin-dependent electronic wave functions (as can arise from spin-orbit coupling); we will investigate this subject in detail in an upcoming publication. Another future direction is to calculate phonon and magnon excitations from DM absorption via in-medium self-energies in a similar EFT framework, refining and extending the calculation in Ref. [5]. Finally, in-medium self-energies are also relevant for DM detection via scattering; one can carry out a calculation similar to what we have done here, but in a different kinematic regime, to include in-medium screening corrections in the study of DM-electron scattering via general EFT interactions [359].

DARK MATTER DIRECT DETECTION IN MATERIALS WITH SPIN-ORBIT COUPLING

10.1 Introduction

Detection of dark matter (DM) through non-gravitational interactions remains one of the main goals of particle physics. Electronic excitations have been identified as a promising path to lead the direct detection of DM to sub-GeV masses, a region not kinematically accessible in experiments based on nuclear recoil. A variety of avenues to search for DM induced electronic excitations have been proposed: ionization in noble gases [14, 19, 24, 35, 177, 244, 333, 334], excitations across a band gap in crystal targets [2, 6, 7, 19, 25, 33–35, 39, 40, 177, 180, 248, 256], superconductors [41, 181], graphene [188], Dirac materials [29, 144, 182, 183, 335], and transitions between molecular orbitals in aromatic organics [243, 383].

In this work we focus on a specific class of semiconductors for which $\mathcal{O}(\text{meV})$ band gaps (as opposed to typical $\mathcal{O}(\text{eV})$ band gaps in semiconductors and insulators) arise as a consequence of spin-orbit coupling (SOC) effects. Targets with such small band gaps can probe DM masses down to $\mathcal{O}(\text{keV})$ via scattering, and $\mathcal{O}(\text{meV})$ via absorption, while still suppressing thermal noise. Moreover, some of these SOC materials have tunable band structures, a property which makes them interesting candidates for direct detection experiments [335].

However, SOC effects introduce some intricacies in the DM-electron interaction rate calculations since the Bloch wave functions are no longer eigenstates of the S_z operator, and therefore become two-component objects in spin space. This implies that electron spin sums cannot be trivially performed, and new transition form factors must be computed. For example, spin-dependent vector mediated scattering can no longer be related to its spin-independent counterpart, and must be computed from first principles. We extend the framework in Sec. 10.2 and implement the new spin-dependent form factors numerically within **EXCEED-DM** [9, 384], which is publicly available on Github .

To showcase the formalism developed in this paper, we apply it to a target with important SOC effects, ZrTe_5 . This material has been extensively studied in the context of DM direct detection [29, 144, 183] as a leading candidate for Dirac material targets. Dirac materials are characterized by low-energy excitations which behave like free electrons and satisfy the Dirac equation. The properties of the electronic excitations can then be understood by a simple extension of the standard QED results. An additional consequence is that they have weak

electromagnetic screening, even with a small energy gap between the valence and conduction bands, making them a desirable target for sub-MeV dark matter coupled to electrons via a dark photon mediator [29]. In this work, however, we will focus only on ZrTe₅ properties which stem from its SOC nature, and we will not exploit any of the ones deriving from its Dirac nature (which is still debated [385–396]).

To illustrate the variety of DM models that an SOC target can probe, we consider several different DM models and processes. Specifically, we will study:

- Standard spin-independent (SI) and spin-dependent (SD) scattering via vector mediators. The fundamental interaction Lagrangians for these models take the form

$$\mathcal{L}_{\text{int}} = \begin{cases} \phi_\mu (g_\chi \bar{\chi} \gamma^\mu \chi + g_e \bar{\psi} \gamma^\mu \psi) & \text{(SI)} \\ \phi_\mu (g_\chi \bar{\chi} \gamma^\mu \gamma^5 \chi + g_e \bar{\psi} \gamma^\mu \gamma^5 \psi) & \text{(SD)} \end{cases} \quad (10.1)$$

where ψ and χ are the electron and DM fermion fields, respectively, and ϕ_μ is the dark mediator field.

- Scalar, pseudoscalar, and vector DM absorption. In this case the fundamental interaction Lagrangians take the form

$$\mathcal{L}_{\text{int}} = \begin{cases} g_e \phi \bar{\psi} \psi & \text{(scalar DM)} \\ g_e \phi \bar{\psi} i \gamma^5 \psi & \text{(pseudoscalar DM)} \\ g_e \phi_\mu \bar{\psi} \gamma^\mu \psi & \text{(vector DM)}. \end{cases} \quad (10.2)$$

The paper is organized as follows. In Sec. 10.2 we generalize the DM interaction rate formalism to account for spin-dependent wave functions in general (spin-orbit coupled, anisotropic) targets. Then in Sec. 10.3 we apply these results to the candidate material ZrTe₅ and compare the results obtained with and without the inclusion of SOC effects. Further details of DFT calculation are presented in App. P.1, and convergence tests for the results shown in Sec. 10.3 can be found in App. P.2.

10.2 DM Interaction Rate Formalism

In this section we derive the rates for transitions between electronic energy levels induced by DM absorption and scattering. For the targets of interest here, the electronic energy levels can be labelled by a band index i and a momentum \mathbf{k} within the first Brillouin zone (1BZ),

which we collectively indicate with an index $I = \{i, \mathbf{k}\}$. The wave functions of the electronic states can be written in the Bloch form as:

$$\Psi_I(\mathbf{x}) = \frac{1}{\sqrt{V}} e^{i\mathbf{k}\cdot\mathbf{x}} \mathbf{u}_I(\mathbf{x}) \quad (10.3)$$

where the periodic Bloch wave functions \mathbf{u}_I are two-component vectors in the spin basis, and V is the crystal volume.

Absorption

In this subsection, we use the non-relativistic (NR) effective field theory (EFT) developed in Ref. [2], and summarized in Appendix Q, to compute DM absorption rates in materials with sizable SOC.

The absorption rate of a state can be derived from the imaginary part of its self-energy. In a medium, care must be taken due to the possible mixing between the DM, ϕ , and SM states (in our case the SM photon, A). In the presence of such mixing effects, the DM absorption rate is related to the imaginary part of the self-energy of the “mostly DM” eigenstate, $\Pi_{\hat{\phi}\hat{\phi}}$:

$$\Gamma_{\text{abs}}^\phi = -\frac{Z_{\hat{\phi}}}{\omega} \text{Im} \Pi_{\hat{\phi}\hat{\phi}}, \quad (10.4)$$

where $\omega \simeq m_\phi$ is the energy of the DM state, and $Z_{\hat{\phi}} = (1 - \frac{d \text{Re}\Pi_{\hat{\phi}\hat{\phi}}}{d\omega^2})^{-1} = 1 + \mathcal{O}(g_e^2)$ is the wave function renormalization which we will approximate as unity in the following. The total absorption rate per unit target mass, R , is given by

$$R = \frac{\rho_\phi}{\rho_T m_\phi} \frac{1}{n} \sum_{\eta=1}^n \Gamma_{\text{abs}}^{\phi_\eta} \quad (10.5)$$

where n is the number of degrees of freedom of the DM particle ($n = 3$ for vector DM and $n = 1$ for scalar and pseudoscalar DM) and we average over the incoming DM polarizations. The DM density, ρ_ϕ , is taken to be 0.4 GeV cm^{-3} , and ρ_T is the target density.

To derive $\Pi_{\hat{\phi}\hat{\phi}}$ we need to diagonalize the in-medium self-energy matrix, which in our case contains a mixing between the DM and the SM photon:

$$\mathcal{S}_{\text{eff}} \supset -\frac{1}{2} \int d^4Q \begin{pmatrix} A^\lambda & \phi^\eta \end{pmatrix} \begin{pmatrix} \Pi_{AA}^{\lambda\lambda'} & \Pi_{A\phi}^{\lambda\eta'} \\ \Pi_{\phi A}^{\eta\lambda'} & m_\phi^2 \delta^{\eta\eta'} + \Pi_{\phi\phi}^{\eta\eta'} \end{pmatrix} \begin{pmatrix} A^{\lambda'} \\ \phi^{\eta'} \end{pmatrix}, \quad (10.6)$$

where the implicit sum over λ, λ' (η, η') runs over the photon (DM) polarizations, and we have introduced the self-energies polarization components defined as:

$$\Pi^{\lambda\lambda'} \equiv \epsilon_\mu^\lambda \Pi^{\mu\nu} \epsilon_\nu^{\lambda'*} \quad (10.7)$$

where ϵ_μ^λ are polarization vectors. In general, the polarization vectors which diagonalize this matrix are not the typical longitudinal and transverse polarization vectors, since mixing can occur (i.e., $\Pi_{AA}^{L,T} \neq 0$). However one can always find an appropriate basis to diagonalize the DM and photon self-energies. In this basis Eq. (10.6) becomes

$$\mathcal{S}_{\text{eff}} \supset -\frac{1}{2} \int d^4Q \begin{pmatrix} A^\lambda & \phi^\eta \end{pmatrix} \begin{pmatrix} \Pi_{AA}^\lambda \delta^{\lambda\lambda'} & \Pi_{A\phi}^{\lambda\eta'} \\ \Pi_{\phi A}^{\eta\lambda'} & (m_\phi^2 + \Pi_{\phi\phi}^\eta) \delta^{\eta\eta'} \end{pmatrix} \begin{pmatrix} A^{\lambda'} \\ \phi^{\eta'} \end{pmatrix}, \quad (10.8)$$

where Π_{AA}^λ and $\Pi_{\phi\phi}^\eta$ are the eigenvalues of $\Pi_{AA}^{\lambda\lambda'}$ and $\Pi_{\phi\phi}^{\eta\eta'}$ respectively.

The off-diagonal terms in Eq. (10.8) are perturbatively suppressed by a factor of g_e with respect to the Π_{AA} terms. Therefore, working at order $\mathcal{O}(g_e^2)$, we find that the in-medium self-energy for the η polarization of the mostly DM eigenstate is given by:

$$\Pi_{\hat{\phi}\hat{\phi}}^\eta = \Pi_{\phi\phi}^\eta + \sum_\lambda \frac{\Pi_{\phi A}^{\eta\lambda} \Pi_{A\phi}^{\lambda\eta}}{m_\phi^2 - \Pi_{AA}^\lambda}. \quad (10.9)$$

Since vector DM couples to electrons in the same way as the photon, one can derive the relevant self-energies by simply replacing the electromagnetic charge with g_e , e.g., $\Pi_{\phi A}^{\eta\lambda} = -(g_e/e) \Pi_{AA}^\lambda \delta^{\eta\lambda}$. Doing so allows us to write Eq. (10.9) in terms of the photon self energy as

$$\Pi_{\hat{\phi}\hat{\phi}}^\eta = \left(\frac{g_e}{e}\right)^2 \frac{m_\phi^2 \Pi_{AA}^\eta}{m_\phi^2 - \Pi_{AA}^\eta} \quad (\text{vector DM}). \quad (10.10)$$

Scalar and pseudoscalar DM only have one degree of freedom, and therefore Eq. (10.9) takes the form

$$\Pi_{\hat{\phi}\hat{\phi}} = \Pi_{\phi\phi} + \sum_\lambda \frac{\Pi_{A\phi}^\lambda \Pi_{\phi A}^\lambda}{m_\phi^2 - \Pi_{AA}^\lambda} \quad ((\text{pseudo})\text{scalar DM}). \quad (10.11)$$

As usual, the self-energies appearing in the previous equations are computed from the sum of 1PI diagrams. Working at one loop, there are two graph topologies that can contribute

$$\begin{array}{c} \begin{array}{c} I' \\ \text{---} \circ \text{---} \\ \text{---} \circ \text{---} \\ I \end{array} \quad \equiv \quad -i \bar{\Pi}_{\mathcal{O}_1, \mathcal{O}_2}(Q), \end{array} \quad (10.12)$$

$$\begin{array}{c} I \\ \text{---} \circ \text{---} \\ I \end{array} \quad \equiv \quad -i \bar{\Pi}'_{\mathcal{O}}(Q), \quad (10.13)$$

where $\mathcal{O}_{(1,2)}$ is any operator to which the external field, A or ϕ (dashed lines), couples. For vector external states these operators carry Lorentz indices that are inherited by $\bar{\Pi}$ and $\bar{\Pi}'$.

The full expressions for the self-energies involved in the absorption calculation can be found in Appendix Q. However, as we discuss in the same appendix, due to the absorption kinematics and the hierarchy between the DM and electron velocities, a few diagrams dominate these self-energies. Specifically, we find that the diagonalization of the photon in-medium self-energy (and therefore the derivation of Π_{AA}^λ) reduces to diagonalizing $\bar{\Pi}_{v^i, v^j}$, where the velocity operator is defined by

$$v^i \equiv \frac{-i \overleftrightarrow{\nabla}_i}{2m_e}. \quad (10.14)$$

From this it follows that the long wavelength limit of the dielectric function, $\varepsilon(0, \omega)$, which will enter explicitly in the scattering rate calculation, can be derived from $\bar{\Pi}_{v^i, v^j}$:

$$[\varepsilon(0, \omega)]^{ij} = \mathbb{1} + \frac{\Pi_{AA}^{ij}}{\omega^2} \simeq \mathbb{1} - e^2 \frac{\bar{\Pi}_{v^i, v^j}}{\omega^2}. \quad (10.15)$$

The long wavelength dielectric function, $\varepsilon(0, \omega)$, together with details of its numeric calculation, is reported in Appendix P.2.¹ For scalar and pseudoscalar DM, the leading order terms in the self-energy of the mostly DM eigenstate are found to be

$$\Pi_{\hat{\phi}\hat{\phi}} \simeq \begin{cases} g_e^2 \bar{\Pi}_{\bar{v}^2, \bar{v}^2} & \text{(scalar DM)} \\ g_e^2 \frac{\omega^2}{4m_e^2} \bar{\Pi}_{\mathbf{v}\cdot\sigma, \mathbf{v}\cdot\sigma} & \text{(pseudoscalar DM)} \end{cases} \quad (10.16)$$

where we have introduced the operator

$$\bar{v}^2 \equiv -\frac{\overleftrightarrow{\nabla}^2}{8m_e^2}. \quad (10.17)$$

Scattering

In this subsection we proceed to derive the DM scattering rate with spin-dependent electronic wave functions. Generalizing the formulas previously derived in Refs. [7, 9, 33, 177, 244, 340],

¹Strictly speaking, the dielectric function is a mixed index tensor, as evident from the defining equation, $J^i = \sigma_j^i A^j = i\omega (1 - \varepsilon_j^i) A^j$, where $\varepsilon_j^i = \delta_j^i - \Pi_j^i/\omega^2 = 1 + \Pi^{ij}/\omega^2$ (see the discussion in Appendix A of Ref. [29] for more details). With a slight abuse of notation we define the matrix ε which has components $[\varepsilon]^{ij} = \varepsilon_j^i$.

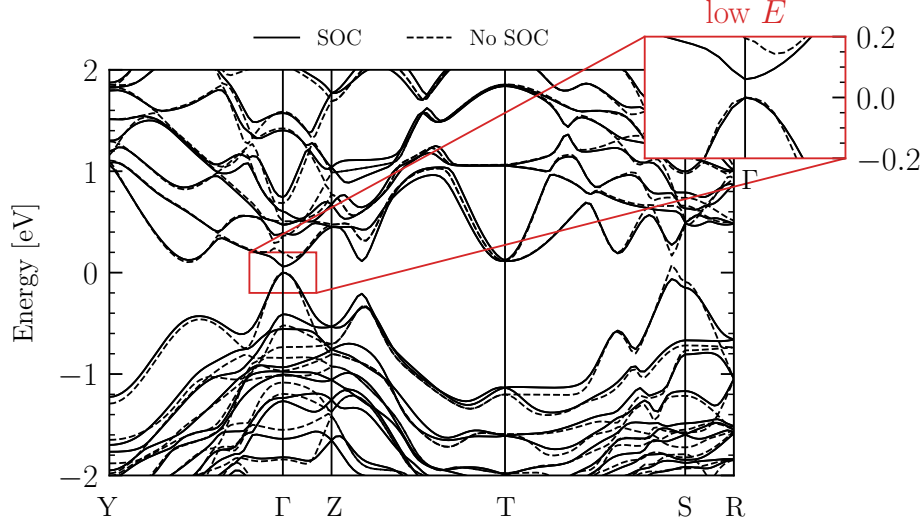


Figure 10.1: ZrTe₅ band structure computed using DFT with SOC (solid lines) and without SOC (dashed lines). The inset highlights the low energy (low E) band dispersion, whose details are sampled using a denser \mathbf{k} -point grid. The band gap for the SOC band structure is set to the experimental value of 23.5 meV [47], and the No SOC band structure is shifted accordingly, which gives a larger band gap of 81.6 meV.

we can write the DM scattering rate as

$$\Gamma_{I \rightarrow I'} = \frac{\pi}{8V m_e^2 m_\chi^2} \int d^3q \delta(E_{I'} - E_I - \omega_{\mathbf{q}}) \times \overline{\left| \int \frac{d^3k}{(2\pi)^3} \tilde{\Psi}_{I'}^*(\mathbf{k} + \mathbf{q}) \cdot \mathcal{M}(\mathbf{q}) \cdot \tilde{\Psi}_I(\mathbf{k}) \right|^2} \quad (10.18)$$

where the bar indicates a spin average (sum) over the incoming (outgoing) DM states, $\tilde{\Psi}_I(\mathbf{k})$ are the Fourier transform of the electronic wave functions defined in Eq. (10.3), and

$$\omega_{\mathbf{q}} \equiv \mathbf{q} \cdot \mathbf{v} - \frac{q^2}{2m_\chi}. \quad (10.19)$$

For the SI and SD models of interest here, we can write the free electron scattering amplitude as

$$\mathcal{M}_{ss',\sigma\sigma'}(\mathbf{q}) = \sqrt{\frac{16\pi m_\chi^2 m_e^2 \bar{\sigma}_e}{\mu_{\chi e}^2} \frac{f_e}{f_e^0}} \mathcal{F}_{\text{med}}\left(\frac{q}{q_0}\right) \mathcal{S}_{ss',\sigma\sigma'}, \quad (10.20)$$

where $\mathcal{F}_{\text{med}}(\frac{q}{q_0})$ encodes the momentum dependence induced by the mediator propagator, $f_e(\mathbf{q})/f_e^0$ is the screening factor introduced by in-medium effects, and $\bar{\sigma}_e$ is a reference cross

section defined by

$$\bar{\sigma}_e \equiv \frac{\mu_{\chi e}^2}{64\pi m_\chi^2 m_e^2} \sum_{ss',\sigma\sigma'} |\mathcal{M}_{ss',\sigma\sigma'}(q_0)|^2, \quad (10.21)$$

with $q_0 = \alpha m_e$. The total rate per unit detector mass is then

$$R = \frac{\pi \bar{\sigma}_e}{V \mu_{\chi e}^2 m_\chi \rho_T} \sum_{I,I'} \int \frac{d^3 q}{(2\pi)^3} \left(\frac{f_e}{f_e^0} \right)^2 \mathcal{F}_{\text{med}}^2(q) g(\mathbf{q}, \omega) \mathcal{F}_{II'}(\mathbf{q}) \quad (10.22)$$

where $g(\mathbf{q}, \omega)$ is the velocity integral defined as

$$g(\mathbf{q}, \omega) \equiv \int d^3 \mathbf{v} f_\chi(\mathbf{v}) 2\pi \delta(\omega - \omega_{\mathbf{q}}), \quad (10.23)$$

with $f_\chi(\mathbf{v})$ being the DM velocity distribution in the laboratory rest frame, which we take to be a boosted Maxwell-Boltzmann distribution with parameters $v_0 = 230 \text{ km s}^{-1}$, $v_{\text{esc}} = 600 \text{ km s}^{-1}$, and $v_e = 240 \text{ km s}^{-1}$.

The crystal form factor $\mathcal{F}_{II'}$ is defined as

$$\mathcal{F}_{II'}(\mathbf{q}) \equiv \left| \int \frac{d^3 k}{(2\pi)^3} \tilde{\Psi}_{I'}^*(\mathbf{k} + \mathbf{q}) \cdot \mathcal{S} \cdot \tilde{\Psi}_I(\mathbf{k}) \right|^2 \quad (10.24)$$

where the spin operators for the models considered in this work are given by

$$\mathcal{S}_{ss',\sigma\sigma'} = \begin{cases} \delta_{ss'} \delta_{\sigma\sigma'} & \text{(SI)}, \\ \frac{1}{\sqrt{3}} \sum_i \sigma_{ss'}^i \sigma_{\sigma\sigma'}^i & \text{(SD)}, \end{cases} \quad (10.25)$$

and σ_i are the Pauli matrices. Given these expressions the form factors, $\mathcal{F}_{II'}$, for the SI and SD models take the form,²

$$\mathcal{F}_{II'} = \begin{cases} |\mathcal{T}_{II'}|^2 & \text{(SI)}, \\ \frac{1}{3} \mathcal{T}_{II'}^* \cdot \mathcal{T}_{II'} & \text{(SD)}, \end{cases} \quad (10.26)$$

where we have defined the DM model independent transition form factors, $\mathcal{T}_{II'}$ and $\mathcal{T}_{II'}$, as

$$\mathcal{T}_{II'} = \int \frac{d^3 k}{(2\pi)^3} \tilde{\Psi}_{I'}^*(\mathbf{k} + \mathbf{q}) \cdot \tilde{\Psi}_I(\mathbf{k}), \quad (10.27)$$


$$\mathcal{T}_{II'} = \int \frac{d^3 k}{(2\pi)^3} \tilde{\Psi}_{I'}^*(\mathbf{k} + \mathbf{q}) \cdot \boldsymbol{\sigma} \cdot \tilde{\Psi}_I(\mathbf{k}). \quad (10.28)$$

²The absence of the overall factor of two, relative to the SI rate formula given in Ref. [9], can be understood from the sum over the states. If the wave functions are spin independent then $\sum_{IF} \rightarrow \sum_{IF} \sum_{ss'}$, where s (s') indexes the initial (final) electron spin state. These spin sums contribute the extra factor of two, bringing Eq. (10.22) and the rate formula in Ref. [9] into agreement.

10.3 Detection Rates in ZrTe_5

We will now apply the formalism developed in the previous section to our benchmark SOC target: ZrTe_5 . The band structure of ZrTe_5 , with and without the inclusion of SOC effects, is shown in Fig. 10.1. The details of the DFT calculation can be found in Appendix P.1. The dominant effect of SOC is to shift the valence and conduction bands closer at the Γ point relative to the No SOC calculation.

While in theory the calculation of DM interaction rates is identical for $\mathcal{O}(\text{meV})$ and $\mathcal{O}(\text{eV})$ gap semiconductors, in practice one must be careful about sampling the 1BZ. This is because these $\mathcal{O}(\text{meV})$ energy differences generally only occur in small volumes within the 1BZ. To account for this we sample the 1BZ with a higher \mathbf{k} -point density in regions corresponding to the low energy band structure. For ZrTe_5 this occurs near the Γ point, and we split the phase space into two separate regions, “low E ” and “high E ”, which we describe now. The low E region consists of the highest two (one) valence bands and lowest two (one) conduction bands, for the calculation with (without) SOC, sampled on a “mini-BZ” grid. This mini-BZ grid is a rescaled uniform Monkhorst-Pack grid [397]; each \mathbf{k} is scaled by a factor of $1/5$, giving a $125 \times$ \mathbf{k} -point sampling in that region. This region will give the dominant contribution to absorption of DM with mass $\lesssim 100$ meV, as well as DM scattering via a light mediator. The high E region includes all the bands outside the low E region, sampled with a standard Monkhorst-Pack uniform grid. The DM absorption rates in Sec. 10.3 are a combination of the low and high E regions. The DM scattering rates in Sec. 10.3 will be shown for both regions, and it will be clear when one dominates the other.

We compute the Bloch wave functions, Eq. (10.3), in both regions within the framework of DFT with QUANTUM ESPRESSO [339, 398, 399]; details can be found in Appendix P.1. The DM absorption and scattering rates are computed with an extended version of EXCEED-DM [9, 384] which includes the formalism developed in Sec. 10.2, and is publicly available on Github .

For each of the models considered in the following subsections, we will show the projected constraints from three different calculations. The curves labelled “SOC” are computed with the inclusion of SOC effects, the curves labelled “No SOC” do not include any SOC effects, and those labelled “Partial SOC” are a combination of the SOC and No SOC calculations, obtained using the energy levels computed with SOC, and the wave functions without SOC. While the Partial SOC results are not a consistent calculation, they aid in understanding how much of the difference between the SOC and No SOC results is due to the changes in the band structure versus the inclusion of the spin dependent wave functions. Generally we find that the changes in the band structure are more influential than the spin dependence

in the wave functions, but the latter can still be important.

Lastly, we note that previous works [29, 144, 183] have derived excitation rates analytically by exploiting the putative Dirac nature of ZrTe_5 . While a direct comparison to assess the validity of the analytic approximations is dubious since we do not observe a conical band structure (see Appendix P.1), previous estimates from Ref. [29] are shown in Figs. (10.2, 10.3). In App. R we discuss the validity of these analytic approximations in more general Dirac materials.

Absorption

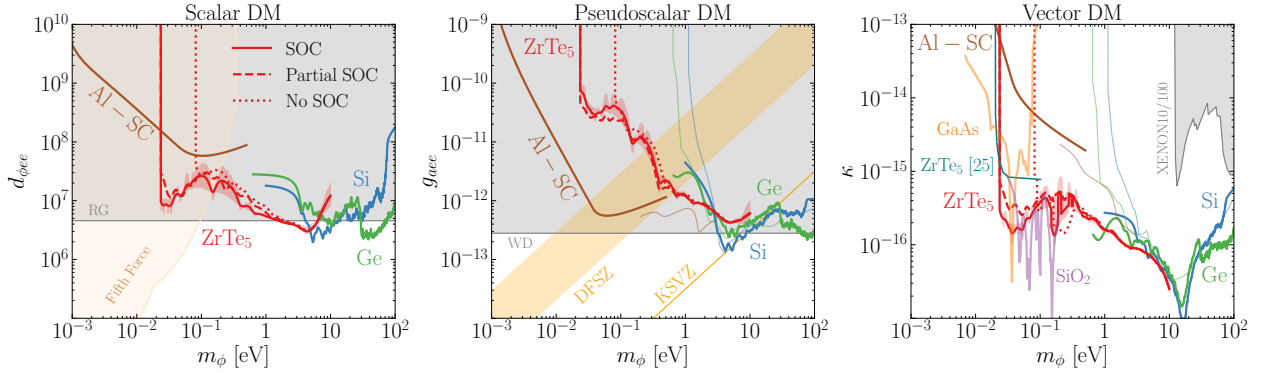


Figure 10.2: Comparison of projected 95% C.L. reach (3 events, no background) assuming one kg-year exposure for scalar (left), pseudoscalar (center) and vector (right) DM. We compare our results with (solid) and without (dotted) SOC for electronic absorption in a ZrTe_5 target (red), with the ones for semiconductor silicon (Si, blue) and germanium (Ge, green) targets [2], superconducting aluminum (Al-SC, brown) [2]), phononic absorption in polar materials [28, 48] (GaAs in orange and SiO_2 in purple), and previous estimates for ZrTe_5 (teal) [29]. We also show the projected constraints combining the SOC energy levels with the No SOC wave functions, (“Partial SOC”, red, dashed) to explicitly show the effect of the spin dependent wave functions. Constraints are expressed in terms of the commonly adopted parameters shown in Eq. (10.29). Shaded red bands correspond to different parameterizations of the electron width $\delta \in [10^{-1.5}, 10^{-0.5}]\omega$ used in calculating the self-energies (see e.g., Eq. (Q.17)), with the solid line corresponding to $\delta = 10^{-1}\omega$. Thin lines indicate results obtained by rescaling the optical data. Also shown are the direct detection limits from XENON10/100 [40], fifth force constraints [45], and stellar cooling constraints from red giants (RG) [46], and white dwarfs (WD) [31]. For the pseudoscalar scenario we also report the couplings corresponding to the QCD axion in KSVZ and DFSZ models, for $0.28 \leq \tan \beta \leq 140$ [43].

For the models considered, Eq. (10.2), our results are shown in Fig. 10.2. For ease of comparison we map the constraints on the g_e parameters in Eq. (10.2) to a more commonly

used notation,

$$g_e = \begin{cases} \frac{4\pi m_e}{M_{\text{Pl}}} d_{\phi ee} & \text{(scalar)} \\ g_{aee} & \text{(pseudoscalar)} \\ e\kappa & \text{(vector)}, \end{cases} \quad (10.29)$$

where $M_{\text{Pl}} = 1.22 \times 10^{19}$ GeV is the Planck mass.

For all the benchmark models, the inclusion of SOC effects dominantly impacts the low mass reach where the SOC corrections to the band structure are most relevant. Most notably, the lowest testable DM mass is shifted as a consequence of the different band gaps: 23.5 meV with SOC, and 81.6 meV without SOC. At higher masses the SOC effects are milder and, as expected, the SOC reach approaches the reach without SOC effects. The close agreement between the ‘‘Partial SOC’’ and ‘‘SOC’’ curves indicates that changes to the energy levels are what is mainly driving the difference in the ‘‘SOC’’ and ‘‘No SOC’’ calculations.

For the scalar and vector DM models we find that ZrTe₅ is superior at low DM masses relative to a superconducting aluminum target, another target material with an $\mathcal{O}(\text{meV})$ gap (0.6 meV for the Al-SC curves shown here). However for pseudoscalar DM, for $m_\phi \lesssim \text{eV}$, Al-SC yields better sensitivity than ZrTe₅. This can be attributed to the large amount of screening present in the vector DM case (but not in the pseudoscalar DM case) for Al-SC.

Shaded bands correspond to different width parameterizations, $\delta \in [10^{-1.5}, 10^{-0.5}] \omega$. In theory, the absorption rate calculation is independent of the choice of width; however, when sampling the 1BZ discretely this is not the case, and practically the goal is to find results that have a weak dependence on this parameter. The discrepancy in the shaded bands should be viewed as an uncertainty in the calculation. The constraints turn up on the left hand side because of the band gap, and on the right hand side because of the finite number of bands used in the calculation. All bands for which $E - E_F < 4 \text{ eV}$, where E_F is the valence band maximum were included; see Appendix P.2 for more details.

Scattering

We now consider DM-electron scattering in ZrTe₅ for the two benchmark models, standard SI and standard SD interactions, shown in Eq. (10.1). Specifically we consider a light mediator for the SI model and a heavy mediator for the SD model. For the SI model a light mediator was chosen due to its high sensitivity to the lowest energy excitations, as well as for ease of comparison with other proposals which commonly report constraints on this model. The SD

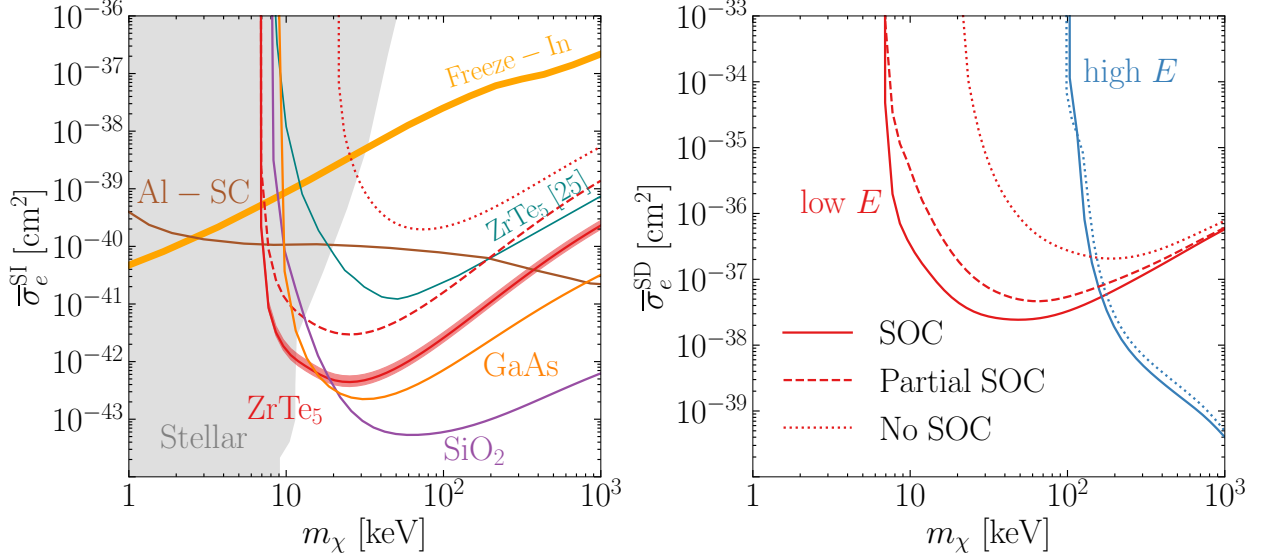


Figure 10.3: Projected constraints on DM-electron scattering cross sections at the 95% C.L. (three events, no background) assuming one kg-year exposure for two benchmark models shown in Eq. (10.1). **Left:** SI model with a light mediator ($\mathcal{F}_{\text{med}} = (q_0/q)^2$), screened with the static dielectric shown in Fig P.3. The red solid (dashed) curve shows the constraints with (without) the inclusion of SOC effects. For comparison we also show projected constraints from single phonon excitations in GaAs (orange) and SiO₂ (purple) computed with PhonoDark [4] (assuming an energy threshold of $\omega_{\text{min}} = 20$ meV), electronic excitations in an aluminum superconductor [49] (brown), and previous estimates for ZrTe₅ (teal) [29]. We also show the projected constraints combining the SOC energy levels with the No SOC wave functions, (“Partial SOC”, red, dashed) to explicitly show the effect of the spin dependent wave functions. Stellar constraints (gray) are taken from Ref. [17] and the freeze-in benchmark (orange) is taken from Ref. [20]. **Right:** SD model with a heavy mediator ($\mathcal{F}_{\text{med}} = 1$). Curves labelled “low/high E ” include transitions restricted to the low/high E regions discussed in Sec. 10.3.

model was chosen to highlight the effect of spin dependent wave functions.³

The results are shown in Fig. 10.3 and we discuss them in detail here. Constraints computed in this work are shown in red, with shaded bands corresponding to the uncertainty in the calculation of the screening factor/dielectric function from the electron width parameter, discussed previously in Sec. 10.3.

When considering the SI model with a light mediator we include anisotropic screening effects in the $f_e(\mathbf{q})/f_e^0 = (\hat{\mathbf{q}} \cdot \boldsymbol{\varepsilon}(\mathbf{q}, \omega) \cdot \hat{\mathbf{q}})^{-1}$ factor. $\boldsymbol{\varepsilon}(\mathbf{q}, \omega)$ is the dielectric tensor, and this screening

³In the SD model, $\mathcal{F}_{\text{med}} = 1$ also for a light mediator due to the dominance of longitudinal component. Here we focus on the heavy mediator case. To avoid perturbativity constraints on the couplings, $g_\chi g_e \lesssim (4\pi)^2$, one needs $m_{A'} \lesssim 3 \text{ GeV} \left(\frac{10^{-37} \text{ cm}^2}{\sigma_e^{\text{SD}}} \right)^{1/4}$ for $\text{keV} < m_\chi < \text{MeV}$.

factor is especially important for the sub-MeV DM masses considered here. Since in this model the scattering rate is dominated by events with small q , we approximate $\epsilon(\mathbf{q}, \omega) \approx \epsilon(0, \omega)$, such that we replace the dielectric with the anisotropic, long wavelength dielectric function shown in Fig. P.3.

For the SI model, we find that the contribution from transitions in the low E region, discussed earlier in Sec. 10.3, dominate the scattering rate. Therefore, in the left panel of Fig. 10.3, we only show the results derived from transitions within the low E region. For the massive mediator SD model, in the right panel of Fig. 10.3, we see that the low E contributions dominate at small DM masses. However for $m_\chi \gtrsim 100$ keV, when the high E contributions at $\mathcal{O}(100$ meV) become kinematically available, the high E contributions are dominant. This is due to the fact that when scattering via a heavy mediator the rate is no longer dominated by the smallest momentum transfers. While we did not explicitly include transitions between the low and high E regions, we note that these are only expected to be important for masses where the reach is comparable between the regions, and will not affect the conclusions.

We find that, for the SI model with a light mediator, the inclusion of SOC effects significantly alters the reach for the whole DM mass range considered since the rate is dominated by small energy/momentum depositions. For the SD model with a massive mediator the SOC effects are most prominent for low DM masses when the scattering is probing the band structure near the band gap, which is the most affected by SOC effects. We also see that at the lowest masses the ‘‘Partial SOC’’ curve is closer to the ‘‘SOC’’ than the ‘‘No SOC’’ lines. This shows that while the change to the energy levels is the dominant effect when including SOC, the spin dependence of the wave functions can give $\mathcal{O}(1)$ variations.

The left hand side of all the constraint curves are determined by the band gap. The smallest kinematically allowed DM mass is $m_\chi = 6$ keV for the SOC calculation with $E_g = 23.5$ meV, and $m_\chi = 21$ keV for the No SOC with $E_g = 81.6$ meV. As mentioned in Sec. 10.3, we only consider bands up to 4 eV above the valence band maximum. Kinematically this means that we are only including all contributions for $m_\chi < \text{MeV}$, and explains why our projections stop there.

10.4 Conclusions

Materials with strong spin-orbit coupling, such as ZrTe_5 , are promising targets in which electronic excitations can be utilized to search for sub-MeV DM. Their $\mathcal{O}(\text{meV})$ band gaps lead to sensitivity to new DM parameter space via both absorption and scattering processes, without relying on detecting single collective excitation modes.

However, due to the spin-orbit coupling, in these materials the electron spin is no longer a

good quantum number, and the spin sums over electronic states cannot be trivially reduced. This introduces interesting wrinkles in the DM absorption and scattering rate calculations, which we extended to account for these effects. In addition, we updated the **EXCEED-DM** program [9, 384], which computes DM-electron interaction rates from first principles, to be compatible with this input for future study of general targets with spin-orbit coupling.

We considered a wide range of DM models and processes to which materials with SOC are sensitive: absorption of vector, pseudoscalar, and scalar DM in Sec. 10.3, and scattering via heavy and light mediators via spin-independent and spin-dependent scattering potentials in Sec. 10.3. We found that for sub-eV vector and scalar DM absorption, ZrTe_5 is a far superior target relative to an aluminum superconductor. We also found more optimistic projections for SI scattering via a light mediator than previous estimates, and computed, for the first time, the projected constraints on an SD model with a heavy mediator. Our projections for ZrTe_5 lay the foundation for further first-principles studies of materials with strong spin-orbit coupling as targets in direct detection experiments.

CONCLUSIONS

The future of direct detection of light DM is bright. The current experimental programs utilizing nuclear recoil and electronic excitations to search for sub-GeV DM are continually improving their sensitivity, exposure, and background mitigation techniques. The coming years should see them either detect DM, or probe down to the neutrino floor, and projected freeze in line respectively; an important benchmark for light DM models. The next frontier, searching for sub-MeV DM, is beginning to take shape. New excitation channels, such as phonons and magnons, are kinematically well suited for these tasks, with their $\mathcal{O}(1 - 100 \text{ meV})$ energies and susceptibility to a wide range of DM models. In addition to these new channels, electronic excitations in small band gap materials also looks like a promising path forward, see, e.g., Ch 10. These advancements have also driven fruitful collaboration between condensed matter/materials scientists and particle physicists, which is catalyzing many novel ideas about how to utilize targets in new ways to detect DM.

While the effectiveness of these detectors is limited by the experimental capabilities, it is also limited by the theoretical understanding of how different DM models can generate signals. That is, to maximize the search over DM parameter space it is crucial to understand these DM-target interactions more generally than by analogy with a few simple benchmark DM models and targets. This requires intimate first principles understanding which has been the backbone of the work presented in this thesis. Even when focused on a simple class of DM models, e.g. spin independent scattering (Chs. 2, 3, 4), care was taken to understand the target dependence of the signal, such that the analysis was general to any target. To facilitate this we created the tools, **PhonoDark**, and **EXCEED-DM**, which can compute the direct detection signals of phonons and electrons, respectively, in any target.

In addition to target independence, to study the influence of general DM models, effective field theory (EFT) is a necessary tool. We used EFTs in two contexts: for general DM-phonon/magnon scattering rate calculations, Ch. 7, and DM absorption on electronic excitations, Ch. 9. These chapters lay the foundation for more general EFT studies, with a final goal of understanding the DM induced signal for a general UV complete model. This will require more development both theoretically, and computationally, for electron, phonon, and magnon excitations, but certainly within reach with the research presented here.

While much of the theoretical groundwork has been laid down, there are still many interest-

ing applications to study. First and foremost is a more intimate connection from the results presented here to experimental projections. All of the projections shown here assume no backgrounds are included; how does the reach for different DM models change when this is included? Additionally, since experiments are actively working their way down to single meV thresholds, are there targets which are sensitive to DM even with higher thresholds? For example targets with higher than normal phonon modes, e.g., organic scintillators at $\omega \sim 500$ meV, as well as a more complete understanding of multiphonon excitations. There are also open experimental questions such as the best way to read out magnon or phonon polariton excitations which are necessary if these are to be used as axion detectors as discussed in Ch. 6.

Appendix A

DFT CALCULATION DETAILS FOR BN

We used the Vienna *Ab initio* Simulation Package (VASP) [295–297, 352] for our density functional theory calculations to obtain the electronic properties of BN. Projector augmented wave (PAW) pseudopotentials [350, 351] with the Perdew-Becke-Ernzerhof (PBE) exchange-correlation functional [347] were used. We included van der Waals interactions between BN layers using the D3 correction method of Grimme et al. with Becke-Johnson damping [400, 401]. In the PAW scheme, we treated *s* and *p* electrons as valence for both B and N.

For structural optimization, we use an energy cutoff of 950 eV for our plane wave basis set, with a Gamma-centered k-point grid of $12 \times 12 \times 12$. The total energy and forces were converged to 1×10^{-8} eV and 1 meV/Å respectively. Wavefunctions were evaluated on two Gamma-centered k-point meshes, $10 \times 10 \times 3$, and $14 \times 14 \times 4$, converging the scattering rate to $\sim 9\%$ at 5 MeV, $\sim 8\%$ at 10 MeV and $\sim 6\%$ at 100 MeV. We extracted the all-electron wavefunction coefficients from our PAW calculations using pawpyseed [354] with an energy cutoff of 450 eV. 68 energy bands were included, incorporating energies up to 60 eV above and below the valence band maximum.

Boron nitride (BN) adopts a hexagonal crystal structure with space group $P6_3/mmc$ (No. 194) as shown in Fig. 2.2. Our calculated lattice parameters are $a = 2.507$ Å and $c = 7.093$ Å which compare well to those from experiment [402] ($a = 2.504$ Å and $c = 6.661$ Å). The PBE-level calculated band gap is 3.61 eV which was corrected to the experimental value of 5.97 eV [403] using a scissors operator.

CALCULATIONS OF TARGET PROPERTIES

We obtain the materials-specific responses using first principles calculations based on density functional theory (DFT) [294]. DFT is a standard method for obtaining solutions to the many-electron interaction problem, and can accurately predict materials properties *ab initio* ranging from electronic and magnetic to mechanical and vibrational properties. For this work, we used DFT to calculate the full electronic and phonon spectra for a range of materials, with the calculation details given below. However, since DFT is a ground-state method, it suffers from the famous ‘band gap’ problem where excited-state properties, including band gaps, are not accurately treated using standard DFT methods. We correct for this in two ways: (i) we performed beyond-DFT calculations (hybrid functional calculations) for several of the compounds where standard DFT gave a zero band gap, and (ii) we adjusted the band gaps to experimentally-reported values for all compounds. We note that the convergence parameters used for the electronic and phonon calculations are different owing to the different physical properties being calculated.

The list of materials calculated with their corresponding space groups and space group numbers is given in Table B.1, with the crystal structures depicted in Fig. C.1. For compounds where several structural isomorphs exist, we considered the reported low-temperature ground state structure. The Brillouin zones for the crystal structures considered in this work are depicted in Fig. C.2 with the high-symmetry points labelled. Both the electronic and phonon band structure plots take paths through these high-symmetry points.

All DFT calculations were performed using the Vienna *Ab initio* Simulation Package (VASP) [295–297, 352] with projector augmented wave (PAW) pseudopotentials [350, 351] using the Perdew-Becke-Ernzerhof (PBE) exchange-correlation functional [347]. In the PAW scheme, we treated *s* and *p* electrons as valence for Li, C, N, O, F, Na, Al, Si, S, Cl, Ca, I, Cs and W, *p* electrons as valence for Mg and *d* electrons as valence for Zn, Ga, Ge, As, In and Sb. Below we summarize the convergence criteria used for the (i) electronic structure and wavefunctions, and (ii) phonon calculations.

Material	Lattice Parameters (\AA)			Space group (number)	Calc. E_g (eV)	Structure		E_g Ref.
	a (el., ph., exp.)	c (el., ph. exp.)				Ref.		
Al ₂ O ₃	4.808, 4.805, 4.759	13.121, 13.116, 12.991		R $\bar{3}c$ (167)	5.84	[404]	[405]	
AlN	3.130, 3.128, 3.111	5.020, 5.016, 4.978		P6 ₃ <i>mc</i> (186)	4.02	[406]	[407]	
CaF ₂	5.507, 5.499, 5.463	–		Fm $\bar{3}m$ (225)	11.81	[408]	[409]	
CaWO ₄	5.317, 5.320, 5.243	11.534, 11.444, 11.376		I4 ₁ / <i>a</i> (88)	4.04	[410]	[411]	
CsI	4.671, 4.669, 4.567	–		Pm $\bar{3}m$ (221)	3.67	[406]	[412]	
Diamond	3.572, 3.572, 3.567	–		Fd $\bar{3}m$ (227)	4.12	[406]	[413]	
GaAs	5.751, 5.756, 5.653	–		F $\bar{4}3m$ (216)	0.141	[406]	[414]	
GaN	3.129, 3.247, 3.189	5.246, 5.280, 5.186		P6 ₃ <i>mc</i> (186)	1.71	[415]	[416]	
GaSb	6.217, 6.223, 6.118	–		F $\bar{4}3m$ (216)	0.47	[406]	[417]	
Ge	5.763, 5.782, 5.657	–		Fd $\bar{3}m$ (227)	0.37	[406]	[418]	
InSb	6.635, 6.634, 6.478	–		F $\bar{4}3m$ (216)	0.06	[406]	[419]	
LiF	4.063, 4.065, 4.020	–		Fm $\bar{3}m$ (225)	8.85	[420]	[421]	
MgF ₂	4.702, 4.684, 4.623	3.097, 3.081, 3.052		P4 ₂ / <i>mnm</i> (136)	6.79	[406]	[422]	
MgO	4.258, 4.250, 4.211	–		Fm $\bar{3}m$ (225)	4.43	[423]	[424]	
NaCl	5.670, 5.696, 5.641	–		Fm $\bar{3}m$ (225)	5.05	[406]	[425]	
NaF	4.682, 4.619, 4.634	–		Fm $\bar{3}m$ (225)	6.14	[426]	[427]	
NaI	6.498, 6.530, 6.473	–		Fm $\bar{3}m$ (225)	3.61	[406]	[428]	
PbS	–, 5.994, 5.936	–		Fm $\bar{3}m$ (225)	–	[406]	[429]	
PbSe	–, 6.206, 6.124	–		Fm $\bar{3}m$ (225)	–	[406]	[429]	
PbTe	–, 6.561, 6.454	–		Fm $\bar{3}m$ (225)	–	[406]	[429]	
Si	5.469, 5.469, 5.431	–		Fd $\bar{3}m$ (227)	0.75	[406]	[430]	
SiO ₂	5.038, 5.016, 4.913	5.526, 5.507, 5.405		P3 ₂ 21 (154)	5.66	[431]	[432]	
ZnO	3.288, 3.287, 3.250	5.308, 5.304, 5.207		P6 ₃ <i>mc</i> (186)	0.72	[406]	[433]	
ZnS	5.449, 5.443, 5.420	–		F $\bar{4}3m$ (216)	2.01	[434]	[435]	

Table B.1: List of material properties used in DFT calculations. The calculated lattice parameters (*a* and *c*) are listed for both those used in the electronic (el.) and phonon (ph.) excitation calculations, along with reported experimental values (exp.). The space group and corresponding space group number are included for the crystal structures considered. The PBE-level calculated band gaps are also listed, with details explained in the text.

B.1 Calculation Details for Electronic Band Structures and Wavefunctions

For structural optimizations, a plane wave cutoff-energy of 950 eV was used with a $12 \times 12 \times 12$ Γ -centered k-point grid. The energy and force convergence criteria were 1×10^{-8} eV and $1 \text{ meV } \text{\AA}^{-1}$ respectively.

All-electron wavefunction coefficients were extracted from PAW calculations using a modification of the pawpyseed code [436]. This enabled recovery of the full wavefunctions as normalized single-particle Kohn-Sham states from the pseudo-wavefunctions obtained by the PAW-method. Initial PAW wavefunctions were calculated with a plane wave energy-cutoff of 1000 eV, from which the all-electron wavefunctions were constructed with a minimum energy-cutoff of 450 eV. Calculations were performed using Γ -centered Monkhorst-Pack grids, with a k-point density of at least 0.27 \AA^{-1} . Energy bands were included up to 60 eV above and below the valence band maximum. However, since there is no pseudopotential containing the low-lying $4d$ -states for indium in VASP, these bands are neglected from the calculations. In NaI and CsI the I $4d$ states are positioned at approximately 43 eV and 42 eV below the valence band maxima respectively. A scissor operator was applied to match the experimental band gaps given in Table 3.1. For Ge, InSb and GaSb, the PBE functional gave partially occupied bands due to underestimation of the band gap. In these cases the HSE06 hybrid functional [437] was applied in a static calculation to introduce a band gap before applying the scissor correction. Electronic band structures were computed on a discrete k-mesh along the high-symmetry directions.

PbS, PbSe and PbTe were excluded from the electron calculations because spin-orbit interactions are required to capture important features of the band structures and spin-orbit coupling is not yet implemented within the pawpyseed code.

Multiple k-point densities, energy-cutoffs, and energy bands included were tested for all materials to ensure convergence of the scattering rates to less than 2% at $m_\chi = 10 \text{ GeV}$, less than 3% at $m_\chi = 10 \text{ MeV}$, and less than 28%, 18%, 18% and 10% for GaAs, GaSb, Ge, and Si at $m_\chi = 1 \text{ MeV}$ respectively. InSb was tested with a $12 \times 12 \times 12$ and $14 \times 14 \times 14$ k-point grid, plotted as dotted and solid curves in Fig. 3.1 respectively. At $m_\chi = 1 \text{ MeV}$ the rate convergence is 5%, and decreases for larger masses. However at smaller masses the $\mathbf{G} = \mathbf{0}$ contribution, from momentum transfers within the 1BZ, and energy depositions below $\sim 1 \text{ eV}$, dominate the rate. The slow convergence here is due to the fact that InSb has rapidly changing band structure near the Γ point, and more k-points are needed for better convergence. These uncertainties are plotted as shaded bands in Fig. 3.1, and accompanying figures in Appendix C, although most are invisible due to the plots being log-log.

B.2 Calculation Details for Phonon Spectra

We obtained the phonon dispersions from Phonopy [50] using the ‘frozen-phonon’ method by diagonalizing the force matrix using VASP as the force calculator. For the VASP calculations, the electronic wavefunctions were expanded in a plane-wave basis with a kinetic-energy cutoff of 600 eV. The Brillouin zone sampling was no less than 0.8 \AA^{-1} in each direction of the unit cell with Monkhorst-Pack grids, and was correspondingly scaled for phonon supercell calculations. Born effective charges were calculated for polar materials using density-functional perturbation theory as implemented in VASP.

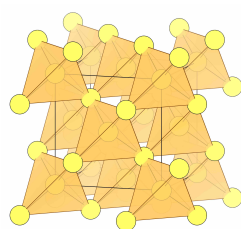
B.3 Parameters in Table 3.1

The experimental electronic band gaps, E_g , are taken from references cited in Table B.1. The speed of sound, \bar{c}_s^{LA} , was calculated by averaging ω^{LA}/q over a uniform 20×20 grid on the surface of a sphere in reciprocal space with radius $q \approx 10 \text{ eV}$ centered at the Γ point. The same averaging procedure was used in calculating the range of optical modes, $\bar{\omega}_O$, when a range exists. The average Born effective charge, \bar{Z}^* , is defined as $\text{Tr} [\mathbf{Z}_+^*] / 3$, where \mathbf{Z}_+^* is the Born effective charge of the positive ion(s) (the other charges can be found by requiring that the primitive cell is neutral). The average high frequency dielectric constant, $\bar{\epsilon}_\infty$, is defined as $\text{Tr} [\boldsymbol{\epsilon}_\infty] / 3$.

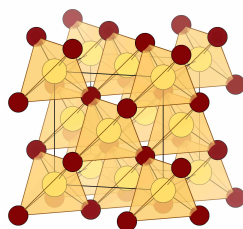
Appendix C

ADDITIONAL TARGET COMPARISON PLOTS

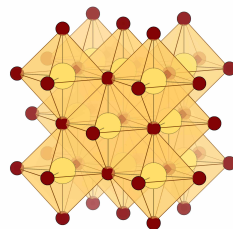
In this Appendix, we provide plots for the remainder of the materials in Table 3.1 not presented in the main text. For concreteness, in all figures we take the local DM density to be $\rho_\chi = 0.4 \text{ GeV/cm}^3$, and assume a Maxwell-Boltzmann distribution with velocity dispersion $v_0 = 230 \text{ km/s}$, truncated at the escape velocity $v_{\text{esc}} = 600 \text{ km/s}$, and boosted to the target rest frame by the Earth velocity in the galactic rest frame $v_E = 240 \text{ km/s}$. We take the direction of the Earth's velocity to be in the \hat{z} direction with respect to the crystal coordinates when computing the reach (for most of the target materials we consider here we expect modulation effects from the Earth's motion to be small). The constraints on $\bar{\sigma}$ correspond to a 95% confidence level (C.L.) assuming Poisson distributed counts and no events are seen (equivalently, the constraint corresponds to the cross section needed to obtain three events). We chose the 95% C.L. for easier comparison with previous literature. Because it is also standard to compute the 90% C.L. exclusion reach, we note that one simply has to multiply the 95% C.L. exclusion reach by 2.3/3 (as the 90% C.L. constraint corresponds to the cross section needed to obtain 2.3 events). We also assume an exposure of one kg-yr.



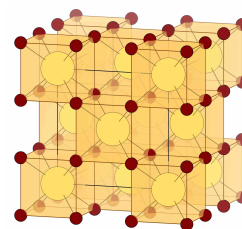
(a) Diamond: diamond-C, Si, Ge. Two interpenetrating face centered cubic lattices, one offset by $1/4$ along the cubic diagonal. Each atom has four nearest neighbors, forming corner-sharing tetrahedra.



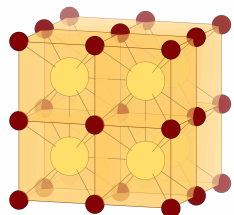
(b) Zincblende: ZnS, GaAs, InSb, GaSb. Same arrangement as diamond cubic, but with two atom types, each occupying one of the face centered cubic lattices.



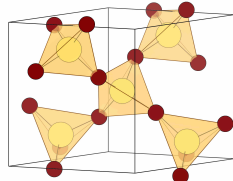
(c) Rock salt: NaCl, MgO, LiF, NaF, NaI, PbS, PbSe, PbTe. The two atom types each form a face centered cubic lattice, offset by $1/2$ along the cubic axis. One atom type is octahedrally coordinated to the other atom type and vice versa.



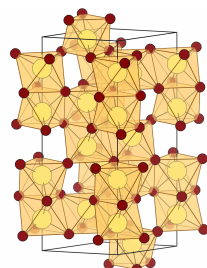
(d) Fluorite: CaF_2 . Ca ions form a face centered cubic lattice. Each Ca ion is surrounded by eight F ions in a cubic geometry.



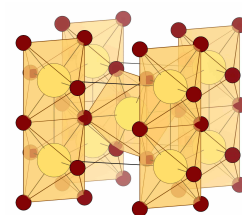
(e) CsI. The two atom types form interpenetrating primitive cubic lattices, with an atom of one type at the center of each cube of the other type.



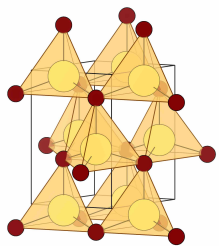
(f) α -quartz: SiO_2 . Each Si ion is bonded to four O ions, forming corner-sharing tetrahedra.



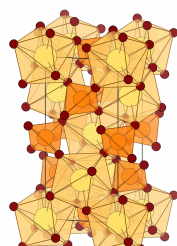
(g) Corundum: Al_2O_3 . Each Al ion is bonded to six O ions, forming octahedra with a mixture of corner, edge and face-sharing connectivities.



(h) Rutile: MgF_2 . Each Mg ion is bonded to six F ions, forming octahedra with a mixture of corner and edge-sharing connectivities.



(i) Wurtzite: GaN, AlN, ZnO. One atom type is tetrahedrally bonded to the other atom type and vice versa. The tetrahedra are corner-sharing and the structure is a member of the hexagonal crystal system.



(j) CaWO_4 . Each Ca ion is bonded to eight O ions, and each W ion is bonded to four O ions, forming corner-sharing octahedra.

Figure C.1: Crystal structures of targets in Table 3.1.

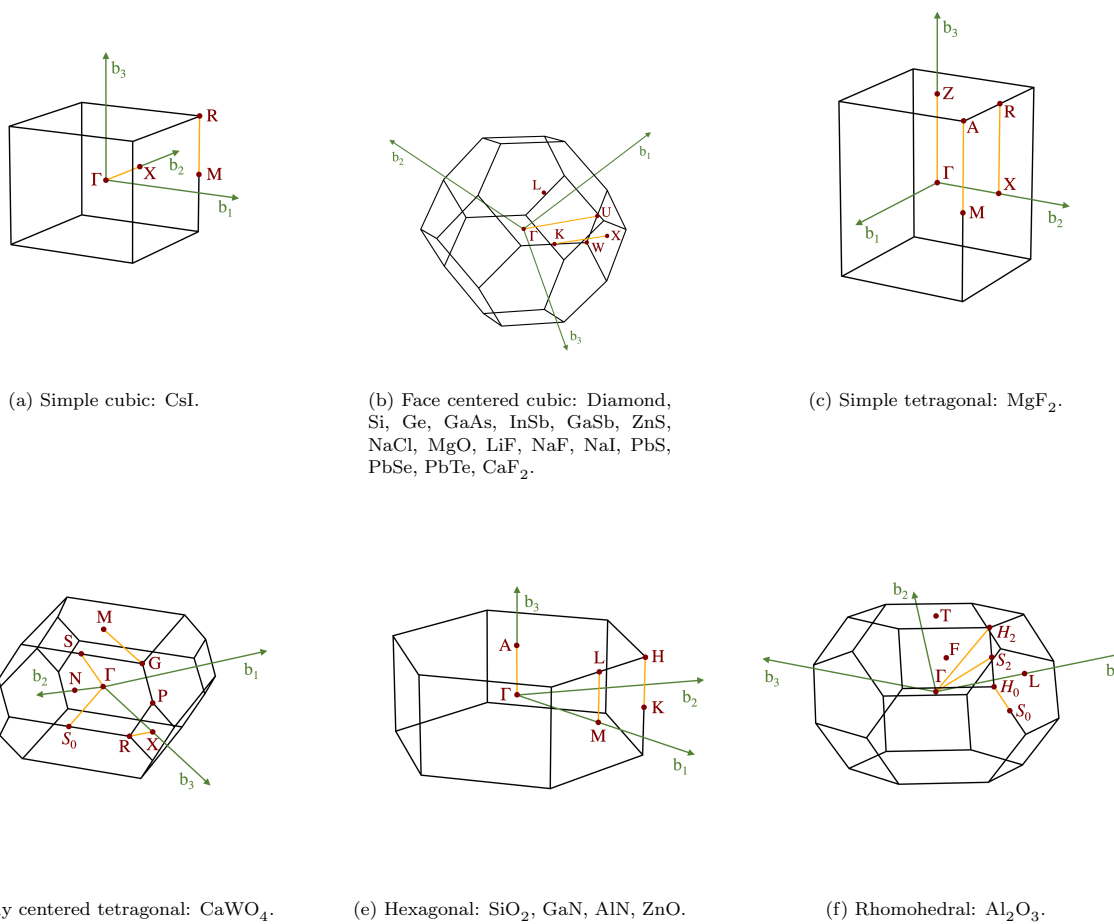


Figure C.2: First Brillouin zones of targets in Table 3.1, with high symmetry points labeled.

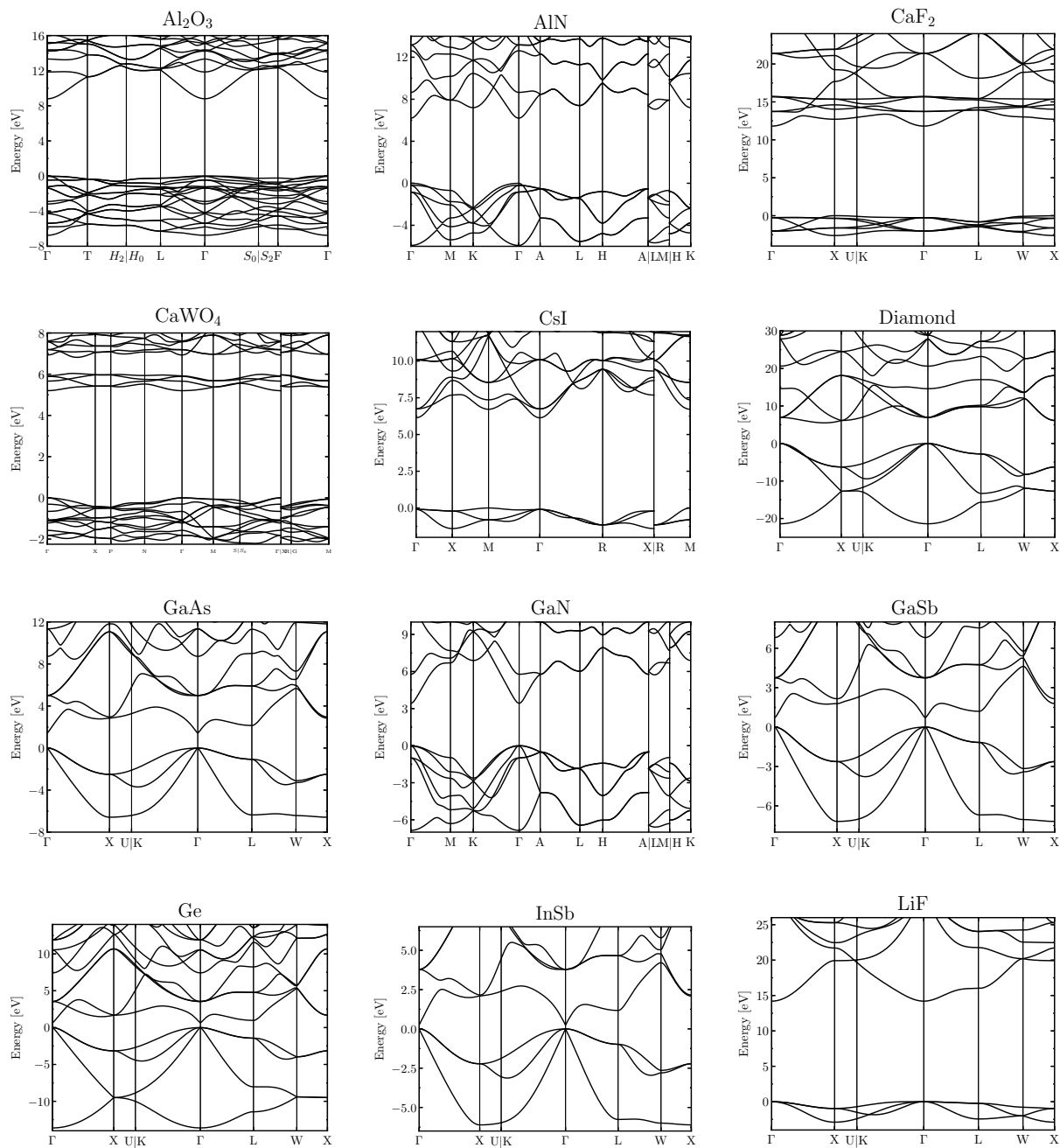


Figure C.3: Calculated electronic band structures of targets in Table 3.1.

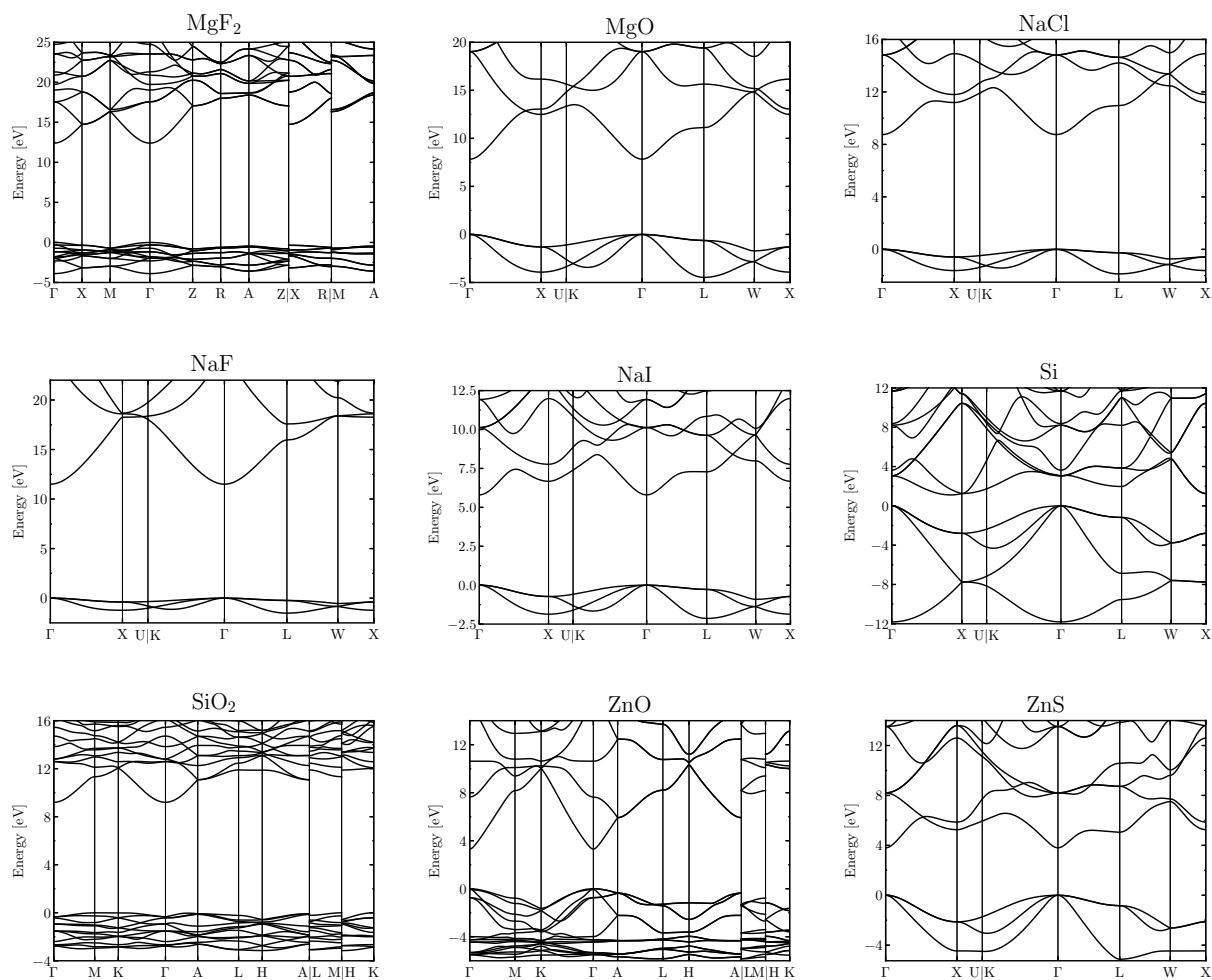


Figure C.4: Calculated electronic band structures of targets in Table 3.1.

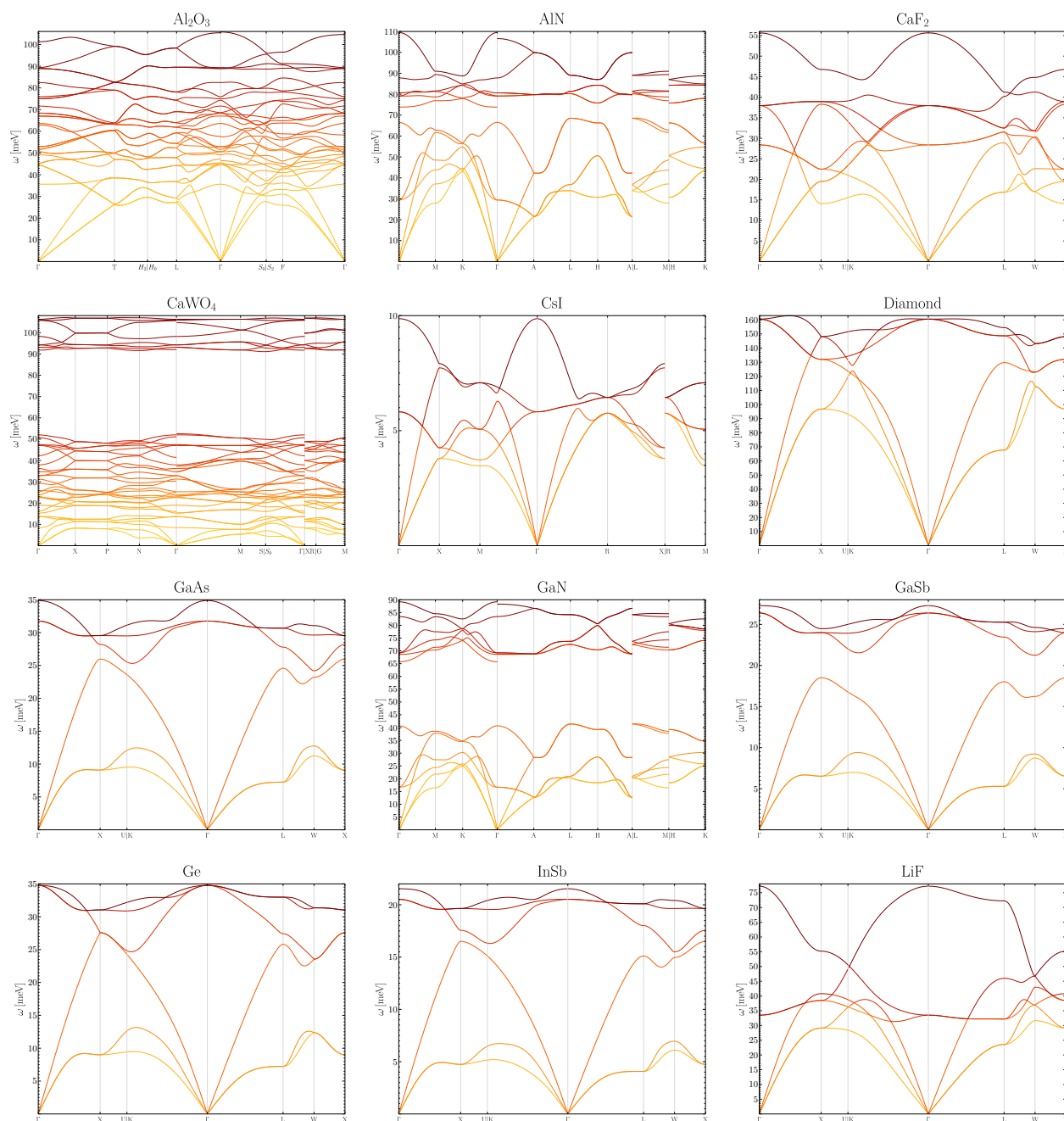


Figure C.5: Phonon dispersions calculated with VASP and phonopy [50] including non-analytic corrections. The path through the high symmetry points is found using SeeK-path [51].

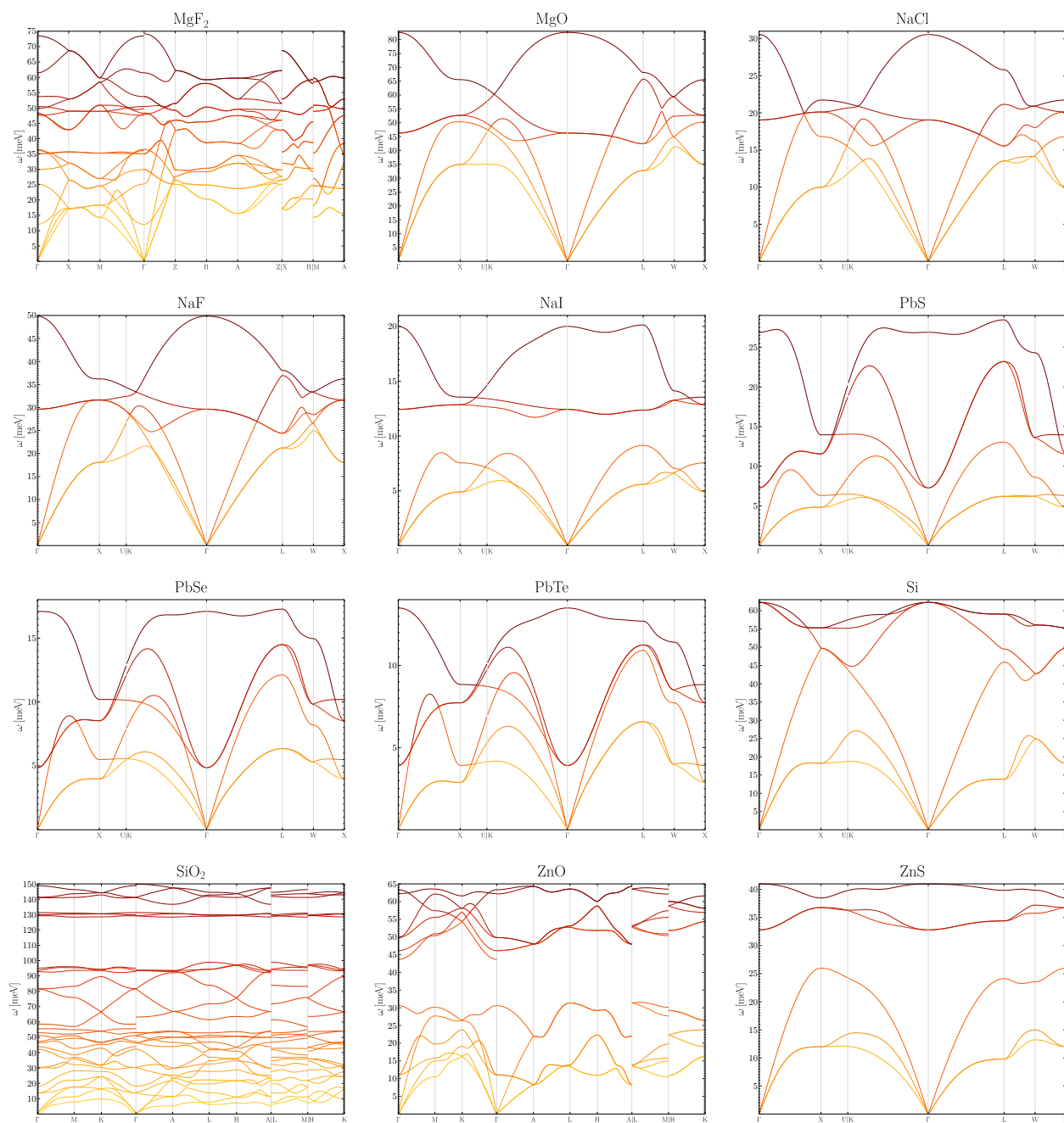


Figure C.6: Phonon dispersions calculated with VASP and phonopy [50] including non-analytic corrections. The path through the high symmetry points is found using SeeK-path [51].

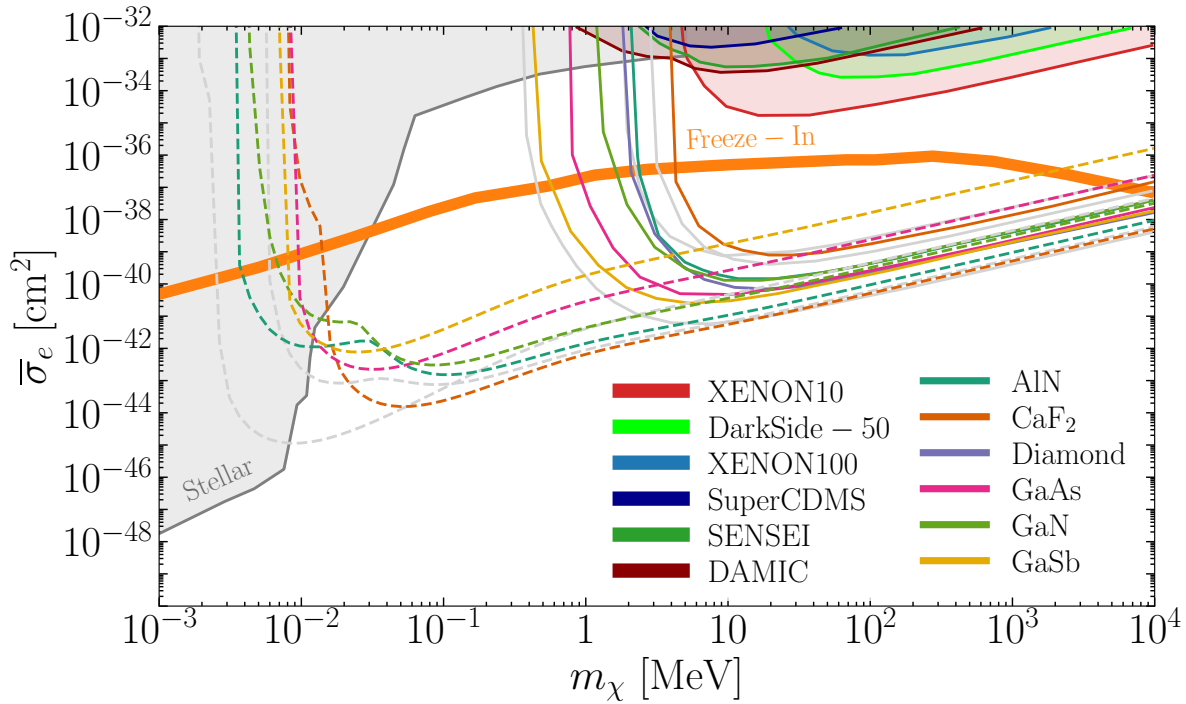


Figure C.7: Same as Fig. 3.1, but with different materials. For reference, gray lines are CsI, Si, and Al_2O_3 taken from Fig. 3.1.

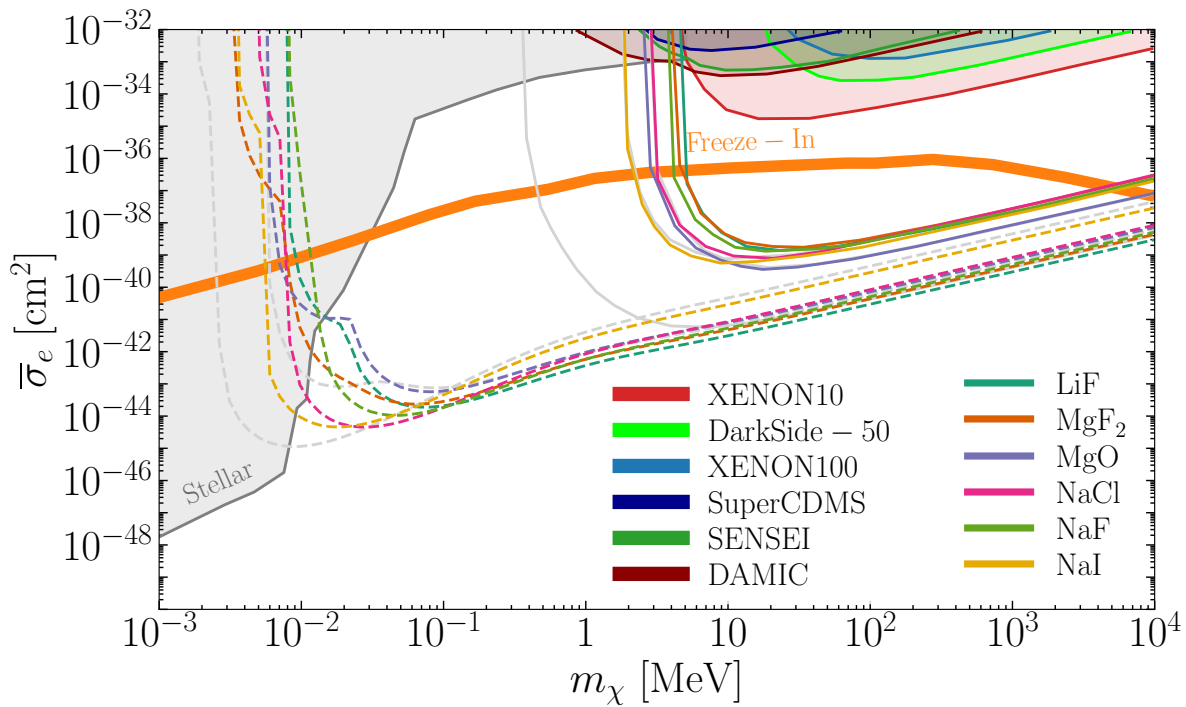


Figure C.8: Same as Fig. 3.1, but with different materials. For reference, gray lines are CsI, Si, and Al_2O_3 taken from Fig. 3.1.

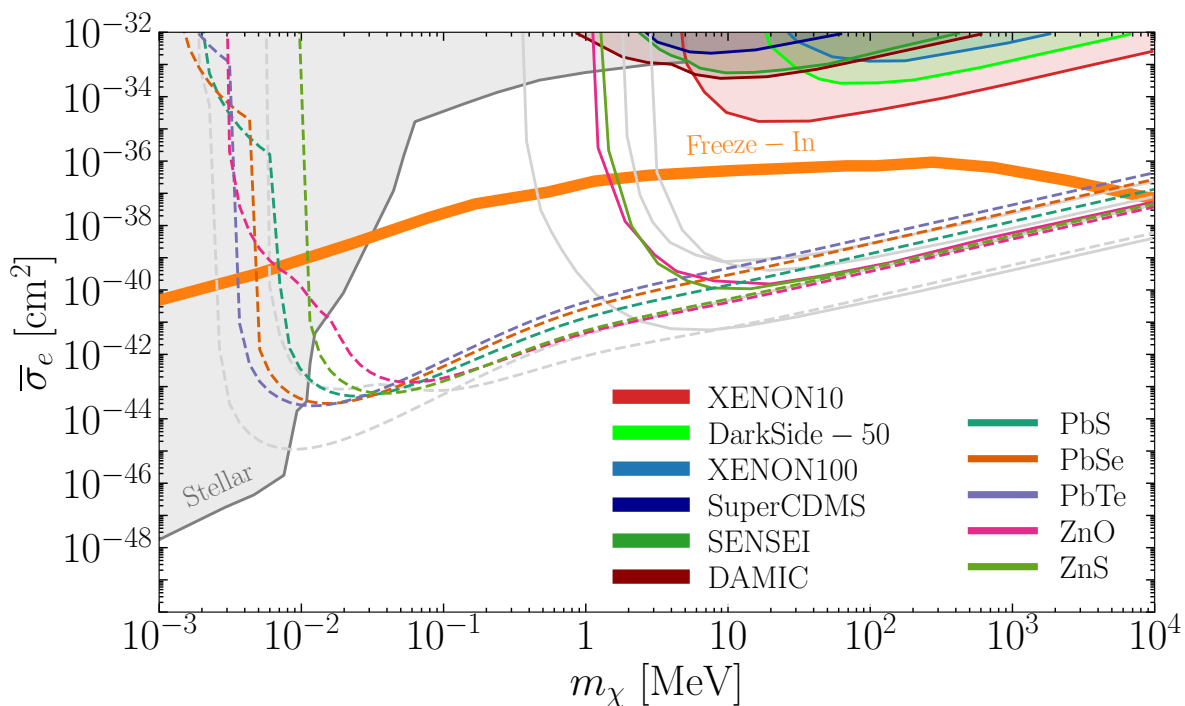


Figure C.9: Same as Fig. 3.1, but with different materials. For reference, gray lines are CsI, Si, and Al_2O_3 taken from Fig. 3.1.

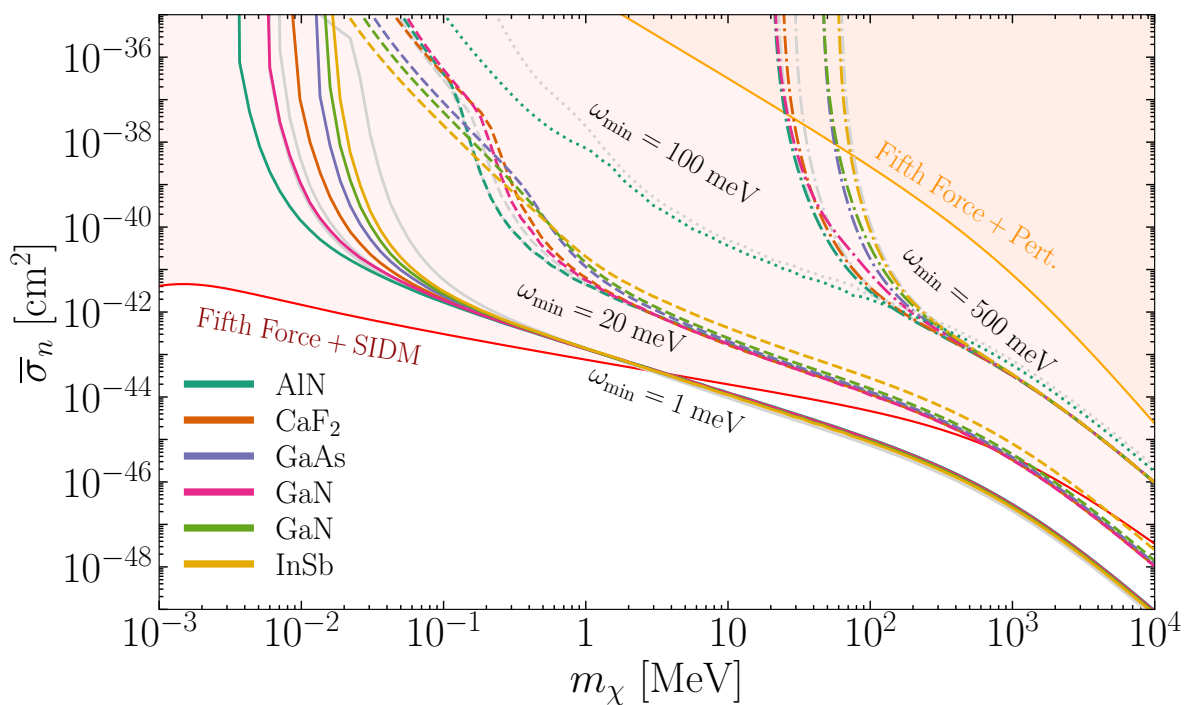


Figure C.10: Same as Fig. 3.2, but with different materials. For reference, gray lines are CsI, Si, and Al_2O_3 taken from Fig. 3.2.

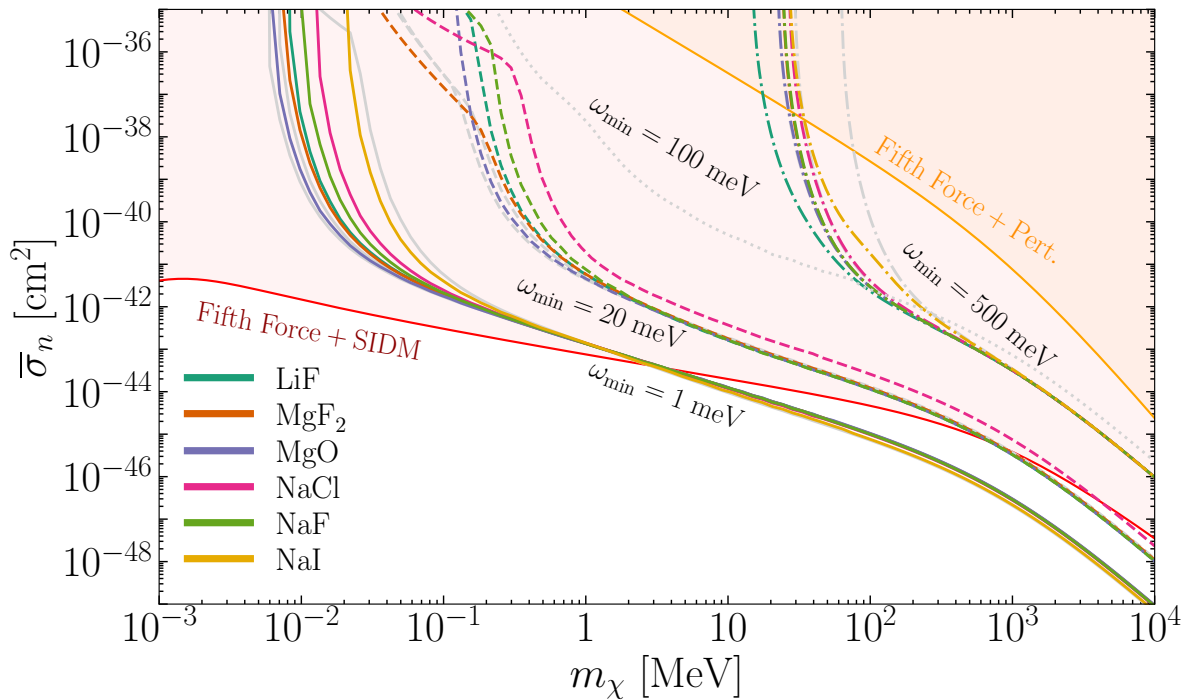


Figure C.11: Same as Fig. 3.2, but with different materials. For reference, gray lines are CsI, Si, and Al₂O₃ taken from Fig. 3.2.

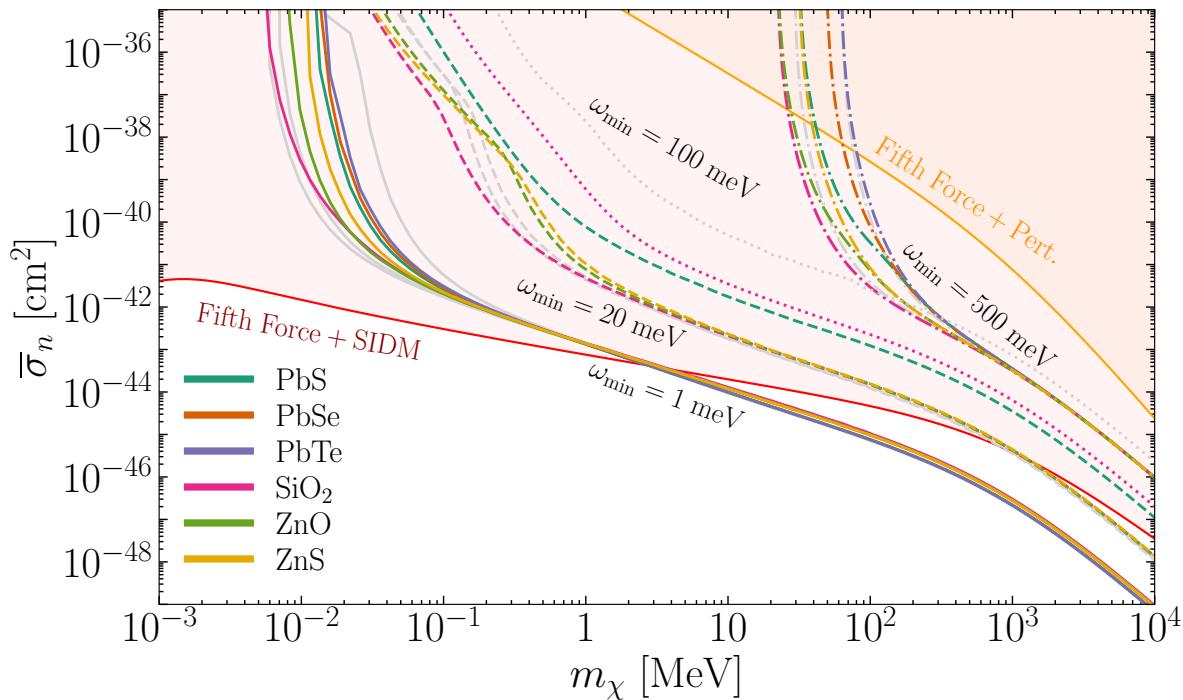


Figure C.12: Same as Fig. 3.2, but with different materials. For reference, gray lines are CsI, Si, and Al₂O₃ taken from Fig. 3.2.

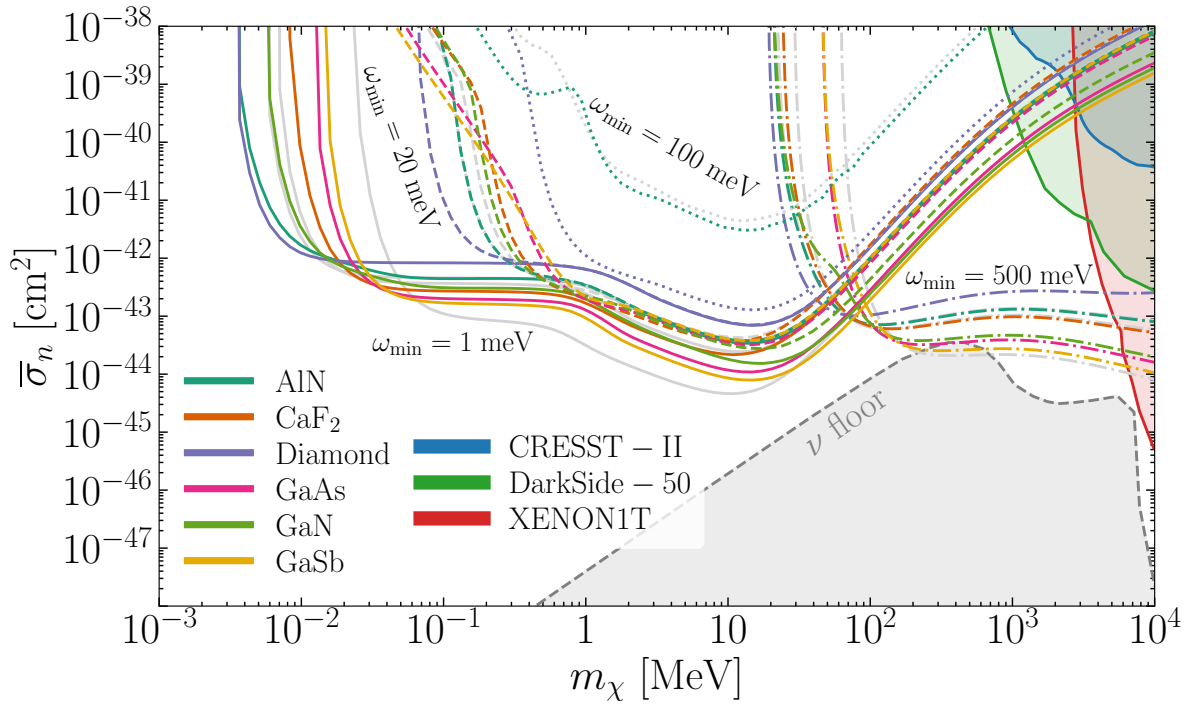


Figure C.13: Same as Fig. 3.3, but with different materials. For reference, gray lines are CsI, Si, and Al_2O_3 taken from Fig. 3.3.

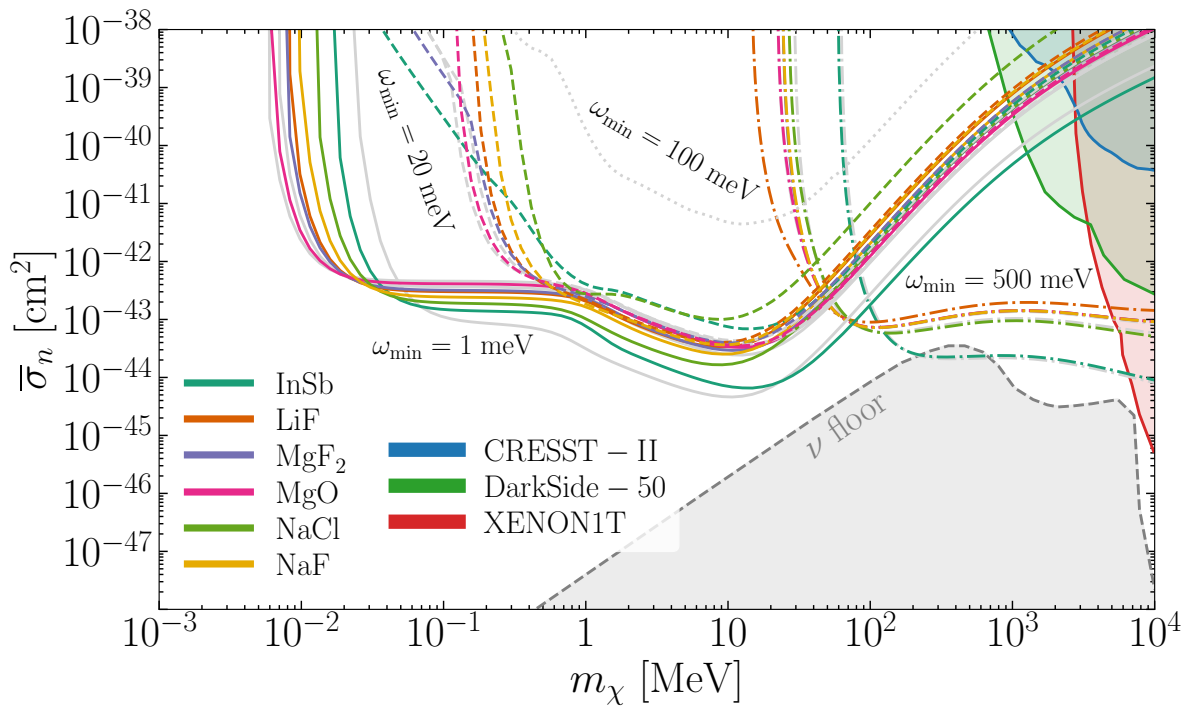


Figure C.14: Same as Fig. 3.3, but with different materials. For reference, gray lines are CsI, Si, and Al_2O_3 taken from Fig. 3.3.

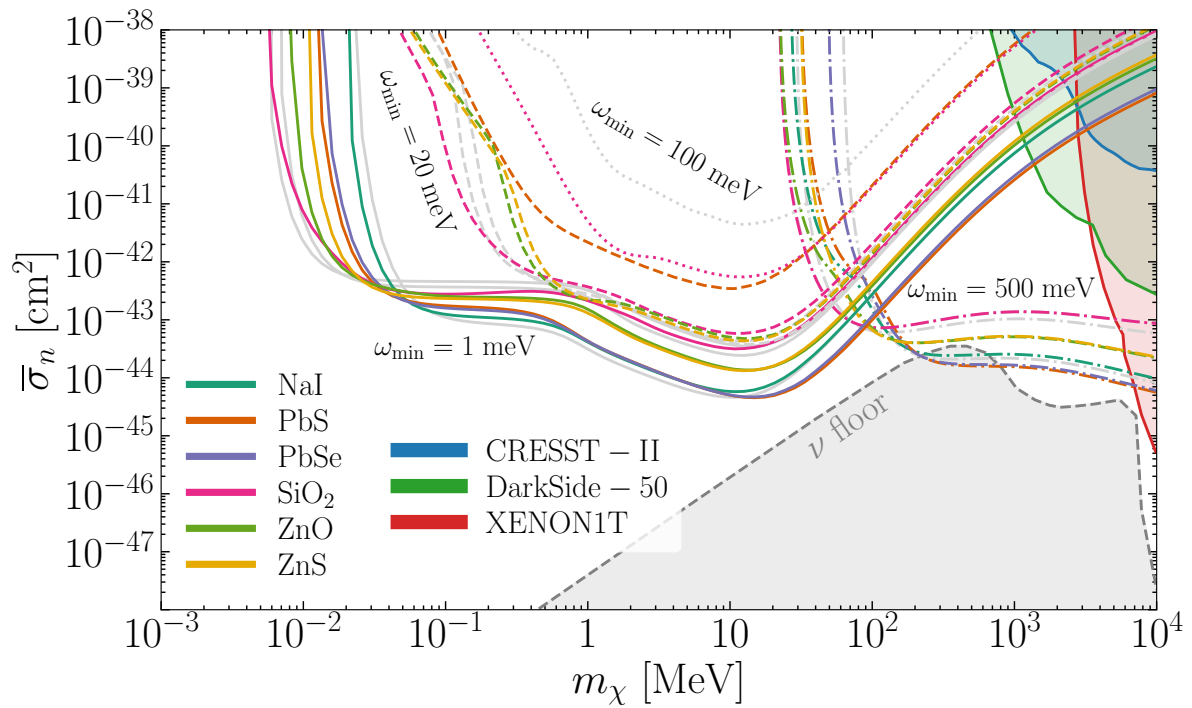


Figure C.15: Fig. 3.3 with different materials. Gray lines are CsI, Si, and Al₂O₃ taken from Fig. 3.3.

Appendix D

DAILY MODULATION AMPLITUDES FOR ADDITIONAL MATERIALS

In addition to the materials discussed in the main text, we have also investigated the daily modulation of the full list of materials considered in Ref. [6]. Their projected reach curves were already computed in Ref. [6] and are included on the interactive webpage [258]. Here we only show the daily modulation amplitude f_{mod} , defined in Eq. (4.15), as in the lower panels of Figs. 4.5, 4.6 and 4.7 in the main text. The results for the dark photon mediator model, the light hadrophilic scalar mediator model and the heavy hadrophilic scalar mediator model are shown in Figs. D.1, D.2 and D.3, respectively. Only materials with $f_{\text{mod}} \geq 10^{-2}$ for at least one m_χ value (at which the material has substantial reach) are shown in each case.

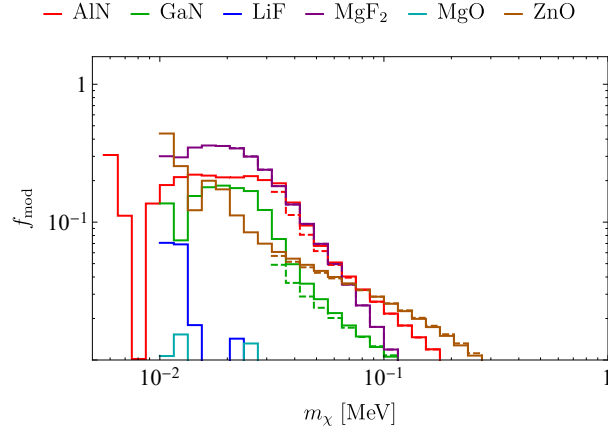


Figure D.1: Daily modulation amplitudes for the dark photon mediator model. Solid and dashed curves assume energy thresholds of 1 meV and 20 meV, respectively. Among the materials studied, only those that have a modulation amplitude greater than 1% for at least one m_χ value (at which the material has substantial reach) are shown. As in the lower panels of Figs. 4.5, 4.6 and 4.7 in the main text, the low mass values where the rate diminishes are excluded for each material. Therefore the shown modulation amplitudes correspond to the mass values where the materials have reach.

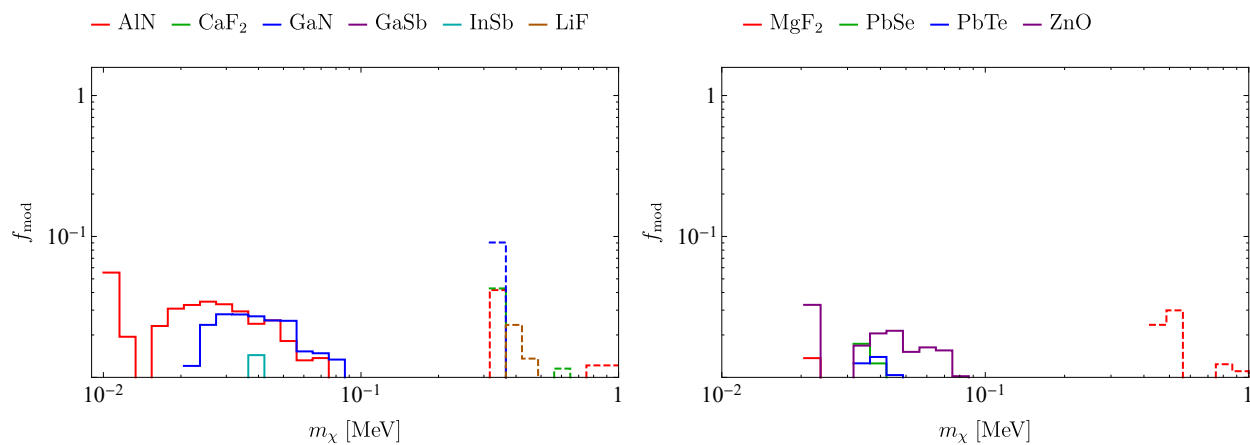


Figure D.2: Same as Fig. D.1, for the light hadrophilic scalar mediator model.

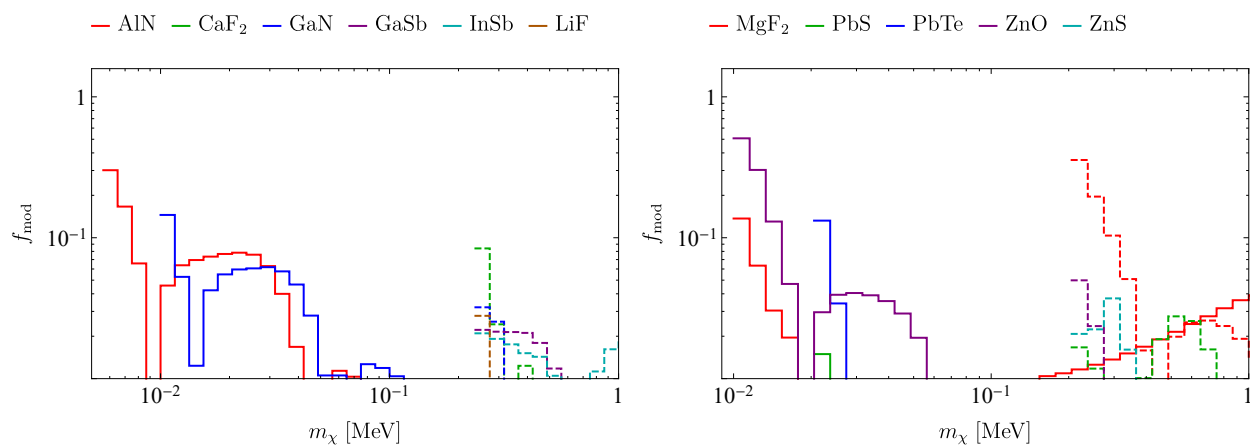


Figure D.3: Same as Fig. D.1, for the heavy hadrophilic scalar mediator model.

A p p e n d i x E

CALCULATION OF THE MODULATION REACH

To establish the statistical significance of a modulating signal, we find the expected number of events needed to reject the non-modulating hypothesis using the following procedure. For a given DM model, with the DM mass m_χ and experimental energy threshold ω_{\min} specified, we first obtain the modulating signal shape $r(t) \equiv R(t)/\langle R \rangle$ as explained in the main text. We divide a sidereal day into $N_{\text{bins}} = 24$ equal-size bins, and denote the bin boundaries by $t_k = (k/N_{\text{bins}})$ days; this binning is fine enough to capture diverse modulation patterns of the large set of materials studied here. Given an expected number of events N_{exp} , we simulate a DM signal sample and a non-modulating sample by generating events following a Poisson distribution in each bin, with mean $\langle N_k \rangle_{\text{sig}} \equiv N_{\text{exp}} \int_{t_{k-1}}^{t_k} r(t) dt/\text{day}$ and $\langle N_k \rangle_{\text{non-mod}} \equiv N_{\text{exp}}/N_{\text{bins}}$ for the k th bin, respectively. We define our test statistic to be the difference between the Pearson's χ^2 values when fitting the simulated data to the non-modulating vs. modulating signal shapes. Concretely, suppose the number of events in the k th bin is N_k . The test statistic is given by

$$\text{TS} = \sum_k \frac{(N_k - \langle N_k \rangle_{\text{non-mod}})^2}{\langle N_k \rangle_{\text{non-mod}}} - \sum_k \frac{(N_k - \langle N_k \rangle_{\text{sig}})^2}{\langle N_k \rangle_{\text{sig}}}. \quad (\text{E.1})$$

Given N_{exp} , we simulate events according to the modulating (DM signal) and non-modulating hypotheses for $N_{\text{sample}} = 10^4$ times each, and obtain the distribution of TS for the modulating and non-modulating samples. For the non-modulating sample, we compute the 95 percentile value $\text{TS}_{\text{non-mod}, 95\%}$. For the modulating signal sample, we compute the mean $\text{TS}_{\text{sig}, \text{mean}}$ and the (50 ± 34) percentiles $\text{TS}_{\text{sig}, \pm 1\sigma}$. These numbers tell us to what extent we can reject the non-modulating hypothesis: $\text{TS}_{\text{non-mod}, 95\%} < \text{TS}_{\text{sig}, \text{mean}}$ means we can reject the non-modulating hypothesis at 95% CL on average, while $\text{TS}_{\text{non-mod}, 95\%} < \text{TS}_{\text{sig}, \pm 1\sigma}$ means we can reject the non-modulating hypothesis at 95% CL given a $\pm 1\sigma$ statistical fluctuation of the signal. Repeating the calculation for many values of N_{exp} , we obtain the interpolating functions $\text{TS}_{\text{non-mod}, 95\%}(N_{\text{exp}})$, $\text{TS}_{\text{sig}, \text{mean}}(N_{\text{exp}})$ and $\text{TS}_{\text{sig}, \pm 1\sigma}(N_{\text{exp}})$. These allow us to solve for the N_{exp} needed for $\text{TS}_{\text{non-mod}, 95\%}$ to drop below $\text{TS}_{\text{sig}, \text{mean}}$, and for it to go below $\text{TS}_{\text{sig}, \pm 1\sigma}$. These then translate into cross sections assuming 1 kg-yr exposure, represented by the modulation reach curves in Figs. 4.5, 4.6 and 4.7. Note that the procedure here largely follows that in Ref. [28], but we have adopted a different test statistic that we find simpler to compute and interpret. We have checked that using instead the test statistic in Ref. [28] produces very similar results in most cases.

A p p e n d i x F

SUPPLEMENTAL MATERIAL: ADDITIONAL DETAILS OF THE
MAGNON RATE CALCULATION

Here we provide additional technical details of the calculations in the *Letter*. We begin by reviewing the derivation of the magnon Hamiltonian (Eq. (3) in the *Letter*). We first define a local coordinate system for each sublattice j , in which the spins point in the z direction in the ground state. Denoting the rotation matrices between global and local coordinates by R_j , we have

$$S_{lj}^\alpha = \sum_{\beta} R_j^{\alpha\beta} S_{lj}^{\prime\beta}, \quad \{\langle S_{lj}^{\prime 1} \rangle, \langle S_{lj}^{\prime 2} \rangle, \langle S_{lj}^{\prime 3} \rangle\} = \{0, 0, S_j\}, \quad (\text{F.1})$$

where α, β are Cartesian coordinates. To find the excitations above the ground state, we map the spin system onto a bosonic system via the Holstein-Primakoff transformation,

$$S_{lj}^{\prime +} = (2S_j - \hat{a}_{lj}^\dagger \hat{a}_{lj})^{1/2} \hat{a}_{lj}, \quad S_{lj}^{\prime -} = \hat{a}_{lj}^\dagger (2S_j - \hat{a}_{lj}^\dagger \hat{a}_{lj})^{1/2}, \quad S_{lj}^{\prime 3} = S_j - \hat{a}_{lj}^\dagger \hat{a}_{lj}, \quad (\text{F.2})$$

where $S_{lj}^{\prime \pm} = S_{lj}^{\prime 1} \pm iS_{lj}^{\prime 2}$. The bosonic creation and annihilation operators satisfy $[\hat{a}_{lj}, \hat{a}_{l'j'}^\dagger] = \delta_{ll'}\delta_{jj'}$, so that commutators between the spin operators $[S_{lj}^{\prime \alpha}, S_{l'j'}^{\prime \beta}] = \delta_{ll'}\delta_{jj'} i\epsilon^{\alpha\beta\gamma} S_{lj}^{\prime \gamma}$ are reproduced. Going to momentum space and diagonalizing the quadratic Hamiltonian (corresponding to the leading terms in the $1/S$ expansion) by a Bogoliubov transformation,

$$\hat{a}_{lj} = \frac{1}{\sqrt{N}} \sum_{\mathbf{k} \in \text{1BZ}} \hat{a}_{j,\mathbf{k}} e^{i\mathbf{k} \cdot \mathbf{x}_{lj}}, \quad (\text{F.3})$$

$$\begin{pmatrix} \hat{a}_{j,\mathbf{k}} \\ \hat{a}_{j,-\mathbf{k}}^\dagger \end{pmatrix} = \mathbf{T}_{\mathbf{k}} \begin{pmatrix} \hat{b}_{\nu,\mathbf{k}} \\ \hat{b}_{\nu,-\mathbf{k}}^\dagger \end{pmatrix} \quad \text{where} \quad \mathbf{T}_{\mathbf{k}} = \begin{pmatrix} \mathbf{U}_{j\nu,\mathbf{k}} & \mathbf{V}_{j\nu,\mathbf{k}} \\ \mathbf{V}_{j\nu,-\mathbf{k}}^* & \mathbf{U}_{j\nu,-\mathbf{k}}^* \end{pmatrix}, \quad (\text{F.4})$$

where \mathbf{x}_{lj} is the position of the j th site in the l th unit cell, we arrive at the free magnon Hamiltonian,

$$H = \sum_{\nu=1}^n \sum_{\mathbf{k} \in \text{1BZ}} \omega_{\nu,\mathbf{k}} \hat{b}_{\nu,\mathbf{k}}^\dagger \hat{b}_{\nu,\mathbf{k}}, \quad (\text{F.5})$$

where $\hat{b}_{\nu,\mathbf{k}}^\dagger, \hat{b}_{\nu,\mathbf{k}}$ are creation and annihilation operators for the canonical magnon modes. The canonical commutators are preserved, $[\hat{b}_{\nu,\mathbf{k}}, \hat{b}_{\nu',\mathbf{k}'}^\dagger] = \delta_{\nu\nu'}\delta_{\mathbf{k}\mathbf{k}'}$, by imposing the following constraint,

$$\mathbf{T}_{\mathbf{k}} \begin{pmatrix} \mathbb{1}_n & \mathbb{0}_n \\ \mathbb{0}_n & -\mathbb{1}_n \end{pmatrix} \mathbf{T}_{\mathbf{k}}^\dagger = \begin{pmatrix} \mathbb{1}_n & \mathbb{0}_n \\ \mathbb{0}_n & -\mathbb{1}_n \end{pmatrix}. \quad (\text{F.6})$$

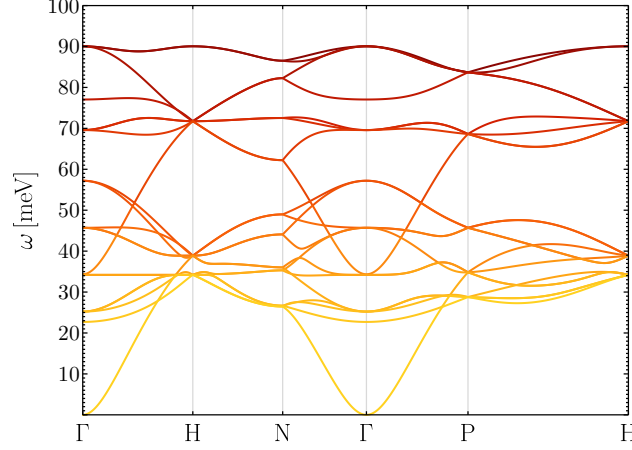


Figure F.1: Calculated magnon dispersion of YIG along the high symmetry lines in the first Brillouin zone.

We follow the algorithm in Ref. [268] to solve the constrained diagonalization problem to obtain $\omega_{\nu,\mathbf{k}}$, $\mathbf{T}_{\mathbf{k}}$. Note that Ref. [268] uses a different Fourier transformation convention, with \mathbf{x}_l rather than \mathbf{x}_{lj} in the exponent of Eq. (F.3). We have consistently followed our convention throughout the calculation, adjusting the equations in Ref. [268] where necessary. In Fig. F.1, we plot our calculated magnon dispersion $\omega_{\nu,\mathbf{k}}$ for YIG along the high symmetry lines in the (body-centered cubic) 1BZ generated using the SeeK-path code [51].

Next, we derive the single magnon production matrix element (Eq. (5) in the *Letter*) from the DM-electron spin coupling (Eq. (4) in the *Letter*). Assuming the absence of orbital angular momentum, a magnetic atom/ion at site l, j sources an effective scattering potential for the incoming DM, which is given by the Fourier transform of the momentum space operator,

$$V_{lj}(\mathbf{x}) = \int \frac{d^3q}{(2\pi)^3} \sum_{\alpha} \hat{O}_{\chi}^{\alpha}(\mathbf{q}) \hat{S}_{lj}^{\alpha} e^{-i\mathbf{q}\cdot(\mathbf{x}-\mathbf{x}_{lj})}. \quad (\text{F.7})$$

For a DM particle with incoming momentum \mathbf{p} and outgoing momentum $\mathbf{p}' = \mathbf{p} - \mathbf{q}$, and a transition $\lambda_i \rightarrow \lambda_f$ in the target system, the matrix element is

$$\begin{aligned} \mathcal{M} &= \langle \chi_f \lambda_f | \hat{V} | \chi_i \lambda_i \rangle \\ &= \frac{1}{N\Omega} \sum_{lj} \int d^3x e^{i\mathbf{q}\cdot\mathbf{x}} \langle s_f \lambda_f | V_{lj}(\mathbf{x}) | s_i \lambda_i \rangle \\ &= \frac{1}{N\Omega} \sum_{\alpha} \langle s_f | \hat{O}_{\chi}^{\alpha}(\mathbf{q}) | s_i \rangle \sum_{lj} e^{i\mathbf{q}\cdot\mathbf{x}_{lj}} \langle \lambda_f | \hat{S}_{lj}^{\alpha} | \lambda_i \rangle. \end{aligned} \quad (\text{F.8})$$

Now focus on the case where λ_i is the ground state $|0\rangle$ and λ_f is a single magnon state $|\nu, \mathbf{k}\rangle$. Plugging in Eqs. (F.1)-(F.4), and keeping only terms proportional to a single power of $\hat{b}_{\nu,\mathbf{k}}^{\dagger}$,

we obtain

$$\begin{aligned}
\sum_{lj} e^{i\mathbf{q}\cdot\mathbf{x}_{lj}} \langle \lambda_f | \hat{S}_{lj}^\alpha | \lambda_i \rangle &= \sum_{lj} e^{i\mathbf{q}\cdot\mathbf{x}_{lj}} \sum_{\beta} \langle \nu, \mathbf{k} | R_j^{\alpha\beta} \hat{S}_{lj}^{\beta} | 0 \rangle = \sum_{lj} \sqrt{\frac{S_j}{2}} e^{i\mathbf{q}\cdot\mathbf{x}_{lj}} \langle \nu, \mathbf{k} | r_j^{\alpha*} \hat{a}_{lj} + r_j^{\alpha} \hat{a}_{lj}^\dagger | 0 \rangle \\
&= \frac{1}{\sqrt{N}} \sum_{\mathbf{k}' \in 1\text{BZ}} \sum_l e^{i(\mathbf{q}-\mathbf{k}')\cdot\mathbf{x}_l} \sum_j \sqrt{\frac{S_j}{2}} e^{i(\mathbf{q}-\mathbf{k}')\cdot\mathbf{x}_j} \langle \nu, \mathbf{k} | r_j^{\alpha*} \hat{a}_{j,-\mathbf{k}'} + r_j^{\alpha} \hat{a}_{j,\mathbf{k}'}^\dagger | 0 \rangle \\
&= \sqrt{N} \sum_{\mathbf{k}' \in 1\text{BZ}} \sum_{\mathbf{G}} \delta_{\mathbf{q}-\mathbf{k}', \mathbf{G}} \sum_{j\nu'} \sqrt{\frac{S_j}{2}} e^{i\mathbf{G}\cdot\mathbf{x}_j} (V_{j\nu', -\mathbf{k}'} r_j^{\alpha*} + U_{j\nu', \mathbf{k}'}^* r_j^{\alpha}) \langle \nu, \mathbf{k} | \hat{b}_{\nu', \mathbf{k}'}^\dagger | 0 \rangle \\
&= \sqrt{N} \sum_{\mathbf{G}} \delta_{\mathbf{q}-\mathbf{k}, \mathbf{G}} \sum_j \sqrt{\frac{S_j}{2}} e^{i\mathbf{G}\cdot\mathbf{x}_j} (V_{j\nu, -\mathbf{k}} r_j^{\alpha*} + U_{j\nu, \mathbf{k}}^* r_j^{\alpha}), \tag{F.9}
\end{aligned}$$

where we have used $\mathbf{x}_{lj} = \mathbf{x}_l + \mathbf{x}_j$, $\sum_l e^{i(\mathbf{q}-\mathbf{k}')\cdot\mathbf{x}_l} = N \sum_{\mathbf{G}} \delta_{\mathbf{q}-\mathbf{k}', \mathbf{G}}$. Plugging Eq. (F.9) into Eq. (F.8) reproduces Eq. (5) in the *Letter* (where the sum over \mathbf{G} is implicit).

Finally, we derive the analytical approximation for the rate in the case of an $n = 1$ ferromagnet target (Eqs. (12) and (13) in the *Letter*). Noting that the \mathbf{k} integral over the 1BZ combined with the \mathbf{G} sum is equivalent to an integral over the entire momentum space, we have

$$R = \frac{n_s \rho_\chi}{\rho_T m_\chi} \int d^3 v_\chi f(\mathbf{v}_\chi) \int \frac{d^3 q}{8\pi^2} \text{tr}(\hat{\rho}_\chi \hat{O}_\chi^+(\mathbf{q}) \hat{O}_\chi^{\dagger-}(\mathbf{q})) \delta\left(\mathbf{q} \cdot \mathbf{v}_\chi - \frac{q^2}{2m_\chi} - \omega_{\mathbf{k}=\mathbf{q}-\mathbf{G}}\right). \tag{F.10}$$

Since the magnon dispersion is near isotropic, the delta function fixes the angle between \mathbf{q} and \mathbf{v}_χ for any given $q = |\mathbf{q}|$ — this is true as long as $\frac{q^2}{2m_\chi} + \omega \leq qv_\chi$, or approximately (since $\omega \ll qv_\chi$), $q \leq 2m_\chi v_\chi$. Thus,

$$R = \frac{n_s \rho_\chi}{\rho_T m_\chi} \int d^3 v_\chi \frac{f(\mathbf{v}_\chi)}{v_\chi} \int_{\Sigma} \frac{dq d\phi}{8\pi^2} q \text{tr}(\hat{\rho}_\chi \hat{O}_\chi^+(\mathbf{q}) \hat{O}_\chi^{\dagger-}(\mathbf{q})), \tag{F.11}$$

where the q integral is now over a two-dimensional surface Σ that satisfies the energy-conserving delta function, which is approximately a sphere of radius $m_\chi v_\chi$ centered at $m_\chi \mathbf{v}_\chi$. The trace generally depends on the angle θ_q between \mathbf{q} and the spins. For the three models in Table 5.1, we have

$$\text{tr}(\hat{\rho}_\chi \hat{O}_\chi^+ \hat{O}_\chi^{\dagger-}) = \begin{cases} \frac{4g_\chi^2 g_e^2}{\Lambda_\chi^2 m_e^2} (1 + \cos^2 \theta_q) & \text{(magnetic dipole DM)}, \\ \frac{g_\chi^2 g_e^2}{\Lambda_\chi^4 m_e^2} q^2 (1 + \cos^2 \theta_q) & \text{(anapole DM)}, \\ \frac{y_\chi^2 y_e^2}{m_e^2} \frac{1}{q^2} \sin^2 \theta_q & \text{(pseudo-mediated DM)}. \end{cases} \tag{F.12}$$

However, since the trigonometric functions are bounded, we have, e.g., $\int dq d\phi f(q) \cos^2 \theta_q = 2\pi \langle c^2 \rangle \int dq f(q)$ for a general function $f(q)$, with $\langle c^2 \rangle \in [0, 1]$ a constant to be understood as

a weighted average of $\cos^2 \theta_q$ over the integration region. Thus,

$$R = \frac{n_s \rho_\chi}{\rho_T m_\chi} \int d^3 v_\chi \frac{f(\mathbf{v}_\chi)}{v_\chi} \int_{q_{\min}(\omega_{\min})}^{q_{\max}(v_\chi)} \frac{dq}{4\pi} q \langle \text{tr}(\hat{\rho}_\chi \hat{\mathcal{O}}_\chi^+(\mathbf{q}) \hat{\mathcal{O}}_\chi^{\dagger-}(\mathbf{q})) \rangle. \quad (\text{F.13})$$

After performing the q integral, we arrive at Eqs. (12) and (13) in the *Letter*.

Appendix G

PHOTON-PHONON MIXING

As outlined in Sec. 6.2, mixing between long-wavelength photon and phonon states needs to be taken into account when computing DM absorption rates in a polar crystal. Our starting point is the Lagrangian for an ionic lattice coupling to electromagnetism:

$$L = \sum_{lj} \left(\frac{1}{2} m_j \dot{\mathbf{u}}_{lj}^2 - \frac{1}{2} \sum_{l'j'} \mathbf{u}_{lj} \cdot \mathbf{V}_{lj,l'j'}^{(2)} \cdot \mathbf{u}_{l'j'} + e \mathbf{E}(\mathbf{x}_{lj}^0) \cdot \mathbf{Z}_j^* \cdot \mathbf{u}_{lj} \right) + \int d^3x \left(-\frac{1}{4} F^{\mu\nu} F_{\mu\nu} + \frac{1}{2} A_\mu \Pi^{\mu\nu} A_\nu \right). \quad (\text{G.1})$$

In the long wavelength limit, the leading electromagnetic coupling is via the electric dipole, as shown in the third term. Plugging in $\mathbf{E} = -\nabla A_0 - \dot{\mathbf{A}}$ and integrate by parts, we can write it in the familiar form of $-\int d^3x J^\mu A_\mu = \int d^3x (-\rho A_0 + \mathbf{J} \cdot \mathbf{A})$, with

$$\rho(\mathbf{x}) = -e \sum_{lj} (\nabla \delta^{(3)}(\mathbf{x} - \mathbf{x}_{lj}^0)) \cdot \mathbf{Z}_j^* \cdot \mathbf{u}_{lj}, \quad \mathbf{J}(\mathbf{x}) = e \sum_{lj} \mathbf{Z}_j^* \cdot \dot{\mathbf{u}}_{lj} \delta^{(3)}(\mathbf{x} - \mathbf{x}_{lj}^0). \quad (\text{G.2})$$

when expanded to linear order in \mathbf{u} . The last term in Eq. (G.1) results from integrating out electron response. As explained in detail in Ref. [7], the photon self-energy $\Pi^{\mu\nu}$ can be related to the dielectric tensor of the medium, $\boldsymbol{\varepsilon}$ (taken to be the electronic contribution, usually denoted by $\boldsymbol{\varepsilon}_\infty$, in the present case), and the photon Lagrangian can be written as

$$-\frac{1}{4} F^{\mu\nu} F_{\mu\nu} + \frac{1}{2} A_\mu \Pi^{\mu\nu} A_\nu = \frac{1}{2} \dot{\mathbf{A}} \cdot \boldsymbol{\varepsilon} \cdot \dot{\mathbf{A}} - \frac{1}{2} A_0 (\nabla \cdot \boldsymbol{\varepsilon} \cdot \nabla) A_0 + \dot{A}_0 (\nabla \cdot \boldsymbol{\varepsilon} \cdot \mathbf{A}) - \frac{1}{2} (\partial_i A^j)^2 + \frac{1}{2} (\nabla \cdot \mathbf{A})^2. \quad (\text{G.3})$$

It is convenient to choose a generalized Coulomb gauge, $\nabla \cdot \boldsymbol{\varepsilon} \cdot \mathbf{A} = 0$, and since the A_0 field is non-dynamical, it can be immediately integrated out. We thus obtain

$$L = \sum_{lj} \frac{1}{2} m_j \dot{\mathbf{u}}_{lj}^2 - \frac{1}{2} \sum_{l'j'} \mathbf{u}_{lj} \cdot \mathbf{V}_{l'j',lj} \cdot \mathbf{u}_{l'j'} + e \mathbf{A}(\mathbf{x}_{lj}^0) \cdot \mathbf{Z}_j^* \cdot \dot{\mathbf{u}}_{lj} + \int d^3x \left[\frac{1}{2} \dot{\mathbf{A}} \cdot \boldsymbol{\varepsilon} \cdot \dot{\mathbf{A}} - \frac{1}{2} (\partial_i A^j)^2 + \frac{1}{2} (\nabla \cdot \mathbf{A})^2 + \frac{1}{2} \rho \frac{1}{\nabla \cdot \boldsymbol{\varepsilon} \cdot \nabla} \rho \right]. \quad (\text{G.4})$$

To derive the Hamiltonian, we note the canonical momenta are:

$$\mathbf{p}_{lj} = \frac{\partial L}{\partial \dot{\mathbf{u}}_{lj}} = m_j \dot{\mathbf{u}}_{lj} + e \mathbf{A}(\mathbf{x}_{lj}^0) \cdot \mathbf{Z}_j^*, \quad \mathbf{P}(\mathbf{x}) = \frac{\partial \mathcal{L}}{\partial \dot{\mathbf{A}}(\mathbf{x})} = \boldsymbol{\varepsilon} \cdot \dot{\mathbf{A}}(\mathbf{x}). \quad (\text{G.5})$$

Therefore,

$$H = \sum_{lj} \mathbf{p}_{lj} \cdot \dot{\mathbf{u}}_{lj} + \int d^3x \mathbf{P} \cdot \dot{\mathbf{A}} - L = H_{\text{ph}} + H_{\text{Coulomb}} + H_{\text{EM}} + H_{\text{mix}}, \quad (\text{G.6})$$

where

$$H_{\text{ph}} = \sum_{lj} \frac{\mathbf{p}_{lj}^2}{2m_j} + \frac{1}{2} \sum_{l'j'j''} \mathbf{u}_{lj} \cdot \mathbf{V}_{l'j'j''} \cdot \mathbf{u}_{l'j'}, \quad (\text{G.7})$$

$$H_{\text{Coulomb}} = -\frac{1}{2} \int d^3x \rho \frac{1}{\nabla \cdot \boldsymbol{\varepsilon} \cdot \nabla} \rho, \quad (\text{G.8})$$

$$H_{\text{EM}} = \frac{1}{2} \int d^3x \left[\mathbf{P} \cdot \boldsymbol{\varepsilon}^{-1} \cdot \mathbf{P} + (\partial_i A^j)^2 - (\nabla \cdot \mathbf{A})^2 + e^2 \sum_{lj} \frac{1}{m_j} \delta^{(3)}(\mathbf{x} - \mathbf{x}_{lj}^0) (\mathbf{A} \cdot \mathbf{Z}_j^*)^2 \right], \quad (\text{G.9})$$

$$H_{\text{mix}} = -e \sum_{lj} \frac{1}{m_j} \mathbf{A}(\mathbf{x}_{lj}^0) \cdot \mathbf{Z}_j^* \cdot \mathbf{p}_{lj}. \quad (\text{G.10})$$

Note that while we have written \mathbf{A} and \mathbf{P} as 3-vectors, they are implicitly assumed to satisfy the gauge condition. This means that, in Eq. (G.9), $\boldsymbol{\varepsilon}$ should be projected onto the subspace satisfying the gauge condition before the inverse is taken.

We now consider the four terms in turn. First, as mentioned in Sec. 6.2, we use the phonopy code with DFT calculations of the force constants $\mathbf{V}_{lj,l'j'}^{(2)}$ to diagonalize the lattice (phonon) Hamiltonian H_{ph} , giving

$$H_{\text{ph}} = \sum_{\nu=1}^{3n} \sum_{\mathbf{k}} \omega_{\nu,\mathbf{k}} \hat{a}_{\nu,\mathbf{k}}^\dagger \hat{a}_{\nu,\mathbf{k}}. \quad (\text{G.11})$$

Second, the Coulomb term, H_{Coulomb} , becomes more transparent when written as a momentum space integral:

$$H_{\text{Coulomb}} = \frac{1}{2} \int \frac{d^3k}{(2\pi)^3} \frac{|\tilde{\rho}(\mathbf{k})|^2}{\mathbf{k} \cdot \boldsymbol{\varepsilon} \cdot \mathbf{k}}, \quad (\text{G.12})$$

with the charge density

$$\tilde{\rho}(\mathbf{k}) = \int d^3x e^{-i\mathbf{k} \cdot \mathbf{x}} \rho(\mathbf{x}) = -ie \sum_{lj} \mathbf{k} \cdot \mathbf{Z}_j^* \cdot \mathbf{u}_{lj} e^{-i\mathbf{k} \cdot \mathbf{x}_{lj}^0}. \quad (\text{G.13})$$

Expanding \mathbf{u}_{lj} in $(\hat{a}_{\nu,\mathbf{k}'} + \hat{a}_{\nu,-\mathbf{k}'}^\dagger)$ as in Eq. (2.79) and summing over l picks out the $\mathbf{k}' = \mathbf{k}$ modes. With the momentum integral discretized, $\int \frac{d^3k}{(2\pi)^3} \rightarrow \frac{1}{N\Omega} \sum_{\mathbf{k}}$, we find

$$H_{\text{Coulomb}} = \frac{e^2}{4\Omega} \sum_{\nu,\nu',\mathbf{k}} \frac{1}{\sqrt{\omega_{\nu',\mathbf{k}} \omega_{\nu,\mathbf{k}}}} \frac{(\mathbf{k} \cdot \boldsymbol{\xi}_{\nu',\mathbf{k}}^*)(\mathbf{k} \cdot \boldsymbol{\xi}_{\nu,\mathbf{k}})}{\mathbf{k} \cdot \boldsymbol{\varepsilon} \cdot \mathbf{k}} (\hat{a}_{\nu',-\mathbf{k}} + \hat{a}_{\nu',\mathbf{k}}^\dagger) (\hat{a}_{\nu,\mathbf{k}} + \hat{a}_{\nu,-\mathbf{k}}^\dagger), \quad (\text{G.14})$$

where

$$\boldsymbol{\xi}_{\nu,\mathbf{k}} \equiv \sum_j \frac{1}{\sqrt{m_j}} \mathbf{Z}_j^* \cdot \boldsymbol{\epsilon}_{\nu,\mathbf{k},j}. \quad (\text{G.15})$$

As a technical note, while there is an option in **phonopy** (non-analytic correction) to also include H_{Coulomb} in the diagonalization calculation, it seems to work only at $k \gtrsim \omega$. Therefore, in our calculation, we use **phonopy** to diagonalize only H_{ph} , and include H_{Coulomb} separately.

Next, we also write the photon Hamiltonian H_{EM} in momentum space:

$$H_{\text{EM}} = \int \frac{d^3k}{(2\pi)^3} \left[\frac{1}{2} \tilde{\mathbf{P}}(\mathbf{k})^* \cdot \boldsymbol{\epsilon}^{-1} \cdot \tilde{\mathbf{P}}(\mathbf{k}) + \frac{1}{2} \tilde{\mathbf{A}}(\mathbf{k})^* \cdot \mathbf{K}^2 \cdot \tilde{\mathbf{A}}(\mathbf{k}) \right], \quad (\text{G.16})$$

where

$$\mathbf{K}^2 = k^2 \mathbb{1} + \frac{e^2}{\Omega} \sum_j \frac{\mathbf{Z}_j^* \mathbf{Z}_j^{*T}}{m_j} - \mathbf{k} \mathbf{k}. \quad (\text{G.17})$$

We decompose the photon field $\tilde{\mathbf{A}}$ into two orthogonal linear polarizations $\mathbf{e}_{1,\mathbf{k}} \perp \mathbf{e}_{2,\mathbf{k}}$ which satisfy the gauge condition, $\mathbf{k} \cdot \boldsymbol{\epsilon} \cdot \mathbf{e}_{\lambda,\mathbf{k}} = 0$ ($\lambda = 1, 2$). We choose the basis in which the projection of $\boldsymbol{\epsilon}$ onto the two-dimensional subspace, $\boldsymbol{\epsilon}_{\lambda'} \cdot \boldsymbol{\epsilon} \cdot \mathbf{e}_{\lambda}$, is diagonal, with eigenvalues $\varepsilon_1, \varepsilon_2$. Denote the projection of \mathbf{K}^2 in this basis by

$$\mathbf{e}_{\lambda',\mathbf{k}}^* \cdot \mathbf{K}^2 \cdot \mathbf{e}_{\lambda,\mathbf{k}} \equiv K_{\lambda'\lambda}^2. \quad (\text{G.18})$$

We introduce phonon creation and annihilation operators $\hat{b}_{\lambda,\mathbf{k}}^\dagger, \hat{b}_{\lambda,\mathbf{k}}$ satisfying the usual (discretized) commutation relations, $[\hat{b}_{\lambda,\mathbf{k}}, \hat{b}_{\lambda',\mathbf{k}'}^\dagger] = \delta_{\lambda,\lambda'} \delta_{\mathbf{k},\mathbf{k}'}$, etc., based on the diagonal piece of the Hamiltonian:

$$\tilde{\mathbf{A}}(\mathbf{k}) = \sqrt{N\Omega} \sum_{\lambda} \frac{1}{\sqrt{2\varepsilon_{\lambda}^{1/2} K_{\lambda\lambda}}} (\hat{b}_{\lambda,\mathbf{k}} + \hat{b}_{\lambda,-\mathbf{k}}^\dagger) \mathbf{e}_{\lambda,\mathbf{k}}, \quad (\text{G.19})$$

$$\tilde{\mathbf{P}}(\mathbf{k}) = \sqrt{N\Omega} \sum_{\lambda} \sqrt{\frac{\varepsilon_{\lambda}^{1/2} K_{\lambda\lambda}}{2}} \frac{1}{i} (\hat{b}_{\lambda,\mathbf{k}} - \hat{b}_{\lambda,-\mathbf{k}}^\dagger) \mathbf{e}_{\lambda,\mathbf{k}}. \quad (\text{G.20})$$

The photon Hamiltonian then becomes

$$H_{\text{EM}} = \sum_{\mathbf{k}} \left[\sum_{\lambda=1}^2 \frac{K_{\lambda\lambda}}{\sqrt{\varepsilon_{\lambda}}} \hat{b}_{\lambda,\mathbf{k}}^\dagger \hat{b}_{\lambda,\mathbf{k}} + \frac{K_{12}^2}{2\sqrt{\varepsilon_1 \varepsilon_2} K_{11} K_{22}} (\hat{b}_{1,-\mathbf{k}} + \hat{b}_{1,\mathbf{k}}^\dagger) (\hat{b}_{2,\mathbf{k}} + \hat{b}_{2,-\mathbf{k}}^\dagger) \right], \quad (\text{G.21})$$

where we have used $K_{12} = K_{21}$.

Finally, the photon-phonon mixing term H_{mix} can be written in terms of the creation and annihilation operators according to Eqs. (6.12) and (G.19):

$$\begin{aligned} H_{\text{mix}} &= -\frac{e}{N\Omega} \sum_{\mathbf{k}} \sum_{l_j} \frac{e^{i\mathbf{k}\cdot\mathbf{x}_{l_j}^0}}{m_j} \tilde{\mathbf{A}}(\mathbf{k}) \cdot \mathbf{Z}_j^* \cdot \mathbf{p}_{l_j} \\ &= \frac{ie}{2\sqrt{\Omega}} \sum_{\mathbf{k}} \sum_{\nu=1}^{3n} \sum_{\lambda=1}^2 \sqrt{\frac{\omega_{\nu,\mathbf{k}}}{\varepsilon_{\lambda}^{1/2} K_{\lambda\lambda}}} (\mathbf{e}_{\lambda,-\mathbf{k}} \cdot \boldsymbol{\xi}_{\nu,\mathbf{k}}) (\hat{a}_{\nu,\mathbf{k}} - \hat{a}_{\nu,-\mathbf{k}}^\dagger) (\hat{b}_{\lambda,-\mathbf{k}} + \hat{b}_{\lambda,\mathbf{k}}^\dagger). \end{aligned} \quad (\text{G.22})$$

The total quadratic Hamiltonian, given by the sum of Eqs. (G.11), Eqs. (G.14), Eqs. (G.21) and Eqs. (G.22), involves the $3n$ phonon and 2 photon creation/annihilation operators, $\hat{a}_{\nu=(1,\dots,3n),\mathbf{k}}^{(\dagger)}$, $\hat{b}_{\lambda=(1,2),\mathbf{k}}^{(\dagger)}$. For simplicity, let us write $\hat{a}_{\nu=(3n+1,3n+2),\mathbf{k}}^{(\dagger)} \equiv \hat{b}_{\lambda=(1,2),\mathbf{k}}^{(\dagger)}$. The quadratic Hamiltonian then has the form:

$$\hat{H} = \sum_{\mathbf{k} \in \text{1BZ}} \mathfrak{a}_{\mathbf{k}}^\dagger \cdot \mathfrak{h}_{\mathbf{k}} \cdot \mathfrak{a}_{\mathbf{k}} \quad \text{with} \quad \mathfrak{a}_{\mathbf{k}} = \left[\hat{a}_{1,\mathbf{k}}, \dots, \hat{a}_{3n+2,\mathbf{k}}, \hat{a}_{1,-\mathbf{k}}^\dagger, \dots, \hat{a}_{3n+2,-\mathbf{k}}^\dagger \right]^\text{T}. \quad (\text{G.23})$$

The matrix $\mathfrak{h}_{\mathbf{k}}$ can be written as:

$$\mathfrak{h}_{\mathbf{k}} = \left(\begin{array}{c|c|c|c} \mathbb{A}_{\mathbf{k}} & \mathbb{B}_{\mathbf{k}}^* & \mathbb{A}_{\mathbf{k}} & \mathbb{B}_{\mathbf{k}}^\dagger \\ \mathbb{B}_{\mathbf{k}}^\text{T} & \mathbb{C}_{\mathbf{k}} & -\mathbb{B}_{\mathbf{k}}^\text{T} & \mathbb{C}_{\mathbf{k}} \\ \hline \mathbb{A}_{\mathbf{k}} & \mathbb{B}_{-\mathbf{k}} & \mathbb{A}_{\mathbf{k}} & \mathbb{B}_{-\mathbf{k}} \\ \mathbb{B}_{\mathbf{k}}^\text{T} & \mathbb{C}_{\mathbf{k}} & -\mathbb{B}_{\mathbf{k}}^\text{T} & \mathbb{C}_{\mathbf{k}} \end{array} \right), \quad (\text{G.24})$$

where $\mathbb{A}_{\mathbf{k}}$ is a $3n \times 3n$ matrix given by:

$$\mathbb{A}_{\mathbf{k},\nu\nu'} = \frac{1}{2} \omega_{\nu} \delta_{\nu\nu'} + \frac{e^2}{4\Omega \sqrt{\omega_{\nu,\mathbf{k}} \omega_{\nu',\mathbf{k}}}} \frac{(\mathbf{k} \cdot \boldsymbol{\xi}_{\nu,\mathbf{k}}^*)(\mathbf{k} \cdot \boldsymbol{\xi}_{\nu',\mathbf{k}})}{\mathbf{k} \cdot \boldsymbol{\varepsilon} \cdot \mathbf{k}}, \quad (\text{G.25})$$

while $\mathbb{B}_{\mathbf{k}}$ is a $3n \times 2$ with the following structure

$$\mathbb{B}_{\mathbf{k},\nu\nu'} = -\sum_{\lambda=1}^2 \frac{ie}{4\sqrt{\Omega}} \sqrt{\frac{\omega_{\nu,\mathbf{k}}}{\varepsilon_{\nu'}^{1/2} K_{\nu'\nu'}}} (\boldsymbol{\xi}_{\nu,\mathbf{k}} \cdot \mathbf{e}_{\nu',-\mathbf{k}}), \quad (\text{G.26})$$

and $\mathbb{C}_{\mathbf{k},\nu\nu'}$ is a 2×2 matrix given by

$$\mathbb{C}_{\mathbf{k},\nu\nu'} = \frac{K_{\nu\nu'}^2}{4\sqrt{\varepsilon_{\nu}\varepsilon_{\nu'}K_{\nu\nu}K_{\nu'\nu'}}}. \quad (\text{G.27})$$

We review a general algorithm for diagonalizing such Hamiltonians in Appendix I.

GENERAL FORM OF THE MAGNON HAMILTONIAN

In this appendix, by following Ref. [268], we review the procedure to derive the quadratic Hamiltonian describing small fluctuations around the ground state of the spin lattice described by Eq. (6.19).¹ The results we review will apply to both commensurate and single- Q incommensurate materials (such as $\text{Ba}_3\text{NbFe}_3\text{Si}_2\text{O}_{14}$ discussed in Sec. 6.3). We conclude the appendix giving the generalization of the rate in Eq. (6.27) for the case of incommensurate materials.

To include in our discussion the case of single- Q incommensurate materials, we need to generalize Eq. (6.20) to

$$\mathbf{S}_{lj} = \mathbf{R}'(\mathbf{x}_{lj}) \cdot \mathbf{R}_j \cdot \mathbf{S}'_{lj}, \quad (\text{H.1})$$

where the additional rotation $\mathbf{R}'(\mathbf{x}_{lj})$ brings to a reference frame where the spin orientation looks the same in all the unit cells (for commensurate ordered materials, $\mathbf{R}' = \mathbf{1}$). Following the Holstein-Primakoff transformation, Eq. (6.21), we we can rewrite Eq. (H.1) as, at leading order,

$$\mathbf{S}_{lj} = \mathbf{R}'(\mathbf{x}_{lj}) \left[\sqrt{\frac{S_j}{2}} \left(\mathbf{r}_j^* \hat{a}_{lj} + \mathbf{r}_j \hat{a}_{lj}^\dagger \right) + \mathbf{t}_j \left(S_j - \hat{a}_{lj}^\dagger \hat{a}_{lj} \right) \right], \quad (\text{H.2})$$

where \mathbf{t}_j is a unit vector pointing along the direction of the j -th spin in the rotating frame (i.e., the reference frame defined by the rotation \mathbf{R}'), while \mathbf{r}_j and \mathbf{r}_j^* span an orthogonal coordinate system. These vectors are related to the components of the matrix \mathbf{R}_j by

$$\mathbf{r}_j^\alpha = \mathbf{R}_j^{\alpha 1} + i\mathbf{R}_j^{\alpha 2} \quad \mathbf{t}_j^\alpha = \mathbf{R}_j^{\alpha 3}. \quad (\text{H.3})$$

By substituting Eq. (H.2) into Eq. (6.19), and going to momentum space, we obtain the following expression for the quadratic part of the Hamiltonian

$$\hat{H} = \sum_{\mathbf{k} \in \text{IBZ}} \mathfrak{a}_{\mathbf{k}}^\dagger \cdot \mathfrak{h}_{\mathbf{k}} \cdot \mathfrak{a}_{\mathbf{k}} \quad \text{with} \quad \mathfrak{a}_{\mathbf{k}} = \left[\hat{a}_{1,\mathbf{k}}, \dots, \hat{a}_{n,\mathbf{k}}, \hat{a}_{1,-\mathbf{k}}^\dagger, \dots, \hat{a}_{n,-\mathbf{k}}^\dagger \right]^\text{T}. \quad (\text{H.4})$$

The matrix $\mathfrak{h}_{\mathbf{k}}$ can be written in terms of $n \times n$ sub-matrices as:

$$\mathfrak{h}_{\mathbf{k}} = \begin{pmatrix} \mathbb{A}_{\mathbf{k}} - \mathbb{C} & \mathbb{B}_{\mathbf{k}} \\ \mathbb{B}_{\mathbf{k}}^\dagger & \mathbb{A}_{-\mathbf{k}}^* - \mathbb{C} \end{pmatrix} \quad (\text{H.5})$$

¹We adopt a different phase convention compared to Ref. [268], by using $e^{i\mathbf{k} \cdot \mathbf{x}_{lj}}$ as oppose to $e^{i\mathbf{k} \cdot \mathbf{x}_l}$, in the Fourier transform Eq. (F.3).

where, by defining $\mathbf{J}'_{lj,l'j'} = \mathbf{R}'(\mathbf{x}_{lj})^\top \cdot \mathbf{J}_{lj,l'j'} \cdot \mathbf{R}'(\mathbf{x}_{l'j'})$, we have

$$\begin{aligned} \mathbb{A}_{\mathbf{k},jj'} &= \mathbb{A}_{\mathbf{k},jj'}^\dagger = \frac{\sqrt{S_j S_{j'}}}{2} \mathbf{r}_j^\top \cdot \mathbf{J}'_{-\mathbf{k},jj'} \cdot \mathbf{r}_{j'}^* - \frac{1}{2} \mu_B \delta_{jj'} \mathbf{B}^\top \cdot g_j \cdot \mathbf{t}_j \\ \mathbb{B}_{\mathbf{k},jj'} &= \mathbb{B}_{\mathbf{k},jj'}^* = \frac{\sqrt{S_j S_{j'}}}{2} \mathbf{r}_j^\top \cdot \mathbf{J}'_{-\mathbf{k},jj'} \cdot \mathbf{r}_{j'} \\ \mathbb{C}_{\mathbf{k},jj'} &= \delta_{jj'} \sum_l S_l \mathbf{t}_j^\top \cdot \mathbf{J}'_{jl}(0) \cdot \mathbf{t}_l \end{aligned} \quad (\text{H.6})$$

The procedure to diagonalize Hamiltonian of this kind is reviewed in Appendix I.

We conclude by generalizing to the incommensurate case the formula for magnon production given in Eq. (6.27). We start by writing the rotation matrix $\mathbf{R}'(\mathbf{x}_{lj})$ in terms of the propagation vector which characterizes the incommensurate order $\mathbf{Q} = (\tau_1, \tau_2, \tau_3)$:

$$\mathbf{R}'(\mathbf{x}_{lj}) = \mathcal{R}(\mathbf{n} | \mathbf{Q} \cdot \mathbf{x}_{lj}), \quad (\text{H.7})$$

where $\mathcal{R}(\mathbf{n} | \varphi)$ is the rotation matrix around the unit vector \mathbf{n} by an angle φ :

$$\mathcal{R}(\mathbf{n} | \varphi) = \text{Re}[e^{i\varphi}(\mathbf{1} - i\mathbf{n}_\times - \mathbf{n}\mathbf{n}^T)] + \mathbf{n}\mathbf{n}^T = \mathbf{R}'_0 + \mathbf{R}'_+ e^{i\varphi} + \mathbf{R}'_- e^{-i\varphi} \quad (\text{H.8})$$

$$\mathbf{R}'_0 = \mathbf{n}\mathbf{n}^T, \quad \mathbf{R}'_\pm = \frac{1}{2}(\mathbf{1} \mp i\mathbf{n}_\times - \mathbf{n}\mathbf{n}^T), \quad \mathbf{n}_\times = \begin{pmatrix} 0 & -n_z & n_y \\ n_z & 0 & -n_x \\ -n_y & n_x & 0 \end{pmatrix}, \quad (\text{H.9})$$

noting that $\mathbf{n}_\times \cdot \mathbf{v} = \mathbf{n} \times \mathbf{v}$ for any vector \mathbf{v} . Then, by using Eq. (H.1) and the interaction given by Eq. (6.4), we find

$$\begin{aligned} \langle \nu, \mathbf{k} | \delta \hat{H}_0 | 0 \rangle &= \sum_{lj} \sqrt{\frac{S_j}{2N}} e^{-i\mathbf{k} \cdot \mathbf{x}_{lj}} \mathbf{f}_j \cdot \mathbf{R}'(\mathbf{x}_{lj}) \cdot (\mathbb{V}_{j\nu, -\mathbf{k}} \mathbf{r}_j^* + \mathbb{U}_{j\nu, \mathbf{k}}^* \mathbf{r}_j) \\ &= \sqrt{\frac{N}{2}} \sum_j \sqrt{S_j} \mathbf{f}_j \cdot (\delta_{\mathbf{k}, 0} \mathbf{R}'_0 + \delta_{\mathbf{k}, \mathbf{Q}} \mathbf{R}'_+ + \delta_{\mathbf{k}, -\mathbf{Q}} \mathbf{R}'_-) \cdot (\mathbb{V}_{j\nu, -\mathbf{k}} \mathbf{r}_j^* + \mathbb{U}_{j\nu, \mathbf{k}}^* \mathbf{r}_j), \end{aligned} \quad (\text{H.10})$$

from which we can obtain the generalized expression for the rate:

$$R_{\mathbf{Q} \neq 0} = \frac{2\omega}{m_{\text{cell}}} \sum_{\nu=1}^n \sum_{\lambda=-1}^1 \frac{\omega_{\nu, \lambda \mathbf{Q}} \gamma_{\nu, \lambda \mathbf{Q}}}{(\omega^2 - \omega_{\nu, \lambda \mathbf{Q}}^2)^2 + (\omega \gamma_{\nu, \lambda \mathbf{Q}})^2} \left| \sum_j \sqrt{S_j} \mathbf{f}_j^T \mathbf{R}'_\lambda (\mathbb{V}_{j\nu, -\lambda \mathbf{Q}} \mathbf{r}_j^* + \mathbb{U}_{j\nu, \lambda \mathbf{Q}}^* \mathbf{r}_j) \right|^2. \quad (\text{H.11})$$

Appendix I

DIAGONALIZATION OF QUADRATIC HAMILTONIANS

In this appendix, by closely following Ref. [268, 298], we review the procedure to diagonalize quadratic Hamiltonians which have the form of Eq. (G.23) and Eq. (H.4). The goal of the procedure is to find a homogeneous linear transformation

$$\mathfrak{a}_{\mathbf{k}} = \mathbb{T}_{\mathbf{k}} \cdot \mathfrak{a}'_{\mathbf{k}} \equiv \mathbb{T}_{\mathbf{k}} \cdot \left[\hat{a}'_{1,\mathbf{k}}, \dots, \hat{a}'_{n,\mathbf{k}}, \hat{a}'_{1,-\mathbf{k}}, \dots, \hat{a}'_{n,-\mathbf{k}} \right]^{\top}, \quad (\text{I.1})$$

such that the operators $\hat{a}'_{\nu,\mathbf{k}}, \hat{a}'_{\nu,\mathbf{k}}^{\dagger}$ satisfy the canonical commutation relations

$$[\mathfrak{a}'_{\mathbf{k}}, \mathfrak{a}'_{\mathbf{k}}^{\dagger}] = \begin{pmatrix} \mathbb{1} & 0 \\ 0 & -\mathbb{1} \end{pmatrix} \equiv \mathfrak{g}, \quad (\text{I.2})$$

and that rewrites the quadratic Hamiltonian as

$$\hat{H} = \sum_{\mathbf{k}} \mathfrak{a}_{\mathbf{k}}^{\dagger} \mathfrak{h}_{\mathbf{k}} \mathfrak{a}_{\mathbf{k}} = \sum_{\mathbf{k}} \mathfrak{a}'_{\mathbf{k}}^{\dagger} \cdot \mathbb{E} \cdot \mathfrak{a}'_{\mathbf{k}}, \quad (\text{I.3})$$

where

$$\mathbb{E}_{\mathbf{k}} \equiv \mathbb{T}_{\mathbf{k}}^{\dagger} \cdot \mathfrak{h}_{\mathbf{k}} \cdot \mathbb{T}_{\mathbf{k}} = \frac{1}{2} \text{diag}(\omega_{1,\mathbf{k}} \dots \omega_{n,\mathbf{k}}, \omega_{1,\mathbf{k}} \dots \omega_{n,\mathbf{k}}) \quad \text{with} \quad \omega_{\nu,\mathbf{k}} > 0. \quad (\text{I.4})$$

By using the commutation relations in Eq. (I.2), it can be easily shown that, up to constant terms, Eq. (I.3) is equivalent to Eq. (6.14) and Eq. (6.23) with the \mathbb{U} and \mathbb{V} matrices implicitly defined as

$$\mathbb{T}_{\mathbf{k}} = \begin{pmatrix} \mathbb{U}_{j\nu,\mathbf{k}} & \mathbb{V}_{j\nu,\mathbf{k}} \\ \mathbb{V}_{j\nu,-\mathbf{k}}^* & \mathbb{U}_{j\nu,-\mathbf{k}}^* \end{pmatrix}. \quad (\text{I.5})$$

Such diagonalization procedure (usually called para-unitary diagonalization) can be achieved if $\mathfrak{h}(\mathbf{k})$ is positive definite. If the spectrum contains zero energy modes, the $\mathfrak{h}(\mathbf{k})$ matrix will be positive *semidefinite* and such para-unitary diagonalization may not exist. This problem can be cured by adding a small ϵ value to the diagonal components of $\mathfrak{h}(\mathbf{k})$ [298]. This introduces a small and negligible shift in the spectrum but makes $\mathfrak{h}(\mathbf{k})$ positive definite and allows for a para-unitary diagonalization. Ref. [298] provides a simple three-step algorithm to find the linear transformation \mathbb{T} and the associated eigenvalues:

- A Cholesky decomposition is applied to find a complex matrix $\mathbb{K}_{\mathbf{k}}$ such that $\mathfrak{h}_{\mathbf{k}} = \mathbb{K}_{\mathbf{k}}^{\dagger} \mathbb{K}_{\mathbf{k}}$.

- The eigenvalue problem for the Hermitian matrix $\mathbb{K}_k \mathfrak{g} \mathbb{K}_k^\dagger$ is solved, and the resulting eigenvalues used to form the columns of the matrix \mathbb{U}_k . The order of the columns is chosen such that the first N elements of the diagonalized matrix $\mathbb{L} = \mathbb{U}^\dagger \mathbb{K}_k \mathfrak{g} \mathbb{K}_k^\dagger \mathbb{U}$ are positive and the last N negative.
- Finally, the matrix \mathbb{E}_k in Eq. (I.4) is simply related to \mathbb{L}_k by $\mathbb{E}_k = \mathfrak{g} \mathbb{L}_k$, and the \mathbb{T}_k matrix is given by $\mathbb{T}_k = \mathbb{K}_k^{-1} \mathbb{U}_k \mathbb{E}_k^{1/2}$.

A p p e n d i x J

NONRELATIVISTIC MATCHING FOR A FERMION FIELD

In this appendix, we review the procedure of decomposing a Dirac fermion field ψ in the NR limit. Consider the following unperturbed relativistic Lagrangian:

$$\mathcal{L}_0 = \bar{\psi} i(\partial_\mu - iA_\mu)\gamma^\mu\psi - m_\psi\bar{\psi}\psi. \quad (\text{J.1})$$

In free space, we would expand the ψ field in plane waves multiplied by the usual u, v spinors satisfying the free particle Dirac equation. Here, we allow the presence of an external gauge potential $A^\mu = (\Phi, \mathbf{A})$, which may not be a small perturbation. For example, if ψ is an electron in a crystal, it is bound by the electromagnetic potential from the ions, and the bound state wavefunctions are very different from plane waves. Generally, we can expand the ψ field in the basis of energy eigenstate wavefunctions. Dropping the antiparticle part, we have

$$\psi(\mathbf{x}, t) = \sum_I u_I(\mathbf{x}, t) \hat{b}_I = \sum_I e^{-iE_I t} u_I(\mathbf{x}) \hat{b}_I, \quad (\text{J.2})$$

where the c -number u_I spinors satisfy

$$(E_I\gamma^0 - i\boldsymbol{\gamma} \cdot \nabla - m_\psi - \gamma^0\Phi(\mathbf{x}) + \boldsymbol{\gamma} \cdot \mathbf{A}(\mathbf{x})) u_I(\mathbf{x}) = 0. \quad (\text{J.3})$$

Writing

$$u_I(\mathbf{x}) = \frac{1}{\sqrt{2}} \begin{pmatrix} \Psi_I(\mathbf{x}) + \Theta_I(\mathbf{x}) \\ \Psi_I(\mathbf{x}) - \Theta_I(\mathbf{x}) \end{pmatrix}, \quad (\text{J.4})$$

with Ψ_I, Θ_I two-component wavefunctions, we see that Eq. (J.3) is solved by

$$\Theta_I(\mathbf{x}) = \frac{i\boldsymbol{\sigma} \cdot (\nabla - i\mathbf{A}(\mathbf{x}))}{E_I + m_\psi - \Phi(\mathbf{x})} \Psi_I(\mathbf{x}). \quad (\text{J.5})$$

This immediately leads to Eq. (7.8), repeated here for easy reference:

$$\psi(\mathbf{x}, t) = e^{-im_\psi t} \frac{1}{\sqrt{2}} \begin{pmatrix} \left(1 - \frac{\boldsymbol{\sigma} \cdot \mathbf{k}}{2m_\psi + \varepsilon}\right) \psi^+(\mathbf{x}, t) \\ \left(1 + \frac{\boldsymbol{\sigma} \cdot \mathbf{k}}{2m_\psi + \varepsilon}\right) \psi^+(\mathbf{x}, t) \end{pmatrix}, \quad (\text{J.6})$$

where $\mathbf{k} = -i\nabla - \mathbf{A}$, $\varepsilon = i\partial_t - \Phi$, and $\psi^+(\mathbf{x}, t) = \sum_I e^{-i\varepsilon_I t} \Psi_I(\mathbf{x}) \hat{b}_I$ with $\varepsilon_I = E_I - m_\psi$. The prefactor has been chosen such that the NR field ψ^\pm 's kinetic term is normalized at leading order as in Eq. (7.11).

In the NR limit, $|\Theta_I| \ll |\Phi_I|$. The large component Ψ_I satisfies

$$\left[-\boldsymbol{\sigma} \cdot (\nabla - i\mathbf{A}(\mathbf{x})) \frac{1}{2m_\psi + \varepsilon_I - \Phi(\mathbf{x})} \boldsymbol{\sigma} \cdot (\nabla - i\mathbf{A}(\mathbf{x})) + \Phi(\mathbf{x}) \right] \Psi_I(\mathbf{x}) = \varepsilon_I \Psi_I(\mathbf{x}). \quad (\text{J.7})$$

At leading order, we replace $\frac{1}{2m_\psi + \varepsilon_I - \Phi(\mathbf{x})} \rightarrow \frac{1}{2m_\psi}$, and recover the NR Schrödinger equation:

$$\left[-\frac{(\nabla - i\mathbf{A}(\mathbf{x}))^2}{2m_\psi} + \frac{1}{2m_\psi} \boldsymbol{\sigma} \cdot (\nabla \times \mathbf{A}(\mathbf{x})) + \Phi(\mathbf{x}) \right] \Psi_I(\mathbf{x}) = \varepsilon_I \Psi_I(\mathbf{x}). \quad (\text{J.8})$$

Corrections to this equation can be incorporated order by order if needed.

PROJECTION OF ANGULAR MOMENTUM OPERATORS

In this appendix, we detail the steps that lead to the numbers $\lambda_{S,j} = -\frac{1}{3}$, $\lambda_{L,j} = -\frac{4}{3}$ in the case of α -RuCl₃, following the projection of angular momentum operators \mathbf{S}_e , \mathbf{L}_e in Eq. (7.36). The formation of effective ionic spins $S_j = \frac{1}{2}$ is due to the combined effect of crystal fields and spin-orbit coupling [325]. First, octahedral crystal fields split the five degenerate $3d$ orbitals ($\ell = 2$) of Ru³⁺ into two higher-energy e_g orbitals and three lower-energy t_{2g} orbitals with an effective orbital moment $\ell_{\text{eff}} = 1$. The energy difference between the e_g and t_{2g} orbitals is $\mathcal{O}(\text{eV})$, rendering the (unoccupied) e_g orbitals irrelevant for the discussion. For the t_{2g} orbitals, spin-orbit coupling further splits these $\ell_{\text{eff}} = 1$ states into $j_{\text{eff}} = \frac{3}{2}$ and $\frac{1}{2}$. With five $3d$ electrons, the lower-energy $j_{\text{eff}} = \frac{3}{2}$ states are fully occupied, while the higher-energy $j_{\text{eff}} = \frac{1}{2}$ Kramers doublet is occupied by a single electron — it is this electron that contributes to the magnetic order. Therefore, the goal is to project the angular momentum operators \mathbf{S} , \mathbf{L} (dropping subscript e from here on for simplicity) onto the $j_{\text{eff}} = \frac{1}{2}$ subspace.

The first step is to project \mathbf{L} onto the t_{2g} subspace. The t_{2g} states are denoted by d_{yz} , d_{zx} , d_{xy} . The angular part of their wavefunctions are linear combinations of spherical harmonics $Y_{\ell=2}^m(\theta, \phi)$ (see e.g., Ref. [263]); equivalently, these t_{2g} states are linear combinations of $|\ell, m_\ell\rangle$ states with $\ell = 2$:

$$|d_{yz}\rangle = \frac{i}{\sqrt{2}}(|2, 1\rangle + |2, -1\rangle), \quad |d_{zx}\rangle = -\frac{1}{\sqrt{2}}(|2, 1\rangle - |2, -1\rangle), \quad |d_{xy}\rangle = -\frac{i}{\sqrt{2}}(|2, 2\rangle - |2, -2\rangle). \quad (\text{K.1})$$

To compute $\mathcal{P}_{t_{2g}} \mathbf{L} \mathcal{P}_{t_{2g}}$, with the projection operator

$$\mathcal{P}_{t_{2g}} = |d_{yz}\rangle\langle d_{yz}| + |d_{zx}\rangle\langle d_{zx}| + |d_{xy}\rangle\langle d_{xy}|, \quad (\text{K.2})$$

we make use of the familiar formulae

$$\langle \ell', m'_\ell | L_z | \ell, m_\ell \rangle = m_\ell \delta_{\ell', \ell} \delta_{m'_\ell, m_\ell}, \quad \langle \ell', m'_\ell | L_\pm | \ell, m_\ell \rangle = \sqrt{(\ell \mp m_\ell)(\ell \pm m_\ell + 1)} \delta_{\ell', \ell} \delta_{m'_\ell, m_\ell \pm 1}, \quad (\text{K.3})$$

where $L_\pm = L_x \pm iL_y$, and obtain, for the matrix representation in the $|d_{yz}\rangle$, $|d_{zx}\rangle$, $|d_{xy}\rangle$ basis:

$$\mathcal{P}_{t_{2g}} L_z \mathcal{P}_{t_{2g}} \doteq \begin{pmatrix} 0 & i & 0 \\ -i & 0 & 0 \\ 0 & 0 & 0 \end{pmatrix}, \quad \mathcal{P}_{t_{2g}} L_\pm \mathcal{P}_{t_{2g}} \doteq \begin{pmatrix} 0 & 0 & \pm 1 \\ 0 & 0 & i \\ \mp 1 & -i & 0 \end{pmatrix}. \quad (\text{K.4})$$

These might not look familiar, but they are nothing but $\ell = 1$ angular momentum operators in the $|p_x\rangle, |p_y\rangle, |p_z\rangle$ basis, which is related to the $|\ell, m_\ell\rangle$ basis with $\ell = 1$ by [263]

$$|p_x\rangle = -\frac{1}{\sqrt{2}}(|1, 1\rangle - |1, -1\rangle), \quad |p_y\rangle = \frac{i}{\sqrt{2}}(|1, 1\rangle + |1, -1\rangle), \quad |p_z\rangle = |1, 0\rangle. \quad (\text{K.5})$$

The angular momentum operators in this basis read

$$L_z \doteq \begin{pmatrix} 0 & -i & 0 \\ i & 0 & 0 \\ 0 & 0 & 0 \end{pmatrix}, \quad L_\pm \doteq \begin{pmatrix} 0 & 0 & \mp 1 \\ 0 & 0 & -i \\ \pm 1 & i & 0 \end{pmatrix}. \quad (\text{K.6})$$

Comparing Eq. (K.4) and (K.6), we see that \mathbf{L} acts as an effective angular momentum with $\ell = 1$ on the t_{2g} subspace:

$$\mathcal{P}_{t_{2g}} \mathbf{L} \mathcal{P}_{t_{2g}} = -\mathbf{L}_{\text{eff}}^{(\ell=1)}. \quad (\text{K.7})$$

The second step is to combine this effective orbital angular momentum $\ell_{\text{eff}} = 1$ with the electron's spin $s = \frac{1}{2}$. This follows the standard angular momentum addition, and we obtain, for the $j_{\text{eff}} = \frac{1}{2}$ states:

$$|j_{\text{eff}} = \frac{1}{2}, m_{j_{\text{eff}}} = \frac{1}{2}\rangle = \sqrt{\frac{2}{3}} |m_{\ell_{\text{eff}}} = 1, m_s = -\frac{1}{2}\rangle - \sqrt{\frac{1}{3}} |m_{\ell_{\text{eff}}} = 0, m_s = \frac{1}{2}\rangle, \quad (\text{K.8})$$

$$|j_{\text{eff}} = \frac{1}{2}, m_{j_{\text{eff}}} = -\frac{1}{2}\rangle = \sqrt{\frac{1}{3}} |m_{\ell_{\text{eff}}} = 0, m_s = -\frac{1}{2}\rangle - \sqrt{\frac{2}{3}} |m_{\ell_{\text{eff}}} = -1, m_s = \frac{1}{2}\rangle, \quad (\text{K.9})$$

where the coefficients are Clebsch-Gordan coefficients. It is now straightforward to project \mathbf{L}_{eff} and \mathbf{S} onto the $j_{\text{eff}} = \frac{1}{2}$ subspace:

$$\mathcal{P}_{j_{\text{eff}}=\frac{1}{2}} L_z^{\text{eff}} \mathcal{P}_{j_{\text{eff}}=\frac{1}{2}} \doteq \begin{pmatrix} \frac{2}{3} & 0 \\ 0 & -\frac{2}{3} \end{pmatrix}, \quad \mathcal{P}_{j_{\text{eff}}=\frac{1}{2}} L_+^{\text{eff}} \mathcal{P}_{j_{\text{eff}}=\frac{1}{2}} \doteq \begin{pmatrix} 0 & \frac{4}{3} \\ 0 & 0 \end{pmatrix}, \quad (\text{K.10})$$

$$\mathcal{P}_{j_{\text{eff}}=\frac{1}{2}} S_z \mathcal{P}_{j_{\text{eff}}=\frac{1}{2}} \doteq \begin{pmatrix} -\frac{1}{6} & 0 \\ 0 & \frac{1}{6} \end{pmatrix}, \quad \mathcal{P}_{j_{\text{eff}}=\frac{1}{2}} S_+ \mathcal{P}_{j_{\text{eff}}=\frac{1}{2}} \doteq \begin{pmatrix} 0 & -\frac{1}{3} \\ 0 & 0 \end{pmatrix}. \quad (\text{K.11})$$

We see that both \mathbf{L}_{eff} and \mathbf{S} are proportional to $\mathbf{J}_{\text{eff}} = \frac{\sigma}{2}$ (identified as the total ionic spin as discussed above) when acting on the $j_{\text{eff}} = \frac{1}{2}$ subspace. So finally, we obtain

$$\mathcal{P}_{j_{\text{eff}}=\frac{1}{2}} \mathbf{L} \mathcal{P}_{j_{\text{eff}}=\frac{1}{2}} = -\mathcal{P}_{j_{\text{eff}}=\frac{1}{2}} \mathbf{L}_{\text{eff}} \mathcal{P}_{j_{\text{eff}}=\frac{1}{2}} = -\frac{4}{3} \mathbf{J}_{\text{eff}}, \quad \mathcal{P}_{j_{\text{eff}}=\frac{1}{2}} \mathbf{S} \mathcal{P}_{j_{\text{eff}}=\frac{1}{2}} = -\frac{1}{3} \mathbf{J}_{\text{eff}}. \quad (\text{K.12})$$

A p p e n d i x L

VELOCITY INTEGRALS

When the velocity dependent rate $\Gamma(\mathbf{v})$, given by Eq. (7.45), is convoluted with the incoming DM's velocity distribution $f_\chi(\mathbf{v})$ to yield the total rate, Eq. (7.46), we encounter the following scalar, vector and tensor velocity integrals:

$$g_0(\mathbf{q}, \omega) \equiv \int d^3v f_\chi(\mathbf{v}) 2\pi\delta(\omega - \omega_{\mathbf{q}}), \quad (\text{L.1})$$

$$\mathbf{g}_1(\mathbf{q}, \omega) \equiv \int d^3v f_\chi(\mathbf{v}) 2\pi\delta(\omega - \omega_{\mathbf{q}}) \mathbf{v}', \quad (\text{L.2})$$

$$\mathbf{g}_2(\mathbf{q}, \omega) \equiv \int d^3v f_\chi(\mathbf{v}) 2\pi\delta(\omega - \omega_{\mathbf{q}}) \mathbf{v}'\mathbf{v}', \quad (\text{L.3})$$

where $\mathbf{v}' = \mathbf{v} - \frac{\mathbf{q}}{2m_\chi}$, and $\omega_{\mathbf{q}} = \mathbf{q} \cdot \mathbf{v} - \frac{q^2}{2m_\chi}$. From the expressions of differential rates $\Sigma_\nu(\mathbf{q})$ throughout Sec. 7.3, it should be easy to see how these integrals emerge. Note that for velocity-independent interactions, only the scalar integral g_0 appears [7, 28, 29].

As we now show, all three velocity integrals above can be evaluated analytically for a boosted and truncated Maxwell-Boltzmann distribution, which we assume in this work:

$$f_\chi(\mathbf{v}) = \frac{1}{N_0} e^{-(\mathbf{v}+\mathbf{v}_e)^2/v_0^2} \Theta(v_{\text{esc}} - |\mathbf{v} + \mathbf{v}_e|), \quad (\text{L.4})$$

where

$$N_0 = \pi^{3/2} v_0^2 \left[v_0 \operatorname{erf}(v_{\text{esc}}/v_0) - \frac{2v_{\text{esc}}}{\sqrt{\pi}} \exp(-v_{\text{esc}}^2/v_0^2) \right], \quad (\text{L.5})$$

and we take $v_0 = 230$ km/s, $v_{\text{esc}} = 600$ km/s, $v_e = 240$ km/s. For all the target materials considered in Sec. 7.3, the rates are insensitive to the direction of \mathbf{v}_e . The analytic results obtained here are key to efficient rate calculations, as they reduce the six-dimensional integral $\int d^3v \int d^3q$ to just a three-dimensional integral $\int d^3q$, which we then compute numerically.

First, the scalar integral g_0 follows from Refs. [7, 28, 29]. Shifting $\mathbf{v} \rightarrow \mathbf{v} - \mathbf{v}_e$, we obtain

$$\begin{aligned} g_0(\mathbf{q}, \omega) &= \frac{2\pi}{N_0} \int d^3v e^{-v^2/v_0^2} \Theta(v_{\text{esc}} - v) \delta\left(\mathbf{q} \cdot \mathbf{v} - \mathbf{q} \cdot \mathbf{v}_e - \frac{q^2}{2m_\chi} - \omega\right) \\ &= \frac{4\pi^2}{N_0} \int_0^{v_{\text{esc}}} dv v^2 e^{-v^2/v_0^2} \int_{-1}^1 d\cos\theta \delta\left(qv\cos\theta - \mathbf{q} \cdot \mathbf{v}_e - \frac{q^2}{2m_\chi} - \omega\right). \end{aligned} \quad (\text{L.6})$$

Let us define

$$v_* \equiv \frac{1}{q} \left(\mathbf{q} \cdot \mathbf{v}_e + \frac{q^2}{2m_\chi} + \omega \right), \quad v_- \equiv \min(|v_*|, v_{\text{esc}}). \quad (\text{L.7})$$

We then obtain

$$\begin{aligned}
g_0(\mathbf{q}, \omega) &= \frac{4\pi^2}{N_0 q} \int_0^{v_{\text{esc}}} dv v e^{-v^2/v_0^2} \int_{-1}^1 d\cos\theta \delta\left(\cos\theta - \frac{v_*}{v}\right) \\
&= \frac{4\pi^2}{N_0 q} \int_{v_-}^{v_{\text{esc}}} dv v e^{-v^2/v_0^2} \\
&= \frac{2\pi^2 v_0^2}{N_0 q} \left(e^{-v^2/v_0^2} - e^{-v_{\text{esc}}^2/v_0^2} \right). \tag{L.8}
\end{aligned}$$

Next, the vector integral \mathbf{g}_1 can be decomposed as

$$\mathbf{g}_1(\mathbf{q}, \omega) = \int d^3v f_\chi(\mathbf{v})(\mathbf{v} + \mathbf{v}_e) - \left(\mathbf{v}_e + \frac{\mathbf{q}}{2m_\chi} \right) g_0(\mathbf{q}, \omega). \tag{L.9}$$

The first term can be computed by shifting $\mathbf{v} \rightarrow \mathbf{v} - \mathbf{v}_e$ as before, but this time the integrand also depends on the azimuthal angle ϕ :

$$\begin{aligned}
\int d^3v f_\chi(\mathbf{v})(\mathbf{v} + \mathbf{v}_e) &= \frac{2\pi}{N_0} \int d^3v e^{-v^2/v_0^2} \Theta(v_{\text{esc}} - v) \delta\left(\mathbf{q} \cdot \mathbf{v} - \mathbf{q} \cdot \mathbf{v}_e - \frac{q^2}{2m_\chi} - \omega\right) \mathbf{v} \\
&= \frac{4\pi^2}{N_0} \int_0^{v_{\text{esc}}} dv v^3 e^{-v^2/v_0^2} \int_{-1}^1 d\cos\theta \delta\left(qv\cos\theta - \mathbf{q} \cdot \mathbf{v}_e - \frac{q^2}{2m_\chi} - \omega\right) \\
&\quad \int_0^{2\pi} \frac{d\phi}{2\pi} [\cos\theta \hat{\mathbf{q}} + \sin\theta (\cos\phi \hat{\mathbf{n}}_1 + \sin\phi \hat{\mathbf{n}}_2)] \\
&= \frac{4\pi^2}{N_0} \hat{\mathbf{q}} \int_0^{v_{\text{esc}}} dv v^3 e^{-v^2/v_0^2} \int_{-1}^1 d\cos\theta \delta\left(qv\cos\theta - \mathbf{q} \cdot \mathbf{v}_e - \frac{q^2}{2m_\chi} - \omega\right) \cos\theta \\
&= \frac{4\pi^2}{N_0 q} \hat{\mathbf{q}} \int_0^{v_{\text{esc}}} dv v^2 e^{-v^2/v_0^2} \int_{-1}^1 d\cos\theta \delta\left(\cos\theta - \frac{v_*}{v}\right) \cos\theta \\
&= \frac{4\pi^2 v_*}{N_0 q} \hat{\mathbf{q}} \int_{v_-}^{v_{\text{esc}}} dv v e^{-v^2/v_0^2} = v_* \hat{\mathbf{q}} g_0(\mathbf{q}, \omega), \tag{L.10}
\end{aligned}$$

where $\hat{\mathbf{n}}_1, \hat{\mathbf{n}}_2$ are orthogonal unit vectors in the plane perpendicular to \mathbf{q} . Plugging in the definition of v_* in Eq. (L.7), we obtain

$$\mathbf{g}_1(\mathbf{q}, \omega) = \left[\frac{\omega}{q} \hat{\mathbf{q}} - (\mathbb{1} - \hat{\mathbf{q}}\hat{\mathbf{q}}) \cdot \mathbf{v}_e \right] g_0(\mathbf{q}, \omega). \tag{L.11}$$

Finally, we compute the tensor integral \mathbf{g}_2 , which can be similarly decomposed as

$$\begin{aligned}
\mathbf{g}_2(\mathbf{q}, \omega) &= \int d^3v f_\chi(\mathbf{v})(\mathbf{v} + \mathbf{v}_e)(\mathbf{v} + \mathbf{v}_e) - \left[\left(\mathbf{v}_e + \frac{\mathbf{q}}{2m_\chi} \right) \hat{\mathbf{q}} + \hat{\mathbf{q}} \left(\mathbf{v}_e + \frac{\mathbf{q}}{2m_\chi} \right) \right] v_* g_0(\mathbf{q}, \omega) \\
&\quad + \left(\mathbf{v}_e + \frac{\mathbf{q}}{2m_\chi} \right) \left(\mathbf{v}_e + \frac{\mathbf{q}}{2m_\chi} \right) g_0(\mathbf{q}, \omega) \\
&= \int d^3v f_\chi(\mathbf{v})(\mathbf{v} + \mathbf{v}_e)(\mathbf{v} + \mathbf{v}_e) \\
&\quad + \left\{ \left[\frac{\omega}{q} \hat{\mathbf{q}} - (\mathbb{1} - \hat{\mathbf{q}}\hat{\mathbf{q}}) \cdot \mathbf{v}_e \right] \left[\frac{\omega}{q} \hat{\mathbf{q}} - (\mathbb{1} - \hat{\mathbf{q}}\hat{\mathbf{q}}) \cdot \mathbf{v}_e \right] - v_*^2 \hat{\mathbf{q}}\hat{\mathbf{q}} \right\} g_0(\mathbf{q}, \omega), \tag{L.12}
\end{aligned}$$

where we have used Eq. (L.10). The remaining integral can be evaluated similarly to Eq. (L.10):

$$\begin{aligned}
& \int d^3v f_\chi(\mathbf{v})(\mathbf{v} + \mathbf{v}_e)(\mathbf{v} + \mathbf{v}_e) \\
&= \frac{4\pi^2}{N_0} \int_0^{v_{\text{esc}}} dv v^4 e^{-v^2/v_0^2} \int_{-1}^1 d\cos\theta \delta\left(qv\cos\theta - \mathbf{q} \cdot \mathbf{v}_e - \frac{q^2}{2m_\chi} - \omega\right) \\
&\quad \int_0^{2\pi} \frac{d\phi}{2\pi} [\cos\theta \hat{\mathbf{q}} + \sin\theta(\cos\phi \hat{\mathbf{n}}_1 + \sin\phi \hat{\mathbf{n}}_2)] \otimes [\cos\theta \hat{\mathbf{q}} + \sin\theta(\cos\phi \hat{\mathbf{n}}_1 + \sin\phi \hat{\mathbf{n}}_2)] \\
&= \frac{4\pi^2}{N_0 q} \int_0^{v_{\text{esc}}} dv v^3 e^{-v^2/v_0^2} \int_{-1}^1 d\cos\theta \delta\left(\cos\theta - \frac{v_*}{v}\right) \left[\cos^2\theta \hat{\mathbf{q}}\hat{\mathbf{q}} + \frac{1}{2}\sin^2\theta(\mathbb{1} - \hat{\mathbf{q}}\hat{\mathbf{q}})\right] \\
&= \frac{4\pi^2}{N_0 q} \int_{v_-}^{v_{\text{esc}}} dv v e^{-v^2/v_0^2} \left[v_*^2 \hat{\mathbf{q}}\hat{\mathbf{q}} + \frac{1}{2}(v^2 - v_*^2)(\mathbb{1} - \hat{\mathbf{q}}\hat{\mathbf{q}})\right] \\
&= v_*^2 \hat{\mathbf{q}}\hat{\mathbf{q}} g_0(\mathbf{q}, \omega) + (\mathbb{1} - \hat{\mathbf{q}}\hat{\mathbf{q}}) \frac{\pi^2 v_0^2}{N_0 q} \left[(v_0^2 - v_*^2 + v_-^2) e^{-v^2/v_0^2} - (v_0^2 - v_*^2 + v_{\text{esc}}^2) e^{-v_{\text{esc}}^2/v_0^2}\right] \\
&= v_*^2 \hat{\mathbf{q}}\hat{\mathbf{q}} g_0(\mathbf{q}, \omega) + (\mathbb{1} - \hat{\mathbf{q}}\hat{\mathbf{q}}) \frac{\pi^2 v_0^2}{N_0 q} \left[v_0^2 e^{-v^2/v_0^2} - (v_0^2 - v_-^2 + v_{\text{esc}}^2) e^{-v_{\text{esc}}^2/v_0^2}\right], \tag{L.13}
\end{aligned}$$

where we have used $\hat{\mathbf{n}}_1\hat{\mathbf{n}}_1 + \hat{\mathbf{n}}_2\hat{\mathbf{n}}_2 = \mathbb{1} - \hat{\mathbf{q}}\hat{\mathbf{q}}$. Therefore,

$$\begin{aligned}
\mathbf{g}_2(\mathbf{q}, \omega) &= \left[\frac{\omega}{q} \hat{\mathbf{q}} - (\mathbb{1} - \hat{\mathbf{q}}\hat{\mathbf{q}}) \cdot \mathbf{v}_e\right] \left[\frac{\omega}{q} \hat{\mathbf{q}} - (\mathbb{1} - \hat{\mathbf{q}}\hat{\mathbf{q}}) \cdot \mathbf{v}_e\right] g_0(\mathbf{q}, \omega) \\
&\quad + (\mathbb{1} - \hat{\mathbf{q}}\hat{\mathbf{q}}) \frac{\pi^2 v_0^2}{N_0 q} \left[v_0^2 e^{-v^2/v_0^2} - (v_0^2 - v_-^2 + v_{\text{esc}}^2) e^{-v_{\text{esc}}^2/v_0^2}\right]. \tag{L.14}
\end{aligned}$$

The following relations between the velocity integrals often help simplify the calculation:

$$\mathbf{q} \cdot \mathbf{g}_1(\mathbf{q}, \omega) = \omega g_0(\mathbf{q}, \omega), \quad \mathbf{q} \cdot \mathbf{g}_2(\mathbf{q}, \omega) = \mathbf{g}_2(\mathbf{q}, \omega) \cdot \mathbf{q} = \omega \mathbf{g}_1(\mathbf{q}, \omega). \tag{L.15}$$

They follow from $\mathbf{q} \cdot \mathbf{v}' = \omega_{\mathbf{q}}$, and can be easily checked using the explicit expressions above.

Appendix M

ESTIMATION OF SINGLE PHONON EXCITATION RATE IN YIG

In this appendix, we explain the analytic estimation that results in the dashed curve in Fig. 7.1. For the standard SD interaction considered in Sec. 7.3, the single phonon excitation rate is

$$\Gamma(\mathbf{v}) = \frac{4g_\chi^2 g_e^2}{m_V^4} \frac{1}{\Omega} \int \frac{d^3 q}{(2\pi)^3} \sum_\nu 2\pi \delta(\omega_{\nu, \mathbf{k}} - \omega_{\mathbf{q}}) |\mathbf{F}_{S, \nu}^{(e)}|^2, \quad (\text{M.1})$$

where

$$\mathbf{F}_{S, \nu}^{(e)}(\mathbf{q}) = \sum_{j=\text{Fe}^{3+}} e^{-W_j(\mathbf{q})} e^{i\mathbf{G} \cdot \mathbf{x}_j^0} \frac{\mathbf{q} \cdot \boldsymbol{\epsilon}_{\nu, \mathbf{k}, j}^*}{\sqrt{2m_j \omega_{\nu, \mathbf{k}}}} \langle \mathbf{S}_e \rangle_j. \quad (\text{M.2})$$

See Eqs. (7.45), (7.49) and (7.43). For YIG, ν runs from 1 to 240. However, since DM has same-sign couplings to all the Fe^{3+} ions (and zero couplings to the other ions), we expect acoustic phonons to give an $\mathcal{O}(1)$ contribution to the total rate at low momentum transfer. Further, the dot product $\mathbf{q} \cdot \boldsymbol{\epsilon}_{\nu, \mathbf{k}, j}^*$ in $\mathbf{F}_{S, \nu}^{(e)}$ singles out the longitudinal acoustic branch, $\nu = 3$, which has the following general properties at low momentum [201]:

$$\omega_{\nu=3, \mathbf{k}} \simeq c_s k, \quad \boldsymbol{\epsilon}_{\nu=3, \mathbf{k}, j} \simeq \sqrt{\frac{m_j}{m_{\text{cell}}}} \hat{\mathbf{k}}, \quad (\text{M.3})$$

where c_s is the longitudinal acoustic sound speed. Also, we can set $\mathbf{G} = \mathbf{0}$, $\mathbf{k} = \mathbf{q}$, and $W_j \simeq 0$ at low q . Therefore,

$$\mathbf{F}_{S, \nu=3}^{(e)}(\mathbf{q}) \simeq \sqrt{\frac{q}{2m_{\text{cell}} c_s}} \sum_{j=\text{Fe}^{3+}} \langle \mathbf{S}_e \rangle_j = \sqrt{\frac{q}{2m_{\text{cell}} c_s}} \mathbf{S}_{\text{cell}}, \quad (\text{M.4})$$

and the velocity-dependent rate becomes

$$\begin{aligned} \Gamma(\mathbf{v}) &\simeq \frac{g_\chi^2 g_e^2}{m_V^4} \frac{2S_{\text{cell}}^2}{\Omega m_{\text{cell}} c_s} \int \frac{d^3 q}{(2\pi)^2} \delta(c_s q - \omega_{\mathbf{q}}) q \\ &= \frac{g_\chi^2 g_e^2}{m_V^4} \frac{S_{\text{cell}}^2}{\pi \Omega m_{\text{cell}} c_s} \int dq q^3 \int d \cos \theta \delta\left(c_s q - qv \cos \theta + \frac{q^2}{2m_\chi}\right) \\ &= \frac{g_\chi^2 g_e^2}{m_V^4} \frac{S_{\text{cell}}^2}{\pi \Omega m_{\text{cell}} c_s} \frac{1}{v} \int dq q^2 \Theta(v - v_{\min}(q)), \end{aligned} \quad (\text{M.5})$$

where

$$v_{\min}(q) \equiv \frac{q}{2m_\chi} + c_s. \quad (\text{M.6})$$

Now we can write the total rate per unit target mass in terms of the commonly used η function, defined by

$$\eta(v_{\min}) \equiv \int d^3v \frac{f(\mathbf{v})}{v} \Theta(v - v_{\min}). \quad (\text{M.7})$$

The result is

$$\begin{aligned} R &\simeq \frac{1}{\rho_T} \frac{\rho_\chi}{m_\chi} \frac{g_\chi^2 g_e^2}{m_V^4} \frac{S_{\text{cell}}^2}{\pi \Omega m_{\text{cell}} c_s} \int dq q^2 \eta(v_{\min}(q)) \\ &= \frac{1}{\pi c_s} \left(\frac{S_{\text{cell}}}{m_{\text{cell}}} \right)^2 \frac{g_\chi^2 g_e^2}{m_V^4} \frac{\rho_\chi}{m_\chi} \int dq q^2 \eta(v_{\min}(q)). \end{aligned} \quad (\text{M.8})$$

This is the formula we use to estimate the single phonon excitation rate in YIG in Sec. 7.3. The material parameters are $c_s = 7.2 \text{ km/s}$ [438], $S_{\text{cell}} = 10$, $m_{\text{cell}} = \rho_T \Omega$, with $\rho_T = 4.95 \text{ g/cm}^3$, $\Omega = 990.683 \text{ \AA}^3$. The analytic expression for the $\eta(v_{\min})$ function for the Maxwell-Boltzmann distribution of Eq. (L.4) can be found in e.g., Ref. [7]. Since the η function has support up to $q_{\max} \simeq 2m_\chi(v_e + v_{\text{esc}})$, we cut off the dashed curve in Fig. 7.1 at the m_χ value for which q_{\max} reaches $\frac{\pi}{\Omega^{1/3}}$, roughly the edge of the 1BZ.

SELF-ENERGY CALCULATIONS

N.1 General Result for the One-Loop Self-Energy

At one-loop level, the self-energies defined in Eqs. (9.23) and (9.24) are given by

$$-i\Pi_{\mathcal{O}_1, \mathcal{O}_2}(Q) = \text{Diagram 1} \quad , \quad -i\Pi'_{\mathcal{O}}(Q) = \text{Diagram 2} \quad , \quad (\text{N.1})$$

where the external states (drawn with curly lines for concreteness) can be either spin-0 or spin-1, and the internal electronic states I, I' are summed over. Using the in-medium Feynman rules (see e.g., Ref. [380]) we obtain, for the first diagram:

$$-i\Pi_{\mathcal{O}_1, \mathcal{O}_2} = \frac{(-1)}{V} \sum_{I'I} \int_{-\infty}^{\infty} \frac{d\varepsilon}{2\pi} \frac{\text{tr}(\langle I' | \mathcal{O}_1 e^{i\mathbf{q}\cdot\mathbf{x}} | I \rangle \langle I | \mathcal{O}_2 e^{-i\mathbf{q}\cdot\mathbf{x}} | I' \rangle)}{(\varepsilon + \omega - \varepsilon_{I'} + i\delta_{I'}) (\varepsilon - \varepsilon_I + i\delta_I)} \quad , \quad (\text{N.2})$$

where V is the total volume, “tr” represents the spin trace, and $\delta_{I^{(\prime)}}$ $\equiv \delta \text{sgn}(\varepsilon_{I^{(\prime)}} - \varepsilon_F)$ with $\delta \rightarrow 0^+$. Note that the $i\delta$ prescription for electron propagators is different from the vacuum theory, and depends on whether the state is above or below the Fermi energy ε_F ; using the correct $i\delta$ prescription is crucial for ensuring causality. Meanwhile, the matrix elements coming from the vertices are

$$\langle I' | \mathcal{O}_1 e^{i\mathbf{q}\cdot\mathbf{x}} | I \rangle = \int d^3x [\Psi_{I'}^*(\mathbf{x}) \mathcal{O}_1 \Psi_I(\mathbf{x})] e^{i\mathbf{q}\cdot\mathbf{x}} \quad , \quad (\text{N.3})$$

and likewise for $\langle I | \mathcal{O}_2 e^{-i\mathbf{q}\cdot\mathbf{x}} | I' \rangle$. Here $\mathcal{O}_{1,2}$ are matrices in spin space, and may involve spatial derivatives acting on the electronic wave functions. For example, for the velocity operator defined in Eq. (9.27) (which is proportional to the identity matrix in spin space), we have

$$\langle I' | v^j e^{i\mathbf{q}\cdot\mathbf{x}} | I \rangle = -\frac{i}{2m_e} \langle I' | \overleftrightarrow{\nabla}_j e^{i\mathbf{q}\cdot\mathbf{x}} | I \rangle = -\frac{i}{2m_e} \int d^3x [\Psi_{I'}^* (\nabla_j \Psi_I) - (\nabla_j \Psi_{I'}^*) \Psi_I] e^{i\mathbf{q}\cdot\mathbf{x}} \quad . \quad (\text{N.4})$$

We can evaluate the energy integral in Eq. (N.2) by examining the pole structure of the integrand in the complex plane. If $\delta_{I'}$ and δ_I have the same sign (i.e., if both I' and I are above or below the Fermi energy), the two poles are on the same side of the real axis and

they have opposite residues; the integral therefore vanishes upon closing the contour via either $+i\infty$ or $-i\infty$. So we must have one state above the Fermi energy and one below it, in which case there is one pole on each side of the real axis; closing the contour via either $+i\infty$ or $-i\infty$ to pick up the residue at one of the poles, we obtain

$$\int_{-\infty}^{\infty} \frac{d\varepsilon}{2\pi} \frac{1}{(\varepsilon + \omega - \varepsilon_{I'} + i\delta_{I'}) (\varepsilon - \varepsilon_I + i\delta_I)} = \begin{cases} \frac{i}{\omega - \omega_{I'I} + i\delta} & \text{if } \delta_{I'} > 0, \delta_I < 0; \\ -\frac{i}{\omega - \omega_{I'I} - i\delta} & \text{if } \delta_{I'} < 0, \delta_I > 0. \end{cases} \quad (\text{N.5})$$

Here $\omega_{I'I} \equiv \varepsilon_{I'} - \varepsilon_I$, and $\delta \rightarrow 0^+$. All cases discussed above can be concisely summarized as:

$$\int_{-\infty}^{\infty} \frac{d\varepsilon}{2\pi} \frac{1}{(\varepsilon + \omega - \varepsilon_{I'} + i\delta_{I'}) (\varepsilon - \varepsilon_I + i\delta_I)} = \frac{-i(f_{I'} - f_I)}{\omega - \omega_{I'I} + i\delta_{I'I}}, \quad (\text{N.6})$$

where $f_I, f_{I'}$ are the occupation numbers (equal to 1 for states below the Fermi energy, 0 for states above it), and $\delta_{I'I} \equiv \delta \operatorname{sgn}(\omega_{I'I})$. We therefore obtain

$$\Pi_{\mathcal{O}_1, \mathcal{O}_2} = -\frac{1}{V} \sum_{I'I} \frac{f_{I'} - f_I}{\omega - \omega_{I'I} + i\delta_{I'I}} \operatorname{tr} \left(\langle I' | \mathcal{O}_1 e^{i\mathbf{q}\cdot\mathbf{x}} | I \rangle \langle I | \mathcal{O}_2 e^{-i\mathbf{q}\cdot\mathbf{x}} | I' \rangle \right). \quad (\text{N.7})$$

As the simplest example, setting $\mathcal{O}_1 = \mathcal{O}_2 = \mathbb{1}$ in Eq. (N.7), we obtain $\Pi_{\mathbb{1}, \mathbb{1}}$, and hence the dielectric via Eq. (9.36), which reproduces the familiar Lindhard formula (see e.g., Ref. [439] and recent discussions in Refs. [36, 49]).

Now move on to the second diagram in Eq. (N.1). While we have shown in Sec. 9.3 that contributions to absorption rates from this diagram can be eliminated using the Ward identity, we present its result here for completeness and also to allow for an explicit check of the Ward identity. In this diagram, the electron propagator starts and ends at the same time point and time-ordering becomes ambiguous. The correct prescription is to take the normal-ordered product of creation and annihilation operators, and the loop is simply proportional to the electron number operator [380]. Again writing the result in terms of occupation number f_I , we find

$$\Pi'_{\mathcal{O}} = -\frac{1}{V} \sum_I f_I \operatorname{tr} \langle I | \mathcal{O} | I \rangle. \quad (\text{N.8})$$

Note that $\Pi'_{\mathcal{O}}$ is purely real at all orders. With Eqs. (N.7) and (N.8) one can readily verify the relations implied by the Ward identity, Eqs. (9.29) and (9.53).

N.2 Real Part of the One-Loop Self-Energy in a Metal

We now apply Eq. (N.7) to the case of a metal. As discussed in Sec. 9.5, we model the electrons near the Fermi surface of a metal as free quasiparticles with an effective mass m_*

and energy eigenstates labeled by momentum. The sum over I, I' becomes integrals over \mathbf{k}, \mathbf{k}' , and we have

$$\begin{aligned} \Pi_{\mathcal{O}_1, \mathcal{O}_2} &= \text{Re } \Pi_{\mathcal{O}_1, \mathcal{O}_2} = \\ &= -\frac{1}{V} \int \frac{V d^3 k'}{(2\pi)^3} \int \frac{V d^3 k}{(2\pi)^3} \frac{f_{\mathbf{k}'} - f_{\mathbf{k}}}{\omega - \frac{k'^2}{2m_*} + \frac{k^2}{2m_*}} \text{tr} \left(\langle \mathbf{k}' | \mathcal{O}_1 e^{i\mathbf{q}\cdot\mathbf{x}} | \mathbf{k} \rangle \langle \mathbf{k} | \mathcal{O}_2 e^{-i\mathbf{q}\cdot\mathbf{x}} | \mathbf{k}' \rangle \right). \end{aligned} \quad (\text{N.9})$$

Note that the $i\delta$ in the denominator is irrelevant since the intermediate states cannot go on-shell and $\Pi_{\mathcal{O}_1, \mathcal{O}_2}$ is real at one-loop level.

Let us first consider $\Pi_{\mathbb{1}, \mathbb{1}}$. For the matrix element part, we have

$$\begin{aligned} &\langle \mathbf{k}' | \mathbb{1} e^{i\mathbf{q}\cdot\mathbf{x}} | \mathbf{k} \rangle \\ &= \frac{1}{V} \int d^3 x e^{i(\mathbf{k}+\mathbf{q}-\mathbf{k}')\cdot\mathbf{x}} \mathbb{1} \\ &= \frac{(2\pi)^3}{V} \delta^3(\mathbf{k} + \mathbf{q} - \mathbf{k}') \mathbb{1}, \end{aligned} \quad (\text{N.10})$$

$$\begin{aligned} &\text{tr} \left(\langle \mathbf{k}' | \mathbb{1} e^{i\mathbf{q}\cdot\mathbf{x}} | \mathbf{k} \rangle \langle \mathbf{k} | \mathbb{1} e^{-i\mathbf{q}\cdot\mathbf{x}} | \mathbf{k}' \rangle \right) \\ &= 2 \frac{(2\pi)^3}{V} \delta^3(\mathbf{k} + \mathbf{q} - \mathbf{k}') \frac{1}{V} \int d^3 x = 2 \frac{(2\pi)^3}{V} \delta^3(\mathbf{k} + \mathbf{q} - \mathbf{k}'). \end{aligned} \quad (\text{N.11})$$

Therefore,

$$\Pi_{\mathbb{1}, \mathbb{1}} = -2 \int \frac{d^3 k}{(2\pi)^3} \frac{f_{\mathbf{k}+\mathbf{q}} - f_{\mathbf{k}}}{\omega - \frac{(\mathbf{k}+\mathbf{q})^2}{2m_*} + \frac{k^2}{2m_*}} = -2 \int \frac{d^3 k}{(2\pi)^3} \frac{f_{\mathbf{k}+\mathbf{q}} - f_{\mathbf{k}}}{\omega - \frac{\mathbf{k}\cdot\mathbf{q}}{m_*} - \frac{q^2}{2m_*}}. \quad (\text{N.12})$$

Expanding in small q and integrating by parts, we find

$$\begin{aligned} \Pi_{\mathbb{1}, \mathbb{1}} &= -2 \int \frac{d^3 k}{(2\pi)^3} (\mathbf{q} \cdot \nabla f_{\mathbf{k}} + \dots) \left(\frac{1}{\omega} + \frac{\mathbf{k} \cdot \mathbf{q}}{m_* \omega^2} + \dots \right) \\ &= 2 \int \frac{d^3 k}{(2\pi)^3} f_{\mathbf{k}} (\mathbf{q} \cdot \nabla + \dots) \left(\frac{1}{\omega} + \frac{\mathbf{k} \cdot \mathbf{q}}{m_* \omega^2} + \dots \right) \\ &\simeq 2 \int \frac{d^3 k}{(2\pi)^3} f_{\mathbf{k}} \frac{q^2}{m_* \omega^2} = \frac{q^2}{\omega^2} \frac{n_e}{m_*}, \end{aligned} \quad (\text{N.13})$$

where the gradients are in \mathbf{k} space, and $n_e = 2 \int \frac{d^3 k}{(2\pi)^3} f_{\mathbf{k}}$ is the free electron density.

We can calculate $\Pi_{\bar{v}^2, \mathbb{1}}$ in a similar way. The matrix element part again yields a momentum-conserving delta function, and the integrand can then be expanded in small q . We find

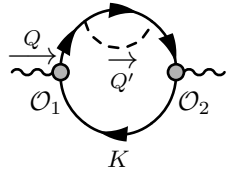
$$\begin{aligned} \Pi_{\bar{v}^2, \mathbb{1}} &= -2 \int \frac{d^3 k}{(2\pi)^3} \frac{f_{\mathbf{k}+\mathbf{q}} - f_{\mathbf{k}}}{\omega - \frac{\mathbf{k}\cdot\mathbf{q}}{m_*} - \frac{q^2}{2m_*}} \frac{(2\mathbf{k} + \mathbf{q})^2}{8m_e^2} \\ &= 2 \int \frac{d^3 k}{(2\pi)^3} f_{\mathbf{k}} \left(\mathbf{q} \cdot \nabla - \frac{1}{2} q^i q^j \nabla_i \nabla_j + \dots \right) \left(\frac{1}{\omega} + \frac{\mathbf{k} \cdot \mathbf{q}}{m_* \omega^2} + \dots \right) \left(\frac{k^2}{2m_e^2} + \frac{\mathbf{k} \cdot \mathbf{q}}{2m_e^2} + \dots \right) \\ &\simeq 2 \int \frac{d^3 k}{(2\pi)^3} f_{\mathbf{k}} \frac{k^2 q^2 + 2(\mathbf{k} \cdot \mathbf{q})^2}{2m_e^2 m_* \omega^2} = \frac{k_F^2}{2m_e^2} \frac{q^2}{\omega^2} \frac{n_e}{m_*}, \end{aligned} \quad (\text{N.14})$$

where we have used $f_{\mathbf{k}} = \Theta(k_F - k)$, and $n_e = \frac{2}{(2\pi)^3} \frac{4}{3} \pi k_F^3$. Finally, since Eq. (N.14) is invariant under $(\omega, \mathbf{q}) \rightarrow (-\omega, -\mathbf{q})$, we have $\Pi_{\mathbb{1},\bar{v}^2}(Q) = \Pi_{\bar{v}^2,\mathbb{1}}(-Q) = \Pi_{\bar{v}^2,\mathbb{1}}(Q)$.

N.3 Imaginary Part of the Two-Loop Self-Energy in a Metal

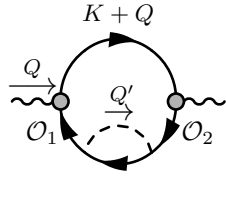
The one-loop self-energies calculated above are purely real: both electrons cannot go on-shell if their energies and momenta differ by $Q^\mu = (\omega, \mathbf{q})$ with $\omega \gg q$. The leading contribution to $\text{Im} \Pi_{\mathcal{O}_1, \mathcal{O}_2}(Q)$ comes from two-loop diagrams with an internal phonon line. In this section, we compute them first in the case of a normal conductor, and then discuss the corrections needed in the superconductor case when ω approaches the gap 2Δ .

Cut diagrams. There are three contributing diagrams:



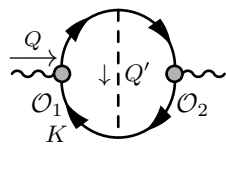
$$= -i \int \frac{d^4 K}{(2\pi)^4} \int \frac{d^4 Q'}{(2\pi)^4} G_K G_{K+Q} G_{K+Q-Q'} G_{K+Q} G_{Q'}^{\text{ph}}$$

$$y_{q'}^2 \text{tr} \left[\tilde{\mathcal{O}}_1(K, K+Q) \tilde{\mathcal{O}}_2(K+Q, K) \right], \quad (\text{N.15})$$



$$= -i \int \frac{d^4 K}{(2\pi)^4} \int \frac{d^4 Q'}{(2\pi)^4} G_K G_{K+Q} G_K G_{K+Q'} G_{Q'}^{\text{ph}}$$

$$y_{q'}^2 \text{tr} \left[\tilde{\mathcal{O}}_1(K, K+Q) \tilde{\mathcal{O}}_2(K+Q, K) \right], \quad (\text{N.16})$$



$$= -i \int \frac{d^4 K}{(2\pi)^4} \int \frac{d^4 Q'}{(2\pi)^4} G_K G_{K+Q} G_{K+Q-Q'} G_{K-Q'} G_{Q'}^{\text{ph}}$$

$$y_{q'}^2 \text{tr} \left[\tilde{\mathcal{O}}_1(K, K+Q) \tilde{\mathcal{O}}_2(K+Q-Q', K-Q') \right]. \quad (\text{N.17})$$

Here each propagator is labeled by a four-momentum that consists of the energy it carries and the momentum label of the electron or phonon state. In each diagram, we denote four-momentum flowing into the \mathcal{O}_1 vertex from the electron propagator as $K^\mu = (\varepsilon, \mathbf{k})$, and the phonon four-momentum (with direction indicated by the arrow) as $Q'^\mu = (\omega', \mathbf{q}')$. The electron and phonon propagators are denoted by iG and iG^{ph} , respectively, with

$$G_K = \frac{1}{\varepsilon - \frac{k^2}{2m_*} + i\delta_\varepsilon}, \quad G_{Q'}^{\text{ph}} = \frac{1}{\omega' - \omega_{q'} + i\delta} - \frac{1}{\omega' + \omega_{q'} - i\delta} = \frac{2\omega_{q'}}{\omega'^2 - \omega_{q'}^2 + i\delta}, \quad (\text{N.18})$$

where $\delta_\varepsilon = \delta \text{sgn}(\varepsilon - \varepsilon_F)$, $\delta \rightarrow 0^+$, and $\omega_{q'} = c_s q'$. The electron-phonon vertex $y_{q'} = \frac{C_{e\text{-ph}q'}}{\sqrt{2\omega_{q'}\rho_T}}$, while the vertices associated with operator insertions $\mathcal{O}_{1,2}$ yield the momentum space

representations of these operators, $\tilde{\mathcal{O}}_{1,2}$, whose arguments are the incoming and outgoing electrons' four-momenta. We have assumed exact momentum conservation and neglected Umklapp processes; the latter may introduce an $\mathcal{O}(1)$ correction to the final results which is more difficult to calculate.

By the optical theorem, $2\text{Im}\Pi_{\mathcal{O}_1, \mathcal{O}_2}$ is given by the sum of cut diagrams. For the first diagram, Eq. (N.15), there is only one possible cut to put all intermediate states on-shell, i.e., the one through the phonon propagator and the two electron propagators carrying momenta K and $K + Q - Q'$. By the cutting rules, we should replace

$$G_{Q'}^{\text{ph}} \rightarrow -2\pi i [\delta(\omega' - \omega_{q'}) + \delta(\omega' + \omega_{q'})], \quad (\text{N.19})$$

$$G_K \rightarrow -2\pi i \text{sgn}(\varepsilon - \varepsilon_F) \delta\left(\varepsilon - \frac{k^2}{2m_*}\right), \quad (\text{N.20})$$

$$G_{K+Q-Q'} \rightarrow -2\pi i \text{sgn}(\varepsilon + \omega - \omega' - \varepsilon_F) \delta\left(\varepsilon + \omega - \omega' - \frac{(\mathbf{k} + \mathbf{q} - \mathbf{q}')^2}{2m_*}\right). \quad (\text{N.21})$$

For $\omega > 0$, the on-shell condition requires $\omega' > 0$, $\varepsilon < \varepsilon_F$ and $\varepsilon + \omega - \omega' > \varepsilon_F$; this corresponds to a process where an electron jumps out of the Fermi sphere by absorbing $Q^\mu = (\omega, \mathbf{q})$ while emitting a phonon to conserve momentum. We therefore obtain

$$\begin{aligned} & \text{Cut}[\text{Eq. (N.15)}] \\ &= - \int \frac{d^4 K}{(2\pi)^3} \int \frac{d^4 Q'}{(2\pi)^3} 2\pi \delta(\omega' - \omega_{q'}) \delta\left(\varepsilon - \frac{k^2}{2m_*}\right) \delta\left(\varepsilon + \omega - \omega' - \frac{(\mathbf{k} + \mathbf{q} - \mathbf{q}')^2}{2m_*}\right) \\ & f_{\mathbf{k}} (1 - f_{\mathbf{k}+\mathbf{q}-\mathbf{q}'}) G_{K+Q}^2 y_{q'}^2 \text{tr} \left[\tilde{\mathcal{O}}_1(K, K+Q) \tilde{\mathcal{O}}_2(K+Q, K) \right] \\ &= - \int \frac{d^3 k}{(2\pi)^3} \int \frac{d^3 q'}{(2\pi)^3} 2\pi \delta\left(\omega + \frac{k^2}{2m_*} - \frac{(\mathbf{k} + \mathbf{q} - \mathbf{q}')^2}{2m_*} - \omega_{q'}\right) f_{\mathbf{k}} (1 - f_{\mathbf{k}+\mathbf{q}-\mathbf{q}'}) y_{q'}^2 \\ & G_{K+Q}^2 \text{tr} \left[\tilde{\mathcal{O}}_1(K, K+Q) \tilde{\mathcal{O}}_2(K+Q, K) \right], \quad (\text{N.22}) \end{aligned}$$

where it is understood that ε (the energy components of K) is set to $\frac{k^2}{2m_*}$ in the final expression. The second diagram, Eq. (N.16), is completely analogous. Cutting the propagators

G_{K+Q} , $G_{Q'}^{\text{ph}}$ and $G_{K+Q'}$, we obtain

$$\begin{aligned}
& \text{Cut}[\text{Eq. (N.16)}] \\
&= - \int \frac{d^3k}{(2\pi)^3} \int \frac{d^3q'}{(2\pi)^3} 2\pi \delta\left(\omega + \frac{(\mathbf{k} + \mathbf{q}')^2}{2m_*} - \frac{(\mathbf{k} + \mathbf{q})^2}{2m_*} - \omega_{q'}\right) f_{\mathbf{k}+\mathbf{q}'} (1 - f_{\mathbf{k}+\mathbf{q}}) y_{q'}^2 \\
& \quad G_K^2 \text{tr}\left[\tilde{\mathcal{O}}_1(K, K+Q) \tilde{\mathcal{O}}_2(K+Q, K)\right] \\
&= - \int \frac{d^3k}{(2\pi)^3} \int \frac{d^3q'}{(2\pi)^3} 2\pi \delta\left(\omega + \frac{k^2}{2m_*} - \frac{(\mathbf{k} + \mathbf{q} - \mathbf{q}')^2}{2m_*} - \omega_{q'}\right) f_{\mathbf{k}} (1 - f_{\mathbf{k}+\mathbf{q}-\mathbf{q}'}) y_{q'}^2 \\
& \quad G_{K-Q'}^2 \text{tr}\left[\tilde{\mathcal{O}}_1(K-Q', K+Q-Q') \tilde{\mathcal{O}}_2(K+Q-Q', K-Q')\right], \tag{N.23}
\end{aligned}$$

where we have shifted the integration variable $\mathbf{k} \rightarrow \mathbf{k} - \mathbf{q}'$ to arrive at the last line.

For the last diagram, Eq. (N.17), there are two possible cuts: through G_K , $G_{Q'}^{\text{ph}}$, $G_{K+Q-Q'}$ and through G_{K+Q} , $G_{Q'}^{\text{ph}}$, $G_{K-Q'}$. Carrying out the same procedure as above, we obtain

$$\begin{aligned}
& \text{Cut}[\text{Eq. (N.17)}] \\
&= - \int \frac{d^3k}{(2\pi)^3} \int \frac{d^3q'}{(2\pi)^3} \left\{ 2\pi \delta\left(\omega + \frac{k^2}{2m_*} - \frac{(\mathbf{k} + \mathbf{q} - \mathbf{q}')^2}{2m_*} - \omega_{q'}\right) f_{\mathbf{k}} (1 - f_{\mathbf{k}+\mathbf{q}-\mathbf{q}'}) y_{q'}^2 \right. \\
& \quad G_{K+Q} G_{K-Q'} \text{tr}\left[\tilde{\mathcal{O}}_1(K, K+Q) \tilde{\mathcal{O}}_2(K+Q-Q', K-Q')\right] \\
& \quad \left. + 2\pi \delta\left(\omega + \frac{(\mathbf{k} - \mathbf{q}')^2}{2m_*} - \frac{(\mathbf{k} + \mathbf{q})^2}{2m_*} - \omega_{q'}\right) f_{\mathbf{k}-\mathbf{q}'} (1 - f_{\mathbf{k}+\mathbf{q}}) y_{q'}^2 \right. \\
& \quad \left. G_K G_{K+Q-Q'} \text{tr}\left[\tilde{\mathcal{O}}_1(K, K+Q) \tilde{\mathcal{O}}_2(K+Q-Q', K-Q')\right] \right\} \\
&= - \int \frac{d^3k}{(2\pi)^3} \int \frac{d^3q'}{(2\pi)^3} 2\pi \delta\left(\omega + \frac{k^2}{2m_*} - \frac{(\mathbf{k} + \mathbf{q} - \mathbf{q}')^2}{2m_*} - \omega_{q'}\right) f_{\mathbf{k}} (1 - f_{\mathbf{k}+\mathbf{q}-\mathbf{q}'}) y_{q'}^2 \\
& \quad G_{K+Q} G_{K-Q'} \text{tr}\left[\tilde{\mathcal{O}}_1(K, K+Q) \tilde{\mathcal{O}}_2(K+Q-Q', K-Q')\right] \\
& \quad + \tilde{\mathcal{O}}_1(K-Q', K+Q-Q') \tilde{\mathcal{O}}_2(K+Q, K), \tag{N.24}
\end{aligned}$$

where we have shifted the integration variable $\mathbf{k} \rightarrow \mathbf{k} + \mathbf{q}'$ and then changed $\mathbf{q} \rightarrow -\mathbf{q}'$ (assuming the phonon energies $\omega_{q'}$ and electron-phonon couplings $y_{q'}$ depend only on the magnitude but not the direction of \mathbf{q}') in the second term.

Adding up Eqs. (N.22), (N.23) and (N.24), we obtain

$$\begin{aligned}
& 2 \operatorname{Im} \Pi_{\mathcal{O}_1, \mathcal{O}_2} \\
&= - \int \frac{d^3 k}{(2\pi)^3} \int \frac{d^3 q'}{(2\pi)^3} 2\pi \delta \left(\omega + \frac{k^2}{2m_*} - \frac{(\mathbf{k} + \mathbf{q} - \mathbf{q}')^2}{2m_*} - \omega_{q'} \right) f_{\mathbf{k}} (1 - f_{\mathbf{k} + \mathbf{q} - \mathbf{q}'}) y_{q'}^2 \\
& \operatorname{tr} \left\{ \left[G_{K+Q} \tilde{\mathcal{O}}_1(K, K+Q) + G_{K-Q'} \tilde{\mathcal{O}}_1(K-Q', K+Q-Q') \right] \right. \\
& \quad \left. \times \left[G_{K+Q} \tilde{\mathcal{O}}_2(K+Q, K) + G_{K-Q'} \tilde{\mathcal{O}}_2(K+Q-Q', K-Q') \right] \right\}. \tag{N.25}
\end{aligned}$$

Small q expansion. As in the previous section, we expand the integrand in small q . The electron propagators become:

$$G_{K+Q} = \frac{1}{\frac{k^2}{2m_*} + \omega - \frac{(\mathbf{k} + \mathbf{q})^2}{2m_*}} = \frac{1}{\omega - \frac{\mathbf{k} \cdot \mathbf{q}}{m_*} - \frac{q^2}{2m_*}} = \frac{1}{\omega} + \frac{\mathbf{k} \cdot \mathbf{q}}{m_* \omega^2} + \dots, \tag{N.26}$$

$$G_{K-Q'} = \frac{1}{\frac{k^2}{2m_*} - \omega_{q'} - \frac{(\mathbf{k} - \mathbf{q}')^2}{2m_*}} = \frac{1}{-\omega + \frac{(\mathbf{k} + \mathbf{q} - \mathbf{q}')^2}{2m_*} - \frac{(\mathbf{k} - \mathbf{q}')^2}{2m_*}} = -\frac{1}{\omega} - \frac{(\mathbf{k} - \mathbf{q}') \cdot \mathbf{q}}{m_* \omega^2} + \dots, \tag{N.27}$$

where we have used the energy-conserving delta function to eliminate $\omega_{q'}$ in $G_{K-Q'}$. Therefore, at leading order in q' ,

$$\begin{aligned}
& G_{K+Q} \tilde{\mathcal{O}}_1(K, K+Q) + G_{K-Q'} \tilde{\mathcal{O}}_1(K-Q', K+Q-Q') \\
&= \begin{cases} G_{K+Q} + G_{K-Q'} \simeq \frac{\mathbf{q}' \cdot \mathbf{q}}{m_* \omega^2} & \text{for } \mathcal{O}_1 = \mathbb{1}, \\ G_{K+Q} \frac{(2\mathbf{k} + \mathbf{q})^2}{8m_e^2} + G_{K-Q'} \frac{(2(\mathbf{k} - \mathbf{q}') + \mathbf{q})^2}{8m_e^2} \simeq -\frac{m_*}{m_e^2} \frac{\omega - \omega_{q'}}{\omega} & \text{for } \mathcal{O}_1 = \bar{v}^2, \end{cases} \tag{N.28}
\end{aligned}$$

where an identity operator in spin space is understood, and we have again used energy conservation to simplify the expression in the $\mathcal{O}_1 = \bar{v}^2$ case. Note in particular how the $\mathcal{O}(q^0)$ terms cancel in the case of $\mathcal{O}_1 = \mathbb{1}$, such that this LO operator gives a q -suppressed contribution. The other factor $G_{K+Q} \tilde{\mathcal{O}}_2(K+Q, K) + G_{K-Q'} \tilde{\mathcal{O}}_2(K+Q-Q', K-Q')$ in Eq. (N.25) is completely analogous, so we obtain, after taking the spin trace (which simply

yields a factor of two) and substituting in $y_{q'} = \frac{C_{\text{e-ph}} q'}{\sqrt{2\omega_{q'} \rho_T}}$, $\omega_{q'} = c_s q'$:

$$\begin{aligned}
& \left\{ \begin{array}{c} \text{Im } \Pi_{\mathbb{1},\mathbb{1}} \\ \text{Im } \Pi_{\bar{v}^2,\mathbb{1}} = \text{Im } \Pi_{\mathbb{1},\bar{v}^2} \\ \text{Im } \Pi_{\bar{v}^2,\bar{v}^2} \end{array} \right\} \\
&= -\frac{C_{\text{e-ph}}^2}{2m_*^2 \rho_T c_s} \int \frac{d^3 k}{(2\pi)^3} \int \frac{d^3 q'}{(2\pi)^3} 2\pi \delta\left(\omega + \frac{k^2}{2m_*} - \frac{(\mathbf{k} + \mathbf{q} - \mathbf{q}')^2}{2m_*} - \omega_{q'}\right) \times \\
& f_{\mathbf{k}} (1 - f_{\mathbf{k}+\mathbf{q}-\mathbf{q}'}) q' \cdot \left\{ \begin{array}{c} \frac{(\mathbf{q}' \cdot \mathbf{q})^2}{\omega^4} \\ -\frac{m_*^2}{m_e^2} \frac{\mathbf{q}' \cdot \mathbf{q}}{\omega^2} \left(1 - \frac{c_s q'}{\omega}\right) \\ \frac{m_*^4}{m_e^4} \left(1 - \frac{c_s q'}{\omega}\right)^2 \end{array} \right\}. \quad (\text{N.29})
\end{aligned}$$

Including the gap. We have presented the calculation of cut diagrams assuming a normal metal for simplicity. Accounting for pairing of electrons in the BCS theory introduces a slight modification in the final result in the form of a coherence factor [381]. Concretely, for the imaginary part of two-loop self-energies computed above, this amounts to replacing

$$2\pi \delta\left(\omega + \frac{k^2}{2m_*} - \frac{k'^2}{2m_*} - \omega_{q'}\right) f_{\mathbf{k}} (1 - f_{\mathbf{k}'}) \rightarrow \frac{\pi}{2} \delta(E_k + E_{k'} + \omega_{q'} - \omega) \left(1 - \frac{\epsilon_k \epsilon_{k'} - \Delta^2}{E_k E_{k'}}\right) \quad (\text{N.30})$$

in Eq. (N.29), where we have abbreviated $\mathbf{k} + \mathbf{q} - \mathbf{q}' \equiv \mathbf{k}'$ and defined $\epsilon_k \equiv \frac{k^2}{2m_*} - \varepsilon_F$, $E_k \equiv \sqrt{\epsilon_k^2 + \Delta^2}$ (and similarly for $\epsilon_{k'}$, $E_{k'}$). The energy of the electron-hole pair is therefore constrained to be $E_k + E_{k'} \geq 2\Delta$.

The \mathbf{k} integral. We now perform the \mathbf{k} integral:

$$\mathcal{I} \equiv \int \frac{d^3 k}{(2\pi)^3} \frac{\pi}{2} \left(1 - \frac{\epsilon_k \epsilon_{k'} - \Delta^2}{E_k E_{k'}}\right) \delta(E_k + E_{k'} + \omega_{q'} - \omega). \quad (\text{N.31})$$

The integrand depends only on the magnitude of k and the angle θ between \mathbf{k} and $\mathbf{q}' - \mathbf{q}$. So the azimuthal angle integral simply yields a factor of 2π and we can use the δ function to perform the integral over $\cos\theta$. The argument of the δ function has two roots in $\cos\theta$

(corresponding to $\epsilon_{k'} = \pm|\epsilon_{k'}|$), both of which are within the range $[-1, 1]$ in most of viable phase space. Noting that $\frac{dE_{k'}}{d\cos\theta} = \frac{\epsilon_{k'}}{E_{k'}} \frac{d\epsilon_{k'}}{d\cos\theta} = -\frac{\epsilon_{k'}}{E_{k'}} \frac{k|\mathbf{q}'-\mathbf{q}|}{m_*}$, we have

$$\mathcal{I} = \frac{m_*}{4\pi|\mathbf{q}'-\mathbf{q}|} \int_0^\infty dk k \frac{E_{k'}}{|\epsilon_{k'}|} \left(1 + \frac{\Delta^2}{E_k E_{k'}}\right) \Theta(\omega - \omega_{q'} - \Delta - E_k). \quad (\text{N.32})$$

where $E_{k'} = \omega - \omega_{q'} - E_k$. Changing the integration variable from k to E_k , we find

$$\mathcal{I} = \frac{m_*^2}{2\pi|\mathbf{q}'-\mathbf{q}|} \int_\Delta^{\omega-\omega_{q'}-\Delta} dE \frac{EE' + \Delta^2}{|\epsilon\epsilon'|} = \frac{m_*^2}{2\pi|\mathbf{q}'-\mathbf{q}|} \int_\Delta^{\omega-\omega_{q'}-\Delta} dE \frac{EE' + \Delta^2}{\sqrt{(E^2 - \Delta^2)(E'^2 - \Delta^2)}}, \quad (\text{N.33})$$

where a factor of two comes from combining contributions from the two values of k above and below k_F that correspond to the same E_k , and we have abbreviated $E_k, E_{k'}, \epsilon_k, \epsilon_{k'}$ to $E, E', \epsilon, \epsilon'$, with $E' = \omega - \omega_{q'} - E$. The integral over E can be reduced to elliptic integrals via $E = \frac{1}{2}[\omega - \omega_{q'} + t(\omega - \omega_{q'} - 2\Delta)]$:

$$\begin{aligned} \mathcal{I} &= \frac{m_*^2}{4\pi|\mathbf{q}'-\mathbf{q}|} \int_{-1}^1 dt \left[(\omega - \omega_{q'} + 2\Delta) \sqrt{\frac{1 - \alpha^2 t^2}{1 - t^2}} - \frac{4\Delta(\omega - \omega_{q'})}{\omega - \omega_{q'} + 2\Delta} \frac{1}{\sqrt{(1 - t^2)(1 - \alpha^2 t^2)}} \right] \\ &= \frac{m_*^2}{2\pi|\mathbf{q}'-\mathbf{q}|} \left[(\omega - \omega_{q'} + 2\Delta) E(\alpha) - \frac{4\Delta(\omega - \omega_{q'})}{\omega - \omega_{q'} + 2\Delta} K(\alpha) \right] \\ &= \frac{m_*^2(\omega - \omega_{q'})}{2\pi|\mathbf{q}'-\mathbf{q}|} \left[(1 + \beta) E(\alpha) - \frac{2\beta}{1 + \beta} K(\alpha) \right] = \frac{m_*^2(\omega - \omega_{q'})}{2\pi|\mathbf{q}'-\mathbf{q}|} E(\sqrt{1 - \beta^2}) \end{aligned} \quad (\text{N.34})$$

where we have introduced

$$\alpha \equiv \frac{\omega - \omega_{q'} - 2\Delta}{\omega - \omega_{q'} + 2\Delta} = \frac{1 - \beta}{1 + \beta}, \quad \beta \equiv \frac{2\Delta}{\omega - \omega_{q'}} \quad (\text{N.35})$$

to simplify notation, and

$$K(z) = \int_0^1 dt \frac{1}{\sqrt{(1 - t^2)(1 - z^2 t^2)}}, \quad E(z) = \int_0^1 dt \sqrt{\frac{1 - z^2 t^2}{1 - t^2}} \quad (\text{N.36})$$

are the complete elliptic integrals of the first and second kind, respectively. In the $\Delta \rightarrow 0$ limit, corresponding to a normal conductor, we have $\alpha \rightarrow 1, \beta \rightarrow 0, E(1) = 1$, and $\mathcal{I} \rightarrow \frac{m_*^2(\omega - \omega_{q'})}{2\pi|\mathbf{q}'-\mathbf{q}|}$.

The q' integral. The remaining integral over the phonon momentum is

$$\begin{aligned}
& \left\{ \begin{array}{c} \text{Im } \Pi_{\mathbf{1},\mathbf{1}} \\ \text{Im } \Pi_{\bar{v}^2,\mathbf{1}} = \text{Im } \Pi_{\mathbf{1},\bar{v}^2} \\ \text{Im } \Pi_{\bar{v}^2,\bar{v}^2} \end{array} \right\} \\
&= -\frac{C_{\text{e-ph}}^2 \omega}{4\pi \rho_T c_s} \int \frac{d^3 q'}{(2\pi)^3} E \left(\sqrt{1 - \frac{(2\Delta/\omega)^2}{(1 - c_s q'/\omega)^2}} \right) \times \\
& \quad \left. \frac{q'}{|\mathbf{q}' - \mathbf{q}|} \left(1 - \frac{c_s q'}{\omega}\right) \cdot \left\{ \begin{array}{c} \frac{(\mathbf{q}' \cdot \mathbf{q})^2}{\omega^4} \\ -\frac{m_*^2}{m_e^2} \frac{\mathbf{q}' \cdot \mathbf{q}}{\omega^2} \left(1 - \frac{c_s q'}{\omega}\right) \\ \frac{m_*^4}{m_e^4} \left(1 - \frac{c_s q'}{\omega}\right)^2 \end{array} \right\} \right. \quad (\text{N.37})
\end{aligned}$$

Expanding $\frac{q'}{|\mathbf{q}' - \mathbf{q}|} = 1 + \frac{\mathbf{q}' \cdot \mathbf{q}}{q'^2} + \dots$ and keeping the leading nonvanishing term, we can easily carry out the angular integration. Finally, changing the radial integration variable to $x = \frac{c_s q'}{\omega}$, we obtain

$$\begin{aligned}
& \left\{ \begin{array}{c} \text{Im } \Pi_{\mathbf{1},\mathbf{1}} \\ \text{Im } \Pi_{\bar{v}^2,\mathbf{1}} = \text{Im } \Pi_{\mathbf{1},\bar{v}^2} \\ \text{Im } \Pi_{\bar{v}^2,\bar{v}^2} \end{array} \right\} \\
&= -\frac{C_{\text{e-ph}}^2 \omega^4}{(2\pi)^3 \rho_T c_s^4} \int_0^{x_{\text{max}}} dx E \left(\sqrt{1 - \frac{(2\Delta/\omega)^2}{(1 - x)^2}} \right) \left\{ \begin{array}{c} \frac{q^2}{3c_s^2 \omega^2} x^4 (1 - x) \\ -\frac{q^2}{3\omega^2} \frac{m_*^2}{m_e^2} x^2 (1 - x)^2 \\ \frac{m_*^4}{m_e^4} x^2 (1 - x)^3 \end{array} \right\}, \quad (\text{N.38})
\end{aligned}$$

where the upper limit

$$x_{\text{max}} \equiv \min \left(1 - \frac{2\Delta}{\omega}, \frac{\omega_D}{\omega} \right) \quad (\text{N.39})$$

is set by the requirements $\omega - \omega_{q'} \geq 2\Delta$ and $\omega_{q'} = c_s q' \leq \omega_D$ (Debye frequency).

When the energy deposition is well above the gap, $\omega \gg 2\Delta$, Eq. (N.38) reproduces the

normal conductor result:

$$\text{Im } \Pi_{\mathbf{1},\mathbf{1}} \xrightarrow{\omega \gg 2\Delta} -\frac{C_{\text{e-ph}}^2}{(2\pi)^3 \rho_T} \frac{\omega^2 q^2}{15 c_s^6} \cdot \begin{cases} \frac{1}{6} (\omega \leq \omega_D), \\ x_D^5 \left(1 - \frac{5}{6} x_D\right) \quad (\omega > \omega_D), \end{cases} \quad (\text{N.40})$$

$$\text{Im } \Pi_{\bar{v}^2,\mathbf{1}} = \text{Im } \Pi_{\mathbf{1},\bar{v}^2} \xrightarrow{\omega \gg 2\Delta} \frac{C_{\text{e-ph}}^2}{(2\pi)^3 \rho_T} \frac{\omega^2 q^2}{9 c_s^4} \frac{m_*^2}{m_e^2} \cdot \begin{cases} \frac{1}{10} (\omega \leq \omega_D), \\ x_D^3 \left(1 - \frac{3}{2} x_D + \frac{3}{5} x_D^2\right) \quad (\omega > \omega_D), \end{cases} \quad (\text{N.41})$$

$$\text{Im } \Pi_{\bar{v}^2,\bar{v}^2} \xrightarrow{\omega \gg 2\Delta} -\frac{C_{\text{e-ph}}^2}{(2\pi)^3 \rho_T} \frac{\omega^4}{3 c_s^4} \frac{m_*^4}{m_e^4} \cdot \begin{cases} \frac{1}{20} (\omega \leq \omega_D), \\ x_D^3 \left(1 - \frac{9}{4} x_D + \frac{9}{5} x_D^2 - \frac{1}{2} x_D^3\right) \quad (\omega > \omega_D), \end{cases} \quad (\text{N.42})$$

where $x_D \equiv \omega_D/\omega$.

Determination of $C_{\text{e-ph}}$. We use resistivity measurements [382] to determine $C_{\text{e-ph}}$. In Refs. [381, 382], a parameter λ_{tr} is introduced for the electron-phonon coupling, which is defined by

$$\lambda_{\text{tr}} = 2 \int_0^\infty \frac{d\omega'}{\omega'} \alpha_{\text{tr}}^2 F(\omega'). \quad (\text{N.43})$$

The function $\alpha_{\text{tr}}^2 F(\omega')$ is in turn defined from the conductivity of a normal conductor,

$$\sigma_1(\omega) = \text{Re } \sigma(\omega) = \frac{\omega_p^2}{\omega^2} \frac{2\pi}{\omega} \int_0^\omega d\omega' (\omega - \omega') \alpha_{\text{tr}}^2 F(\omega'). \quad (\text{N.44})$$

Note that the normalization convention in Ref. [381] is such that $4\pi\sigma_1$ there equals σ_1 in our notation. From Eqs. (9.36) and (N.38) (in the limit $\Delta \rightarrow 0$) we can readily identify

$$\alpha_{\text{tr}}^2 F(\omega') = \begin{cases} \frac{C_{\text{e-ph}}^2 e^2 \omega'^4}{3 (2\pi)^4 \rho_T c_s^6 \omega_p^2} & (\omega' \leq \omega_D), \\ 0 & (\omega' > \omega_D), \end{cases} \quad (\text{N.45})$$

and therefore

$$\lambda_{\text{tr}} = \frac{C_{\text{e-ph}}^2 e^2 \omega_D^4}{6 (2\pi)^4 \rho_T c_s^6 \omega_p^2}. \quad (\text{N.46})$$

For Al, using $\lambda_{\text{tr}} = 0.39$ together with values of the other parameters in Table 9.2, we find $C_{\text{e-ph}} = 56 \text{ eV}$.

ABSORPTION IN ANISOTROPIC TARGETS

Since the benchmark materials considered in this work (Si, Ge and Al-SC) are near-isotropic, in the main text of the paper we worked under the simplifying assumption that the medium is isotropic. However, it is straightforward to extend the calculation to anisotropic targets. In this appendix, we discuss the modifications needed to go beyond the isotropic limit.

First, the in-medium photon self-energy matrix $\Pi_{\lambda\lambda'}$ may have nonzero off-diagonal entries, and its eigenvalues can be found by diagonalization [29]:

$$\begin{pmatrix} \Pi_{++} & \Pi_{+-} & \Pi_{+L} \\ \Pi_{-+} & \Pi_{--} & \Pi_{-L} \\ \Pi_{L+} & \Pi_{L-} & \Pi_{LL} \end{pmatrix} \xrightarrow{\text{diagonalize}} \begin{pmatrix} \Pi_1 & 0 & 0 \\ 0 & \Pi_2 & 0 \\ 0 & 0 & \Pi_3 \end{pmatrix}. \quad (\text{O.1})$$

A DM state ϕ may mix with all three photon polarizations, and Eq. (9.22) generalizes to

$$R = -\frac{\rho_\phi}{\rho_T} \frac{1}{\omega^2} \text{Im} \left(\Pi_{\phi\phi} + \sum_{i=1,2,3} \frac{\Pi_{\phi i} \Pi_{i\phi}}{m_\phi^2 - \Pi_i} \right), \quad (\text{O.2})$$

where $\Pi_{\phi i}$ is obtained from $\Pi_{\phi A}^\mu$ by first projecting onto $e_{\pm,L}^\mu$ and then rotating into the diagonal basis.

For vector DM ϕ , the same rotation in Eq. (O.1) diagonalizes also the $\phi\phi$ and ϕA self-energy matrices. So each of the three polarizations of ϕ mixes only with the one corresponding photon polarization, and we simply replace $\Pi_{T,L}$ in Eq. (9.22) by $\Pi_{1,2,3}$ and average over the three polarizations to obtain the rate in the anisotropic case:

$$R_{\text{vector}} = -\frac{1}{3} \kappa^2 \frac{\rho_\phi}{\rho_T} m_\phi^2 \sum_{i=1,2,3} \text{Im} \left(\frac{1}{m_\phi^2 - \Pi_i} \right). \quad (\text{O.3})$$

For pseudoscalar DM, still assuming spin-degenerate electronic states, we obtain from Eq. (9.44):

$$R_{\text{pseudoscalar}} = -g_{aee}^2 \frac{\rho_\phi}{\rho_T} \frac{1}{4m_e^2\omega^2} \frac{1}{e^2} \left[\omega^2 \text{Im} (\Pi_{++} + \Pi_{--}) + m_\phi^2 \text{Im} \Pi_{LL} \right], \quad (\text{O.4})$$

which generalizes Eq. (9.45). Note that while anisotropy allows for a nonzero mixing between the DM ϕ and the photon (via its coupling to the electron's magnetic dipole), its contribution to absorption rate is at $\mathcal{O}(q^2)$ and negligible. On the other hand, if the electronic states

are not spin-degenerate (e.g., due to spin-orbit coupling), one would need to explicitly compute additional matrix elements of the spin operator Σ between the spin part of the wave functions, and the absorption rate cannot be written in terms of components of the photon self-energy matrix. Also, mixing between the DM and the photon becomes relevant in this case.

For scalar DM, anisotropy may introduce mixing with all three photon polarizations, and Eq. (O.2) applies. The final result, however, is still expected to be dominated by the $\Pi_{\bar{v}^2, \bar{v}^2}$ term from $\Pi_{\phi\phi}$, and we therefore have the same formula, Eq. (9.56), as in the isotropic case:

$$R_{\text{scalar}} \simeq -d_{\phi ee}^2 \frac{4\pi m_e^2}{M_{\text{Pl}}^2} \frac{\rho_\phi}{\rho_T} \frac{1}{m_\phi^2} \text{Im} \Pi_{\bar{v}^2, \bar{v}^2}. \quad (\text{O.5})$$

NUMERICAL DETAILS

P.1 Density Functional Theory (DFT)

The DFT calculations are carried out within the generalized gradient approximation (GGA) [347] using the QUANTUM ESPRESSO code [399] with and without spin-orbit coupling (SOC) included. We use the ZrTe_5 experimental lattice constants, $a = 3.9797 \text{ \AA}$, $b = 14.470 \text{ \AA}$, and $c = 13.676 \text{ \AA}$ of the orthorhombic crystal structure [440]. We employ fully relativistic pseudopotentials for calculations including SOC, and scalar relativistic pseudopotentials for calculations without SOC, in both cases generated with Pseudo Dojo [441–443]. In each case, we use a 3265 eV kinetic energy cutoff on a uniform $4 \times 4 \times 2$ Brillouin zone (BZ) grid to compute the electron density. To systematically converge the absorption and scattering rates, for the high E region we compute the electronic wave functions with 200, 300, and 400 eV cutoffs on $10 \times 10 \times 10$, $12 \times 12 \times 12$, and $14 \times 14 \times 14$ \mathbf{k} -grids. For the low E region, we compute the wave functions with 650, 750, and 850 eV cutoffs on $8 \times 8 \times 8$, $9 \times 9 \times 9$, and $10 \times 10 \times 10$ uniform \mathbf{k} -grids in a small reciprocal-space volume that includes the low-energy band dispersion. The convergence of these calculations is discussed in Appendix P.2.

The computed band structure of ZrTe_5 is presented in Fig. 10.1, where we correct the band gap with a scissor shift to match the experimental band gap for the calculation with SOC. The inset shows in detail the dispersion near the band edges, highlighting the linear dispersion along the intralayer directions Γ -Y and Γ -Z. Note that in interlayer directions (not shown in Fig. 10.1) the dispersion is not linear or conical. This band structure obtained by combining the experiment lattice constant and the Perdew-Burke-Ernzerhof (PBE) exchange correlation functional is consistent with a previous study [444]. While the presence of a Dirac cone in ZrTe_5 is still under debate [385–396], pursuing more extensive tests of crystal structure and DFT functionals, or carrying out beyond-DFT band structure calculations, is beyond the scope of this work.

P.2 DM Interaction Constraint Convergence and Dielectric Function

In this appendix we will discuss some details of the DM scattering and absorption rate calculations, as well as the long wavelength, anisotropic dielectric function, $\epsilon(0, \omega)$. Since the main focus of this paper is the effect of SOC, only the electronic wave functions near the Fermi surface are needed. This is because, in ZrTe_5 , SOC effects are approximately $\mathcal{O}(10 \text{ meV})$, and therefore a very small perturbation for states $> \text{eV}$ away from the Fermi

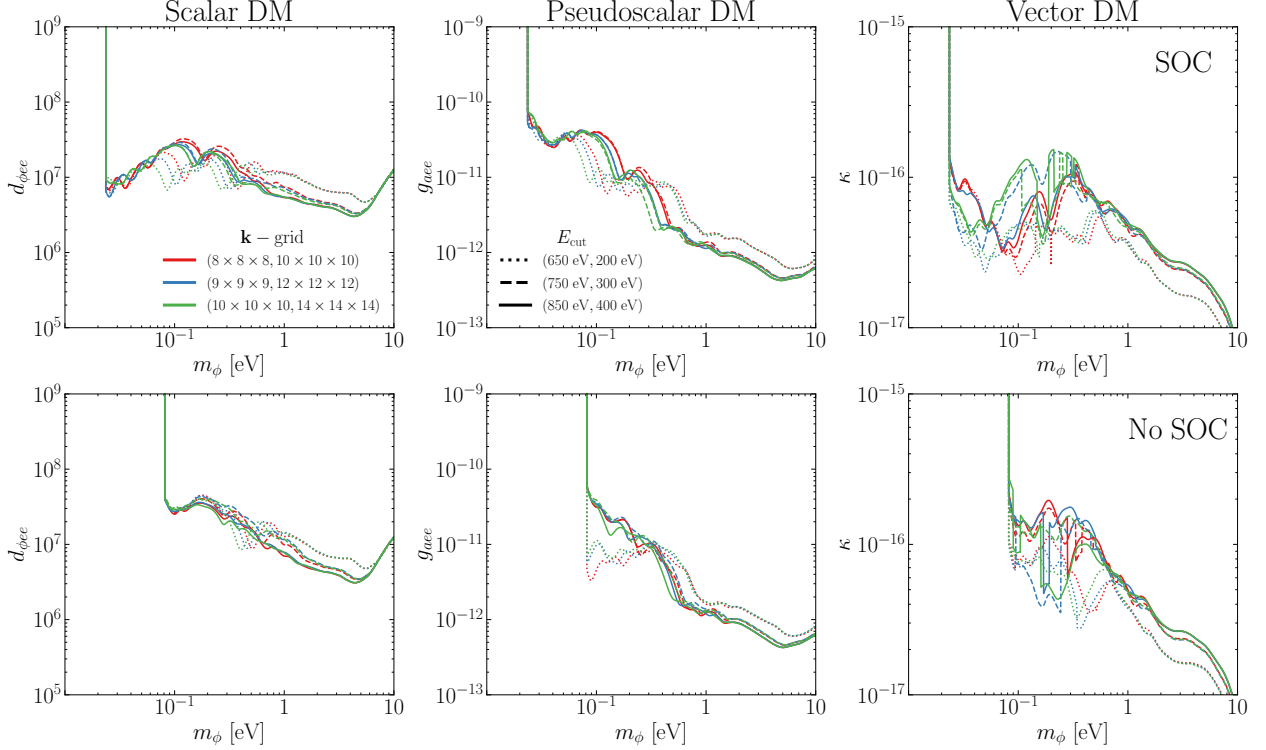


Figure P.1: Convergence of the constraints on DM absorption, for the models discussed in Sec. 10.3, with respect to the \mathbf{k} point sampling (\mathbf{k} -grid) and plane wave energy cutoff, E_{cut} . The first row includes SOC effects while the second row does not. Absorption rates were computed by adding the contributions from the low E and high E regions, and the first (second) value in the legends corresponds to the parameter used in the low (high) E calculation. For example, the red dotted line corresponds to a calculation in which the low (high) E region was sampled on an $8 \times 8 \times 8$ ($10 \times 10 \times 10$) Monkhorst-Pack grid in the 1BZ, with $E_{\text{cut}} = 650$ (200) eV. All curves assume a width parameter of $\delta = 10^{-1}\omega$.

surface. We are therefore safely within the “valence to conduction” regime, discussed in more detail in Ref. [9], and do not need to study deeper, core electronic levels, or larger energy states where the electrons are close to free. DFT is the preferred tool for studying these transitions, and the two main convergence parameters are the number of \mathbf{k} -points in the 1BZ sampling, and the plane wave expansion cutoff, E_{cut} . In both the low E and high E regions we sample \mathbf{k} points uniformly with a Monkhorst-Pack grid. The only difference is that the low E points are scaled by 1/5 relative to the high E region. Convergence of the DM absorption and scattering constraints with respect to the \mathbf{k} point sampling and E_{cut} parameters are shown in Fig. P.1 and Fig. P.2 respectively. The constraints in the main text are identical to the most converged constraints shown in Figs. (P.1, P.2). Generally we see faster convergence with respect to E_{cut} than the \mathbf{k} point density, and slightly faster convergence for the DFT calculation which omits SOC effects than those which include

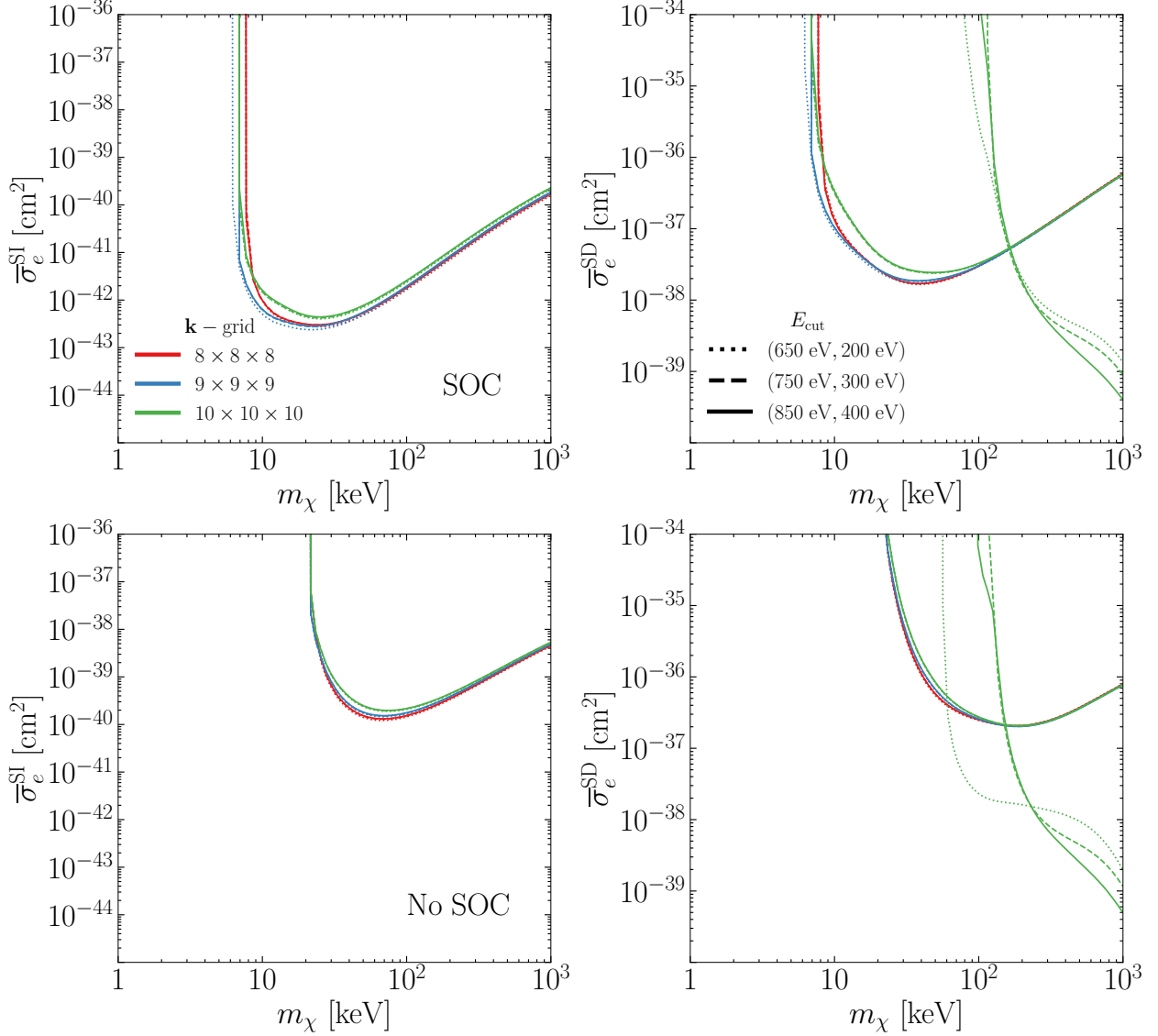


Figure P.2: Convergence of the constraints on DM scattering, for the models discussed in Sec. 10.3, with respect to the \mathbf{k} point sampling (\mathbf{k} -grid) and plane wave energy cutoff, E_{cut} . The first row includes SOC effects while the second row does not. The collection of constraints dominant at the lowest masses corresponds to the low E transitions, and the other set corresponds to the high E transitions. Similar to Fig. P.1, the E_{cut} parameters in the legend correspond to the values used for the low/high E regions.

them. We also note that all-electron reconstruction effects were omitted here since we are focusing on very small DM masses, and therefore kinematically limited to small q transitions. However these effects could be important for studies of DM scattering in ZrTe_5 at higher masses, or for larger experimental thresholds.

The dielectric function in the long wavelength limit is shown in Fig. P.3, was used as an

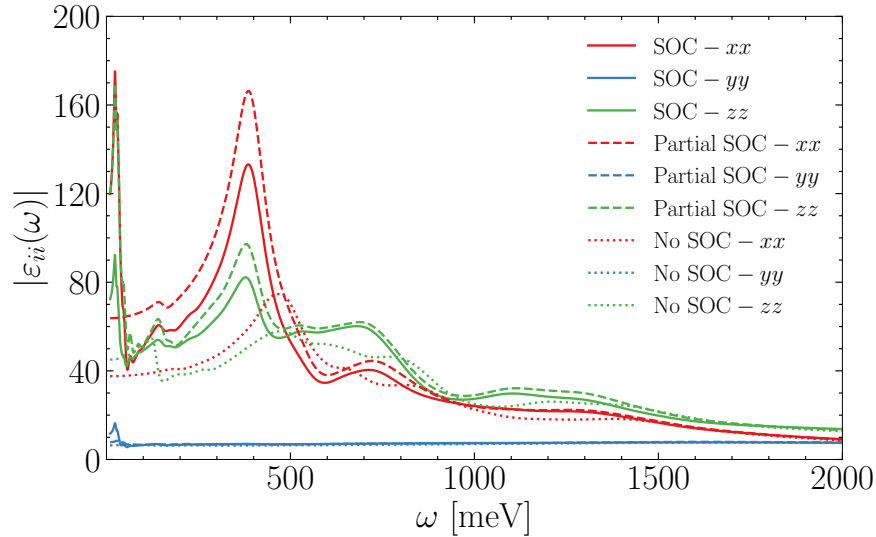


Figure P.3: Magnitude of the dielectric function of ZrTe_5 computed with SOC (solid), without SOC (dotted), and a combination of the calculations with and without SOC (dashed), as described in Sec. 10.3. The directional dependence of the dielectric function is due to the anisotropic nature of ZrTe_5 . Note that while non-local corrections are not included in this figure we found they have a small $\mathcal{O}(10\%)$ effect. These results are obtained with an electronic broadening of $\delta = 10^{-1}\omega$.

intermediate to compute a few different constraints. Specifically it was used to screen the SI scattering rate, and it can be shown that the vector DM absorption rate, as well as the pseudoscalar DM absorption rate when wave functions are spin independent, can be related to the dielectric function. Moreover this calculation serves as a useful benchmark to compare future DFT calculations.

A p p e n d i x Q

GENERALIZED SELF-ENERGIES

In this appendix we provide the expressions for the self-energies used in the main text, namely Π_{AA} , $\Pi_{A\phi}$, and $\Pi_{\phi\phi}$. Since electrons in the target are non-relativistic, we will work in the framework of NR EFT closely following Ref. [2], generalizing the results to anisotropic materials with sizable SOC.

At leading order in the NR EFT, it can be shown [2] that the electron-photon coupling reads:

$$\mathcal{L}_{\psi A}^{\text{eff}} = -e A_0 \psi_+^\dagger \psi_+ - \frac{ie}{2m_e} \mathbf{A} \cdot \left(\psi_+^\dagger \overleftrightarrow{\nabla} \psi_+ \right) + \frac{e}{2m_e} (\nabla \times \mathbf{A}) \cdot \left(\psi_+^\dagger \boldsymbol{\Sigma} \psi_+ \right) - \frac{e^2}{2m_e} \mathbf{A}^2 \psi_+^\dagger \psi_+, \quad (\text{Q.1})$$

where $\boldsymbol{\Sigma} = \text{diag}(\boldsymbol{\sigma}, \boldsymbol{\sigma})$, and $\psi_+ = \frac{1}{2}(1 + \gamma^0)\psi_{\text{NR}}$ with ψ_{NR} being the NR electron field defined as

$$\psi(\mathbf{x}, t) = e^{-im_e t} \psi_{\text{NR}}(\mathbf{x}, t). \quad (\text{Q.2})$$

For vector DM, by simply replacing $eA^\mu \rightarrow eA^\mu - g_e\phi^\mu$ in eq. (Q.1), we obtain:

$$\begin{aligned} \mathcal{L}_{\text{int}}^{\text{eff}} = & g \phi_0 \hat{\psi}_+^\dagger \hat{\psi}_+ + \frac{ig}{2m_e} \boldsymbol{\phi} \cdot \left(\hat{\psi}_+^\dagger \overleftrightarrow{\nabla} \hat{\psi}_+ \right) - \frac{g}{2m_e} (\nabla \times \boldsymbol{\phi}) \cdot \left(\hat{\psi}_+^\dagger \boldsymbol{\Sigma} \hat{\psi}_+ \right) \\ & + \frac{ge}{m_e} \boldsymbol{\phi} \cdot \mathbf{A} \hat{\psi}_+^\dagger \hat{\psi}_+ - \frac{g^2}{2m_e} \boldsymbol{\phi}^2 \hat{\psi}_+^\dagger \hat{\psi}_+ \quad (\text{Q.3}) \\ & (\text{vector DM}). \end{aligned}$$

In deriving the effective interaction Lagrangian for scalar and pseudoscalar DM, we have to keep some NLO terms in the NR expansion. This is because, as discussed in [2], the LO order terms contain factors of the momentum transfer, q , which in the absorption limit induces a larger suppression compared to the electron velocity. Therefore, keeping all the NLO order terms that do not contain factors of q we obtain

$$\mathcal{L}_{\text{int}}^{\text{eff}} = \begin{cases} g \phi \hat{\psi}_+^\dagger \hat{\psi}_+ + \frac{g}{8m_e^2} \boldsymbol{\phi} \cdot \left(\hat{\psi}_+^\dagger \overleftrightarrow{\nabla}^2 \hat{\psi}_+ \right) - \frac{ige}{2m_e^2} \boldsymbol{\phi} \cdot \mathbf{A} \cdot \left(\hat{\psi}_+^\dagger \overleftrightarrow{\nabla} \hat{\psi}_+ \right) & (\text{scalar DM}), \\ -\frac{g}{2m_e} (\nabla \phi) \cdot \hat{\psi}_+^\dagger \boldsymbol{\Sigma} \hat{\psi}_+ + \frac{ig}{4m_e^2} (\partial_t \phi) \left(\hat{\psi}_+^\dagger \boldsymbol{\Sigma} \cdot \overleftrightarrow{\nabla} \hat{\psi}_+ \right) & (\text{pseudoscalar DM}). \end{cases} \quad (\text{Q.4})$$

With these effective interactions, we are now ready to derive the expressions for the self-energies. By using the photon-electron coupling given in eq. (Q.1), we obtain the expression

for $\Pi_{AA}^{\mu\nu}$ in terms of the loop diagrams $\Pi_{\mathcal{O}_1\mathcal{O}_2}$ and $\Pi'_{\mathcal{O}}$ defined in eq. (9.23) and (9.24):

$$\Pi_{AA}^{00} = -e^2 \bar{\Pi}_{\mathbb{1}\mathbb{1}} \quad (\text{Q.5})$$

$$\Pi_{AA}^{i0} = -e^2 \left(\bar{\Pi}_{v^i\mathbb{1}} + \frac{iq^l}{2m_e} \epsilon_{iml} \bar{\Pi}_{\sigma^m\mathbb{1}} \right) \quad (\text{Q.6})$$

$$\Pi_{AA}^{ij} = -e^2 \left[\bar{\Pi}_{v^i v^j} + \frac{iq^l}{2m_e} (\epsilon_{jml} \bar{\Pi}_{v^i\sigma^m} + \epsilon_{iml} \bar{\Pi}_{\sigma^m v^j}) - \frac{q^l q^r}{4m_e^2} \epsilon_{ilm} \epsilon_{jrn} \bar{\Pi}_{\sigma^m \sigma^n} \right] - \omega_p^2 \delta^{ij} \quad (\text{Q.7})$$

where $\omega_p = \sqrt{\frac{n_e e^2}{m_e}}$ is the plasma frequency, and we have highlighted in red terms that vanish in absence of sizable spin-orbit coupling (in this specific case, they vanish because $\text{tr}[\boldsymbol{\sigma}^i] = 0$ in absence of SOC). Since vector DM couples to electrons in the same way of the photon but with a rescaled coupling, $\kappa = g_e/e$, we have

$$\Pi_{\phi\phi}^{\mu\nu} = -\kappa \Pi_{\phi A}^{\mu\nu} = \kappa^2 \Pi_{AA}^{\mu\nu}. \quad (\text{Q.8})$$

For scalar DM, by using the interactions given in eq. (Q.4), we get

$$\Pi_{\phi A}^0 = -g_e e \left(\bar{\Pi}_{\mathbb{1}\mathbb{1}} - \bar{\Pi}_{\mathbb{1}\tilde{v}^2} + \frac{iq^k}{4m_e} \epsilon_{ijk} \bar{\Pi}_{\mathbb{1}\tilde{v}^{ij}} \right) \quad (\text{Q.9})$$

$$\begin{aligned} \Pi_{\phi A}^i &= -g_e e \left[\bar{\Pi}_{\mathbb{1}v^i} - \bar{\Pi}_{\tilde{v}^2 v^i} + \frac{iq^k}{4m_e} \epsilon_{ljk} \bar{\Pi}_{\tilde{v}^{lj} v^i} + \frac{iq^l}{4m_e} \epsilon_{lim} (\bar{\Pi}_{\mathbb{1}\sigma^m} - \bar{\Pi}_{\tilde{v}^2 \sigma^m}) \right. \\ &\quad \left. + \frac{iq^k}{4m_e} \frac{iq^r}{4m_e} \epsilon_{ijk} \epsilon_{mlr} \bar{\Pi}_{\tilde{v}^{ij} \sigma^m} + \frac{1}{m_e} \bar{\Pi}'_{v^i} \right] \quad (\text{Q.10}) \end{aligned}$$

$$\begin{aligned} \Pi_{\phi\phi} &= g_e^2 \left[\bar{\Pi}_{\mathbb{1}\mathbb{1}} - \bar{\Pi}_{\mathbb{1}\tilde{v}^2} - \bar{\Pi}_{\tilde{v}^2\mathbb{1}} + \bar{\Pi}_{\tilde{v}^2\tilde{v}^2} \right. \\ &\quad \left. + \frac{iq^k}{4m_e} \epsilon_{ijk} (\bar{\Pi}_{\mathbb{1}\tilde{v}^{ij}} + \bar{\Pi}_{\tilde{v}^{ij}\mathbb{1}} + \bar{\Pi}_{\tilde{v}^2\tilde{v}^{ij}} + \bar{\Pi}_{\tilde{v}^{ij}\tilde{v}^2}) + \frac{iq^k}{4m_e} \frac{iq^r}{4m_e} \epsilon_{ijk} \epsilon_{mlr} \bar{\Pi}_{\tilde{v}^{ij} \tilde{v}^{ml}} \right], \quad (\text{Q.11}) \end{aligned}$$

where we have introduced the operator $\tilde{v}^{ij} \equiv \sigma^i v^j$, and as before highlighted in red the terms that vanish in absence of sizable SOC. The terms highlighted in blue, instead, vanish in isotropic materials without SOC.

Similarly, by using the couplings given in eq. (Q.4), we derive the expression for the self-energies of pseudoscalar DM:

$$\Pi_{\phi A}^0 = -ig_e e \left(\frac{q^i}{2m_e} \bar{\Pi}_{\sigma^i\mathbb{1}} - \frac{\omega}{2m_e} \bar{\Pi}_{\tilde{v}^{ii}\mathbb{1}} \right) \quad (\text{Q.12})$$

$$\Pi_{\phi A}^i = g_e e \left(\frac{q^j}{2m_e} \bar{\Pi}_{\sigma^j v^i} - \frac{\omega}{2m_e} \bar{\Pi}_{\tilde{v}^{jj} v^i} - \frac{q^j}{2m_e} \frac{q^l}{2m_e} \epsilon_{lir} \bar{\Pi}_{\sigma^j \sigma^r} + \bar{\Pi}'_{\sigma^i} \right) \quad (\text{Q.13})$$

$$\Pi_{\phi\phi} = -g_e^2 \left[\frac{q^i}{2m_e} \frac{q^j}{2m_e} \bar{\Pi}_{\sigma^i \sigma^j} - \frac{q^i}{2m_e} \frac{\omega}{2m_e} (\bar{\Pi}_{\sigma^i \tilde{v}^{jj}} + \bar{\Pi}_{\tilde{v}^{jj} \sigma^i}) + \frac{\omega^2}{4m_e^2} \bar{\Pi}_{\tilde{v}^{ii} \tilde{v}^{jj}} \right]. \quad (\text{Q.14})$$

$\bar{\Pi}_{\mathcal{O}_1\mathcal{O}_2}$	$\mathbb{1}$	σ	v, \tilde{v}	\bar{v}^2
$\mathbb{1}$	$v_e^2 v_\phi^2$	$\frac{m_\phi}{m_e} v_\phi^2$	$v_e^2 v_\phi$	$\frac{m_\phi}{m_e} v_e^2 v_\phi^2$
σ		1	$\frac{m_\phi}{m_e} v_\phi$	v_e^2
v, \tilde{v}			v_e^2	$\frac{m_\phi}{m_e} v_e^2 v_\phi$
\bar{v}^2				v_e^4

Table Q.1: Self-energies scaling with the DM and electron velocities in the absorption limit. Notice that each insertion of the identity operator induces a suppression of order $v_e v_\phi$ due to the wave-function orthogonality, and that parity odd self-energies receive an additional suppression of order q/k .

Due to the absorption kinematics ($q \sim m_\phi v_\phi \ll \omega \sim m_\phi$), and the hierarchy that exists between the DM velocity, $v_\phi \sim 10^{-3}$, and the electrons' typical velocity in a crystal, $v_e \sim 10^{-2}$; only a few terms are actually relevant in the self-energy expressions given above. To facilitate the following discussion, in Table Q.1 we summarize the velocity scaling of all the terms appearing in the self-energy expression given above. By using these scaling relations it is easy to see that the photon self-energy (and therefore also the DM self-energy) is dominated by its spatial components, specifically by the $\bar{\Pi}_{v^i v^j}$ term. For scalar DM, $\Pi_{\phi\phi}$ is dominated by the term $\bar{\Pi}_{\bar{v}^2 \bar{v}^2}$, and the mixing self-energies $\Pi_{A\phi}$ are suppressed by one power of v_ϕ . Finally, for pseudoscalar DM, $\Pi_{\phi\phi}$ is dominated by $\bar{\Pi}_{\bar{v}\bar{v}}$ and the mixing self-energies are again suppressed.

So far we have ignored the tadpole terms $\bar{\Pi}'_{\mathcal{O}}$. They can be written in terms of the electronic wave functions as [2]:

$$\bar{\Pi}'_{\mathcal{O}} = -\frac{1}{V} \sum_I f_I \langle I | \mathcal{O} | I \rangle, \quad (\text{Q.15})$$

and are usually related to macroscopic quantities of the material. Specifically, $\bar{\Pi}'_{v_i}$ and $\bar{\Pi}'_{\sigma_i}$ are related to the current and spin densities of the material (which both vanish for the case of ZrTe_5). For the case of ZrTe_5 , the only non-vanishing tadpole term is $\bar{\Pi}'_{\mathbb{1}} = n_e$, which enters in the expression for the vector self-energy. However, we never explicitly compute this term. Instead, we exploit the relation

$$\bar{\Pi}_{\mathbb{1}\mathbb{1}}^{ij} = \frac{m_e^2}{\omega^2} \left(\bar{\Pi}_{v^i v^j} - \frac{\delta^{ij}}{m_e} \bar{\Pi}'_{\mathbb{1}} \right) \quad (\text{Q.16})$$

where $\bar{\Pi}_{\mathbb{1}\mathbb{1}} = \frac{q^i}{m_e} \bar{\Pi}_{\mathbb{1}\mathbb{1}}^{ij} \frac{q^j}{m_e}$. Indeed, as discussed in [445], a direct numerical derivation of $\bar{\Pi}_{v^i v^j} - \frac{\delta^{ij}}{m_e} \bar{\Pi}'_{\mathbb{1}}$ would be affected by numerical errors in the $\omega \rightarrow 0$ limit.

Let's conclude this section by discussing more in detail the scaling relations given in Table Q.1. Indeed, while some of them are trivial, others require some explanation. The expression for the loop diagrams $\bar{\Pi}_{\mathcal{O}_1, \mathcal{O}_2}$ is given by [2]:

$$-i \bar{\Pi}_{\mathcal{O}_1, \mathcal{O}_2} = \frac{i}{V} \sum_{I'I} \frac{f_{I'} - f_I}{\omega - \omega_{I'I} + i\delta_{I'I}} \langle I' | \mathcal{O}_1 e^{i\mathbf{q}\cdot\mathbf{x}} | I \rangle \langle I | \mathcal{O}_2 e^{-i\mathbf{q}\cdot\mathbf{x}} | I' \rangle, \quad (\text{Q.17})$$

where V is the total volume, $\omega_{I'I} \equiv E_{I'} - E_I$, $\delta_{I'I} \equiv \delta \operatorname{sgn}(\omega_{I'I})$, and $f_I, f_{I'}$ are the occupation numbers (which, at zero temperature, equal one for states below the Fermi surface, and zero for states above it). From this expression we can see that self-energies involving the identity operators contain the matrix element $\langle i', \mathbf{k}' | e^{i\mathbf{q}\cdot\mathbf{x}} | i, \mathbf{k} \rangle$ which vanishes in the $q \rightarrow 0$ limit since $|i', \mathbf{k}' \rangle$ and $|i, \mathbf{k} \rangle$ are distinct energy eigenstates and therefore orthogonal. At $\mathcal{O}(q)$, we have $\langle i', \mathbf{k}' | e^{i\mathbf{q}\cdot\mathbf{x}} | i, \mathbf{k} \rangle \simeq i\mathbf{q} \cdot \langle i', \mathbf{k}' | \mathbf{x} | i, \mathbf{k} \rangle$. One way to compute this matrix element is to trade the position operator for the momentum operator via its commutator with the Hamiltonian. Here we will assume that the Hamiltonian has the form $H = \frac{\mathbf{p}^2}{2m_e} + V(\mathbf{x})$, ignoring the possibility of momentum-dependent or non-local terms in the potential. While these terms can introduce mild corrections ($\mathcal{O}(10\%)$) we do not expect them to change the overall scaling of the self-energies so we can ignore them in this context. With this assumption in mind, we can write the matrix element involving the position operator as

$$\langle i', \mathbf{k}' | \mathbf{x} | i, \mathbf{k} \rangle = -\frac{1}{E_{i', \mathbf{k}'} - E_{i, \mathbf{k}}} \langle i', \mathbf{k}' | [\mathbf{x}, H] | i, \mathbf{k} \rangle = -\frac{i}{m_e(E_{i', \mathbf{k}'} - E_{i, \mathbf{k}})} \langle i', \mathbf{k}' | \mathbf{p} | i, \mathbf{k} \rangle. \quad (\text{Q.18})$$

Writing the wave functions in the Bloch form, we find:

$$\langle i', \mathbf{k}' | e^{i\mathbf{q}\cdot\mathbf{x}} | i, \mathbf{k} \rangle = \delta_{\mathbf{k}', \mathbf{k}} \frac{\mathbf{q}}{m_e \omega_{i', \mathbf{k}}} \cdot \sum_{\mathbf{G}} (\mathbf{k} + \mathbf{G}) (u_{i', \mathbf{k}, \mathbf{G}}^s)^* u_{i, \mathbf{k}, \mathbf{G}}^s + \mathcal{O}(q^2). \quad (\text{Q.19})$$

where $\omega_{i', \mathbf{k}} \equiv E_{i', \mathbf{k}} - E_{i, \mathbf{k}}$. Therefore, in the absorption limit, each identity operator entering in a self-energy diagram induces a suppression of order $v_e v_\phi$.

Parity-odd self energies also vanish in the $q \rightarrow 0$ limit. Let's show this explicitly for the case of $\bar{\Pi}_{v^i v^2}$. By rewriting the electronic wave function in the Bloch form, we can write $\bar{\Pi}_{v^i v^2}$ as

$$\Pi_{v^2 v^i} = \frac{1}{V} \frac{1}{16m_e^3} \sum_{\substack{i' \in \text{con.} \\ i \in \text{val.}}} \sum_{\mathbf{k}} \left(\frac{[\sum_{\mathbf{G}} (2\mathbf{k} + \mathbf{G} + \mathbf{q}) u_{i', \mathbf{k}, \mathbf{G}}^{s*} u_{i, \mathbf{k}, \mathbf{G}}^s] [\sum_{\mathbf{G}} (2\mathbf{k} + \mathbf{G} + \mathbf{q})^2 u_{i', \mathbf{k}, \mathbf{G}}^{\lambda*} u_{i, \mathbf{k}, \mathbf{G}}^\lambda]}{\omega - \omega_{i', \mathbf{k}, \mathbf{k} + \mathbf{q}} + i\delta_{i', \mathbf{k}, \mathbf{k} + \mathbf{q}}} - i \rightarrow i' \right). \quad (\text{Q.20})$$

By parity invariance the Bloch coefficients satisfy the relation $u_{i\mathbf{k}\mathbf{G}}^s = u_{i-\mathbf{k}-\mathbf{G}}^s$, therefore, at order q^0 we have $\bar{\Pi}_{v^i\bar{v}^2} = -\bar{\Pi}_{v^i\bar{v}^2} = 0$. The first non-vanishing contribution arises at order q and is given by

$$\bar{\Pi}_{\bar{v}^2 v^i} = \frac{1}{V} \frac{q^i}{4m_e^3} \sum_{\substack{i' \in \text{con.} \\ i \in \text{val.}}} \sum_{\mathbf{k}} \left(\frac{[\sum_{\mathbf{G}} u_{i'\mathbf{k}+\mathbf{q}\mathbf{G}}^{s*} u_{i\mathbf{k}\mathbf{G}}^s] [\sum_{\mathbf{G}} (2\mathbf{k} + \mathbf{G})^2 u_{i'\mathbf{k}\mathbf{G}}^{\lambda*} u_{i\mathbf{k}\mathbf{G}}^\lambda]}{\omega - \omega_{i'i, \mathbf{k}} + i\delta_{i'i, \mathbf{k}}} - i \rightarrow i' \right). \quad (\text{Q.21})$$

Therefore, instead of the naive v_e^3 scaling, $\bar{\Pi}_{\bar{v}^2 v^i}$ scales as $(m_\phi/m_e)v_e^2 v_\phi$ in the absorption limit. By following an analogous derivation, we can conclude that any parity-odd operator receives an additional $\frac{m_\phi v_\phi}{m_e v_e} \sim \frac{q}{k}$ suppression respect to its naive scaling.

ANALYTIC APPROXIMATIONS IN DIRAC MATERIALS

Dirac materials are defined by having a conical band structure near the Fermi surface. They are “Dirac” since the electronic dispersion relation in this conical region is linear in k , similar to the solutions to the Dirac equation,

$$(i\cancel{\partial} - m)\psi(x) = 0 \quad (\text{R.1})$$

describing free fermions. The presence of this conical structure in Dirac materials implies the existence of low energy excitations which satisfy a rescaled version of this equation,

$$(i\tilde{\cancel{\partial}} - \Delta)\psi(x) = 0, \quad (\text{R.2})$$

where 2Δ is a band gap between the two cones, and $\tilde{\partial}_\mu \equiv (\partial_t, v_F^x \partial_x, v_F^y \partial_y, v_F^z \partial_z)$, with \mathbf{v}_F the directionally dependent Fermi velocity. The solutions to Eq. (R.2) can be found analytically, and most previous works [29, 144, 183] studying DM-electron interactions in 3D Dirac materials used these analytic solutions as the Bloch wave functions in Eq. (10.3). Specifically, they used these analytic wave functions to derive scattering and absorption rates.

However, the subtlety is that solutions to Eq. (R.2) cannot be the electronic Bloch wave functions since they are not eigenstates of the crystal Hamiltonian, $H = \mathbf{p}^2/2m_e + V$. Therefore while the excitations which satisfy the rescaled Dirac equation, Eq. (R.2), are certainly related to the electronic Bloch wavefunctions, they are, generally, not the appropriate wave functions to use when computing DM interaction rates.

To further illustrate this point we will briefly discuss the most well known Dirac material, graphene. Even though it is only two dimensional it will serve as a good example to illustrate the difference between the electronic Bloch wave functions and those which satisfy the Dirac equation. Our discussion here will closely follow Ref. [446], to which we refer the reader for further details.

Graphene has two carbon atoms within a unit cell which form a hexagonal lattice structure. The Bloch wave functions, satisfying the crystal Hamiltonian, are typically found using the “tight-binding” method, which assumes that the Bloch wave functions are a linear combination of the atomic wave functions of each of the carbon atoms,

$$\Psi_{i,\mathbf{k}}(\mathbf{x}) = \sum_{j=A,B} \psi_{j,\mathbf{k}}(\mathbf{x}) X_{j,\mathbf{k}}(\mathbf{x}) \quad (\text{R.3})$$

where the “A” and “B” indexes refer to the individual carbon atoms (equivalently the individual carbon atom sublattices), $\psi_{j,\mathbf{k}}$ are some coefficient functions and $X_{j,\mathbf{k}}$ are the specific linear combination of the atomic wave functions which forms a Bloch state,

$$X_{j,\mathbf{k}}(\mathbf{x}) = \frac{1}{\sqrt{N}} \sum_{\mathbf{r}} e^{i\mathbf{k}\cdot\mathbf{r}} \psi_j^{\text{atom}}(\mathbf{x} - \mathbf{r} - \mathbf{r}_j^0). \quad (\text{R.4})$$

Here \mathbf{r} is a lattice vector, \mathbf{r}_j^0 is the equilibrium position of the carbon atom on the j^{th} sublattice, and N is the number of unit cells in the lattice. The Bloch nature of the $X_{j,\mathbf{k}}$ functions can be seen explicitly by noticing that $X_{j,\mathbf{k}}(\mathbf{x} + \mathbf{r}) = e^{i\mathbf{k}\cdot\mathbf{r}} X_{j,\mathbf{k}}(\mathbf{x})$. Assuming that the $\psi_{j,\mathbf{k}}$'s are lattice periodic implies that $\Psi_{i,\mathbf{k}}$ is also a valid Bloch state. The idea behind this decomposition is that the $\psi_{j,\mathbf{k}}$'s are slowly varying functions, or envelope functions, in position space, while the atomic wave functions contain the high frequency behavior, being very localized to the atomic sites. Using this intuition we can simplify the full Schrödinger equation near the Dirac point

$$\left(-\frac{\nabla^2}{2m_e} + V(\mathbf{x}) - E_{i,\mathbf{k}} \right) \Psi_{i,\mathbf{k}} = 0 \quad (\text{R.5})$$

to

$$0 = \sum_{j=A,B} -\frac{1}{m_e} \nabla \psi_{j,\mathbf{k}} \cdot \nabla X_{j,\mathbf{k}} + \psi_{j,\mathbf{k}} \left(-\frac{\nabla^2}{2m_e} + V - E_{i,\mathbf{k}} \right) X_{j,\mathbf{k}}. \quad (\text{R.6})$$

This equation can now be “coarse-grained” by integrating out the pieces close to the center of the atoms with the operator, $\int_{\Omega_l} d^3\mathbf{x} X_{l,\mathbf{k}}^*$ for both $l \in \{A, B\}$ sublattices. Assuming that ψ varies slowly over these regions, we can pull $\psi_{j,\mathbf{k}}$ out of these integrals and Eq. (R.6) becomes two equations,

$$0 = \sum_{j=A,B} \left(-\frac{1}{m_e} \langle X_{l,\mathbf{k}} | \nabla | X_{j,\mathbf{k}} \rangle \cdot \nabla - \delta_{l,j} E_{i,\mathbf{k}} \right) \psi_{j,\mathbf{k}} \quad (\text{R.7})$$

for each $l = A, B$, where the expectation value of $-\nabla^2/2m_e + V$ with respect to $X_{i,\mathbf{k}}$ vanishes since we are implicitly assuming \mathbf{k} is close to the Dirac point, i.e. at the peak of the conical band.. From symmetry arguments it can be shown that $\langle X_{A,\mathbf{k}} | \nabla | X_{B,\mathbf{k}} \rangle \propto \hat{\mathbf{x}} - i\hat{\mathbf{y}}$ and therefore Eq. (R.7) can be further simplified to,

$$v_F (\boldsymbol{\sigma} \cdot \mathbf{k}) \begin{pmatrix} \psi_{A,\mathbf{k}} \\ \psi_{B,\mathbf{k}} \end{pmatrix} = E_{i,\mathbf{k}} \begin{pmatrix} \psi_{A,\mathbf{k}} \\ \psi_{B,\mathbf{k}} \end{pmatrix} \quad (\text{R.8})$$

which is exactly the rescaled Dirac equation, with v_F the Fermi velocity parameter.

Therefore we see that the $\psi_{i,\mathbf{k}}$ components of the total Bloch wave functions in Eq. (R.3) are what satisfies the Dirac equation, not the $\Psi_{i,\mathbf{k}}$ which should be used in the excitation

rate calculations. Moreover note that the σ operator does not act in spin-space but rather in “sublattice” space, and therefore for spin-dependent excitation rates the spin dependence follows from the $X_{j,\mathbf{k}}$ functions.

There are circumstances where the analytic expressions can be used as an approximation. If the tight-binding approximation is valid, and the Bloch wave functions can be cleanly separated into high and low momentum components (as was just done for graphene), then for q much smaller than typical momentum scale of the X functions the spin independent transition form factors, e.g., Eq. (10.27) if Ψ is spin-independent, can reduce to the previously used analytic expressions. In these targets the agreement between an analytic and numeric approach is then indicative of how good the tight-binding approximation is. However not all Dirac cones necessarily appear from the same tight-binding approximation as in graphene, and a detailed study of the Bloch wave functions, along with the band structure, should be done to understand whether any analytic approximations will be valid.

BIBLIOGRAPHY

- [1] H.-Y. Chen, A. Mitridate, T. Trickle, Z. Zhang, M. Bernardi, and K. M. Zurek, “Dark Matter Direct Detection in Materials with Spin-Orbit Coupling,” *arXiv:2202.11716 [cond-mat, physics:hep-ph]* (Feb., 2022) . <http://arxiv.org/abs/2202.11716>. TT participated in the conception of this project, aided in the derivation of the new dark matter-electron interaction rates, implemented and computed all dark matter-electron interaction rates with EXCEED-DM, created Figures 2-6, and participated in the writing of the manuscript.
- [2] A. Mitridate, T. Trickle, Z. Zhang, and K. M. Zurek, “Dark matter absorption via electronic excitations,” *JHEP* **09** (September, 2021) 123, [arXiv:2106.12586 \[hep-ph\]](https://arxiv.org/abs/2106.12586). <http://arxiv.org/abs/2106.12586>. TT participated in the conception of this project, aided in the derivation of the novel dark matter induced electronic absorption rate formulas, created the Fortran package EXCEED-DM to compute the dark matter - electron absorption rates, created all the Figures, and participated in the writing of the manuscript.
- [3] A. Coskuner, T. Trickle, Z. Zhang, and K. M. Zurek, “Directional detectability of dark matter with single phonon excitations: Target comparison,” *Physical Review D* **105** (Jan., 2022) 015010. <https://link.aps.org/doi/10.1103/PhysRevD.105.015010>. TT participated in the conception of this project, helped develop the Python package, PhonoDark, to compute the dark matter single-phonon scattering rate, and participated in the writing of the manuscript.
- [4] T. Trickle, Z. Zhang, and K. M. Zurek, “Effective Field Theory of Dark Matter Direct Detection With Collective Excitations,” *Phys. Rev. D* **105** (9, 2020) 015001, [arXiv:2009.13534 \[hep-ph\]](https://arxiv.org/abs/2009.13534). TT participated in the conception of this project, aided in the derivation of the effective field theory for phonon and magnon excitations, developed and utilized the program PhonoDark to compute the dark matter single-phonon excitation rates, helped in the numeric calculation of dark matter single-magnon scattering, created all the Figures, and participated in the writing of the manuscript.
- [5] A. Mitridate, T. Trickle, Z. Zhang, and K. M. Zurek, “Detectability of Axion Dark Matter with Phonon Polaritons and Magnons,” *Phys. Rev. D* **102** (5, 2020) 095005, [arXiv:2005.10256 \[hep-ph\]](https://arxiv.org/abs/2005.10256). TT participated in the conception of this project, aided in the derivation of the axion absorption rate formulas, numerically computed all of the absorption rates, created Figures 2-5, and participated in the writing of the manuscript.
- [6] S. M. Griffin, K. Inzani, T. Trickle, Z. Zhang, and K. M. Zurek, “Multichannel direct detection of light dark matter: Target comparison,” *Phys. Rev. D* **101** (2020) no. 5, 055004, [arXiv:1910.10716 \[hep-ph\]](https://arxiv.org/abs/1910.10716). TT aided in the derivation of the dark

- matter induced scattering rates, created the preliminary versions of PhonoDark and EXCEED-DM tools which compute dark matter single-phonon, electron excitation rates, respectively, created all Figures with the exception of the crystal structures and electronic band structures, and participated in the writing of the manuscript.
- [7] T. Trickle, Z. Zhang, K. M. Zurek, K. Inzani, and S. Griffin, “Multi-Channel Direct Detection of Light Dark Matter: Theoretical Framework,” *JHEP* **03** (2020) 036, [arXiv:1910.08092 \[hep-ph\]](#). TT aided in the derivation of the dark matter induced scattering rates, created the preliminary versions of PhonoDark and EXCEED-DM tools which compute dark matter single-phonon, electron excitation rates, respectively, created Figures 3-6, and participated in the writing of the manuscript.
- [8] T. Trickle, Z. Zhang, and K. M. Zurek, “Detecting Light Dark Matter with Magnons,” *Phys. Rev. Lett.* **124** (2020) no. 20, 201801, [arXiv:1905.13744 \[hep-ph\]](#). TT participated in the conception of this project, aided in the derivation of the novel dark matter-magnon scattering rate calculation, helped perform the numeric calculation of the scattering rates, created Figure 2, and participated in the writing of the manuscript.
- [9] S. M. Griffin, K. Inzani, T. Trickle, Z. Zhang, and K. M. Zurek, “Extended calculation of dark matter-electron scattering in crystal targets,” *Phys. Rev. D* **104** (5, 2021) 095015, [arXiv:2105.05253 \[hep-ph\]](#). TT participated in the conception of this project, aided in the derivation of the novel dark matter induced electronic scattering rate formulas, created the Fortran package EXCEED-DM to compute the dark matter - electron scattering rates, created all of the Figures, and participated in the writing of the manuscript.
- [10] S. Knapen, T. Lin, and K. M. Zurek, “Light Dark Matter: Models and Constraints,” *Phys. Rev.* **D96** (2017) no. 11, 115021, [arXiv:1709.07882 \[hep-ph\]](#).
- [11] M. Battaglieri *et al.*, “US Cosmic Visions: New Ideas in Dark Matter 2017: Community Report,” in *U.S. Cosmic Visions: New Ideas in Dark Matter College Park, MD, USA, March 23-25, 2017*. 2017. [arXiv:1707.04591 \[hep-ph\]](#). <http://lss.fnal.gov/archive/2017/conf/fermilab-conf-17-282-ae-ppd-t.pdf>.
- [12] **DarkSide** Collaboration, P. Agnes *et al.*, “Low-Mass Dark Matter Search with the DarkSide-50 Experiment,” *Phys. Rev. Lett.* **121** (2018) no. 8, 081307, [arXiv:1802.06994 \[astro-ph.HE\]](#).
- [13] **XENON** Collaboration, E. Aprile *et al.*, “Dark matter search results from a one ton-year exposure of xenon1t,” *Phys. Rev. Lett.* **121** (2018) no. 11, 111302, [arXiv:1805.12562 \[astro-ph.CO\]](#).
- [14] **XENON** Collaboration, E. Aprile *et al.*, “Light Dark Matter Search with Ionization Signals in XENON1T,” *Phys. Rev. Lett.* **123** (2019) no. 25, 251801, [arXiv:1907.11485 \[hep-ex\]](#).

- [15] **CRESST** Collaboration, G. Angloher *et al.*, “Results on light dark matter particles with a low-threshold CRESST-II detector,” *Eur. Phys. J. C* **76** (2016) no. 1, 25, [arXiv:1509.01515 \[astro-ph.CO\]](#).
- [16] **LUX** Collaboration, D. S. Akerib *et al.*, “Extending light wimp searches to single scintillation photons in lux,” *Phys. Rev. D* **101** (2019) no. 4, 042001, [arXiv:1907.06272 \[astro-ph.CO\]](#).
- [17] H. Vogel and J. Redondo, “Dark Radiation constraints on minicharged particles in models with a hidden photon,” *JCAP* **1402** (2014) 029, [arXiv:1311.2600 \[hep-ph\]](#).
- [18] X. Chu, T. Hambye, and M. H. G. Tytgat, “The Four Basic Ways of Creating Dark Matter Through a Portal,” *JCAP* **1205** (2012) 034, [arXiv:1112.0493 \[hep-ph\]](#).
- [19] R. Essig, J. Mardon, and T. Volansky, “Direct Detection of Sub-GeV Dark Matter,” *Phys. Rev.* **D85** (Aug., 2012) 076007, [arXiv:1108.5383 \[hep-ph\]](#).
- [20] C. Dvorkin, T. Lin, and K. Schutz, “Making dark matter out of light: freeze-in from plasma effects,” *Phys. Rev. D* **99** (2019) no. 11, 115009, [arXiv:1902.08623 \[hep-ph\]](#).
- [21] **DAMIC** Collaboration, A. Aguilar-Arevalo *et al.*, “Constraints on light dark matter particles interacting with electrons from damic at snolab,” *Phys. Rev. Lett.* **123** (2019) no. 18, 181802, [arXiv:1907.12628 \[astro-ph.CO\]](#).
- [22] **SENSEI** Collaboration, O. Abramoff *et al.*, “SENSEI: Direct-Detection Constraints on Sub-GeV Dark Matter from a Shallow Underground Run Using a Prototype Skipper-CCD,” *Phys. Rev. Lett.* **122** (2019) no. 16, 161801, [arXiv:1901.10478 \[hep-ex\]](#).
- [23] **SuperCDMS** Collaboration, R. Agnese *et al.*, “First Dark Matter Constraints from a SuperCDMS Single-Charge Sensitive Detector,” *Phys. Rev. Lett.* **121** (aug, 2018) 051301, [arXiv:1804.10697 \[hep-ex\]](#). [Erratum: *Phys.Rev.Lett.* 122, 069901 (2019)].
- [24] R. Essig, T. Volansky, and T.-T. Yu, “New constraints and prospects for sub-GeV dark matter scattering off electrons in xenon,” *Physical Review D* **96** (aug, 2017) 043017, [arXiv:1703.00910 \[hep-ph\]](#).
- [25] R. Essig, A. Manalaysay, J. Mardon, P. Sorensen, and T. Volansky, “First Direct Detection Limits on sub-GeV Dark Matter from XENON10,” *Phys. Rev. Lett.* **109** (2012) 021301, [arXiv:1206.2644 \[astro-ph.CO\]](#).
- [26] **XENON100** Collaboration, E. Aprile *et al.*, “First Axion Results from the XENON100 Experiment,” *Phys. Rev.* **D90** (2014) no. 6, 062009, [arXiv:1404.1455 \[astro-ph.CO\]](#).

- [27] **XENON** Collaboration, E. Aprile *et al.*, “Constraining the spin-dependent wimp-nucleon cross sections with xenon1t,” *Phys. Rev. Lett.* **122** (2019) no. 14, 141301, [arXiv:1902.03234 \[astro-ph.CO\]](#).
- [28] S. Griffin, S. Knapen, T. Lin, and K. M. Zurek, “Directional Detection of Light Dark Matter with Polar Materials,” *Phys. Rev. D* **98** (2018) no. 11, 115034, [arXiv:1807.10291 \[hep-ph\]](#).
- [29] A. Coskuner, A. Mitridate, A. Olivares, and K. M. Zurek, “Directional Dark Matter Detection in Anisotropic Dirac Materials,” *Phys. Rev. D* **103** (9, 2021) 016006, [arXiv:1909.09170 \[hep-ph\]](#).
- [30] A. Ayala, I. Domínguez, M. Giannotti, A. Mirizzi, and O. Straniero, “Revisiting the bound on axion-photon coupling from globular clusters,” *Phys. Rev. Lett.* **113** (2014) no. 19, 191302, [arXiv:1406.6053 \[astro-ph.SR\]](#).
- [31] M. M. Miller Bertolami, B. E. Melendez, L. G. Althaus, and J. Isern, “Revisiting the axion bounds from the Galactic white dwarf luminosity function,” *JCAP* **10** (2014) no. 10, 069, [arXiv:1406.7712 \[hep-ph\]](#).
- [32] S. Chigusa, T. Moroi, and K. Nakayama, “Detecting light boson dark matter through conversion into magnon,” [arXiv:2001.10666 \[hep-ph\]](#).
- [33] R. Essig, M. Fernandez-Serra, J. Mardon, A. Soto, T. Volansky, and T.-T. Yu, “Direct Detection of sub-GeV Dark Matter with Semiconductor Targets,” *JHEP* **05** (2016) 046, [arXiv:1509.01598 \[hep-ph\]](#).
<https://arxiv.org/pdf/1509.01598.pdf><https://link.springer.com/content/pdf/10.1007%7B%7D2FJHEP05%7B%7D282016%7B%7D29046.pdf>.
- [34] S. Derenzo, R. Essig, A. Massari, A. Soto, and T.-T. Yu, “Direct Detection of sub-GeV Dark Matter with Scintillating Targets,” *Phys. Rev. D* **96** (July, 2017) 016026, [arXiv:1607.01009 \[hep-ph\]](#).
- [35] S. K. Lee, M. Lisanti, S. Mishra-Sharma, and B. R. Safdi, “Modulation Effects in Dark Matter-Electron Scattering Experiments,” *Phys. Rev. D* **92** (2015) no. 8, 083517, [arXiv:1508.07361 \[hep-ph\]](#).
- [36] S. Knapen, J. Kozaczuk, and T. Lin, “Dark matter-electron scattering in dielectrics,” [arXiv:2101.08275 \[hep-ph\]](#).
- [37] *Handbook of Optical Constants of Solids*. Elsevier, 1985.
- [38] R. L. Benbow and D. W. Lynch, “Optical absorption in Al and dilute alloys of Mg and Li in Al at 4.2 K,” *Phys. Rev. B* **12** (Dec, 1975) 5615–5621.
<http://link.aps.org/doi/10.1103/PhysRevB.12.5615>.
- [39] Y. Hochberg, T. Lin, and K. M. Zurek, “Absorption of light dark matter in semiconductors,” *Phys. Rev.* **D95** (2017) no. 2, 023013, [arXiv:1608.01994 \[hep-ph\]](#).

- [40] I. M. Bloch, R. Essig, K. Tobioka, T. Volansky, and T.-T. Yu, “Searching for Dark Absorption with Direct Detection Experiments,” *JHEP* **06** (June, 2017) 087, [arXiv:1608.02123 \[hep-ph\]](https://arxiv.org/abs/1608.02123). [https://doi.org/10.1007/JHEP06\(2017\)087](https://doi.org/10.1007/JHEP06(2017)087).
- [41] Y. Hochberg, T. Lin, and K. M. Zurek, “Detecting Ultralight Bosonic Dark Matter via Absorption in Superconductors,” *Phys. Rev.* **D94** (2016) no. 1, 015019, [arXiv:1604.06800 \[hep-ph\]](https://arxiv.org/abs/1604.06800).
- [42] H. An, M. Pospelov, and J. Pradler, “New stellar constraints on dark photons,” *Phys. Lett.* **B725** (2013) 190–195, [arXiv:1302.3884 \[hep-ph\]](https://arxiv.org/abs/1302.3884).
- [43] **Particle Data Group** Collaboration, M. Tanabashi *et al.*, “Review of Particle Physics,” *Phys. Rev. D* **98** (2018) no. 3, 030001.
- [44] G. B. Gelmini, V. Takhistov, and E. Vitagliano, “Scalar Direct Detection: In-Medium Effects,” *Phys. Lett. B* **809** (2020) 135779, [arXiv:2006.13909 \[hep-ph\]](https://arxiv.org/abs/2006.13909).
- [45] E. G. Adelberger, B. R. Heckel, and A. E. Nelson, “Tests of the gravitational inverse square law,” *Ann. Rev. Nucl. Part. Sci.* **53** (2003) 77–121, [arXiv:hep-ph/0307284 \[hep-ph\]](https://arxiv.org/abs/hep-ph/0307284).
- [46] E. Hardy and R. Lasenby, “Stellar cooling bounds on new light particles: plasma mixing effects,” *JHEP* **02** (2017) 033, [arXiv:1611.05852 \[hep-ph\]](https://arxiv.org/abs/1611.05852).
- [47] H. Xiong, J. A. Sobota, S.-L. Yang, H. Soifer, A. Gauthier, M.-H. Lu, Y.-Y. Lv, S.-H. Yao, D. Lu, M. Hashimoto, P. S. Kirchmann, Y.-F. Chen, and Z.-X. Shen, “Three-dimensional nature of the band structure of ZrTe_5 measured by high-momentum-resolution photoemission spectroscopy,” *Physical Review B* **95** (May, 2017) 195119. <https://link.aps.org/doi/10.1103/PhysRevB.95.195119>.
- [48] S. Knapen, J. Kozaczuk, and T. Lin, “python package for dark matter scattering in dielectric targets,” *Phys. Rev. D* **105** (4, 2022) 015014, [arXiv:2104.12786 \[hep-ph\]](https://arxiv.org/abs/2104.12786).
- [49] Y. Hochberg, Y. Kahn, N. Kurinsky, B. V. Lehmann, T. C. Yu, and K. K. Berggren, “Determining dark matter-electron scattering rates from the dielectric function,” 1, 2021.
- [50] A. Togo and I. Tanaka, “First principles phonon calculations in materials science,” *Scr. Mater.* **108** (Nov, 2015) 1–5.
- [51] Y. Hinuma, G. Pizzi, Y. Kumagai, F. Oba, and I. Tanaka, “Band structure diagram paths based on crystallography,” [arXiv:1602.06402](https://arxiv.org/abs/1602.06402). <http://arxiv.org/abs/1602.06402>.
- [52] M. Pospelov and T. ter Veldhuis, “Direct and indirect limits on the electromagnetic form-factors of WIMPs,” *Phys. Lett. B* **480** (2000) 181–186, [arXiv:hep-ph/0003010 \[hep-ph\]](https://arxiv.org/abs/hep-ph/0003010).

- [53] K. Sigurdson, M. Doran, A. Kurylov, R. R. Caldwell, and M. Kamionkowski, “Dark-matter electric and magnetic dipole moments,” *Phys. Rev. D* **70** (2004) 083501, [arXiv:astro-ph/0406355 \[astro-ph\]](#). [Erratum: *Phys.Rev.D* 73, 089903 (2006)].
- [54] E. Masso, S. Mohanty, and S. Rao, “Dipolar Dark Matter,” *Phys. Rev. D* **80** (2009) 036009, [arXiv:0906.1979 \[hep-ph\]](#).
- [55] A. Fitzpatrick and K. M. Zurek, “Dark Moments and the DAMA-CoGeNT Puzzle,” *Phys. Rev. D* **82** (2010) 075004, [arXiv:1007.5325 \[hep-ph\]](#).
- [56] S. Chang, N. Weiner, and I. Yavin, “Magnetic Inelastic Dark Matter,” *Phys. Rev. D* **82** (2010) 125011, [arXiv:1007.4200 \[hep-ph\]](#).
- [57] V. Barger, W.-Y. Keung, and D. Marfatia, “Electromagnetic properties of dark matter: Dipole moments and charge form factor,” *Phys. Lett. B* **696** (2011) 74–78, [arXiv:1007.4345 \[hep-ph\]](#).
- [58] T. Banks, J.-F. Fortin, and S. Thomas, “Direct Detection of Dark Matter Electromagnetic Dipole Moments,” [arXiv:1007.5515 \[hep-ph\]](#).
- [59] C. M. Ho and R. J. Scherrer, “Anapole Dark Matter,” *Phys. Lett. B* **722** (2013) 341–346, [arXiv:1211.0503 \[hep-ph\]](#).
- [60] M. I. Gresham and K. M. Zurek, “On the Effect of Nuclear Response Functions in Dark Matter Direct Detection,” *Phys. Rev. D* **89** (jan, 2014) 123521, [arXiv:1401.3739 \[hep-ph\]](#). <http://arxiv.org/abs/1401.3739><http://dx.doi.org/10.1103/PhysRevD.89.123521>.
- [61] E. Del Nobile, G. B. Gelmini, P. Gondolo, and J.-H. Huh, “Direct detection of Light Anapole and Magnetic Dipole DM,” *JCAP* **1406** (2014) 002, [arXiv:1401.4508 \[hep-ph\]](#).
- [62] B. J. Kavanagh, P. Panci, and R. Ziegler, “Faint Light from Dark Matter: Classifying and Constraining Dark Matter-Photon Effective Operators,” *JHEP* **04** (2019) 089, [arXiv:1810.00033 \[hep-ph\]](#).
- [63] X. Chu, J. Pradler, and L. Semmelrock, “Light dark states with electromagnetic form factors,” *Phys. Rev. D* **99** (2019) no. 1, 015040, [arXiv:1811.04095 \[hep-ph\]](#).
- [64] S. Knapen, T. Lin, M. Pyle, and K. M. Zurek, “Detection of Light Dark Matter With Optical Phonons in Polar Materials,” *Phys. Lett. B* **785** (2018) 386–390, [arXiv:1712.06598 \[hep-ph\]](#).
- [65] G. Cappellini, R. Del Sole, L. Reining, and F. Bechstedt, “Model dielectric function for semiconductors,” *Phys. Rev. B* **47** (Apr, 1993) 9892–9895. <https://link.aps.org/doi/10.1103/PhysRevB.47.9892>.

- [66] F. Zwicky, “Republication of: The redshift of extragalactic nebulae,” *General Relativity and Gravitation* **41** (Jan., 2009) 207–224.
<https://doi.org/10.1007/s10714-008-0707-4>.
- [67] J. Amaré *et al.*, “First Results on Dark Matter Annual Modulation from the ANAIS-112 Experiment,” *Phys. Rev. Lett.* **123** (2019) no. 3, 031301,
[arXiv:1903.03973](https://arxiv.org/abs/1903.03973) [astro-ph.IM].
- [68] C. Cozzini *et al.*, “Results of CRESST phase I,” *AIP Conf. Proc.* **605** (2002) no. 1, 481–484.
- [69] **CRESST** Collaboration, F. Petricca *et al.*, “First results on low-mass dark matter from the CRESST-III experiment,” in *15th International Conference on Topics in Astroparticle and Underground Physics (TAUP 2017) Sudbury, Ontario, Canada, July 24-28, 2017*. 2017. [arXiv:1711.07692](https://arxiv.org/abs/1711.07692) [astro-ph.CO].
- [70] S. Baum, K. Freese, and C. Kelso, “Dark Matter implications of DAMA/LIBRA-phase2 results,” *Phys. Lett.* **B789** (feb, 2019) 262–269,
[arXiv:1804.01231](https://arxiv.org/abs/1804.01231) [astro-ph.CO].
- [71] **DAMIC** Collaboration, J. R. T. de Mello Neto *et al.*, “The DAMIC dark matter experiment,” *PoS ICRC2015* (2016) 1221, [arXiv:1510.02126](https://arxiv.org/abs/1510.02126) [physics.ins-det].
- [72] **DM-Ice** Collaboration, J. H. Jo, “Results from the DM-Ice17 Dark Matter Experiment at the South Pole,” *PoS ICHEP2016* (2017) 1223,
[arXiv:1612.07426](https://arxiv.org/abs/1612.07426) [physics.ins-det].
- [73] **KIMS** Collaboration, K. Kim, “Status of the KIMS-NaI experiment,” in *Proceedings, Meeting of the APS Division of Particles and Fields (DPF 2015): Ann Arbor, Michigan, USA, 4-8 Aug 2015*. 2015. [arXiv:1511.00023](https://arxiv.org/abs/1511.00023) [physics.ins-det].
- [74] **LUX** Collaboration, D. S. Akerib *et al.*, “Liquid xenon scintillation measurements and pulse shape discrimination in the LUX dark matter detector,” *Phys. Rev.* **D97** (2018) no. 11, 112002, [arXiv:1802.06162](https://arxiv.org/abs/1802.06162) [physics.ins-det].
- [75] **LUX** Collaboration, D. Akerib *et al.*, “Results of a Search for Sub-GeV Dark Matter Using 2013 LUX Data,” *Phys. Rev. Lett.* **122** (2019) no. 13, 131301,
[arXiv:1811.11241](https://arxiv.org/abs/1811.11241) [astro-ph.CO].
- [76] E. Shields, J. Xu, and F. Calaprice, “SABRE: A New NaI(Tl) Dark Matter Direct Detection Experiment,” *Phys. Procedia* **61** (2015) 169–178.
- [77] **SuperCDMS** Collaboration, R. Agnese *et al.*, “Search for Low-Mass Weakly Interacting Massive Particles with SuperCDMS,” *Phys. Rev. Lett.* **112** (2014) no. 24, 241302, [arXiv:1402.7137](https://arxiv.org/abs/1402.7137) [hep-ex].

- [78] **SuperCDMS** Collaboration, R. Agnese *et al.*, “Projected Sensitivity of the SuperCDMS SNOLAB experiment,” *Phys. Rev.* **D95** (Apr, 2017) 082002, [arXiv:1610.00006 \[physics.ins-det\]](#).
<https://link.aps.org/doi/10.1103/PhysRevD.95.082002>.
- [79] **SuperCDMS** Collaboration, R. Agnese *et al.*, “New Results from the Search for Low-Mass Weakly Interacting Massive Particles with the CDMS Low Ionization Threshold Experiment,” *Phys. Rev. Lett.* **116** (Sept., 2016) 071301, [arXiv:1509.02448 \[astro-ph.CO\]](#).
- [80] **SuperCDMS** Collaboration, R. Agnese *et al.*, “Search for Low-Mass Dark Matter with CDMSlite Using a Profile Likelihood Fit,” *Phys. Rev. D* **99** (2019) no. 6, 062001, [arXiv:1808.09098 \[astro-ph.CO\]](#).
- [81] **DAMIC**, **DAMIC-M** Collaboration, M. Settimo, “Search for low-mass dark matter with the DAMIC experiment,” in *16th Rencontres du Vietnam: Theory meeting experiment: Particle Astrophysics and Cosmology*. 4, 2020. [arXiv:2003.09497 \[hep-ex\]](#).
- [82] **EDELWEISS** Collaboration, E. Armengaud *et al.*, “Searches for electron interactions induced by new physics in the EDELWEISS-III Germanium bolometers,” *Phys. Rev. D* **98** (2018) no. 8, 082004, [arXiv:1808.02340 \[hep-ex\]](#).
- [83] **EDELWEISS** Collaboration, E. Armengaud *et al.*, “Searching for low-mass dark matter particles with a massive Ge bolometer operated above-ground,” *Phys. Rev. D* **99** (2019) no. 8, 082003, [arXiv:1901.03588 \[astro-ph.GA\]](#).
- [84] **EDELWEISS** Collaboration, Q. Arnaud *et al.*, “First germanium-based constraints on sub-MeV Dark Matter with the EDELWEISS experiment,” *Phys. Rev. Lett.* **125** (2020) no. 14, 141301, [arXiv:2003.01046 \[astro-ph.GA\]](#).
- [85] **SENSEI** Collaboration, J. Tiffenberg, M. Sofo-Haro, A. Drlica-Wagner, R. Essig, Y. Guardincerri, S. Holland, T. Volansky, and T.-T. Yu, “Single-electron and single-photon sensitivity with a silicon Skipper CCD,” *Phys. Rev. Lett.* **119** (2017) no. 13, 131802, [arXiv:1706.00028 \[physics.ins-det\]](#).
- [86] **SENSEI** Collaboration, M. Crisler, R. Essig, J. Estrada, G. Fernandez, J. Tiffenberg, M. Sofo haro, T. Volansky, and T.-T. Yu, “SENSEI: First Direct-Detection Constraints on sub-GeV Dark Matter from a Surface Run,” *Phys. Rev. Lett.* **121** (2018) no. 6, 061803, [arXiv:1804.00088 \[hep-ex\]](#).
- [87] **SENSEI** Collaboration, L. Barak *et al.*, “SENSEI: Direct-Detection Results on sub-GeV Dark Matter from a New Skipper-CCD,” *Phys. Rev. Lett.* **125** (4, 2020) 171802, [arXiv:2004.11378 \[astro-ph.CO\]](#).
- [88] **SuperCDMS** Collaboration, R. Agnese *et al.*, “Low-mass dark matter search with cdmslite,” *Phys. Rev.* **D97** (2018) no. 2, 022002, [arXiv:1707.01632 \[astro-ph.CO\]](#).

- [89] **SuperCDMS** Collaboration, D. W. Amaral *et al.*, “Constraints on low-mass, relic dark matter candidates from a surface-operated SuperCDMS single-charge sensitive detector,” *Phys. Rev. D* **102** (2020) no. 9, 091101, [arXiv:2005.14067 \[hep-ex\]](#).
- [90] C. Chang *et al.*, “Snowmass 2021 Letter of Interest: The TESSARACT Dark Matter Project,” 2020. https://www.snowmass21.org/docs/files/summaries/CF/SNOWMASS21-CF1_CF2-IF1_IF8-120.pdf.
- [91] G. Ruoso, A. Lombardi, A. Ortolan, R. Pengo, C. Braggio, G. Carugno, C. S. Gallo, and C. C. Speake, “The QUAX proposal: a search of galactic axion with magnetic materials,” *J. Phys. Conf. Ser.* **718** (2016) no. 4, 042051, [arXiv:1511.09461 \[hep-ph\]](#).
- [92] R. Barbieri, C. Braggio, G. Carugno, C. S. Gallo, A. Lombardi, A. Ortolan, R. Pengo, G. Ruoso, and C. C. Speake, “Searching for galactic axions through magnetized media: the QUAX proposal,” *Phys. Dark Univ.* **15** (2017) 135–141, [arXiv:1606.02201 \[hep-ph\]](#).
- [93] N. Crescini *et al.*, “Operation of a ferromagnetic axion haloscope at $m_a = 58 \mu\text{eV}$,” *Eur. Phys. J.* **C78** (2018) no. 9, 703, [arXiv:1806.00310 \[hep-ex\]](#). [Erratum: *Eur. Phys. J.*C78,no.9,813(2018)].
- [94] D. Alesini *et al.*, “Galactic axions search with a superconducting resonant cavity,” *Phys. Rev. D* **99** (2019) no. 10, 101101, [arXiv:1903.06547 \[physics.ins-det\]](#).
- [95] **QUAX** Collaboration, N. Crescini *et al.*, “Axion search with a quantum-limited ferromagnetic haloscope,” *Phys. Rev. Lett.* **124** (2020) no. 17, 171801, [arXiv:2001.08940 \[hep-ex\]](#).
- [96] C. Csáki and P. Tanedo, “Beyond the Standard Model,” [arXiv:1602.04228 \[hep-ph\]](#) (2015) . <http://arxiv.org/abs/1602.04228>. arXiv: 1602.04228.
- [97] A. Padilla, “Lectures on the Cosmological Constant Problem,” [arXiv:1502.05296 \[astro-ph, physics:gr-qc, physics:hep-ph, physics:hep-th\]](#) (Feb., 2015) . <http://arxiv.org/abs/1502.05296>. arXiv: 1502.05296.
- [98] R. D. Peccei and H. R. Quinn, “CP Conservation in the Presence of Pseudoparticles,” *Physical Review Letters* **38** (jun, 1977) 1440–1443.
- [99] R. D. Peccei and H. R. Quinn, “Constraints imposed by CP conservation in the presence of pseudoparticles,” *Physical Review D* **16** (sep, 1977) 1791–1797.
- [100] A. Hook, “TASI Lectures on the Strong CP Problem and Axions,” [arXiv:1812.02669 \[hep-ph\]](#) (July, 2021) . <http://arxiv.org/abs/1812.02669>. arXiv: 1812.02669.
- [101] Particle Data Group, P. A. Zyla, R. M. Barnett, J. Beringer, O. Dahl, D. A. Dwyer, D. E. Groom, C. J. Lin, K. S. Lugovsky, E. Pianori, D. J. Robinson, C. G. Wohl, W. M. Yao, K. Agashe, G. Aielli, B. C. Allanach, C. Amsler, M. Antonelli, E. C. Aschenauer, D. M. Asner, H. Baer, S. Banerjee, L. Baudis, C. W. Bauer, J. J. Beatty,

- V. I. Belousov, S. Bethke, A. Bettini, O. Biebel, K. M. Black, E. Blucher, O. Buchmuller, V. Burkert, M. A. Bychkov, R. N. Cahn, M. Carena, A. Ceccucci, A. Cerri, D. Chakraborty, R. S. Chivukula, G. Cowan, G. D'Ambrosio, T. Damour, D. de Florian, A. de Gouvêa, T. DeGrand, P. de Jong, G. Dissertori, B. A. Dobrescu, M. D'Onofrio, M. Doser, M. Drees, H. K. Dreiner, P. Eerola, U. Egede, S. Eidelman, J. Ellis, J. Erler, V. V. Ezhela, W. Fetscher, B. D. Fields, B. Foster, A. Freitas, H. Gallagher, L. Garren, H. J. Gerber, G. Gerbier, T. Gershon, Y. Gershtein, T. Gherghetta, A. A. Godizov, M. C. Gonzalez-Garcia, M. Goodman, C. Grab, A. V. Griksan, C. Grojean, M. Grünewald, A. Gurtu, T. Gutsche, H. E. Haber, C. Hanhart, S. Hashimoto, Y. Hayato, A. Hebecker, S. Heinemeyer, B. Heltsley, J. J. Hernández-Rey, K. Hikasa, J. Hisano, A. Höcker, J. Holder, A. Holtkamp, J. Huston, T. Hyodo, K. F. Johnson, M. Kado, M. Karliner, U. F. Katz, M. Kenzie, V. A. Khoze, S. R. Klein, E. Klempt, R. V. Kowalewski, F. Krauss, M. Kreps, B. Krusche, Y. Kwon, O. Lahav, J. Laiho, L. P. Lellouch, J. Lesgourgues, A. R. Liddle, Z. Ligeti, C. Lippmann, T. M. Liss, L. Littenberg, C. Lourenço, S. B. Lugovsky, A. Lusiani, Y. Makida, F. Maltoni, T. Mannel, A. V. Manohar, W. J. Marciano, A. Masoni, J. Matthews, U. G. Meißner, M. Mikhasenko, D. J. Miller, D. Milstead, R. E. Mitchell, K. Mönig, P. Molaro, F. Moortgat, M. Moskovic, K. Nakamura, M. Narain, P. Nason, S. Navas, M. Neubert, P. Nevski, Y. Nir, K. A. Olive, C. Patrignani, J. A. Peacock, S. T. Petcov, V. A. Petrov, A. Pich, A. Piepke, A. Pomarol, S. Profumo, A. Quadt, K. Rabbertz, J. Rademacker, G. Raffelt, H. Ramani, M. Ramsey-Musolf, B. N. Ratcliff, P. Richardson, A. Ringwald, S. Roesler, S. Rolli, A. Romaniouk, L. J. Rosenberg, J. L. Rosner, G. Rybka, M. Ryskin, R. A. Ryutin, Y. Sakai, G. P. Salam, S. Sarkar, F. Sauli, O. Schneider, K. Scholberg, A. J. Schwartz, J. Schwiening, D. Scott, V. Sharma, S. R. Sharpe, T. Shutt, M. Silari, T. Sjöstrand, P. Skands, T. Skwarnicki, G. F. Smoot, A. Soffer, M. S. Sozzi, S. Spanier, C. Spiering, A. Stahl, S. L. Stone, Y. Sumino, T. Sumiyoshi, M. J. Syphers, F. Takahashi, M. Tanabashi, J. Tanaka, M. Taševský, K. Terashi, J. Terning, U. Thoma, R. S. Thorne, L. Tiator, M. Titov, N. P. Tkachenko, D. R. Tovey, K. Trabelsi, P. Urquijo, G. Valencia, R. Van de Water, N. Varelas, G. Venanzoni, L. Verde, M. G. Vinster, P. Vogel, W. Vogelsang, A. Vogt, V. Vorobyev, S. P. Wakely, W. Walkowiak, C. W. Walter, D. Wands, M. O. Wascko, D. H. Weinberg, E. J. Weinberg, M. White, L. R. Wiencke, S. Willocq, C. L. Woody, R. L. Workman, M. Yokoyama, R. Yoshida, G. Zanderighi, G. P. Zeller, O. V. Zenin, R. Y. Zhu, S. L. Zhu, F. Zimmermann, J. Anderson, T. Basaglia, V. S. Lugovsky, P. Schaffner, and W. Zheng, “Review of Particle Physics,” *Progress of Theoretical and Experimental Physics* **2020** (Aug., 2020) 083C01. <https://doi.org/10.1093/ptep/ptaa104>.
- [102] H. W. Babcock, “The rotation of the Andromeda Nebula,” *Lick Observatory Bulletin* **498** (Jan., 1939) 41–51. <https://ui.adsabs.harvard.edu/abs/1939LicOB..19...41B>. ADS Bibcode: 1939LicOB..19...41B.
- [103] V. C. Rubin and W. K. Ford, Jr., “Rotation of the Andromeda Nebula from a Spectroscopic Survey of Emission Regions,” *The Astrophysical Journal* **159** (Feb.,

- 1970) 379. <https://ui.adsabs.harvard.edu/abs/1970ApJ...159..379R>. ADS Bibcode: 1970ApJ...159..379R.
- [104] Y. Sofue, “Rotation Curve of the Milky Way and the Dark Matter Density,” *arXiv:2004.11688 [astro-ph]* (Apr., 2020) . <http://arxiv.org/abs/2004.11688>. arXiv: 2004.11688.
- [105] M. Milgrom, “A modification of the Newtonian dynamics as a possible alternative to the hidden mass hypothesis.,” *The Astrophysical Journal* **270** (July, 1983) 365–370. <https://ui.adsabs.harvard.edu/abs/1983ApJ...270..365M>. ADS Bibcode: 1983ApJ...270..365M.
- [106] S. Dodelson, “The Real Problem with MOND,” *International Journal of Modern Physics D* **20** (Dec., 2011) 2749–2753. <http://arxiv.org/abs/1112.1320>. arXiv: 1112.1320.
- [107] G. F. Smoot, “COBE observations and results,” in *Conference on 3K cosmology*. ASCE, 1999.
- [108] G. Hinshaw, D. Larson, E. Komatsu, D. N. Spergel, C. L. Bennett, J. Dunkley, M. R. Nolta, M. Halpern, R. S. Hill, N. Odegard, L. Page, K. M. Smith, J. L. Weiland, B. Gold, N. Jarosik, A. Kogut, M. Limon, S. S. Meyer, G. S. Tucker, E. Wollack, and E. L. Wright, “Nine-year wilkinson microwave anisotropy probe (wmap) observations: Cosmological parameter results,” [arXiv:1212.5226 \[astro-ph.CO\]](https://arxiv.org/abs/1212.5226).
- [109] P. Collaboration, N. Aghanim, Y. Akrami, M. Ashdown, J. Aumont, C. Baccigalupi, M. Ballardini, A. J. Banday, R. B. Barreiro, N. Bartolo, S. Basak, R. Battye, K. Benabed, J.-P. Bernard, M. Bersanelli, P. Bielewicz, J. J. Bock, J. R. Bond, J. Borrill, F. R. Bouchet, F. Boulanger, M. Bucher, C. Burigana, R. C. Butler, E. Calabrese, J.-F. Cardoso, J. Carron, A. Challinor, H. C. Chiang, J. Chluba, L. P. L. Colombo, C. Combet, D. Contreras, B. P. Crill, F. Cuttaia, P. de Bernardis, G. de Zotti, J. Delabrouille, J.-M. Delouis, E. Di Valentino, J. M. Diego, O. Doré, M. Douspis, A. Ducout, X. Dupac, S. Dusini, G. Efstathiou, F. Elsner, T. A. Enßlin, H. K. Eriksen, Y. Fantaye, M. Farhang, J. Fergusson, R. Fernandez-Cobos, F. Finelli, F. Forastieri, M. Frailis, A. A. Fraisse, E. Franceschi, A. Frolov, S. Galeotta, S. Galli, K. Ganga, R. T. Génova-Santos, M. Gerbino, T. Ghosh, J. González-Nuevo, K. M. Górski, S. Gratton, A. Gruppuso, J. E. Gudmundsson, J. Hamann, W. Handley, F. K. Hansen, D. Herranz, S. R. Hildebrandt, E. Hivon, Z. Huang, A. H. Jaffe, W. C. Jones, A. Karakci, E. Keihänen, R. Keskitalo, K. Kiiveri, J. Kim, T. S. Kisner, L. Knox, N. Krachmalnicoff, M. Kunz, H. Kurki-Suonio, G. Lagache, J.-M. Lamarre, A. Lasenby, M. Lattanzi, C. R. Lawrence, M. L. Jeune, P. Lemos, J. Lesgourgues, F. Levrier, A. Lewis, M. Liguori, P. B. Lilje, M. Lilley, V. Lindholm, M. López-Caniego, P. M. Lubin, Y.-Z. Ma, J. F. Macías-Pérez, G. Maggio, D. Maino, N. Mandolesi, A. Mangilli, A. Marcos-Caballero, M. Maris, P. G. Martin, M. Martinelli, E. Martínez-González, S. Matarrese, N. Mauri, J. D. McEwen, P. R. Meinhold, A. Melchiorri, A. Mennella, M. Migliaccio, M. Millea, S. Mitra, M.-A. Miville-Deschênes, D. Molinari, L. Montier, G. Morgante, A. Moss, P. Natoli, H. U.

- Nørgaard-Nielsen, L. Pagano, D. Paoletti, B. Partridge, G. Patanchon, H. V. Peiris, F. Perrotta, V. Pettorino, F. Piacentini, L. Polastri, G. Polenta, J.-L. Puget, J. P. Rachen, M. Reinecke, M. Remazeilles, A. Renzi, G. Rocha, C. Rosset, G. Roudier, J. A. Rubiño-Martín, B. Ruiz-Granados, L. Salvati, M. Sandri, M. Savelainen, D. Scott, E. P. S. Shellard, C. Sirignano, G. Sirri, L. D. Spencer, R. Sunyaev, A.-S. Suur-Uski, J. A. Tauber, D. Tavagnacco, M. Tenti, L. Toffolatti, M. Tomasi, T. Trombetti, L. Valenziano, J. Valiviita, B. Van Tent, L. Vibert, P. Vielva, F. Villa, N. Vittorio, B. D. Wandelt, I. K. Wehus, M. White, S. D. M. White, A. Zacchei, and A. Zonca, “Planck 2018 results. VI. Cosmological parameters,” *Astronomy & Astrophysics* **641** (Sept., 2020) A6, [arXiv:1807.06209 \[astro-ph.CO\]](https://arxiv.org/abs/1807.06209). <http://arxiv.org/abs/1807.06209>. arXiv: 1807.06209.
- [110] S. Dodelson, *Modern cosmology*. Academic Press, 2003.
- [111] E. W. Kolb and M. S. Turner, *The Early Universe (Frontiers in Physics)*. Perseus Books Group.
- [112] J. S. Bullock and M. Boylan-Kolchin, “Small-scale challenges to the Λ CDM paradigm,” *Annual Review of Astronomy and Astrophysics*, vol. 55, pp. 343–387 (2017) (July, 2017), [arXiv:1707.04256 \[astro-ph.CO\]](https://arxiv.org/abs/1707.04256).
- [113] R. Hlozek, D. Grin, D. J. Marsh, and P. G. Ferreira, “A search for ultralight axions using precision cosmological data,” *Physical Review D* **91** (may, 2015) 103512.
- [114] R. Hložek, D. J. Marsh, D. Grin, R. Allison, J. Dunkley, and E. Calabrese, “Future CMB tests of dark matter: Ultralight axions and massive neutrinos,” *Physical Review D* **95** (jun, 2017) 123511.
- [115] R. Hložek, D. J. E. Marsh, and D. Grin, “Using the full power of the cosmic microwave background to probe axion dark matter,” *Monthly Notices of the Royal Astronomical Society* **476** (feb, 2018) 3063–3085.
- [116] V. Iršič, M. Viel, M. G. Haehnelt, J. S. Bolton, and G. D. Becker, “First constraints on fuzzy dark matter from Lyman- α forest data and hydrodynamical simulations,” *Physical Review Letters* **119** (jul, 2017) 031302.
- [117] M. Nori, R. Murgia, V. Iršič, M. Baldi, and M. Viel, “Lyman α forest and non-linear structure characterization in fuzzy dark matter cosmologies,” *Monthly Notices of the Royal Astronomical Society* **482** (oct, 2018) 3227–3243.
- [118] E. Armengaud, N. Palanque-Delabrouille, C. Yèche, D. J. E. Marsh, and J. Baur, “Constraining the mass of light bosonic dark matter using SDSS Lyman- α forest,” *Monthly Notices of the Royal Astronomical Society* **471** (jul, 2017) 4606–4614.
- [119] E. O. Nadler, V. Gluscevic, K. K. Boddy, and R. H. Wechsler, “Constraints on dark matter microphysics from the Milky Way satellite population,” *The Astrophysical Journal* **878** (jun, 2019) L32.

- [120] K. Schutz, “Subhalo mass function and ultralight bosonic dark matter,” *Physical Review D* **101** (jun, 2020) 123026.
- [121] J. Zhang, H. Liu, and M.-C. Chu, “Cosmological simulation for fuzzy dark matter model,” *Frontiers in Astronomy and Space Sciences* **5** (jan, 2019) .
- [122] D. Clowe, A. Gonzalez, and M. Markevitch, “Weak lensing mass reconstruction of the interacting cluster 1E0657-558: Direct evidence for the existence of dark matter,” *The Astrophysical Journal* **604** (Apr., 2004) 596–603.
<http://arxiv.org/abs/astro-ph/0312273>. arXiv: astro-ph/0312273.
- [123] D. Clowe, M. Bradač, A. H. Gonzalez, M. Markevitch, S. W. Randall, C. Jones, and D. Zaritsky, “A direct empirical proof of the existence of dark matter,” *The Astrophysical Journal* **648** (Sept., 2006) L109–L113.
<http://arxiv.org/abs/astro-ph/0608407>. arXiv: astro-ph/0608407.
- [124] M. Markevitch, A. H. Gonzalez, D. Clowe, A. Vikhlinin, L. David, W. Forman, C. Jones, S. Murray, and W. Tucker, “Direct constraints on the dark matter self-interaction cross-section from the merging galaxy cluster 1E0657-56,” *The Astrophysical Journal* **606** (May, 2004) 819–824.
<http://arxiv.org/abs/astro-ph/0309303>. arXiv: astro-ph/0309303.
- [125] K. E. Andrade, J. Fuson, S. Gad-Nasr, D. Kong, Q. Minor, M. G. Roberts, and M. Kaplinghat, “A Stringent Upper Limit on Dark Matter Self-Interaction Cross Section from Cluster Strong Lensing,” *Monthly Notices of the Royal Astronomical Society* **510** (Dec., 2021) 54–81. <http://arxiv.org/abs/2012.06611>. arXiv: 2012.06611.
- [126] S. Tremaine and J. E. Gunn, “Dynamical role of light neutral leptons in cosmology,” *Physical Review Letters* **42** (Feb., 1979) 407–410.
<https://ui.adsabs.harvard.edu/abs/1979PhRvL..42..407T>. ADS Bibcode: 1979PhRvL..42..407T.
- [127] C. Di Paolo, F. Nesti, and F. L. Villante, “Phase space mass bound for fermionic dark matter from dwarf spheroidal galaxies,” *Monthly Notices of the Royal Astronomical Society* **475** (Apr., 2018) 5385–5397.
<http://arxiv.org/abs/1704.06644>. arXiv: 1704.06644.
- [128] D. Savchenko and A. Rudakovskiy, “New mass bound on fermionic dark matter from a combined analysis of classical dSphs,” *Monthly Notices of the Royal Astronomical Society* **487** (Aug., 2019) 5711–5720. <http://arxiv.org/abs/1903.01862>. arXiv: 1903.01862.
- [129] J. Alvey, N. Sabti, V. Tiki, D. Blas, K. Bondarenko, A. Boyarsky, M. Escudero, M. Fairbairn, M. Orkney, and J. I. Read, “New Constraints on the Mass of Fermionic Dark Matter from Dwarf Spheroidal Galaxies,” *Monthly Notices of the Royal Astronomical Society* **501** (Dec., 2020) 1188–1201.
<http://arxiv.org/abs/2010.03572>. arXiv: 2010.03572.

- [130] H. Davoudiasl, P. B. Denton, and D. A. McGady, “Ultralight Fermionic Dark Matter,” *Physical Review D* **103** (Mar., 2021) 055014. <http://arxiv.org/abs/2008.06505>. arXiv: 2008.06505.
- [131] B. Audren, J. Lesgourgues, G. Mangano, P. D. Serpico, and T. Tram, “Strongest model-independent bound on the lifetime of Dark Matter,” *Journal of Cosmology and Astroparticle Physics* **2014** (Dec., 2014) 028–028. <http://arxiv.org/abs/1407.2418>. arXiv: 1407.2418.
- [132] A. Bilal, “Introduction to supersymmetry,” 2001.
- [133] G. Arcadi, M. Dutra, P. Ghosh, M. Lindner, Y. Mambrini, M. Pierre, S. Profumo, and F. S. Queiroz, “The waning of the wimp? a review of models, searches, and constraints,” [arXiv:1703.07364](https://arxiv.org/abs/1703.07364) [hep-ph].
- [134] C. Giovanetti, M. Lisanti, H. Liu, and J. T. Ruderman, “Joint CMB and BBN Constraints on Light Dark Sectors with Dark Radiation,” *arXiv:2109.03246 [astro-ph, physics:hep-ph]* (Sept., 2021) . <http://arxiv.org/abs/2109.03246>. arXiv: 2109.03246.
- [135] D. Green and S. Rajendran, “The Cosmology of Sub-MeV Dark Matter,” *JHEP* **10** (Oct., 2017) 013, [arXiv:1701.08750](https://arxiv.org/abs/1701.08750) [hep-ph]. <http://arxiv.org/abs/1701.08750>. arXiv: 1701.08750.
- [136] N. Bernal, M. Heikinheimo, T. Tenkanen, K. Tuominen, and V. Vaskonen, “The Dawn of FIMP Dark Matter: A Review of Models and Constraints,” *Int. J. Mod. Phys. A* **32** (June, 2017) 1730023, [arXiv:1706.07442](https://arxiv.org/abs/1706.07442) [hep-ph].
- [137] L. J. Hall, K. Jedamzik, J. March-Russell, and S. M. West, “Freeze-In Production of FIMP Dark Matter,” *JHEP* **03** (Nov., 2010) 080, [arXiv:0911.1120](https://arxiv.org/abs/0911.1120) [hep-ph].
- [138] K. Petraki and R. R. Volkas, “Review of asymmetric dark matter,” *Int. J. Mod. Phys. A* **28** (2013) 1330028, [arXiv:1305.4939](https://arxiv.org/abs/1305.4939) [hep-ph].
- [139] K. M. Zurek, “Asymmetric Dark Matter: Theories, Signatures, and Constraints,” *Phys. Rept.* **537** (2014) 91–121, [arXiv:1308.0338](https://arxiv.org/abs/1308.0338) [hep-ph].
- [140] T. Lin, H.-B. Yu, and K. M. Zurek, “On Symmetric and Asymmetric Light Dark Matter,” *Phys. Rev.* **D85** (2012) 063503, [arXiv:1111.0293](https://arxiv.org/abs/1111.0293) [hep-ph].
- [141] A. Coskuner, D. M. Grabowska, S. Knapen, and K. M. Zurek, “Direct Detection of Bound States of Asymmetric Dark Matter,” *Phys. Rev.* **D100** (2019) no. 3, 035025, [arXiv:1812.07573](https://arxiv.org/abs/1812.07573) [hep-ph].
- [142] D. E. Kaplan, M. A. Luty, and K. M. Zurek, “Asymmetric Dark Matter,” *Phys. Rev.* **D79** (2009) 115016, [arXiv:0901.4117](https://arxiv.org/abs/0901.4117) [hep-ph].
- [143] T. Cohen, D. J. Phalen, A. Pierce, and K. M. Zurek, “Asymmetric Dark Matter from a GeV Hidden Sector,” *Phys. Rev.* **D82** (2010) 056001, [arXiv:1005.1655](https://arxiv.org/abs/1005.1655) [hep-ph].

- [144] Y. Hochberg, Y. Kahn, M. Lisanti, K. M. Zurek, A. G. Grushin, R. Ilan, S. M. Griffin, Z.-F. Liu, S. F. Weber, and J. B. Neaton, “Detection of sub-MeV Dark Matter with Three-Dimensional Dirac Materials,” *Phys. Rev. D* **97** (January, 2018) 015004, [arXiv:1708.08929](https://arxiv.org/abs/1708.08929) [hep-ph].
<https://link.aps.org/doi/10.1103/PhysRevD.97.015004>.
- [145] J. Preskill, M. B. Wise, and F. Wilczek, “Cosmology of the Invisible Axion,” *Phys. Lett. B* **120** (jan, 1983) 127–132.
- [146] L. Abbott and P. Sikivie, “A Cosmological Bound on the Invisible Axion,” *Phys. Lett. B* **120** (jan, 1983) 133–136.
- [147] M. Dine and W. Fischler, “The Not So Harmless Axion,” *Phys. Lett. B* **120** (jan, 1983) 137–141.
- [148] C.-F. Chang and Y. Cui, “New perspectives on axion misalignment mechanism,” *Phys. Rev. D* **102**, 015003 (2020) (Nov., 2019) , [arXiv:1911.11885](https://arxiv.org/abs/1911.11885) [hep-ph].
- [149] R. T. Co, L. J. Hall, and K. Harigaya, “Kinetic Misalignment Mechanism,” *Phys. Rev. Lett.* **124** (10, 2019) 251802, [arXiv:1910.14152](https://arxiv.org/abs/1910.14152) [hep-ph].
- [150] M. Buschmann, J. W. Foster, A. Hook, A. Peterson, D. E. Willcox, W. Zhang, and B. R. Safdi, “Dark matter from axion strings with adaptive mesh refinement,” *Nature Communications* **13** (feb, 2022) .
- [151] **ADMX** Collaboration, S. J. Asztalos *et al.*, “A SQUID-based microwave cavity search for dark-matter axions,” *Phys. Rev. Lett.* **104** (2010) 041301, [arXiv:0910.5914](https://arxiv.org/abs/0910.5914) [astro-ph.CO].
- [152] **ADMX** Collaboration, N. Du *et al.*, “A Search for Invisible Axion Dark Matter with the Axion Dark Matter Experiment,” *Phys. Rev. Lett.* **120** (2018) no. 15, 151301, [arXiv:1804.05750](https://arxiv.org/abs/1804.05750) [hep-ex].
- [153] **HAYSTAC** Collaboration, L. Zhong *et al.*, “Results from phase 1 of the HAYSTAC microwave cavity axion experiment,” *Phys. Rev.* **D97** (2018) no. 9, 092001, [arXiv:1803.03690](https://arxiv.org/abs/1803.03690) [hep-ex].
- [154] B. T. McAllister, G. Flower, E. N. Ivanov, M. Goryachev, J. Bourhill, and M. E. Tobar, “The ORGAN Experiment: An axion haloscope above 15 GHz,” *Phys. Dark Univ.* **18** (2017) 67–72, [arXiv:1706.00209](https://arxiv.org/abs/1706.00209) [physics.ins-det].
- [155] J. L. Ouellet *et al.*, “First Results from ABRACADABRA-10 cm: A Search for Sub- μ eV Axion Dark Matter,” *Phys. Rev. Lett.* **122** (2019) no. 12, 121802, [arXiv:1810.12257](https://arxiv.org/abs/1810.12257) [hep-ex].
- [156] A. Garcon *et al.*, “Constraints on bosonic dark matter from ultralow-field nuclear magnetic resonance,” [arXiv:1902.04644](https://arxiv.org/abs/1902.04644) [hep-ex].

- [157] **CAST** Collaboration, V. Anastassopoulos *et al.*, “New CAST Limit on the Axion-Photon Interaction,” *Nature Phys.* **13** (2017) 584–590, [arXiv:1705.02290 \[hep-ex\]](#).
- [158] **MADMAX Working Group** Collaboration, A. Caldwell, G. Dvali, B. Majorovits, A. Millar, G. Raffelt, J. Redondo, O. Reimann, F. Simon, and F. Steffen, “Dielectric Haloscopes: A New Way to Detect Axion Dark Matter,” *Phys. Rev. Lett.* **118** (2017) no. 9, 091801, [arXiv:1611.05865 \[physics.ins-det\]](#).
- [159] **MADMAX** Collaboration, P. Brun *et al.*, “A new experimental approach to probe QCD axion dark matter in the mass range above 40 μeV ,” *Eur. Phys. J.* **C79** (2019) no. 3, 186, [arXiv:1901.07401 \[physics.ins-det\]](#).
- [160] W. DeRocco and A. Hook, “Axion interferometry,” *Phys. Rev. D* **98** (2018) no. 3, 035021, [arXiv:1802.07273 \[hep-ph\]](#).
- [161] I. Obata, T. Fujita, and Y. Michimura, “Optical Ring Cavity Search for Axion Dark Matter,” *Phys. Rev. Lett.* **121** (2018) no. 16, 161301, [arXiv:1805.11753 \[astro-ph.CO\]](#).
- [162] M. Goryachev, B. Mcallister, and M. E. Tobar, “Axion Detection with Precision Frequency Metrology,” *Phys. Dark Univ.* **26** (2019) 100345, [arXiv:1806.07141 \[physics.ins-det\]](#).
- [163] H. Liu, B. D. Elwood, M. Evans, and J. Thaler, “Searching for Axion Dark Matter with Birefringent Cavities,” *Phys. Rev. D* **100** (2019) no. 2, 023548, [arXiv:1809.01656 \[hep-ph\]](#).
- [164] G. Flower, J. Bourhill, M. Goryachev, and M. E. Tobar, “Broadening frequency range of a ferromagnetic axion haloscope with strongly coupled cavity–magnon polaritons,” *Phys. Dark Univ.* **25** (2019) 100306, [arXiv:1811.09348 \[physics.ins-det\]](#).
- [165] K. Nagano, T. Fujita, Y. Michimura, and I. Obata, “Axion Dark Matter Search with Interferometric Gravitational Wave Detectors,” *Phys. Rev. Lett.* **123** (2019) no. 11, 111301, [arXiv:1903.02017 \[hep-ph\]](#).
- [166] M. Lawson, A. J. Millar, M. Pancaldi, E. Vitagliano, and F. Wilczek, “Tunable axion plasma haloscopes,” *Phys. Rev. Lett.* **123** (Apr., 2019) 141802, [arXiv:1904.11872 \[hep-ph\]](#).
- [167] A. Berlin, R. T. D’Agnolo, S. A. Ellis, C. Nantista, J. Neilson, P. Schuster, S. Tantawi, N. Toro, and K. Zhou, “Axion Dark Matter Detection by Superconducting Resonant Frequency Conversion,” [arXiv:1912.11048 \[hep-ph\]](#).
- [168] R. Lasenby, “Microwave cavity searches for low-frequency axion dark matter,” [arXiv:1912.11056 \[hep-ph\]](#).
- [169] R. Lasenby, “Parametrics of electromagnetic searches for axion dark matter,” [arXiv:1912.11467 \[hep-ph\]](#).

- [170] M. Fabbrichesi, E. Gabrielli, and G. Lanfranchi, “The Dark Photon,” [arXiv:2005.01515](https://arxiv.org/abs/2005.01515) [hep-ph].
- [171] P. Agrawal, N. Kitajima, M. Reece, T. Sekiguchi, and F. Takahashi, “Relic Abundance of Dark Photon Dark Matter,” *Phys. Lett. B* **801** (2020) 135136, [arXiv:1810.07188](https://arxiv.org/abs/1810.07188) [hep-ph].
- [172] P. W. Graham, J. Mardon, and S. Rajendran, “Vector Dark Matter from Inflationary Fluctuations,” *Phys. Rev. D* **93** (2016) no. 10, 103520, [arXiv:1504.02102](https://arxiv.org/abs/1504.02102) [hep-ph].
- [173] D. Smith and N. Weiner, “Inelastic Dark Matter,” *Physical Review D* **64** (July, 2001) 043502. <http://arxiv.org/abs/hep-ph/0101138>. arXiv: hep-ph/0101138.
- [174] R. Catena and P. Ullio, “A novel determination of the local dark matter density,” *Journal of Cosmology and Astroparticle Physics* **2010** (Aug., 2010) 004–004. <https://doi.org/10.1088/1475-7516/2010/08/004>.
- [175] J. D. Lewin and P. F. Smith, “Review of mathematics, numerical factors, and corrections for dark matter experiments based on elastic nuclear recoil,” *Astroparticle Physics* **6** (Dec., 1996) 87–112. <https://www.sciencedirect.com/science/article/pii/S0927650596000473>.
- [176] N. W. Evans, C. A. J. O’Hare, and C. McCabe, “SHM⁺⁺: A Refinement of the Standard Halo Model for Dark Matter Searches in Light of the Gaia Sausage,” [arXiv:1810.11468](https://arxiv.org/abs/1810.11468) [astro-ph, physics:hep-ex, physics:hep-ph] (Dec., 2018) . <http://arxiv.org/abs/1810.11468>. arXiv: 1810.11468.
- [177] P. W. Graham, D. E. Kaplan, S. Rajendran, and M. T. Walters, “Semiconductor Probes of Light Dark Matter,” *Phys. Dark Univ.* **1** (2012) 32–49, [arXiv:1203.2531](https://arxiv.org/abs/1203.2531) [hep-ph].
- [178] T. Trickle, Z. Zhang, and K. M. Zurek, “<https://phonodark.caltech.edu>.” 2021.
- [179] EXCEED-DM Collaboration, “EXCEED-DM-v0.2.0,” June, 2021. <https://doi.org/10.5281/zenodo.5009167>.
- [180] N. A. Kurinsky, T. C. Yu, Y. Hochberg, and B. Cabrera, “Diamond Detectors for Direct Detection of Sub-GeV Dark Matter,” *Phys. Rev.* **D99** (2019) no. 12, 123005, [arXiv:1901.07569](https://arxiv.org/abs/1901.07569) [hep-ex].
- [181] Y. Hochberg, Y. Zhao, and K. M. Zurek, “Superconducting Detectors for Superlight Dark Matter,” *Phys. Rev. Lett.* **116** (Apr., 2016) 011301, [arXiv:1504.07237](https://arxiv.org/abs/1504.07237) [hep-ph].
- [182] Y. Hochberg, M. Pyle, Y. Zhao, and K. M. Zurek, “Detecting Superlight Dark Matter with Fermi-Degenerate Materials,” *JHEP* **08** (Dec., 2016) 057, [arXiv:1512.04533](https://arxiv.org/abs/1512.04533) [hep-ph].

- [183] R. M. Geilhufe, F. Kahlhoefer, and M. W. Winkler, “Dirac Materials for Sub-MeV Dark Matter Detection: New Targets and Improved Formalism,” *Phys. Rev. D* **101** (2020) no. 5, 055005, [arXiv:1910.02091 \[hep-ph\]](#).
- [184] K. Schutz and K. M. Zurek, “Detectability of Light Dark Matter with Superfluid Helium,” *Phys. Rev. Lett.* **117** (2016) no. 12, 121302, [arXiv:1604.08206 \[hep-ph\]](#).
- [185] S. Knapen, T. Lin, and K. M. Zurek, “Light Dark Matter in Superfluid Helium: Detection with Multi-excitation Production,” *Phys. Rev.* **D95** (2017) no. 5, 056019, [arXiv:1611.06228 \[hep-ph\]](#).
- [186] F. Acanfora, A. Esposito, and A. D. Polosa, “Sub-GeV Dark Matter in Superfluid He-4: an Effective Theory Approach,” *Eur. Phys. J.* **C79** (2019) no. 7, 549, [arXiv:1902.02361 \[hep-ph\]](#).
- [187] A. Caputo, A. Esposito, and A. D. Polosa, “Sub-MeV Dark Matter and the Goldstone Modes of Superfluid Helium,” *Phys. Rev. D* **100** (2019) no. 11, 116007, [arXiv:1907.10635 \[hep-ph\]](#).
- [188] Y. Hochberg, Y. Kahn, M. Lisanti, C. G. Tully, and K. M. Zurek, “Directional detection of dark matter with two-dimensional targets,” *Phys. Lett.* **B772** (September, 2017) 239–246, [arXiv:1606.08849 \[hep-ph\]](#).
<https://arxiv.org/pdf/1606.08849.pdf><http://arxiv.org/abs/1606.08849><https://linkinghub.elsevier.com/retrieve/pii/S0370269317305270>.
- [189] G. Cavoto, F. Luchetta, and A. D. Polosa, “Sub-GeV Dark Matter Detection with Electron Recoils in Carbon Nanotubes,” *Phys. Lett.* **B776** (2018) 338–344, [arXiv:1706.02487 \[hep-ph\]](#).
- [190] F. Kadribasic, N. Mirabolfathi, K. Nordlund, A. E. Sand, E. Holmström, and F. Djurabekova, “Directional Sensitivity In Light-Mass Dark Matter Searches With Single-Electron Resolution Ionization Detectors,” *Phys. Rev. Lett.* **120** (2018) no. 11, 111301, [arXiv:1703.05371 \[physics.ins-det\]](#).
- [191] R. Budnik, O. Chesnovsky, O. Slone, and T. Volansky, “Direct Detection of Light Dark Matter and Solar Neutrinos via Color Center Production in Crystals,” *Phys. Lett.* **B782** (2018) 242–250, [arXiv:1705.03016 \[hep-ph\]](#).
- [192] S. Rajendran, N. Zobrist, A. O. Sushkov, R. Walsworth, and M. Lukin, “A method for directional detection of dark matter using spectroscopy of crystal defects,” *Phys. Rev.* **D96** (2017) no. 3, 035009, [arXiv:1705.09760 \[hep-ph\]](#).
- [193] R. Essig, J. Mardon, O. Slone, and T. Volansky, “Detection of sub-GeV Dark Matter and Solar Neutrinos via Chemical-Bond Breaking,” *Phys. Rev.* **D95** (2017) no. 5, 056011, [arXiv:1608.02940 \[hep-ph\]](#).

- [194] A. Arvanitaki, S. Dimopoulos, and K. Van Tilburg, “Resonant absorption of bosonic dark matter in molecules,” *Phys. Rev.* **X8** (2018) no. 4, 041001, [arXiv:1709.05354 \[hep-ph\]](#).
- [195] R. Essig, J. Pérez-Ríos, H. Ramani, and O. Slone, “Direct Detection of Spin-(In)dependent Nuclear Scattering of Sub-GeV Dark Matter Using Molecular Excitations,” *Phys. Rev. Research.* **1** (2019) 033105, [arXiv:1907.07682 \[hep-ph\]](#).
- [196] S. Chang, A. Pierce, and N. Weiner, “Momentum Dependent Dark Matter Scattering,” *JCAP* **1001** (2010) 006, [arXiv:0908.3192 \[hep-ph\]](#).
- [197] A. Fitzpatrick, W. Haxton, E. Katz, N. Lubbers, and Y. Xu, “The Effective Field Theory of Dark Matter Direct Detection,” *JCAP* **02** (mar, 2013) 004, [arXiv:1203.3542 \[hep-ph\]](#). <http://arxiv.org/abs/1203.3542><http://dx.doi.org/10.1088/1475-7516/2013/02/004>.
- [198] T. Lin, “Dark matter models and direct detection,” *PoS* **333** (2019) 009, [arXiv:1904.07915 \[hep-ph\]](#).
- [199] S. Knapen and T. Lin *private communications*.
- [200] R. H. Helm, “Inelastic and Elastic Scattering of 187-Mev Electrons from Selected Even-Even Nuclei,” *Phys. Rev.* **104** (1956) 1466–1475.
- [201] P. Cox, T. Melia, and S. Rajendran, “Dark matter phonon coupling,” *Phys. Rev. D* **100** (2019) no. 5, 055011, [arXiv:1905.05575 \[hep-ph\]](#).
- [202] X. Wang and D. Vanderbilt, “First-principles perturbative computation of dielectric and born charge tensors in finite electric fields,” *Phys. Rev. B* **75** (Mar, 2007) 115116. <https://link.aps.org/doi/10.1103/PhysRevB.75.115116>.
- [203] C. Boehm and P. Fayet, “Scalar dark matter candidates,” *Nucl. Phys.* **B683** (2004) 219–263, [arXiv:hep-ph/0305261 \[hep-ph\]](#).
- [204] M. Pospelov, A. Ritz, and M. B. Voloshin, “Secluded WIMP Dark Matter,” *Phys. Lett.* **B662** (2008) 53–61, [arXiv:0711.4866 \[hep-ph\]](#).
- [205] D. Hooper and K. M. Zurek, “A Natural Supersymmetric Model with MeV Dark Matter,” *Phys. Rev.* **D77** (2008) 087302, [arXiv:0801.3686 \[hep-ph\]](#).
- [206] J. Kumar and J. L. Feng, “WIMPless Dark Matter,” *AIP Conf. Proc.* **1200** (2010) no. 1, 1059–1062, [arXiv:0909.2877 \[hep-ph\]](#).
- [207] N. Arkani-Hamed and N. Weiner, “LHC Signals for a SuperUnified Theory of Dark Matter,” *JHEP* **12** (2008) 104, [arXiv:0810.0714 \[hep-ph\]](#).
- [208] C. Cheung, J. T. Ruderman, L.-T. Wang, and I. Yavin, “Kinetic Mixing as the Origin of Light Dark Scales,” *Phys. Rev. D* **80** (2009) 035008, [arXiv:0902.3246 \[hep-ph\]](#).

- [209] D. E. Morrissey, D. Poland, and K. M. Zurek, “Abelian Hidden Sectors at a GeV,” *JHEP* **07** (2009) 050, [arXiv:0904.2567 \[hep-ph\]](#).
- [210] Y. Hochberg, E. Kuflik, T. Volansky, and J. G. Wacker, “Mechanism for Thermal Relic Dark Matter of Strongly Interacting Massive Particles,” *Phys. Rev. Lett.* **113** (2014) 171301, [arXiv:1402.5143 \[hep-ph\]](#).
- [211] M. Heikinheimo, K. Nordlund, K. Tuominen, and N. Mirabolfofathi, “Velocity Dependent Dark Matter Interactions in Single-Electron Resolution Semiconductor Detectors with Directional Sensitivity,” *Phys. Rev.* **D99** (2019) no. 10, 103018, [arXiv:1903.08654 \[hep-ph\]](#).
- [212] T. Emken, R. Essig, C. Kouvaris, and M. Sholapurkar, “Direct Detection of Strongly Interacting Sub-GeV Dark Matter via Electron Recoils,” *JCAP* **1909** (2019) no. 09, 070, [arXiv:1905.06348 \[hep-ph\]](#).
- [213] M. Ibe, W. Nakano, Y. Shoji, and K. Suzuki, “Migdal Effect in Dark Matter Direct Detection Experiments,” *JHEP* **03** (2018) 194, [arXiv:1707.07258 \[hep-ph\]](#).
- [214] M. J. Dolan, F. Kahlhoefer, and C. McCabe, “Directly detecting sub-GeV dark matter with electrons from nuclear scattering,” *Phys. Rev. Lett.* **121** (2018) no. 10, 101801, [arXiv:1711.09906 \[hep-ph\]](#).
- [215] N. F. Bell, J. B. Dent, J. L. Newstead, S. Sabharwale, and T. J. Weiler, “The Migdal Effect and Photon Bremsstrahlung in effective field theories of dark matter direct detection and coherent elastic neutrino-nucleus scattering,” [arXiv:1905.00046 \[hep-ph\]](#).
- [216] D. Baxter, Y. Kahn, and G. Krnjaic, “Electron Ionization via Dark Matter-Electron Scattering and the Migdal Effect,” [arXiv:1908.00012 \[hep-ph\]](#).
- [217] R. Essig, J. Pradler, M. Sholapurkar, and T.-T. Yu, “On the relation between Migdal effect and dark matter-electron scattering in atoms and semiconductors,” [arXiv:1908.10881 \[hep-ph\]](#).
- [218] C. J. Riedel, “Direct detection of classically undetectable dark matter through quantum decoherence,” *Phys. Rev.* **D88** (2013) no. 11, 116005, [arXiv:1212.3061 \[quant-ph\]](#).
- [219] C. Kouvaris and J. Pradler, “Probing sub-GeV Dark Matter with conventional detectors,” *Phys. Rev. Lett.* **118** (2017) no. 3, 031803, [arXiv:1607.01789 \[hep-ph\]](#).
- [220] C. J. Riedel and I. Yavin, “Decoherence as a way to measure extremely soft collisions with dark matter,” *Phys. Rev.* **D96** (2017) no. 2, 023007, [arXiv:1609.04145 \[quant-ph\]](#).
- [221] D. J. E. Marsh, K.-C. Fong, E. W. Lentz, L. Smejkal, and M. N. o. Ali, “A Proposal to Detect Dark Matter Using Axionic Topological Antiferromagnets,” *Phys. Rev. Lett.* **123** (2019) no. 12, 121601, [arXiv:1807.08810 \[hep-ph\]](#).

- [222] R. Alonso, D. Blas, and P. Wolf, “Exploring the ultra-light to sub-MeV dark matter window with atomic clocks and co-magnetometers,” *JHEP* **07** (2019) 069, [arXiv:1810.00889 \[hep-ph\]](#).
- [223] B. M. Roberts *et al.*, “Search for transient variations of the fine structure constant and dark matter using fiber-linked optical atomic clocks,” [arXiv:1907.02661 \[astro-ph.CO\]](#).
- [224] M. Zarei, S. Shakeri, M. Abdi, D. J. E. Marsh, and S. Matarrese, “Probing Virtual Axion-Like Particles by Precision Phase Measurements,” [arXiv:1910.09973 \[hep-ph\]](#).
- [225] M. W. Goodman and E. Witten, “Detectability of certain dark-matter candidates,” *Physical Review D* **31** (jun, 1985) 3059–3063.
- [226] A. K. Drukier, K. Freese, and D. N. Spergel, “Detecting cold dark-matter candidates,” *Physical Review D* **33** (jun, 1986) 3495–3508.
- [227] T. Trickle, Z. Zhang, K. M. Zurek, K. Inzani, and S. Griffin, “Multi-channel direct detection of light dark matter: Theoretical framework,” [arXiv:http://arxiv.org/abs/1910.08092v1 \[hep-ph\]](#).
- [228] **KIMS** Collaboration, S. K. Kim and the KIMS Collaboration, “New results from the KIMS experiment,” *Journal of Physics: Conference Series* **120** (jul, 2008) 042021.
- [229] K. Miuchi, M. Minowa, A. Takeda, H. Sekiya, Y. Shimizu, Y. Inoue, W. Ootani, and Y. Ootuka, “First results from dark matter search experiment with LiF bolometer at Kamioka underground laboratory,” *Astropart. Phys.* **19** (2003) 135–144, [arXiv:astro-ph/0204411 \[astro-ph\]](#).
- [230] F. Detraux, P. Ghosez, and X. Gonze, “Anomalously large born effective charges in cubic wo_3 ,” *Phys. Rev. B* **56** (Jul, 1997) 983–985. <https://link.aps.org/doi/10.1103/PhysRevB.56.983>.
- [231] J. E. Peralta, J. Heyd, G. E. Scuseria, and R. L. Martin, “Spin-orbit splittings and energy band gaps calculated with the heyd-scuseria-ernzerhof screened hybrid functional,” *Physical Review B* **74** (aug, 2006) .
- [232] J. Amaré *et al.*, “ANAIS-112 status: two years results on annual modulation,” *J. Phys. Conf. Ser.* **1468** (2020) no. 1, 012014, [arXiv:1910.13365 \[astro-ph.IM\]](#).
- [233] F. Pröbst *et al.*, “Results of CRESST Phase I,” *Nucl. Phys. Proc. Suppl.* **110** (2002) 67–69.
- [234] **CRESST** Collaboration, G. Angloher *et al.*, “Limits on Dark Matter Effective Field Theory Parameters with CRESST-II,” *Eur. Phys. J. C* **79** (2019) no. 1, 43, [arXiv:1809.03753 \[hep-ph\]](#).

- [235] **CRESST** Collaboration, H. Kluck *et al.*, “Latest results of CRESST-III’s search for sub-GeV/c² dark matter,” *J. Phys. Conf. Ser.* **1468** (2020) no. 1, 012038.
- [236] R. Bernabei *et al.*, “The DAMA project: Achievements, implications and perspectives,” *Prog. Part. Nucl. Phys.* **114** (2020) 103810.
- [237] **DAMIC** Collaboration, A. Aguilar-Arevalo *et al.*, “Results on low-mass weakly interacting massive particles from a 11 kg-day target exposure of DAMIC at SNOLAB,” *Phys. Rev. Lett.* **125** (2020) 241803, [arXiv:2007.15622](#) [[astro-ph.CO](#)].
- [238] **LUX** Collaboration, D. S. Akerib *et al.*, “An Effective Field Theory Analysis of the First LUX Dark Matter Search,” [arXiv:2003.11141](#) [[astro-ph.CO](#)].
- [239] **SABRE** Collaboration, M. Antonello *et al.*, “The SABRE project and the SABRE Proof-of-Principle,” *Eur. Phys. J. C* **79** (2019) no. 4, 363, [arXiv:1806.09340](#) [[physics.ins-det](#)].
- [240] **SuperCDMS** Collaboration, I. Alkhatib *et al.*, “Light Dark Matter Search with a High-Resolution Athermal Phonon Detector Operated Above Ground,” [arXiv:2007.14289](#) [[hep-ex](#)].
- [241] M. J. Strassler and K. M. Zurek, “Echoes of a hidden valley at hadron colliders,” *Phys. Lett.* **B651** (2007) 374–379, [arXiv:hep-ph/0604261](#) [[hep-ph](#)].
- [242] Y. Hochberg, E. Kuflik, H. Murayama, T. Volansky, and J. G. o. Wacker, “Model for Thermal Relic Dark Matter of Strongly Interacting Massive Particles,” *Phys. Rev. Lett.* **115** (2015) no. 2, 021301, [arXiv:1411.3727](#) [[hep-ph](#)].
- [243] C. Blanco, J. I. Collar, Y. Kahn, and B. Lillard, “Dark Matter-Electron Scattering from Aromatic Organic Targets,” *Phys. Rev. D* **101** (2020) no. 5, 056001, [arXiv:1912.02822](#) [[hep-ph](#)].
- [244] R. Catena, T. Emken, N. A. Spaldin, and W. Tarantino, “Atomic responses to general dark matter-electron interactions,” *Phys. Rev. Res.* **2** (2020) no. 3, 033195, [arXiv:1912.08204](#) [[hep-ph](#)].
- [245] G. Baym, D. Beck, J. P. Filippini, C. Pethick, and J. Shelton, “Searching for low mass dark matter via phonon creation in superfluid ⁴He,” *Phys. Rev. D* **102** (5, 2020) 035014, [arXiv:2005.08824](#) [[hep-ph](#)].
- [246] A. Caputo, A. Esposito, F. Piccinini, A. D. Polosa, and G. Rossi, “Directional detection of light dark matter from three-phonon events in superfluid ⁴He,” [arXiv:2012.01432](#) [[hep-ph](#)].
- [247] B. Campbell-Deem, P. Cox, S. Knapen, T. Lin, and T. Melia, “Multiphonon excitations from dark matter scattering in crystals,” *Phys. Rev. D* **101** (2020) no. 3, 036006, [arXiv:1911.03482](#) [[hep-ph](#)]. [Erratum: *Phys.Rev.D* 102, 019904 (2020)].

- [248] S. M. Griffin, Y. Hochberg, K. Inzani, N. Kurinsky, T. Lin, and T. Chin, “Silicon carbide detectors for sub-GeV dark matter,” *Phys. Rev. D* **103** (8, 2021) 075002, [arXiv:2008.08560 \[hep-ph\]](#).
- [249] Y. Kahn, G. Krnjaic, and B. Mandava, “Dark Matter Detection With Bound Nuclear Targets: The Poisson Phonon Tail,” [arXiv:2011.09477 \[hep-ph\]](#).
- [250] S. Knapen, J. Kozaczuk, and T. Lin, “The Migdal effect in semiconductors,” [arXiv:2011.09496 \[hep-ph\]](#).
- [251] M. Pyle, E. Figueroa-Feliciano, and B. Sadoulet, “Optimized Designs for Very Low Temperature Massive Calorimeters,” *ArXiv e-prints* (3, 2015) , [arXiv:1503.01200 \[astro-ph.IM\]](#).
- [252] H. J. Maris, G. M. Seidel, and D. Stein, “Dark matter detection using helium evaporation and field ionization,” *Phys. Rev. Lett.* **119** (Nov, 2017) 181303, [arXiv:1706.00117 \[astro-ph.IM\]](#).
<https://link.aps.org/doi/10.1103/PhysRevLett.119.181303>.
- [253] J. Rothe *et al.*, “TES-Based Light Detectors for the CRESST Direct Dark Matter Search,” *J. Low Temp. Phys.* **193** (2018) no. 5-6, 1160–1166.
- [254] I. Colantoni *et al.*, “BULLKID: BULky and Low-Threshold Kinetic Inductance Detectors,” *J. Low Temp. Phys.* **199** (2020) no. 3-4, 593–597.
- [255] C. Fink *et al.*, “Characterizing TES Power Noise for Future Single Optical-Phonon and Infrared-Photon Detectors,” *AIP Adv.* **10** (2020) no. 8, 085221, [arXiv:2004.10257 \[physics.ins-det\]](#).
- [256] P. Du, D. Egana-Ugrinovic, R. Essig, and M. Sholapurkar, “Sources of Low-Energy Events in Low-Threshold Dark Matter Detectors,” [arXiv:2011.13939 \[hep-ph\]](#).
- [257] T. Trickle, Z. Zhang, and K. M. Zurek <https://phonodark.caltech.edu>.
- [258] <https://demo-phonon-web-app.herokuapp.com>.
- [259] A. Togo, “Phonon Database at Kyoto University.” 2020.
- [260] E. D. Carlson, M. E. Machacek, and L. J. Hall, “Self-interacting dark matter,” *Astrophys. J.* **398** (1992) 43–52.
- [261] J. L. Feng and J. Kumar, “The WIMPless Miracle: Dark-Matter Particles without Weak-Scale Masses or Weak Interactions,” *Phys. Rev. Lett.* **101** (2008) 231301, [arXiv:0803.4196 \[hep-ph\]](#).
- [262] A. Auerbach, *Interacting Electrons and Quantum Magnetism*. Springer, New York, NY, 1994.
- [263] J. M. D. Coey, *Magnetism and Magnetic Materials*. Cambridge University Press, jan, 2001. , Sec. 4.4.2.

- [264] V. Cherepanov, I. Kolokolov, and V. L'vov, "The saga of YIG: Spectra, thermodynamics, interaction and relaxation of magnons in a complex magnet," *Physics Reports* **229** (jul, 1993) 81.
<https://www.sciencedirect.com/science/article/pii/0370157393901070>.
- [265] A. J. Princep, R. A. Ewings, S. Ward, S. Tóth, C. Dubs, *et al.*, "The full magnon spectrum of yttrium iron garnet," *npj Quantum Materials* **2** (nov, 2017) 63.
<http://www.nature.com/articles/s41535-017-0067-y>.
- [266] R. Barbieri, M. Cerdonio, G. Fiorentini, and S. Vitale, "AXION TO MAGNON CONVERSION: A SCHEME FOR THE DETECTION OF GALACTIC AXIONS," *Phys. Lett.* **B226** (1989) 357–360.
- [267] A. Jain *et al.*, "The Materials Project: A materials genome approach to accelerating materials innovation," *APL Materials* **1** (2013) no. 1, 011002.
<http://link.aip.org/link/AMPADS/v1/i1/p011002/s1&Agg=doi>.
- [268] S. Toth and B. Lake, "Linear spin wave theory for single-Q incommensurate magnetic structures," *Journal of Physics: Condensed Matter* **27** (feb, 2014) 166002, [arXiv:1402.6069](https://arxiv.org/abs/1402.6069). <http://arxiv.org/abs/1402.6069>
<http://dx.doi.org/10.1088/0953-8984/27/16/166002>.
- [269] R. Essig, M. Sholapurkar, and T.-T. Yu, "Solar Neutrinos as a Signal and Background in Direct-Detection Experiments Searching for Sub-GeV Dark Matter With Electron Recoils," *Phys. Rev.* **D97** (2018) no. 9, 095029, [arXiv:1801.10159](https://arxiv.org/abs/1801.10159) [hep-ph].
- [270] S. Davidson, S. Hannestad, and G. Raffelt, "Updated bounds on millicharged particles," *JHEP* **05** (2000) 003, [arXiv:hep-ph/0001179](https://arxiv.org/abs/hep-ph/0001179) [hep-ph].
- [271] X. Chu, J.-L. Kuo, J. Pradler, and L. Semmelrock, "Stellar probes of dark sector-photon interactions," *Phys. Rev.* **D100** (2019) no. 8, 083002, [arXiv:1908.00553](https://arxiv.org/abs/1908.00553) [hep-ph].
- [272] E. Masso and J. Redondo, "Compatibility of CAST search with axion-like interpretation of PVLAS results," *Phys. Rev. Lett.* **97** (2006) 151802, [arXiv:hep-ph/0606163](https://arxiv.org/abs/hep-ph/0606163) [hep-ph].
- [273] D. Lachance-Quirion, Y. Tabuchi, S. Ishino, A. Noguchi, T. Ishikawa, R. Yamazaki, and Y. Nakamura, "Resolving quanta of collective spin excitations in a millimeter-sized ferromagnet," *Science Advances* **3** (jul, 2017) e1603150.
- [274] D. Lachance-Quirion, Y. Tabuchi, A. Gloppe, K. Usami, and Y. Nakamura, "Hybrid quantum systems based on magnonics," *Applied Physics Express* **12** (Feb., 2019) 070101, [arXiv:1902.03024](https://arxiv.org/abs/1902.03024) [quant-ph].
- [275] S. Weinberg, "The U(1) problem," *Physical Review D* **11** (jun, 1975) 3583–3593.

- [276] F. Wilczek, “Problem of Strong P and T Invariance in the Presence of Instantons,” *Physical Review Letters* **40** (jan, 1978) 279–282.
- [277] M. S. Turner, “Cosmic and Local Mass Density of Invisible Axions,” *Phys. Rev. D* **33** (1986) 889–896.
- [278] D. Lyth, “Axions and inflation: Sitting in the vacuum,” *Phys. Rev. D* **45** (1992) 3394–3404.
- [279] L. Visinelli and P. Gondolo, “Dark Matter Axions Revisited,” *Phys. Rev. D* **80** (2009) 035024, [arXiv:0903.4377 \[astro-ph.CO\]](#).
- [280] L. Visinelli and P. Gondolo, “Axion cold dark matter in non-standard cosmologies,” *Phys. Rev. D* **81** (2010) 063508, [arXiv:0912.0015 \[astro-ph.CO\]](#).
- [281] T. Hiramatsu, M. Kawasaki, and K. Saikawa, “Evolution of String-Wall Networks and Axionic Domain Wall Problem,” *JCAP* **08** (2011) 030, [arXiv:1012.4558 \[astro-ph.CO\]](#).
- [282] T. Hiramatsu, M. Kawasaki, K. Saikawa, and T. Sekiguchi, “Axion cosmology with long-lived domain walls,” *JCAP* **01** (2013) 001, [arXiv:1207.3166 \[hep-ph\]](#).
- [283] M. Kawasaki, K. Saikawa, and T. Sekiguchi, “Axion dark matter from topological defects,” *Phys. Rev. D* **91** (2015) no. 6, 065014, [arXiv:1412.0789 \[hep-ph\]](#).
- [284] A. Ringwald and K. Saikawa, “Axion dark matter in the post-inflationary Peccei-Quinn symmetry breaking scenario,” *Phys. Rev. D* **93** (2016) no. 8, 085031, [arXiv:1512.06436 \[hep-ph\]](#). [Addendum: *Phys.Rev.D* 94, 049908 (2016)].
- [285] R. T. Co, L. J. Hall, and K. Harigaya, “QCD Axion Dark Matter with a Small Decay Constant,” *Phys. Rev. Lett.* **120** (2018) no. 21, 211602, [arXiv:1711.10486 \[hep-ph\]](#).
- [286] K. Harigaya and M. Kawasaki, “QCD axion dark matter from long-lived domain walls during matter domination,” *Phys. Lett. B* **782** (2018) 1–5, [arXiv:1802.00579 \[hep-ph\]](#).
- [287] R. T. Co, E. Gonzalez, and K. Harigaya, “Axion Misalignment Driven to the Hilltop,” *JHEP* **05** (2019) 163, [arXiv:1812.11192 \[hep-ph\]](#).
- [288] F. Takahashi and W. Yin, “QCD axion on hilltop by a phase shift of π ,” *JHEP* **10** (2019) 120, [arXiv:1908.06071 \[hep-ph\]](#).
- [289] K. Harigaya and J. M. Leedom, “QCD Axion Dark Matter from a Late Time Phase Transition,” [arXiv:1910.04163 \[hep-ph\]](#).
- [290] R. T. Co, L. J. Hall, K. Harigaya, K. A. Olive, and S. Verner, “Axion Kinetic Misalignment and Parametric Resonance from Inflation,” *JCAP* **08** (4, 2020) 036, [arXiv:2004.00629 \[hep-ph\]](#).

- [291] **IAXO** Collaboration, E. Armengaud *et al.*, “Physics potential of the International Axion Observatory (IAXO),” *JCAP* **06** (2019) 047, [arXiv:1904.09155 \[hep-ph\]](#).
- [292] D. Horns, J. Jaeckel, A. Lindner, A. Lobanov, J. Redondo, and A. Ringwald, “Searching for WISPy Cold Dark Matter with a Dish Antenna,” *JCAP* **1304** (2013) 016, [arXiv:1212.2970 \[hep-ph\]](#).
- [293] M. Baryakhtar, J. Huang, and R. Lasenby, “Axion and hidden photon dark matter detection with multilayer optical haloscopes,” *Phys. Rev.* **D98** (2018) no. 3, 035006, [arXiv:1803.11455 \[hep-ph\]](#).
- [294] R. M. Martin, *Electronic Structure*. Cambridge University Press, apr, 2004.
- [295] G. Kresse and J. Hafner, “Ab initio molecular dynamics for liquid metals,” *Phys. Rev. B* **47** (jan, 1993) 558–561.
- [296] G. Kresse and J. Hafner, “Ab initio molecular-dynamics simulation of the liquid-metal–amorphous-semiconductor transition in germanium,” *Phys. Rev. B* **49** (may, 1994) 14251–14269. <http://link.aps.org/doi/10.1103/PhysRevB.49.14251>.
- [297] G. Kresse and J. Furthmüller, “Efficient iterative schemes for ab initio total-energy calculations using a plane-wave basis set,” *Physical Review B* **54** (oct, 1996) 11169–11186. <http://link.aps.org/doi/10.1103/PhysRevB.54.11169>.
- [298] J. Colpa, “Diagonalization of the quadratic boson hamiltonian,” *Physica A: Statistical Mechanics and its Applications* **93** (sep, 1978) 327–353.
- [299] S. Bhagavantam and T. Venkatarayudu, “Raman effect in relation to crystal structure,” *Proceedings of the Indian Academy of Sciences - Section A* **9** (mar, 1939) 224–258.
- [300] A. S. Barker, “Infrared lattice vibrations and dielectric dispersion in corundum,” *Phys. Rev.* **132** (Nov, 1963) 1474–1481. <https://link.aps.org/doi/10.1103/PhysRev.132.1474>.
- [301] M. Schubert, T. E. Tiwald, and C. M. Herzinger, “Infrared dielectric anisotropy and phonon modes of sapphire,” *Phys. Rev. B* **61** (Mar, 2000) 8187–8201. <https://link.aps.org/doi/10.1103/PhysRevB.61.8187>.
- [302] Y. Tabuchi, S. Ishino, A. Noguchi, T. Ishikawa, R. Yamazaki, K. Usami, and Y. Nakamura, “Quantum magnonics: magnon meets superconducting qubit,” [arXiv:1508.05290v1 \[quant-ph\]](#).
- [303] H. B. Nielsen and S. Chadha, “On How to Count Goldstone Bosons,” *Nucl. Phys. B* **105** (1976) 445–453.
- [304] H. Watanabe and T. Brauner, “On the number of Nambu-Goldstone bosons and its relation to charge densities,” *Phys. Rev. D* **84** (2011) 125013, [arXiv:1109.6327 \[hep-ph\]](#).

- [305] H. Watanabe and H. Murayama, “Unified Description of Nambu-Goldstone Bosons without Lorentz Invariance,” *Phys. Rev. Lett.* **108** (2012) 251602, [arXiv:1203.0609 \[hep-th\]](#).
- [306] H. Watanabe and H. Murayama, “Effective Lagrangian for Nonrelativistic Systems,” *Phys. Rev. X* **4** (2014) no. 3, 031057, [arXiv:1402.7066 \[hep-th\]](#).
- [307] K. Kim, S. Y. Lim, J.-U. Lee, S. Lee, T. Y. Kim, K. Park, G. S. Jeon, C.-H. Park, J.-G. Park, and H. Cheong, “Suppression of magnetic ordering in XXZ-type antiferromagnetic monolayer NiPS₃,” *Nature Communications* **10** (jan, 2019) .
- [308] L. Visinelli, “Axion-electromagnetic waves,” *Mod. Phys. Lett.* **A28** (2013) no. 35, 1350162, [arXiv:1401.0709 \[physics.class-ph\]](#).
- [309] A. J. Millar, G. G. Raffelt, J. Redondo, and F. D. Steffen, “Dielectric Haloscopes to Search for Axion Dark Matter: Theoretical Foundations,” *JCAP* **01** (2017) 061, [arXiv:1612.07057 \[hep-ph\]](#).
- [310] A. R. Wildes, V. Simonet, E. Ressouche, G. J. McIntyre, M. Avdeev, E. Suard, S. A. J. Kimber, D. Lançon, G. Pepe, B. Moubaraki, and T. J. Hicks, “Magnetic structure of the quasi-two-dimensional antiferromagnet NiPS₃,” *Physical Review B* **92** (dec, 2015) .
- [311] M. Goryachev, W. G. Farr, D. L. Creedon, Y. Fan, M. Kostylev, and M. E. Tobar, “High-cooperativity cavity qed with magnons at microwave frequencies,” *Physical Review Applied* **2** (Nov, 2014) , [arXiv:1408.2905 \[quant-ph\]](#).
<http://dx.doi.org/10.1103/PhysRevApplied.2.054002>.
- [312] G. Flower, M. Goryachev, J. Bourhill, and M. E. Tobar, “Experimental implementations of cavity-magnon systems: from ultra strong coupling to applications in precision measurement,” *New J. Phys.* **21** (2019) no. 9, 095004, [arXiv:1905.04002 \[quant-ph\]](#).
- [313] **PandaX-II** Collaboration, X. Cui *et al.*, “Dark Matter Results From 54-Ton-Day Exposure of PandaX-II Experiment,” *Phys. Rev. Lett.* **119** (2017) no. 18, 181302, [arXiv:1708.06917 \[astro-ph.CO\]](#).
- [314] E. Andersson, A. Bökmark, R. Catena, T. Emken, H. K. Moberg, and E. Åstrand, “Projected sensitivity to sub-GeV dark matter of next-generation semiconductor detectors,” *JCAP* **05** (2020) 036, [arXiv:2001.08910 \[hep-ph\]](#).
- [315] A. Caputo, A. Esposito, E. Geoffray, A. D. Polosa, and S. Sun, “Dark Matter, Dark Photon and Superfluid He-4 from Effective Field Theory,” *Phys. Lett. B* **802** (2020) 135258, [arXiv:1911.04511 \[hep-ph\]](#).
- [316] M. Cirelli, E. Del Nobile, and P. Panci, “Tools for model-independent bounds in direct dark matter searches,” *JCAP* **10** (2013) 019, [arXiv:1307.5955 \[hep-ph\]](#).

- [317] N. Anand, A. L. Fitzpatrick, and W. Haxton, “Weakly interacting massive particle-nucleus elastic scattering response,” *Phys. Rev. C* **89** (2014) no. 6, 065501, [arXiv:1308.6288](https://arxiv.org/abs/1308.6288) [hep-ph].
- [318] N. Anand, A. L. Fitzpatrick, and W. Haxton, “Model-independent Analyses of Dark-Matter Particle Interactions,” *Phys. Procedia* **61** (2015) 97–106, [arXiv:1405.6690](https://arxiv.org/abs/1405.6690) [nucl-th].
- [319] E. Del Nobile, “Complete Lorentz-to-Galileo dictionary for direct dark matter detection,” *Phys. Rev. D* **98** (2018) no. 12, 123003, [arXiv:1806.01291](https://arxiv.org/abs/1806.01291) [hep-ph].
- [320] B. Grzadkowski, M. Iskrzynski, M. Misiak, and J. Rosiek, “Dimension-Six Terms in the Standard Model Lagrangian,” *JHEP* **10** (2010) 085, [arXiv:1008.4884](https://arxiv.org/abs/1008.4884) [hep-ph].
- [321] G. D. Kribs, T. S. Roy, J. Terning, and K. M. Zurek, “Quirky Composite Dark Matter,” *Phys. Rev. D* **81** (2010) 095001, [arXiv:0909.2034](https://arxiv.org/abs/0909.2034) [hep-ph].
- [322] X. Gonze and C. Lee, “Dynamical matrices, born effective charges, dielectric permittivity tensors, and interatomic force constants from density-functional perturbation theory,” *Physical Review B* **55** (apr, 1997) 10355–10368.
- [323] G. Jackeli and G. Khaliullin, “Mott insulators in the strong spin-orbit coupling limit: From heisenberg to a quantum compass and kitaev models,” *Physical Review Letters* **102** (Jan, 2009) . <http://dx.doi.org/10.1103/PhysRevLett.102.017205>.
- [324] W. Witczak-Krempa, G. Chen, Y. B. Kim, and L. Balents, “Correlated quantum phenomena in the strong spin-orbit regime,” *Annual Review of Condensed Matter Physics* **5** (Mar, 2014) 57–82. <http://dx.doi.org/10.1146/annurev-conmatphys-020911-125138>.
- [325] S. Trebst, “Kitaev materials,” 2017.
- [326] B. J. Kim, H. Jin, S. J. Moon, J.-Y. Kim, B.-G. Park, C. S. Leem, J. Yu, T. W. Noh, C. Kim, S.-J. Oh, and et al., “Novel $j=1/2$ mott state induced by relativistic spin-orbit coupling insr2iro4,” *Physical Review Letters* **101** (Aug, 2008) . <http://dx.doi.org/10.1103/PhysRevLett.101.076402>.
- [327] S. M. Winter, A. A. Tsirlin, M. Daghofer, J. van den Brink, Y. Singh, P. Gegenwart, and R. Valentí, “Models and materials for generalized kitaev magnetism,” *Journal of Physics: Condensed Matter* **29** (Nov, 2017) 493002. <http://dx.doi.org/10.1088/1361-648X/aa8cf5>.
- [328] K. W. Plumb, J. P. Clancy, L. J. Sandilands, V. V. Shankar, Y. F. Hu, K. S. Burch, H.-Y. Kee, and Y.-J. Kim, “ —rucl_3 : A spin-orbit assisted mott insulator on a honeycomb lattice,” *Physical Review B* **90** (Jul, 2014) . <http://dx.doi.org/10.1103/PhysRevB.90.041112>.

- [329] L. Janssen, E. C. Andrade, and M. Vojta, “Magnetization processes of zigzag states on the honeycomb lattice: Identifying spin models for RuCl_3 and Na_2IrO_3 ,” *Physical Review B* **96** (Aug, 2017) . <http://dx.doi.org/10.1103/PhysRevB.96.064430>.
- [330] A. Banerjee *et al.*, “Proximate Kitaev quantum spin liquid behaviour in a honeycomb magnet,” *Nature Materials* **15** (2016) no. 7, 733–740. <https://doi.org/10.1038/nmat4604>.
- [331] L.-W. Wang, L.-S. Xie, P.-X. Xu, and K. Xia, “First-principles study of magnon-phonon interactions in gadolinium iron garnet,” *Physical Review B* **101** (Apr, 2020) . <http://dx.doi.org/10.1103/PhysRevB.101.165137>.
- [332] G. Arcadi, A. Djouadi, and M. Raidal, “Dark Matter through the Higgs portal,” *Phys. Rept.* **842** (2020) 1–180, [arXiv:1903.03616](https://arxiv.org/abs/1903.03616) [hep-ph].
- [333] **DarkSide** Collaboration, P. Agnes *et al.*, “Constraints on Sub-GeV Dark-Matter–Electron Scattering from the DarkSide-50 Experiment,” *Phys. Rev. Lett.* **121** (2018) no. 11, 111303, [arXiv:1802.06998](https://arxiv.org/abs/1802.06998) [astro-ph.CO].
- [334] **XENON** Collaboration, E. Aprile *et al.*, “Excess electronic recoil events in XENON1T,” *Phys. Rev. D* **102** (2020) no. 7, 072004, [arXiv:2006.09721](https://arxiv.org/abs/2006.09721) [hep-ex].
- [335] K. Inzani, A. Faghaninia, and S. M. Griffin, “Prediction of tunable spin-orbit gapped materials for dark matter detection,” *Physical Review Research* **3** (2021) no. 1, 013069, [arXiv:2008.05062](https://arxiv.org/abs/2008.05062) [cond-mat.mtrl-sci].
- [336] C. Bunge, J. Barrientos, and A. Bunge, “Roothaan-Hartree-Fock Ground-State Atomic Wave Functions: Slater-Type Orbital Expansions and Expectation Values for $Z = 2-54$,” *Atom. Data Nucl. Data Tabl.* **53** (1993) 113–162.
- [337] P. Giannozzi *et al.*, “Quantum espresso: a modular and open-source software project for quantum simulations of materials,” *Journal of Physics: Condensed Matter* **21** (2009) no. 39, 395502 (19pp). <http://www.quantum-espresso.org>.
- [338] P. Giannozzi *et al.*, “Advanced capabilities for materials modelling with quantum espresso,” *Journal of Physics: Condensed Matter* **29** (2017) no. 46, 465901. <http://stacks.iop.org/0953-8984/29/i=46/a=465901>.
- [339] P. Giannozzi *et al.*, “Quantum espresso toward the exascale,” *The Journal of Chemical Physics* **152** (apr, 2020) 154105, <https://doi.org/10.1063/5.0005082>. <https://doi.org/10.1063/5.0005082>.
- [340] Z.-L. Liang, L. Zhang, P. Zhang, and F. Zheng, “The wavefunction reconstruction effects in calculation of DM-induced electronic transition in semiconductor targets,” *JHEP* **01** (2019) 149, [arXiv:1810.13394](https://arxiv.org/abs/1810.13394) [cond-mat.mtrl-sci].
- [341] A. Coskuner, T. Trickle, Z. Zhang, and K. M. Zurek, “Directional Detectability of Dark Matter With Single Phonon Excitations: Target Comparison,” [arXiv:2102.09567](https://arxiv.org/abs/2102.09567) [hep-ph].

- [342] T. Trickle, “tanner-trickle/EXCEED-DM: EXCEED-DM-v0.1.0,” Zenodo, May, 2021. <https://doi.org/10.5281/zenodo.4747696>.
- [343] T. Trickle, “EXCEED-DM: DFT-computed electronic wave functions for Si and Ge,” Zenodo, May, 2021. <https://doi.org/10.5281/zenodo.4735777>.
- [344] T. Trickle, “EXCEED-DM: Calculated Scattering Rate Data for Si and Ge,” Zenodo, 2021.
- [345] P. Hohenberg and W. Kohn, “Inhomogeneous Electron Gas,” *Phys. Rev.* **136** (1964) B864–B871.
- [346] W. Kohn and L. J. Sham, “Self-Consistent Equations Including Exchange and Correlation Effects,” *Phys. Rev.* **140** (1965) A1133–A1138.
- [347] J. P. Perdew, K. Burke, and M. Ernzerhof, “Generalized Gradient Approximation Made Simple,” *Physical Review Letters* **77** (Oct, 1996) 3865–3868. <http://link.aps.org/doi/10.1103/PhysRevLett.77.3865>.
- [348] J. Heyd, G. E. Scuseria, and M. Ernzerhof, “Hybrid functionals based on a screened Coulomb potential,” *Journal of Chemical Physics* **118** (2003) no. 18, 8207–8215.
- [349] J. Heyd, G. E. Scuseria, and M. Ernzerhof, “Erratum: Hybrid functionals based on a screened Coulomb potential (Journal of Chemical Physics (2003) 118 (8207)),” *Journal of Chemical Physics* **124** (2006) no. 21, . <https://doi.org/10.1063/1.2204597>.
- [350] P. Blöchl, “Projector augmented-wave method,” *Physical Review B* **50** (Dec, 1994) 17953–17979. <https://link.aps.org/doi/10.1103/PhysRevB.50.17953>.
- [351] G. Kresse and D. Joubert, “From ultrasoft pseudopotentials to the projector augmented-wave method,” *Physical Review B* **59** (jan, 1999) 1758–1775.
- [352] G. Kresse and J. Furthmüller, “Efficiency of ab initio total energy calculations for metals and semiconductors using a plane-wave basis set,” *Computational Materials Science* **6** (jul, 1996) 15–50.
- [353] C. Rostgaard, “The projector augmented-wave method,” [arXiv:0910.1921](https://arxiv.org/abs/0910.1921) [[cond-mat.mtrl-sci](https://arxiv.org/abs/0910.1921)].
- [354] K. Bystrom, D. Broberg, S. Dwaraknath, K. A. Persson, and M. Asta, “Pawpyseed: Perturbation-extrapolation band shifting corrections for point defect calculations,” *arXiv e-prints* (Apr, 2019) arXiv:1904.11572, [arXiv:1904.11572](https://arxiv.org/abs/1904.11572) [[cond-mat.mtrl-sci](https://arxiv.org/abs/1904.11572)].
- [355] G. H. S. E. U. Condon, *The Theory of Atomic Spectra*. Cambridge University Press, January, 1935. https://www.ebook.de/de/product/4287067/e_u_condon_george_h_shortley_the_theory_of_atomic_spectra.html.

- [356] D. Belkić and H. S. Taylor, “A unified formula for the fourier transform of slater-type orbitals,” *Physica Scripta* **39** (feb, 1989) 226–229.
- [357] A. Radick, A.-M. Taki, and T.-T. Yu, “Dependence of Dark Matter - Electron Scattering on the Galactic Dark Matter Velocity Distribution,” *JCAP* **02** (2021) 004, [arXiv:2011.02493 \[hep-ph\]](#).
- [358] T. N. Maity, T. S. Ray, and S. Sarkar, “Halo uncertainties in electron recoil events at direct detection experiments,” [arXiv:2011.12896 \[hep-ph\]](#).
- [359] R. Catena, T. Emken, M. Matas, N. A. Spaldin, and E. Urdshals, “Crystal responses to general dark matter-electron interactions,” *Phys. Rev. Res.* **3** (5, 2021) 033149, [arXiv:2105.02233 \[hep-ph\]](#).
- [360] M. Pospelov, A. Ritz, and M. B. Voloshin, “Bosonic super-WIMPs as keV-scale dark matter,” *Phys. Rev.* **D78** (2008) 115012, [arXiv:0807.3279 \[hep-ph\]](#).
- [361] V. A. Dzuba, V. V. Flambaum, and M. Pospelov, “Atomic Ionization by keV-scale Pseudoscalar Dark Matter Particles,” *Phys. Rev. D* **81** (2010) 103520, [arXiv:1002.2979 \[hep-ph\]](#).
- [362] H. An, M. Pospelov, J. Pradler, and A. Ritz, “Direct Detection Constraints on Dark Photon Dark Matter,” *Phys. Lett. B* **747** (2015) 331–338, [arXiv:1412.8378 \[hep-ph\]](#).
- [363] G. B. Gelmini, A. J. Millar, V. Takhistov, and E. Vitagliano, “Probing dark photons with plasma haloscopes,” *Phys. Rev. D* **102** (2020) no. 4, 043003, [arXiv:2006.06836 \[hep-ph\]](#).
- [364] I. M. Bloch, A. Caputo, R. Essig, D. Redigolo, M. Sholapurkar, and T. Volansky, “Exploring new physics with O(keV) electron recoils in direct detection experiments,” *JHEP* **01** (2021) 178, [arXiv:2006.14521 \[hep-ph\]](#).
- [365] H. B. T. Tan, A. Derevianko, V. A. Dzuba, and V. V. Flambaum, “Atomic ionization by scalar dark matter and solar scalars,” [arXiv:2105.08296 \[hep-ph\]](#).
- [366] J. A. Dror, K. Harigaya, and V. Narayan, “Parametric Resonance Production of Ultralight Vector Dark Matter,” *Phys. Rev. D* **99** (2019) no. 3, 035036, [arXiv:1810.07195 \[hep-ph\]](#).
- [367] R. T. Co, A. Pierce, Z. Zhang, and Y. Zhao, “Dark Photon Dark Matter Produced by Axion Oscillations,” *Phys. Rev. D* **99** (2019) no. 7, 075002, [arXiv:1810.07196 \[hep-ph\]](#).
- [368] M. Bastero-Gil, J. Santiago, L. Ubaldi, and R. Vega-Morales, “Vector dark matter production at the end of inflation,” *JCAP* **04** (2019) 015, [arXiv:1810.07208 \[hep-ph\]](#).
- [369] A. J. Long and L.-T. Wang, “Dark Photon Dark Matter from a Network of Cosmic Strings,” *Phys. Rev. D* **99** (2019) no. 6, 063529, [arXiv:1901.03312 \[hep-ph\]](#).

- [370] R. L. Davis, “Cosmic Axions from Cosmic Strings,” *Phys. Lett. B* **180** (1986) 225–230.
- [371] M. Gorghetto, E. Hardy, and G. Villadoro, “Axions from Strings: the Attractive Solution,” *JHEP* **07** (2018) 151, [arXiv:1806.04677 \[hep-ph\]](#).
- [372] M. Gorghetto, E. Hardy, and G. Villadoro, “More Axions from Strings,” *SciPost Phys.* **10** (2021) 050, [arXiv:2007.04990 \[hep-ph\]](#).
- [373] I. Z. Rothstein, “TASI lectures on effective field theories,” 8, 2003. [arXiv:hep-ph/0308266](#).
- [374] R. Penco, “An Introduction to Effective Field Theories,” [arXiv:2006.16285 \[hep-th\]](#).
- [375] H. An, M. Pospelov, and J. Pradler, “Dark Matter Detectors as Dark Photon Helioscopes,” *Phys. Rev. Lett.* **111** (2013) 041302, [arXiv:1304.3461 \[hep-ph\]](#).
- [376] A. Derevianko, V. A. Dzuba, V. V. Flambaum, and M. Pospelov, “Axio-electric effect,” *Phys. Rev. D* **82** (2010) 065006, [arXiv:1007.1833 \[hep-ph\]](#).
- [377] G. G. Raffelt, *Stars as laboratories for fundamental physics: The astrophysics of neutrinos, axions, and other weakly interacting particles*. 5, 1996. <http://wwwth.mpp.mpg.de/members/raffelt/mypapers/199613.pdf>.
- [378] J. Redondo and G. Raffelt, “Solar constraints on hidden photons re-visited,” *JCAP* **08** (2013) 034, [arXiv:1305.2920 \[hep-ph\]](#).
- [379] C. Kittel, *Introduction to Solid State Physics*. Wiley, 8 ed., 2004.
- [380] G. D. Mahan, *Many Particle Physics, Third Edition*. Plenum, New York, 2000.
- [381] P. B. Allen, “Electron-Phonon Effects in the Infrared Properties of Metals,” *Phys. Rev. B* **3** (Jan, 1971) 305–320. <http://link.aps.org/doi/10.1103/PhysRevB.3.305>.
- [382] P. B. Allen, “Empirical electron-phonon λ values from resistivity of cubic metallic elements,” *Phys. Rev. B* **36** (Aug, 1987) 2920–2923. <http://link.aps.org/doi/10.1103/PhysRevB.36.2920>.
- [383] C. Blanco, Y. Kahn, B. Lillard, and S. D. McDermott, “Dark Matter Daily Modulation With Anisotropic Organic Crystals,” *Phys. Rev. D* **104** (2021) 036011, [arXiv:2103.08601 \[hep-ph\]](#).
- [384] EXCEED-DM Collaboration, “tanner-trickle/exceed-dm: Exceed-dm-v0.3.0,” 2021.
- [385] G. Zheng, J. Lu, X. Zhu, W. Ning, Y. Han, H. Zhang, J. Zhang, C. Xi, J. Yang, H. Du, K. Yang, Y. Zhang, and M. Tian, “Transport evidence for the three-dimensional Dirac semimetal phase in ZrTe_5 ,” *Physical Review B* **93** (March, 2016) 115414. <https://link.aps.org/doi/10.1103/PhysRevB.93.115414>.

- [386] R. Y. Chen, Z. G. Chen, X.-Y. Song, J. A. Schneeloch, G. D. Gu, F. Wang, and N. L. Wang, “Magnetoinfrared Spectroscopy of Landau Levels and Zeeman Splitting of Three-Dimensional Massless Dirac Fermions in $\{\mathrm{ZrTe}\}_5$,” *Physical Review Letters* **115** (October, 2015) 176404. <https://link.aps.org/doi/10.1103/PhysRevLett.115.176404>.
- [387] S. Liu, M. X. Wang, C. Chen, X. Xu, J. Jiang, L. X. Yang, H. F. Yang, Y. Y. Lv, J. Zhou, Y. B. Chen, S. H. Yao, M. H. Lu, Y. F. Chen, C. Felser, B. H. Yan, Z. K. Liu, and Y. L. Chen, “Experimental observation of conductive edge states in weak topological insulator candidate HfTe_5 ,” *APL Materials* **6** (dec, 2018) 121111.
- [388] Q. Li, D. E. Kharzeev, C. Zhang, Y. Huang, I. Pletikoscic, A. V. Fedorov, R. D. Zhong, J. A. Schneeloch, G. D. Gu, and T. Valla, “Observation of the chiral magnetic effect in ZrTe_5 ,” *Nature Phys.* **12** (2016) 550–554, [arXiv:1412.6543](https://arxiv.org/abs/1412.6543) [[cond-mat.str-el](https://arxiv.org/abs/1412.6543)].
- [389] R. Y. Chen, S. J. Zhang, J. A. Schneeloch, C. Zhang, Q. Li, G. D. Gu, and N. L. Wang, “Optical spectroscopy study of the three-dimensional Dirac semimetal $\{\mathrm{ZrTe}\}_5$,” *Physical Review B* **92** (August, 2015) 075107. <https://link.aps.org/doi/10.1103/PhysRevB.92.075107>.
- [390] X. Yuan, C. Zhang, Y. Liu, A. Narayan, C. Song, S. Shen, X. Sui, J. Xu, H. Yu, Z. An, J. Zhao, S. Sanvito, H. Yan, and F. Xiu, “Observation of quasi-two-dimensional Dirac fermions in ZrTe_5 ,” *NPG Asia Materials* **8** (November, 2016) e325–e325. <https://www.nature.com/articles/am2016166>.
- [391] Z.-G. Chen, R. Y. Chen, R. D. Zhong, J. Schneeloch, C. Zhang, Y. Huang, F. Qu, R. Yu, Q. Li, G. D. Gu, and N. L. Wang, “Spectroscopic evidence for bulk-band inversion and three-dimensional massive Dirac fermions in ZrTe_5 ,” *Proceedings of the National Academy of Sciences* **114** (January, 2017) 816–821. <https://www.pnas.org/content/114/5/816>.
- [392] B. Monserrat and A. Narayan, “Unraveling the topology of zrte_5 by changing temperature,” *Phys. Rev. Research* **1**, 033181 (2019) (September, 2019) , [arXiv:1909.07613](https://arxiv.org/abs/1909.07613) [[cond-mat.mtrl-sci](https://arxiv.org/abs/1909.07613)].
- [393] R. Wu, J.-Z. Ma, S.-M. Nie, L.-X. Zhao, X. Huang, J.-X. Yin, B.-B. Fu, P. Richard, G.-F. Chen, Z. Fang, X. Dai, H.-M. Weng, T. Qian, H. Ding, and S. H. Pan, “Evidence for Topological Edge States in a Large Energy Gap near the Step Edges on the Surface of $\{\mathrm{ZrTe}\}_5$,” *Physical Review X* **6** (May, 2016) 021017. <https://link.aps.org/doi/10.1103/PhysRevX.6.021017>.
- [394] N. L. Nair, P. T. Dumitrescu, S. Channa, S. M. Griffin, J. B. Neaton, A. C. Potter, and J. G. Analytis, “Thermodynamic signatures for the existence of dirac electrons in zrte_5 ,” *Phys. Rev. B* **97**, 041111 (2018) (August, 2017) , [arXiv:1708.03320](https://arxiv.org/abs/1708.03320) [[cond-mat.mes-hall](https://arxiv.org/abs/1708.03320)].

- [395] Y. Zhang, C. Wang, L. Yu, G. Liu, A. Liang, J. Huang, S. Nie, X. Sun, Y. Zhang, B. Shen, J. Liu, H. Weng, L. Zhao, G. Chen, X. Jia, C. Hu, Y. Ding, W. Zhao, Q. Gao, C. Li, S. He, L. Zhao, F. Zhang, S. Zhang, F. Yang, Z. Wang, Q. Peng, X. Dai, Z. Fang, Z. Xu, C. Chen, and X. J. Zhou, “Electronic evidence of temperature-induced Lifshitz transition and topological nature in ZrTe_5 ,” *Nature Communications* **8** (May, 2017) 15512. <https://www.nature.com/articles/ncomms15512>.
- [396] L. Moreschini, J. C. Johanssen, H. Berger, J. Denlinger, C. Jozwiak, E. Rotenberg, K. S. Kim, A. Bostwick, and M. Grioni, “Nature and topology of the low-energy states in ZrTe_5 ,” *Physical Review B* **94** (August, 2016) 081101. <https://link.aps.org/doi/10.1103/PhysRevB.94.081101>.
- [397] H. J. Monkhorst and J. D. Pack, “Special points for Brillouin-zone integrations,” *Phys. Rev. B* **13** (1976) 5188–5192.
- [398] P. Giannozzi, S. Baroni, N. Bonini, M. Calandra, R. Car, C. Cavazzoni, D. Ceresoli, G. L. Chiarotti, M. Cococcioni, I. Dabo, *et al.*, “Quantum espresso: a modular and open-source software project for quantum simulations of materials,” *Journal of physics: Condensed matter* **21** (sep, 2009) 395502.
- [399] P. Giannozzi, O. Andreussi, T. Brumme, O. Bunau, M. B. Nardelli, M. Calandra, R. Car, C. Cavazzoni, D. Ceresoli, M. Cococcioni, N. Colonna, I. Carnimeo, A. D. Corso, S. de Gironcoli, P. Delugas, R. A. DiStasio Jr., A. Ferretti, A. Floris, G. Fratesi, G. Fugallo, R. Gebauer, U. Gerstmann, F. Giustino, T. Gorni, J. Jia, M. Kawamura, H.-Y. Ko, A. Kokalj, E. Küçükbenli, M. Lazzeri, M. Marsili, N. Marzari, F. Mauri, N. L. Nguyen, H.-V. Nguyen, A. Otero-de-la Roza, L. Paulatto, S. Poncé, D. Rocca, R. Sabatini, B. Santra, M. Schlipf, A. P. Seitsonen, A. Smogunov, I. Timrov, T. Thonhauser, P. Umari, N. Vast, X. Wu, and S. Baroni, “Advanced capabilities for materials modelling with Quantum ESPRESSO,” *Journal of Physics: Condensed Matter* **29** (November, 2017) 465901. <http://arxiv.org/abs/1709.10010>. arXiv: 1709.10010.
- [400] S. Grimme, J. Antony, S. Ehrlich, and H. Krieg, “A consistent and accurate ab initio parametrization of density functional dispersion correction (DFT-D) for the 94 elements H-Pu,” *Journal of Chemical Physics* **132** (2010) no. 15, .
- [401] S. Grimme, S. Ehrlich, and L. Goerigk, “Effect of the damping function in dispersion corrected density functional theory,” *Journal of Computational Chemistry* **32** (may, 2011) 1456–1465. <http://www.ncbi.nlm.nih.gov/pubmed/18988249><http://doi.wiley.com/10.1002/jcc.21759>.
- [402] R. W. Lynch and H. G. Drickamer, “Effect of High Pressure on the Lattice Parameters of Diamond, Graphite, and Hexagonal Boron Nitride,” *The Journal of Chemical Physics* **44** (jan, 1966) 181–184. <http://aip.scitation.org/doi/10.1063/1.1726442>.

- [403] K. Watanabe, T. Taniguchi, and H. Kanda, "Direct-bandgap properties and evidence for ultraviolet lasing of hexagonal boron nitride single crystal," *Nature Materials* **3** (2004) no. 6, 404–409. <https://doi.org/10.1038/nmat1134>.
- [404] X.-L. Wang, C. R. Hubbard, K. B. Alexander, P. F. Becher, J. A. Fernandez-Baca, and S. Spooner, "Neutron diffraction measurements of the residual stresses in $\text{Al}_2\text{O}_3\text{-ZrO}_2$ (CeO_2) ceramic composites," *Journal of the American Ceramic Society* **77** (jun, 1994) 1569–1575.
- [405] R. H. French, "Electronic band structure of Al_2O_3 , with comparison to AlON and AlN ," *Journal of the American Ceramic Society* **73** (mar, 1990) 477–489.
- [406] J. Zemann, "Crystal structures, 2nd edition. vol. 1 by R. W. G. Wyckoff," *Acta Crystallographica* **18** (jan, 1965) 139–139.
- [407] W. M. Yim, E. J. Stofko, P. J. Zanzucchi, J. I. Pankove, M. Ettenberg, and S. L. Gilbert, "Epitaxially grown AlN and its optical band gap," *Journal of Applied Physics* **44** (jan, 1973) 292–296.
- [408] S. Speziale and T. S. Duffy, "Single-crystal elastic constants of fluorite (CaF_2) to 9.3 GPa," *Physics and Chemistry of Minerals* **29** (aug, 2002) 465–472.
- [409] G. W. Rubloff, "Far-ultraviolet reflectance spectra and the electronic structure of ionic crystals," *Physical Review B* **5** (jan, 1972) 662–684.
- [410] A. Senyshyn, H. Kraus, V. B. Mikhailik, and V. Yakovyna, "Lattice dynamics and thermal properties of CaWO_4 ," *Physical Review B* **70** (dec, 2004) .
- [411] V. B. Mikhailik, H. Kraus, D. Wahl, M. Itoh, M. Koike, and I. K. Bailiff, "One- and two-photon excited luminescence and band-gap assignment in CaWO_4 ," *Physical Review B* **69** (may, 2004) .
- [412] M. J. Lipp, C. H. Yoo, D. Strachan, and W. B. Daniels, "Band-structure parameters and fermi resonances of exciton-polaritons in CsI and CsBr under hydrostatic pressure," *Physical Review B* **73** (feb, 2006) .
- [413] P. J. D. C. D. Clark and P. V. Harris, "Intrinsic edge absorption in diamond," *Proceedings of the Royal Society of London. Series A. Mathematical and Physical Sciences* **277** (feb, 1964) 312–329.
- [414] M. Levinshtein, S. Rumyantsev, and M. Shur, *Handbook Series on Semiconductor Parameters*. WORLD SCIENTIFIC, jan, 1996.
- [415] W. Paszkowicz, S. Podsiadło, and R. Minikayev, "Rietveld-refinement study of aluminium and gallium nitrides," *Journal of Alloys and Compounds* **382** (nov, 2004) 100–106.
- [416] H. Teisseyre, P. Perlin, T. Suski, I. Grzegory, S. Porowski, J. Jun, A. Pietraszko, and T. D. Moustakas, "Temperature dependence of the energy gap in GaN bulk single crystals and epitaxial layer," *Journal of Applied Physics* **76** (aug, 1994) 2429–2434.

- [417] S. Adachi, "Optical dispersion relations for GaP, GaAs, GaSb, InP, InAs, InSb, $\text{Al}_x\text{Ga}_{1-x}\text{As}$, and $\text{In}_{1-x}\text{Ga}_x\text{As}_y\text{P}_{1-y}$," *Journal of Applied Physics* **66** (dec, 1989) 6030–6040.
- [418] S. Sze and J. Irvin, "Resistivity, mobility and impurity levels in GaAs, Ge, and Si at 300°K," *Solid-State Electronics* **11** (jun, 1968) 599–602.
- [419] C. L. Littler and D. G. Seiler, "Temperature dependence of the energy gap of InSb using nonlinear optical techniques," *Applied Physics Letters* **46** (may, 1985) 986–988.
- [420] H.-J. Ullrich, A. Uhlig, G. Geise, H. Horn, and H. Waltinger, "Precise determination of the lattice constant of LiF by means of x-ray divergent beam (pseudo kossel-) technique via computer graphics and multiple intersections," *Mikrochimica Acta* **107** (may, 1992) 283–293.
- [421] G. Singh and T. Gallon, "The electron energy loss spectrum of LiF in the band gap region," *Solid State Communications* **51** (aug, 1984) 281–284.
- [422] J. Thomas, G. Stephan, J. C. Lemonnier, M. Nisar, and S. Robin, "Optical anisotropy of MgF₂ in its UV absorption region," *Physica Status Solidi (b)* **56** (mar, 1973) 163–170.
- [423] "Magnesium oxide (MgO) crystal structure, lattice parameters, thermal expansion," in *II-VI and I-VII Compounds; Semimagnetic Compounds*, pp. 1–6. Springer-Verlag.
- [424] R. Whited, C. J. Flaten, and W. Walker, "Exciton thermoreflectance of MgO and CaO," *Solid State Communications* **13** (dec, 1973) 1903–1905.
- [425] F. C. Brown, C. Gähwiller, H. Fujita, A. B. Kunz, W. Scheifley, and N. Carrera, "Extreme-ultraviolet spectra of ionic crystals," *Physical Review B* **2** (sep, 1970) 2126–2138.
- [426] V. T. Deshpande, "Thermal expansion of sodium fluoride and sodium bromide," *Acta Crystallographica* **14** (jul, 1961) 794–794.
- [427] G. Roy, G. Singh, and T. Gallon, "The electron energy loss spectra of some alkali halides in the band gap region," *Surface Science* **152-153** (apr, 1985) 1042–1050.
- [428] P. A. Rodnyi, *Physical Processes in Inorganic Scintillators (Laser & Optical Science & Technology)*. CRC Press, 1997. <https://www.amazon.com/Physical-Processes-Inorganic-Scintillators-Technology/dp/0849337887?SubscriptionId=AKIAIOBINVZYXZQZ2U3A&tag=chimb0ri05-20&linkCode=xm2&camp=2025&creative=165953&creativeASIN=0849337887>.
- [429] W. H. Strehlow and E. L. Cook, "Compilation of energy band gaps in elemental and binary compound semiconductors and insulators," *Journal of Physical and Chemical Reference Data* **2** (jan, 1973) 163–200.

- [430] R. Ahrenkiel, S. Johnston, W. Metzger, and P. Dippo, “Relationship of band-edge luminescence to recombination lifetime in silicon wafers,” *Journal of Electronic Materials* **37** (nov, 2007) 396–402.
- [431] Y. L. Page and G. Donnay, “Refinement of the crystal structure of low-quartz,” *Acta Crystallographica Section B Structural Crystallography and Crystal Chemistry* **32** (aug, 1976) 2456–2459.
- [432] S. A. Sato, K. Yabana, Y. Shinohara, T. Otobe, K.-M. Lee, and G. F. Bertsch, “Time-dependent density functional theory of high-intensity short-pulse laser irradiation on insulators,” *Physical Review B* **92** (nov, 2015) .
- [433] V. Srikant and D. R. Clarke, “On the optical band gap of zinc oxide,” *Journal of Applied Physics* **83** (may, 1998) 5447–5451.
- [434] E. A. Jumpertz, “Electron-density distribution in zinc blende,” *Zeitschrift für Elektrochemie und angewandte physikalische Chemie* **59** (1955) 419–425.
- [435] B. Khamala, L. Franklin, Y. Malozovsky, A. Stewart, H. Saleem, and D. Bagayoko, “Calculated electronic, transport, and bulk properties of zinc-blende zinc sulphide (zb-ZnS),” *Computational Condensed Matter* **6** (mar, 2016) 18–23.
- [436] K. Bystrom, D. Broberg, S. Dwaraknath, K. A. Persson, and M. Asta, “Pawpyseed: Perturbation-extrapolation band shifting corrections for point defect calculations,” [arXiv:http://arxiv.org/abs/1904.11572v1](http://arxiv.org/abs/1904.11572v1) [cond-mat.mtrl-sci].
- [437] A. V. Krukau, O. A. Vydrov, A. F. Izmaylov, and G. E. Scuseria, “Influence of the exchange screening parameter on the performance of screened hybrid functionals,” *The Journal of Chemical Physics* **125** (dec, 2006) 224106.
- [438] A. E. Clark and R. E. Strakna, “Elastic constants of single-crystal yig,” *Journal of Applied Physics* **32** (jun, 1961) 1172–1173. <https://doi.org/10.1063/1.1736184>.
- [439] M. Dressel and G. Grüner, *Electrodynamics of Solids: Optical Properties of Electrons in Matter*. Cambridge University Press, 2 ed., 2002.
- [440] H. Fjellvåg and A. Kjekshus, “Structural properties of ZrTe₅ and HfTe₅ as seen by powder diffraction,” *Solid State Communications* **60** (Oct., 1986) 91–93. <https://www.sciencedirect.com/science/article/pii/0038109886905363>.
- [441] J. P. Perdew and A. Zunger, “Self-interaction correction to density-functional approximations for many-electron systems,” *Phys. Rev. B* **23** (May, 1981) 5048–5079. <https://link.aps.org/doi/10.1103/PhysRevB.23.5048>.
- [442] N. Troullier and J. L. Martins, “Efficient pseudopotentials for plane-wave calculations,” *Phys. Rev. B* **43** (Jan, 1991) 1993–2006. <https://link.aps.org/doi/10.1103/PhysRevB.43.1993>.

- [443] M. J. van Setten, M. Giantomassi, E. Bousquet, M. J. Verstraete, D. R. Hamann, X. Gonze, and G.-M. Rignanese, “The pseudodojo: Training and grading a 85 element optimized norm-conserving pseudopotential table,” *Computer Physics Communications* **226** (2018) 39–54.
- [444] Z. Fan, Q.-F. Liang, Y. Chen, S.-H. Yao, and J. Zhou, “Transition between strong and weak topological insulator in zrte5 and hfte5,” *Scientific reports* **7** (2017) no. 1, 1–7.
- [445] D. Sangalli, J. A. Berger, C. Attaccalite, M. Grüning, and P. Romaniello, “Optical properties of periodic systems within the current-current response framework: Pitfalls and remedies,” *Phys. Rev. B* **95** (Apr, 2017) 155203. <https://link.aps.org/doi/10.1103/PhysRevB.95.155203>.
- [446] Y. E. Lozovik, S. P. Merkulova, A. A. Sokolik, S. V. Morozov, K. S. Novoselov, and A. K. Geim, “Collective electron phenomena and electron transport in graphene scientific session of the physical sciences division of the russian academy of sciences (27 february 2008),” *Physics-Uspekhi* **51** (aug, 2008) 727–748.